

Thermodynamically stable and metastable solids: New approaches  
to the synthesis of anhydrous phosphates containing  
vanadium, molybdenum, and/or tungsten

Dissertation  
zur  
Erlangung des Doktorgrades (Dr. rer. nat.)  
der  
Mathematisch-Naturwissenschaftlichen Fakultät  
der  
Rheinischen Friedrich-Wilhelms-Universität Bonn

vorgelegt von  
**M.Sc. Subrata Chandra Roy**  
aus Narsingdi, Bangladesh

Bonn, September 2015



Angefertigt mit Genehmigung der Mathematisch-naturwissenschaftlichen Fakultät  
der Rheinischen Friedrich-Wilhelms-Universität Bonn

1. Gutachter: Prof. Dr. Robert Glaum
  2. Gutachter: Prof. Dr. Werner Mader
  3. Gutachter: Prof. Dr. Thomas Bredow
  4. Gutachter: Prof. Dr. Hartmut Schmieden
- Tag der Promotion: November 10, 2015
- Erscheinungsjahr: 2015





*Dedicated to my Parents*



*Knowledge, the object of knowledge, and the knower are the three factors which motivate action. The senses, the work, and the doer comprises the threefold base of action.*

~Srimad Bhagavad Gita, Chapter 18, Verse 18



# Contents

<b>Contents</b>	<b>V</b>
<b>List of Figures</b>	<b>IX</b>
<b>List of Tables</b>	<b>XXIII</b>
<b>1 Introduction</b>	<b>1</b>
<b>2 Experimental techniques</b>	<b>6</b>
2.1 Introduction	6
2.2 Preparation of silica tubes	6
2.3 Vacuum line	7
2.4 High temperature furnaces	8
2.5 Solid states reactions	9
2.6 Chemical vapor transport	10
2.7 Solution combustion synthesis	11
2.7.1 Selection of fuel	12
2.7.2 Metal to fuel ratio in SCS	12
2.7.3 Oxidizer to fuel ratio	13
2.7.4 Procedure for SCS	13
<b>3 Characterization techniques</b>	<b>15</b>
3.1 X-ray diffraction techniques	15
3.1.1 The Guinier technique	16
3.1.2 Single crystal investigations	18
3.2 Spectroscopic investigations	26
3.2.1 UV/Vis/NIR spectroscopy	26
3.2.2 Electron paramagnetic resonance (EPR) spectroscopy	29
3.2.3 Solid state <sup>31</sup> P-MAS-NMR spectroscopy	31
3.2.4 X-ray photoelectron spectroscopy (XPS)	32
3.2.5 Energy Dispersive X-ray (EDX) analysis	34
3.3 Magnetic behavior	34
<b>4 Chemicals used throughout this thesis</b>	<b>37</b>
4.1 Chemicals purchased	37
4.2 Chemicals synthesized	38
4.2.1 Platinum(II) chloride, PtCl <sub>2</sub>	38
4.2.2 Tungsten(VI) oxide-phosphate, W <sub>2</sub> O <sub>3</sub> (PO <sub>4</sub> ) <sub>2</sub>	39
4.2.3 Tungsten(VI) oxide-pyrophosphate, WOP <sub>2</sub> O <sub>7</sub>	41
4.2.4 Molybdenum(VI) oxide-pyrophosphate, (MoO <sub>2</sub> ) <sub>2</sub> (P <sub>2</sub> O <sub>7</sub> )	42

## VI Contents

4.2.5	$\beta$ -Vanadium(V) oxide-phosphate, $\beta$ -VOPO <sub>4</sub>	43
4.2.6	Vanadyl(IV) pyrophosphate, (VO) <sub>2</sub> P <sub>2</sub> O <sub>7</sub>	45
4.2.7	Vanadium(III) phosphate, VPO <sub>4</sub>	47
4.2.8	Vanadium phosphide, VP	48
4.2.9	Iron(III) phosphate, FePO <sub>4</sub>	49
4.2.10	Indium(III) phosphate, InPO <sub>4</sub>	50
<b>5</b>	<b>Crystal structures of <math>m</math>-W<sub>2</sub>O<sub>3</sub>(PO<sub>4</sub>)<sub>2</sub> and WOPO<sub>4</sub> revisited</b>	<b>51</b>
5.1	Introduction	51
5.2	Equilibrium phase relations in the system W/P/O	52
5.3	Synthesis and crystallization of $m$ -W <sub>2</sub> O <sub>3</sub> (PO <sub>4</sub> ) <sub>2</sub>	54
5.4	Crystal structure and <sup>31</sup> P-MAS-NMR spectrum of $m$ -W <sub>2</sub> O <sub>3</sub> (PO <sub>4</sub> ) <sub>2</sub>	56
5.5	XPS study of $m$ -W <sub>2</sub> O <sub>3</sub> (PO <sub>4</sub> ) <sub>2</sub>	57
5.6	UV/Vis/NIR spectroscopic studies of $m$ -W <sub>2</sub> O <sub>3</sub> (PO <sub>4</sub> ) <sub>2</sub>	58
5.7	Synthesis and crystallization of W <sup>V</sup> OPO <sub>4</sub>	59
5.8	Single crystal structure refinement of WOPO <sub>4</sub>	60
5.9	Crystal structure of WOPO <sub>4</sub>	62
5.10	Magnetic behaviour of W <sup>V</sup> OPO <sub>4</sub>	64
5.11	Conclusion	65
<b>6</b>	<b>Solid solutions (V<sub>1-x</sub>W<sub>x</sub>)OPO<sub>4</sub> (0 ≤ x ≤ 1)</b>	<b>66</b>
6.1	Introduction	66
6.2	Equilibrium phase relations in systems WO <sub>x</sub> /VO <sub>y</sub> /PO <sub>2.5</sub> (2.0 ≤ x ≤ 3.0; 1.5 ≤ y ≤ 2.5)	67
6.3	Synthesis and crystallization	68
6.4	Crystal structure of the α <sub>II</sub> -type solid solution	77
6.5	Electronic structure	83
6.5.1	EPR spectroscopic studies of α <sub>II</sub> - and β-(V <sub>1-x</sub> W <sub>x</sub> )OPO <sub>4</sub>	83
6.5.2	X-ray photoelectron spectroscopic study of α <sub>II</sub> -(V <sub>0.80</sub> W <sub>0.20</sub> )OPO <sub>4</sub>	85
6.5.3	UV/Vis/NIR spectroscopy	87
6.5.4	Magnetic behavior of α <sub>II</sub> -(V <sub>1-x</sub> W <sub>x</sub> )OPO <sub>4</sub>	90
6.5.5	Electronic conductivity of α <sub>II</sub> -(V <sub>0.74</sub> W <sub>0.26</sub> )OPO <sub>4</sub>	91
6.5.6	<sup>31</sup> P-MAS-NMR spectra of α <sub>II</sub> -(V <sub>1-x</sub> W <sub>x</sub> )OPO <sub>4</sub>	93
6.6	The solid solution (V <sub>1-x</sub> W <sub>x</sub> )OPO <sub>4</sub> (WOPO <sub>4</sub> type) at high tungsten concentration (0.67 ≤ x ≤ 1)	94
6.7	Conclusion	99
<b>7</b>	<b>Solid solutions (V<sub>1-x</sub>Mo<sub>x</sub>)OPO<sub>4</sub></b>	<b>100</b>
7.1	Introduction	100
7.2	Equilibrium phases in systems MoO <sub>x</sub> /VO <sub>y</sub> /PO <sub>2.5</sub> (2.0 ≤ x ≤ 3.0; 1.5 ≤ y ≤ 2.5)	100

7.3	Synthesis and crystallization	102
7.4	X-ray single crystal structure refinement of $\beta$ -(V <sub>0.90</sub> Mo <sub>0.10</sub> )OPO <sub>4</sub>	109
7.5	Results and discussion	111
7.6	Charge distribution in (V <sub>1-x</sub> Mo <sub>x</sub> )OPO <sub>4</sub>	116
7.7	Conclusion	123
<b>8</b>	<b>Metal(III) tungsten(VI) ortho-pyrophosphates</b>	<b>125</b>
8.1	Introduction	125
8.2	Synthesis and crystallization	125
8.3	Single crystal structure analysis	134
8.4	Conclusion	153
<b>9</b>	<b>Metastable tungsten phosphates with structures related to ReO<sub>3</sub> and WOPO<sub>4</sub></b>	<b>155</b>
9.1	Introduction	155
9.2	Synthesis	158
9.3	X-ray powder pattern	164
9.4	Transmission Electron Microscopy (TEM)	166
9.5	<sup>31</sup> P-MAS-NMR spectroscopy	167
9.6	Mixed metal phosphates with WOPO <sub>4</sub> structure type	171
9.7	Single crystal structure refinements of (M <sup>III</sup> <sub>0.333</sub> W <sup>VI</sup> <sub>0.667</sub> )OPO <sub>4</sub> (M: Cr, Mo)	173
9.8	Magnetic behavior of (M <sub>0.333</sub> W <sub>0.667</sub> )OPO <sub>4</sub> ; M: Cr, Fe	178
9.9	Discussion	179
<b>10</b>	<b>Mixed metal monophosphate tungsten bronzes (W<sub>1-x</sub>M<sub>x</sub>)<sub>8</sub>(PO<sub>2</sub>)<sub>4</sub> (M: Cr, V)</b>	<b>181</b>
10.1	Introduction	181
10.2	Synthesis	182
10.3	Results and discussion	186
<b>11</b>	<b>Access to thermodynamically metastable oxo-compounds via reduction by moist hydrogen</b>	<b>189</b>
11.1	Introduction	189
11.2	Reduction of $\beta$ -VOPO <sub>4</sub>	190
11.2.1	Experimental	192
11.2.2	Results and discussion	192
11.2.3	Characterization of V <sup>III</sup> PO <sub>4</sub> -m1	195
11.2.4	Characterization of V <sup>III</sup> PO <sub>4</sub> -m2, V <sub>2</sub> (VO)(P <sub>2</sub> O <sub>7</sub> )(PO <sub>4</sub> )	200
11.3	Synthesis of the metastable vanadium oxides V <sup>IV</sup> O <sub>2</sub> (B) and (V <sup>IV</sup> O) <sub>2</sub> V <sup>V</sup> <sub>2</sub> O <sub>7</sub>	203

## VIII Contents

11.3.1	Experimental	203
11.3.2	Results and discussion	203
11.4	Conclusion	205
<b>12</b>	<b>Catalytic testing</b>	<b>206</b>
12.1	Introduction	206
12.2	Construction and operation of multi-tube fixed bed reactor	207
12.3	Results and discussion	207
<b>13</b>	<b>Summary</b>	<b>210</b>
<b>14</b>	<b>Appendix</b>	<b>216</b>
14.1	The crystal structures of $m\text{-W}_2\text{O}_3(\text{PO}_4)_2$ and $\text{WOPO}_4$ revisited	216
14.2	Solid solutions $(\text{V}_{1-x}\text{W}_x)\text{OPO}_4$ ( $0 < x < 1.0$ )	219
14.3	Solid solutions $(\text{V}_{1-x}\text{Mo}_x)\text{OPO}_4$ ( $0 \leq x \leq 1.0$ )	233
14.4	Metal(III) tungstenyl(VI) ortho-pyrophosphates	243
14.5	Metastable tungsten phosphates with structures related to $\text{ReO}_3$ and $\text{WOPO}_4$	263
14.6	Mixed metal monophosphate tungsten bronzes $(\text{W}_{1-x}\text{M}_x)_8(\text{PO}_2)_4$ ( $M$ : Cr, V)	270
14.7	Access to thermodynamically metastable oxo-compounds via reduction by moist hydrogen	272
<b>15</b>	<b>References</b>	<b>275</b>



## List of Figures

Figure 1.1	Polyhedral representation of the crystal structure of $(VO)_2P_2O_7$ [10], purple $VO_6$ octahedra, yellow $P_2O_7$ groups.....	1
Figure 2.1	Sketch of the vacuum line [41]. .....	7
Figure 2.2	Temperature profile over the length of a transport ampoule in a two zone horizontal furnace. ....	8
Figure 2.3	Sketch of the hydraulic press and the tools for the preparation of pellets [41]. .....	9
Figure 2.4	Layout of a sealed silica ampoule in the temperature gradient of a two-zone tubular furnace. ....	10
Figure 2.5	Flow chart of a SCS experiment. ....	13
Figure 3.1	Optical path of Guinier camera. ....	17
Figure 3.2	Schematic representation of single crystal mounted at the tip of a glass fiber for x-ray data collection in order to structural investigation. ....	19
Figure 3.3	Principle of the area detector in terms of the Ewald construction. ....	20
Figure 3.4	Schematic diagram of the microcrystal UV/Vis/NIR spectrophotometer CARY 17 [67]. ....	28
Figure 3.5	Instrumentation of XPS system [70]. ....	32
Figure 4.1	Synthesis of $PtCl_2$ . Comparison of the Guinier photograph of the obtained product (a) and simulated diffraction pattern (b) [74]. ....	39
Figure 4.2	Synthesis of orthorhombic $W_2O_3(PO_4)_2$ . Comparison of the Guinier photograph of the obtained product (a) and simulated diffraction pattern (b) [75], * indicate $m-WO_3$ .....	40
Figure 4.3	Synthesis of monoclinic $W_2O_3(PO_4)_2$ . Comparison of the Guinier photograph of the obtained product (a) and simulated diffraction pattern (b) [78]. ....	40
Figure 4.4	Photograph of crystals of $m-WOP_2O_7$ obtained by vapor phase moderated solid state reaction using water as mineralizer. ....	41
Figure 4.5	Synthesis of monoclinic $WOP_2O_7$ . Comparison of the Guinier photograph of the obtained product (a) and simulated diffraction pattern (b) [79]. * indicate a small impurity of $m-W_2O_3(PO_4)_2$ [78]. ....	41
Figure 4.6	Synthesis of $\alpha-(MoO_2)_2P_2O_7$ . Comparison of the Guinier photograph of the obtained product (a) and simulated diffraction pattern (b) [80]. ....	42
Figure 4.7	Synthesis of $\beta-VOPO_4$ . Comparison of the Guinier photograph of the obtained product (a) and simulated diffraction pattern (b) [161]. ....	43
Figure 4.8	SCS of $\beta-VOPO_4$ [161]. Phase formation during prolonged heating in air monitored by Guinier photographs. ....	44

Figure 4.9	Photographs of $\beta$ -VOPO <sub>4</sub> crystals (obtained by CVT using H <sub>2</sub> O as TA) showing dichroism (yellow/green), same crystal at two different orientations.....	45
Figure 4.10	Synthesis of (VO) <sub>2</sub> P <sub>2</sub> O <sub>7</sub> . Comparison of the Guinier photograph of the obtained product (a) and simulated diffraction pattern (b) [10]. .....	45
Figure 4.11	Photograph of (VO) <sub>2</sub> P <sub>2</sub> O <sub>7</sub> crystals obtained from a melt by slow cooling. ....	46
Figure 4.12	Synthesis of VPO <sub>4</sub> . Comparison of the Guinier photograph of the obtained product (a) and simulated diffraction pattern (b) [83]. .....	47
Figure 4.13	Synthesis of VP. Comparison of the Guinier photograph of the obtained product (a) and simulated diffraction pattern (b) [84]. .....	48
Figure 4.14	Synthesis of FePO <sub>4</sub> . Comparison of the Guinier photograph of the obtained product (a) and simulated diffraction pattern (b) [85]. .....	49
Figure 4.15	Synthesis of InPO <sub>4</sub> . Comparison of the Guinier photograph of the obtained product (a) and simulated diffraction pattern (b) [87]. .....	50
Figure 5.1	Ternary phase diagram of the system W/P/O at 900 °C according to [92].....	53
Figure 5.2	Photographs of <i>m</i> -W <sub>2</sub> O <sub>3</sub> (PO <sub>4</sub> ) <sub>2</sub> crystals obtained by CVT using Cl <sub>2</sub> (a) and HCl (b) as transporting agent. ....	54
Figure 5.3	Comparison of Guinier photographs of <i>m</i> -W <sub>2</sub> O <sub>3</sub> (PO <sub>4</sub> ) <sub>2</sub> . Stoichiometric pale-yellow crystals (a), under-stoichiometric dichroic blue/colorless crystals (b) and simulated diffraction pattern based on data in [78] (c). ....	55
Figure 5.4	Polyhedral representation (left) of <i>m</i> -W <sub>2</sub> O <sub>3</sub> (PO <sub>4</sub> ) <sub>2</sub> [77], [W <sub>2</sub> O <sub>11</sub> ] double octahedra green (W1) and magenta (W2 and W3) at $y = 0$ and $\frac{1}{4}$ , respectively, [PO <sub>4</sub> ] tetrahedra yellow. Ball and stick model (right), open circle oxygen showing that the tungstenyl bonds are pointing in opposite directions. ....	56
Figure 5.5	Quantitative <sup>31</sup> P-MAS-NMR spectrum of stoichiometric <i>m</i> -W <sub>2</sub> O <sub>3</sub> (PO <sub>4</sub> ) <sub>2</sub> .....	57
Figure 5.6	XP spectrum of stoichiometric <i>m</i> -W <sub>2</sub> O <sub>3</sub> (PO <sub>4</sub> ) <sub>2</sub> with fitted curves for W4f <sub>7/2</sub> , W4f <sub>5/2</sub> and W4p <sub>3/2</sub> .....	58
Figure 5.7	Polarized single crystal UV/Vis/NIR absorption spectra of stoichiometric, pale-yellow <i>m</i> -W <sub>2</sub> O <sub>3</sub> (PO <sub>4</sub> ) <sub>2</sub> (a) and slightly oxygen-deficient dichroic blue/colorless <i>m</i> -W <sub>2</sub> O <sub>3-<math>\delta</math></sub> (PO <sub>4</sub> ) <sub>2</sub> (b), hpol and vpol are presumably parallel and perpendicular to the <i>b</i> -axis, respectively. ....	59
Figure 5.8	Photograph of WOPO <sub>4</sub> crystals obtained by CVT using iodine as TA. ....	60
Figure 5.9	Guinier-photograph of WOPO <sub>4</sub> (middle) and simulated diffraction pattern based on single-crystal structure refinement (bottom, [this thesis]). Magnified peak profiles showing the splitting due to a slight monoclinic distortion of the unit cell (top). ....	61
Figure 5.10	Crystal structure of WOPO <sub>4</sub> , green and yellow represent [WO <sub>6</sub> ] octahedra and [PO <sub>4</sub> ] tetrahedra, respectively. ....	63

Figure 5.11	ORTEP representation of [WO <sub>6</sub> ] and [PO <sub>4</sub> ] polyhedra in WOPO <sub>4</sub> . Ellipsoids are at 50% probability level, software DIAMOND [128].	64
Figure 5.12	Temperature dependent molar susceptibility, $\chi_{\text{mol}}$ and its reciprocal, $\chi_{\text{mol}}^{-1}$ of WOPO <sub>4</sub> .	64
Figure 6.1	The system W/V/P/O with three quasi-ternary oxide systems (a) and the oxygen co-existence pressure diagrams at 1000 K for tungsten, vanadium, and phosphorus oxides (b) [136].	66
Figure 6.2	Visualization of the existing compounds in systems WO <sub>x</sub> /VO <sub>y</sub> /PO <sub>2.5</sub> , ( $2.0 \leq x \leq 3.0$ ; $1.5 \leq y \leq 2.5$ ) within a phase triangle. The reduced phases containing W <sup>5+</sup> , M <sup>4+</sup> (M: W, V), and V <sup>3+</sup> are indicated by red, green and violet color, respectively.	67
Figure 6.3	Comparison of Guinier-photographs of members of the solid solutions (V <sub>1-x</sub> W <sub>x</sub> )OPO <sub>4</sub> obtained by SCS followed by heating in air where $0.0 \leq x \leq 0.01$ is only $\beta$ -VOPO <sub>4</sub> type, $0.02 \leq x \leq 0.03$ shows a mixture of $\beta$ - and $\alpha_{\text{II}}$ -VOPO <sub>4</sub> type, and $x \geq 0.04$ is only $\alpha_{\text{II}}$ -VOPO <sub>4</sub> structure type solid solution, arrows indicate the $\beta$ -VOPO <sub>4</sub> type.	71
Figure 6.4	Guinier-photographs of (V <sub>0.95</sub> W <sub>0.05</sub> )OPO <sub>4</sub> ( $\alpha_{\text{II}}$ -VOPO <sub>4</sub> type [160]) (a), (V <sub>0.95</sub> W <sub>0.05</sub> )OPO <sub>4</sub> ·2H <sub>2</sub> O (b) obtained due to hydration of (a) by exposing it to lab atmosphere, compared with a simulated XRPD pattern of (V <sub>0.95</sub> W <sub>0.05</sub> )OPO <sub>4</sub> ·2H <sub>2</sub> O (structure model VOPO <sub>4</sub> ·2H <sub>2</sub> O [173]) (c). Asterisks and dots indicate small impurities of $\alpha$ -V <sup>IV</sup> O(PO <sub>3</sub> ) <sub>2</sub> [156] and Pt, respectively.	74
Figure 6.5	Guinier-photographs of reaction products from experiments aiming at synthesis of the solid solution (V <sub>1-x</sub> W <sub>x</sub> )OPO <sub>4</sub> ( $0.10 \leq x \leq 0.35$ ) via SCS after subsequent heating at 600 °C in air. Asterisks indicate phases with $\alpha_{\text{I}}$ -VOPO <sub>4</sub> structure type [159], dots indicate VOPO <sub>4</sub> ·2H <sub>2</sub> O structure type [173], and down arrows indicate a ReO <sub>3</sub> type [174] phosphate.	75
Figure 6.6	Influence of post-annealing treatment on phases occurring in the Guinier photographs of (V <sub>0.80</sub> W <sub>0.20</sub> )OPO <sub>4</sub> . XRPD after sample quenching and using x-ray transparent adhesive tape (a), slow cooling (b), and slow cooling followed by grinding with water (c). Asterisks indicate $\alpha_{\text{I}}$ -VOPO <sub>4</sub> type [159], dots indicate VOPO <sub>4</sub> ·2H <sub>2</sub> O type [173], down arrows indicate ReO <sub>3</sub> type [174] phases.	76
Figure 6.7	Microphotographs of crystals $\beta$ -(VO <sub>1-<math>\beta</math></sub> )PO <sub>4</sub> (a), $\beta$ -(V <sub>0.01</sub> W <sub>0.99</sub> )OPO <sub>4</sub> (b), $\alpha_{\text{II}}$ -(V <sub>0.10</sub> W <sub>0.90</sub> )OPO <sub>4</sub> (c), and $\alpha_{\text{II}}$ -(V <sub>0.74</sub> W <sub>0.26</sub> )OPO <sub>4</sub> (d) obtained by CVT.	77
Figure 6.8	Lattice parameters $a$ and $c$ of members of the solid solution (V <sub>1-x</sub> W <sub>x</sub> )OPO <sub>4</sub> ( $0.0 \leq x \leq 0.26$ ; $\alpha_{\text{II}}$ -VOPO <sub>4</sub> structure type). Data from Guinier photographs of powder samples in black, single crystal data are light grey, and open circles for pure $\alpha_{\text{II}}$ -VOPO <sub>4</sub> from literature [160].	78

## XII List of Figures

Figure 6.9	Guinier-photographs of $\alpha_{II}-(V_{0.74}W_{0.26})OPO_4$ (a) and $\alpha_{II}-(V_{0.90}W_{0.10})OPO_4$ (b) compared to diffraction patterns simulated on the basis of the corresponding single crystal structure refinements [this thesis]; * indicate Pt from transport additive $PtCl_2$ .....	79
Figure 6.10	Crystal structure of $\alpha_{II}-VOPO_4$ (according to [160]). Projections on the <i>ab</i> - and <i>ac</i> -plane, respectively. $[VO_6]$ octahedra: orange, $[PO_4]$ tetrahedra: yellow. Red spheres represent oxygen atoms of vanadyl(V) groups $(V=O)^{3+}$ .....	81
Figure 6.11	Crystal structure of $\beta-VOPO_4$ (according to [161]). Projection along the crystallographic <i>b</i> -axis, $[VO_6]$ octahedra: orange, $[PO_4]$ tetrahedra: yellow, red spheres represent oxygen atoms of vanadyl(V) groups $(V=O)^{3+}$ .....	81
Figure 6.12	Comparison of the co-ordination polyhedra $[(V_{1-x}W_x)O_6]$ with $x = 0$ (a) in $\alpha_{II}-VOPO_4$ [160], $x = 0.10$ (b) in $(V_{0.90}W_{0.10})OPO_4$ , and $x = 0.26$ (c) in $(V_{0.74}W_{0.26})OPO_4$ . ORTEP style graphics (Ellipsoids are at 50% probability level, software: DIAMOND [128])......	82
Figure 6.13	Room temperature continuous wave (CW) powder EPR spectra of $(V_{1-x}^{IV}V_{2x}^{V}W_x^{VI})OPO_4$ with $x = 0.01, 0.10$ , and $0.26$ at X-band (a), for $x = 0.01$ (b) at three different bands (S, X, Q) with their simulations shown in red. The orientation of <i>A</i> and <i>g</i> is shown in the inset of (b). .....	84
Figure 6.14	Continuous wave X-band EPR spectrum of a powder of slightly under-stoichiometric $\beta-VO_{1-\delta}PO_4$ (powder from crystals obtained by CVT). .....	85
Figure 6.15	XP spectra of $\alpha_{II}-(V_{0.2}^{IV}V_{0.6}^{V}W_{0.2}^{VI})OPO_4$ with fitted curves for V2p (a), W4f (b), and O1s (c). .....	87
Figure 6.16	UV/Vis/NIR powder reflectance spectra of $(V_{1-x}W_x)OPO_4$ ( $\beta-VOPO_4$ structure type) with $x = 0.00$ (stoichiometric bright yellow) and $x = 0.01$ (olive). .....	88
Figure 6.17	UV/Vis/NIR powder reflectance spectra of $(V_{1-x}W_x)OPO_4$ ( $\alpha_{II}-VOPO_4$ structure type) with $x = 0.05, 0.10$ , and $0.20$ .....	89
Figure 6.18	Polarized single crystal UV/Vis/NIR absorption spectra of slightly oxygen-deficient $\beta-VO_{1-\delta}PO_4$ (a, b) and $\alpha_{II}-(V_{0.90}W_{0.10})OPO_4$ (c). Due to very thin plate like crystals, measurements of the spectra with light polarized along the <i>c</i> -axis of $\alpha_{II}-(V_{0.90}W_{0.10})OPO_4$ was not possible.....	90
Figure 6.19	Reciprocal molar susceptibility $\chi_{mol}^{-1}$ vs. temperature of $(V_{0.10}^{IV}V_{0.80}^{V}W_{0.10}^{VI})OPO_4$ (open circles, $\mu_{exp} = 1.74 \mu_B/V^{4+}$ ) and $(V_{0.26}^{IV}V_{0.48}^{V}W_{0.26}^{VI})OPO_4$ (black circles, $\mu_{exp} = 1.62 \mu_B/V^{4+}$ ). .....	91
Figure 6.20	Temperature dependent resistance of $\alpha_{II}-(V_{0.26}^{IV}V_{0.48}^{V}W_{0.26}^{VI})OPO_4$ (crushed crystals obtained from CVT). .....	92
Figure 6.21	The <i>I-V</i> relationship of $(V_{0.26}^{IV}V_{0.48}^{V}W_{0.26}^{VI})OPO_4$ ( $\alpha_{II}-VOPO_4$ type).....	93
Figure 6.22	Room temperature $^{31}P$ -MAS-NMR spectra of $(V_{1-x}W_x)OPO_4$ ; $x = 0.20$ (a) and $x = 0.05$ (b) (both $\alpha_{II}-VOPO_4$ structure type) measured at spin rates 15 KHz. ....	94

Figure 6.23	Guinier-photographs of members of the solid solution $(V_{1-x}W_x)OPO_4$ ; (WOPO <sub>4</sub> type) with $x = 0.67$ (a), 0.75 (b), 0.90 (c), and 1.0 (d) compared to the simulations based on the single-crystal data of WOPO <sub>4</sub> [this thesis]. Asterisks, down arrows, black dots, cross, and up arrows indicate P <sub>4</sub> W <sub>8</sub> O <sub>32</sub> [95], V(WO <sub>2</sub> ) <sub>2</sub> (P <sub>2</sub> O <sub>7</sub> )(PO <sub>4</sub> ) [this thesis], WP <sub>2</sub> O <sub>7</sub> [94], Pt and unknown phase, respectively. The samples were obtained via SCS followed by heating in argon atmosphere (a), by vapor phase moderated solid state reactions (b) and (c), and by CVT (d). .....	95
Figure 6.24	Guinier photograph of $(V_{0.20}W_{0.80})OPO_4$ (member of WOPO <sub>4</sub> type solid solution) obtained by a three step procedure (a), compared to simulation (b) based on the single-crystal data of WOPO <sub>4</sub> [this thesis], mixed occupancy of the W sites by V and W, asterisks indicate a small impurity of (WO <sub>3</sub> ) <sub>8</sub> (PO <sub>2</sub> ) <sub>4</sub> [95].....	96
Figure 6.25	Variation of lattice parameters of members of WOPO <sub>4</sub> structure type solid solution $(V^{III}_{1-x}W^V_{3x-2}W^{VI}_{2(1-x)})OPO_4$ with $0.67 \leq x \leq 1.0$ .....	98
Figure 7.1	The quaternary system Mo/V/P/O with quasi-ternary oxide systems (a) and the oxygen co-existence pressure diagram of Mo, V, and P oxides (b) [136].....	100
Figure 7.2	Visualization of compounds in systems MoO <sub>x</sub> /VO <sub>y</sub> /PO <sub>2.5</sub> , ( $2.0 \leq x \leq 3.0$ ; $1.5 \leq y \leq 2.5$ ), the reduced phases with Mo(V), M(IV) and M(III); (M: Mo, V) are indicated by red, green and violet color, respectively. ....	101
Figure 7.3	Comparison of Guinier photographs of members of the solid solution $(V_{1-x}Mo_x)OPO_4$ ; $0.0 \leq x \leq 0.30$ ( $\beta$ -VOPO <sub>4</sub> structure type [161]) obtained via SCS followed by heating in air ( $\vartheta = 725$ °C for $x = 0.0$ , decreasing to $\vartheta = 600$ °C for $x = 0.30$ ). .....	106
Figure 7.4	Comparison of Guinier photographs of members of the metastable solid solution $(V_{1-x}Mo_x)OPO_4$ ; $0.0 \leq x \leq 0.20$ ( $\gamma$ -VOPO <sub>4</sub> structure type) with the simulation based on data of $\gamma$ -VOPO <sub>4</sub> [162]). .....	107
Figure 7.5	Conversion of the member of solid solution $(V_{0.8}Mo_{0.2})OPO_4$ ( $\omega$ -VOPO <sub>4</sub> (ht) type [166]) (a), into $(V_{0.8}Mo_{0.2})OPO_4 \cdot 2H_2O$ (b) by absorbing H <sub>2</sub> O from lab. atmosphere, and a simulated XRPD pattern of $(V_{0.8}Mo_{0.2})OPO_4 \cdot 2H_2O$ (c), structure model VOPO <sub>4</sub> ·2H <sub>2</sub> O [173] with adjusted lattice parameters, $a = 6.131$ Å and $c = 7.216$ Å.....	107
Figure 7.6	Conversion of the member of solid solution $(V_{0.9}Mo_{0.1})OPO_4$ ( $\gamma$ -VOPO <sub>4</sub> type [162]) (a), into $(V_{0.9}Mo_{0.1})OPO_4 \cdot 2H_2O$ (b) by absorbing H <sub>2</sub> O from lab. atmosphere, and a simulated XRPD pattern of $(V_{0.9}Mo_{0.1})OPO_4 \cdot 2H_2O$ (c) (structure model VOPO <sub>4</sub> ·2H <sub>2</sub> O [173]), with adjusted lattice parameters, $a = 6.201$ and $c = 7.189$ Å. ....	108
Figure 7.7	Guinier photograph of the solidified melt of “ $(V_{0.60}Mo_{0.40})OPO_4$ ” showing rather bad signal to noise ratio and a hump around $4\theta \approx 42^\circ$ indicating the presence of amorphous material. ....	109

Figure 7.8	Guinier-photograph ( $V_{0.9}Mo_{0.1}OPO_4$ ( $\beta$ -VOPO <sub>4</sub> structure type) compared to the simulation based on the data from the single crystal structure refinement [this thesis] with mixed V/Mo occupancy on metal site. ....	111
Figure 7.9	Guinier-photographs of two members of the solid solution ( $V_{1-x}Mo_xOPO_4$ ( $\beta$ -VOPO <sub>4</sub> structure type) at $x = 0.30$ (a) and $x = 0.20$ (b), compared to simulations based on the single crystal structure refinement of ( $V_{0.90}Mo_{0.10}OPO_4$ [this thesis, $\beta$ - type] with adjusted lattice parameters.....	112
Figure 7.10	Variation of lattice parameters and cell volume ( $\text{\AA}^3$ ) of members of the solid solution ( $V_{1-x}Mo_xOPO_4$ ; $0.0 \leq x \leq 0.30$ ( $\beta$ -VOPO <sub>4</sub> structure type). ....	113
Figure 7.11	Comparison of the co-ordination polyhedra [MO <sub>6</sub> ] in $\beta$ -VOPO <sub>4</sub> [161] (a), ( $V_{0.90}Mo_{0.10}OPO_4$ [this thesis] (b), and $\beta$ -MoOPO <sub>4</sub> (c) [88]. ORTEP style graphics (ellipsoids are at 50% probability level, software: DIAMOND [128])....	114
Figure 7.12	Crystal structure of $\gamma$ -VOPO <sub>4</sub> [162]. [VO <sub>6</sub> ] octahedra: orange, [VO <sub>5</sub> ] square pyramids: green, [PO <sub>4</sub> ] tetrahedra: yellow, open circles represent oxygen atoms of vanadyl(V) groups (V=O) <sup>3+</sup> . ....	114
Figure 7.13	Guinier photograph of ( $V_{0.8}Mo_{0.2}OPO_4$ , $\gamma$ -VOPO <sub>4</sub> structure type (a) obtained by SCS compared to simulated patterns based on the structure model of $\gamma$ -VOPO <sub>4</sub> [162] with different metal distributions. Mo in octahedral metal site (b) which shows best fit with the experimental XRPD, in contrast to Mo in statistical distribution of metal sites (c) and in square pyramidal metal site (d). ....	115
Figure 7.14	Continuous wave X-band powder EPR spectra of ( $V^{IV}_xV^{V}_{1-2x}Mo^{VI}_xOPO_4$ ; $x = 0.005, 0.01, 0.02$ and $0.30$ (all $\beta$ -VOPO <sub>4</sub> structure type [161]) measured at RT.....	117
Figure 7.15	Comparison of X-band powder CW-EPR spectra (measured at RT) of ( $V^{IV}_{0.005}V^{V}_{0.990}Mo^{VI}_{0.005}OPO_4$ (green) and ( $V^{IV}_{0.01}V^{V}_{0.98}W^{VI}_{0.01}OPO_4$ (red, both are $\beta$ -VOPO <sub>4</sub> structure type). ....	117
Figure 7.16	Continuous wave (CW) X-band powder EPR spectra (measured at RT) of ( $V^{IV}_xV^{V}_{1-2x}Mo^{VI}_xOPO_4$ ; $x = 0.02$ and $0.10$ ( $\gamma$ -VOPO <sub>4</sub> structure type).....	118
Figure 7.17	UV/Vis/NIR powder reflectance spectra of ( $V_{1-x}Mo_xOPO_4$ ; $x = 0.00, 0.005, 0.01, 0.05,$ and $0.20$ ( $\beta$ -VOPO <sub>4</sub> structure type).....	119
Figure 7.18	Photographs of microcrystalline powders of members of the solid solution ( $V_{1-x}Mo_xOPO_4$ ; $0 \leq x \leq 0.30$ ( $\beta$ -VOPO <sub>4</sub> type [161]) obtained via SCS followed by heating in air. ....	119
Figure 7.19	UV/Vis/NIR powder reflectance spectra of ( $V_{1-x}Mo_xOPO_4$ ; $x = 0.02,$ and $0.10$ ( $\gamma$ -VOPO <sub>4</sub> structure type).....	120
Figure 7.20	( $V^{IV}_{0.20}V^{V}_{0.60}Mo^{VI}_{0.20}OPO_4$ . Reciprocal molar susceptibility vs. temperature.....	121
Figure 7.21	Temperature dependent resistance of ( $V^{IV}_{0.20}V^{V}_{0.60}Mo^{VI}_{0.20}OPO_4$ powder ( $\beta$ -VOPO <sub>4</sub> structure type [161]). ....	121

Figure 7.22	Room temperature $^{31}\text{P}$ -MAS-NMR spectra of paramagnetic solid solution $(\text{V}_{1-x}\text{Mo}_x)\text{OPO}_4$ ; $x = 0.05, 0.20$ , $\beta$ - $\text{VOPO}_4$ structure type (a), $x = 0.10, 0.20$ , $\gamma$ - $\text{VOPO}_4$ structure type (b), $x = 0.02$ , $\text{VOPO}_4 \cdot 2\text{H}_2\text{O}$ structure type (c). In fig (b) the impurity signal at 6.8 ppm is due to partial conversion into $\text{VOPO}_4 \cdot 2\text{H}_2\text{O}$ type [173] phase. All spectra were measured at rotation frequency of 15 KHz. .... 123	123
Figure 7.23	Structure types, their homogeneity ranges, and formation temperatures in the quasi-binary system $\text{MoOPO}_4$ - $\text{VOPO}_4$ . .... 124	124
Figure 8.1	Comparison of Guinier photographs of products from experiments aiming at the synthesis of $\text{Cr}^{\text{III}}(\text{W}^{\text{VI}}\text{O}_2)_{1.8}(\text{Cr}^{\text{III}}\text{O}_2)_{0.2}(\text{P}_2\text{O}_7)(\text{PO}_4)$ (a) and $\text{Cr}(\text{WO}_2)_2(\text{P}_2\text{O}_7)(\text{PO}_4)$ (b) to simulated XRPD based on structure data of $\text{Rh}(\text{WO}_2)_2(\text{P}_2\text{O}_7)(\text{PO}_4)$ [this thesis] with adjusted lattice parameters (c). Asterisks indicate mixed-metal MPTB phase ( $m = 4$ ) $(\text{Cr}_{0.17}\text{W}_{0.83}\text{O}_3)_8(\text{PO}_2)_4$ [see Chapter 10]. .... 128	128
Figure 8.2	Comparison of Guinier photographs of products from experiments aiming at the synthesis of the lpb composition $(\text{V}^{\text{III}}_{0.6}\text{V}^{\text{IV}}_{0.4})(\text{W}^{\text{VI}}\text{O}_2)_{1.8}(\text{V}^{\text{III}}\text{O}_2)_{0.2}(\text{P}_2\text{O}_7)(\text{PO}_4)$ with $x = 0.60$ at ca. 20 ppm $\text{O}_2$ (a) and at 1000 ppm $\text{O}_2$ (b), and simulated XRPD pattern of $\text{V}(\text{WO}_2)_2(\text{P}_2\text{O}_7)(\text{PO}_4)$ (c), down arrows in (a) indicate mixed-metal MPTB $(\text{V}_{0.17}\text{W}_{0.83}\text{O}_3)_8(\text{PO}_2)_4$ [197, Chapter 10]. .... 129	129
Figure 8.3	Comparison of the Guinier photographs of $M^{\text{III}}(\text{W}^{\text{VI}}\text{O}_2)_2(\text{P}_2\text{O}_7)(\text{PO}_4)$ where $M^{\text{III}}$ : Sc, V, Cr, Fe, Ru, Rh, In, and Ir. Small impurities of $m$ - $\text{W}_2\text{O}_3(\text{PO}_4)_2$ [76, 77, 78] and $(\text{Rh}_{0.667}\text{W}_{0.333})\text{O}_2$ [233] are indicated by (*) and (x), respectively. .... 132	132
Figure 8.4	Microphotograph of brown crystals of $\text{V}(\text{WO}_2)_2(\text{P}_2\text{O}_7)(\text{PO}_4)$ obtained by vapor phase moderated solid state reaction. .... 133	133
Figure 8.5	Guinier photographs of $\text{Ru}(\text{WO}_2)_2(\text{P}_2\text{O}_7)(\text{PO}_4)$ (a), $\text{Rh}(\text{WO}_2)_2(\text{P}_2\text{O}_7)(\text{PO}_4)$ (b), and $\text{V}(\text{WO}_2)_2(\text{P}_2\text{O}_7)(\text{PO}_4)$ (c) obtained from vapor phase moderated solid state reactions (see Table 8.1), compared to the simulated diffraction pattern based on the models from the crystal structure refinements (Table 8.5 to Table 8.7). Crosses indicate small impurity of $(\text{Rh}_{0.667}\text{W}_{0.333})\text{O}_2$ [233]. .... 136	136
Figure 8.6	ORTEP representation of $[(\text{W}/\text{V})\text{O}_6]$ , $[\text{P}_2\text{O}_7]$ , and $[\text{PO}_4]$ groups in $\text{V}(\text{WO}_2)_2(\text{P}_2\text{O}_7)(\text{PO}_4)$ . Ellipsoids (50% probability level, DIAMOND [128]) in light grey represent metals on sites $M1$ to $M6$ with mixed occupancy $\text{V}/\text{W}$ ( $M1$ to $M4$ are predominantly $\text{W}$ ), grey $\text{O}$ , and white $\text{P}$ . .... 142	142
Figure 8.7	Crystal structure of polynary phosphate $\text{V}^{\text{III}}(\text{W}^{\text{VI}}\text{O}_2)_2(\text{P}_2\text{O}_7)\text{PO}_4$ projected along the crystallographic $b$ -axis (a); and $c$ -axis (b). Dark grey fairly regular octahedra $\text{VO}_6$ (2 sites) show an occupancy of about $\text{V}_{0.5}\text{W}_{0.5}$ , light grey distorted octahedra $\text{WO}_6$ (4 sites, $\text{WO}_2^{2+}$ groups) show an occupancy of about $\text{V}_{0.25}\text{W}_{0.75}$ , medium grey $[\text{P}_2\text{O}_7]$ group and white $[\text{PO}_4]$ tetrahedra, white circles represent oxygen atoms of tungstenyl(VI) groups $(\text{WO}_2)^{2+}$ . .... 143	143

Figure 8.8	Scandium(III) tungstenyl(VI) ortho-pyrophosphate. Comparison of the observed XRPD pattern (a) to simulations based on the structure of $\text{Rh}^{\text{III}}(\text{W}^{\text{VI}}\text{O}_2)_2(\text{P}_2\text{O}_7)(\text{PO}_4)$ (Sc substituting Ru on sites <i>M</i> 5 and <i>M</i> 6, no Sc/W disorder) (c) and full inversion of the occupancy of the sites <i>M</i> 5 and <i>M</i> 6 according to $\text{W}(\text{Sc}_{1/2}\text{W}_{1/2}\text{O}_2)_2(\text{P}_2\text{O}_7)(\text{PO}_4)$ (b). A small impurity of <i>m</i> - $\text{W}_2\text{O}_3(\text{PO}_4)_2$ is indicated by (*). .....	144
Figure 8.9	BF TEM image of crushed $\text{V}(\text{WO}_2)_2(\text{P}_2\text{O}_7)(\text{PO}_4)$ crystals (left) and ED pattern along [012]; * : $18.3 \text{ \AA } d(\bar{2}00)$ ; ** : $5.3 \text{ \AA } d(021)$ (right). .....	146
Figure 8.10	HRTEM image of $\text{V}(\text{WO}_2)_2(\text{P}_2\text{O}_7)(\text{PO}_4)$ along [012] (a); enlargement of the boxed area with a polyhedra drawing of the structure model (b); HRTEM simulation: $d = 43$ ; $\Delta f = -7.5 \text{ nm}$ (c). .....	146
Figure 8.11	Room temperature $^{31}\text{P}$ -MAS-NMR spectra of $\text{W}(\text{Sc}_{0.5}\text{W}_{0.5}\text{O}_2)_2(\text{P}_2\text{O}_7)(\text{PO}_4)$ (a), $\text{In}(\text{WO}_2)_2(\text{P}_2\text{O}_7)(\text{PO}_4)$ (b), and $\text{Ir}(\text{WO}_2)_2(\text{P}_2\text{O}_7)(\text{PO}_4)$ (c), $\text{InPO}_4$ [87, this thesis] (d), <i>m</i> - $\text{W}_2\text{O}_3(\text{PO}_4)_2$ [this thesis] (e), and $\text{WO}(\text{P}_2\text{O}_7)$ [this thesis] (f). Resonances from an impurity of <i>m</i> - $\text{W}_2\text{O}_3(\text{PO}_4)_2$ are indicated by (•). .....	147
Figure 8.12	XP spectra of $\text{V}^{\text{III}}(\text{W}^{\text{VI}}\text{O}_2)_2(\text{P}_2\text{O}_7)\text{PO}_4$ with fitted curves for V2p (a), W4f (b), and O1s (c). .....	150
Figure 8.13	UV/Vis/NIR powder reflectance spectra of $\text{Cr}^{\text{III}}(\text{W}^{\text{VI}}\text{O}_2)_2(\text{P}_2\text{O}_7)\text{PO}_4$ and $\text{Fe}^{\text{III}}(\text{W}^{\text{VI}}\text{O}_2)_2(\text{P}_2\text{O}_7)\text{PO}_4$ . .....	151
Figure 8.14	Temperature dependence molar susceptibility, $\chi_{\text{mol}}$ and its reciprocal $\chi_{\text{mol}}^{-1}$ of $M^{\text{III}}(\text{WO}_2)_2(\text{P}_2\text{O}_7)\text{PO}_4$ , <i>M</i> : V, Cr, Fe. ....	152
Figure 8.15	Room temperature continuous wave (CW) X-band powder EPR spectra of $\text{Cr}^{\text{III}}(\text{W}^{\text{VI}}\text{O}_2)_2(\text{P}_2\text{O}_7)\text{PO}_4$ and $\text{Fe}^{\text{III}}(\text{W}^{\text{VI}}\text{O}_2)_2(\text{P}_2\text{O}_7)\text{PO}_4$ . ....	153
Figure 9.1	Summary on phase transitions and structural parameters of $\text{WO}_3$ [245, 246, 247, 248, 249]. .....	155
Figure 9.2	Crystal structures of $\text{WO}_{2.90}$ ( $\text{W}_{20}\text{O}_{58}$ ) showing the CS{103} plane [257] (a) and $\text{WO}_{2.72}$ ( $\text{W}_{18}\text{O}_{49}$ ) showing the pentagonal columns of $\text{WO}_7$ pentagonal bipyramids with edge sharing and hexagonal tunnels [261] (b). .....	156
Figure 9.3	Powder diffraction patterns showing the progress of phase formation with temperature during SCS followed by heating in air. The formation of two metastable phases, <i>cub</i> - $\text{WO}_3$ and $\text{WOPO}_4$ type prior to the occurrence of the thermodynamically stable phase $\text{Cr}(\text{WO}_2)_2(\text{P}_2\text{O}_7)(\text{PO}_4)$ is obvious. ....	160
Figure 9.4	XRPD patterns of members of the solid solution $(\text{V}_{1-x}\text{W}_x\text{P}_{0.5})\text{O}_{2.5+\delta}$ ( $0.25 \leq x \leq 0.50$ ) with <i>cub</i> - $\text{WO}_3$ structure type obtained via SCS followed by heating in air. ....	161
Figure 9.5	Guinier photograph of $(\text{Fe}_{0.10}\text{V}_{0.10}\text{W}_{0.30}\text{P}_{0.50})\text{O}_{2.5+\delta}$ ( <i>cub</i> - $\text{WO}_3$ structure type) (a) obtained by via SCS followed by heating in air at $450 \text{ }^\circ\text{C}$ for one day, compared with the simulated pattern (b) with adjusted lattice parameter (structure model <i>cub</i> - $\text{WO}_3$ [252]). .....	161



Figure 9.6	Comparison of Guinier photographs of $(W_{1-x}P_x)O_{3-x/2}$ ; $0 \leq x < 0.5$ obtained by SCS followed by heating in air. Asterisks indicate small impurities of <i>m</i> -WO <sub>3</sub> . .....	163
Figure 9.7	Guinier photographs of metastable phosphates $(M^{III}_{0.167}W^{VI}_{0.333}P_{0.50})O_{2.5}$ and simulated patterns based on the structure model of <i>cab</i> -WO <sub>3</sub> [252], for <i>M</i> : V, Cr, Fe, In and <i>tet</i> -WO <sub>3</sub> [249] for <i>M</i> : Sc with adjusted lattice parameters. ....	165
Figure 9.8	TEM image showing an volume of $(Cr_{0.17}W_{0.33}P_{0.50})O_{2.5}$ selected by a “selected area aperture” for diffraction (left), inverted electron diffraction pattern (right).....	166
Figure 9.9	<sup>31</sup> P-MAS-NMR spectra of $(W_{1-x}P_x)O_{3-x/2}$ ; $x = 0.25$ , (a), $x = 0.33$ (b), $x = 0.50$ (c) obtained by SCS followed by heating in air at 500 °C, 650°C and 500 °C, respectively and after leaching with hot water of sample <i>b</i> (d).....	168
Figure 9.10	Comparison of Guinier photographs (no background correction) of $(W_{0.67}P_{0.33})O_{2.835}$ (phosphate with <i>tet</i> - WO <sub>3</sub> related, P:W = 6:12) obtained via SCS followed by heating at 650 °C (a) then leaching with hot water (b). Asterisk (*) indicate might be the appearance of monoclinic WO <sub>3</sub> phase. ....	169
Figure 9.11	Development of <sup>31</sup> P-MAS-NMR spectra $(W_{0.923}P_{0.077})O_{2.962}$ obtained via SCS followed by heating at three different temperatures 400 °C (a), 600 °C (b), and 900 °C (c). ....	170
Figure 9.12	Comparison of the Guinier photographs of $(M^{III}_{0.33}W^{VI}_{0.67})OPO_4$ ; <i>M</i> : V, Cr, Fe (WOPO <sub>4</sub> structure type) with their simulated pattern based on the single crystal data of WOPO <sub>4</sub> [this thesis] with adjusted lattice parameters, the W sites are statistically occupied by $Mo_{0.33}W_{0.67}$ . * indicate small impurities of $(W_{0.83}V_{0.17}O_3)_8(PO_2)_4$ [197]. ....	172
Figure 9.13	Guinier photographs of $(Cr^{III}_{0.333}W^{VI}_{0.667})OPO_4$ (powder from SCS; a) and $(Mo^{III}_{0.333}W^{VI}_{0.667})OPO_4$ (powder from selected crystals; b) are compared to the simulated diffraction patterns based on data sets from the crystal structure refinements [this thesis]. ....	174
Figure 9.14	ORTEP representation (Ellipsoids are at 50% probability level, [128]) of [(Mo/W)O <sub>6</sub> ], and [PO <sub>4</sub> ] groups in $(Mo_{0.33}W_{0.67})OPO_4$ .....	178
Figure 9.15	Temperature dependence of molar susceptibility, $\chi_{mol}$ and its reciprocal $\chi_{mol}^{-1}$ of $(Cr^{III}_{0.33}W^{VI}_{0.67})OPO_4$ and $(Fe^{III}_{0.33}W^{VI}_{0.67})OPO_4$ . ....	178
Figure 10.1	Crystal structure of $(W^{V,VI}O_3)_8(PO_2)_4$ [95], green and yellow represent [WO <sub>6</sub> ] and [PO <sub>4</sub> ] polyhedra, respectively. ....	181

Figure 10.2	Synthesis of $(\text{Cr}^{\text{III}}_{1/6}\text{W}^{\text{VI}}_{5/6}\text{O}_3)_8(\text{PO}_2)_4$ . Guinier photograph of the product obtained by vapour phase moderated solid state reaction (a), simulation based on the data of $(\text{W}^{\text{V,VI}}\text{O}_3)_8(\text{PO}_2)_4$ [95] however transformed into monoclinic symmetry ( $P2_1$ ) with statistical Cr/W distribution of metal sites and adjusted lattice parameters (see section 10.3). Asterisks indicate a very small impurity of $m\text{-WO}_3$ [264].....	182
Figure 10.3	Phases obtained during annealing in air after ignition in SCS aiming at $(\text{Cr}^{\text{III}}_{1/6}\text{W}^{\text{VI}}_{5/6}\text{O}_3)_8(\text{PO}_2)_4$ . Asterisks indicate small impurity of $m\text{-WO}_3$ [264]. .....	183
Figure 10.4	Visualization of the three calculated stoichiometric compositions (A, B, C) of vanadium-tungsten mixed transition metal MPTBs. Experiments are indicated by red circles. ....	184
Figure 10.5	Reaction products in experiments aiming at the synthesis of $(\text{V}^{\text{III}}_{1/6}\text{W}^{\text{VI}}_{5/6}\text{O}_3)_8(\text{PO}_2)_4$ (A, middle) and $(\text{V}^{\text{V}}_{3/6}\text{W}^{\text{VI}}_{3/6}\text{O}_3)_8(\text{PO}_2)_4$ (C, top). Simulation based on data of $(\text{WO}_3)_8(\text{PO}_2)_4$ [95] (bottom) however through transforming the cell from $P2_12_12_1$ to $P2_1$ with statistical distribution of V/W in metal sites and adjusted lattice parameters. Asterisks and black dots indicate $m\text{-WO}_3$ [264] and $\text{V}(\text{WO}_2)_2(\text{P}_2\text{O}_7)(\text{PO}_4)$ [this thesis], respectively. ....	185
Figure 10.6	Phases obtained during SCS aiming at $(\text{V}^{\text{III}}_{1/6}\text{W}^{\text{VI}}_{5/6}\text{O}_3)_8(\text{PO}_2)_4$ . Asterisks indicate a very small impurity of $m\text{-WO}_3$ [264].....	186
Figure 10.7	Guinier photograph of $(\text{V}^{\text{III}}_{1/6}\text{W}^{\text{VI}}_{5/6}\text{O}_3)_8(\text{PO}_2)_4$ , obtained from crystals of experiment G2 (Table 10.1), showing the splitting of some of reflections (a) which is explained by the simulation based on data of $(\text{WO}_3)_8(\text{PO}_2)_4$ , S. G. $P2_12_12_1$ [95] however with transforming into lower symmetry ( $P2_1$ ) and statistical distribution of V and W in metal sites and adjusted lattice parameters. Asterisks indicate little impurity. ....	187
Figure 11.1	Diagram of $\log p(\text{O}_2)$ vs. $1/T$ for a gas mixture $\text{H}_2/\text{H}_2\text{O}$ $\{p(\text{total}) = 1\text{ bar}, p(\text{H}_2\text{O}) = 0.023\text{ bar}\}$ .....	190
Figure 11.2	Barogram of the coexisting phases $\text{VPO}_n$ ( $n = 5, 4.5, 4, 0$ ) [this thesis, for thermodynamic data see Table 11.1]. ....	192
Figure 11.3	Reduction of $\beta\text{-VOPO}_4$ by moist hydrogen at different temperatures. ( $\circ$ ) $(\text{VO})_2\text{P}_2\text{O}_7$ [10], ( $\blacksquare$ ) $\text{VPO}_4\text{-m1}$ [this thesis], ( $\bullet$ ) $\text{VPO}_4\text{-m2}$ phase [this thesis], ( $\Delta$ ) $\text{VPO}_4$ [83], and (*) indicate $\beta\text{-V}_2\text{OPO}_4$ [148]. The down arrow indicates unassigned reflections. ....	193
Figure 11.4	Sketch of the reaction tube designed for stepwise oxidation of $\text{VPO}_4\text{-m1}$ to $(\text{V}^{\text{IV}}\text{O})_2\text{P}_2\text{O}_7$ and $\beta\text{-V}^{\text{V}}\text{OPO}_4$ .....	194
Figure 11.5	First structure model of metastable $\text{V}^{\text{III}}\text{PO}_4\text{-m1}$ (a) with square planar $[\text{VO}_4]$ derived by removing the vanadyl oxygen from $\beta\text{-V}^{\text{V}}\text{OPO}_4$ (b) [161]. ....	195

Figure 11.6	Guinier photographs of VPO <sub>4</sub> -m1 with x-ray exposure time 15 min (a) and 5 hour (b), simulation based on the structure model related to $\beta$ -VOPO <sub>4</sub> without vanadyl-oxygen atoms (square-planar VO <sub>4</sub> groups) (c). Reflections marked by asterisks might originate from VPO <sub>4</sub> -m2. ....	196
Figure 11.7	Second structure model of metastable VPO <sub>4</sub> -m1 derived from $\beta$ -V <sub>2</sub> OPO <sub>4</sub> . ....	197
Figure 11.8	Guinier photograph of VPO <sub>4</sub> -m1 (a) compared to the simulation based on the second structure model derived from $\beta$ -V <sub>2</sub> OPO <sub>4</sub> (b), reflections marked by asterisks see text. ....	197
Figure 11.9	Second structure model of VPO <sub>4</sub> -m1 with square planar [VO <sub>4</sub> ] (b) and (c) obtained from $\beta$ -V <sub>2</sub> OPO <sub>4</sub> (a). ....	198
Figure 11.10	Predicted structure for new metastable VPO <sub>4</sub> ( <i>Pnma</i> ) polymorph with [VO <sub>4</sub> ] tetrahedra in red and PO <sub>4</sub> in yellow obtained from DFT calculation. ....	199
Figure 11.11	Simulated XRPD patterns of new metastable VPO <sub>4</sub> polymorphs predicted by DFT calculation with <i>Pnma</i> (top) and <i>P2<sub>1</sub>/m</i> (bottom). Both structure model consist of VO <sub>4</sub> tetrahedra. ....	199
Figure 11.12	Temperature dependent effective magnetic moment of V <sup>III</sup> PO <sub>4</sub> -m1. ....	200
Figure 11.13	Guinier photograph of VPO <sub>4</sub> -m2, V <sub>2</sub> (VO)(P <sub>2</sub> O <sub>7</sub> )(PO <sub>4</sub> ) (a). Simulation based on single crystal data of Fe <sub>2</sub> (VO)(P <sub>2</sub> O <sub>7</sub> )(PO <sub>4</sub> ) [133] (b) via substituting the iron sites by vanadium, and simulation based on relaxed crystal structure (c). Adjusted lattice parameters from the experimental XRPD pattern are used for both cases. (■) and down arrows indicate reflections of VPO <sub>4</sub> -m1 and an unknown phase, respectively. ....	201
Figure 11.14	Polyhedral representation of the crystal structure of metastable VPO <sub>4</sub> -m2, V <sub>2</sub> (VO)(P <sub>2</sub> O <sub>7</sub> )(PO <sub>4</sub> ) (a) and (b), and $\beta$ -V <sub>2</sub> OPO <sub>4</sub> [148] (c). Green string of phase sharing VO <sub>6</sub> octahedra, purple dimer of phase sharing VO <sub>6</sub> octahedra, and yellow PO <sub>4</sub> tetrahedra. ....	202
Figure 11.15	Reduction of V <sub>2</sub> O <sub>5</sub> by moist hydrogen at different temperatures. ....	204
Figure 11.16	Crystal structures of V <sub>2</sub> O <sub>5</sub> (a), metastable (VO) <sub>2</sub> V <sub>2</sub> O <sub>7</sub> (b), metastable VO <sub>2</sub> (B) (c) related to V <sub>2</sub> O <sub>5</sub> structure, and VO <sub>2</sub> (M) (d) distorted rutile structure type. ....	205
Figure 13.1	Solid solutions (V <sub>1-x</sub> W <sub>x</sub> )OPO <sub>4</sub> . Structure types and compositional ranges. ....	211
Figure 13.2	Crystal structure of new polynary phosphate V <sup>III</sup> (W <sup>VI</sup> O <sub>2</sub> ) <sub>2</sub> (P <sub>2</sub> O <sub>7</sub> )PO <sub>4</sub> . Fairly regular octahedra VO <sub>6</sub> (2 sites) show an occupancy of about V <sub>0.5</sub> W <sub>0.5</sub> . Distorted octahedra WO <sub>6</sub> (4 sites, WO <sub>2</sub> <sup>2+</sup> groups) show an occupancy of about V <sub>0.25</sub> W <sub>0.75</sub> . ....	212
Figure 13.3	Schematic diagram of annealing condition and typically observed phases of post-SCS process ( <i>M</i> : Sc, V, Cr, Fe, In). ....	213
Figure 13.4	Structure types, their homogeneity ranges, and formation temperatures in the quasi-binary system MoOPO <sub>4</sub> -VOPO <sub>4</sub> . ....	214

Figure 13.5	Structural derivation of $V^{III}PO_4$ -m1, model 1 (a) and $V^{III}PO_4$ -m1, model 2 (c) derived from $\beta$ -VOPO <sub>4</sub> (b) and $\beta$ -V <sub>2</sub> OPO <sub>4</sub> (d), respectively. ....	214
Figure 13.6	Polyhedral representation of the structures of metastable VPO <sub>4</sub> -m2, V <sub>2</sub> (VO)(P <sub>2</sub> O <sub>7</sub> )(PO <sub>4</sub> ) (a) and (b), and $\beta$ -V <sub>2</sub> OPO <sub>4</sub> [148] (c). Green: string of phase sharing VO <sub>6</sub> octahedra, purple: dimer of phase sharing VO <sub>6</sub> octahedra, and yellow: PO <sub>4</sub> tetrahedra. ....	215
Figure 14.1	Comparison of Guinier photographs of solid solutions (V <sub>1-x</sub> W <sub>x</sub> )OPO <sub>4</sub> ; $0 \leq x \leq 1.0$ obtained by SCS followed by heating in air with exceptions, where heating is done at argon (j), and at H <sub>2</sub> flow followed by sealed tube experiment at 800 °C (l), simulation of $\alpha_{II}$ -VOPO <sub>4</sub> [160] (a), the symbols (*) represent (W <sub>0.83</sub> V <sub>0.17</sub> O <sub>3</sub> ) <sub>8</sub> (PO <sub>2</sub> ) <sub>4</sub> [this thesis], (▼) $\alpha_{II}$ -(V <sub>1-x</sub> W <sub>x</sub> )OPO <sub>4</sub> , (×) (WO <sub>3</sub> ) <sub>8</sub> (PO <sub>2</sub> ) <sub>4</sub> [95], (+) $m$ -(W <sub>2</sub> O <sub>3</sub> )(PO <sub>4</sub> ) <sub>2</sub> [78]. ....	219
Figure 14.2	Reduction of $m$ -(W <sub>2</sub> O <sub>3</sub> )(PO <sub>4</sub> ) <sub>2</sub> (b) by moist H <sub>2</sub> at different temperatures. At 550°C partially reduced violet $m$ -(W <sub>2</sub> O <sub>3-<math>\delta</math>)</sub> (PO <sub>4</sub> ) <sub>2</sub> (c), at 700°C black powder of WP [105] (d), and simulated pattern of $m$ -(W <sub>2</sub> O <sub>3</sub> )(PO <sub>4</sub> ) <sub>2</sub> (a) based on single crystal structure data [78].....	231
Figure 14.3	Guinier photograph of two phase mixture $m$ -(W <sub>2</sub> O <sub>3</sub> )(PO <sub>4</sub> ) <sub>2</sub> and P <sub>8</sub> W <sup>V,VI</sup> <sub>12</sub> O <sub>52</sub> (indicated by *), obtained after partial reduction of $m$ -(W <sub>2</sub> O <sub>3</sub> )(PO <sub>4</sub> ) <sub>2</sub> [78] by moist H <sub>2</sub> at 550 °C followed by heating in sealed silica ampoule at 800 °C. ....	231
Figure 14.4	Reduction of $\beta$ -VOPO <sub>4</sub> (b) by moist H <sub>2</sub> at different temperatures. At 550 and 900 °C lead to metastable VPO <sub>4</sub> -m1 (c), and $\beta$ -V <sub>2</sub> OPO <sub>4</sub> (d) [148], respectively. Simulation of $\beta$ -VOPO <sub>4</sub> (a) based on single crystal structure data [161]. Down arrows indicate small amount of unknown impurities. ....	232
Figure 14.5	Comparison of the Guinier photographs aiming at the synthesis of “(V <sub>1-x</sub> Mo <sub>x</sub> )OPO <sub>4</sub> ” at $x = 0.95$ (a) and 1.0 (b) via SCS followed by heating in air with the simulation of $\alpha$ -(MoO <sub>2</sub> ) <sub>2</sub> P <sub>2</sub> O <sub>7</sub> [88] (c). ....	242
Figure 14.6	Aiming to the synthesis of “Sb(WO <sub>2</sub> ) <sub>2</sub> (P <sub>2</sub> O <sub>7</sub> )(PO <sub>4</sub> )” (a) in air leads to multiphase mixture of $m$ -W <sub>2</sub> O <sub>3</sub> (PO <sub>4</sub> ) <sub>2</sub> (indicated by dots), a unknown phase X2 (indicated by *) and $o$ -W <sub>2</sub> O <sub>3</sub> (PO <sub>4</sub> ) <sub>2</sub> shown as simulation of $o$ -W <sub>2</sub> O <sub>3</sub> (PO <sub>4</sub> ) <sub>2</sub> [75] (b).....	243
Figure 14.7	Synthesis of Mo(WO <sub>2</sub> ) <sub>2</sub> (P <sub>2</sub> O <sub>7</sub> )(PO <sub>4</sub> ) in sealed silica tube leads to the formation of multiphase mixtures: XRPD of mechanically separated black powders of MoP <sub>2</sub> O <sub>7</sub> [207] (a), bronze powders (b) comprising WOPO <sub>4</sub> [this thesis, 90, 91], (WO <sub>3</sub> ) <sub>8</sub> (PO <sub>2</sub> ) <sub>4</sub> [95] indicated by * and down arrows, respectively. Simulation of Mo(WO <sub>2</sub> ) <sub>2</sub> (P <sub>2</sub> O <sub>7</sub> )(PO <sub>4</sub> ) (c) based on data of Ru(WO <sub>2</sub> ) <sub>2</sub> (P <sub>2</sub> O <sub>7</sub> )(PO <sub>4</sub> ) with adjusted lattice parameters, open circle indicate small impurity. ....	243

Figure 14.8	Sequential changes in powder diffraction patterns with temperatures during SCS followed by heating in air. The formation of two metastable phases, <i>tet</i> -WO <sub>3</sub> and WOPO <sub>4</sub> type prior to the occurrence of the thermodynamically stable phase Sc(WO <sub>2</sub> ) <sub>2</sub> (P <sub>2</sub> O <sub>7</sub> )(PO <sub>4</sub> ) is obvious. * indicate <i>m</i> -(W <sub>2</sub> O <sub>3</sub> )(PO <sub>4</sub> ) <sub>2</sub> [76, 77, 78].	244
Figure 14.9	Sequential changes in powder diffraction patterns with temperatures during SCS followed by heating in air. The formation of two metastable phases, <i>cub</i> -WO <sub>3</sub> and WOPO <sub>4</sub> structure type prior to the occurrence of the thermodynamically stable phase V(WO <sub>2</sub> ) <sub>2</sub> (P <sub>2</sub> O <sub>7</sub> )(PO <sub>4</sub> ) is obvious. * indicated (W <sub>0.83</sub> V <sub>0.17</sub> O <sub>3</sub> ) <sub>8</sub> (PO <sub>2</sub> ) <sub>4</sub> .	245
Figure 14.10	Sequential changes in powder diffraction patterns with temperatures during SCS followed by heating in air. The formation of two metastable phases, <i>cub</i> -WO <sub>3</sub> and WOPO <sub>4</sub> structure type prior to the occurrence of the thermodynamically stable phase Fe(WO <sub>2</sub> ) <sub>2</sub> (P <sub>2</sub> O <sub>7</sub> )(PO <sub>4</sub> ) is obvious.	246
Figure 14.11	Sequential changes in powder diffraction patterns with temperatures during SCS followed by heating in air. The formation of two metastable phases, <i>cub</i> -WO <sub>3</sub> and WOPO <sub>4</sub> structure type prior to the occurrence of the thermodynamically stable phase In(WO <sub>2</sub> ) <sub>2</sub> (P <sub>2</sub> O <sub>7</sub> )(PO <sub>4</sub> ) is obvious.	247
Figure 14.12	Guinier photographs of Ir(WO <sub>2</sub> ) <sub>2</sub> (P <sub>2</sub> O <sub>7</sub> )(PO <sub>4</sub> ) (a), In(WO <sub>2</sub> ) <sub>2</sub> (P <sub>2</sub> O <sub>7</sub> )(PO <sub>4</sub> ) (b), Fe(WO <sub>2</sub> ) <sub>2</sub> (P <sub>2</sub> O <sub>7</sub> )(PO <sub>4</sub> ) (c), and Cr(WO <sub>2</sub> ) <sub>2</sub> (P <sub>2</sub> O <sub>7</sub> )(PO <sub>4</sub> ) (d) obtained via SCS followed by heating in air except (a) which is obtained from vapor phase moderated solid state reactions (see Table 8.1 and Table 8.2), compared to the simulated diffraction patterns based on the model from the single crystal structure refinements (Table 8.5).	250
Figure 14.13	TEM EDX spectra of V(WO <sub>2</sub> ) <sub>2</sub> (P <sub>2</sub> O <sub>7</sub> )(PO <sub>4</sub> ); V-K : W-L : P-K = 16.2(5) : 31.7(9) : 52.2(9) (a) and 16.8(7) : 29(1) : 53(2) (b) atom%. Cu and C from TEM grid.	260
Figure 14.14	ED pattern (a) and ED simulation (b) based on the structure model of V(WO <sub>2</sub> ) <sub>2</sub> (P <sub>2</sub> O <sub>7</sub> )(PO <sub>4</sub> ) (Table 8.5); Top: [012]:*:(40 $\bar{2}$ );**:( $\bar{2}21$ ); Middle: [110]:*:(00 $\bar{2}$ );**:( $\bar{2}20$ ); Bottom: [122]:*:(40 $\bar{2}$ ) and **:( $\bar{2}21$ )	261
Figure 14.15	ED pattern (a) and ED simulation (b) based on the structure model of Cr(WO <sub>2</sub> ) <sub>2</sub> (P <sub>2</sub> O <sub>7</sub> )(PO <sub>4</sub> ) (model from Table 8.5 with adjusted lattice parameters from powder XRPD); Top: [110]:*:(00 $\bar{2}$ );**:( $\bar{2}20$ ); Middle: [121]:*:( $\bar{2}2\bar{2}$ );**:( $\bar{2}21$ ); Bottom: [122].	262
Figure 14.16	<sup>31</sup> P-MAS-NMR spectra of (In <sub>0.167</sub> W <sub>0.333</sub> P <sub>0.50</sub> )O <sub>2.5</sub> □ <sub>0.5</sub> ( <i>cub</i> -WO <sub>3</sub> type) obtained by SCS followed by heating in air at 700 °C. The broadness of the signal might be due to low crystallinity as well as coupling of In nuclei.	266

Figure 14.17	Monitoring the changes of metastable $VPO_4$ -m1 [this thesis] into thermodynamically stable $VPO_4$ [83] phase from heating experiments in sealed silica ampoules by XRPD patterns. X-ray exposure time 15 min except 2 <sup>nd</sup> pattern from bottom where the x-ray exposure time is 5 hours. .... 272
Figure 14.18	Monitoring the synthesis of $V_4O_9$ by XRPD from the reduction process of $V_2O_5$ with moist hydrogen. .... 274

## List of Tables

Table 2.1	Different fuels and their structure. ....	12
Table 3.1	Experimental set ups for diffuse powder reflectance measurements. ....	27
Table 4.1	List of commercially available reagent grade starting materials. ....	37
Table 5.1	Summay of the crystallographic information of the existing compounds in system W/P/O, S.G.: space group, Z: formula units per unit cell. ....	53
Table 5.2	Details on data collection and single crystal structure refinement of WOPO <sub>4</sub> . ....	62
Table 6.1	Crystallographic information on tungsten-vanadium oxides and vanadium phosphates (tungsten phosphates are given in Table 5.1), S.G.: space group, Z: formula units per unit cell. ....	68
Table 6.2	Experiments aiming at the synthesis of solid solutions (V <sub>1-x</sub> W <sub>x</sub> )OPO <sub>4</sub> ; 0.0 ≤ x ≤ 1.0 in sealed ampoules. Heating protocol, pre-reaction 550 ← 700 °C for t <sub>1</sub> (days) and final transport reaction temperature 800 → 700 °C for t <sub>2</sub> (days). ....	69
Table 6.3	SCS experiments aiming at the synthesis of solid solutions (V <sub>1-x</sub> W <sub>x</sub> )OPO <sub>4</sub> . Heating of the combustion products was typically in air. Heating at reduced p(O <sub>2</sub> ) in some experiments is pointed out. ....	72
Table 6.4	Summary of crystallographic data and information on x-ray single crystal structure refinements of members of the solid solution series (V <sub>1-x</sub> W <sub>x</sub> )OPO <sub>4</sub> with x = 0.10 and 0.26. ....	80
Table 6.5	XPS results of α <sub>II</sub> -(V <sup>IV</sup> <sub>0.2</sub> V <sup>V</sup> <sub>0.6</sub> W <sup>VI</sup> <sub>0.2</sub> )OPO <sub>4</sub> and literature value. ....	86
Table 6.6	Summary of isotropic chemical shifts δ <sub>iso</sub> in <sup>31</sup> P-MAS-NMR spectra of members of the solid solution (V <sub>1-x</sub> W <sub>x</sub> )OPO <sub>4</sub> ; 0 ≤ x ≤ 0.20. ....	93
Table 7.1	Crystallographic information on molybdenum phosphates MoO <sub>x</sub> -PO <sub>2.5</sub> and molybdenum vanadium oxides MoO <sub>x</sub> -VO <sub>y</sub> (2.0 ≤ x ≤ 3.0; 1.5 ≤ y ≤ 2.5), a summary on vanadium phosphates was given in Table 6.1, S.G.: space group, Z: formula units per unit cell. ....	102
Table 7.2	Experiments aiming at the synthesis of solid solutions (V <sub>1-x</sub> Mo <sub>x</sub> )OPO <sub>4</sub> (0 ≤ x ≤ 1.0) via SCS followed by heating in air, heating protocol θ (°C) and t (h). ....	104
Table 7.3	Summary of crystallographic data and information on x-ray single crystal structure refinement of β-(V <sub>0.90</sub> Mo <sub>0.10</sub> )OPO <sub>4</sub> . ....	110
Table 7.4	Lattice parameters of members of the solid solution (V <sub>1-x</sub> Mo <sub>x</sub> )OPO <sub>4</sub> ; 0.0 ≤ x ≤ 0.20 (γ-VOPO <sub>4</sub> structure type [162], space group: <i>Pbam</i> ). ....	116
Table 7.5	Summary of isotropic chemical shifts δ <sub>iso</sub> in <sup>31</sup> P-MAS-NMR spectra of members of the solid solutions (V <sub>1-x</sub> Mo <sub>x</sub> )OPO <sub>4</sub> ; 0.02 ≤ x ≤ 0.20 and reference compounds. ....	122

XXIV List of Tables

Table 8.1	Experiments aiming at the synthesis of phosphates $M^{\text{III}}(\text{W}^{\text{VI}}\text{O}_2)_2(\text{P}_2\text{O}_7)(\text{PO}_4)$ via vapor phase moderated solid state reactions in sealed ampoules using $\text{Cl}_2$ (from $\text{PtCl}_2$ ) as mineralizer, heating protocol $\vartheta$ ( $^\circ\text{C}$ ) and $t$ (d). ....	126
Table 8.2	Experiments aiming at the synthesis of phosphates $M^{\text{III}}(\text{W}^{\text{VI}}\text{O}_2)_2(\text{P}_2\text{O}_7)(\text{PO}_4)$ via SCS followed by heating in air. For the vanadium phosphate various $p(\text{O}_2)$ were used, heating protocol $\vartheta$ ( $^\circ\text{C}$ ) and $t$ (d). ....	130
Table 8.3	Lattice parameters and colors of anhydrous ortho-pyrophosphates $M^{\text{III}}(\text{W}^{\text{VI}}\text{O}_2)_2(\text{P}_2\text{O}_7)(\text{PO}_4)$ ( $C2/c$ , $Z = 16$ , from IP-Guinier photographs, $\text{Cu-K}\alpha_1$ ). ....	133
Table 8.4	Summary of crystallographic data and information on x-ray single crystal structure refinements of $M(\text{WO}_2)_2(\text{P}_2\text{O}_7)(\text{PO}_4)$ with $M$ : V, Ru, Rh. ....	137
Table 8.5	Atomic coordinates and isotropic displacement parameters ( $\text{\AA}^2$ ) with estimated standard deviations in parentheses of $\text{V}(\text{WO}_2)_2(\text{P}_2\text{O}_7)(\text{PO}_4)$ . ....	138
Table 8.6	Atomic coordinates and isotropic displacement parameters ( $\text{\AA}^2$ ) with estimated standard deviations in parentheses of $\text{Ru}(\text{WO}_2)_2(\text{P}_2\text{O}_7)(\text{PO}_4)$ . ....	139
Table 8.7	Atomic coordinates and isotropic displacement parameters ( $\text{\AA}^2$ ) with estimated standard deviations in parentheses of $\text{Rh}(\text{WO}_2)_2(\text{P}_2\text{O}_7)(\text{PO}_4)$ . ....	140
Table 8.8	Selected interatomic distances ( $\text{\AA}$ ) of phosphates $M(\text{WO}_2)_2(\text{P}_2\text{O}_7)(\text{PO}_4)$ ; $M$ : V, Ru, Rh with estimated standard deviations in parentheses. ....	141
Table 8.9	Summary of $^{31}\text{P}$ -MAS-NMR isotropic chemical shifts $\delta_{\text{iso}}$ of phosphates $M(\text{WO}_2)_2(\text{P}_2\text{O}_7)(\text{PO}_4)$ with $M$ : Sc, In, Ir, and reference compounds. A: Integrated intensities of resonances. ....	148
Table 8.10	XPS results of $\text{V}^{\text{III}}(\text{W}^{\text{VI}}\text{O}_2)_2(\text{P}_2\text{O}_7)(\text{PO}_4)$ and literature value. ....	149
Table 9.1	Summary of the crystallographic information on the existing compounds in system W-O, S.G.: space group, Z: formula units per unit cell. ....	157
Table 9.2	Experiments aiming at the synthesis of phosphates $M^{\text{III}}(\text{W}^{\text{VI}}\text{O}_2)_2(\text{P}_2\text{O}_7)(\text{PO}_4)$ by SCS followed by heating in air. For vanadium the use of various $p(\text{O}_2)$ is given as footnotes, heating protocol $\vartheta$ ( $^\circ\text{C}$ ) and $t$ (d). ....	158
Table 9.3	Experiments aiming at the synthesis of $(\text{W}_{1-x}\text{P}_x)\text{O}_{3-x/2}\square_{x/2}$ ( $0 \leq x \leq 0.5$ ) via SCS, molar ratio of metal:glycine:nitric acid is 1:3:6, heating protocol $\vartheta$ ( $^\circ\text{C}$ ) and $t$ (h). ....	162
Table 9.4	Lattice parameters of the metastable phosphates with crystal structures related to <i>cub-tet</i> - $\text{WO}_3$ . ....	164
Table 9.5	EDX analysis of powder sample of $(\text{Cr}_{0.17}\text{W}_{0.33}\text{P}_{0.50})\text{O}_{2.5}\square_{0.5}$ . ....	167
Table 9.6	EDX analysis of powder samples of $(\text{W}_{0.67}\text{P}_{0.33})\text{O}_{2.83}\square_{0.17}$ before and after leaching with hot water. ....	169
Table 9.7	Lattice parameters of phosphates $(M^{\text{III}}_{0.333}\text{W}^{\text{VI}}_{0.667})\text{OPO}_4$ ; $M$ : V, Cr, Fe, Mo, S.G. $P2_1/m$ , i.r. of $\text{W}^{5+}$ and $\text{W}^{6+}$ are 62 and 60 pm, respectively [266]. ....	171
Table 9.8	Crystallographic data and information on x-ray single-crystal structure refinements of $(\text{Cr}_{0.333}\text{W}_{0.667})\text{OPO}_4$ and $(\text{Mo}_{0.333}\text{W}_{0.667})\text{OPO}_4$ . ....	175



Table 9.9	Atomic coordinates and isotropic displacement parameters ( $\text{\AA}^2$ ) for $(\text{Cr}_{0.33}\text{W}_{0.67})\text{OPO}_4$ (WOPO <sub>4</sub> structure type) with estimated standard deviations in parentheses. ....	176
Table 9.10	Atomic coordinates and isotropic displacement parameters ( $\text{\AA}^2$ ) for $(\text{Mo}_{0.33}\text{W}_{0.67})\text{OPO}_4$ (WOPO <sub>4</sub> structure type) with estimated standard deviations in parentheses. ....	176
Table 9.11	Selected interatomic distances ( $\text{\AA}$ ) of $(\text{Cr}_{0.33}\text{W}_{0.67})\text{OPO}_4$ and $(\text{Mo}_{0.33}\text{W}_{0.67})\text{OPO}_4$ with estimated standard deviations in parentheses. ....	177
Table 10.1	Experiments aiming at the synthesis of vanadium containing MPTB $(\text{V}_x\text{W}_{1-x}\text{O}_3)_8(\text{PO}_2)_4$ , heating protocol $\vartheta$ ( $^\circ\text{C}$ ) and $t$ (d). ....	185
Table 10.2	Lattice parameters of $(\text{M}^{\text{III}}_{1/6}\text{W}^{\text{VI}}_{5/6}\text{O}_3)_8(\text{PO}_2)_4$ ; (M: V, Cr) space group $P2_1$ ; ionic radii (i.r.) of $\text{W}^{5+}$ and $\text{W}^{6+}$ are 62 and 60 pm, respectively [266]. ....	188
Table 10.3	Lattice parameters of metastable phosphates with structure related to <i>cub-/tet</i> -WO <sub>3</sub> type obtained via SCS followed by heating in air. ....	188
Table 11.1	Thermodynamic data of the coexisting phases in $\text{VPO}_n$ ( $n = 5, 4.5, 4, 0$ ) [291]. ....	191
Table 11.2	Atomic coordinates for the first structure model of metastable $\text{VPO}_{4\text{-m}1}$ , S.G. <i>Pnma</i> ; $a = 7.341 \text{ \AA}$ , $b = 6.389 \text{ \AA}$ , $c = 7.329 \text{ \AA}$ based on $\beta\text{-VOPO}_4$ . ....	195
Table 11.3	Atomic coordinates for the second structure model of metastable $\text{VPO}_{4\text{-m}1}$ S.G. <i>C2/c</i> ; $a = 7.73411 \text{ \AA}$ , $b = 7.33411 \text{ \AA}$ , $c = 7.36658 \text{ \AA}$ , $\beta = 119.854^\circ$ based on $\beta\text{-V}_2\text{OPO}_4$ . ....	196
Table 11.4	Atomic coordinates of $\text{VPO}_{4\text{-m}2}$ , $\text{V}_2(\text{VO})(\text{P}_2\text{O}_7)(\text{PO}_4)$ obtained by DFT calculation. ....	202
Table 12.1	Tested materials, results of catalytic testing and characterization of the catalyst materials after testing, $S_{\text{MA}} = \{n(\text{MA}_{\text{product}})/n(\text{n-butane}_{\text{feed}})\} * 100$ , $X_{\text{n-butane}} = \{n(\text{All}_{\text{product}})/n(\text{n-butane}_{\text{feed}})\}$ . ....	208
Table 14.1	Atomic coordinates and isotropic displacement parameters ( $\text{\AA}^2$ ) for WOPO <sub>4</sub> with estimated standard deviations in parentheses. ....	216
Table 14.2	Anisotropic displacement parameters ( $\text{\AA}^2$ ) for WOPO <sub>4</sub> with estimated standard deviations in parentheses. ....	216
Table 14.3	Selected interatomic distances ( $\text{\AA}$ ) of WOPO <sub>4</sub> with estimated standard deviations in parentheses. ....	217
Table 14.4	Assignment of the Guinier photograph of WOPO <sub>4</sub> , S. G. $P2_1/m$ ; $a = 6.5541(4) \text{ \AA}$ , $b = 5.2234(7) \text{ \AA}$ , $c = 11.1862(8) \text{ \AA}$ , $\beta = 90.331(6)^\circ$ . ....	217
Table 14.5	Lattice parameters of members of the solid solution $(\text{V}_{1-x}\text{W}_x)\text{OPO}_4$ ; $0.0 \leq x \leq 0.26$ . ( $\alpha_{\text{II}}$ -VOPO <sub>4</sub> structure type, S.G. $P4/n$ , $Z = 4$ ). ....	220
Table 14.6	Lattice parameters of members of WOPO <sub>4</sub> structure type solid solution $(\text{V}^{\text{III}}_{1-x}\text{W}^{\text{V}}_{3x-2}\text{W}^{\text{VI}}_{2(1-x)})\text{OPO}_4$ ( $0.67 \leq x \leq 1.0$ ) S.G. $P2_1/m$ , $Z = 4$ ). i.r. of $\text{W}^{6+}$ , $\text{W}^{5+}$ , and $\text{V}^{3+}$ are 60, 62, 64 pm, respectively [266]. ....	220

Table 14.7	Atomic coordinates and isotropic displacement parameters ( $\text{\AA}^2$ ) for $(V_{0.90}W_{0.10})OPO_4$ ( $\alpha_{II}$ -VOPO <sub>4</sub> structure type).....	220
Table 14.8	Atomic coordinates and isotropic displacement parameters ( $\text{\AA}^2$ ) for $(V_{0.74}W_{0.26})OPO_4$ ( $\alpha_{II}$ -VOPO <sub>4</sub> structure type).....	221
Table 14.9	Anisotropic displacement parameters ( $\text{\AA}^2$ ) for $(V_{0.90}W_{0.10})OPO_4$ ( $\alpha_{II}$ -VOPO <sub>4</sub> structure type).....	221
Table 14.10	Anisotropic displacement parameters ( $\text{\AA}^2$ ) for $(V_{0.74}W_{0.26})OPO_4$ ( $\alpha_{II}$ -VOPO <sub>4</sub> structure type).....	221
Table 14.11	Interatomic distances ( $\text{\AA}$ ) for $(V_{0.90}W_{0.10})OPO_4$ and $(V_{0.74}W_{0.26})OPO_4$ ( $\alpha_{II}$ -VOPO <sub>4</sub> structure type).....	221
Table 14.12	Assignment of the Guinier photograph of $\beta$ -VOPO <sub>4</sub> , S.G. <i>Pnma</i> ; $a = 7.7863(5) \text{\AA}$ , $b = 6.1329(4) \text{\AA}$ , $c = 6.9674(5) \text{\AA}$ .....	222
Table 14.13	Assignment of the Guinier photograph of $(V_{0.99}W_{0.01})OPO_4$ ( $\beta$ -VOPO <sub>4</sub> structure type, S.G. <i>Pnma</i> ; $a = 7.7794(5) \text{\AA}$ , $b = 6.1360(3) \text{\AA}$ , $c = 6.9733(4) \text{\AA}$ ).....	223
Table 14.14	Assignment of the Guinier photograph of $(V_{0.95}W_{0.05})OPO_4$ ( $\alpha_{II}$ -VOPO <sub>4</sub> structure type, S.G. <i>P4/n</i> ; $a = 6.0297(2) \text{\AA}$ , $c = 4.3960(3) \text{\AA}$ ).....	224
Table 14.15	Assignment of the Guinier photograph of $(V_{0.90}W_{0.10})OPO_4$ ( $\alpha_{II}$ -VOPO <sub>4</sub> structure type, S.G. <i>P4/n</i> ; $a = 6.0503(3) \text{\AA}$ , $c = 4.3618(4) \text{\AA}$ ).....	224
Table 14.16	Assignment of the Guinier photograph of $(V_{0.875}W_{0.125})OPO_4$ ( $\alpha_{II}$ -VOPO <sub>4</sub> structure type, S.G. <i>P4/n</i> ; $a = 6.0599(5) \text{\AA}$ , $c = 4.3456(8) \text{\AA}$ ).....	225
Table 14.17	Assignment of the Guinier photograph of $(V_{0.834}W_{0.166})OPO_4$ ( $\alpha_{II}$ -VOPO <sub>4</sub> structure type, S.G. <i>P4/n</i> ; $a = 6.0729(3) \text{\AA}$ , $c = 4.3295(6) \text{\AA}$ ).....	225
Table 14.18	Assignment of the Guinier photograph of $(V_{0.80}W_{0.20})OPO_4$ ( $\alpha_{II}$ -VOPO <sub>4</sub> structure type, S.G. <i>P4/n</i> ; $a = 6.0875(6) \text{\AA}$ , $c = 4.3141(13) \text{\AA}$ ).....	226
Table 14.19	Assignment of the Guinier photograph of $(V_{0.75}W_{0.25})OPO_4$ ( $\alpha_{II}$ -VOPO <sub>4</sub> structure type, S.G. <i>P4/n</i> ; $a = 6.0928(8) \text{\AA}$ , $c = 4.3055(6) \text{\AA}$ ).....	226
Table 14.20	Assignment of the Guinier photograph of $(V_{0.10}W_{0.90})OPO_4$ (WOPO <sub>4</sub> structure type, S.G. <i>P2<sub>1</sub>/m</i> ; $a = 6.5450(11) \text{\AA}$ , $b = 5.2189(9) \text{\AA}$ , $c = 11.1739(14) \text{\AA}$ , $\beta = 90.21(1)^\circ$ ).....	227
Table 14.21	Assignment of the Guinier photograph of $(V_{0.20}W_{0.80})OPO_4$ (WOPO <sub>4</sub> structure type, S.G. <i>P2<sub>1</sub>/m</i> ; $a = 6.531(1) \text{\AA}$ , $b = 5.206(7) \text{\AA}$ , $c = 11.124(2) \text{\AA}$ , $\beta = 90.12(2)^\circ$ ).....	228
Table 14.22	Assignment of the Guinier photograph of $(V_{0.25}W_{0.75})OPO_4$ (WOPO <sub>4</sub> structure type, S.G. <i>P2<sub>1</sub>/m</i> ; $a = 6.521(1) \text{\AA}$ , $b = 5.2164(7) \text{\AA}$ , $c = 11.1143(8) \text{\AA}$ , $\beta = 90.13(1)^\circ$ ).....	229
Table 14.23	Assignment of the Guinier photograph of $(V_{0.33}W_{0.67})OPO_4$ (WOPO <sub>4</sub> structure type, S.G. <i>P2<sub>1</sub>/m</i> ; $a = 6.513(2) \text{\AA}$ , $b = 5.202(1) \text{\AA}$ , $c = 11.056(2) \text{\AA}$ , $\beta = 90.12(2)^\circ$ ).....	230

Table 14.24	Lattice parameters of members of the solid solution $(V_{1-x}Mo_x)OPO_4$ ; $0.0 \leq x \leq 0.30$ ( $\beta$ -VOPO <sub>4</sub> structure type [161], space group: <i>Pnma</i> ).....	233
Table 14.25	Atomic coordinates and isotropic displacement parameters ( $\text{\AA}^2$ ) for $(V_{0.90}Mo_{0.10})OPO_4$ ( $\beta$ -VOPO <sub>4</sub> structure type). .....	233
Table 14.26	Anisotropic displacement parameters ( $\text{\AA}^2$ ) for $(V_{0.90}Mo_{0.10})OPO_4$ ( $\beta$ -VOPO <sub>4</sub> structure type). .....	233
Table 14.27	Interatomic distances ( $\text{\AA}$ ) for $(V_{0.90}Mo_{0.10})OPO_4$ ( $\beta$ -VOPO <sub>4</sub> structure type).....	233
Table 14.28	Assignment of the Guinier photograph of $(V_{0.99}Mo_{0.01})OPO_4$ ( $\beta$ -VOPO <sub>4</sub> structure type, S. G. <i>Pnma</i> ; $a = 7.7822(5)$ $\text{\AA}$ , $b = 6.1352(7)$ $\text{\AA}$ , $c = 6.9610(4)$ $\text{\AA}$ ). .....	234
Table 14.29	Assignment of the Guinier photograph of $(V_{0.98}Mo_{0.02})OPO_4$ ( $\beta$ -VOPO <sub>4</sub> structure type, S. G. <i>Pnma</i> ; $a = 7.7818(7)$ $\text{\AA}$ , $b = 6.1375(4)$ $\text{\AA}$ , $c = 6.9732(7)$ $\text{\AA}$ ). .....	235
Table 14.30	Assignment of the Guinier photograph of $(V_{0.95}Mo_{0.05})OPO_4$ ( $\beta$ -VOPO <sub>4</sub> structure type, S.G. <i>Pnma</i> ; $a = 7.7781(4)$ $\text{\AA}$ , $b = 6.1426(2)$ $\text{\AA}$ , $c = 6.9793(4)$ $\text{\AA}$ ). .....	236
Table 14.31	Assignment of the Guinier photograph of $(V_{0.90}Mo_{0.10})OPO_4$ ( $\beta$ -VOPO <sub>4</sub> structure type, S.G. <i>Pnma</i> ; $a = 7.7698(6)$ $\text{\AA}$ , $b = 6.1495(6)$ $\text{\AA}$ , $c = 6.9905(5)$ $\text{\AA}$ ). .....	237
Table 14.32	Assignment of the Guinier photograph of $(V_{0.80}Mo_{0.20})OPO_4$ ( $\beta$ -VOPO <sub>4</sub> structure type, S.G. <i>Pnma</i> ; $a = 7.7761(7)$ $\text{\AA}$ , $b = 6.1460(5)$ $\text{\AA}$ , $c = 6.9945(8)$ $\text{\AA}$ ). .....	238
Table 14.33	Assignment of the Guinier photograph of $(V_{0.70}Mo_{0.30})OPO_4$ ( $\beta$ -VOPO <sub>4</sub> structure type, S.G. <i>Pnma</i> ; $a = 7.7762(7)$ $\text{\AA}$ , $b = 6.1596(7)$ $\text{\AA}$ , $c = 7.0016(8)$ $\text{\AA}$ ). .....	239
Table 14.34	Assignment of the Guinier photograph of $(V_{0.90}Mo_{0.10})OPO_4$ ( $\gamma$ -VOPO <sub>4</sub> structure type, S.G. <i>Pbam</i> ; $a = 17.327(2)$ $\text{\AA}$ , $b = 8.875(2)$ $\text{\AA}$ , $c = 4.918(1)$ $\text{\AA}$ ). .....	240
Table 14.35	Assignment of the Guinier photograph of $(V_{0.80}Mo_{0.20})OPO_4$ ( $\gamma$ -VOPO <sub>4</sub> structure type, S.G. <i>Pbam</i> ; $a = 17.318(4)$ $\text{\AA}$ , $b = 8.880(3)$ $\text{\AA}$ , $c = 4.915(11)$ $\text{\AA}$ ). .....	241
Table 14.36	$V(WO_2)_2(P_2O_7)(PO_4)$ . Anisotropic displacement parameters ( $\text{\AA}^2$ ) with estimated standard deviations in parentheses. ....	248
Table 14.37	$Ru(WO_2)_2(P_2O_7)(PO_4)$ . Anisotropic displacement parameters ( $\text{\AA}^2$ ) with estimated standard deviations in parentheses. ....	249
Table 14.38	Assignment of the Guinier photograph of $W^{VI}(Sc^{III}_{0.5}W^{VI}_{0.5}O_2)_2(P_2O_7)(PO_4)$ , S.G. <i>C2/c</i> ; $a = 38.201(7)$ $\text{\AA}$ , $b = 12.919(8)$ $\text{\AA}$ , $c = 9.608(2)$ $\text{\AA}$ , $\beta = 102.10(1)^\circ$ .....	251
Table 14.39	Assignment of the Guinier photograph of $V^{III}(W^{VI}O_2)_2(P_2O_7)(PO_4)$ , S.G. <i>C2/c</i> ; $a = 37.1696(31)$ $\text{\AA}$ , $b = 12.7899(8)$ $\text{\AA}$ , $c = 9.4769(13)$ $\text{\AA}$ , $\beta = 102.319(8)^\circ$ . .....	252

XXVIII List of Tables

Table 14.40	Assignment of the XRPD of $(V_{0.6}^{III}V_{0.4}^{IV})(V_{0.1}^{IV}W_{0.9}^{VI}O_2)_2(P_2O_7)(PO_4)$ , S.G. $C2/c$ ; $a = 37.1714(31) \text{ \AA}$ , $b = 12.7884(12) \text{ \AA}$ , $c = 9.4852(8) \text{ \AA}$ , $\beta = 102.278(8)^\circ$ .....	253
Table 14.41	Assignment of the Guinier photograph of $Cr^{III}(W^{VI}O_2)_2(P_2O_7)(PO_4)$ , S.G. $C2/c$ ; $a = 37.016(3) \text{ \AA}$ , $b = 12.756(1) \text{ \AA}$ , $c = 9.428(1) \text{ \AA}$ , $\beta = 102.275(9)^\circ$ .....	254
Table 14.42	Assignment of the Guinier photograph of $Fe^{III}(W^{VI}O_2)_2(P_2O_7)(PO_4)$ , S.G. $C2/c$ ; $a = 37.187(4) \text{ \AA}$ , $b = 12.789(1) \text{ \AA}$ , $c = 9.484(1) \text{ \AA}$ , $\beta = 102.36(1)^\circ$ .....	255
Table 14.43	Assignment of the Guinier photograph of $Mo^{III}(W^{VI}O_2)_2(P_2O_7)(PO_4)$ , S.G. $C2/c$ $a = 37.355(7) \text{ \AA}$ , $b = 12.902(2) \text{ \AA}$ , $c = 9.550(2) \text{ \AA}$ , $\beta = 102.33(1)^\circ$ .....	256
Table 14.44	Assignment of the Guinier photograph of $Ru^{III}(W^{VI}O_2)_2(P_2O_7)(PO_4)$ , S.G. $C2/c$ $a = 37.054(4) \text{ \AA}$ , $b = 12.807(1) \text{ \AA}$ , $c = 9.454(1) \text{ \AA}$ , $\beta = 102.139(12)^\circ$ .....	257
Table 14.45	Assignment of the Guinier photograph of $Rh^{III}(W^{VI}O_2)_2(P_2O_7)(PO_4)$ , S.G. $C2/c$ ; $a = 37.043(3) \text{ \AA}$ , $b = 12.7768(9) \text{ \AA}$ , $c = 9.434(1) \text{ \AA}$ , $\beta = 102.245(9)^\circ$ .....	258
Table 14.46	Assignment of the Guinier photograph of $Ir^{III}(W^{VI}O_2)_2(P_2O_7)(PO_4)$ , S.G. $C2/c$ ; $a = 37.113(2) \text{ \AA}$ , $b = 12.819(1) \text{ \AA}$ , $c = 9.4610(8) \text{ \AA}$ , $\beta = 102.314(6)^\circ$ .....	259
Table 14.47	Assignment of the Guinier photograph of $In^{III}(W^{VI}O_2)_2(P_2O_7)(PO_4)$ , S.G. $C2/c$ $a = 37.839(7) \text{ \AA}$ , $b = 12.930(3) \text{ \AA}$ , $c = 9.530(2) \text{ \AA}$ , $\beta = 102.15(2)^\circ$ .....	260
Table 14.48	Assignment of the Guinier photograph of $cub-(V_{0.25}W_{0.25}P_{0.50})O_{2.5+\delta}$ , S.G. $Pm\bar{3}m$ ; $a = 3.7732(9) \text{ \AA}$ .....	263
Table 14.49	Assignment of the Guinier photograph of $cub-(V_{0.167}W_{0.333}P_{0.50})O_{2.5+\delta}$ , S.G. $Pm\bar{3}m$ ; $a = 3.7708(9) \text{ \AA}$ .....	263
Table 14.50	Assignment of the Guinier photograph of $cub-(V_{0.10}W_{0.40}P_{0.50})O_{2.5+\delta}$ , S.G. $Pm\bar{3}m$ ; $a = 3.770(1) \text{ \AA}$ .....	263
Table 14.51	Assignment of the Guinier photograph of $cub-(Cr_{0.167}W_{0.333}P_{0.50})O_{2.5}\square_{0.5}$ , S.G. $Pm\bar{3}m$ ; $a = 3.7712(9) \text{ \AA}$ .....	264
Table 14.52	Assignment of the Guinier photograph of $cub-(Fe_{0.167}W_{0.333}P_{0.50})O_{2.5}\square_{0.5}$ , S.G. $Pm\bar{3}m$ ; $a = 3.766(2) \text{ \AA}$ .....	264
Table 14.53	Assignment of the Guinier photograph of $cub-(In_{0.167}W_{0.333}P_{0.50})O_{2.5+\delta}$ , S.G. $Pm\bar{3}m$ ; $a = 3.761(5) \text{ \AA}$ .....	264
Table 14.54	Assignment of the Guinier photograph of $cub-(W_{0.50}P_{0.50})O_{2.75}\square_{0.25}$ , S.G. $Pm\bar{3}m$ ; $a = 3.771(2) \text{ \AA}$ .....	264

Table 14.55	Assignment of the Guinier photograph of $tet\text{-}(W_{0.75}P_{0.25})O_{2.5+0.375}$ , S.G. $P4/ncc$ ; $a = 5.290(2) \text{ \AA}$ , $c = 7.698(3) \text{ \AA}$ . .....	265
Table 14.56	Assignment of the Guinier photograph of $cub\text{-}(Fe_{0.1}V_{0.1}W_{0.3}P_{0.5})O_{2.5+\delta}$ , S.G. $Pm\bar{3}m$ ; $a = 3.7732(8) \text{ \AA}$ . .....	265
Table 14.57	Assignment of the Guinier photograph of $tet\text{-}(Sc_{0.167}W_{0.333}P_{0.5})O_{2.5}\square_{0.5}$ , S.G. $P4/ncc$ ; $a = 5.2760(6) \text{ \AA}$ , $c = 7.717(2) \text{ \AA}$ . .....	266
Table 14.58	Anisotropic displacement parameters ( $\text{\AA}^2$ ) for $(Mo_{0.33}W_{0.67})OPO_4$ ( $WOPO_4$ structure type). .....	267
Table 14.59	Assignment of the XRPD of $(Fe^{III}_{0.33}W^{VI}_{0.67})OPO_4$ ( $W^VOPO_4$ structure type) S.G. $P2_1/m$ ; $a = 6.5158(11) \text{ \AA}$ , $b = 5.1771(6) \text{ \AA}$ , $c = 11.0542(15) \text{ \AA}$ , $\beta = 90.20(1)^\circ$ . .....	267
Table 14.60	Assignment of the Guinier photograph of $(Cr^{III}_{0.33}W^{VI}_{0.67})OPO_4$ ( $W^VOPO_4$ structure type, S.G. $P2_1/m$ ; $a = 6.4740(10) \text{ \AA}$ , $b = 5.1569(4) \text{ \AA}$ , $c = 11.0486(18) \text{ \AA}$ , $\beta = 90.11(1)^\circ$ . .....	268
Table 14.61	Assignment of the Guinier photograph of $(Mo^{III}_{0.33}W^{VI}_{0.67})OPO_4$ ( $W^VOPO_4$ structure type, S.G. $P2_1/m$ ; $a = 6.5418(6) \text{ \AA}$ , $b = 5.2176(5) \text{ \AA}$ , $c = 11.1730(7) \text{ \AA}$ , $\beta = 90.307(6)^\circ$ . .....	269
Table 14.62	Assignment of the Guinier photograph of $(Cr^{III}_{1/6}W^{VI}_{5/6}O_3)_8(PO_2)_4$ {structure type $(WO_3)_8(PO_2)_4$ [95]; S.G. $P2_1$ ; $a = 6.483(2) \text{ \AA}$ , $b = 5.216(1) \text{ \AA}$ , $c = 17.22(1) \text{ \AA}$ , $\beta = 90.32(3)^\circ$ }. .....	270
Table 14.63	Assignment of the Guinier photograph of $(V^{III}_{1/6}W^{VI}_{5/6}O_3)_8(PO_2)_4$ {structure type $(WO_3)_8(PO_2)_4$ [95], S.G. $P2_1$ ; $a = 6.4929(8) \text{ \AA}$ , $b = 5.2217(5) \text{ \AA}$ , $c = 17.322(3) \text{ \AA}$ , $\beta = 90.486(7)^\circ$ }. .....	271
Table 14.64	Atomic coordinates of predicted new metastable polymorph of $VPO_4$ containing $VO_4$ and $PO_4$ tetrahedra obtained from DFT calculation, S.G. $Pnma$ ; $a = 8.4891 \text{ \AA}$ , $b = 5.6533 \text{ \AA}$ , $c = 9.0598 \text{ \AA}$ (left) and S. G. $P2_1/m$ ; $a = 5.5289 \text{ \AA}$ , $b = 9.1850 \text{ \AA}$ , $c = 8.8903 \text{ \AA}$ , $\beta = 95.6362^\circ$ (right). .....	273
Table 14.65	Assignment of the Guinier photograph of metastable $VPO_4\text{-m2}$ , $V_2(VO)(P_2O_7)(PO_4)$ obtained by moist $H_2$ reduction of $\beta\text{-VOPO}_4$ at $700^\circ\text{C}$ for one day, S.G. $P2_1/m$ ; $a = 8.794(4) \text{ \AA}$ , $b = 5.269(2) \text{ \AA}$ , $c = 10.398(6) \text{ \AA}$ , $\beta = 112.60(4)^\circ$ . .....	273
Table 14.66	Selected interatomic distances ( $\text{\AA}$ ) of $VPO_4\text{-m2}$ , $V_2(VO)(P_2O_7)(PO_4)$ obtained by DFT calculation with adjusted lattice parameters from the experimental XRPD pattern. ....	274



# 1 Introduction

More than 350 anhydrous phosphates containing just a single transition metal have already been structurally characterized [1, 2, 3]. The existence of this rather large number of transition metal phosphates can be attributed to the stability of the particular transition metal in different oxidation states, formation of various metal-oxygen coordination polyhedra, and various degrees of condensation of  $\text{PO}_4$  tetrahedra ( $Q^0$ ,  $Q^1$ ,  $Q^2$ ,  $Q^3$ ) [4]. Transition metal phosphates are attracting intense interest in solid state chemistry and materials science since many of their properties are economically promising. Phosphates are used in rechargeable batteries as cathode materials ( $\text{LiFePO}_4$  [5]), in fuel cells as hybrid proton exchange membrane (made of nafion and  $\text{Zr}(\text{HPO}_4)_2$  [6]), in hydrogen storage (porous nickel(II) phosphate [7]), as ionic conductors (NASICON and related compounds [8]), as non-linear optical materials ( $\text{KTiOPO}_4$  [9]), and as heterogeneous catalysts for the oxidation of small hydrocarbons (V/P/O based materials [10]).

Vanadyl pyrophosphate,  $(\text{VO})_2\text{P}_2\text{O}_7$  (VPP) has been extensively studied during the last decades due to its unique catalytic properties for the selective oxidation of *n*-butane to maleic anhydride (MA, Furan-2,5-dione) [11, 12]. To date VPP is the most active and selective catalyst material for that purpose [13]. The catalytic behavior is attributed to its unique physico-chemical properties and crystal structure (see Figure 1.1).

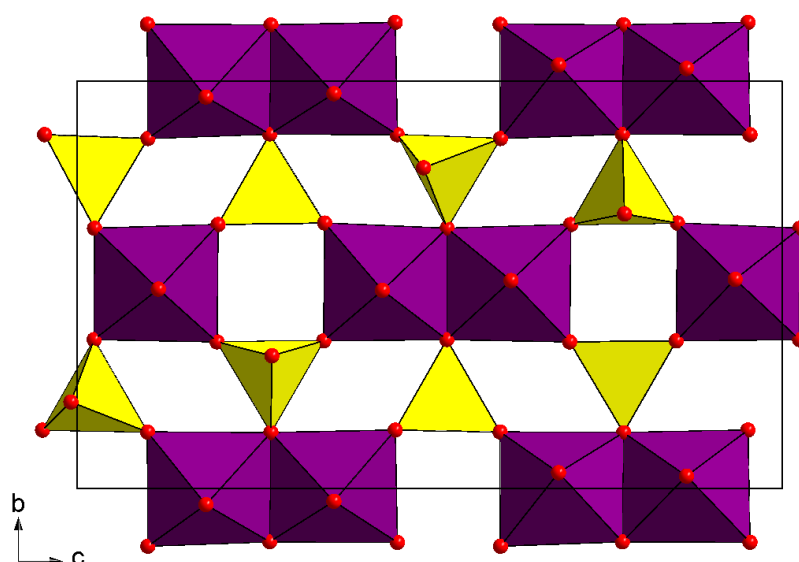


Figure 1.1 Polyhedral representation of the crystal structure of  $(\text{VO})_2\text{P}_2\text{O}_7$  [10], purple  $\text{VO}_6$  octahedra, yellow  $\text{P}_2\text{O}_7$  groups.

Formation of MA by oxidation of *n*-butane is exothermic (eq. 1.1) yet the key by-products (CO, CO<sub>2</sub>, H<sub>2</sub>O) are thermodynamically even more stable (eq. 1.2) and (eq. 1.3).



The enhancement of MA production and suppression of by-products (CO and CO<sub>2</sub>) formation can only be controlled kinetically by using a catalyst and securing adequate heat transfer from the reactor. Oxidative transformation of *n*-butane to MA occurs at the top one or two atomic surface layer of the VPP catalyst material which follows the generally accepted Mars-van Krevelen type (MvK) mechanism [14, 15, 16]. The catalytic reaction allows the insertion of three lattice oxygen atoms into and abstraction of eight hydrogen atoms from *n*-butane which is accompanied by the transfer of 14 electrons (oxidation) and ring closing to yield MA.

Instead of *n*-butane benzene was previously used for the industrial production of MA. Vanadium oxide supported on an inert oxide (alumina, silica, kieselguhr) with low surface area was then used as catalyst material. Benzene is easily oxidized to MA, however only four out of six carbon atoms are recovered in the final product (MA) which makes it an insufficient feedstock. Recognition of benzene as hazardous material and its rapid price rise, enforced the search for an alternative feedstock. Moreover, the natural gas exploration at huge scale in Northern Europe and the USA made available supplies of *n*-butane. Therefore, oxidative transformation of *n*-butane became the prevailing technology for MA production.

The use of a VPP catalyst for the heterogeneous catalytic reaction of *n*-butane was first reported by Bergman and Frisch about half a century ago yielding only 31 mol% of MA at 550 °C [17]. Commercial manufacturing was started four years later [18]. During the years, optimized synthesis procedure, developed engineering process, and improved characterization techniques could raise the production yield. Up to now the most active and selective catalyst material (V<sup>IV</sup>O)<sub>2</sub>P<sub>2</sub>O<sub>7</sub> is produced via topotactic transformation of the hemihydrate (VOHPO<sub>4</sub>·0.5H<sub>2</sub>O) [19, 20] precursor at about 360 °C as described in (eq. 1.4) and (eq. 1.5). This catalyst shows a conversion and yield of about 85% and 65% [21], respectively.





By characterization of both the surface and bulk of the catalyst material, it was shown that an amorphous surface layer on crystalline  $(\text{VO})_2\text{P}_2\text{O}_7$  might be the active phase for butane based MA production [22]. In situ spectroscopic and diffraction studies showed the existence of other polymorphs ( $\alpha$ -,  $\beta$ -,  $\gamma$ -,  $\delta$ -,  $\omega$ -) of  $\text{V}^{\text{V}}\text{OPO}_4$  [23, 24, 25] which can be attributed to the oxidation of VPP as shown in (eq. 1.6).



Since there is enough room to improve the yield of MA, scientists are still trying to tune the existing catalyst by addition of promoters or dopants. However, studies on the application of catalytic promoters did not lead to an improved catalyst performance [26, 27, 28, 29]. In addition, scientists went through considerable efforts to synthesize new catalyst materials. The catalytic activity and selectivity of various, more recently characterized, polynary vanadium(IV) phosphates containing a transition metal (Cr, Fe, Ni, Cu) in the phosphate framework do not reach the conventional vanadyl(IV) pyrophosphate catalyst [30, 31]. Nevertheless, a thin layer of porous silica coating prepared by spray drying from colloidal polysilicic acid (5-10% wt) in presence of catalyst precursor [32] has higher selectivity. However, due to longer equilibration time and expensive synthesis this material is not used in industry.

The metal center in the catalyst material is reduced after transfer of surface oxygen to the reactants and therefore rapid re-oxidation (re-generation) is necessary to complete the catalytic cycle which is performed by the combination of oxygen migration from the catalyst bulk (deeper layer) and gas-phase re-oxidation. P. K. Grasselli has explained that for the oxidative catalytic transformation, the catalyst material must have redox active centers [33] besides other criteria, e.g. appropriate lattice oxygen [33, 34], covalence and an amphoteric nature of the M-O bonds [33, 34], optimum bulk structure to recover anion vacancies, transfer of electron and oxygen without breakdown of the structure [34], and isolation of the active surface oxygen sites [34]. One of the strategies to optimize the catalyst material is insertion of a second redox active transition metal. Redox active transition metals with specific oxidation states are vanadium(IV, V), iron(II, III),

copper(I, II), manganese(III, IV), molybdenum(V, VI), and rhenium(IV, V, VI, VII) which could be potential components of oxidation catalyst materials.

The significance of MA can well be understood by its huge annual production of 2.7 million tones [35] by several companies (BASF, Germany; Sasol-Huntsman, Germany; DuPont-Monsanto, USA; Flint Hills Resources LP, USA; Mitsubishi, Japan; Denka-Scientific Design, Japan; Lonza Group AG, Switzerland; Polynt SpA, Italy; Suzhou Synthetic Chemical Co. Ltd, China). MA is used nearly in every field of chemical industry. For instances, MA is used:

- ❖ for the production of raw material (unsaturated polyester resin, UPR) in the manufacturing of stronger and lighter fiberglass which is used in automobiles, pleasure boats, wind turbine blades and constructions.
- ❖ for the production of raw material (1,4-butanediol) in the manufacturing of synthetic fibers (spandex/elastane) which have exceptional elasticity (polybutylene terephthalate, PBT).
- ❖ as lubricating oil additives to inhibit corrosion.
- ❖ as preservatives, artificial sweeteners (aspartame), flavor enhancers.
- ❖ in personal care products for example, in hair spray, detergents (acrylic acid), and paper-sizing agent (poly-acrylic acid).
- ❖ as insecticides, fungicides, herbicides in pharmaceuticals and also in water treatment plants.

Despite the vast body of literature (over 225 US patents since 1980) and the huge commercial production of MA (2.7 million tones/year) [35] the true chemical composition and the structural properties of the active site for this catalytic reaction under operando conditions are still under debate [36, 37]. Consequently, scientists are still investing their efforts to explore the mystery of this complicated catalytic reaction process.

**The prime object** of this research work was to synthesize and crystallize new ternary oxides  $MO_x/VO_y/PO_{2.5}$  ( $M$ : Mo, W;  $2.5 \leq x \leq 3$  and  $2 \leq y \leq 2.5$ ). Although research on the binary oxides, mentioned above was performed [38, 92, 97, 133, 134, 135, 217] no reports on the ternary systems are known in literature. In addition, one of the most important targets in this study was the quest for new catalyst materials within these systems for the oxidation of *n*-butane to MA.

One strategy to achieve this goal was to set an intermediate average oxidation state of vanadium in vanadyl phosphate via incorporation of another redox-active metal to enhance the catalytic performance [33]. The average oxidation state of vanadium in the active VPP catalyst is in the range of 4.1 to 4.2 [22, 39].

Besides the crystal-chemical aspect a further goal of this study was to establish in detail the electronic structure of the transition metal ions in newly synthesized phosphates. This knowledge should help to understand structure-property relations for the new compounds.

## 2 Experimental techniques

### 2.1 Introduction

In this research work chemical vapor transport reactions (CVT, in closed ampoules), classical solid state reactions, vapor phase moderated solid state reactions and heat treatment of the intermediate product after solution combustion synthesis (SCS) are performed at relatively high temperatures (400 to 1050 °C). Since the normal borosilicate glass can only withstand temperatures up to 600 °C, for high temperature reactions silica glass is used. It can persist up to 1100 °C. To work with silica glass certain glass-blowing skills are necessary.

### 2.2 Preparation of silica tubes

Sealed silica tubes and half ampoules are prepared by the following procedure.

- ❖ The supplied silica tubes ( $l \approx 150$  cm,  $d \approx 1.5$  mm, company GVB, Aachen, Germany) were cut equally into three pieces with the help of a diamond cutter. Then every piece was parted into two in an oxy-hydrogen flame to obtain so called half ampoule (only one side open silica tubes). These half ampoules are also used as vessels for high temperature solid state reactions in air.
- ❖ To make sealed ampoules, firstly the open end of the silica half ampoule is joined to the inner standard taper ground joint by help of an oxy-hydrogen flame and then washed with normal glass cleaning agent, dried in a drying oven at 100 °C and afterwards fitted to the vacuum line ( $10^{-3}$  to  $10^{-4}$  atm).
- ❖ Before the ampoules were charged with reactants, they are simultaneously heated ( $T \sim 800$  °C for at least four hours) and evacuated to remove moisture, adsorbed to the inner wall of the silica tubes [40].
- ❖ After that the empty ampoules are cooled down to ambient temperature and filled with commercial argon gas (4N). The reactants and transporting agent or mineralizer are transferred carefully to the bottom end of the ampoule avoiding the adherences of the reactants to the ampoule wall.

- ❖ The bottom end of the ampoule was cooled to liquid nitrogen to prevent the vaporization of the reactants during capillary shaping at  $l \sim 10$  cm away from the end by oxy-hydrogen flame and again connected to the evacuation line.
- ❖ Afterwards the ampoule was tested for appropriate evacuation using a spark tester (Edwards High voltage, part of BOC Ltd., England) and sealed on-line with the oxy-hydrogen flame.

### 2.3 Vacuum line

The vacuum line is used for the preparation of evacuated sealed silica tubes. It is the combination of drying furnace and vacuum oil pump (model E2M2, Edwards High vacuum Int., part of BOC Ltd., England) and drying towers (Figure 2.1 [41]). The silica tubes were heated by the heating furnace and evacuated simultaneously by the vacuum pump. The commercial argon (4N) gas was purged into the tube before transferring the reactants inside the tube to maintain the inert atmosphere. The commercial argon gas was connected to safety bubbler (concentrated sulfuric acid) prior to pass through four different drying towers to purify the gas. The drying towers were filled with potassium hydroxide, silica gel, molecular sieve and phosphorus pentoxide, accordingly.

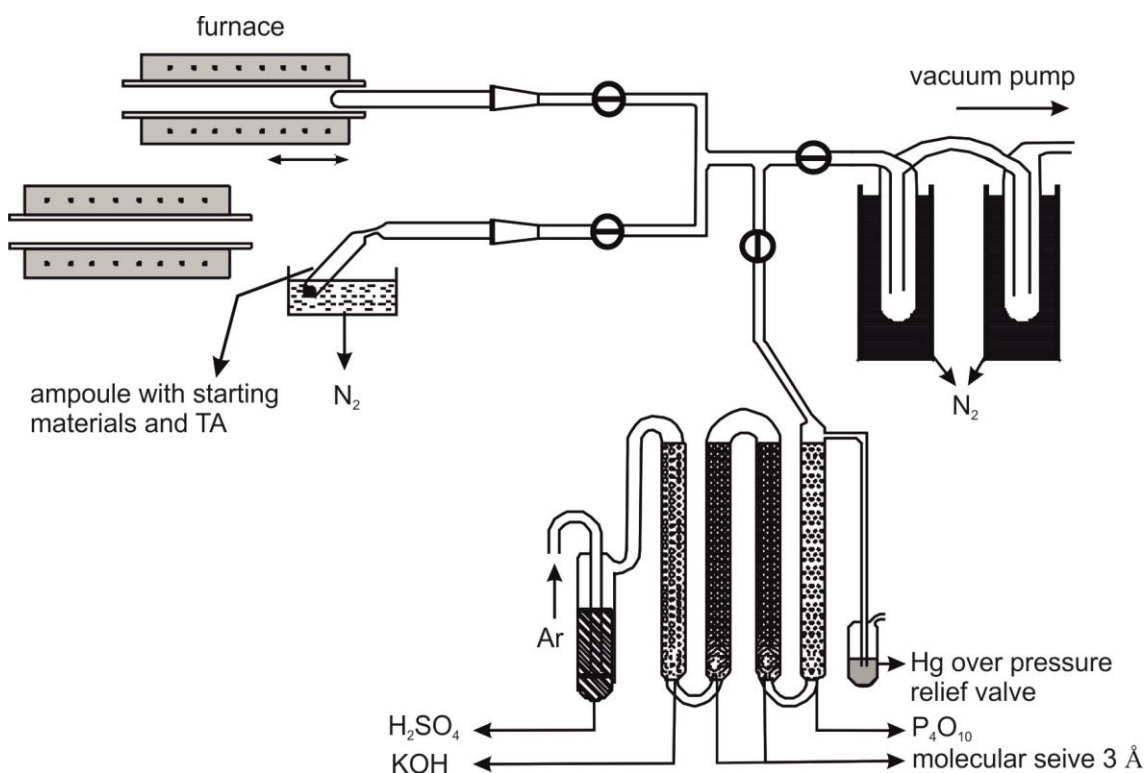


Figure 2.1 Sketch of the vacuum line [41].

## 2.4 High temperature furnaces

In this present work different kinds of high temperature furnaces were used for the synthesis and crystallization process.

Two-zone horizontal tubular furnaces (HTM Reetz GmbH, type LOBA, Berlin, Germany) were used for CVT experiments. Their maximum working temperature is 1150 °C. It is also called “transport furnace”. A continuous temperature gradient (Figure 2.2) is maintained between two defined temperatures. The temperature of the furnace is controlled by Ni/Ni-Cr thermocouples. Ceramic stoppers were used at both ends of the furnace to stabilize the inside temperature by minimizing thermal convection.

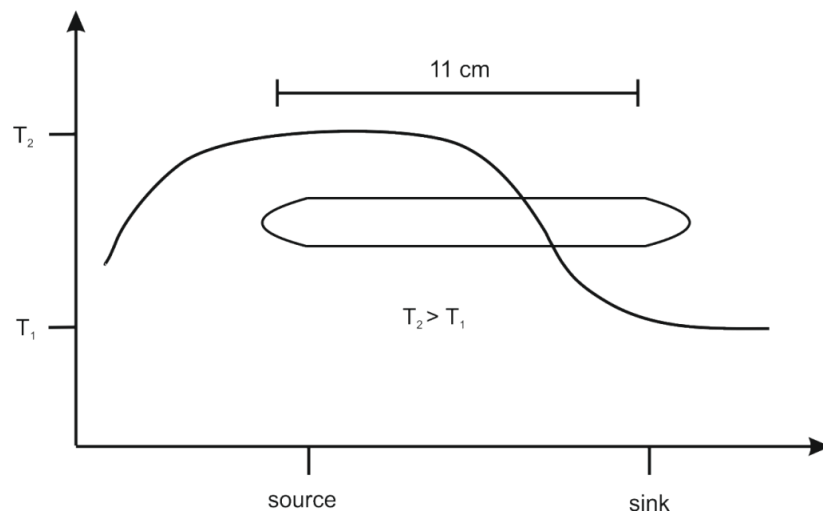


Figure 2.2 Temperature profile over the length of a transport ampoule in a two zone horizontal furnace.

Muffle furnaces with flap door (model L5/11 controller B170 and L5/12 controller B180, Nabertherm, Germany) were used for isothermal heating experiments. The muffle is heated by ceramic heating plates from two sides (top and bottom). The maximum working temperature is 1100 °C or 1200 °C.

Single zone tubular furnaces were used to dry the ampoules during evacuation. In such furnace a heating coil made of Kanthal A1 wire (Fe: 72.2%, Cr: 22%, Al: 5.8%,) wound to the ceramic tube of 4 cm inner diameter which is made of Pythagorasmass is surrounded by the insulator and the outer surface is made of steel. The temperature of the furnace is controlled by a Ni/Ni-Cr thermocouples.

## 2.5 Solid states reactions

In solid states reactions the rate of reaction is slow due to slow diffusion rate of the reactants. Annealing at higher temperature increases the diffusion rate and hence increases the rate of reaction. However, “vapor phase moderated solid state reaction” can speed up the reaction rate due to increased diffusion via the gas phase as an effect of the mineralizer. Some mineralizers (e.g.  $\text{Cl}_2$ ) can corrode the silica tube and might dissolve the  $\text{SiO}_2$  from the ampoule wall into the system. Moreover, by reducing the diffusion path length, the rate of reaction can be increased which can be achieved by intimate mixing of the reactants. This can be attained through making a pellet of the reactants mixture at high pressure by following way:

- ❖ All the reactants were ground thoroughly in an agate mortar until a fine homogeneous powder was obtained.
- ❖ Ca. 200 mg of the finely ground mixture were transferred to the clean and dry mould and then 25 kN pressure was applied for 25 minutes by a hydraulic press (Figure 2.3).
- ❖ After that the pressure was released cautiously and a pellet of about  $12 \times 2 \times 2 \text{ mm}^3$  was removed carefully from the mould.

The pellet has less contact with the surface of silica ampoule. This minimizes the reactions between the sample and the silica wall which is regarded as a second advantage of this method.

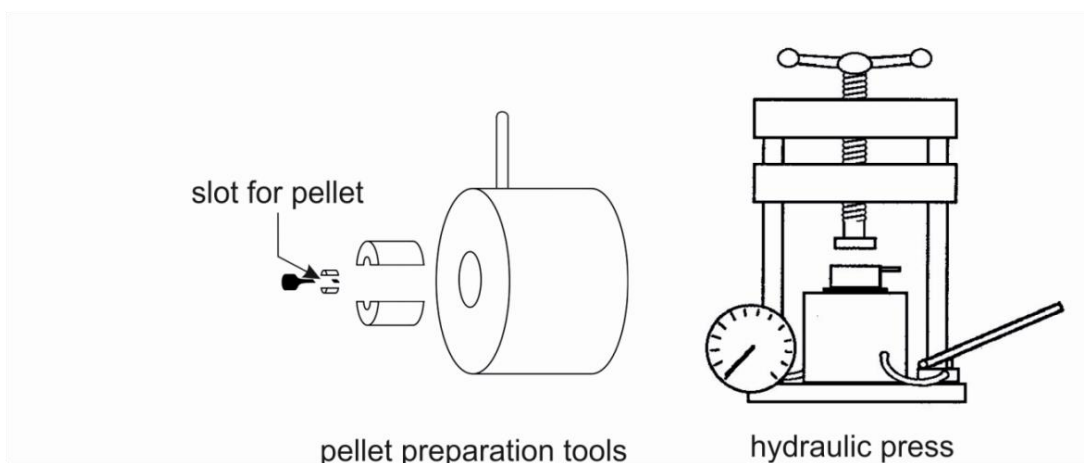


Figure 2.3 Sketch of the hydraulic press and the tools for the preparation of pellets [41].

## 2.6 Chemical vapor transport

Chemical vapor transport is a very powerful crystallization method developed by Schäfer [42, 43]. This technique is also useful for the purification of solids and for the preparation of doped materials. This technique consists of reaction of a condensed source material,  $A(s)$  with a transporting agent,  $L(g)$  forming gaseous species  $AL(g)$  at the source side of evacuated sealed ampoule. And then transportation of  $AL(g)$  to the sink side of the ampoule due to temperature gradient and deposition of condensed phase under release of transport agent (Figure 2.4).

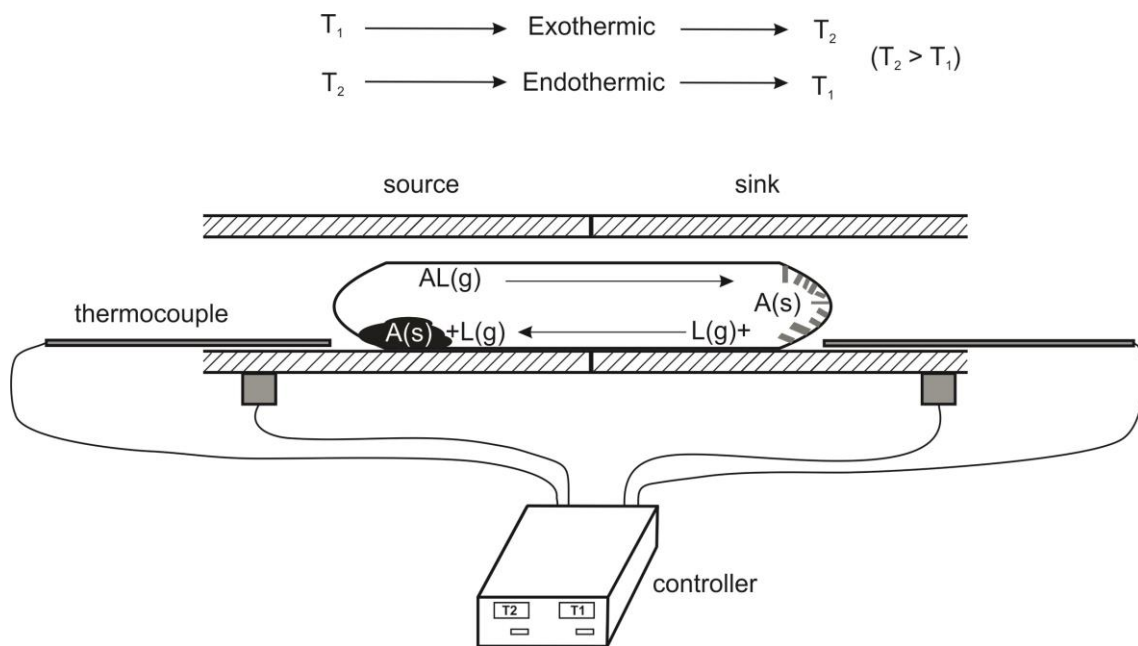


Figure 2.4 Layout of a sealed silica ampoule in the temperature gradient of a two-zone tubular furnace.

For most of the transport experiments the following procedures are maintained.

- ❖ The two-zone tubular furnaces (transport furnaces) are kept in horizontal position to maintain convection as small as possible.
- ❖ The already prepared sealed ampoule is put into the transport furnace in such a way that two-thirds of the ampoule are in the source temperature region and one-third remains at the sink to make sure of a small crystallization zone.
- ❖ For pre-reactions the ampoule is heated at lower temperature before heating to the final equilibration temperature.



- ❖ After that the ampoule is kept in a reverse temperature gradient for one day. Thus unwanted crystal seeds are transported from the sink region. This procedure is called *cleaning transport*.
- ❖ Usually the time of transport experiments ranges from a couple of days to some weeks. When the transport experiment is finished the source side of the ampoule is taken out from the furnace first and cooled by cold water or liquid nitrogen so that the gas phase is condensed at the source side. It keeps the crystals at the sink side clean from the condensed gaseous species.
- ❖ The cold ampoule is cut into two parts by a diamond saw. The crystals from the sink and the solid from the source are collected very carefully. If they are attached firmly to the ampoule wall, the half ampoules are filled with 5% hydrofluoric acid (prepared by dilution with H<sub>2</sub>O from 35% HF). After a couple of hours, the unsoldered crystals are washed 2 to 3 times with distilled water and collected. Later, they are dried in the drying oven for about one hour and then examined under a microscope.

## 2.7 Solution combustion synthesis

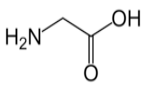
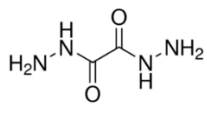
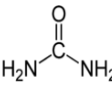
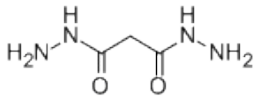
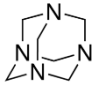
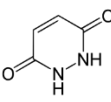
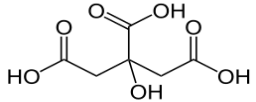
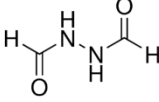
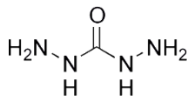
A common example of combustion is the burning of natural gas (CH<sub>4</sub>) in air. It leads in an exothermic reaction to the formation of CO<sub>2</sub>(g), H<sub>2</sub>O(g) and “fire”, a huge amount of energy. CH<sub>4</sub> acts as fuel and O<sub>2</sub> from air as oxidizer. The combustion synthesis is also called fire synthesis or **S**elf-propagating **H**igh temperature **S**ynthesis (SHS). For fire synthesis or combustion synthesis the necessary components are fuel and oxidizer [44]. To ignite the combustion reaction choosing the right temperature is crucial. The reaction between the fuel and the oxidizer is actually a redox reaction with liberation of a huge amount of energy and gaseous reaction products.

Solution combustion synthesis (SCS) refers to the combustion of the dry mass or gel obtained from a homogeneous solution of precursors, fuel and oxidizer. Here nitric acid or ammonium nitrate or metal nitrates are used as oxidizer and the low melting high energy material containing C, N, H is used as fuel, e.g. glycine, urea etc (see Table 2.1). They liberate small gaseous molecules, CO<sub>2</sub>, H<sub>2</sub>O, N<sub>2</sub> during the combustion process.

### 2.7.1 Selection of fuel

Although there is no hard and fast rule for the use of a particular type of fuel for a particular transition metal, glycine is relatively good for chromium and related oxides. Similarly, urea is good for alumina and related oxides [44]. Eventually the fuels are also used as chelating agent to form coordination polymers with the metal atom to ensure the homogeneous solution and distribution of components in the gel evenly which is very important for successful SCS.

Table 2.1 Different fuels and their structure.

Type of fuel	Structure	Type of fuel	Structure
Glycine		Oxalic acid dihydrazide	
Urea		Malonic acid dihydrazide	
Hexamethylene-tetramine		Maleic hydrazide	
Citric acid		Diformyl hydrazide	
Carbohydrazide			

### 2.7.2 Metal to fuel ratio in SCS

Metal nitrates are the preferred precursor materials in SCS. As a general requirement, metal oxide precursors should decompose at low temperature with evolution of a large amount of gas. Metal to fuel (m/f) ratio is very important since the fuel serve as chelating agent. Ideally, the amount of fuel/chelator should allow formation of a homogeneous coordination polymer (“gel”) with the metal precursors on evaporation. Typically in the experiments reported in this thesis  $m/f \approx 1:3$  was used. Since the amount of fuel used for a particular reaction has been set, from the balanced redox reaction the required amount of oxidizer can be calculated.

### 2.7.3 Oxidizer to fuel ratio

To ensure complete combustion and for the maximum release of energy, the equivalence ratio of oxidizer to fuel (o/f) should be unity so that no residual carbon is present in the combustion products. Deviation of (o/f) ratio from unity is known as fuel rich ( $o/f < 1$ ) and fuel lean ( $o/f > 1$ ). The equivalence ratio ( $o/f = 1$ ) can be transformed into a molar ratio from the completely balanced redox reaction between fuel and oxidizer (eq. 2.1).



### 2.7.4 Procedure for SCS

The complete procedure for a SCS is given by the flow chart in Figure 2.5.

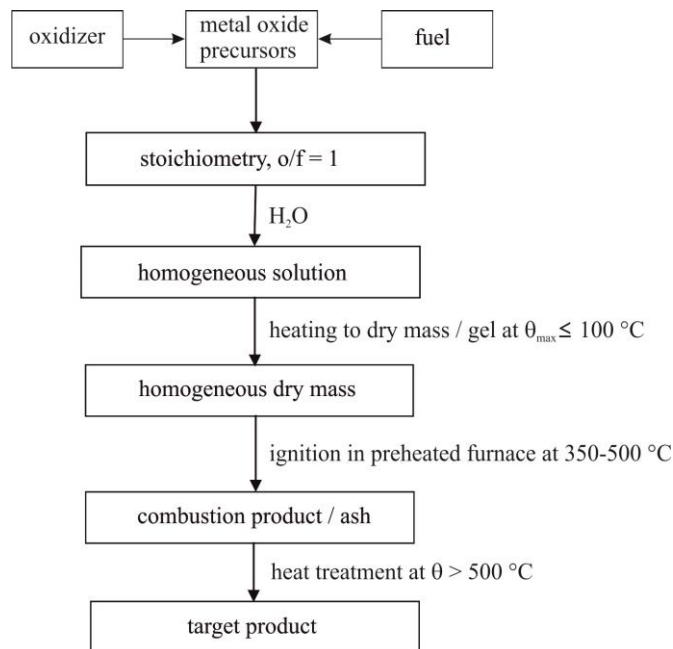


Figure 2.5 Flow chart of a SCS experiment.

The combustion process starts with evaporation of the rest water molecules from the partially dry or gel type mass before melting and decomposition occurs. Afterwards ignition starts with a hot spot. The redox mixture burns off and the reaction propagates by itself with further swelling of the reaction mixture and liberation of large amounts of gaseous products. The red hot spot observed during combustion indicates the temperature would be around 800 °C which is sustained for a very short period of time, only. However, the temperature during combustion was reported to be over 1200 °C [44]. Both the short duration of reaction time and evolution of the large amounts of gases

favor the formation of materials with small particle size. Fuel rich condition favors the formation of materials with higher specific surface area [45]. Instead of high temperature, the short persistent time allows to use normal glass beakers as reaction containers. The whole process needs around two to three minutes. The high temperature treatment of the reaction intermediates after SCS leads to the formation of the target compound.

The dried reaction mixture (“gel”) will not combust in a self-propagating reaction if:

- ❖ the concentration of the fuel and oxidizer in the gel is too low
- ❖ already during the drying process partial reaction starts
- ❖ the ignition temperature is low

Since in SCS temperatures up to 800 °C are obtained within a very short time (few seconds) the system could be described as isolated. As a result the maximum adiabatic temperature,  $T_{ad}$  experienced by the system can be estimated according to (eq. 2.2) taking the thermodynamic data from literature. The value of  $\Delta H_r^0$  can be calculated according to (eq. 2.3). A typical example is given in ref. [44].

$$-\Delta H_r^0 = \int_{T_0}^{T_{ad}} (\sum \Delta C_p)_{\text{product}} dT \quad (\text{eq. 2.2})$$

$$\Delta H_r^0(\text{reaction}) = \Delta H_f^0(\text{products}) - \Delta H_f^0(\text{reactants}) \quad (\text{eq. 2.3})$$

Where  $\Delta H_r^0$  is the enthalpy of reaction at 298 K ( $T_0$ ),  $n$  is the stoichiometric coefficient,  $C_p$  is the heat capacity of the solid reaction products.

The advantages of solution combustion synthesis over classical solid state reactions are:

- ❖ SCS leads to the formation of particles with high specific area (nano particles) due to formation of large amounts of volatile products during combustion
- ❖ The homogeneous dispersion of all elements on an atomic level allows synthesis of uniform materials
- ❖ SCS is a comparatively fast and cost effective method of synthesis
- ❖ Solid reaction intermediates from SCS frequently allow formation of thermodynamically metastable phases which are hardly accessible by classical solid state reactions.

### 3 Characterization techniques

A combination of techniques have been used to characterize the compounds synthesized throughout this research work including x-ray single crystal data analysis, XRPD, <sup>31</sup>P-MAS-NMR spectroscopy. The oxidation states of some selected compounds are determined by XPS measurements and presence of paramagnetic center is established by EPR as well as magnetic measurements. The band gap of some compounds was determined by conductivity measurement and compared with the results obtained from UV/Vis/NIR measurements. The elemental analyses were performed with EDX spectroscopy. The basic principle of above mentioned techniques, instrumentations and the specific experimental set up employed in this work are discussed here after.

#### 3.1 X-ray diffraction techniques

The electromagnetic radiation with photon energy of 100 eV to 100 keV is in the range of x-rays. Since the x-ray with low wavelength or high energy is comparable with atomic size and can penetrate through the sample and provides bulk structural information.

The most important physical phenomenon in XRD is the interaction of x-ray with the electrons of atoms. This type of collision is called elastic interaction or Compton scattering i.e. the diffracted x-ray do not change its energy, changes only the momentum. Most of the time diffracted waves from the periodic arrangement of atoms (crystal) have destructive interference but in few specific directions they interfere constructively following the Brags equation (eq. 3.1) to have sharp reflexes of same symmetry as the arrangement of atoms which allow us to get structural information of the material.

$$n \cdot \lambda = 2 \cdot d \cdot \sin \theta \quad (\text{eq. 3.1})$$

$n$  an integer determine the order of diffraction peak

$\lambda$  wavelength of the x-ray

$d$  interspacing distance of the atomic lattice planes

$\theta$  incident or scattering angle of x-ray

### 3.1.1 The Guinier technique

XRPD (Guinier technique) is the most widely used technique for the characterization of crystalline materials in this thesis. The primary source of x-ray is the x-ray tube. Synchrotron radiation is another source of x-ray which has thousands to millions times higher intensity than that of lab x-ray.

In laboratory x-ray tube, a focused electron beam is accelerated across the high voltage field and bombard to the stationary or rotating solid target material. As the electrons decelerated a continuous white radiation is generated which is called “Bremsstrahlung” or white radiation. However, in diffraction technique monochromatic x-ray radiation is used which is produced by ionization of  $1s$  (K shell) electron of target material by the high energy electron beam. That means after ionization the vacant  $1s$  level is filled by the higher energy electron ( $2p$  or  $3p$ , outer shell electron) via emitting the excess energy as an x-ray which is characteristic. The transition  $2p \rightarrow 1s$  and  $3p \rightarrow 1s$  is called  $K\alpha$  and  $K\beta$ , respectively where  $K\beta$  has higher energy than  $K\alpha$ . Indeed  $K\alpha$  is splitted into  $K\alpha_1$  and  $K\alpha_2$  due to two possible spin state of  $2p$  electron relative to vacant  $1s$  orbital.

The generated x-ray leaves the x-ray tube through the beryllium window. For XRPD the monochromatic x-ray is used. This is obtained by placing a large (1 to 2 cm long) bent quartz ( $\alpha$ -SiO<sub>2</sub>) crystal in the path of x-ray (see Figure 3.1). The crystal is placed in such a plane (101) that allows to pass only intense convergent  $K\alpha_1$  x-ray beam by separation of it from the others rays.

The monochromatic x-ray beam hits the powder sample where the crystalline domains i.e. set of lattice planes are randomly oriented in every possible orientation. For each set of lattice planes at least few crystallites have the possibility to orient at Bragg angle,  $\theta$  to the incident beam to fulfil the diffraction condition. The film is arranged so that the diffracted beam focuses at the surface of the film. The undiffracted radiation is stopped by a beam stopper, placed in front of the film which prevents it from blackening.

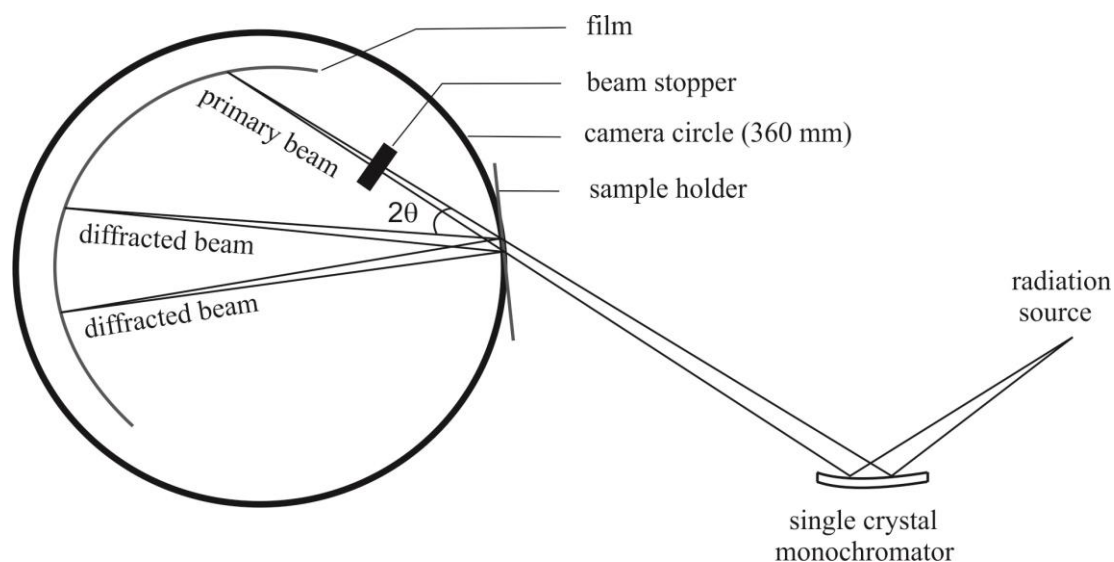


Figure 3.1 Optical path of Guinier camera.

### 3.1.1.1 Recording of an X-ray powder diffraction (XRPD) pattern

- ❖ A few mg of sample are finely ground in an agate mortar.
- ❖ The powder is transferred to Mylar foil (Fluxana GmbH & Co. KG, type TF-160) which is fixed by a ring in the sample holder.
- ❖ 1-2 drops of ethanol help the sample to adhere on the foil and to spread over the irradiation area of the foil to ensure statistical distribution of particles.
- ❖ The powder diffraction pattern were recorded at ambient temperature using an image plate [46] Guinier camera (HUBER G670, Cu- $K\alpha_1$  radiation,  $\lambda = 1.54051 \text{ \AA}$ ) with integrated read out system.
- ❖ The intensity vs.  $2\theta$  raw data are obtained as *gdf* format and converted into *ASCII*.
- ❖ *ASCII* data are processed (background correction, data smoothing) by using the program Match [47].
- ❖ Using the program ORIGIN [48] the two-dimensional XRPD (also called Guiner photograph), normalized intensity vs  $4\theta$  is plotted and evaluated. In the  $4\theta$  scale one mm equals one degree.

### 3.1.1.2 Simulation and analysis of X-ray powder diffraction pattern

To check the purity of the synthesized (already known) compounds the powder diffraction pattern of that compound is compared with the simulated diffraction pattern obtained from *Inorganic Crystal Structure Database* (ICSD) [2]. The starting positional parameters are obtained from the program with the help of *Direct methods* by using the

program LAZY PULVERIX [49]. Here the relative intensity,  $I/I_0$  of each diffraction peak was calculated according to the equation (eq. 3.2).

$$I/I_0 = |F_c|^2 \cdot PLG \cdot H \cdot T \cdot A \quad (\text{eq. 3.2})$$

$F_c$	Calculated structure factor
$PLG$	Polarization, Lorentz and Geometric factor
$H$	Multiplicity factor
$T$	Temperature factor
$A$	Absorption factor

The structure solution of new compounds is also checked by comparing the simulated diffraction pattern obtained from the single crystal structure solution data set with the original powder diffraction pattern.

The peak position and the intensities are characteristics for every material. The peak position depends on the unit cell parameters and the intensities depend on the type of element i.e. scattering factor of the lattice point. The unit cell parameters of a compound are determined from the XRPD by using the program SOS [50]. The SOS1 makes zero point correction with the help of internal standard,  $\alpha$ -quartz and peak position correction by the corresponding polynomial regression of the fourth order. Accurate peak position and indexing allows the program SOS2 to determine the unit cell parameters by using “Least square errors” principle. However, for a new compound the indexing can be attained either from the structure solution or by using computer programs like TREOR-90 [51], DICVOL [52], VISSER [53] which are included in one package program WinPLOTTR [54]. All of these programs use the Wolf algorithm.

### 3.1.2 Single crystal investigations

Single-crystal X-ray diffraction is a powerful nondestructive analytical technique which provides complete information about the structure of crystalline substances, including unit cell dimensions, bond-distances, bond-angles, and on site-occupancy.

#### 3.1.2.1 Crystal selection and mounting

To get the good quality x-ray diffraction data the selection of good quality crystal is very important. The screening of single crystal is done under cross polarizing microscope. A good quality single crystal should have the following criteria:



- ❖ uniform internal structure i.e. should not be fractured, twined or physically distorted.
- ❖ proper size and shape i.e. in the range of 0.1 to 0.3 mm in order to maintain minimum absorption extinction.

For x-ray data collection single crystal is mounted by the following way:

- ❖ the x-ray amorphous glass fiber of diameter of 20 to 70  $\mu\text{m}$  is made by pulling the molten silica.
- ❖ the prepared glass fiber (1 to 1.5 cm long) is glued with the sealing wax on single crystal holder (made of brass) which is suitable to insert into goniometer head.
- ❖ the already selected good quality single crystal is then mounted on the tip of the silica glass fiber with minimum amount of adhesive in such a way so that there is minimum absorption of x-ray due to glass fiber and adhesive during data collection (see Figure 3.2).

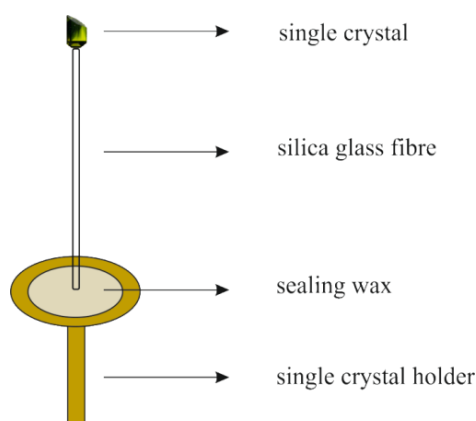


Figure 3.2 Schematic representation of single crystal mounted at the tip of a glass fiber for x-ray data collection in order to structural investigation.

### 3.1.2.2 Intensity data collection

**Charge Coupled Device (CCD)** detector uses large chips (dia. 1-2 inches,  $4096 \times 4096$  pixels) based on x-ray sensitive layer of fluorescent material, Gadolinium oxide sulfide. To collect as much data as possible the detector surface is magnified to  $95 \times 95 \text{ mm}^2$  using bundles of conical optical fibers. Although the reflections are recorded in short time the background noise level is problematic especially when long exposure time is needed for weakly scattering materials or the crystal containing weak superstructure reflections.

**Image Plate (IP)** detector is useful to avoid the high background noise level. Nevertheless, due to its large diameter (350 mm) the entire data set can be measured while rotating the crystal about a single axis. However, IP detector is slower than CCD detector. The surface of the IP consists of  $\text{Eu}^{2+}$  doped BaBrF. During x-ray exposure  $\text{Eu}^{2+}$  is oxidized to  $\text{Eu}^{3+}$  and the free electron stay at the interstitial lattice sites forming color centers. The latent image is read out by red laser scan. The red laser reduces the  $\text{Eu}^{3+}$  to  $\text{Eu}^{2+}$  with the emission of photons. The intensity of the emission by each pixel is then measured by a photocell with photomultiplier. The IP detector can be recycled by removing all color centers by exposing with intense white light. Besides the sensitivity both systems are similar.

The data collection strategy of both area detectors (CCD and IP) is same. The crystal is precisely centered at the goniometer with the help of video camera. Few orientation photographs at that stage provide information about the crystal quality and the diffracting power and also about tentative unit cell. The crystal is rotated ( $0.3\text{-}1.0^\circ$  for CCD,  $0.5\text{-}2.0^\circ$  for IP) about the vertical axis to bring the range of reciprocal lattice points near the Ewald sphere to cut those in gray area (see Figure 3.3).

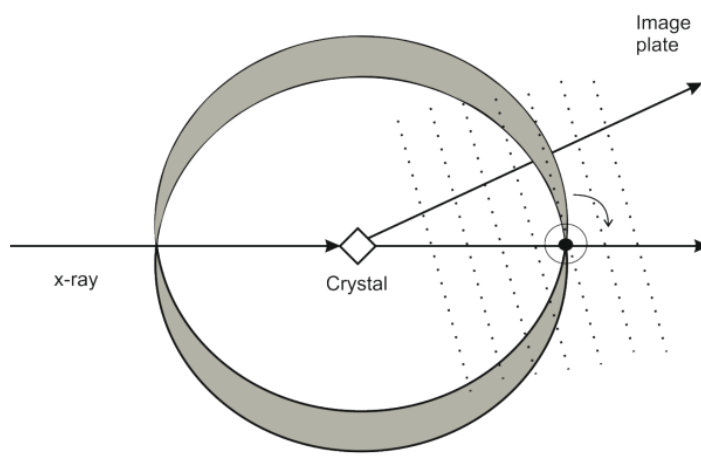


Figure 3.3 Principle of the area detector in terms of the Ewald construction.

After the first 10-20 minutes exposure probable crystal system can be selected on the basis of the differences between the scattering vectors which can be described as reciprocal base vectors. Considering the initially determined intensities and the unit cell the suitable parameters for the measurement, for example, exposure time, rotation angle range, detector to crystal distance, and angle increment were chosen.

One of the great advantages of the area detector is that the complete diffraction properties of the crystal can be obtained from different reciprocal lattice photographs. From the

reciprocal lattice the presence of twinning, satellites, any foreign reflections, diffuse reflection streaks can be identified. This area is also suitable for the identification of systematic absence. To obtain a more accurate orientation matrix the actual intensity measurement is compulsory which is done by selecting a range of spots through the data. Then the software can determine the reflection profile for all data to provide a new matrix which ultimately determine the exposure and the component of the each reflection position. A circular area, determined by the profile function is scanned and all pixels inside the area are summarized to the raw intensity whereas intensities around the edge are used to calculate the background. Therefore, the net intensities are obtained by scaling and subtracting from the raw intensity. The well-determined peak positions obtained by calculating of their direction cosines and standard deviation from each reflection are used for final refinement of the cell parameters. After data collection and data reduction the corrected intensities are converted to observed structure factor  $F_0$ , which is comparable to the calculated structure factor  $F_c$ . The starting positional parameters are achieved from corrected data set with using *Direct methods* [55] or *Charge Flipping* [56] and final refinement is carried out using the program SHELX-97 [55].

### 3.1.2.3 Interpretation of results

The solution of the crystal structure is to find the atomic positions within the unit cell from the intensity data set containing the information of unit cell parameters and space group. By Fourier transformation x-ray diffraction phenomenon is converted through the periodic array of electron density into the individual structure factor  $F_0(hkl)$ . If all of the individual wave with their phases and amplitude (i.e.  $F_0$ ) are known the Fourier synthesis will provide the electron density map and therefore the crystal structure. The Fourier summation equation is given in (eq. 3.3).

$$\rho(x, y, z) = \frac{1}{V} \sum_{h,k,l=-\infty}^{+\infty} F_{hkl} \cdot e^{-i2\pi[hx+ky+lz-\phi(hkl)]} \quad (\text{eq. 3.3})$$

$\rho(x, y, z)$  electron density function at the coordinates  $xyz$  in unit cell

$V$  volume of the unit cell

$hkl$  miller indices

The electron density  $\rho(x,y,z)$  can be determined for every point  $x,y,z$  for a single asymmetric unit of a unit cell. The location of electron density maxima corresponds to the atomic coordinates in the unit cell. The experimental intensity data provide only the

amplitude, however the phase information  $\phi(hkl)$  is missing which is known as *phase problem*. Currently three methods are available to recover the phase from the corresponding diffraction amplitude obtained by regular x-ray single crystal experimental measurements.

**Patterson method** was introduced by Aurther Lindo Patterson [57, 58] to determine the structure model based on Fourier synthesis by using (eq. 3.4)

$$P_{u,v,w} = \frac{1}{V} \sum_h \sum_k \sum_l |F_{hkl}|^2 \cdot \cos[2\pi(hu + kv + lv)] \quad (\text{eq. 3.4})$$

Where,  $P_{u,v,w}$  is the Patterson function at coordinate  $u,v,w$  of Patterson space. They are not directly related to the atomic coordinates  $x,y,z$  but refer to the same axes and unit cell within the unit cell volume  $V$ , and the structure factor  $|F_{hkl}|$  of the plane  $hkl$  indices.

The maxima in the calculated Patterson function for the whole unit cell corresponds to the ends of the interatomic vectors. The relative intensity of Patterson maxima is the product of the atomic numbers and the highest peak corresponds to the origin of the cell. This method is very useful for molecules containing few heavier atoms than the rest of the atoms. However it become complicated with roughly equal atomic number of atoms.

**Direct methods** use the relationships between the intensities of the various reflections which lead to the direct solution of phase problem, “*electron density in a structure can never have a negative value and that is concentrated in well-defined maxima*”. Based on this assumptions Sayre developed the following (eq. 3.5).

$$F_{hkl} = k \sum_{h'k'l'} F_{h'k'l'} \cdot F_{h-h',k-k',l-l'} \quad (\text{eq. 3.5})$$

In other words, the structure factor for any reflection  $hkl$  can be calculated as the sum of the products of the structure factors of all pairs of reflections whose miller indices sum to  $hkl$ . *i.e*

$$E_{321} = E_{100} \cdot E_{221} + E_{110} \cdot E_{211} + E_{111} \cdot E_{210} + \dots \quad (\text{eq. 3.6})$$

Karle and Hauptman developed the *Triplet relationship* (eq. 3.7) [59, 60] for centrosymmetric structures where the phase problem is reduced to sign problem.

$$S_{hkl} \approx S_{h'k'l'} \cdot S_{h-h',k-k',l-l'} \quad (\text{eq. 3.7})$$

For noncentrosymmetric structures the phase angle  $\Phi$  must be determined which is analogous to the triplet sign relationship (eq. 3.8).

$$\Phi_{hkl} \approx \Phi_{h'k'l'} \cdot \Phi_{h-h', k-k', l-l'} \quad (\text{eq. 3.8})$$

On the basis of a starting data set from well known or arbitrarily specified phase solutions the final structure model can be computed and that can be cross examined with the help of higher members of Sayre equations, e.g quartet, quintet relations.

**Charge flipping** method [61, 62, 63] is useful when the structure solution is difficult or impossible by direct methods or related techniques. Charge flipping uses the iterative algorithm and alternates between the real and reciprocal space to solve the phase problem. Using this algorithm, the charge flipping reconstruct approximate electron density from structure amplitude. One of the most important advantages of this method is that it does not need any preliminary knowledge about the atom types, chemical composition or space group symmetry. Therefore, this method is mostly suitable for the structure solution where the atoms form continuous domain in more than 3D space, for instance, modulated structures, structures with pseudo symmetry, quasicrystals. The computer program SUPERFIIP [56] stands for *charge flipping in superspace* is an effective tool for the application of charge flipping algorithm.

### 3.1.2.4 Structure solution and refinement

**Least Squares Refinement** is a powerful analytical method used to compare the observed data with the calculated data to have an idea about the actuality of the structure model. However, to solve the structure by this method directly from the intensity data without developing a model first using one of the methods described before is not possible.

**R-values** refer to *residual* or *R-factor* (eq. 3.9) which is one of the descriptor to confirm the structure model to the reality.

$$R = \frac{\sum_{hkl} ||F_0| - F_c||}{\sum_{hkl} |F_0|} \quad (\text{eq. 3.9})$$

*R-factor*, multiplying by 100% corresponds to the relative deviation from the true structure. Due to some random errors the ideal structure solution ( $R = 0$ ) never observed. The high quality refinements often show *R-value* less than 2.5%. However the *R-factor* increases

if the weight is counted. The sophisticated weighted  $R$ -factors ( $wR$ , based on  $F_0$  and  $wR_2$  based on  $F_0^2$ ) (eq. 3.10) are directly related to the quantity which is minimized in the least squares refinements.

$$wR = \sqrt{\frac{\sum_{hkl} w \cdot (F_0 - F_c)^2}{\sum_{hkl} w \cdot (F_0)^2}} \quad \text{and} \quad wR_2 = \sqrt{\frac{\sum_{hkl} w \cdot (F_0^2 - F_c^2)^2}{\sum_{hkl} w \cdot (F_0^2)^2}} \quad (\text{eq. 3.10})$$

$$w = \frac{1}{\sigma^2(F_0^2) + (u \cdot P)^2 + v \cdot P} \quad \text{and} \quad P = \frac{1}{3}(F_0^2 + 2F_c^2) \quad (\text{eq. 3.11})$$

The  $u$  and  $v$  terms in (eq. 3.11) are chosen to minimize the differences in the variances for reflections in different ranges of intensity and diffraction angle and the weighting schemes are applied in the last stage of the refinement.

Since the terms in  $wR_2$  are squared, the  $wR_2$  values are generally twice larger than that of  $wR$ . A complete structure model should have the  $wR_2$  values less than 0.15. Another important descriptor to indicate the quality of the refinement is the  $Goof$  which stands for *Goodness of fit* represented by (eq. 3.12).

$$Goof = \sqrt{\frac{\sum_{hkl} w(F_0 - F_c)^2}{(m - n)}} \quad (\text{eq. 3.12})$$

The terms  $m$  and  $n$  are the number of reflections and parameters, respectively. The value of  $Goof$  is close to one with a suitable weighting scheme represents high quality structure solution.

**Anisotropic Displacement Parameters** are the vibrational mode of the atoms which are accounted for getting a true structure model. It is represented by ellipsoid or by six parameters. The spatial propagation and the direction of vibration can be shown by ellipsoidal representation. It is calculated for the structure amplitude  $F_c(hkl)$  of a reflection ( $hkl$ ) by introducing of an anisotropic temperature factor  $T_j$  for each atom,  $j$ .

$$F_c(hkl) = \sum_{j=1}^n f_j \cdot T_j(hkl) \cdot e^{[2i\pi(hx_j + ky_j + lz_j)]} \quad (\text{eq. 3.13})$$

$$T_j(hkl) = e^{-2\pi^2 \{U_{11}(ha^*)^2 + U_{22}(kb^*)^2 + U_{33}(lc^*)^2 + 2U_{12}(hka^*b^*) + 2U_{23}(klb^*c^*) + 2U_{13}(lhc^*a^*)\}} \quad (\text{eq. 3.14})$$

$a^*$ ,  $b^*$ ,  $c^*$  are the reciprocal lattice constant and  $U_{ij}$  is the coefficient of thermal ellipsoid of an atom,  $j/\text{\AA}^2$ .

In structure representation the atoms are effectively shown by thermal ellipsoids. Among the six thermal vibrational orientations of an atom the diagonal terms  $U_{11}$ ,  $U_{22}$ ,  $U_{33}$  which are mutually perpendicular to each other represent the principle axes of the thermal vibration of an atom. The off diagonal terms  $U_{12}$ ,  $U_{13}$ ,  $U_{21}$ ,  $U_{23}$ ,  $U_{31}$ ,  $U_{32}$  represent the orientation of the ellipsoid to that of the reciprocal axes. The shape of the displacement parameter is another sensitive descriptor for the accuracy of the structure determination. The causes of the poor displacement parameter are as follows:

- ❖ very small or even negative displacement parameter is the indication of heavier atom should occupy this site.
- ❖ significantly large value is the indications of light atom or no atom should occupy this site.
- ❖ cigar or dishes shaped or empty volume (Non Positive Definite, NPD) displacement ellipsoid is the indication of poor data set and in this regard structure determination with isotropic displacement is recommended rather than anisotropic refinement.

**Extinction correction** is desired when systematically the reflections of high intensity and low scattering angle has  $|F_0| < |F_c|$ . There are two types of extinction namely primary and secondary. *Primary extinction* occurs when strong diffracted rays weakened by further diffraction like “Primary beam”. *Secondary extinction* occurs when the planes into the crystal experienced a reduced primary beam as the first layers experienced. The *Secondary extinction* is more common. Therefore the reflection is weakened. In an *ideally imperfect* crystal (real crystal with significant uniform mosaic spread, [64]) the primary beam intensity is affected less than 1% (ignorable) by the scattering. Here, the extinction correction is done by using the SHLEX program at the final stage of refinement.

**Absorption correction** is important for anisotropic crystals, for instance, very thin plate shape or needle shape crystals. Because the path length of x-ray beam travels through the crystal is different in different orientations of crystal. This may cause huge errors in measured relative intensities. During the travels through the crystal the x-ray intensities is weakened due to Rayleigh scattering, Compton scattering and ionization. This depends on the atomic number of the scattering atom and the wavelength of the radiation used. In terms of linear absorption  $\mu$  ( $\text{mm}^{-1}$ ) and path length of x-ray through the crystal  $x$  (mm), the absorption coefficient can be elucidates by (eq. 3.15).

$$I = I_0 e^{-\mu x} \quad (\text{eq. 3.15})$$

Among the different types of absorption methods *Numerical absorption correction* is one of the best because for each reflection all possible path lengths of incident and scattered beam through the crystal are calculated. Semi-empirical method is predominantly appropriate when the crystal faces are impossible to index or the crystal is very irregular and other absorption effects are considerable, for instance, due to the adhesive and the glass rod used for crystal mounting. The IUCr recommended absorption correction is  $0.1 < \mu x < 1$  for a semi-empirical correction,  $1 < \mu x < 3$  for possibly numerical correction and  $\mu x > 3$  for a numerical correction.

## 3.2 Spectroscopic investigations

Spectroscopic study is the interaction of matter with radiation and the data are usually represented as spectrum which is a plot of response as a function of energy. Here several spectroscopic techniques are discussed.

### 3.2.1 UV/Vis/NIR spectroscopy

The UV/Vis/NIR spectroscopic measurements provide us the information about the symmetry of chromophores, ligand-field splitting and consequently the electronic structure of the compound. The transition metal complexes are colored due to electronic transitions caused by the absorption of visible light. If the transition metal compound absorbed a particular wavelength of radiation, it appears with its complimentary color. The absorbance maxima in a spectrum correspond to the absorbing color and the absorbance minima correspond to the color of the compound.

The intra-atomic electronic transition from the low energy to high energy transition metal  $d$  orbitals with conserving the spin multiplicity is the spin allowed  $d-d$  transition. The spin-forbidden transitions are observed with very low intensity (frequently sharp peaks for  $d$  block transition metals) compared with the spin-allowed transition. Similarly, the Laporte-forbidden transition, which conserves parity during electronic transition in centro-symmetric chromospheres ( $O_h$ ), is also observed experimentally with very low intensity.

The inter-atomic electronic transitions either from a metal  $d$  orbital (filled or partially filled) to a ligand (vacant) orbital or from a ligand orbital (filled) to a metal  $d$  orbital (empty or partially filled) are termed MLCT (Metal to Ligand Charge Transfer) and



LMCT (Ligand to Metal Charge Transfer) transitions, respectively. Besides these two CT transitions exists another CT which is Metal to Metal Charge Transfer (MMCT) transition. As the CT transitions are both spin and Laporte allowed, they are approximately three orders of magnitude higher in intensity than  $d-d$  transition.

### 3.2.1.1 Diffuse reflectance

The diffuse powder reflectance spectra were recorded at ambient temperature by two different spectrophotometers, CARY 14 (UV range, 200-600 nm) and CARY 17 (Vis/NIR range, 300-2600 nm) OLIS Inc. USA, equipped with integrating sphere, halogen lamp ( $5000 \leq \tilde{\nu} \leq 50000 \text{ cm}^{-1}$ ) as light source, prism and grating as a monochromator. For the whole spectral range three different experimental set ups were used (Table 3.1).

Table 3.1 Experimental set ups for diffuse powder reflectance measurements.

spectral region	ranges (nm)	data points	step width (nm)	scan rate (nm/sec)	slit width (mm)	band width (nm)	integration time (sec)	detector
UV	200-600	800	0.5	1	0.10	0.11-0.37	0.5	PMT
Vis	300-900	600	1	1	0.06	0.14-0.22	1	PMT
NIR	600-2600	500	4	4	1.4-2.2	5	1	PbS

PMT: Photomultiplier tube; PbS : Lead sulphide

In the UV and visible region the data points were collected with a fixed slit width of 0.10 mm and 0.06 mm, respectively which results in the variable band width of 0.11 to 0.37 nm and 0.14 to 0.22 nm, accordingly. Whereas in the NIR region the data points were collected with fixed band width of 5 nm which corresponds to a variable slit width of 1.4 to 2.2 mm.

For measurement of diffuse reflectance spectra about 500 mg of powder sample were placed on a white Teflon sample holder and polished to make a smooth surface. In every case the intensity of  $\text{BaSO}_4$  powder was measured as white standard. The diffuse reflectance ( $K/S$ ) was calculated using the Kubelka-Munk function [65] (eq. 3.16) with diffuse reflectance,  $R_{diff} = I_{sample} / I_{standard}$ .

$$K/S = \frac{(1 - R_{diff})^2}{2R_{diff}} \quad (\text{eq. 3.16})$$

### 3.2.1.2 Single crystal UV/Vis/NIR spectroscopy

Single crystal UV/Vis/NIR spectra were recorded at ambient temperature using a modified CARY 17 microcrystal spectrophotometer (Figure 3.4, spectral service, ANU Canberra, Australia) [66, 67]. The CARY 17 enables to measure the spectrum ( $5800 \leq \tilde{\nu} \leq 36000 \text{ cm}^{-1}$ ) of single crystal with dimension down to 0.1 mm edge length. A halogen lamp is used as light source. From 280 to 900 nm (UV/Vis region) the intensity data was recorded by a PMT detector system with scan rates and slit width of 1 nm/sec and 0.07 mm, respectively, whereas from 600 to 1700 nm (NIR region) a Ge semiconductor detector cooled with liquid nitrogen was used to record the intensity data with the scan rate of 2 nm/sec and the same slit width was maintained. In the Vis and NIR regions the step widths were 1 and 2 nm, respectively which corresponds to 621 and 550 collected data points.

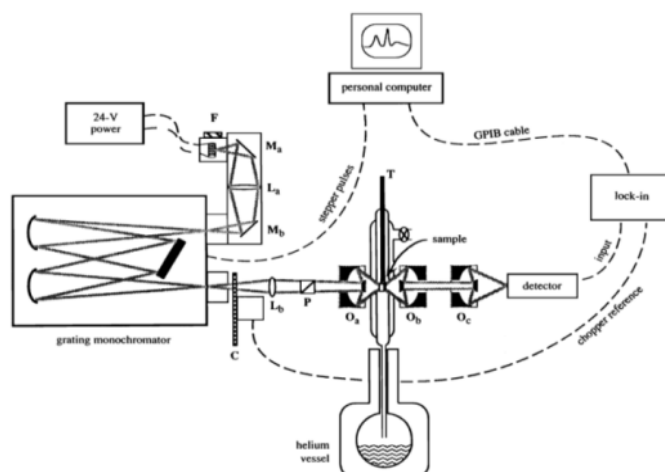


Figure 3.4 Schematic diagram of the microcrystal UV/Vis/NIR spectrophotometer CARY 17 [67].

### 3.2.1.3 Single crystal UV/Vis/NIR spectra measurement

The sample holder (made of brass) is rapped with aluminum foil to mask the holes in order to obstruct any unnecessary radiation from the spectrometer light source to the detector. A very small aperture is created into the foil with a sharp pin to allow certain amount of radiation to the detector. The transparent single crystal selected under the microscope is placed on the aperture and attached to the foil with small amount of grease. It is worth mentioning that the crystal should cover the whole aperture so that the detector can get the radiation only through the crystal. Afterwards the sample holder with the crystal is placed at the appropriate place of the spectrophotometer to collect the absorption spectra

with respect to vertical polarization (v-pole) direction and horizontal polarization (h-pole) direction of the incident light. In every measurement the base line correction was done by a sample holder with an aperture without the crystal. The Optical density,  $A$  is calculated by using the Lambert-Beer law (eq. 3.17).

$$A = -\log \frac{I}{I_0} = \varepsilon \cdot d \cdot c \quad (\text{eq. 3.17})$$

$I$	intensity of light transmitted through the crystal
$I_0$	intensity of light transmitted through the aperture without crystal
$\varepsilon$	molar extinction coefficient
$d$	thickness of the crystal
$c$	concentration of chromospheres

### 3.2.2 Electron paramagnetic resonance (EPR) spectroscopy

EPR spectroscopy, closely related to the NMR technique is a versatile spectroscopic method for the electronic structure determination of materials with unpaired electron. Only the transition metal complexes with a residual electron spin, paramagnetic system and radicals are EPR active. In presence of magnetic field the electron spin angular momentum,  $S$  gives rise to magnetic momentum,  $\mu$ .

$$\mu = h\gamma_e S = -g_e \beta_e S \quad (\text{eq. 3.18})$$

$\gamma_e$	magnetogyric ratio of electron
$g_e$	g-factor of free electron, 2.00232
$\beta_e$	Bohr magnetron, $(\hbar/2m_e)$
$S$	total spin angular momentum, individual spin is fundamental property of subatomic particle which is multiple integer of +1/2 or -1/2.

The negative sign arises due to the negative charge on the electron. In the presence of external magnetic field,  $B_0$  the degenerate spin state will split (eq. 3.19) depending on their magnetic quantum number,  $m_s$  and the applied magnetic field.

$$E = \pm \frac{1}{2} g_e \beta_e B_0 \quad (\text{eq. 3.19})$$

Resonance or absorption occurs when the frequency,  $\nu_0$  of same energy as the differences between two spin energy states is applied (eq. 3.20).

$$\Delta E = h\nu_0 = g_e \beta_e B_0 \quad (\text{eq. 3.20})$$

If the electron is in certain chemical environment instead of free state then the second magnetic field produced by the nuclei will influence the local structure of electron and the resonance condition will be modified (eq. 3.21).

$$h\nu = g_e\beta_e B_0(1-\sigma) = g\beta B_0 \quad (\text{eq. 3.21})$$

Where,  $g$ -factor is  $g_e(1-\sigma)$  and  $\sigma$  indicate the effects of local field which can be positive and negative. As the EPR signal for paramagnetic center can be obtained at different frequency by sweeping the magnetic field, the signal at particular magnetic field is not the unique for identification of compounds. Thus values of  $g$ -factor calculated from the EPR spectra which will be different from the free electron would give information about the local electronic structure. The  $g$ -factor values also give hints about the anisotropy.

Sometimes the EPR spectra consist of multi-lined instead of single lined. This is due to the hyperfine interaction between the unpaired electron and the near by non-zero spin nuclei (odd atomic and even mass numbers). Nuclei with residual spin angular momentum create local magnetic moment and affect the magnetic moment on the electron. The resulting magnetic moment depends on the orientation of the nuclei dipole. Nuclei with non-zero nuclear spin quantum number contribute for hyperfine interaction. The number of hyperfine lines having  $M$  equivalent nuclei, each with  $I$  nuclear spin can be determined by the formula,  $2MI+1$ . The measured separation between two lines is the hyperfine coupling constant in magnetic field unit which also gives information about the distance from the unpaired electron, torsion angle and the extent of delocalization.

The electromagnets with magnetic strength of 0.1 to 1.5 Tesla (easily reachable) could give the resonance frequencies in the microwave (mw) region of 2.8 to 42 GHz. The mw frequencies are termed as band, for example, X-band (~9.5 GHz), Q-band (~36 GHz) W-band (~95 GHz) and so on. As the production of variable microwave frequencies with sufficient amplitude and frequency stability is extremely difficult, the most EPR experiments were done by continuous microwave (CW) irradiation, i.e the microwave frequency is kept constant while the magnetic field is swepted till the resonance occurs.

**The measurement of EPR Spectra** was performed using a Bruker Elexsys E580 spectrometer equipped with EN 4118X-MD4 and EN5107D2 Bruker dielectric resonators for X-band and Q-band, respectively. For the CW-EPR spectra a spherical TE011 cavity (SHQ, Bruker, ER 4119HS) was used. All spectra were acquired at room temperature. Simulations and fitting of the EPR data was executed by using EasySpin program

package under MATLAB software [68], from which the function *pepper* was used to simulate the EPR spectra for comparison with their experimental data.

### 3.2.3 Solid state $^{31}\text{P}$ -MAS-NMR spectroscopy

NMR spectroscopy is a powerful and sophisticated analytical technique not only in various scientific research areas but also in industries. NMR spectroscopy together with x-ray crystallography are the prominent technologies for chemical structure determination. In the presence of applied magnetic field materials with non-zero nuclear spin ( $I \neq 0$ ) lift up the degenerate energy level into  $2I+1$  states. The difference among the energy level depends on the type of nuclei and the strength of the applied field. The lower energetic nuclei can jump to the higher energy level by absorbing the electromagnetic radiation. The energy or the frequency of the radiation should be exactly same as their energy level difference. This frequency is called Larmor frequency or resonance frequency. Such resonance frequency is typically in the range of radio frequency region. However, nuclei with same type of  $\gamma$  (gyromagnetic ratio) do not resonate at same frequency. Since the nucleus is surrounded by electrons which have also spin momentum like nuclei. These circulations create a magnetic field which is opposite the induced magnetic field of nucleus. Therefore the nucleus experienced reduced magnetic field due to this electronic shielding which is called shielding effect. Therefore, the gap between the energy level reduced and the required resonance frequency is reduced, too. Consequently the NMR absorption peak shifts which termed as chemical shift,  $\delta$  in ppm unit.

In solid there are direction dependent interactions due to spatial proximity and chemical bonding. This orientation dependent interactions is termed as chemical shift anisotropy,  $\delta_{\text{anis}}$ . However, in liquid state NMR this orientation dependent interaction is overlooked by Brownian motion. As a result the range of line width in solid state NMR is  $10^5$  Hz whereas in liquid state NMR is 0.1 Hz. This is attributed to the dipolar coupling,  $D$  which depends on the type of nuclei, internuclear distance, and specifically on the orientation of the vector connecting two nuclear spins with respect to the applied magnetic field (eq. 3.22).

$$D \propto 3\cos^2 \theta - 1 \quad (\text{eq. 3.22})$$

This dipolar coupling become zero at  $\theta = 54.7^\circ$  which is called Magic Angle. Therefore by introducing an artificial motion of the solid at an angle  $54.7^\circ$  w.r.t the applied magnetic field the anisotropic dipolar interaction can be suppressed. Spinning at this specific angle is called magic angle spinning (MAS). However, the rate of MAS must be greater or equal

to the magnitude of the anisotropic interaction otherwise a manifold of spinning sidebands separated by the rate of spinning will appear.

**$^{31}\text{P}$ -MAS-NMR measurements** were carried out on a Varian Infinity+ spectrometer equipped with a commercial 2.5 mm MAS double-resonance probe (Chemagnetics) operating at 162.532 MHz. The  $^{31}\text{P}$ -MAS spectra are the average of up to 64 transients acquired with a repetition delay up to 3600 s, a  $90^\circ$  pulse duration of  $1.9 \mu\text{s}$ , and 10 Hz line broadening during data processing. For the measurement the magnetization was extinguished by a series of pulses followed by a rectangular pulse with different delay. The chemical shift parameters were determined by numerical fitting of the observed spectra (software SPINSIGHT 4.3.2 [69]). The isotropic chemical shift parameters are reported in parts per million (ppm) referred to an external standard of 85%  $\text{H}_3\text{PO}_4$ .

### 3.2.4 X-ray photoelectron spectroscopy (XPS)

X-ray photoelectron spectroscopy also called electron spectroscopy for chemical analysis (ESCA) is a widely used surface analytical technique that uses x-ray in an ultra-high vacuum atmosphere to study the chemical composition and the chemical states of the specimen. In XPS the surface of the sample is focused by x-rays and the energy of the x-ray photons,  $h\nu$  is absorbed by the inner shell electrons of the sample (Figure 3.5, [70]).

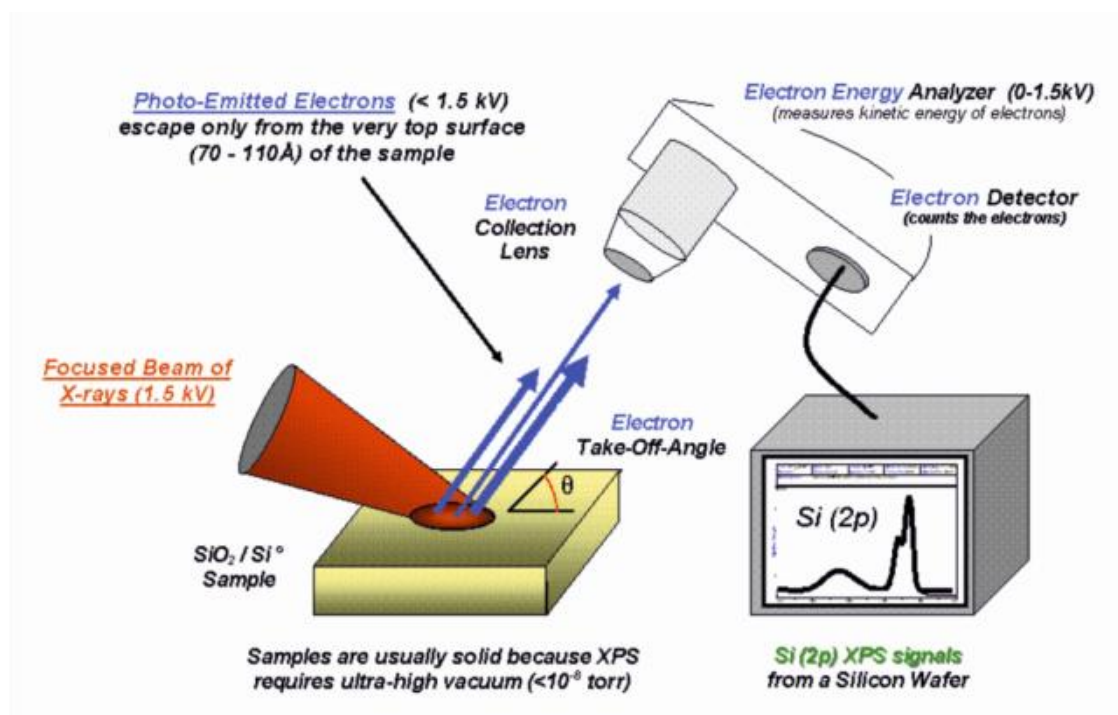


Figure 3.5 Instrumentation of XPS system [70].

If the photon energy of the incident x-rays is high enough to overcome the binding energies (BEs) then the electrons are emitted with a specific kinetic energy (KE) which can be described as Einstein Photo emission process (eq. 3.23).

$$BE = h\nu - KE - \phi_{spec} \quad (\text{eq. 3.23})$$

$h\nu$  is the energy of incident x-rays and  $KE$  is the kinetic energy of the emitted electron and the detector of the XPS instrument collect the readings of  $KE$ . Since the  $KE$  of the ejected electron is characteristic for a particular element, it can be used as a qualitative elemental characterization. However, the  $KE$  of the ejected electron is directly related to the energy of the incident x-rays photon, and every XPS instrument is not using the same kind of x-rays source, so it is not recommended to use the value of  $KE$  as a standard to compare the experimental results obtained from different source. Therefore,  $BEs$  are the unique to the elemental characterization and comparing from different XPS instruments. Moreover, once the  $KEs$  data are available the  $BEs$  can be calculated easily. The last term,  $\phi_{spec}$  is a correction function which is unique to the instrument.

The area under the particular binding energy peak is directly proportional to the number of atoms that emit the electrons at that BE. Therefore the ratio of the areas under the BE signal for each element give the estimation of the surface composition. The well-known splitting phenomenon of the binding energy peaks in XPS spectrum is observed due to spin-orbit coupling for the orbitals with  $p$ ,  $d$  and  $f$ . The total angular momentum,  $j$  is the sum of individual angular momentum and spin momenta (eq. 3.24).

$$j = l + s \quad (\text{eq. 3.24})$$

For instance, the BE peak of Vanadium 2p orbital (V2p) is supposed to be split into V2p<sub>3/2</sub> and V2p<sub>1/2</sub> since  $J = 1 \pm 1/2$ .

All the XPS measurements and evaluation were performed in the research group of Prof. Dr. Kwang-Hwa Lii with his co-worker Nguyen Quang Bac, National Central University, Taiwan. The spectra of X-ray photoelectron were measured by a PHI Quantera SXM Spectrometer equipped with Al K $\alpha$  anode (1486.6 eV) operated at 24.8 W, with the typical beam diameter of 100  $\mu\text{m}$  under a vacuum of about  $4.5 \times 10^{-8}$  torr. The data were analyzed with the MultiPak software [71] for peak fitting with suitable background and peak profiles.

### 3.2.5 Energy Dispersive X-ray (EDX) analysis

Energy Dispersive X-ray, EDX [72, 73] is a non-destructive surface analytical technique, sometimes also called Energy Dispersive Spectroscopy (EDS) or Energy Dispersive X-ray Micro Analysis (EDXMA) which is used for elemental characterization of a sample.

In EDX analysis the sample to be measured is bombarded with high energy electron beam or x-ray. During collision some of the electrons from the inner shell atomic orbital of the specimen are ejected, creating the electron holes. These electron holes are filled up by the upper shell electrons which have higher energy than the inner shell electrons and releasing the extra energy as an x-ray. The energy of the emitted x-ray is same as the difference between the two energy levels which is characteristic of each element. This number and energy of the x-ray is measured by energy dispersive spectrometer which also allows the quantitative analysis of the probe.

EDX measurements are performed by REM, DSM-940, Zeiss, operated in 20 Kv, equipped with PV 9800 energy dispersive detector which is cooled by liquid nitrogen. Electrically non-conducting samples were sputtered with gold before the bombardment with high energy beam which allows a path for the incident electron beam to flow to the ground.

### 3.3 Magnetic behavior

Electrons orbiting a nucleus generate magnetic field due to its spin and the spin magnetic dipole moment of an orbiting electron,  $\mu_s$  also termed as Bohr Magnetron,  $\mu_B$

$$\mu_s \approx \gamma J = \left( \frac{e}{2m} \right) \left( \frac{nh}{2\pi} \right) = \mu_B \quad (\text{eq. 3.25})$$

$J$  is spin angular momentum,  $h$  is plank constant,  $e$  and  $m$  is the electron's charge and mass, respectively. Similarly every material placed in a external magnetic field,  $H$  acquires magnetic moment,  $\mu$  due to magnetic field induction,  $B$  (eq. 3.26). The magnetic moment per unit volume is called magnetization,  $M$ .

$$B = H + 4\pi M \quad (\text{eq. 3.26})$$

In some materials magnetization is proportional to the applied magnetic field (eq. 3.27).

$$\chi = \frac{M}{H} \quad (\text{eq. 3.27})$$



$\chi$  is a proportionality constant which is dimensionless and is called magnetic susceptibility of the material. Conveniently the magnetic behavior of different materials is characterized by the value of molar magnetic susceptibility and its dependency on temperature and applied field. The molar magnetic susceptibility,  $\chi_m$  ( $\text{cm}^3 \cdot \text{mol}^{-1}$ ) of a material with formula unit  $F$ , and density  $d$  is expressed as (eq. 3.28)

$$\chi_m = \frac{\chi F}{d} \quad (\text{eq. 3.28})$$

In diamagnetic substance the elementary charges of the material try to shield the interior body from the applied magnetic field results an antiparallel induced magnetic field or magnetization to the applied field i.e  $\chi_m$  is slightly negative and independent to the temperature. All materials have diamagnetism to the magnetic effort but are masked due to very weak contribution. According to Langevin expression for a simple element with atomic number  $Z$ , average radius of the electron from nucleus  $R$ , and atoms per unit volume  $N$ , the diamagnetic susceptibility is given by (eq. 3.29).

$$\chi_m^{dia} = -\frac{\mu_0 Z N e^2}{6m_e} \langle R^2 \rangle \quad (\text{eq. 3.29})$$

In ferromagnetic substance, in presence of applied field the atomic permanent dipole moment align themselves in the direction of applied field due to cooperative spin interaction among the neighboring ions. Therefore the  $\chi_m$  is positive and very large but not proportional to the applied magnetic field. It depends on the history of applied field. Because the magnetization sometimes remains even at zero applied field. With increasing temperature the  $\chi_m$  decreases rapidly up to certain temperature called Curie temperature then behave like paramagnetic substance. However for anti-ferromagnetic substance  $\chi_m$  increases till certain temperature called Neel temperature,  $N_T$  then act like paramagnetism.

In paramagnetic substance the permanent atomic magnetic moment align themselves parallel to the applied magnetic field and hence the  $\chi_m$  is positive, temperature dependent and proportional to the low field response. In lighter elements ( $Z < 40$ ) the electronic spin interact themselves to form total spin angular momentum,  $S$ . Therefore the paramagnetic susceptibility  $\chi_m^{para}$  and effective magnetic moment  $\mu_{eff}$  for spin only contribution with  $g = 2$  is

$$\chi_m^{para} = \frac{N_A g^2 \mu_B^2}{3k_B T} S(S+1) \quad (\text{eq. 3.30})$$

$$\mu_{eff} = 2\mu_B \sqrt{S(S+1)} \quad (\text{eq. 3.31})$$

$N_A$  is the Avogadro constant,  $k_B$  is the Boltzmann constant and  $T$  is the temperature (K). However, in case of heavier element total spin angular momentum,  $S$  interact with total orbital angular momentum,  $L$  called Russel-Saunders coupling or LS coupling. Considering this spin-orbit coupling the paramagnetic susceptibility and effective magnetic moment expressed as

$$\chi_m^{para} = \frac{N_A g^2 \mu_B^2}{3k_B T} J(J+1) \quad (\text{eq. 3.32})$$

$$\mu_{eff} = g\mu_B \sqrt{J(J+1)} \quad (\text{eq. 3.33})$$

$$g = 1 + \frac{S(S+1) - L(L+1) + J(J+1)}{2J(J+1)} \quad \text{and } J = \text{from } (L-S) \text{ to } (L+S), \text{ for less than half}$$

filled and more than half filled orbital, respectively with increments of 1. In this work, the  $\mu_{eff}$  was calculated by using (eq. 3.34), simplified from (eq. 3.30)

$$\mu_{eff} = 2.83\sqrt{\chi T} \quad (\text{eq. 3.34})$$

where it follows the Curie behavior.

**Magnetic measurements.** The temperature dependence of molar magnetic susceptibility,  $\chi_m$  was measured by a vibrating sample magnetometer (VSM) in the temperature range 2 to 300 K. The VSM operates on Faraday's law of induction by measuring the induced current which is proportional to the magnetic moment of the sample. In VSM technique the sample is placed inside a homogeneous magnetic field to magnetize the sample by water cooled electromagnet and the induced magnetic dipole moment of the sample will create a magnetic field around the sample which is called magnetic stray field. The magnetic stray field is changing as a function of time due to sample vibration and recognized by a set of pick-up coils. This alternating magnetic field will create electric field in the pick-up coils which is proportional to the magnetization of the sample. The signal is amplified by a lock-in amplifier to avoid noise from the environment.

## 4 Chemicals used throughout this thesis

### 4.1 Chemicals purchased

Commercially available reagent grade starting materials used during this research work are listed in Table 4.1. Other pure (according to Guinier photograph) starting materials  $\text{MoO}_2$ ,  $\text{Ir}(\text{PO}_3)_3$ ,  $\text{CrPO}_4$ , and  $\text{RhPO}_4$  were collected from the research group stock.

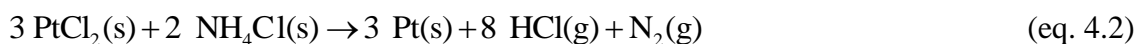
Table 4.1 List of commercially available reagent grade starting materials.

Substance	Company	Purity
Acetone	Merck, Darmstadt	99%
Argon	Air products, Hattingen	99.996%
$\text{AgO}_2$	Sigma Aldrich, Steinheim	99.99%
$\text{BaSO}_4$	Merck, Darmstadt	p. A.
$\text{Cr}(\text{NO}_3)_3 \cdot 9\text{H}_2\text{O}$	Acros, New Jersey	99%
$\text{Fe}(\text{NO}_3)_3 \cdot 9\text{H}_2\text{O}$	Acros, New Jersey	99%
Glycine	Grüssing Filsum	99.5%
Hydrogen	Air products, Hattingen	99.9%
Hydrofluoric acid	Merck, Darmstadt	38-40% reinst
$\text{I}_2$	Grüssing, Filsum	99.5%
$\text{InCl}_3$	Alfa products, Karlsruhe	99% + reinst
$\text{In}_2\text{O}_3$	Alfa Aesar, Karlsruhe	99.9%
$\text{LuCl}_3 \cdot 6\text{H}_2\text{O}$	Alfa products, Karlsruhe	99% + reinst
$\text{MoO}_3$	Merck, Darmstadt	99%
Nitric acid	VWR, France	65% reinst
$\text{NH}_4\text{Cl}$	Th. Geyer, Germany	99.50%
$(\text{NH}_4)_2\text{HPO}_4$	Merck, Darmstadt	p. A.
$\text{NH}_4\text{VO}_3$	Chempur, Karlsruhe	p. A.
$(\text{NH}_4)_6\text{W}_{12}\text{O}_{39} \cdot 4.8\text{H}_2\text{O}$	Alfa Aesar, Karlsruhe	p. A.
$(\text{NH}_4)_6\text{Mo}_7\text{O}_{24} \cdot 4\text{H}_2\text{O}$	Alfa Aesar, Karlsruhe	p. A.
Oxygen	Praxair, Hürth	99.9%
Phosphorus, red	Merck, Darmstadt	p. A.
Phosphorus, red	Clariant (Knapsack electronics), Hürth	6 N
$\text{P}_4\text{O}_{10}$	KML Laborchemie, Lohmar	97%
$\text{RuO}_2$	Alfa Aesar, Karlsruhe	99.9%
$\text{Sc}_2\text{O}_3$	Sigma Aldrich, Steinheim	99.999%
$\alpha\text{-SiO}_2$	Merck, Darmstadt	p. A.
$\text{V}_2\text{O}_5$	Merck, Darmstadt	99.99%
$\text{WO}_3$	Sigma Aldrich, Steinheim	99.99%

## 4.2 Chemicals synthesized

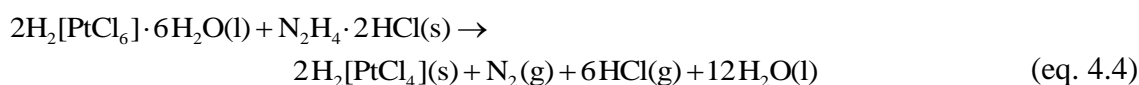
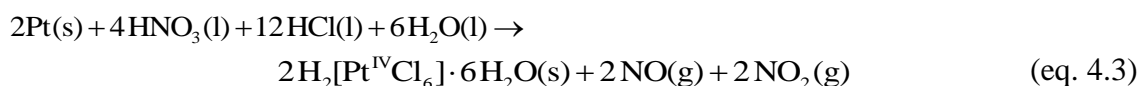
### 4.2.1 Platinum(II) chloride, PtCl<sub>2</sub>

Platinum(II) chloride [74] was used for the in situ preparation of chlorine (eq. 4.1) and hydrogen chloride (eq. 4.2). These were used as transport agents in CVT experiments.



It is easier to handle solid PtCl<sub>2</sub> (at RT) which can liberate Cl<sub>2</sub> gas above 525 °C rather than a cylinder containing gaseous chlorine. Anhydrous CuCl<sub>2</sub> (dehydrated from CuCl<sub>2</sub>·2H<sub>2</sub>O at 140 °C) could be an alternative option. However, here the maximum decomposition temperature should be 350 °C because beyond this temperature gaseous CuCl is formed.

PtCl<sub>2</sub> was synthesized by thermal decomposition of tetrachloroplatinic acid, H<sub>2</sub>[Pt<sup>IV</sup>Cl<sub>6</sub>] at 150 °C. To get H<sub>2</sub>[Pt<sup>II</sup>Cl<sub>4</sub>], metallic platinum bars (9.1106 g, 0.0467 mol) were dissolved in aqua regia (50 mL 65% HNO<sub>3</sub> and 150 mL 35% HCl) at about 150 °C for three days with continuous refluxing. After complete dissolution of the platinum the resulting clear solution was orange-brown due to the formation of the [Pt<sup>IV</sup>Cl<sub>6</sub>]<sup>2-</sup> ion and nitrogen oxides (eq. 4.3). This solution was evaporated to orange-red viscous liquid and washed again with large amount of HCl to avoid the formation of PtCl<sub>4</sub>·NOCl. Reduction of hexa-chloroplatinic acid, H<sub>2</sub>[Pt<sup>IV</sup>Cl<sub>6</sub>] by hydrazinium dihydrochloride, N<sub>2</sub>H<sub>4</sub>·2HCl with 1:2 molar ratio leads to the formation of H<sub>2</sub>[Pt<sup>II</sup>Cl<sub>4</sub>] (eq. 4.4). The obtained material is dried at 100 °C for 12 hours to evaporate HCl and then ground and dried again at 150 °C for four hours (eq. 4.5). Finally, the brown colored PtCl<sub>2</sub> powder (according to Guinier photograph shown in Figure 4.1) was obtained by several times washing with hot water to remove the traces of H<sub>2</sub>[Pt<sup>II</sup>Cl<sub>4</sub>]. The Cl<sub>2</sub> content of this batch is 92% (gravimetric analysis) compare to theoretical value.



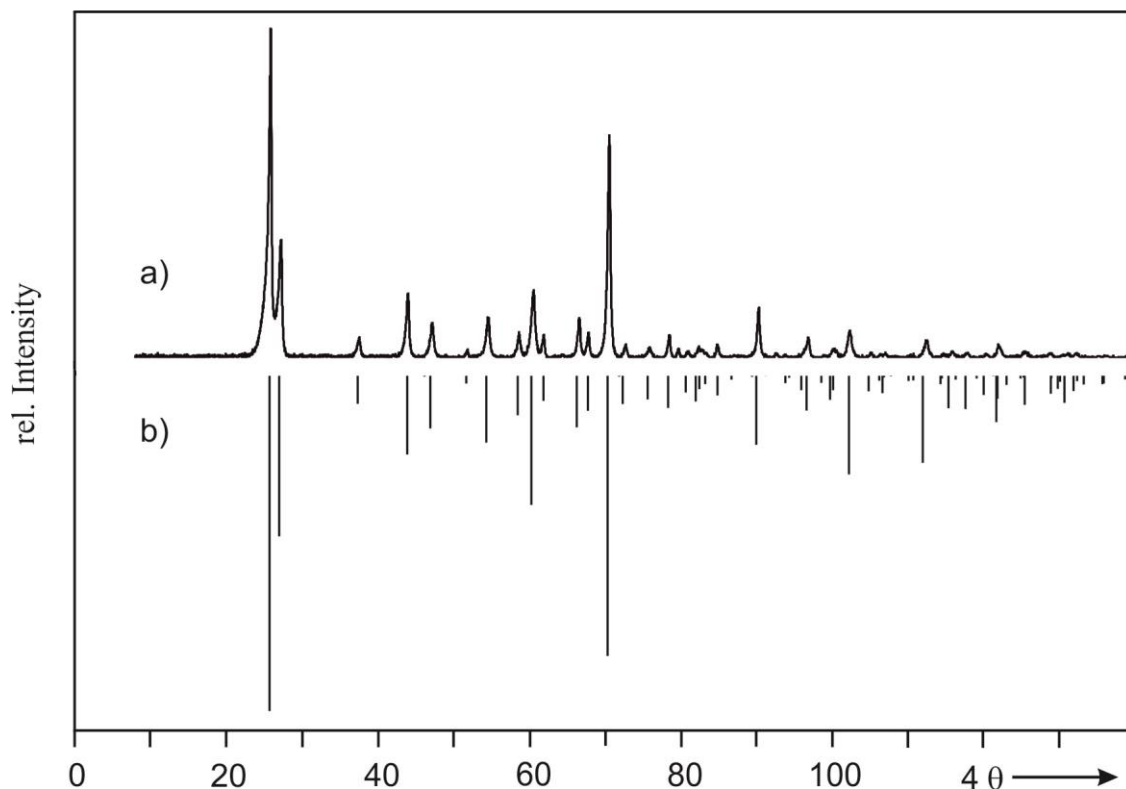
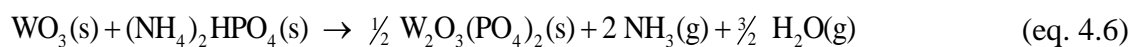


Figure 4.1 Synthesis of  $\text{PtCl}_2$ . Comparison of the Guinier photograph of the obtained product (a) and simulated diffraction pattern (b) [74].

#### 4.2.2 Tungsten(VI) oxide-phosphate, $\text{W}_2\text{O}_3(\text{PO}_4)_2$

Two polymorphs, orthorhombic (low temperature form) [75] and monoclinic (high temperature form) [76, 77, 78] of  $\text{W}_2\text{O}_3(\text{PO}_4)_2$  are known in literature. Microcrystalline powders of the phase pure polymorphs of  $\text{W}_2\text{O}_3(\text{PO}_4)_2$  were prepared from equivalent mixtures of  $\text{WO}_3$  (3245.75 mg, 14 mmol) and  $(\text{NH}_4)_2\text{HPO}_4$  (1848.78 mg, 14 mmol) in an open silica tube according to (eq. 4.6). In the first step the mixture of reactants was heated from room temperature to 400 °C for 24 hours and 600 °C for another two days in order to release  $\text{NH}_3$  and  $\text{H}_2\text{O}$  from  $(\text{NH}_4)_2\text{HPO}_4$  followed by grinding in intermediate steps. The orthorhombic polymorph of  $\text{W}_2\text{O}_3(\text{PO}_4)_2$  was obtained at 700 °C for three days (Figure 4.2). A grayish white powder of the monoclinic polymorph was obtained by heating the orthorhombic polymorph at 950 °C for three days (Figure 4.3). This phase transition is irreversible.



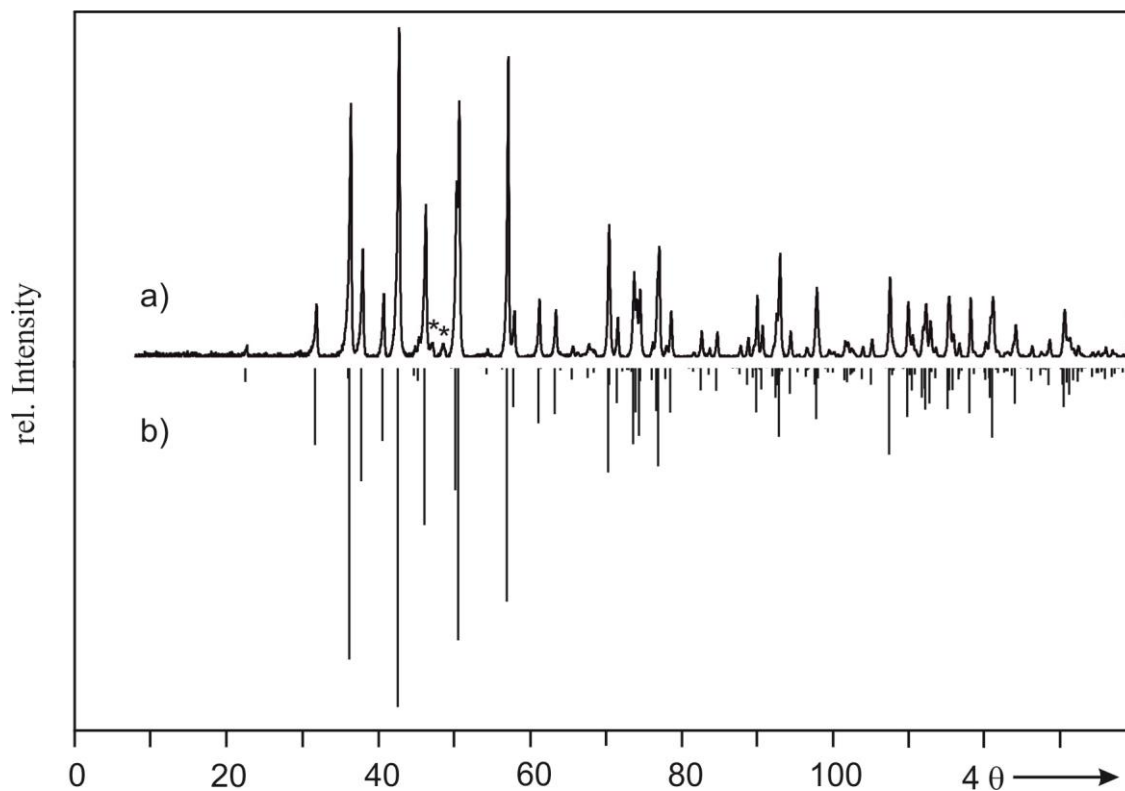


Figure 4.2 Synthesis of orthorhombic  $W_2O_3(PO_4)_2$ . Comparison of the Guinier photograph of the obtained product (a) and simulated diffraction pattern (b) [75], \* indicate *m*-WO<sub>3</sub>.

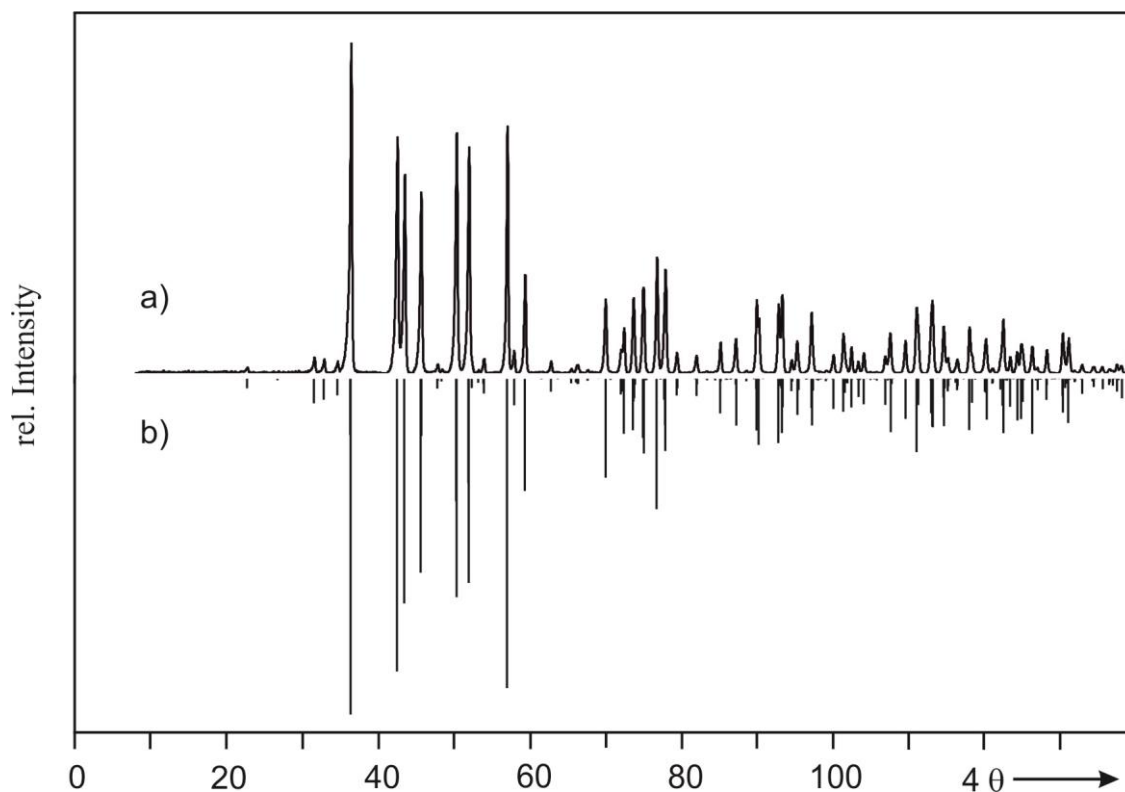


Figure 4.3 Synthesis of monoclinic  $W_2O_3(PO_4)_2$ . Comparison of the Guinier photograph of the obtained product (a) and simulated diffraction pattern (b) [78].

### 4.2.3 Tungsten(VI) oxide-pyrophosphate, $WOP_2O_7$

For  $WOP_2O_7$  an orthorhombic [75] and a monoclinic [79] polymorph are known. Colorless single crystals of *m*- $WOP_2O_7$  (Figure 4.4) were obtained by vapor phase moderated solid state reaction from a mixture of  $WO_3$  (231.5 mg, 1 mmol) and  $P_4O_{10}$  (213.1 mg, 0.75 mmol) in an evacuated and sealed ampoule at 800 °C for seven days where the water molecules (due to hygroscopic nature of  $P_4O_{10}$ ) act as mineralizer. The layer-type structure of *m*- $WOP_2O_7$  results in a non-statistical distribution of the particles orientation during the x-ray exposure. Therefore, the intensity distribution of the XRPD does not fit to the simulated pattern (Figure 4.5).

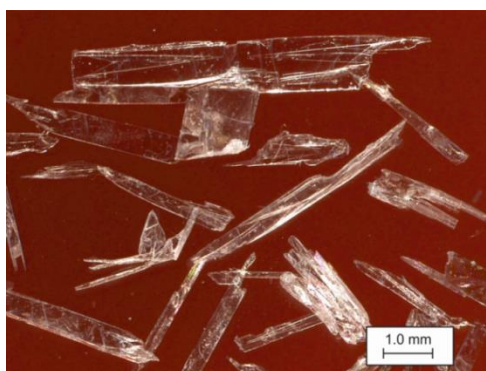


Figure 4.4 Photograph of crystals of *m*- $WOP_2O_7$  obtained by vapor phase moderated solid state reaction using water as mineralizer.

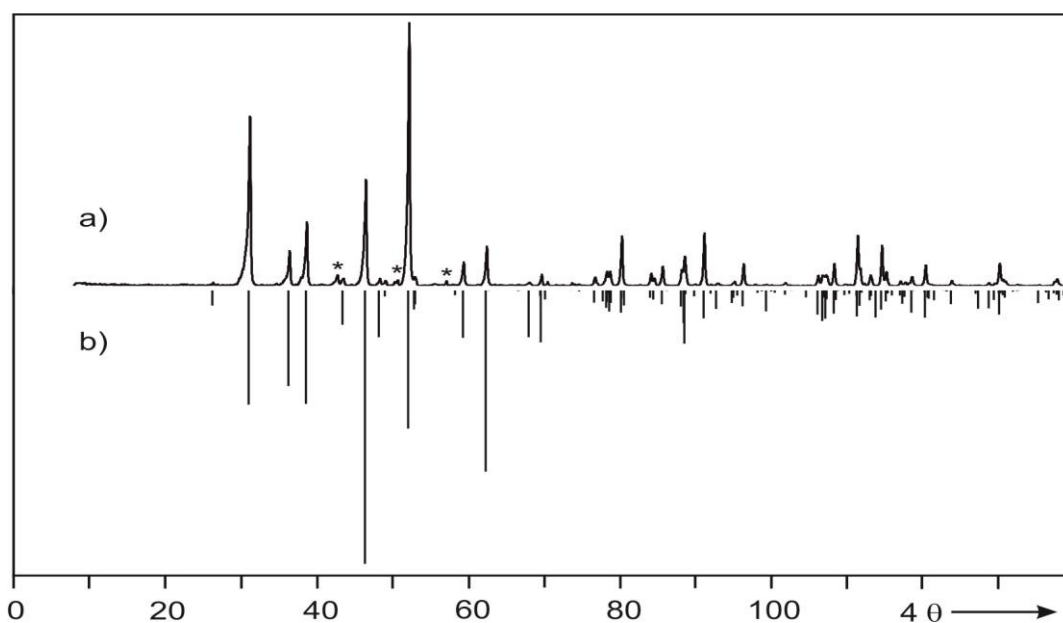


Figure 4.5 Synthesis of monoclinic  $WOP_2O_7$ . Comparison of the Guinier photograph of the obtained product (a) and simulated diffraction pattern (b) [79]. \* indicate a small impurity of *m*- $W_2O_3(PO_4)_2$  [78].

#### 4.2.4 Molybdenum(VI) oxide-pyrophosphate, $(\text{MoO}_2)_2(\text{P}_2\text{O}_7)$

A microcrystalline powder of  $\alpha$ - $(\text{MoO}_2)_2(\text{P}_2\text{O}_7)$  [80, 88] was prepared by heating a mixture of  $\text{MoO}_3$  (437.7 mg, 3 mmol) and  $(\text{NH}_4)_2\text{HPO}_4$  (396.2 mg, 3 mmol) in an open silica tube according to (eq. 4.7). The heat treatment was conducted initially at 250 °C (two days) and 400 °C (two days) in order to remove volatile gaseous species from  $(\text{NH}_4)_2\text{HPO}_4$  followed by subsequent heating at 600 °C for two days. The Guinier photograph of the product was compared with the simulated pattern as shown in Figure 4.6.

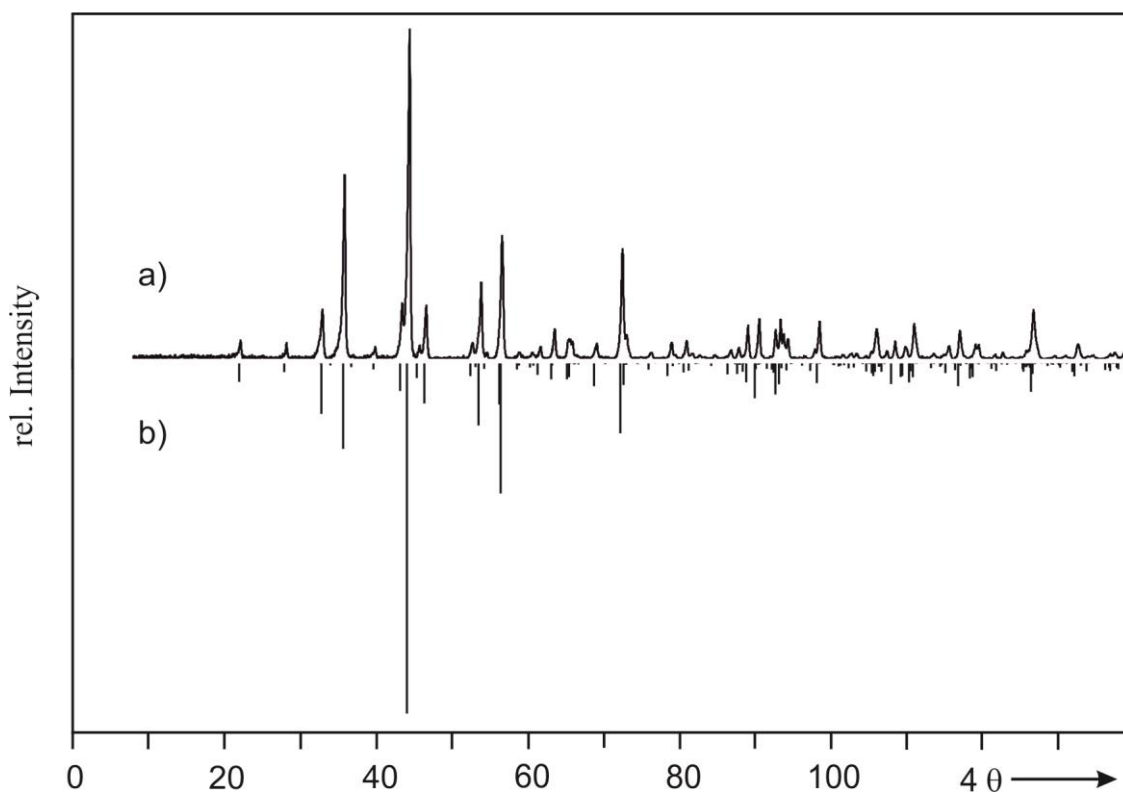
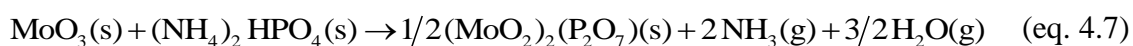


Figure 4.6 Synthesis of  $\alpha$ - $(\text{MoO}_2)_2\text{P}_2\text{O}_7$ . Comparison of the Guinier photograph of the obtained product (a) and simulated diffraction pattern (b) [80].



#### 4.2.5 $\beta$ -Vanadium(V) oxide-phosphate, $\beta$ -VOPO<sub>4</sub>

$\beta$ -VOPO<sub>4</sub> [161] was prepared according to (eq. 4.8). The mixture of equivalent amounts of NH<sub>4</sub>VO<sub>3</sub> (7798.5 mg, 66.67 mmol) and (NH<sub>4</sub>)<sub>2</sub>HPO<sub>4</sub> (8803.7 mg, 66.67 mmol) was heated in an open silica tube at 200 °C for one day and then 400 °C for another day in order to evaporate the volatile products (NH<sub>3</sub> and H<sub>2</sub>O). A bright yellow powder of  $\beta$ -VOPO<sub>4</sub> was obtained by heating at 650 °C for five days in air.

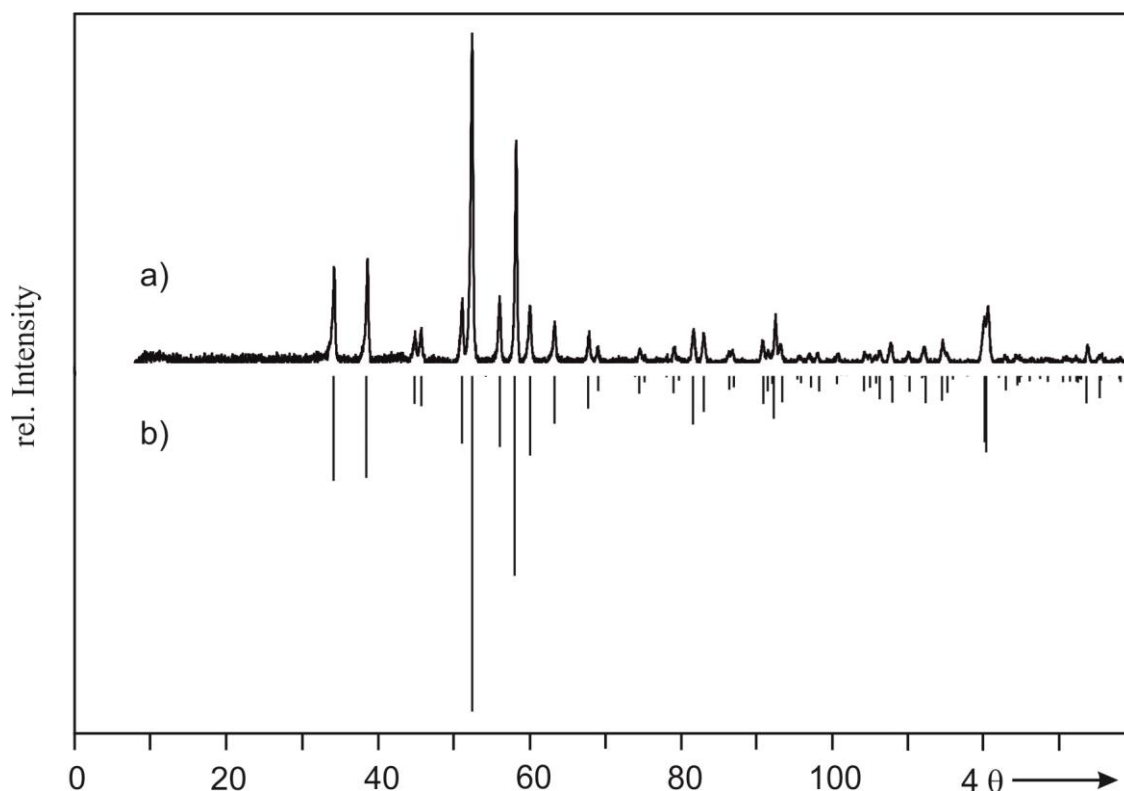
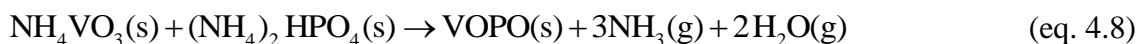


Figure 4.7 Synthesis of  $\beta$ -VOPO<sub>4</sub>. Comparison of the Guinier photograph of the obtained product (a) and simulated diffraction pattern (b) [161].

Moreover,  $\beta$ -VOPO<sub>4</sub> was also prepared by solution combustion synthesis from an equimolar mixture of (NH<sub>4</sub>)<sub>2</sub>HPO<sub>4</sub> (8.8037g, 66.67mmol) and (NH<sub>4</sub>)VO<sub>3</sub> (7.7985 mg, 66.67 mmol). Nitric acid and glycine were taken as oxidizer and fuel, respectively. The molar ratio of fuel:oxidizer was 1:8. The starting materials together with fuel and oxidizer were dissolved in a minimum amount of water and dried to a gel at about 100 °C on a hot plate with magnetic stirrer. The dry gel was ignited in a preheated (550 °C) muffle furnace and kept at this temperature for ten minutes. The sponge like brownish

black intermediate was finely ground and identified as a mixture of  $\alpha_1$ -VOPO<sub>4</sub> [159] and VOPO<sub>4</sub>·2H<sub>2</sub>O [173] by XRPD (Figure 4.8). These phases are still present after advanced heating at 650 °C. It was shown in separate experiments that the di-hydrate forms from  $\alpha_1$ -VOPO<sub>4</sub> already on cooling to room temperature. Therefore, formation of the  $\alpha_1$ -phase at the high temperature appears reasonable (see section 6.3). Subsequent heating of the solid at 725 °C for two days leads to the thermodynamically stable, bright yellow  $\beta$ -polymorph of VOPO<sub>4</sub>, which is not hygroscopic.

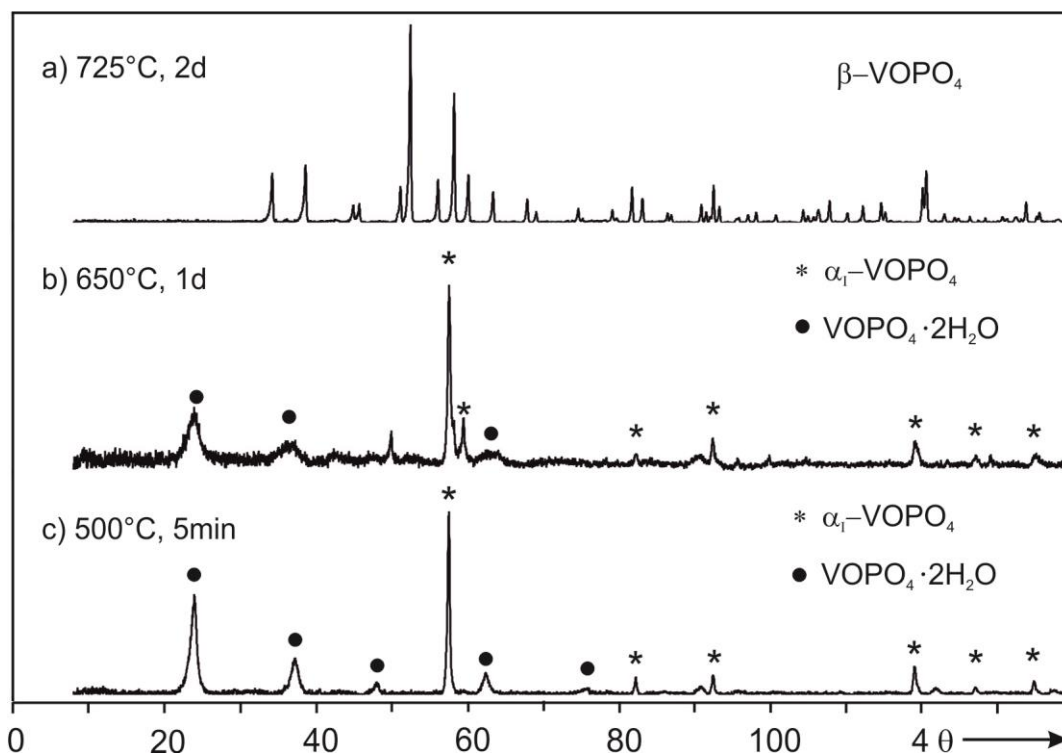
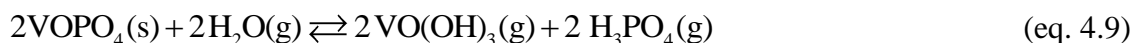


Figure 4.8 SCS of  $\beta$ -VOPO<sub>4</sub> [161]. Phase formation during prolonged heating in air monitored by Guinier photographs.

Yellow/green, dichroic single crystals of slightly under-stoichiometric  $\beta$ -VOPO<sub>4</sub> (see section 6.5) were obtained by chemical vapor transport (TA: H<sub>2</sub>O from VOPO<sub>4</sub>·2H<sub>2</sub>O; 700 → 600 °C; ten days). Crystals (shown in Figure 4.9) with edge lengths up one mm were obtained at transport rates,  $\dot{m} = 0.1 \text{ mg}\cdot\text{h}^{-1}$ . The transport reaction can be written as (eq. 4.9).



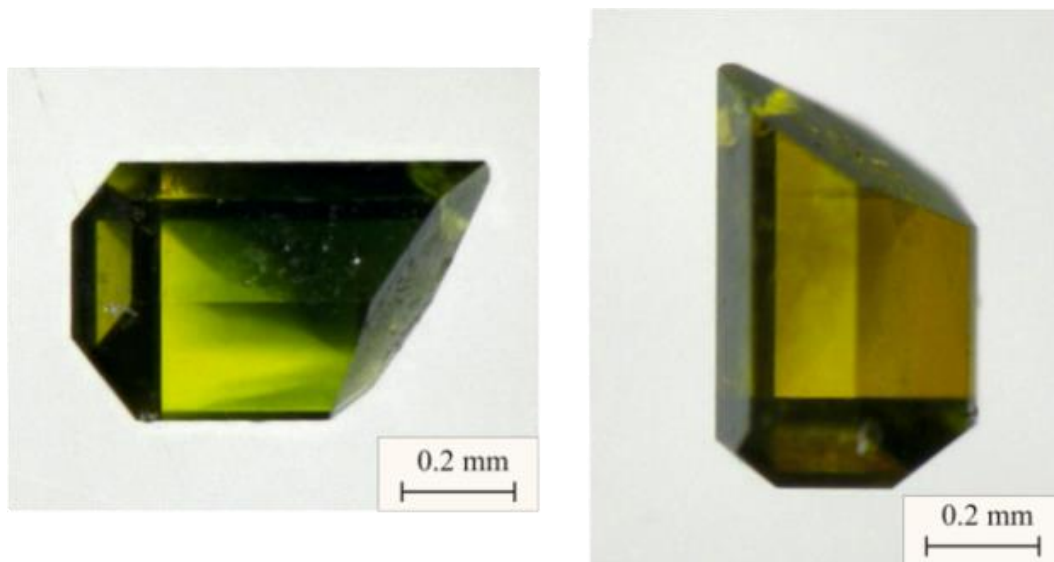


Figure 4.9 Photographs of  $\beta$ -VOPO<sub>4</sub> crystals (obtained by CVT using H<sub>2</sub>O as TA) showing dichroism (yellow/green), same crystal at two different orientations.

#### 4.2.6 Vanadyl(IV) pyrophosphate, (VO)<sub>2</sub>P<sub>2</sub>O<sub>7</sub>

Grey powders of (VO)<sub>2</sub>P<sub>2</sub>O<sub>7</sub> [10] were obtained by heating bright yellow powders of  $\beta$ -VOPO<sub>4</sub> [161] in  $p(\text{O}_2) \approx 20$  ppm (4N argon flow) at 700°C for one day. A silica boat charged with  $\beta$ -V<sup>V</sup>OPO<sub>4</sub> ( $m \approx 500$  mg) was inserted into a horizontal tubular furnace which was equipped with reaction tube of silica and controlled by Ni/Ni-Cr thermocouple. Argon was passed for 30 minutes through the reaction tube before rising the temperature. The flow of Ar gas was controlled by a valve. The furnace temperature was raised 50°h<sup>-1</sup>.

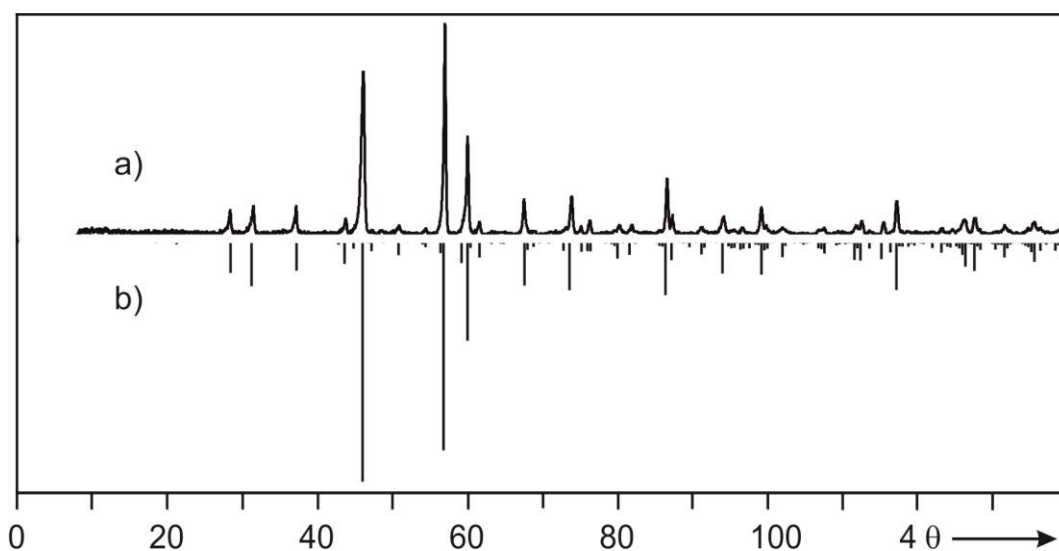


Figure 4.10 Synthesis of (VO)<sub>2</sub>P<sub>2</sub>O<sub>7</sub>. Comparison of the Guinier photograph of the obtained product (a) and simulated diffraction pattern (b) [10].

Dichroic single crystals of  $(VO)_2P_2O_7$  (see Figure 4.11) up to two mm edge-lengths were achieved by slow cooling of a melt. A silica boat charged with bright yellow powder of  $\beta$ -VOPO<sub>4</sub> was heated up to 1000°C (ramp 50 °h<sup>-1</sup>) in argon atmosphere and kept at this temperature for two days before cooling down to 700 °C at a cooling rate of 1 °h<sup>-1</sup>. Then the furnace was switched off and the material was allowed to cool to ambient temperature under argon. Very small variation in the oxidation state of vanadium in  $(VO)_2P_2O_7$  might causes different colors, which has already been reported. Crystals grown by pulling melt and slow cooling under pressure (3 kbar of Ar) are reported to be dark green [81] and blue [82], respectively.



Figure 4.11 Photograph of  $(VO)_2P_2O_7$  crystals obtained from a melt by slow cooling.

#### 4.2.7 Vanadium(III) phosphate, $VPO_4$

Single phase  $VPO_4$  [83] (see Figure 4.12) was prepared by vapor phase moderated solid state reaction in a sealed silica tube using iodine as mineralizer from a mixture of appropriate molar ratio of  $\beta$ - $VOPO_4$  (323.83 mg, 2 mmol) and VP [84] (40.96 mg, 0.5 mmol) at 800 °C according to the (eq. 4.10). Both the starting materials were grinded in a mortar. The ampoule was filled with the reactants, sealed and preheated at 450 °C for three days before heating to the final equilibration temperature.

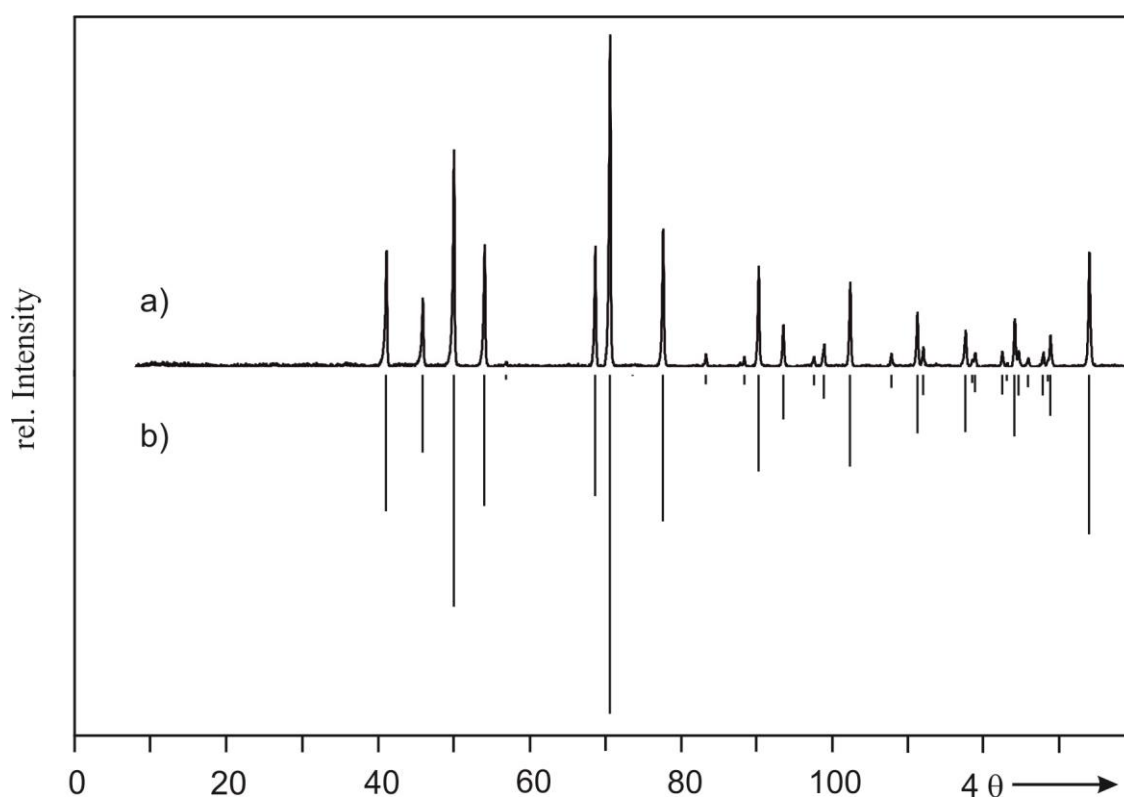


Figure 4.12 Synthesis of  $VPO_4$ . Comparison of the Guinier photograph of the obtained product (a) and simulated diffraction pattern (b) [83].

#### 4.2.8 Vanadium phosphide, VP

Single phase microcrystalline powders of VP [84] (Figure 4.13) were prepared by solid state reaction in sealed silica tubes from equimolar mixtures of granular vanadium (203.80 mg, 4 mmol) and red phosphorus (123.92 mg, 4 mmol P) at 700 °C according to the (eq. 4.11). The commercial granular greenish vanadium was washed with hot HCl to remove the slightly oxidized greenish surface, which gives the granules a metallic luster. The starting materials were sealed in a cleaned and dried (at 800 °C) silica tube. The ampoule was filled with the reactants and preheated at 450 °C for three days before heating to the final temperature.

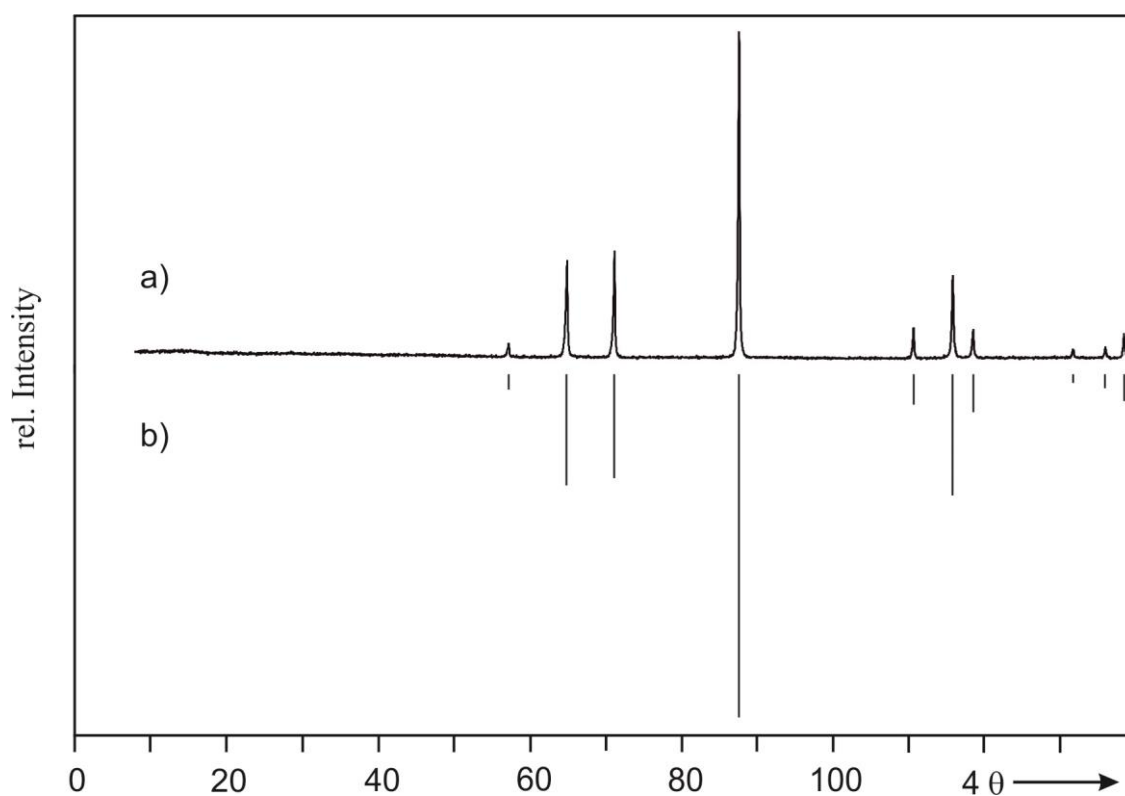


Figure 4.13 Synthesis of VP. Comparison of the Guinier photograph of the obtained product (a) and simulated diffraction pattern (b) [84].

### 4.2.9 Iron(III) phosphate, FePO<sub>4</sub>

Single phase light brown powder of Fe<sup>III</sup>PO<sub>4</sub> [85] was prepared according to literature [86]. A warm aqueous solution containing appropriate amounts of Fe(NO<sub>3</sub>)<sub>3</sub>·9H<sub>2</sub>O (808.05 mg, 2 mmol) and (NH<sub>4</sub>)<sub>2</sub>HPO<sub>4</sub> (528.26 mg, 2 mmol) was neutralized with aqueous ammonia. The resulting yellow precipitate was filtered, washed, and heated in an open silica tube at 200 °C for one day. Subsequent heating at 700 °C for three days led to the final product (see Figure 4.14).

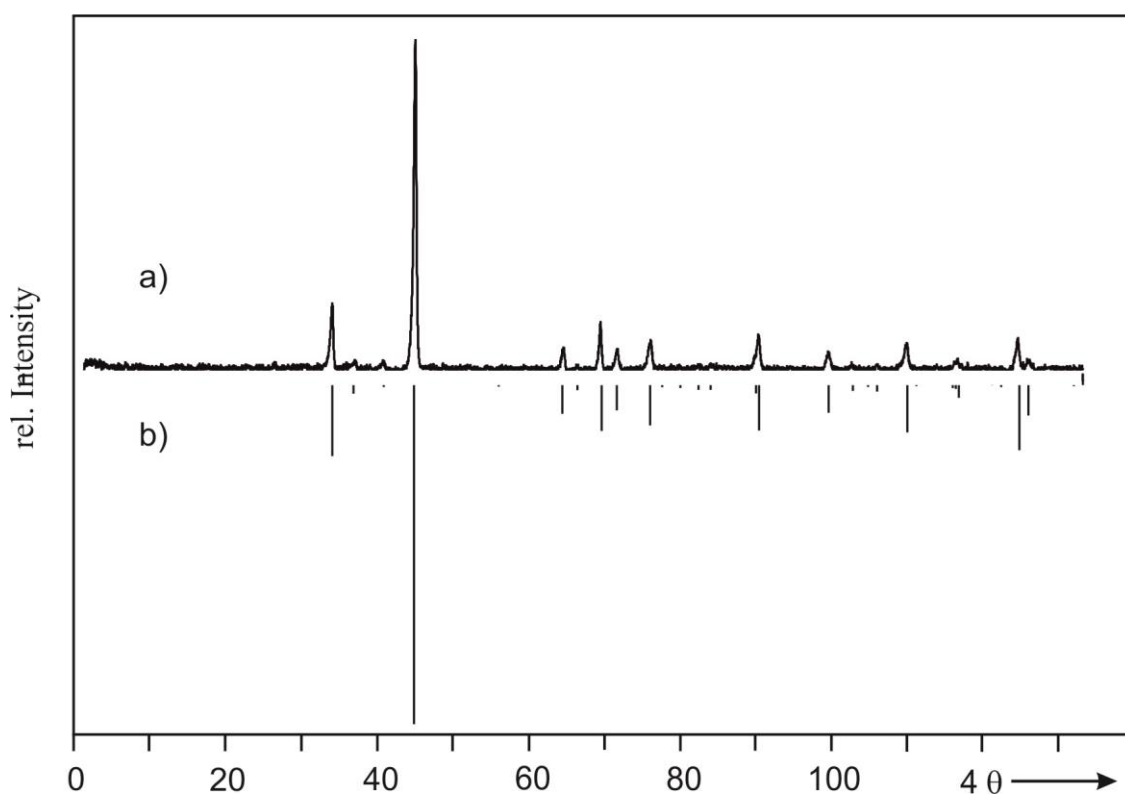


Figure 4.14 Synthesis of FePO<sub>4</sub>. Comparison of the Guinier photograph of the obtained product (a) and simulated diffraction pattern (b) [85].

#### 4.2.10 Indium(III) phosphate, $\text{InPO}_4$

$\text{In}^{\text{III}}\text{PO}_4$  [87] was prepared according to (eq. 4.12). The mixture of equivalent amounts of  $\text{In}_2\text{O}_3$  (832.60 mg, 3 mmol) and  $(\text{NH}_4)_2\text{HPO}_4$  (794.33 mg, 6 mmol) was heated in an open silica tube at 200 °C for one day and then at 400 °C for another day in order to evaporate the volatile products ( $\text{NH}_3$  and  $\text{H}_2\text{O}$ ). A single phase white powder of  $\text{In}^{\text{III}}\text{PO}_4$  (see Figure 4.15) was obtained by stepwise raising the temperature (100 °/day) with thorough grinding at every intermediate steps up to 1000 °C for two days.

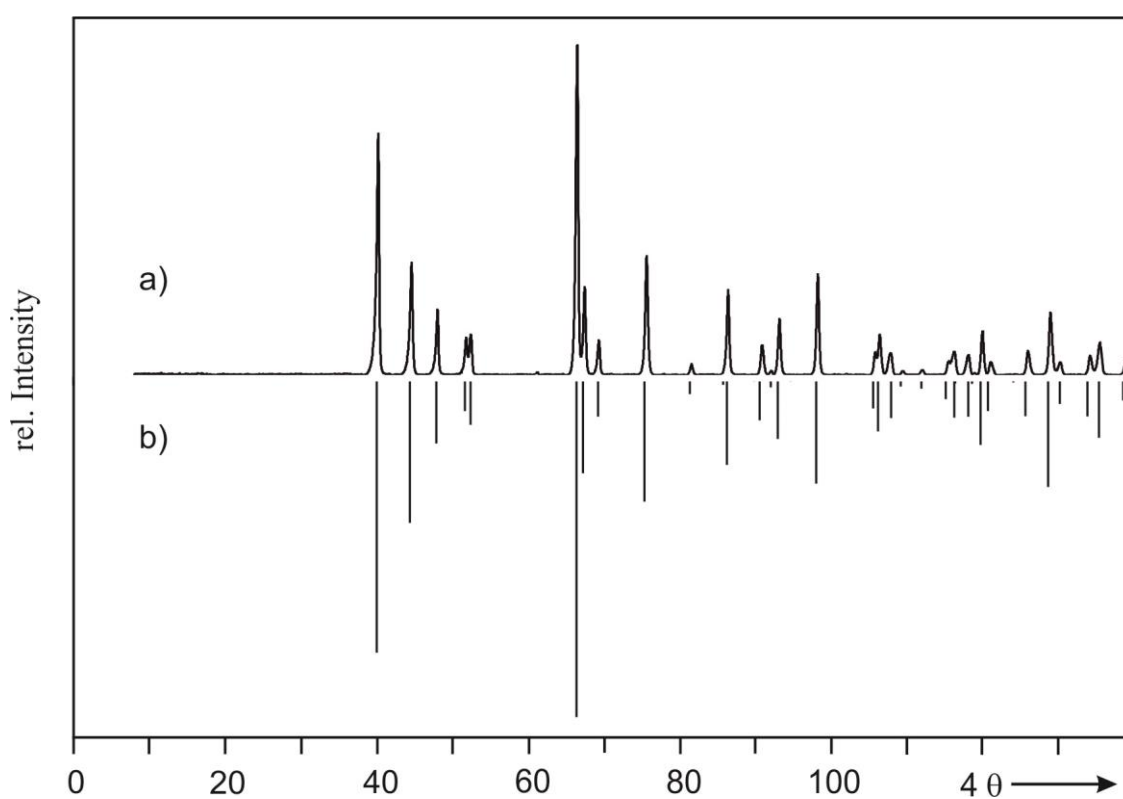
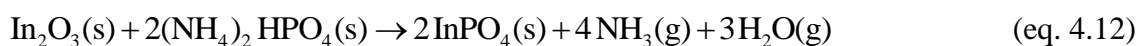


Figure 4.15 Synthesis of  $\text{InPO}_4$ . Comparison of the Guinier photograph of the obtained product (a) and simulated diffraction pattern (b) [87].



## 5 Crystal structures of $m\text{-W}_2\text{O}_3(\text{PO}_4)_2$ and $\text{WOPO}_4$ revisited

### 5.1 Introduction

Molybdenum, as element of group 6 forms anhydrous phosphates at different oxidation states +III, +IV, +V, +VI. Recently, the anhydrous phosphate of rhenium, diagonally related to molybdenum have been found to occur with oxidation states +IV, +V, +VI, and +VII [88]. Plenty of literature is available about the formation of anhydrous phosphates containing tungsten at oxidation states +IV, +V, +VI. Two fully oxidized tungsten phosphates with two different polymorphs for each have already been synthesized and characterized. They are  $o\text{-W}^{\text{VI}}\text{OP}_2\text{O}_7$  [75],  $m\text{-W}^{\text{VI}}\text{OP}_2\text{O}_7$  [79] and  $o\text{-W}^{\text{VI}}_2\text{O}_3(\text{PO}_4)_2$  [75] (isotypic to  $\text{W}^{\text{VI}}_2\text{O}_3(\text{AsO}_4)_2$  [89]) and  $m\text{-W}^{\text{VI}}_2\text{O}_3(\text{PO}_4)_2$  [76, 77, 78]. The crystal structure of  $m\text{-W}_2\text{O}_3(\text{PO}_4)_2$  was first solved in the monoclinic space group  $P2_1/m$  by Kierkegaard [76] with a high residual ( $R = 17\%$ ). Later Kierkegaard et al. [77] improved the quality of the structure refinement to 11.7%, however, in space group  $P2_1$ . Litterscheid [78] crystallized  $m\text{-W}_2\text{O}_3(\text{PO}_4)_2$  by CVT using  $\text{NH}_4\text{Cl}$  as transport additive and improved the quality of the refinement to  $R = 2.7\%$  with space group  $P2_1/m$ . For complete characterization of the fully oxidized anhydrous phosphate the  $^{31}\text{P}$ -MAS-NMR was missing. The white color of microcrystalline  $\text{W}_2\text{O}_3(\text{PO}_4)_2$  already expresses the oxidation state of tungsten. Therefore the XPS measurement of  $\text{W}_2\text{O}_3(\text{PO}_4)_2$  can be used as reference to determine the surface oxidation states of other tungsten phosphates. These open topics triggered the reinvestigation of  $m\text{-W}_2\text{O}_3(\text{PO}_4)_2$  which is one of the mostly used starting materials in this research work.

Tungsten(V) phosphate,  $\text{W}^{\text{V}}\text{OPO}_4$ , the second member of the series of monophosphate tungsten bronzes (MPTB,  $(\text{W}^{\text{V}}\text{O}_3)_{2m}(\text{PO}_2)_4$ ,  $m = 2$ ) was synthesized and characterized more than two decades ago by Lii et al. [90]. They reported orthorhombic symmetry and space group  $Pna2_1$ . In earlier work  $\text{W}^{\text{V}}\text{OPO}_4$  was reported as pseudo-orthorhombic [91], although from x-ray single crystal diffraction, the symmetry was identified as monoclinic. The single crystal structure refinement of  $\text{W}^{\text{V}}\text{OPO}_4$  by Lii et al. [90] allowed only isotropic thermal parameters for the oxygen atoms, to avoid physically meaningless numbers (NPD). Additionally the displacement parameters of some oxygen atoms were quite large. Furthermore, during their work on space group determination the  $hk0$  reflections were excluded. Peak multiplets in that plane were described as twinning. The Guinier photograph of  $\text{WOPO}_4$  obtained in this work showed splitting of

several reflections. All of these findings suggested a re-examination of the crystal structure of  $WOPO_4$  which is also used as starting material in this research work.

## 5.2 Equilibrium phase relations in the system W/P/O

In the ternary system W/P/O (Figure 5.1, [92]) exist the two fully oxidized tungsten phosphates  $W^{VI}_2O_3(PO_4)_2$  and  $W^{VI}OP_2O_7$  (with an orthorhombic and a monoclinic polymorph for each). The reduced phases,  $W^V_2O_3P_2O_7$  [93],  $W^VOPO_4$  [91, this thesis], and  $W^{IV}P_2O_7$  [94] have been synthesized and characterized, too. For partially reduced anhydrous tungsten(V,VI) phosphates two compositional series are known. These are  $(WO_3)_{2m}(PO_2)_4$ ;  $2 \leq m \leq 14$  [95, 96, 97] and  $(WO_3)_{2m}(P_2O_4)_4$ ;  $4 \leq m \leq 10$  [98] called MPTBp (mono-phosphate tungsten bronzes with pentagonal tunnel) and DPTBh (Di-phosphate tungsten bronzes with hexagonal tunnel), respectively. Smaller cations like  $Na^+$ ,  $K^+$ , and  $Pb^{2+}$  can be partially inserted into the empty tunnels of the MPTB structure [99, 100]. Larger metal ions,  $A^+$ : Rb, Cs, Ba, Tl can also be partially inserted into the hexagonal tunnels of DPTB structure [100, 101, 102] without any further change in the tunnel structure. The existence of  $\gamma$ - $Mo_4O_{11}$  [103] and  $\eta$ - $Mo_4O_{11}$  [104] with MPTBp and MPTBh structure types and empty tunnels confirm that the insertion of A ions is not regarded to stabilize the hexagonal tunnel structure. The structure of these compounds can be described as slabs of corner sharing  $WO_6$  octahedra ( $ReO_3$  type) separated by  $PO_4$  or  $P_2O_7$  units for MPTB and DPTB, respectively. The integer  $m$  is defining the MPTB or DPTB phases and can be interpreted as the width of the  $ReO_3$  related slabs ( $m = 2$ , two octahedra wide).

In the binary system W/P the known phosphides are WP [105],  $WP_2$  [106], and  $W_3P$  [107]. The binary system P/O consists of five condensed oxides with different oxidation states of phosphorus,  $P_4O_n$  ( $n = 6, 7, 8, 9, 10$ ). Phosphorus(V) oxide,  $P_4O_{10}$  [108, 109, 110, 111] with three modifications and phosphorus(III) oxide [112] are well-known. The mixed-valent(III, V) oxides are  $P_4O_n$  ( $n = 7, 8, 9$ ) [113, 114, 115]. At high temperatures ( $T > 300$  °C) and reducing conditions these oxides occur in the equilibrium gas phase. The binary system W/O has already been discussed in section 9.1. Crystallographic information on the existing compounds in system W/P/O are given in table Table 5.1.

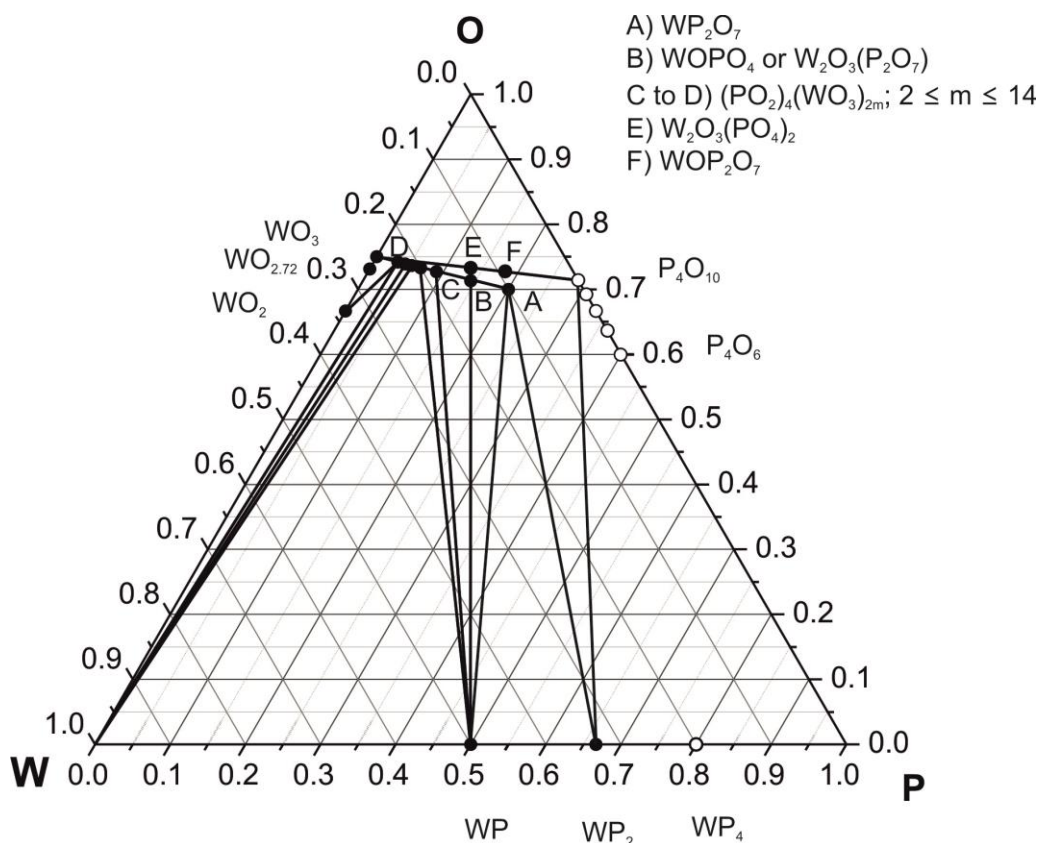


Figure 5.1 Ternary phase diagram of the system W/P/O at 900 °C according to [92].

Table 5.1 Summary of the crystallographic information of the existing compounds in system W/P/O, S.G.: space group, Z: formula units per unit cell.

Phases	S.G., Z	Unit cell parameters (Å, °)	Ref.
WP	$Pnma$ , 4	5.731(4), 3.248(2), 6.227(4)	[105]
$\alpha$ - $WP_2$	$C2/m$ , 4	8.500(3), 3.168(1), 7.466(2), 119.367(5)	[106]
$\beta$ - $WP_2$	$Cmc2_1$ , 4	3.1649(1), 11.1599(5), 4.9732(2)	[106]
$W_3P$	$I\bar{4}$ , 8	9.890, 4.808	[107]
$WP_2O_7$	$Pa\bar{3}$ , 4	7.9502(3)	[94]
$W^V_2O_3P_2O_7$	$Pnma$ , 4	5.2886(4), 12.3391(10), 13.0321(6)	[93]
$o$ - $W^{VI}OP_2O_7$	$Pnma$ , 4	16.6620(20), 5.147(2), 6.612(4)	[75]
$m$ - $W^{VI}OP_2O_7$	$C2/m$ , 4	15.710(5), 5.162(5), 6.917(5), 102.41(5)	[79]
$o$ - $W^{VI}_2O_3(PO_4)_2$	$Pnma$ , 4	15.683(1), 6.249(1), 7.934(1)	[75]
$m$ - $W^{VI}_2O_3(PO_4)_2$	$P2_1/m$ , 4	7.83(1), 12.48(2), 7.76(1), 91.9(1)	[76]
$m$ - $W^{VI}_2O_3(PO_4)_2$	$P2_1/m$ , 4	7.83(1), 12.48(2), 7.76(1), 91.9(1)	[78]
$m$ - $W^{VI}_2O_3(PO_4)_2$	$P2_1$ , 4	7.822(4), 12.50(1), 7.754(7), 91.05(5)	[77]
$W^V_2O_3(P_2O_7)$	$Pnma$ , 4	5.2886(4), 12.3391(10), 13.0321(6)	[93]
$W^VOPO_4$	$Pna2_1$ , 4	11.174(3), 6.550(2), 5.228(1)	[90]
$W^VOPO_4$	monoclinic	11.172(8), 5.217(1), 6.543(2), 90.34(4)	[91]
$W^VOPO_4^a$	tetragonal	6.250(1), 4.066(1)	[91]
$(PO_2)_4(W^{V,VI}O_3)_{2m}$ ( $2 \leq m \leq 14$ )	$P2_12_12_1$ , 1	5.312(1), 6.5557(8), 42.196(8) (for $m = 12$ )	[97]

<sup>a</sup>) high pressure form

### 5.3 Synthesis and crystallization of $m\text{-W}_2\text{O}_3(\text{PO}_4)_2$

Synthesis of grayish white powder of  $m\text{-W}_2\text{O}_3(\text{PO}_4)_2$  was described in section 4.2.2. Single crystals of  $m\text{-W}_2\text{O}_3(\text{PO}_4)_2$  with pale-yellowish shade (see Figure 5.2a) were obtained by CVT via endothermic reaction at  $1000 \rightarrow 900$  °C using chlorine as transport agent (in situ decomposition of  $\text{PtCl}_2$ ). Crystals with edge length up to one mm were obtained at transport rates  $\dot{m} = 0.3 \text{ mg}\cdot\text{h}^{-1}$ . The dichroic blue/colorless single crystals of  $m\text{-W}_2\text{O}_3(\text{PO}_4)_2$  (see Figure 5.2b) were crystallized using HCl as TA (in-situ decomposition of  $2 \text{ NH}_4\text{Cl} + 3 \text{ PtCl}_2$  with slight excess of  $\text{NH}_4\text{Cl}$ ).

The blue color points to a small oxygen deficiency that can be attributed to the slightly reducing synthetic condition, slight excess of  $\text{NH}_4\text{Cl}$  might lead to further decomposition of  $\text{NH}_3$  into hydrogen and nitrogen. A Guinier photograph of a powder of the blue crystals (maintaining same x-ray exposure time) shows a very slightly reduced intensity of the (040) reflection compare to the pale-yellow crystals as shown in Figure 5.3. However, the lattice parameters of blue crystals ( $a = 7.7766(8) \text{ \AA}$ ,  $b = 12.4985(7) \text{ \AA}$ ,  $c = 7.7905(7) \text{ \AA}$ ,  $\beta = 92.295(8)^\circ$ ,  $V = 756.60(11) \text{ \AA}^3$ ) and the reported  $m\text{-W}_2\text{O}_3(\text{PO}_4)_2$  ( $a = 7.751(4) \text{ \AA}$ ,  $b = 12.5054(6) \text{ \AA}$ ,  $c = 7.7903(5) \text{ \AA}$ ,  $\beta = 92.221(5)^\circ$ ,  $V = 756.89(7) \text{ \AA}^3$ ) [78] do not differ significantly.

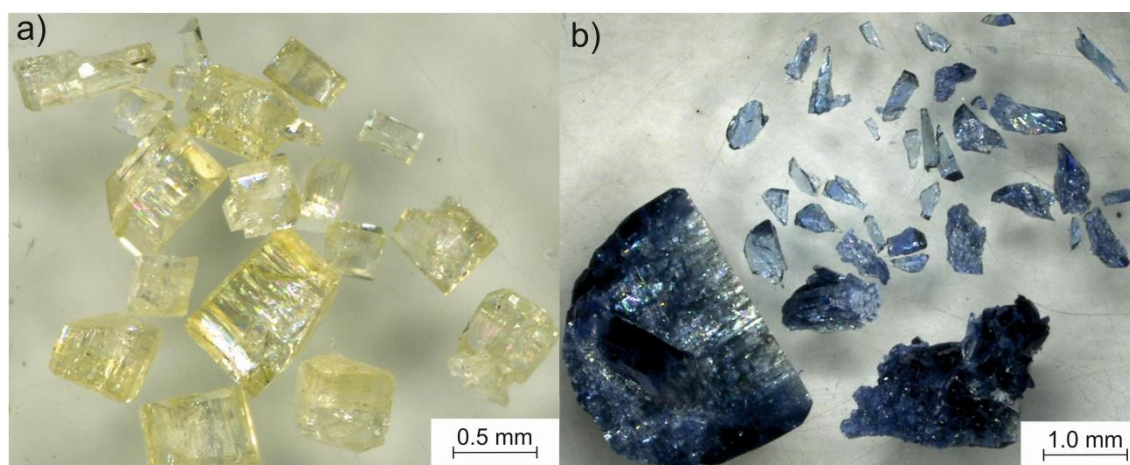


Figure 5.2 Photographs of  $m\text{-W}_2\text{O}_3(\text{PO}_4)_2$  crystals obtained by CVT using  $\text{Cl}_2$  (a) and HCl (b) as transporting agent.

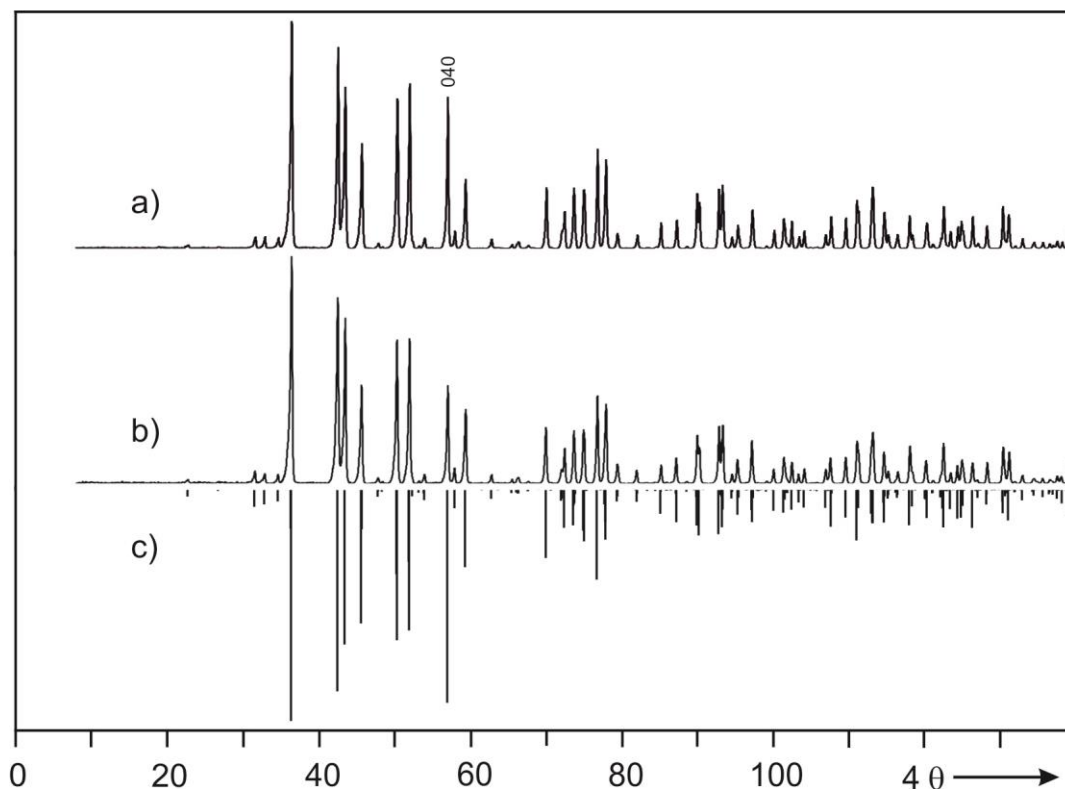
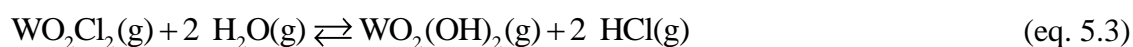
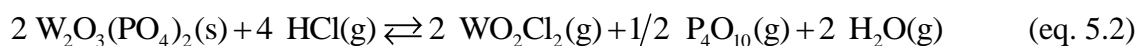
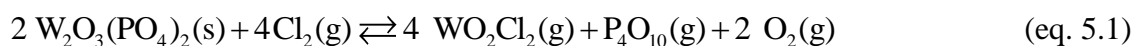


Figure 5.3 Comparison of Guinier photographs of  $m\text{-W}_2\text{O}_3(\text{PO}_4)_2$ . Stoichiometric pale-yellow crystals (a), under-stoichiometric dichroic blue/colorless crystals (b) and simulated diffraction pattern based on data in [78] (c).

Crystallization of  $m\text{-W}_2\text{O}_3(\text{PO}_4)_2$  was done by CVT using  $\text{Cl}_2$  or  $\text{HCl}$  as transporting agents. According to the literature on CVT of anhydrous phosphates [1, 43] and  $\text{WO}_3$  using chlorine [116] or  $\text{HCl}$  [117] as TA, the most important transport effective gaseous species are expected to be  $\text{WO}_2\text{Cl}_2$ ,  $\text{WO}_2(\text{OH})_2$ ,  $\text{P}_4\text{O}_{10}$  and  $\text{O}_2$ . Therefore, transport reactions of  $\text{W}_2\text{O}_3(\text{PO}_4)_2$  with  $\text{Cl}_2$  can be described by (eq. 5.1) and with  $\text{HCl}$  can be described by combination of the two reactions (eq. 5.2) and (eq. 5.3).



## 5.4 Crystal structure and $^{31}\text{P}$ -MAS-NMR spectrum of $m\text{-W}_2\text{O}_3(\text{PO}_4)_2$

The crystal structure of  $m\text{-W}_2\text{O}_3(\text{PO}_4)_2$  is built of corner sharing  $[\text{W}_2\text{O}_{11}]$  double octahedra and  $[\text{PO}_4]$  tetrahedra as shown in Figure 5.4. The structure contains three crystallographically independent sites for tungsten (Wyckoff positions  $4f$ ,  $2e$ ,  $2e$ ) and phosphorus (Wyckoff positions  $4f$ ,  $2e$ ,  $2e$ ) as well. Four of the six oxygen atoms of the  $\text{WO}_6$  octahedra are shared with four different  $\text{PO}_4$  units. The fifth one is shared with another  $\text{WO}_6$  unit leading to the double octahedra  $[\text{W}_2\text{O}_{11}]$  and the remaining oxygen bound to one tungsten atom ( $\text{W}=\text{O}^{4+}$  group).  $[\text{W}_2\text{O}_{11}]$  units are connected by  $[\text{PO}_4]$  tetrahedra to create ribbons running parallel to the crystallographic  $b$ -axis at  $y = 0$  and  $1/4$  level. The ribbons are only connected through  $\text{PO}_4$  units along the crystallographic  $b$ -axis leading to a 3D structure. It is worthwhile to mention that the formation of terminal tungstenyl bonds ( $-\text{W}=\text{O}$ ) in  $m\text{-W}_2\text{O}_3(\text{PO}_4)_2$  is the consequence of incorporation of  $\text{PO}_4$  tetrahedra in  $\text{WO}_3$  structure. This type of terminal metallyl group is unique to the structure of tungstenyl(VI) orthophosphate. Incorporation of additional redox active metals into  $m\text{-W}_2\text{O}_3(\text{PO}_4)_2$  structure might lead to good candidates for oxidation catalyst materials.

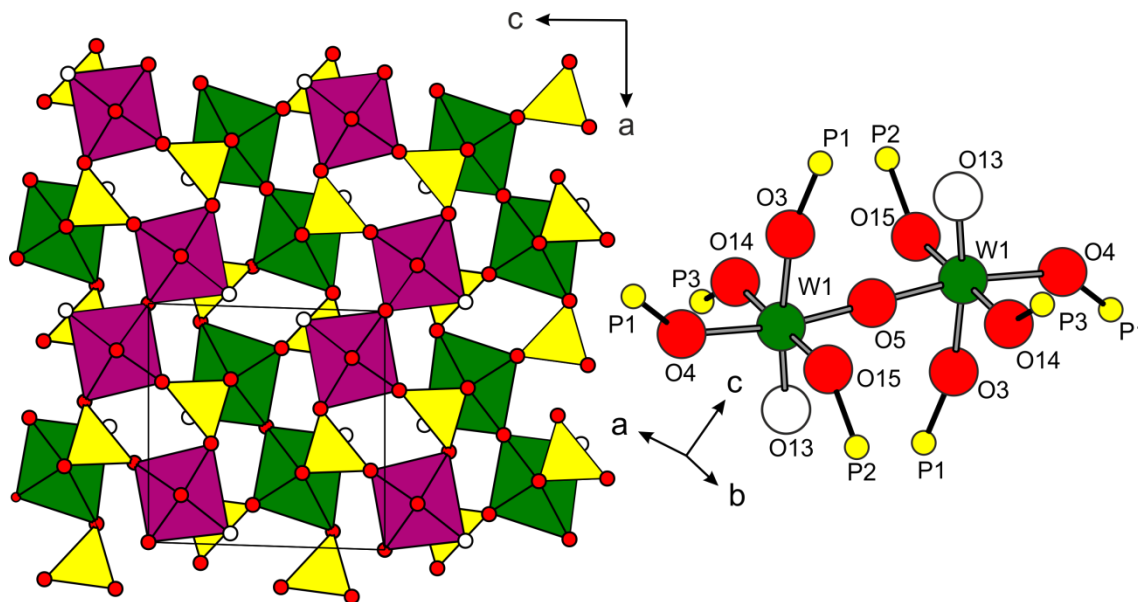


Figure 5.4 Polyhedral representation (left) of  $m\text{-W}_2\text{O}_3(\text{PO}_4)_2$  [77],  $[\text{W}_2\text{O}_{11}]$  double octahedra green (W1) and magenta (W2 and W3) at  $y = 0$  and  $1/4$ , respectively,  $[\text{PO}_4]$  tetrahedra yellow. Ball and stick model (right), open circle oxygen showing that the tungstenyl bonds are pointing in opposite directions.

The  $^{31}\text{P}$ -MAS-NMR spectrum of  $m\text{-W}_2\text{O}_3(\text{PO}_4)_2$  displayed in Figure 5.5 was measured at spin rates of 25 KHz where the saturation time is 512 s. The isotropic chemical shift parameters obtained from the measurement are  $\delta_{\text{iso}} = -14.9$  and  $-17.0$  ppm. Including the spinning side bands the relative intensity ratio is 3.14 : 1 which is in accordance with the crystal structure of  $m\text{-W}_2\text{O}_3(\text{PO}_4)_2$  containing three independent phosphorus sites at Wyckoff positions of  $4f$ ,  $2e$ , and  $2e$ .

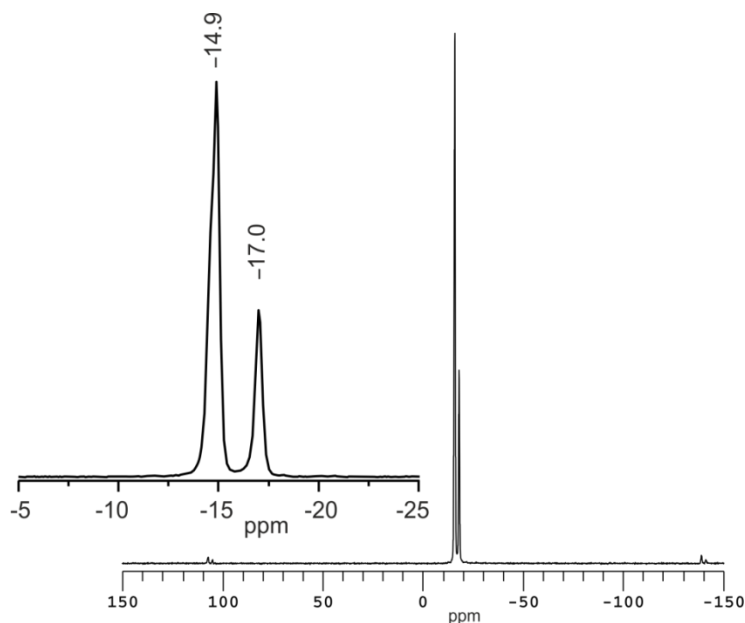


Figure 5.5 Quantitative  $^{31}\text{P}$ -MAS-NMR spectrum of stoichiometric  $m\text{-W}_2\text{O}_3(\text{PO}_4)_2$ .

### 5.5 XPS study of $m\text{-W}_2\text{O}_3(\text{PO}_4)_2$

There is no doubt about the oxidation state of tungsten (+6) in stoichiometric white powders of  $m\text{-W}_2\text{O}_3(\text{PO}_4)_2$  which is identified by XPS measurement (as shown in Figure 5.6). The binding energies (BEs) of tungsten were referenced to that of C1s level at 285.0 eV. Here the observed BEs of C1s is 284.47 eV which is 0.53 eV less than the corresponding reference BE. Hence, to get the corrected BE, 0.53 eV was added to the observed W4f BEs. The corrected BE of the  $\text{W}4f_{7/2}$  level is 36.77 eV, which is very close to that of  $\text{W}^{6+}$  in  $\text{WO}_3$  (35.4 - 36.6 eV) or in  $\text{Al}_2(\text{WO}_4)_3$  (35.8 - 36.7 eV) [118]. Therefore,  $m\text{-W}_2\text{O}_3(\text{PO}_4)_2$  might be used as XPS standard.



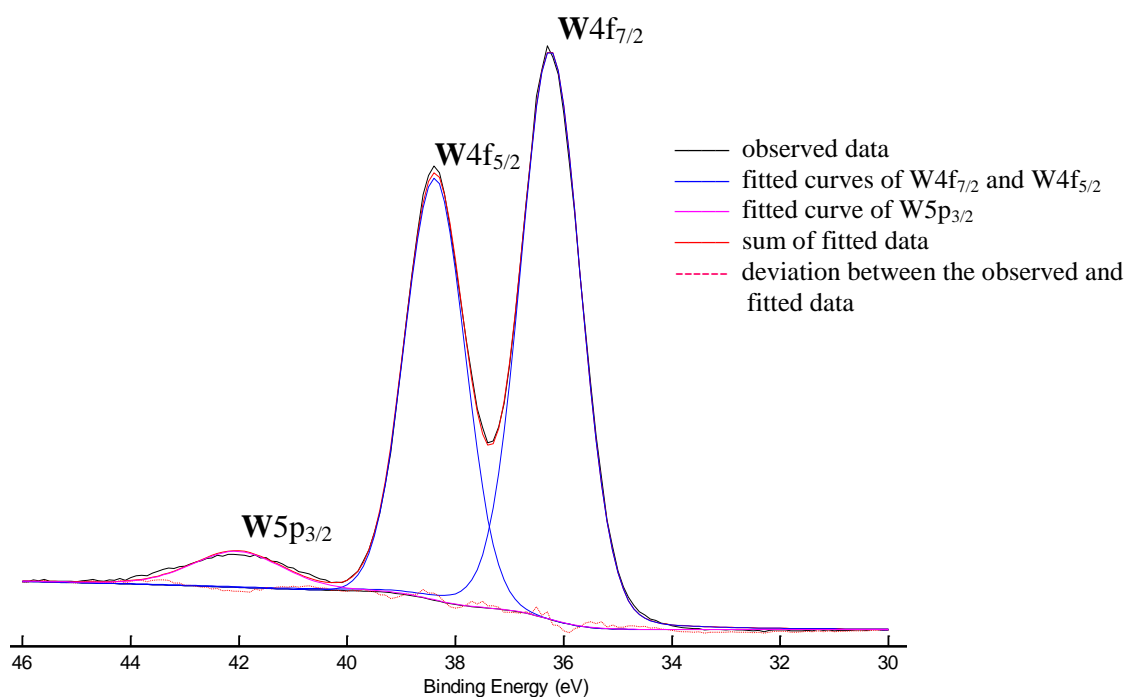


Figure 5.6 XPS spectrum of stoichiometric  $m\text{-W}_2\text{O}_3(\text{PO}_4)_2$  with fitted curves for  $\text{W}4f_{7/2}$ ,  $\text{W}4f_{5/2}$  and  $\text{W}4p_{3/2}$ .

## 5.6 UV/Vis/NIR spectroscopic studies of $m\text{-W}_2\text{O}_3(\text{PO}_4)_2$

The single crystal UV/Vis/NIR absorption spectra of a slightly under-stoichiometric dichroic (blue/colorless)  $m\text{-W}_2\text{O}_{3-\delta}(\text{PO}_4)_2$  show a broad and strong absorption band (10500 to 16000  $\text{cm}^{-1}$ ) centered at  $\tilde{\nu} \sim 13000 \text{ cm}^{-1}$  and a shoulder at 17800  $\text{cm}^{-1}$  (see Figure 5.7b). In agreement to the electronic absorption spectra of Keggin type anions containing mixed valent molybdenum or tungsten [119, 120], these absorption bands might be assigned as IVCT( $\text{W}^{5+} \rightarrow \text{W}^{6+}$ ). In addition, this assignment is supported by the observed broad absorption band at  $\tilde{\nu} \sim 14000 \text{ cm}^{-1}$  of a bluish single crystal and of blue amorphous lamella of  $\alpha\text{-(MoO}_2)_2(\text{P}_2\text{O}_7)$  reported in Ref. [88]. The stoichiometric crystals of pale-yellow  $m\text{-W}_2\text{O}_3(\text{PO}_4)_2$  do not show any IVCT transition (see Figure 5.7a).



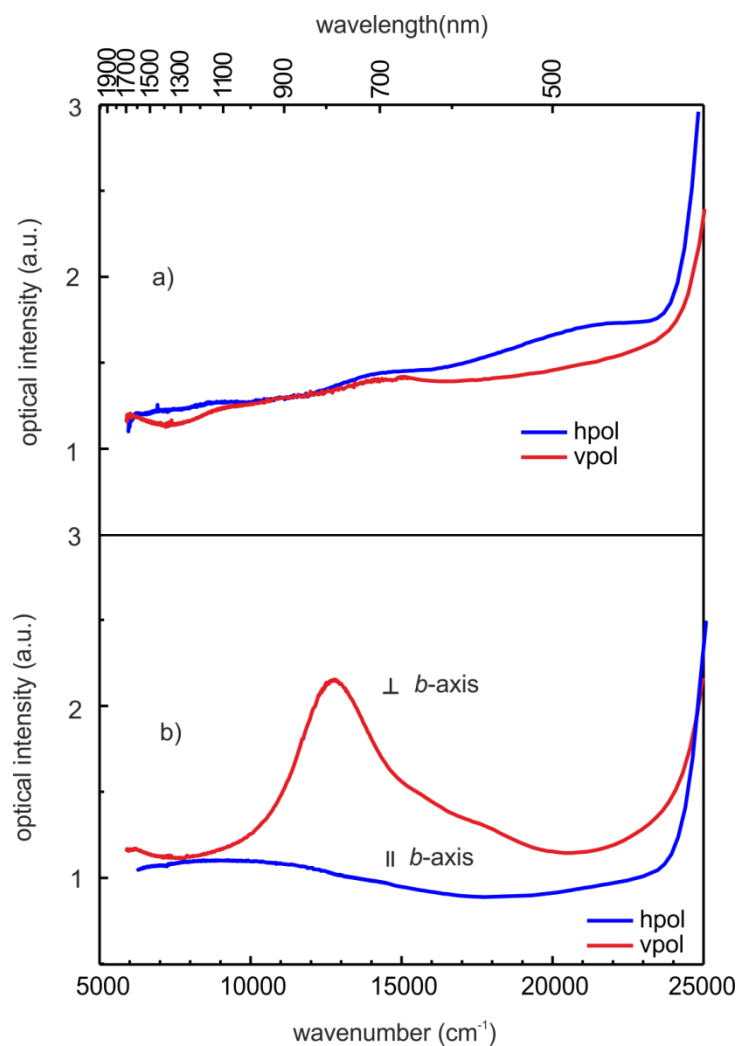


Figure 5.7 Polarized single crystal UV/Vis/NIR absorption spectra of stoichiometric, pale-yellow  $m\text{-W}_2\text{O}_3(\text{PO}_4)_2$  (a) and slightly oxygen-deficient dichroic blue/colorless  $m\text{-W}_2\text{O}_{3-\delta}(\text{PO}_4)_2$  (b), hpol and vpol are presumably parallel and perpendicular to the  $b$ -axis, respectively.

## 5.7 Synthesis and crystallization of $\text{W}^{\text{V}}\text{OPO}_4$

Microcrystalline dark brown powders of  $\text{WOPO}_4$  were prepared from the appropriate molar ratio of  $\text{W}_2\text{O}_3(\text{PO}_4)_2$ ,  $\text{WO}_3$  and red phosphorus at 1000 °C in sealed ampoules according to (eq. 5.4).



The starting materials were finely ground in an agate mortar and sealed in a preheated, evacuated silica tube ( $l = 11$  cm and  $d = 1.5$  cm) and subsequently heated in a muffle furnace for seven days at  $1000$  °C.

Single crystals of  $\text{WOPO}_4$  were obtained by CVT in a temperature gradient  $1000 \rightarrow 900$  °C for seven days using iodine as a transport agent. Crystals of up to four mm edge length (see Figure 5.8) were obtained at transport rate  $\dot{m} = 3$  mg·h<sup>-1</sup>.

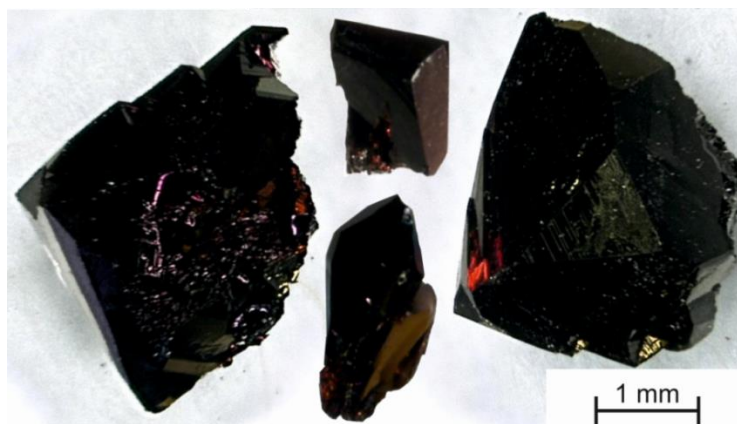
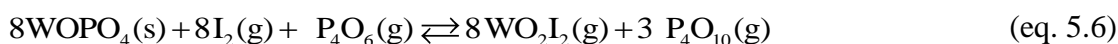
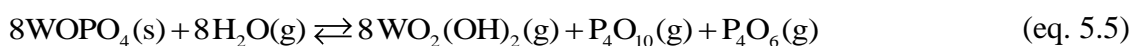


Figure 5.8 Photograph of  $\text{WOPO}_4$  crystals obtained by CVT using iodine as TA.

According to literature the CVT of anhydrous phosphates [43] and  $\text{WO}_3$  [116] using water or iodine as transport agent, the most effective transport species are expected to be  $\text{WO}_2(\text{OH})_2$ ,  $\text{WO}_2\text{I}_2$ ,  $\text{P}_4\text{O}_6$ , and  $\text{P}_4\text{O}_{10}$ . The transport agent, iodine is added and the water comes from the ampoule inside, because it is difficult to exclude the presence of water inside the ampoule although the ampoule was evacuated at  $800$  °C [121]. Therefore, CVT of  $\text{WOPO}_4$  is expected to proceed according to (eq. 5.5) and (eq. 5.6).



## 5.8 Single crystal structure refinement of $\text{WOPO}_4$

A suitable crystal of  $0.02 \times 0.06 \times 0.10$  mm<sup>3</sup> size was chosen under a polarizing microscope and glued on a thin vitreous silica fiber. Single crystal diffraction data were collected on a Bruker APEX-II CCD diffractometer controlled by the Bruker APEX2 and SAINT software [122] using graphite-monochromated Mo-K $\alpha$  ( $\lambda = 0.71073$  Å) radiation at ambient temperature. Crystal system, lattice type was determined from simulated precession

photographs. The starting parameters for the least square refinement were obtained by Direct methods with SHELX-97. Full-matrix least-squares refinement was carried out by using SHELX-97 [123] in the WinGX [124] framework.

The observed x-ray powder diffraction pattern (Guinier photograph) of  $W^V OPO_4$  shows splitting in some of the reflections (see Figure 5.9, top) compared to the already reported orthorhombic  $WOPO_4$  [90] which is clearly pointing to lower symmetry (monoclinic). The single crystal structure refinement (see Table 5.2) confirms the monoclinic angle,  $\beta = 90.12^\circ$  and symmetry. All the atoms were refined with anisotropic temperature factors and the W-O-P bridging oxygen atom (O8) showed relatively large anisotropic displacement parameter. The x-ray powder pattern is compared with the simulated pattern based on the single crystal structure refinement ( $P2_1/m$ ) in Figure 5.9. The atomic coordinates and anisotropic displacement parameters ( $\text{\AA}^2$ ) for  $WOPO_4$  are given in Table 14.1 and Table 14.2, respectively. Assigning of the Guinier photograph is given in Table 14.4.

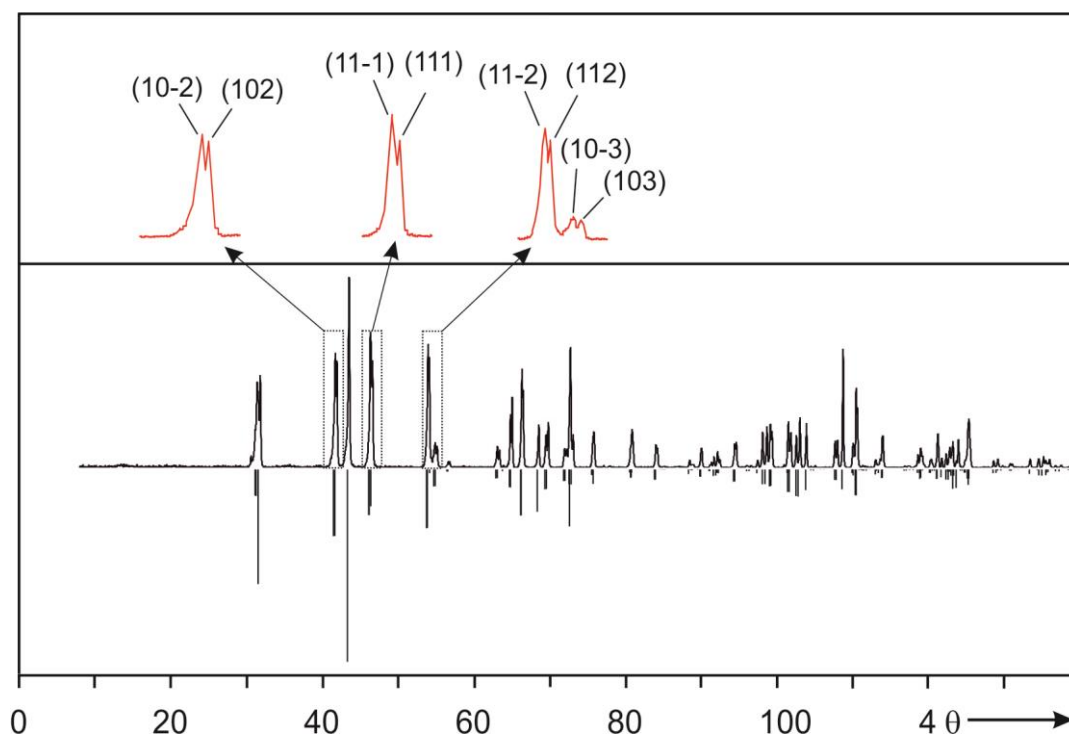


Figure 5.9 Guinier-photograph of  $WOPO_4$  (middle) and simulated diffraction pattern based on single-crystal structure refinement (bottom, [this thesis]). Magnified peak profiles showing the splitting due to a slight monoclinic distortion of the unit cell (top).

Table 5.2 Details on data collection and single crystal structure refinement of WOPO<sub>4</sub>.

Empirical formula	WPO <sub>5</sub>
Structural formula	(PO <sub>2</sub> ) <sub>4</sub> (WO <sub>3</sub> ) <sub>4</sub>
Formula weight	294.8119
Crystal system	monoclinic (11)
Space group	$P2_1/m$
$T$ (K)	295
$\lambda$ (Å)	0.71073
$a$ (Å) <sup>a)</sup>	6.5541(4)
$b$ (Å) <sup>a)</sup>	5.2234(7)
$c$ (Å) <sup>a)</sup>	11.1862(7)
$\beta$ <sup>a)</sup>	90.330(6)
$V$ (Å <sup>3</sup> ) <sup>a)</sup>	382.97(7)
$Z$	4
$D_{\text{calc}}$ (g·cm <sup>-3</sup> )	5.115
$\mu$ (mm <sup>-1</sup> )	30.48
Crystal dimensions (mm <sup>3</sup> )	0.02 × 0.06 × 0.10
Crystal color	bronze
$F(0\ 0\ 0)$	516
Measured refls.	5605
Independent refls.	1832
Absorption correction	empirical
No. of parameters	80
Theta range (°)	1.82 - 35.00
Index ranges	$-10 \leq h \leq 6, -8 \leq k \leq 8; -13 \leq l \leq 18$
$Goof$	1.027
$R_{\text{int}}$	0.039
$R$ indices [ $I > 2\sigma(I)$ ]: $R_1, wR_2$ <sup>b)</sup>	0.027, 0.073
$R$ indices (all data): $R_1, wR_2$ <sup>b)</sup>	0.035, 0.078

<sup>a)</sup> lattice parameters from XRPD, <sup>b)</sup>  $R_I = \frac{\sum |F_o| - |F_c|}{\sum |F_o|}$ ,  $F^2 > 2\sigma(F^2)$ ,  $w = 1/[\sigma^2(F_o^2) + (AP)^2 + BP]$ ,  $P = (F_o^2 + 2F_c^2)/3$ .

## 5.9 Crystal structure of WOPO<sub>4</sub>

The mixed-valence tungsten(V,VI) phosphates (PO<sub>2</sub>)<sub>4</sub>(WO<sub>3</sub>)<sub>2 $m$</sub>  ( $2 \leq m \leq 14$ ) [100] are termed Monophosphate Tungsten Bronzes (MPTB). This series of phosphates contains potential candidates for quasi-one or -two dimensional properties due to their strong structural anisotropy [125]. W<sup>V</sup>OPO<sub>4</sub> is considered as second member ( $m = 2$ ) of the MPTB series as shown in Figure 5.10b. The structure of WOPO<sub>4</sub> is isostructural to the high temperature form of NbOPO<sub>4</sub> [126] and the low pressure form of TaOPO<sub>4</sub> [127]. The structure of MPTB can be described as ReO<sub>3</sub>-type slabs/layers of corner sharing WO<sub>6</sub> octahedra with thickness of  $m$  octahedra, separated by PO<sub>4</sub> groups. Thus pentagonal

tunnels between the junction of  $\text{WO}_6$  slabs and  $\text{PO}_4$  tetrahedra are created. However, the second member of this series actually doesn't have any  $\text{ReO}_3$ -type slabs. Due to smaller  $m$  value corner sharing  $\text{W}_2\text{O}_{10}$  double octahedra form one dimensional zig-zag chains and these chains are isolated from another by  $\text{PO}_4$  tetrahedra (Figure 5.10a). The oxidation states of tungsten in  $\text{WOPO}_4$  is exclusively 5+ which is different from the other members of the series. This average oxidation state increases with increasing value of  $m$ . According to the formula of MPTB series,  $\text{WP}_2\text{O}_7$  [94] can be considered as the first member ( $m = 1$ ). This consideration is not backed by the crystal structure of  $\text{WP}_2\text{O}_7$ .

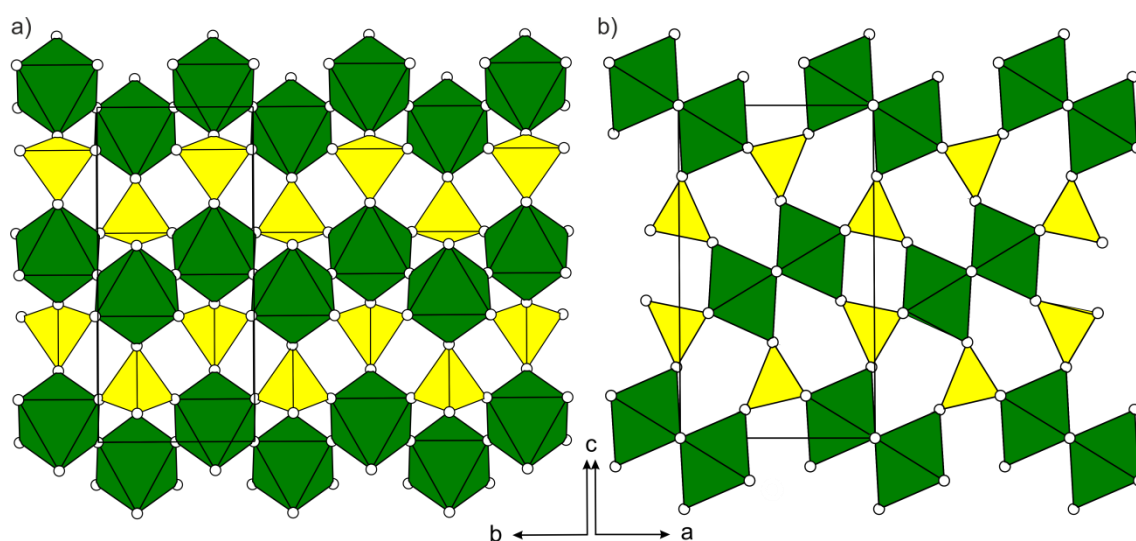


Figure 5.10 Crystal structure of  $\text{WOPO}_4$ , green and yellow represent  $[\text{WO}_6]$  octahedra and  $[\text{PO}_4]$  tetrahedra, respectively.

Each of the  $\text{WO}_6$  octahedra are sharing corners with four different  $\text{PO}_4$  tetrahedra and two  $\text{WO}_6$  octahedra in cis position. The  $\text{WO}_6$  octahedra are distorted with two short distances ( $d(\text{W1-O7}) = 1.8448(2) \text{ \AA}$  and  $d(\text{W2-O6}) = 1.8474(2) \text{ \AA}$ ) and four long distances ( $1.947(6) \leq d(\text{W1-O}) \leq 1.976(5) \text{ \AA}$  and  $1.962(6) \leq d(\text{W2-O}) \leq 1.971(6) \text{ \AA}$ ) (see Figure 5.11, [128]). The short distances are along the bridging oxygen atoms ( $\text{O6}$  and  $\text{O7}$ , both at special sites) of two  $\text{WO}_6$  octahedra. The two crystallographically independent  $\text{PO}_4$  units are fairly regular ( $1.491(3) \leq d(\text{P1-O}) \leq 1.517(7) \text{ \AA}$ ) and ( $1.506(6) \leq d(\text{P2-O}) \leq 1.526(6) \text{ \AA}$ ). Selected interatomic distances for  $\text{WOPO}_4$  are given in Table 14.3.

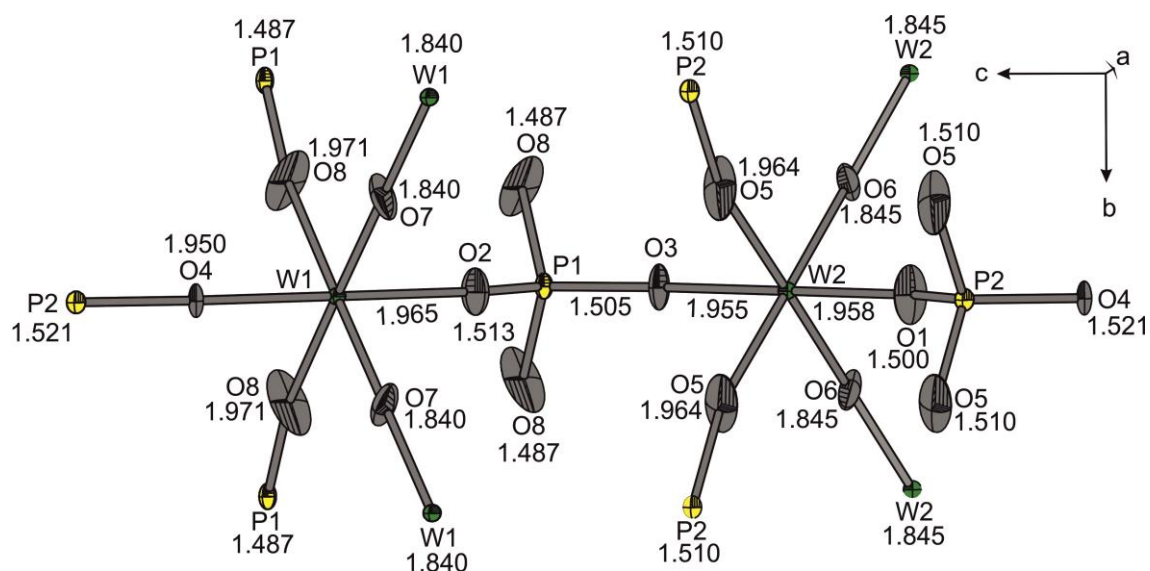


Figure 5.11 ORTEP representation of  $[WO_6]$  and  $[PO_4]$  polyhedra in  $WOPO_4$ . Ellipsoids are at 50% probability level, software DIAMOND [128].

## 5.10 Magnetic behaviour of $W^V OPO_4$

The temperature dependence of the molar magnetic susceptibility  $\chi_m^{-1}$  of crushed crystals of  $WOPO_4$  was measured as a function of temperature ( $2 \leq T \leq 300$  K, Figure 5.12) using a vibrating sample magnetometer, VSM. The magnetization measurement was performed by first cooling the sample from room temperature to 2 K under applied magnetic field and then rising the temperature using the same temperature sweep rate. A diamagnetic correction was applied to the observed weight data according to the method of atom and group increments [129].

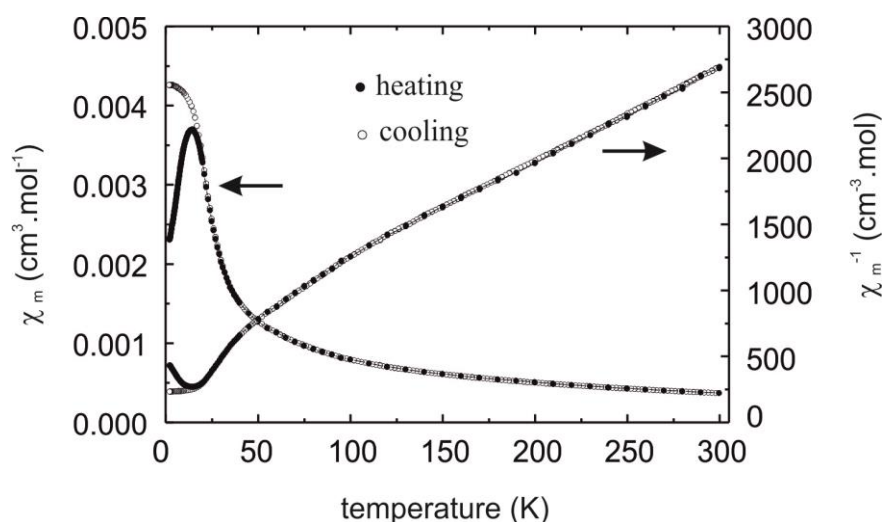


Figure 5.12 Temperature dependent molar susceptibility,  $\chi_{mol}$  and its reciprocal,  $\chi_{mol}^{-1}$  of  $WOPO_4$ .

$\text{WOPO}_4$  shows Curie-Weiss behavior [130]. At high temperature range ( $50 \leq T \leq 300$  K) the observed constant magnetic moment is  $\mu_{\text{exp}} = 1.06\mu_{\text{B}}/ \text{W}^{5+}$  and the paramagnetic Curie temperature is calculated to  $\theta_{\text{p}} = -78$  K by using (eq. 3.34). The moment is distinctly lower than the spin-only value of  $1.73 \mu_{\text{B}}$  for one unpaired electron. The observed reduced magnetic moment can be attributed to the strong spin-orbit coupling of the  $5d^1$  ( $\text{W}^{5+}$ ) system. Below 100 K the susceptibility deviates significantly from the Curie-Weiss behavior and at 15.6 K  $\text{WOPO}_4$  shows some antiferromagnetic ordering. The deviation from the linearity or change in magnetic exchange interaction below 50 K would be the consequence of distorted  $\text{WO}_6$  octahedra which was postulated by Greenblatt and et al. [131]. The magnetization curves for both heating and cooling are the same above 15.6 K however, they deviate from each other below this temperature. The orientation dependent magnetic and conductivity measurements conducted by Greenblatt and et al. [131] also showed anisotropic magnetic and electronic properties as expected due to its 1D chain structure. Although  $\text{WOPO}_4$  shows paramagnetic behavior due to the unpaired electron of  $\text{W}^{5+}$ , no EPR resonance is observed even at low temperature (10 K). This can be attributed to the high concentration of paramagnetic centers.

## 5.11 Conclusion

Pale-yellow crystals of stoichiometric  $m\text{-W}_2\text{O}_3(\text{PO}_4)_2$  [76, 77, 78] of up to one mm edge length were crystallized by CVT using chlorine as transport agent. Slightly reducing condition using hydrogen chloride as TA lead to the formation of under-stoichiometric dichroic (blue/colorless) crystals of  $m\text{-W}_2\text{O}_{3-\delta}(\text{PO}_4)_2$ . The oxygen vacancy in  $m\text{-W}_2\text{O}_{3-\delta}(\text{PO}_4)_2$  can be compared to non-stoichiometric  $\text{WO}_{3-\delta}$  [256, 257]. In contrast to the pale-yellow stoichiometric  $m\text{-W}_2\text{O}_3(\text{PO}_4)_2$ , under-stoichiometric  $m\text{-W}_2\text{O}_{3-\delta}(\text{PO}_4)_2$  shows dichroic (blue/colorless) behaviour. This can be explained by an IVCT transition ( $\text{W}^{5+} \rightarrow \text{W}^{6+}$ ) which is observed at  $\tilde{\nu} \approx 13000 \text{ cm}^{-1}$ . White powder of  $m\text{-W}_2\text{O}_3(\text{PO}_4)_2$  confirm its stoichiometry and the oxidation states which might be used as XPS standard. The BE of the  $\text{W}4f_{7/2}$  level in  $m\text{-W}_2\text{O}_3(\text{PO}_4)_2$  is 36.77 eV. The quantitative  $^{31}\text{P}$ -MAS-NMR studies of  $m\text{-W}_2\text{O}_3(\text{PO}_4)_2$  are in agreement with three crystallographic phosphorus sites within the crystal structure. Refinement of the dark brown single crystal of  $\text{W}^{\text{V}}\text{OPO}_4$  obtained by CVT has revealed the monoclinic ( $Z = 4$ , S.G.  $P2_1/m$ ) in contrast to the previously reported orthorhombic symmetry ( $Z = 4$ , S.G.  $Pna2_1$ ).

## 6 Solid solutions $(V_{1-x}W_x)OPO_4$ ( $0 \leq x \leq 1$ )

### 6.1 Introduction

The well established quasi-binary oxide systems  $WO_x$ - $PO_{2.5}$  [1, 92, 97],  $VO_y$ - $PO_{2.5}$  [132, 133] and  $VO_y$ - $WO_x$  [134, 135] ( $2.5 \leq x \leq 3$  and  $2 \leq y \leq 2.5$ ) are shown in Figure 6.1a (the oxygen co-existence pressures for the binary systems are shown in Figure 6.1b [136]). However, no investigation is known in literature about the quasi-ternary systems  $WO_x$ - $VO_y$ - $PO_{2.5}$ . Therefore, exploration of new materials in these systems appeared to be scientifically valuable. Besides, the search for new catalyst materials for butane based MA production would be worthwhile and economically lucrative. In addition, it had already been reported that V/W mixed oxides are catalytically active for the selective oxidation of acrolein to acrylic acid [137].

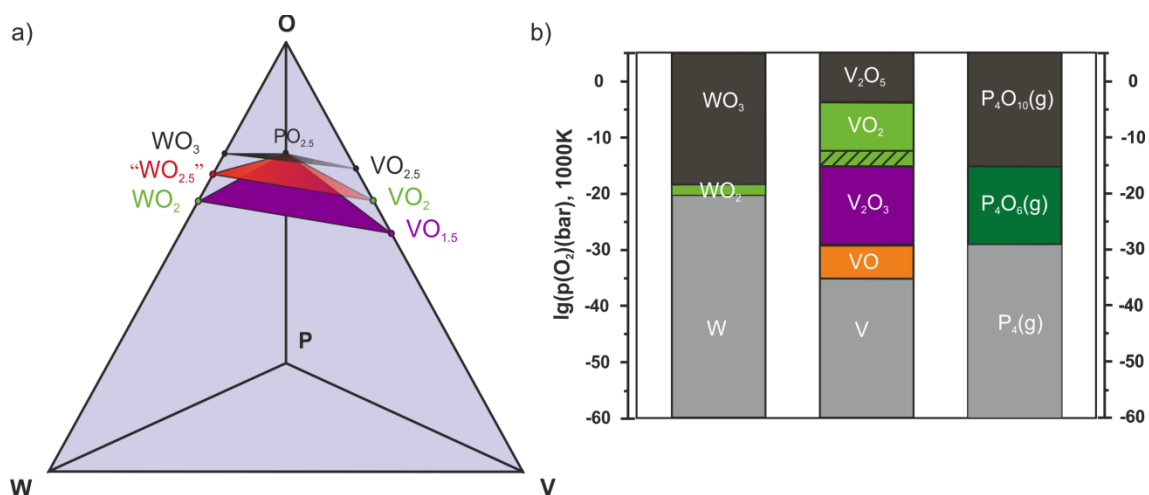


Figure 6.1 The system W/V/P/O with three quasi-ternary oxide systems (a) and the oxygen co-existence pressure diagrams at 1000 K for tungsten, vanadium, and phosphorus oxides (b) [136].

Experiments aiming at the introduction of mixed-valency in  $\alpha_{II}$ - $VOPO_4$  by solid solution formation with  $(V^{IV}O)Mo^VI O_4$  or  $(Mo^VO)PO_4$  led, according to the authors, to only small amounts (up to 7%) of heterovalent substitution of phosphate by molybdate and  $V^{5+}$  by  $V^{4+}$  [138]. On the other hand, partial substitution of niobium by tungsten in  $\alpha$ - $NbOPO_4$  (S.G.  $P4/n$  [139]) lead to  $(Nb^{V}_{0.787}W^{V}_{0.213})OPO_4$  [140] (S.G.  $P4/nmm$ ) which is closely related to the host structure. It is worth to be mentioned that the high temperature polymorph  $\beta$ - $NbOPO_4$  [141] is isotypic to  $WOPO_4$  [90, this thesis]. However, information on solid solution formation between  $VOPO_4$  and  $WOPO_4$  was lacking in literature. This



might be attributed to their two different crystal structures and the quite different redox behavior of  $V^{5+}$  and  $W^{5+}$ .

In this chapter, the redox chemistry of the anhydrous transition metal phosphates  $V^V OPO_4$  and  $W^V OPO_4$  and formation of three different solid solutions with the structure types of  $\alpha_{II}$ -,  $\beta$ - $VOPO_4$ , and  $WOPO_4$  is reported. Single crystal structure refinements along with the results of various other techniques for characterization (EPR, XPS, UV/Vis/NIR, magnetic behavior, and electric conductivity measurement) are also included.

## 6.2 Equilibrium phase relations in systems $WO_x/VO_y/PO_{2.5}$

$$(2.0 \leq x \leq 3.0; 1.5 \leq y \leq 2.5)$$

The quaternary system W/V/P/O can be represented by a Gibbs phase tetrahedron as shown in Figure 6.1 where the quasi-ternary section  $WO_3/VO_{2.5}/PO_{2.5}$  is the fully oxidized plane (see Figure 6.2). The other quasi-ternary sections " $WO_{2.5}$ "/ $VO_2/PO_{2.5}$  and  $WO_2/VO_{1.5}/PO_{2.5}$  are the two successive planes just below the fully oxidized one where W and V are in reduced oxidation states. (see Figure 6.2). Compounds known in these quasi-binary oxides are listed in Table 6.1.

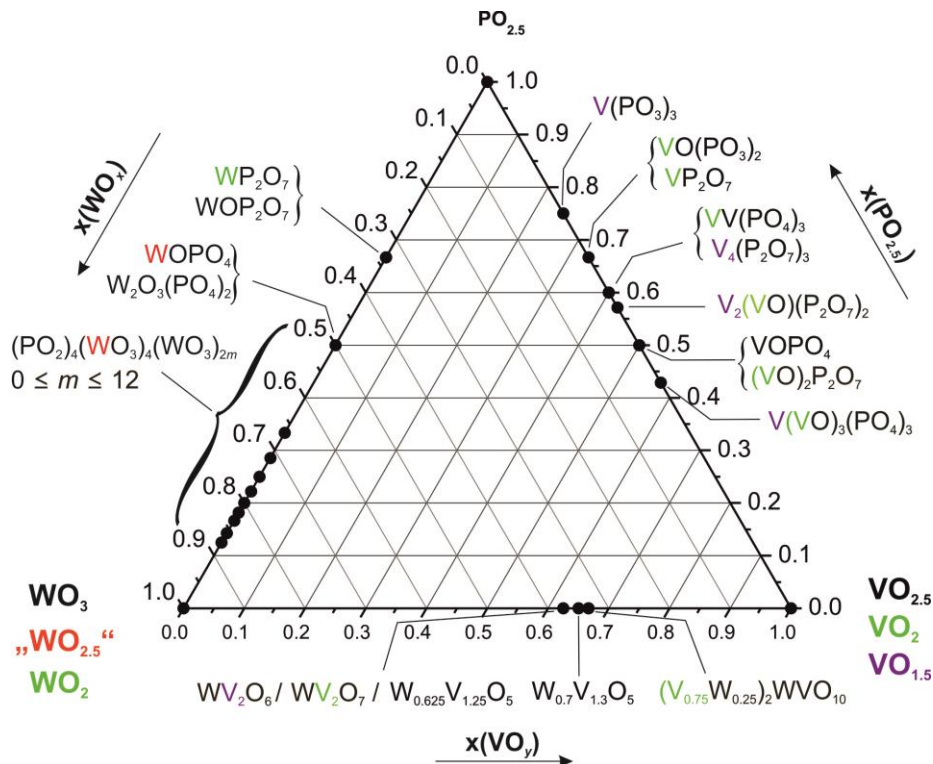


Figure 6.2 Visualization of the existing compounds in systems  $WO_x/VO_y/PO_{2.5}$ , ( $2.0 \leq x \leq 3.0$ ;  $1.5 \leq y \leq 2.5$ ) within a phase triangle. The reduced phases containing  $W^{5+}$ ,  $M^{4+}$  ( $M$ : W, V), and  $V^{3+}$  are indicated by red, green and violet color, respectively.

Table 6.1 Crystallographic information on tungsten-vanadium oxides and vanadium phosphates (tungsten phosphates are given in Table 5.1), S.G.: space group, Z: formula units per unit cell.

Phase	S.G., Z	Unit cell parameters (Å, °)	Ref.
WV <sub>2</sub> O <sub>6</sub>	<i>P4<sub>2</sub>/mmm</i> , 2	4.6213(5), 8.8864(6)	[142]
WV <sub>2</sub> O <sub>7</sub>	<i>C2</i> , 6	24.4, 7.44, 3.95, 90.0	[143]
W <sub>0.625</sub> V <sub>1.25</sub> O <sub>5</sub>	<i>I4/mmm</i> , 16	19.5, 3.7	[144]
W <sub>0.7</sub> V <sub>1.3</sub> O <sub>5</sub>	<i>I4/mmm</i> , 16	19.506(1), 3.7039(7)	[145]
W <sub>3</sub> V <sub>5</sub> O <sub>20</sub> <sup>a)</sup>	<i>C2/m</i> , 2	24.413(3), 7.446(2), 3.950(1), 91.03(2)	[146]
V <sub>16</sub> W <sub>9</sub> O <sub>65</sub>	<i>I4/mmm</i> , 2	25.074(4), 3.714(1)	[147, 134]
β-V <sub>2</sub> O(PO <sub>4</sub> )	<i>I4<sub>1</sub>/amd</i> , 4	5.362(5), 12.378(9)	[148]
VPO <sub>4</sub>	<i>Cmcm</i> , 4	5.2316(5), 7.7738(7), 6.2847(5)	[83]
V <sub>4</sub> (P <sub>2</sub> O <sub>7</sub> ) <sub>3</sub>	<i>Pmcn</i> , 4	7.443(1), 9.560(2), 21.347(4)	[149]
V(PO <sub>3</sub> ) <sub>3</sub>	<i>Ic</i> , 12	10.615(2), 19.095(4), 9.432(1), 97.94(1)	[150, 151]
V(VO) <sub>3</sub> (PO <sub>4</sub> ) <sub>3</sub>	<i>F2dd</i> , 24	7.2596(8), 21.786(2), 38.904(4)	[31]
V <sub>2</sub> (VO)(P <sub>2</sub> O <sub>7</sub> ) <sub>2</sub>	<i>Pnma</i> , 4	17.459(3), 12.185(2), 5.2431(7)	[152]
VP <sub>2</sub> O <sub>7</sub> <sup>b)</sup>	<i>P2<sub>1</sub></i> , 2	4.7725(1), 7.8710(2), 6.8618(2), 106.1417(10)	[153]
(VO) <sub>2</sub> P <sub>2</sub> O <sub>7</sub>	<i>Pca2<sub>1</sub></i> , 8	7.729(1), 9.583(1), 16.581(2)	[10]
(VO) <sub>2</sub> P <sub>2</sub> O <sub>7</sub>	<i>Pb2<sub>1</sub>a</i> , 8	7.725(3), 16.576(4), 9.573(3)	[154]
(VO) <sub>2</sub> P <sub>2</sub> O <sub>7</sub>	<i>P2<sub>1</sub></i> , 8	7.7276(3), 16.58849(40), 9.5796(5), 89.975(3)	[155]
α-VO(PO <sub>3</sub> ) <sub>2</sub>	<i>C2/c</i> , 4	15.0924(4), 4.1919(1), 9.5706(3), 126.464(2)	[156]
β-VO(PO <sub>3</sub> ) <sub>2</sub>	<i>I4̄ 2d</i> , 4	10.99(1), 4.258(6)	[157]
V <sub>2</sub> (PO <sub>4</sub> ) <sub>3</sub> <sup>b)</sup>	<i>P2<sub>1</sub>/n</i> , 4	8.4067(8), 8.5152(8), 11.5903(11), 89.129(6)	[158]
α <sub>I</sub> -VOPO <sub>4</sub>	<i>P4/n</i> , 2	6.20, 4.11	[159]
α <sub>II</sub> -VOPO <sub>4</sub>	<i>P4/n</i> , 2	6.014(7), 4.434(2)	[160]
β-VOPO <sub>4</sub>	<i>Pnma</i> , 4	7.770(3), 6.143(3), 6.965(3)	[161]
γ-VOPO <sub>4</sub>	<i>Pbam</i> , 8	17.3970(5), 8.8199(2), 4.9079(1)	[162]
δ-VOPO <sub>4</sub>	<i>P4<sub>2</sub>/mbc</i> , 8	9.0547(7), 8.6080(8)	[163]
ε-VOPO <sub>4</sub>	<i>Cc</i> , 4	7.2659(3), 6.8934(2), 7.2651(3), 115.340(1)	[164]
ω-VOPO <sub>4</sub>	<i>P4<sub>2</sub>/mmc</i> , 2	4.8552(3), 8.4301(6)	[165]
ω-VOPO <sub>4</sub> (Ht)	<i>tetragonal</i>	6.839, 8.42	[166]

<sup>a)</sup> W<sub>1.8</sub>V<sub>3.2</sub>O<sub>13</sub> or (V<sup>IV</sup><sub>0.75</sub>W<sup>VI</sup><sub>0.25</sub>)<sub>2</sub>W<sup>VI</sup>V<sup>V</sup>O<sub>10</sub>, <sup>b)</sup> VP<sub>2</sub>O<sub>7</sub> and V<sub>2</sub>(PO<sub>4</sub>)<sub>3</sub> are thermodynamically metastable and can be obtained only by electrochemical de-intercalation of LiVP<sub>2</sub>O<sub>7</sub> and LiV<sub>2</sub>(PO<sub>4</sub>)<sub>3</sub>, respectively.

### 6.3 Synthesis and crystallization

Single-phase, microcrystalline powders of three different solid solutions (V<sub>1-x</sub>W<sub>x</sub>)OPO<sub>4</sub> (0 ≤ x ≤ 0.01, β-VOPO<sub>4</sub> structure type [161], 0.04 ≤ x ≤ 0.26, α<sub>II</sub>-VOPO<sub>4</sub> structure type [160]; and 0.67 ≤ x ≤ 1.0, WOPO<sub>4</sub> structure type [90, 91, this thesis]) have been prepared according to (eq. 6.1) at 800 °C by *vapor phase moderated solid state synthesis* from mixtures of W<sup>V</sup>OPO<sub>4</sub> and β-V<sup>V</sup>OPO<sub>4</sub> in sealed silica ampoules using small amounts of chlorine as mineralizer (Table 6.2).

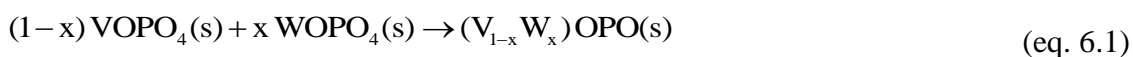


Table 6.2 Experiments aiming at the synthesis of solid solutions (V<sub>1-x</sub>W<sub>x</sub>)OPO<sub>4</sub>; 0.0 ≤ x ≤ 1.0 in sealed ampoules. Heating protocol, pre-reaction 550 ← 700 °C for t<sub>1</sub> (days) and final transport reaction temperature 800 → 700 °C for t<sub>2</sub> (days).

<i>x</i>	Starting Materials	Amount (mg)	PtCl <sub>2</sub> (mg)	t <sub>1</sub> , t <sub>2</sub> (d)	Source Products (according to IP Guinier photographs)	Sink Products
0.01	WOPO <sub>4</sub> VOPO <sub>4</sub>	3.70 200.37	3.9	3, 7	β-(V <sub>0.99</sub> W <sub>0.01</sub> )OPO <sub>4</sub>	β-(V <sub>0.99</sub> W <sub>0.01</sub> )OPO <sub>4</sub>
0.03	WOPO <sub>4</sub> VOPO <sub>4</sub>	11.05 196.37	4.9	3, 7	β-(V <sub>0.99</sub> W <sub>0.01</sub> )OPO <sub>4</sub> , α-VO(PO <sub>3</sub> ) <sub>2</sub>	β-(V <sub>0.99</sub> W <sub>0.01</sub> )OPO <sub>4</sub>
0.05	WOPO <sub>4</sub> VOPO <sub>4</sub>	17.6 183.11	4.9	3, 7	α <sub>II</sub> -(V <sub>0.95</sub> W <sub>0.05</sub> )OPO <sub>4</sub> , α-VO(PO <sub>3</sub> ) <sub>2</sub>	---
0.10	WOPO <sub>4</sub> VOPO <sub>4</sub>	42.54 208.17	5.7	2, 7	α <sub>II</sub> -(V <sub>0.90</sub> W <sub>0.10</sub> )OPO <sub>4</sub>	α <sub>II</sub> -(V <sub>0.90</sub> W <sub>0.10</sub> )OPO <sub>4</sub>
0.111	WOPO <sub>4</sub> VOPO <sub>4</sub>	36.85 161.91	5.1	2, 7	α <sub>II</sub> -(V <sub>0.899</sub> W <sub>0.111</sub> )OPO <sub>4</sub>	---
0.125	WOPO <sub>4</sub> VOPO <sub>4</sub>	42.11 161.91	5.1	2, 7	α <sub>II</sub> -(V <sub>0.875</sub> W <sub>0.125</sub> )OPO <sub>4</sub>	---
0.142	WOPO <sub>4</sub> VOPO <sub>4</sub>	46.81 154.47	10.1	2, 7	α <sub>II</sub> -(V <sub>0.858</sub> W <sub>0.142</sub> )OPO <sub>4</sub>	---
0.166	WOPO <sub>4</sub> VOPO <sub>4</sub>	53.62 147.19	10.1	2, 7	α <sub>II</sub> -(V <sub>0.833</sub> W <sub>0.166</sub> )OPO <sub>4</sub> , (VO)Si(PO <sub>4</sub> ) <sub>2</sub> <sup>a)</sup>	---
0.20	WOPO <sub>4</sub> VOPO <sub>4</sub>	117.92 259.06	4.9	2, 7	α <sub>II</sub> -(V <sub>0.80</sub> W <sub>0.20</sub> )OPO <sub>4</sub>	---
0.25	WOPO <sub>4</sub> VOPO <sub>4</sub>	109.15 180.01	5.3	2, 7	α <sub>II</sub> -(V <sub>0.75</sub> W <sub>0.25</sub> )OPO <sub>4</sub>	α <sub>II</sub> -(V <sub>0.75</sub> W <sub>0.25</sub> )OPO <sub>4</sub>
0.30	WOPO <sub>4</sub> VOPO <sub>4</sub>	88.52 133.40	5.3	2, 7	α <sub>II</sub> -(V <sub>0.74</sub> W <sub>0.26</sub> )OPO <sub>4</sub>	(W <sub>0.83</sub> V <sub>0.17</sub> ) <sub>8</sub> (PO <sub>2</sub> ) <sub>8</sub> <sup>c)</sup> , (VO)Si(PO <sub>4</sub> ) <sub>2</sub> <sup>a)</sup>
0.50	WOPO <sub>4</sub> VOPO <sub>4</sub>	147.45 81.03	10.0	2, 7	V(W <sub>0.9</sub> V <sub>0.1</sub> O <sub>2</sub> ) <sub>2</sub> (P <sub>2</sub> O <sub>7</sub> )PO <sub>4</sub> <sup>b)</sup> , α <sub>II</sub> -(V <sub>0.74</sub> W <sub>0.26</sub> )OPO <sub>4</sub> , (W <sub>0.83</sub> V <sub>0.17</sub> ) <sub>8</sub> (PO <sub>2</sub> ) <sub>4</sub> <sup>c)</sup> , α-VO(PO <sub>3</sub> ) <sub>2</sub>	---
0.60	WOPO <sub>4</sub> VOPO <sub>4</sub>	147.40 53.70	20.5	2, 8	V(W <sub>0.9</sub> V <sub>0.1</sub> O <sub>2</sub> ) <sub>2</sub> (P <sub>2</sub> O <sub>7</sub> )PO <sub>4</sub> <sup>b)</sup>	--
0.67	WOPO <sub>4</sub> VOPO <sub>4</sub>	64.78 235.85	5.0	2, 7	V(WO <sub>2</sub> ) <sub>2</sub> (P <sub>2</sub> O <sub>7</sub> )PO <sub>4</sub> <sup>b)</sup>	---
0.75	WOPO <sub>4</sub> VOPO <sub>4</sub>	176.88 32.38	29	1, 7	(V <sub>0.25</sub> W <sub>0.75</sub> )OPO <sub>4</sub> <sup>d)</sup> , WP <sub>2</sub> O <sub>7</sub> <sup>e)</sup> , phase X <sup>e, f)</sup>	---
0.80	WOPO <sub>4</sub> VOPO <sub>4</sub>	168.45 23.13	5	1, 7	(V <sub>0.20</sub> W <sub>0.80</sub> )OPO <sub>4</sub> <sup>d)</sup> , WP <sub>2</sub> O <sub>7</sub> <sup>e)</sup> , phase X <sup>e, f)</sup>	---
0.85	WOPO <sub>4</sub> VOPO <sub>4</sub>	278.43 26.98	5	1, 7	(V <sub>0.15</sub> W <sub>0.85</sub> )OPO <sub>4</sub> <sup>d)</sup> , WP <sub>2</sub> O <sub>7</sub> <sup>e)</sup>	---
0.90	WOPO <sub>4</sub> VOPO <sub>4</sub>	189.52 17.99	5.1	1, 7	(V <sub>0.10</sub> W <sub>0.90</sub> )OPO <sub>4</sub> <sup>d)</sup> , WP <sub>2</sub> O <sub>7</sub> <sup>e)</sup>	---

<sup>a)</sup> due to reaction with silica ampoule, <sup>b)</sup> new structure type, for details see Chapter 8, <sup>c)</sup> vanadium substituted MPTB structure type with *m* = 4 (see Chapter 10), <sup>d)</sup> WOPO<sub>4</sub> structure type, <sup>e)</sup> trace amount, <sup>f)</sup> highest intensity at 4θ = 40.5, 51.8, 57.2°.

The reaction mixtures with different molar ratios of  $W^V OPO_4$  and  $\beta\text{-}V^V OPO_4$  were finely ground in an agate mortar. Cleaned and dried silica tubes ( $l = 11$  cm,  $d = 1.5$  cm) were loaded with these mixtures (see Table 6.2) evacuated and sealed. Subsequently the reaction mixtures were preheated at a lower temperature ( $550 \rightarrow 700$  °C, for one to three days) prior to the final transport experiment ( $800 \rightarrow 700$  °C, for seven days).

The compositions  $(V_{1-x}W_x)OPO_4$ ,  $0.26 < x < 0.60$  lead to the formation of four phase equilibrium mixtures. These consist of  $\alpha_{II}\text{-}(V_{0.74}W_{0.26})OPO_4$ ,  $(V^{IV}O)(PO_3)_2$  (monoclinic modification [167]), a vanadium-substituted mono-phosphate tungsten bronze of approximate composition  $(W_{0.83}V_{0.17}O_3)_8(PO_2)_4$  ( $P2_1/m$ ,  $a = 6.492(1)$  Å,  $b = 5.2214(3)$  Å,  $c = 17.313(3)$  Å,  $\beta = 90.495(9)^\circ$  [Chapter 10] structure type of *MPTB*  $(WO_3)_{2m}(PO_2)_4$  with  $m = 4$  [95]) and a lower phase boundary composition  $V(W_{0.9}V_{0.1}O_2)_2(P_2O_7)PO_4$  which is extended up to  $x = 0.67$ ,  $V(WO_2)_2(P_2O_7)PO_4$  [see Chapter 8].

Single-phase powders of solid solutions  $(V_{1-x}W_x)OPO_4$  with  $\alpha_{II}\text{-}$  and  $\beta\text{-}VOPO_4$  structure type were also obtained by *solution combustion synthesis* (SCS) [168, 169, 170], followed by heating the reaction intermediates after combustion in air at 700 °C (see Figure 6.3 and Table 6.3). To obtain powders of  $(V_{1-x}W_x)OPO_4$  ( $0.0 \leq x \leq 0.26$ ) with higher specific surface area solution combustion synthesis (SCS) was employed.

In SCS the precursor materials  $(NH_4)_6W_{12}O_{39} \cdot xH_2O$  ( $x = 4.8$  gravimetrically determined),  $NH_4VO_3$ , and  $(NH_4)_2HPO_4$  were used as source of  $WO_3$ ,  $V_2O_5$ , and  $P_4O_{10}$ , respectively. Glycine and nitric acid were used as chelator/fuel and oxidizer, accordingly. The appropriate molar ratios of precursor materials (Table 6.3) were dissolved in a minimum amount of water together with oxidizer ( $HNO_3$ ). The fuel is added to the clear solution at continuous stirring. The molar ratio of metal to glycine to oxidizer was kept at  $n(\text{metal}):n(\text{glycine}):n(HNO_3) = 1:3:6$ . An excess of oxidizer was used with respect to the stoichiometrically required amount, which is called fuel lean condition. This allows the complete burning of the fuel or in other words, eliminates the probability of any carbon residue. Eventually, the solution was dried to a gel on a hot plate at  $\vartheta \approx 100$  °C. The dry mass was ignited in a preheated (400 to 550 °C) muffle furnace, and kept at this temperature for ten minutes. The combustion products were allowed to cool to room temperature, ground and heated by stepwise rising the temperature to obtain the thermodynamically stable products. At each intermediate step the products were ground and characterized by XRPD (Table 6.3). In SCS aiming at about 5-8 g target material occasionally partial ignition occurred at the hot plate (during drying process). Since the

temperature at the hot plate is too low for complete combustion the partial ignition should be avoided. This is achieved by using less amount of fuel (about half equivalent) than redox equivalent which is called fuel lean condition.

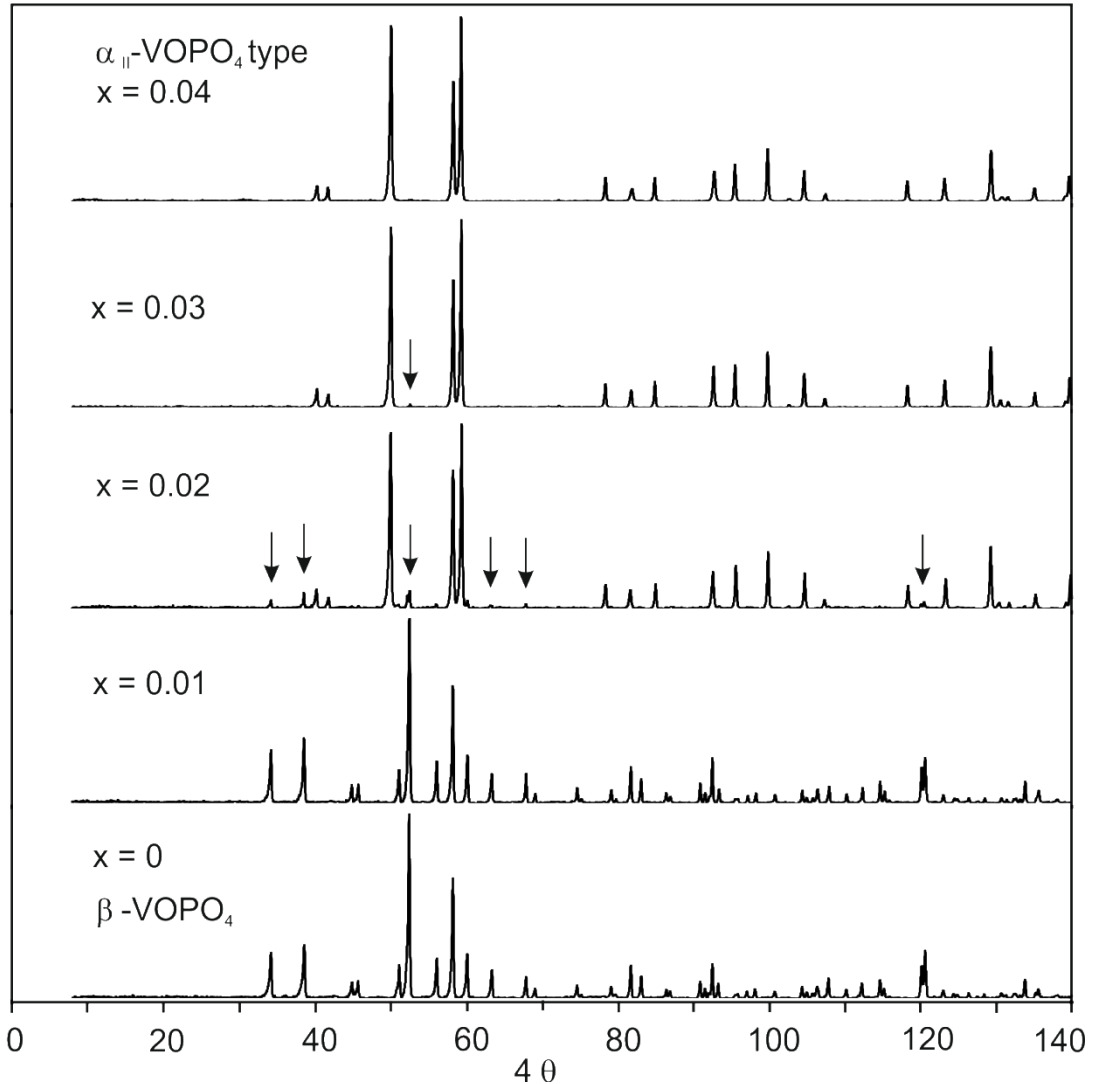


Figure 6.3 Comparison of Guinier-photographs of members of the solid solutions  $(V_{1-x}W_x)OPO_4$  obtained by SCS followed by heating in air where  $0.0 \leq x \leq 0.01$  is only  $\beta$ - $VOPO_4$  type,  $0.02 \leq x \leq 0.03$  shows a mixture of  $\beta$ - and  $\alpha_{II}$ - $VOPO_4$  type, and  $x \geq 0.04$  is only  $\alpha_{II}$ - $VOPO_4$  structure type solid solution, arrows indicate the  $\beta$ - $VOPO_4$  type.

Table 6.3 SCS experiments aiming at the synthesis of solid solutions (V<sub>1-x</sub>W<sub>x</sub>)OPO<sub>4</sub>. Heating of the combustion products was typically in air. Heating at reduced  $p(\text{O}_2)$  in some experiments is pointed out.

$x$	Starting Materials	Amount (mg)	$\vartheta$ (°C)	$t$ (h)	Reaction Products (according to IP Guinier photographs)
0.0	NH <sub>4</sub> VO <sub>3</sub>	1169.92	500	0.1	$\alpha_1$ -VOPO <sub>4</sub> , VOPO <sub>4</sub> ·2H <sub>2</sub> O <sup>a)</sup>
	(NH <sub>4</sub> ) <sub>2</sub> HPO <sub>4</sub>	1320.85	600	24	$\alpha_1$ -VOPO <sub>4</sub> , VOPO <sub>4</sub> ·2H <sub>2</sub> O <sup>a)</sup>
	(NH <sub>4</sub> ) <sub>6</sub> W <sub>12</sub> O <sub>39</sub> ·xH <sub>2</sub> O	---	725	72	$\beta$ -VOPO <sub>4</sub>
0.01	NH <sub>4</sub> VO <sub>3</sub>	694.92	500	0.1	$\alpha_1$ -(V <sub>0.99</sub> W <sub>0.01</sub> )OPO <sub>4</sub> , (V <sub>0.99</sub> W <sub>0.01</sub> )OPO <sub>4</sub> ·2H <sub>2</sub> O <sup>a)</sup>
	(NH <sub>4</sub> ) <sub>2</sub> HPO <sub>4</sub>	792.60	600	24	$\alpha_1$ -(V <sub>0.99</sub> W <sub>0.01</sub> )OPO <sub>4</sub> , (V <sub>0.99</sub> W <sub>0.01</sub> )OPO <sub>4</sub> ·2H <sub>2</sub> O <sup>a)</sup>
	(NH <sub>4</sub> ) <sub>6</sub> W <sub>12</sub> O <sub>39</sub> ·xH <sub>2</sub> O	15.18	700	72	$\beta$ -(V <sub>0.99</sub> W <sub>0.01</sub> )OPO <sub>4</sub>
0.02	NH <sub>4</sub> VO <sub>3</sub>	687.91	500	0.1	$\alpha_1$ -(V <sub>0.98</sub> W <sub>0.02</sub> )OPO <sub>4</sub> , (V <sub>0.98</sub> W <sub>0.02</sub> )OPO <sub>4</sub> ·2H <sub>2</sub> O <sup>a)</sup>
	(NH <sub>4</sub> ) <sub>2</sub> HPO <sub>4</sub>	792.34	600	24	$\alpha_1$ -(V <sub>0.98</sub> W <sub>0.02</sub> )OPO <sub>4</sub> , (V <sub>0.98</sub> W <sub>0.02</sub> )OPO <sub>4</sub> ·2H <sub>2</sub> O <sup>a)</sup>
	(NH <sub>4</sub> ) <sub>6</sub> W <sub>12</sub> O <sub>39</sub> ·xH <sub>2</sub> O	30.43	700	72	$\beta$ -(V <sub>0.99</sub> W <sub>0.01</sub> )OPO <sub>4</sub> , $\alpha_{II}$ -(V <sub>0.96</sub> W <sub>0.04</sub> )OPO <sub>4</sub>
0.03	NH <sub>4</sub> VO <sub>3</sub>	907.74	500	0.1	$\alpha_1$ -(V <sub>0.97</sub> W <sub>0.03</sub> )OPO <sub>4</sub> , (V <sub>0.97</sub> W <sub>0.03</sub> )OPO <sub>4</sub> ·2H <sub>2</sub> O <sup>a)</sup>
	(NH <sub>4</sub> ) <sub>2</sub> HPO <sub>4</sub>	1056.51	600	24	$\alpha_1$ -(V <sub>0.97</sub> W <sub>0.03</sub> )OPO <sub>4</sub> , (V <sub>0.97</sub> W <sub>0.03</sub> )OPO <sub>4</sub> ·2H <sub>2</sub> O <sup>a)</sup>
	(NH <sub>4</sub> ) <sub>6</sub> W <sub>12</sub> O <sub>39</sub> ·xH <sub>2</sub> O	60.52	700	24	$\beta$ -(V <sub>0.99</sub> W <sub>0.01</sub> )OPO <sub>4</sub> + $\alpha_{II}$ -(V <sub>0.96</sub> W <sub>0.04</sub> )OPO <sub>4</sub>
0.04	NH <sub>4</sub> VO <sub>3</sub>	673.85	500	0.1	$\alpha_1$ -(V <sub>0.96</sub> W <sub>0.04</sub> )OPO <sub>4</sub> , (V <sub>0.96</sub> W <sub>0.04</sub> )OPO <sub>4</sub> ·2H <sub>2</sub> O <sup>a)</sup>
	(NH <sub>4</sub> ) <sub>2</sub> HPO <sub>4</sub>	792.60	600	24	$\alpha_1$ -(V <sub>0.96</sub> W <sub>0.04</sub> )OPO <sub>4</sub> , (V <sub>0.96</sub> W <sub>0.04</sub> )OPO <sub>4</sub> ·2H <sub>2</sub> O <sup>a)</sup>
	(NH <sub>4</sub> ) <sub>6</sub> W <sub>12</sub> O <sub>39</sub> ·xH <sub>2</sub> O	60.53	700	24	$\alpha_{II}$ -(V <sub>0.96</sub> W <sub>0.04</sub> )OPO <sub>4</sub>
0.05	NH <sub>4</sub> VO <sub>3</sub>	1333.61	500	0.1	$\alpha_1$ -(V <sub>0.95</sub> W <sub>0.05</sub> )OPO <sub>4</sub> , (V <sub>0.95</sub> W <sub>0.05</sub> )OPO <sub>4</sub> ·2H <sub>2</sub> O <sup>a)</sup>
	(NH <sub>4</sub> ) <sub>2</sub> HPO <sub>4</sub>	1584.80	600	24	$\alpha_1$ -(V <sub>0.95</sub> W <sub>0.05</sub> )OPO <sub>4</sub> , (V <sub>0.95</sub> W <sub>0.05</sub> )OPO <sub>4</sub> ·2H <sub>2</sub> O <sup>a)</sup>
	(NH <sub>4</sub> ) <sub>6</sub> W <sub>12</sub> O <sub>39</sub> ·xH <sub>2</sub> O	151.30	700	24	$\alpha_{II}$ -(V <sub>0.95</sub> W <sub>0.05</sub> )OPO <sub>4</sub>
0.10	NH <sub>4</sub> VO <sub>3</sub>	1263.42	500	0.1	$\alpha_1$ -(V <sub>0.90</sub> W <sub>0.10</sub> )OPO <sub>4</sub> , (V <sub>0.90</sub> W <sub>0.10</sub> )OPO <sub>4</sub> ·2H <sub>2</sub> O <sup>a)</sup>
	(NH <sub>4</sub> ) <sub>2</sub> HPO <sub>4</sub>	1584.83	600	24	$\alpha_1$ -(V <sub>0.90</sub> W <sub>0.10</sub> )OPO <sub>4</sub> , (V <sub>0.90</sub> W <sub>0.10</sub> )OPO <sub>4</sub> ·2H <sub>2</sub> O <sup>a)</sup>
	(NH <sub>4</sub> ) <sub>6</sub> W <sub>12</sub> O <sub>39</sub> ·xH <sub>2</sub> O	302.48	700	24	$\alpha_{II}$ -(V <sub>0.90</sub> W <sub>0.10</sub> )OPO <sub>4</sub>
0.15	NH <sub>4</sub> VO <sub>3</sub>	795.336	500	0.1	“ $t$ -WO <sub>3</sub> ” <sup>b)</sup> , $\alpha_1$ -(V <sub>0.85</sub> W <sub>0.15</sub> )OPO <sub>4</sub> ,
	(NH <sub>4</sub> ) <sub>2</sub> HPO <sub>4</sub>	1056.40			(V <sub>0.85</sub> W <sub>0.15</sub> )OPO <sub>4</sub> ·2H <sub>2</sub> O <sup>a)</sup>
	(NH <sub>4</sub> ) <sub>6</sub> W <sub>12</sub> O <sub>39</sub> ·xH <sub>2</sub> O	302.68	600	24	“ $t$ -WO <sub>3</sub> ” <sup>b)</sup> , $\alpha_1$ -(V <sub>0.85</sub> W <sub>0.15</sub> )OPO <sub>4</sub> ,
				(V <sub>0.85</sub> W <sub>0.15</sub> )OPO <sub>4</sub> ·2H <sub>2</sub> O <sup>a)</sup> ,	
			700	72	$\alpha_{II}$ -(V <sub>0.85</sub> W <sub>0.15</sub> )OPO <sub>4</sub>
0.20	NH <sub>4</sub> VO <sub>3</sub>	1123.01	400	0.1	“ $t$ -WO <sub>3</sub> ” <sup>b)</sup> , “Keggin” <sup>d)</sup>
	(NH <sub>4</sub> ) <sub>2</sub> HPO <sub>4</sub>	1584.92	450	24	“ $t$ -WO <sub>3</sub> ” <sup>b)</sup>
	(NH <sub>4</sub> ) <sub>6</sub> W <sub>12</sub> O <sub>39</sub> ·xH <sub>2</sub> O	604.98	600	24	$\alpha_1$ -(V <sub>0.80</sub> W <sub>0.20</sub> )OPO <sub>4</sub> , (V <sub>0.80</sub> W <sub>0.20</sub> )OPO <sub>4</sub> ·2H <sub>2</sub> O <sup>a)</sup> ,
				“ $t$ -WO <sub>3</sub> ” <sup>b)</sup>	
			700	48	$\alpha_{II}$ -(V <sub>0.80</sub> W <sub>0.20</sub> )OPO <sub>4</sub>
0.25	NH <sub>4</sub> VO <sub>3</sub>	421.12	500	0.1	“ $c$ -WO <sub>3</sub> ” <sup>c)</sup>
	(NH <sub>4</sub> ) <sub>2</sub> HPO <sub>4</sub>	633.98	600	24	“ $c$ -WO <sub>3</sub> ” <sup>c)</sup> , $\alpha_1$ -(V <sub>0.75</sub> W <sub>0.25</sub> )OPO <sub>4</sub> ,
	(NH <sub>4</sub> ) <sub>6</sub> W <sub>12</sub> O <sub>39</sub> ·xH <sub>2</sub> O	302.47			(V <sub>0.75</sub> W <sub>0.25</sub> )OPO <sub>4</sub> ·2H <sub>2</sub> O <sup>a)</sup>
			700	24	$\alpha_{II}$ -(V <sub>0.75</sub> W <sub>0.25</sub> )OPO <sub>4</sub>
0.35	NH <sub>4</sub> VO <sub>3</sub>	364.97	500	0.1	“ $c$ -WO <sub>3</sub> ” <sup>c)</sup> , $\alpha_1$ -(V <sub>0.74</sub> W <sub>0.26</sub> )OPO <sub>4</sub>
	(NH <sub>4</sub> ) <sub>2</sub> HPO <sub>4</sub>	633.87	600	24	“ $c$ -WO <sub>3</sub> ” <sup>c)</sup> , $\alpha_1$ -(V <sub>0.74</sub> W <sub>0.26</sub> )OPO <sub>4</sub> ,
	(NH <sub>4</sub> ) <sub>6</sub> W <sub>12</sub> O <sub>39</sub> ·xH <sub>2</sub> O	426.49			(V <sub>0.74</sub> W <sub>0.26</sub> )OPO <sub>4</sub> ·2H <sub>2</sub> O <sup>a)</sup>
			700	24	$\alpha_{II}$ -(V <sub>0.74</sub> W <sub>0.26</sub> )OPO <sub>4</sub> , (W <sub>0.83</sub> V <sub>0.17</sub> O <sub>3</sub> ) <sub>8</sub> (PO <sub>2</sub> ) <sub>4</sub>
0.40	NH <sub>4</sub> VO <sub>3</sub>	140.40	500	1	“ $c$ -WO <sub>3</sub> ” <sup>c)</sup> , (V <sub>0.74</sub> W <sub>0.24</sub> )OPO <sub>4</sub> ·2H <sub>2</sub> O <sup>a)</sup>
	(NH <sub>4</sub> ) <sub>2</sub> HPO <sub>4</sub>	397.0	600	24	“ $c$ -WO <sub>3</sub> ” <sup>c)</sup> , $\alpha_{II}$ -(V <sub>0.74</sub> W <sub>0.24</sub> )OPO <sub>4</sub>
	(NH <sub>4</sub> ) <sub>6</sub> W <sub>12</sub> O <sub>39</sub> ·xH <sub>2</sub> O	302.78	700	144	$\alpha_{II}$ -(V <sub>0.74</sub> W <sub>0.26</sub> )OPO <sub>4</sub> , (W <sub>0.83</sub> V <sub>0.17</sub> O <sub>3</sub> ) <sub>8</sub> (PO <sub>2</sub> ) <sub>4</sub>

0.50	$NH_4VO_3$	175.46	400	0.1	“Keggin” <sup>d)</sup>
	$(NH_4)_2HPO_4$	396.16	450	24	“c-WO <sub>3</sub> ” <sup>c)</sup>
	$(NH_4)_6W_{12}O_{39} \cdot xH_2O$	380.80	550	24	“t-WO <sub>3</sub> ” <sup>b)</sup>
			700	144	$(W_{0.83}V_{0.17}O_3)_8(PO_2)_4$ , $o$ -W <sub>2</sub> O <sub>3</sub> (PO <sub>4</sub> ) <sub>2</sub> , $\alpha_{II}$ -(V <sub>0.74</sub> W <sub>0.26</sub> )OPO <sub>4</sub>
		800	72	$m$ -W <sub>2</sub> O <sub>3</sub> (PO <sub>4</sub> ) <sub>2</sub>	
0.67	$NH_4VO_3$	1052.8	400	0.1	“Keggin” <sup>d)</sup>
	$(NH_4)_2HPO_4$	3569.6	450	1	“c-WO <sub>3</sub> ” <sup>c)</sup>
	$(NH_4)_6W_{12}O_{39} \cdot xH_2O$	4537.32	550	24	“t-WO <sub>3</sub> ” <sup>b)</sup>
			750	120	$m$ -W <sub>2</sub> O <sub>3</sub> (PO <sub>4</sub> ), $o$ -W <sub>2</sub> O <sub>3</sub> (PO <sub>4</sub> ) <sub>2</sub>
			800	72	$m$ -W <sub>2</sub> O <sub>3</sub> (PO <sub>4</sub> ) <sub>2</sub>
850			168	$m$ -W <sub>2</sub> O <sub>3</sub> (PO <sub>4</sub> ) <sub>2</sub> (solidified melt)	
0.67	$NH_4VO_3$	1158.15	600 <sup>e)</sup>	24	“c-WO <sub>3</sub> ” <sup>c)</sup>
	$(NH_4)_2HPO_4$	3962.56	750 <sup>e)</sup>	48	“c-WO <sub>3</sub> ” <sup>c)</sup> , (V <sub>0.33</sub> W <sub>0.67</sub> )OPO <sub>4</sub>
	$(NH_4)_6W_{12}O_{39} \cdot xH_2O$	5066.67	780 <sup>e)</sup>	72	(V <sub>0.33</sub> W <sub>0.67</sub> )OPO <sub>4</sub> , (W <sub>0.83</sub> V <sub>0.17</sub> O <sub>3</sub> ) <sub>8</sub> (PO <sub>2</sub> ) <sub>4</sub> <sup>x)</sup>
0.80	$NH_4VO_3$	701.90	400	0.1	“Keggin” <sup>d)</sup>
	$(NH_4)_2HPO_4$	3966.40	450	24	“c-WO <sub>3</sub> ” <sup>c)</sup>
	$(NH_4)_6W_{12}O_{39} \cdot xH_2O$	6049.77	550	24	“t-WO <sub>3</sub> ” <sup>b)</sup>
			600	120	“t-WO <sub>3</sub> ” <sup>b)</sup>
			700	48	“t-WO <sub>3</sub> ” <sup>b)</sup> , $o$ -W <sub>2</sub> O <sub>3</sub> (PO <sub>4</sub> )
			750	72	$m$ -W <sub>2</sub> O <sub>3</sub> (PO <sub>4</sub> ) + <sup>x)</sup>
800				$m$ -W <sub>2</sub> O <sub>3</sub> (PO <sub>4</sub> )	
0.80	$NH_4VO_3$	70.18	750	48	$m$ -W <sub>2</sub> O <sub>3</sub> (PO <sub>4</sub> ) + <sup>x)</sup>
	$(NH_4)_2HPO_4$	396.16	550 <sup>f)</sup>	48	$m$ -W <sub>2</sub> O <sub>3-<math>\delta</math></sub> (PO <sub>4</sub> ) + <sup>x)</sup>
	$(NH_4)_6W_{12}O_{39} \cdot xH_2O$	609.28	800 <sup>g)</sup>	168	(V <sub>0.2</sub> W <sub>0.8</sub> )OPO <sub>4</sub> (WOPO <sub>4</sub> type), (WO <sub>3</sub> ) <sub>8</sub> (PO <sub>2</sub> ) <sub>4</sub>
1.0	$(NH_4)_2HPO_4$	1584.99	400	0.1	“Keggin” <sup>d)</sup>
	$(NH_4)_6W_{12}O_{39} \cdot xH_2O$	3025.00	500	24	amorphous
			600	24	“c-WO <sub>3</sub> ” <sup>c)</sup>
			700	120	$o$ -(W <sub>2</sub> O <sub>3</sub> )(PO <sub>4</sub> ) <sub>2</sub> , “t-WO <sub>3</sub> ” <sup>b)</sup>
			900	144	$m$ -(W <sub>2</sub> O <sub>3</sub> )(PO <sub>4</sub> ) <sub>2</sub> , $m$ -WO <sub>3</sub> <sup>x)</sup>

<sup>a)</sup> from hydration of  $\alpha_I$ -VOPO<sub>4</sub> type, <sup>b)</sup> phosphates  $(W_{0.5-x}V_xP_{0.5})O_{2.5+\square_{0.5}}$  with structure type of tetragonal WO<sub>3</sub> [249] see Chapter 9, <sup>c)</sup> phosphates  $(W_{0.5-x}V_xP_{0.5})O_{2.5+\square_{0.5}}$  with structure type of cubic WO<sub>3</sub> [252, 253] see Chapter 9, <sup>d)</sup>  $(NH_4)_3[PW_{12}O_{40}] \cdot xH_2O$  [171] type, <sup>e)</sup> at argon atm  $p(O_2) \approx 20$  ppm, <sup>f)</sup> at H<sub>2</sub> atmosphere, <sup>g)</sup> sealed tube experiment, <sup>x)</sup> very small impurity,  $o$ : orthorhombic type,  $m$ : monoclinic type.

The  $\alpha_{II}$ - and  $\beta$ -VOPO<sub>4</sub> structure type solid solutions are formed by heating the combustion products at 700 °C for at least one day. Longer heating times increases the crystallinity (according to XRPD). The solid solutions are thermodynamically stable up to 800 °C. Within this temperature range their stability increases with increasing the tungsten concentration. Heating the  $\alpha_{II}$ - and  $\beta$ -VOPO<sub>4</sub> structure type solid solutions in air at  $T \geq 800$  °C leads to melting of the material, which froze upon quenching to an amorphous solids. Occasionally, the XRPD pattern of the solidified melts showed very weak reflections of (VO)Si(PO<sub>4</sub>)<sub>2</sub> [172] due to reaction with the silica crucible. The observed redox-stability of V<sup>4+</sup> in  $(V_{1-x}W_x)OPO_4$ , which is  $(V^{IV}_xV^{V}_{1-2x}W^{VI}_x)OPO_4$  (for  $0 \leq x \leq 0.26$ ) is quite

remarkable, since heating of  $(V^{IV}O)_2P_2O_7$  [10] in air at 700 °C leads to complete oxidation and formation of  $V^VOPO_4$  [161].

Exposure of solid solution  $(V_{1-x}W_x)OPO_4$   $\alpha_{II}$ - $VOPO_4$  structure type to lab atmosphere over a period of several weeks led to their complete hydration, as it is suggested by the XRPD pattern of the phases (see Figure 6.4), which is very similar to the one observed for  $VOPO_4 \cdot 2H_2O$  [173].

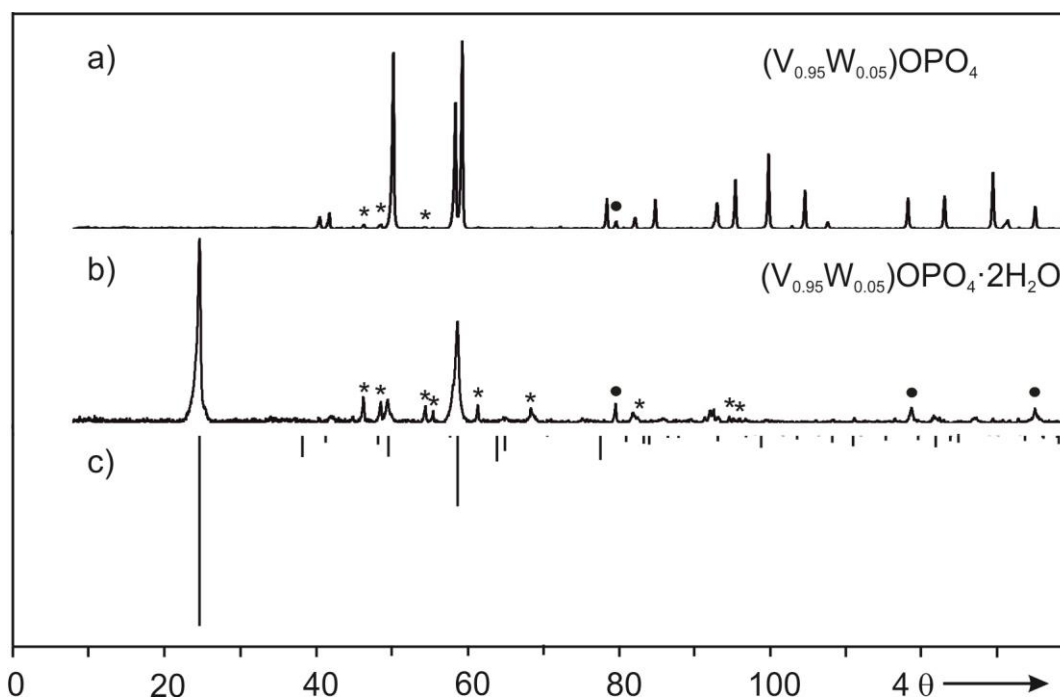


Figure 6.4 Guinier-photographs of  $(V_{0.95}W_{0.05})OPO_4$  ( $\alpha_{II}$ - $VOPO_4$  type [160]) (a),  $(V_{0.95}W_{0.05})OPO_4 \cdot 2H_2O$  (b) obtained due to hydration of (a) by exposing it to lab atmosphere, compared with a simulated XRPD pattern of  $(V_{0.95}W_{0.05})OPO_4 \cdot 2H_2O$  (structure model  $VOPO_4 \cdot 2H_2O$  [173]) (c). Asterisks and dots indicate small impurities of  $\alpha$ - $V^{IV}O(PO_3)_2$  [156] and Pt, respectively.

Immediately after ignition at 400 °C the XRPD of the combustion product shows weak reflections of  $(NH_4)_3PW_{12}O_{40} \cdot 9.5H_2O$  [171]. It was observed that the formation of  $(NH_4)_3PW_{12}O_{40} \cdot 9.5H_2O$  can be avoided if the ignition was performed at 500 °C. Further heating of the material after grinding in an agate mortar shows a mixture of  $\alpha_I$ - $VOPO_4$  [159] and  $VOPO_4 \cdot 2H_2O$  [173] type compounds up to  $0.0 \leq x \leq 0.35$  (according to Guinier photographs). Since the  $\alpha_I$ - $VOPO_4$  polymorph is metastable and it can be solvated very easily to the dihydrated phase [173] by absorption water from the lab atmosphere during the cooling process. At lower temperature in the range of  $0.50 < x \leq 1.0$  besides the



above mentioned two phases another phase is observed which is isotypic to  $ReO_3$  [174]. Details of these two structure type phases discussed in Chapter 9. After further heating for one day at  $600^\circ C$  these phases were still present (see Figure 6.5).

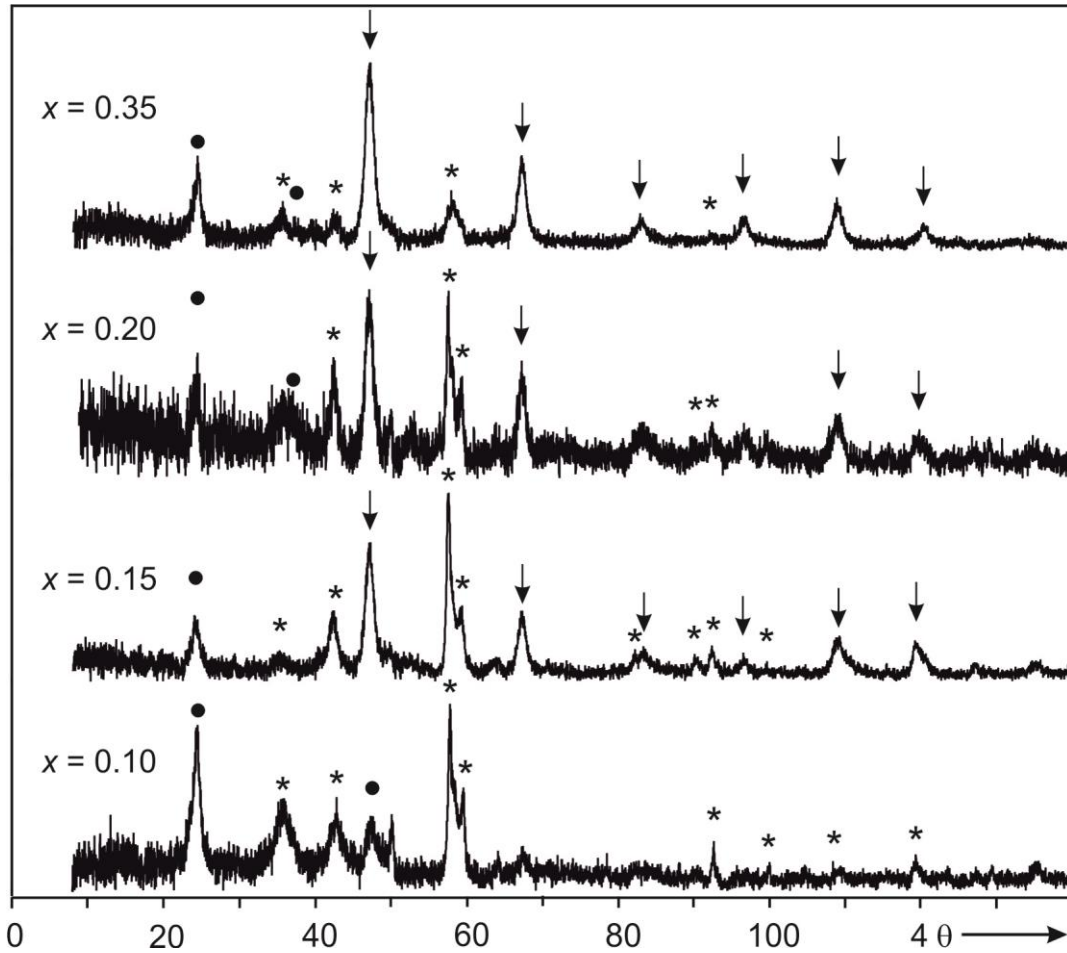


Figure 6.5 Guinier-photographs of reaction products from experiments aiming at synthesis of the solid solution  $(V_{1-x}W_x)OPO_4$  ( $0.10 \leq x \leq 0.35$ ) via SCS after subsequent heating at  $600^\circ C$  in air. Asterisks indicate phases with  $\alpha_I$ - $VOPO_4$  structure type [159], dots indicate  $VOPO_4 \cdot 2H_2O$  structure type [173], and down arrows indicate a  $ReO_3$  type [174] phosphate.

Hydration of  $\alpha_I$ - $VOPO_4$  structure type solid solution,  $(V_{1-x}W_x)OPO_4$  which formed as reaction intermediate during SCS was avoided by the following procedure. Firstly, rapid cooling of the sample (quenching) with water and then using x-ray transparent adhesive tape instead of mylar foil and ethanol solvent for preparation of the sample. These two procedures allow to avoid formation of the dihydrated phase ( $VOPO_4 \cdot 2H_2O$  [173]) (see Figure 6.6).

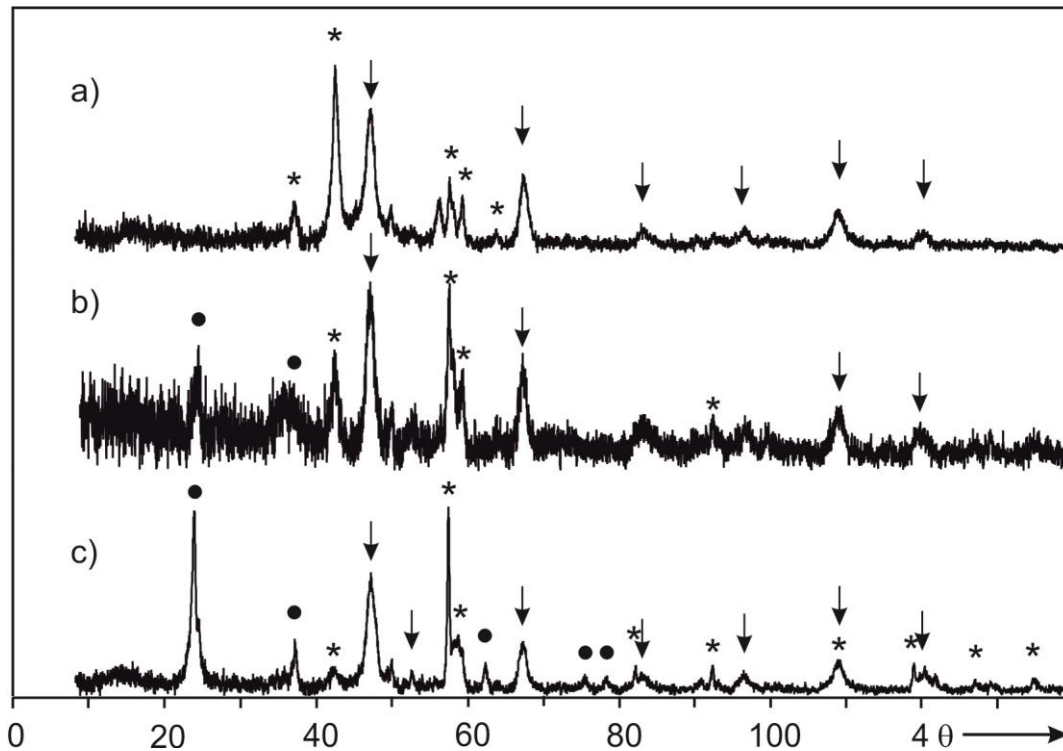
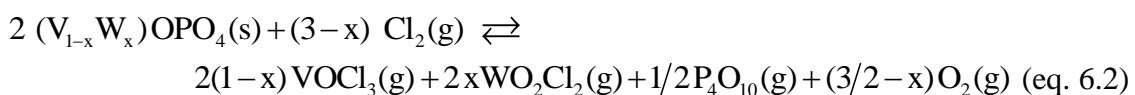


Figure 6.6 Influence of post-annealing treatment on phases occurring in the Guinier photographs of  $(V_{0.80}W_{0.20})OPO_4$ . XRPD after sample quenching and using x-ray transparent adhesive tape (a), slow cooling (b), and slow cooling followed by grinding with water (c). Asterisks indicate  $\alpha_I$ - $VOPO_4$  type [159], dots indicate  $VOPO_4 \cdot 2H_2O$  type [173], down arrows indicate  $ReO_3$  type [174] phases.

Crystallization of  $(V_{1-x}W_x)OPO_4$ ;  $x = 0.01$  ( $\beta$ -type),  $0.10$  ( $\alpha_{II}$ -type), and  $0.26$  ( $\alpha_{II}$ -type) was achieved by chemical vapor transport (CVT) [43] via endothermic reactions using chlorine as transport agent in a temperature gradient  $800 \rightarrow 700$  °C. Crystals with edge-lengths up to 2 mm were obtained (see Figure 6.7) at transport rates  $\dot{m} = 0.25$   $mg \cdot h^{-1}$ . Crystals of  $(V_{0.90}W_{0.10})OPO_4$  and  $(V_{0.74}W_{0.26})OPO_4$  can easily be cleaved parallel to (001) as a consequence of their layer-type structure. EDX analysis of these crystals showed only V, W, and P and provided no hints on impurity elements. According to literature on CVT of  $VO_2$ ,  $V_2O_5$  [175, 176],  $WO_3$  [116] and anhydrous phosphates [43] using chlorine as transport agent the most important transport effective gaseous species are expected to be  $VOCl_3$ ,  $WO_2Cl_2$ ,  $P_4O_{10}$  and  $O_2$ . Therefore, CVT of the solid solutions  $\alpha_{II}$ - and  $\beta$ - $(V_{1-x}W_x)OPO_4$  is expected to proceed according to (eq. 6.2).



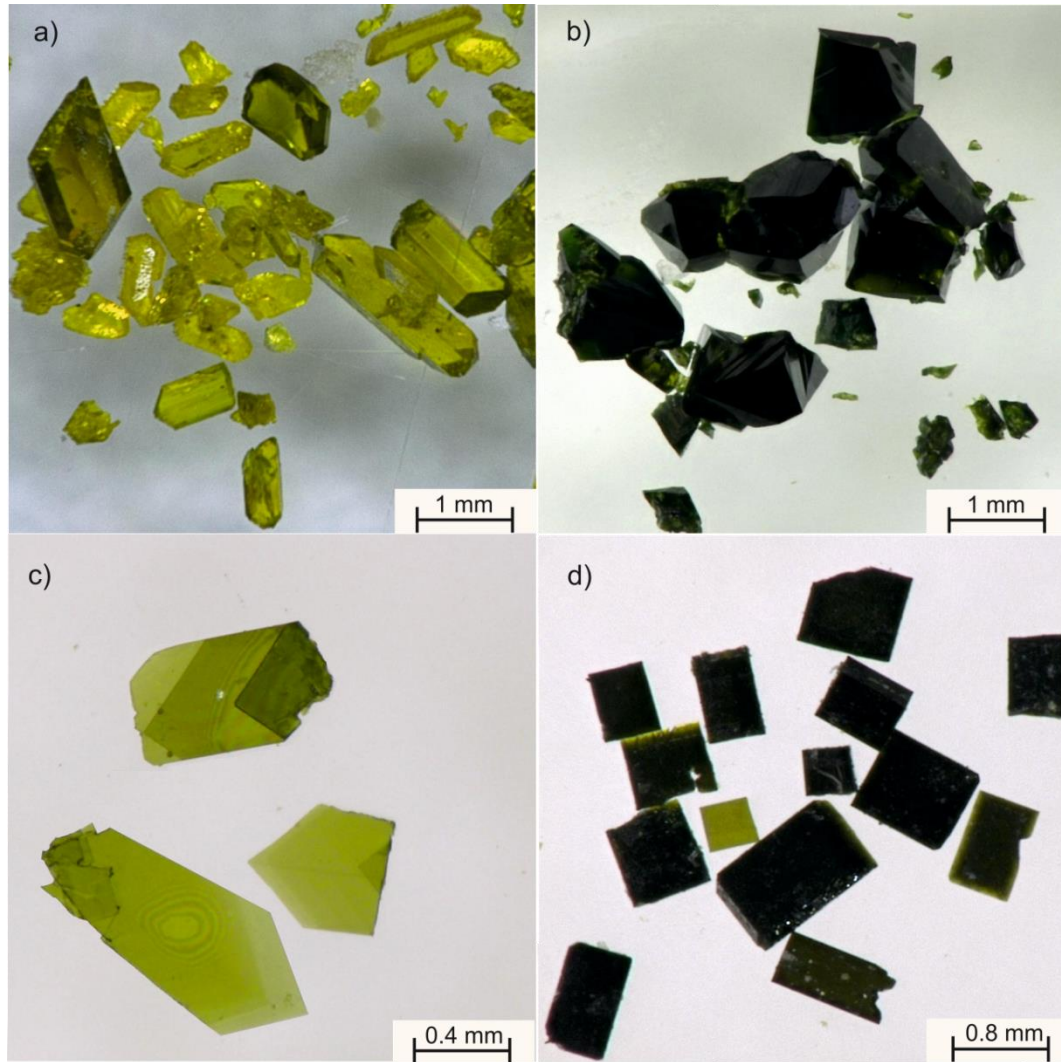


Figure 6.7 Microphotographs of crystals  $\beta$ -( $VO_{1-\delta}$ ) $PO_4$  (a),  $\beta$ -( $V_{0.01}W_{0.99}$ ) $OPO_4$  (b),  $\alpha_{II}$ -( $V_{0.10}W_{0.90}$ ) $OPO_4$  (c), and  $\alpha_{II}$ -( $V_{0.74}W_{0.26}$ ) $OPO_4$  (d) obtained by CVT.

#### 6.4 Crystal structure of the $\alpha_{II}$ -type solid solution

According to the X-ray powder diffraction study (Guinier technique) the solid solutions  $(V_{1-x}W_x)OPO_4$  ( $0 \leq x \leq 0.01$ ) synthesized at  $800^\circ\text{C}$  adopt the  $\beta$ - $VOPO_4$  structure type [161]. Lattice parameters of pure  $\beta$ - $VOPO_4$  (space group  $Pnma$ ) and  $(V_{0.99}W_{0.01})OPO_4$  [in brackets] are  $a = 7.7863(5)$  [ $7.7794(5)$ ] Å,  $b = 6.1329(3)$  [ $6.1360(3)$ ] Å, and  $c = 6.9673(5)$  [ $6.9733(4)$ ] Å, respectively. For  $0.01 < x < 0.04$  a two phase region consisting of  $(V_{0.99}W_{0.01})OPO_4$  and  $(V_{0.96}W_{0.04})OPO_4$  ( $\alpha_{II}$ - $VOPO_4$  structure type [160]) is observed. The solubility for  $WOPO_4$  in  $VOPO_4$  extends up to  $(V_{0.74}W_{0.26})OPO_4$  ( $\alpha_{II}$ - $VOPO_4$  structure type). Lattice parameters of  $(V_{1-x}W_x)OPO_4$  with  $0.04 \leq x \leq 0.26$  and for pure  $\alpha_{II}$ - $VOPO_4$  [160], which is metastable with respect to the  $\beta$ -form, are given in Figure 6.8 (and Table 14.5). With increasing tungsten content a shrinking of the

crystallographic  $c$ -axis ( $\Delta c/c_0 = -29\%$ ) and a moderate increase of the  $a$ -axis ( $\Delta a/a_0 = +14\%$ ) are observed. Fully assigned Guinier photographs of several members of the solid solutions ( $\alpha_{II}$ - and  $\beta$ - type) are provided in Table 14.12 to Table 14.19.

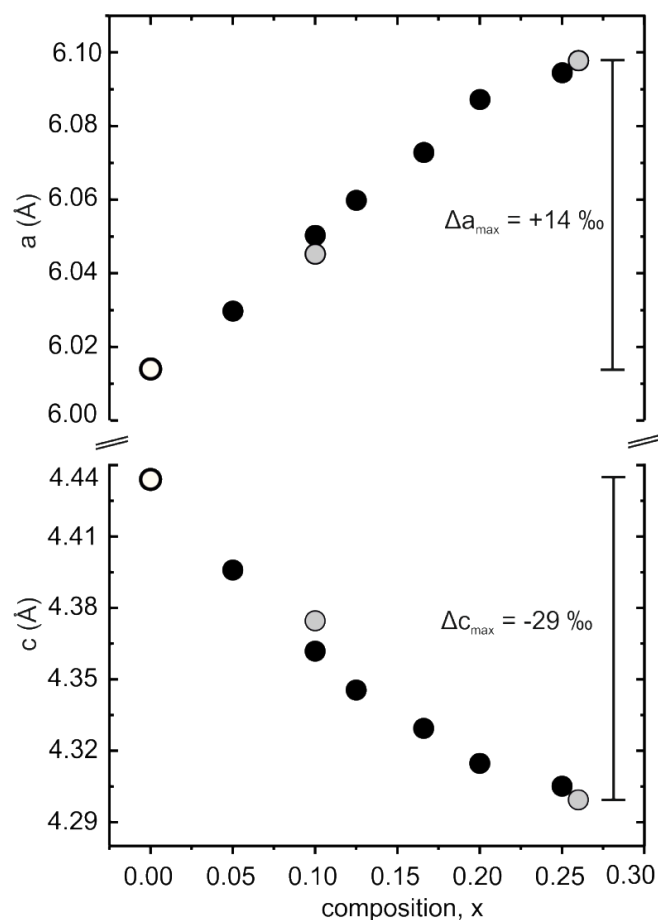


Figure 6.8 Lattice parameters  $a$  and  $c$  of members of the solid solution  $(V_{1-x}W_x)OPO_4$  ( $0.0 \leq x \leq 0.26$ ;  $\alpha_{II}$ -VOPO<sub>4</sub> structure type). Data from Guinier photographs of powder samples in black, single crystal data are light grey, and open circles for pure  $\alpha_{II}$ -VOPO<sub>4</sub> from literature [160].

Single crystals of  $(V_{1-x}W_x)OPO_4$  at  $x = 0.10$  and  $0.26$  were selected carefully under a polarizing microscope and glued on a thin vitreous silica fiber. Single crystal diffraction data were collected on a  $\kappa$ -CCD diffractometer (Enraf-Nonius Inc.) controlled by the HKL2000 software [177] using graphite-monochromated Mo-K $\alpha$  ( $\lambda = 0.71073 \text{ \AA}$ ) radiation at ambient temperature. Crystal system, lattice type were determined from simulated precession photographs. The starting parameters for the least squares refinement were obtained by Direct methods with SHELX-97. Full-matrix least-squares refinement was carried out by using SHELX-97 [123] in the WinGX [124] framework.

After the initial refinement cycles one independent site for the metal atoms was localized in the structures of  $(V_{0.90}W_{0.10})OPO_4$  and  $(V_{0.74}W_{0.26})OPO_4$ . However, the displacement parameters were unreasonable for this site. This problem was solved by allowing for mixed occupancy of the metal site by vanadium and tungsten. Thus, the residuals  $R_1$  dropped from 14% to about 5% for both structures. During further refinement the  $\Delta$ -Fourier electron density map showed some electron density at a rather small distance to the metal site. Eventually, the crystals of both compositions turned out to be twinned with the twin components related by a mirror plane parallel to  $(1\ 1\ 0)$ . Taking the twinning into account reduced the residuals even further. No hints were found for the presence of a superstructure due to vanadium/tungsten ordering. Details regarding single crystal data collection and structure refinements of  $(V_{0.90}W_{0.10})OPO_4$  and  $(V_{0.74}W_{0.26})OPO_4$  are summarized in Table 6.4. In Figure 6.9 the observed powder diffraction patterns of  $(V_{1-x}W_x)OPO_4$  at  $x = 0.10$  and  $x = 0.26$  are compared to simulations which are based on the data from the single crystal structure refinements. The final atomic coordinates and anisotropic displacement parameters are provided in Table 14.7 to Table 14.10. Selected inter-atomic distances are provided in Table 14.11.

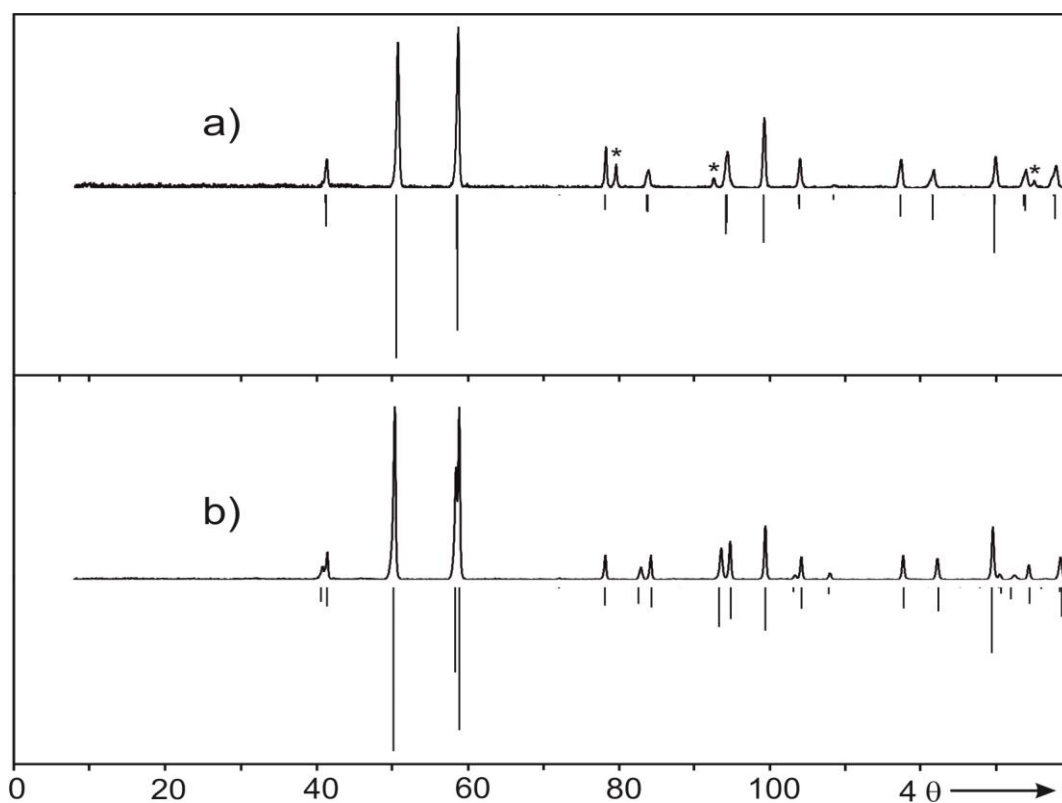


Figure 6.9 Guinier-photographs of  $\alpha_{II}\text{-}(V_{0.74}W_{0.26})OPO_4$  (a) and  $\alpha_{II}\text{-}(V_{0.90}W_{0.10})OPO_4$  (b) compared to diffraction patterns simulated on the basis of the corresponding single crystal structure refinements [this thesis]; \* indicate Pt from transport additive  $PtCl_2$ .

Table 6.4 Summary of crystallographic data and information on x-ray single-crystal structure refinements of members of the solid solution series (V<sub>1-x</sub>W<sub>x</sub>)OPO<sub>4</sub> with x = 0.10 and 0.26.

	V <sub>0.90</sub> W <sub>0.10</sub> PO <sub>5</sub>	V <sub>0.74</sub> W <sub>0.26</sub> PO <sub>5</sub>
Structural formula	α <sub>II</sub> -(V <sub>0.90</sub> W <sub>0.10</sub> )OPO <sub>4</sub>	α <sub>II</sub> -(V <sub>0.74</sub> W <sub>0.26</sub> )OPO <sub>4</sub>
Formula weight	175.2026	196.4662
Crystal system	tetragonal	tetragonal
Space group	<i>P4/n</i>	<i>P4/n</i>
<i>T</i> (K)	293(2)	293(2)
λ (Å)	0.71073	0.71073
<i>a</i> (Å)	6.0452(2)	6.0979(2)
<i>c</i> (Å)	4.3746(6)	4.2995(1)
<i>V</i> (Å <sup>3</sup> )	159.67(1)	159.874(1)
<i>Z</i>	2	2
<i>D</i> <sub>calc</sub> (g·cm <sup>-3</sup> )	3.469	4.095
μ (mm <sup>-1</sup> )	6.94	12.22
Crystal dimensions (mm <sup>3</sup> )	0.24×0.10×0.002	0.15×0.01×0.05
Crystal color	greenish yellow	green
<i>F</i> (0 0 0)	167.0	183
Measured refls.	5751	6836
Independent refls.	344	346
Absorption correction	multiscan	multiscan
Twin matrix	0 1 0 1 0 0 0 1	0 1 0 1 0 0 0 1
Batch scale factors	0.92	0.33
No. of parameters	21	21
Theta range (°)	2.91 - 34.97	3.34 - 34.86
Index ranges	-9 ≤ <i>h</i> ≤ 9; -7 ≤ <i>k</i> ≤ 7; -6 ≤ <i>l</i> ≤ 6	-9 ≤ <i>h</i> ≤ 9; -9 ≤ <i>k</i> ≤ 9; -6 ≤ <i>l</i> ≤ 6
<i>GOOF</i>	1.164	1.00
<i>R</i> <sub>int</sub>	0.065	0.068
<i>R</i> <sub>1</sub> , <i>wR</i> <sub>2</sub> [ <i>I</i> > 2σ( <i>I</i> )] <sup>a)</sup>	0.020, 0.049	0.027, 0.067
<i>R</i> <sub>1</sub> , <i>wR</i> <sub>2</sub> (all data) <sup>a)</sup>	0.021, 0.058	0.030, 0.081

<sup>a)</sup>  $R_1 = \sum ||F_0| - |F_c|| / \sum |F_0|$ ,  $F^2 > 2\sigma(F^2)$ ,  $w = 1/[\sigma^2(F_0^2) + (A \cdot P)^2 + B \cdot P]$ ,  $P = (F_0^2 + 2F_c^2)/3$ .

The crystal structures of α<sub>II</sub>-VOPO<sub>4</sub> [160] and β-VOPO<sub>4</sub> [161] are visualized in Figure 6.10 and Figure 6.11, respectively. In both structures chains of octahedra ...-O=V-O=V-O=V-... with alternating short and long distances *d*(V-O) along the chains are linked by phosphate tetrahedra. In α<sub>II</sub>-VOPO<sub>4</sub> these chains are straight and run parallel to the tetragonal *c*-axis. The chains in the β-form show a zig-zag pattern and extend along the orthorhombic *a*-axis. The crystal structure of α<sub>II</sub>-VOPO<sub>4</sub> (Figure 6.10) is characterized by layers  $\frac{2}{\infty}[\text{V}^{\text{V}}\text{OPO}_4]$  with only weak Lewis-acid-base inter-layer interactions due to a rather long distance *d*(V-O) = 2.85 Å [160]. In contrast the crystal structure of β-VOPO<sub>4</sub>



[161] exhibits a 3-D linkage of  $[PO_4]$  tetrahedra and distorted  $[(V^V=O)O_5]$  octahedra (Figure 6.11) and a significantly shorter sixth distance  $d(V-O) = 2.59 \text{ \AA}$ .

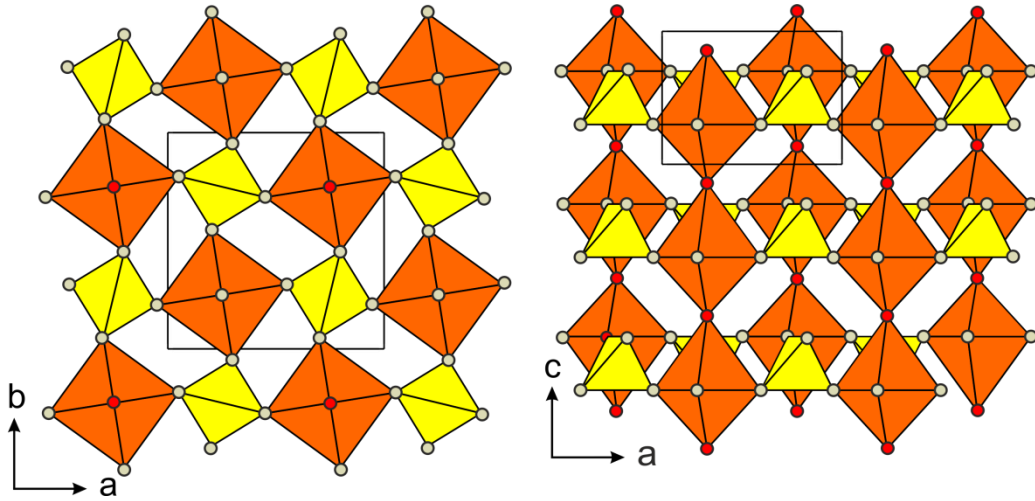


Figure 6.10 Crystal structure of  $\alpha_{II}$ -VOPO<sub>4</sub> (according to [160]). Projections on the  $ab$ - and  $ac$ -plane, respectively.  $[VO_6]$  octahedra: orange,  $[PO_4]$  tetrahedra: yellow. Red spheres represent oxygen atoms of vanadyl(V) groups  $(V=O)^{3+}$ .

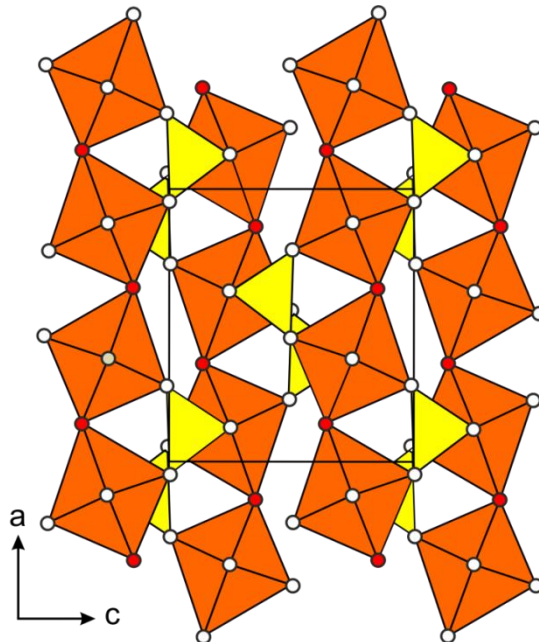


Figure 6.11 Crystal structure of  $\beta$ -VOPO<sub>4</sub> (according to [161]). Projection along the crystallographic  $b$ -axis,  $[VO_6]$  octahedra: orange,  $[PO_4]$  tetrahedra: yellow, red spheres represent oxygen atoms of vanadyl(V) groups  $(V=O)^{3+}$ .

Single-crystal structure refinements (see Table 6.4) of members at  $x = 0.10$  and  $0.26$  of the solid solution series  $(V_{1-x}W_x)OPO_4$  confirm the  $\alpha_{II}$ -VOPO<sub>4</sub> structure type. Thus obtained site occupation factors (see Table 14.7 and Table 14.8) clearly show the mixed occupancy of V/W at the metal site. In Figure 6.12 coordination polyhedra  $[MO_6]$  for  $V_{0.74}W_{0.26}OPO_4$  and  $V_{0.90}W_{0.10}OPO_4$  are compared to the distorted  $[VO_6]$  octahedron in  $\alpha_{II}$ -VOPO<sub>4</sub> [160]. Substitution of vanadium by the larger tungsten ion leads to an increase of the distance  $d(V-O_{eq})$  and, as a consequence, of the  $a$ -axis of the unit cell. The length of the crystallographic  $c$ -axis of the  $\alpha_{II}$ -structure is determined by the distances between the cation and the axial oxygen atoms. The substitution leads to an elongation of the short bond between the metal and the "double-bonded" oxygen from 1.58 to 1.67 Å. In contrast, the long axial bond is shortened from 2.85 to 2.63 Å (Figure 6.12). Thus, the overall effect of substituting vanadium by tungsten is a shrinking of the  $c$ -axis (Figure 6.8 and Figure 6.12). It might be assumed, that in parallel to the structural change the intra-layer interactions, which are very weak in  $\alpha_{II}$ -VOPO<sub>4</sub>, will be strengthened and the well-known intercalation behavior of  $\alpha_{II}$ -VOPO<sub>4</sub> towards Lewis acid-bases [178] should be modified.

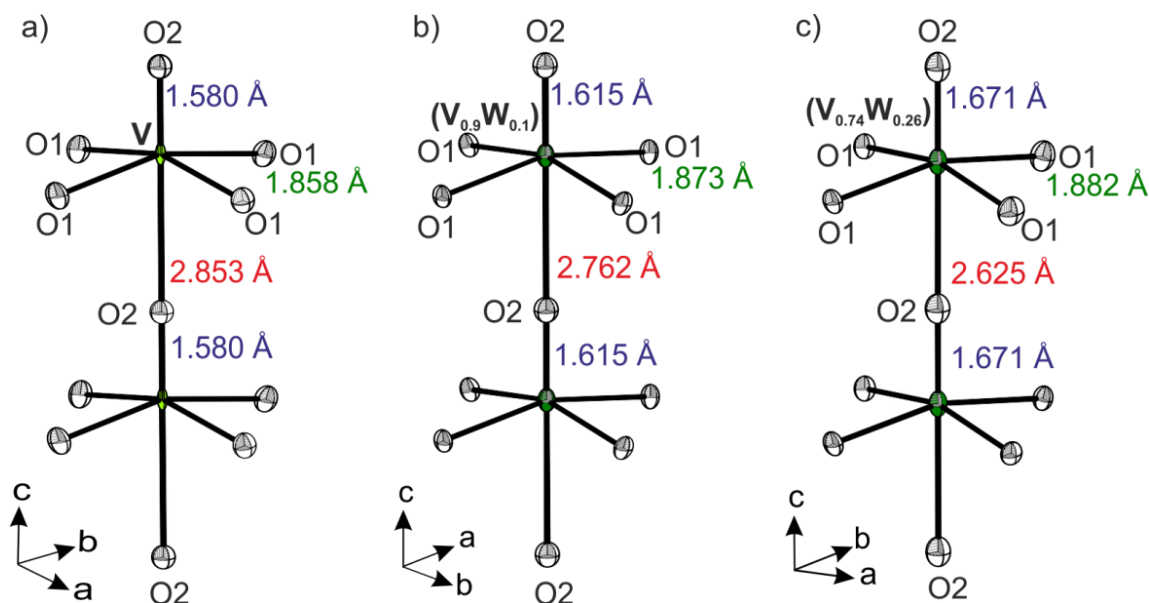


Figure 6.12 Comparison of the co-ordination polyhedra  $[(V_{1-x}W_x)O_6]$  with  $x = 0$  (a) in  $\alpha_{II}$ -VOPO<sub>4</sub> [160],  $x = 0.10$  (b) in  $(V_{0.90}W_{0.10})OPO_4$ , and  $x = 0.26$  (c) in  $(V_{0.74}W_{0.26})OPO_4$ . ORTEP style graphics (Ellipsoids are at 50% probability level, software: DIAMOND [128]).



## 6.5 Electronic structure

The electronic properties of (V<sub>1-x</sub>W<sub>x</sub>)OPO<sub>4</sub> (0 ≤ x ≤ 0.01, β-VOPO<sub>4</sub> structure type [161]; 0.04 ≤ x ≤ 0.26, α<sub>II</sub>-VOPO<sub>4</sub> structure type [160]) were studied by X-ray photoelectron spectroscopy (XPS), EPR spectroscopy, UV/Vis/NIR spectroscopy, magnetic susceptibility measurements and temperature dependent measurements of the electric conductivity of (V<sub>0.74</sub>W<sub>0.26</sub>)OPO<sub>4</sub>. The results of these experiments are consistent with the quantitative oxidation of W<sup>5+</sup> by V<sup>5+</sup> and, as a consequence, the presence of V<sup>4+</sup> at equivalent amounts to W<sup>6+</sup>. Accordingly, the solid solution has to be formulated as (V<sup>IV</sup><sub>x</sub>V<sup>V</sup><sub>1-2x</sub>W<sup>VI</sup><sub>x</sub>)OPO<sub>4</sub>, 0 ≤ x ≤ 0.26.

### 6.5.1 EPR spectroscopic studies of α<sub>II</sub>- and β-(V<sub>1-x</sub>W<sub>x</sub>)OPO<sub>4</sub>

All the EPR studies were performed in the research group of Prof. Olav Schiemann, University of Bonn, Germany. Further evidence for the presence of the paramagnetic V<sup>4+</sup> ions in the (V<sub>1-x</sub>W<sub>x</sub>)OPO<sub>4</sub> solid solutions has been obtained from EPR measurements of the corresponding phosphate powders (as shown in Figure 6.13). Since the V<sup>5+</sup> and W<sup>6+</sup> ions are EPR silent, all obtained spectra are attributed to V<sup>4+</sup> ions. For (V<sup>IV</sup><sub>x</sub>V<sup>V</sup><sub>1-2x</sub>W<sup>VI</sup><sub>x</sub>)OPO<sub>4</sub> with x = 0.01 an EPR spectrum is found that is typical for tetragonally distorted octahedral coordination of V<sup>4+</sup> ions (Figure 8a) [179, 180, 181]. The spectrum was simulated with an axial g-tensor (g<sub>||</sub> = 1.935±0.001, g<sub>⊥</sub> = 1.965±0.001) and an axial <sup>51</sup>V hyperfine coupling tensor (A<sub>||</sub> = 506±3 MHz, A<sub>⊥</sub> = 159±1 MHz). Note that the symmetry of the fitted EPR parameters is consistent with the crystallographic data, which show four symmetry equivalent V-O bonds in the equatorial plane of the VO<sub>6</sub> octahedra and different bond lengths for the axial oxygen atoms. The hyperfine coupling is more prominent in magnetically diluted phase and it is almost obscured at the member with highest concentration of the solid solution.

A splitting of the EPR lines of (V<sup>IV</sup><sub>0.01</sub>V<sup>V</sup><sub>0.98</sub>W<sup>VI</sup><sub>0.01</sub>)OPO<sub>4</sub> is observed at Q-band (Figure 6.13b) which could not be fitted with the simplification of co-linear alignment of the g and A(<sup>51</sup>V) tensors. The true rhombic symmetry of the chromophore as well as the non-colinear alignment of the g and A(<sup>51</sup>V) tensors {[0° 18° 0°] Euler angles (α, β, δ)} had to be accounted for. Eventually, this led to a good fit of the simulations with the corresponding lower frequency (X- and S-band) EPR spectra.

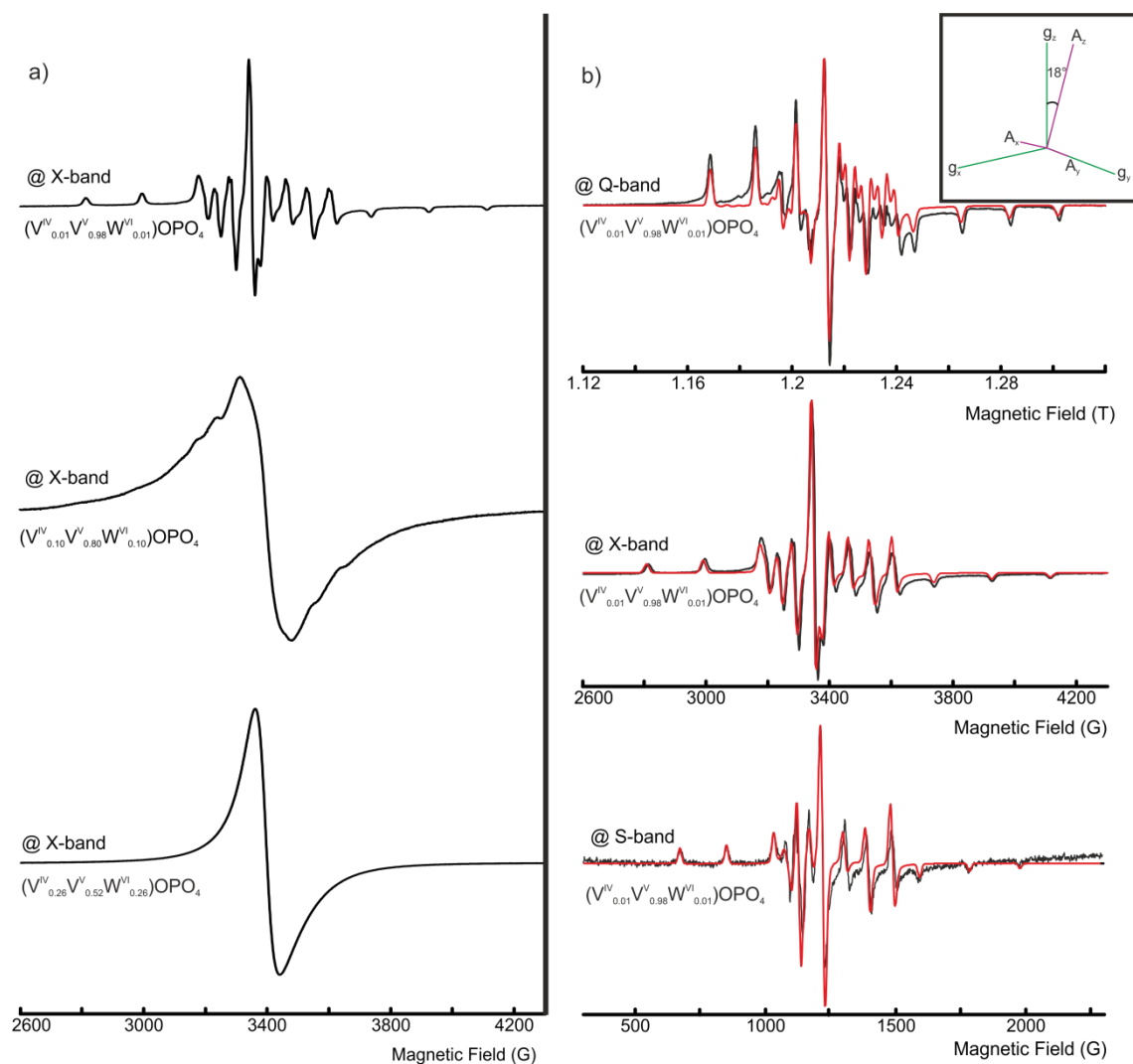


Figure 6.13 Room temperature continuous wave (CW) powder EPR spectra of  $(V_{1-x}^{IV}V_{2x}^{V}W_x^{VI})OPO_4$  with  $x = 0.01, 0.10$ , and  $0.26$  at X-band (a), for  $x = 0.01$  (b) at three different bands (S, X, Q) with their simulations shown in red. The orientation of  $A$  and  $g$  is shown in the inset of (b).

For the solid solution with  $x = 0.10$  all lines of the  $V^{4+}$  spectrum are strongly broadened providing the maximum of absorption at  $g = 1.974 \pm 0.001$ . A further increase of  $V^{4+}$  content up to  $x = 0.26$  yields an EPR spectrum, which consists of an exchange-narrowed line at the same  $g$ -value. The line broadening and narrowing with increasing number of  $V^{4+}$  sites is due to an increase in the electron spin-spin exchange coupling because on average the spin sites are closer in distance when their concentration increases [182, 183].

The EPR spectrum of tungsten-free slightly non-stoichiometric  $\beta$ - $VO_{1-\delta}PO_4$  as it is obtained from chemical vapor transport experiments consists of a weak anisotropic signal which has an absorption maximum at  $g = 1.963 \pm 0.001$ . Since the obtained spectrum (Figure 6.14)

does not show the characteristic hyperfine structure of the  $V^{4+}$  ion, it can not be assigned unambiguously to  $V^{4+}$  ions as it was done in [161] where a nonstoichiometry with respect to the V content of 1% was estimated for  $\beta\text{-VO}_{1-\delta}\text{PO}_4$ . The comparison of the EPR signal intensities observed for  $\beta\text{-VO}_{1-\delta}\text{PO}_4$  and  $(V_{0.99}W_{0.01})OPO_4$  in this study suggests that the content of the spin centers determining the EPR spectrum of  $\beta\text{-VO}_{1-\delta}\text{PO}_4$  is far below 1% per formula.

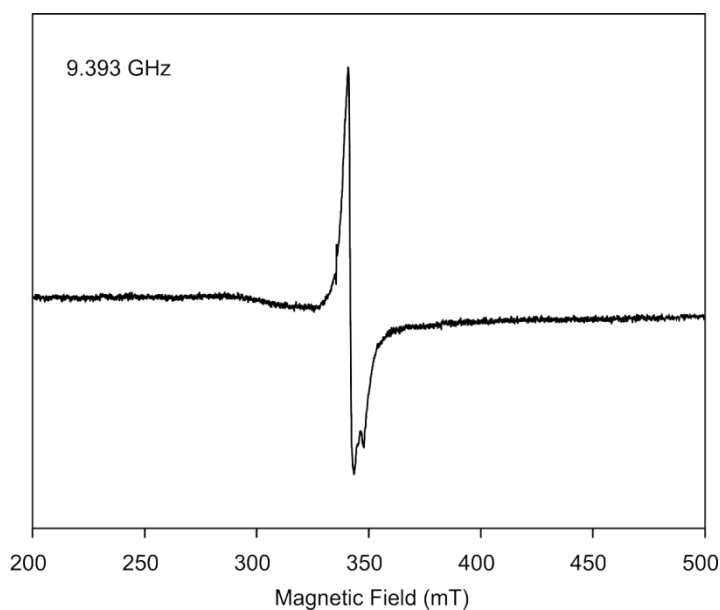


Figure 6.14 Continuous wave X-band EPR spectrum of a powder of slightly under-stoichiometric  $\beta\text{-VO}_{1-\delta}\text{PO}_4$  (powder from crystals obtained by CVT).

### 6.5.2 X-ray photoelectron spectroscopic study of $\alpha_{II}\text{-}(V_{0.80}W_{0.20})OPO_4$

The X-ray photoelectron spectra were measured using a PHI Quantera SXM Spectrometer equipped with Al  $K\alpha$  anode (1486.6 eV) operated at 24.8 W, with the typical beam diameter of 100  $\mu\text{m}$  under the vacuum of about  $4.5 \times 10^{-8}$  torr. The data are analyzed with the MultiPak software [71] for peak fitting with suitable background and peak profiles. The binding energies (BEs) of tungsten were referenced to that of C1s level at 285.0 eV whereas for vanadium, the best energy reference is, O1s at 529.8 eV for  $V_2O_5$  because C1s is not a good reference for determination BEs of vanadium [118]. Here the observed BE of C1s and O1s are 284.47 eV and 530.8 eV, respectively which are 0.53 eV less and 0.84 eV higher than the corresponding reference BE. Therefore to get the corrected BE, 0.53 eV was added to the observed W4f and 0.84 eV was subtracted from the V2p BEs (see Table 6.5). The ranges of binding energy (BE) were recorded from 28 to 46 eV for W4f,

510 to 540 eV for both V2p and O1s, and 280 to 292 eV for C1s, with the resolution of 0.1 eV, and preset time of 2.4, 3.6 and 1.2 seconds per point, respectively.

Table 6.5 XPS results of α<sub>II</sub>-(V<sup>IV</sup><sub>0.2</sub>V<sup>V</sup><sub>0.6</sub>W<sup>VI</sup><sub>0.2</sub>)OPO<sub>4</sub> and literature value.

component	BEs (eV)		Δ (eV)	Ref.
	Observed	Corrected		
O 1s	530.84	530.00		[this thesis, 186]
V 2p <sub>3/2</sub>	516.49	515.65	14.35	[this thesis]
		515.65	14.35	V <sup>IV</sup> O <sub>2</sub> [186]
		516.20	13.70	V <sup>IV</sup> O <sub>2</sub> [184]
V 2p <sub>3/2</sub>	518.00	517.16	12.84	[this thesis]
		517.00	12.80	V <sup>V</sup> <sub>2</sub> O <sub>5</sub> [186]
		516.90	12.90	V <sup>V</sup> <sub>2</sub> O <sub>5</sub> [184]
C 1s	284.47	285.00		
W 4f <sub>7/2</sub>	35.86	36.39	--	[this thesis]
		35.4 - 36.6	--	W <sup>VI</sup> O <sub>3</sub> [118]
		35.8 - 36.7	--	Al <sub>2</sub> (W <sup>VI</sup> O <sub>4</sub> ) <sub>3</sub> [118]

$$\Delta = |O1s - V2p_{3/2}|$$

The oxidation states of tungsten and vanadium in (V<sub>0.8</sub>W<sub>0.2</sub>)OPO<sub>4</sub> were identified by XPS. The V2p (Figure 6.15a) and W4f (Figure 6.15b) XP spectra show that vanadium has two and tungsten just a single valence state. The corrected observed binding energies (BE) for an electron in the vanadium 2p<sub>3/2</sub> state are 515.65 eV and 517.14 eV, respectively. The first energy is very close to that of V(IV) and the latter one is very close to that of V(V) in reference compounds [185]. The separation of BEs between O1s and V2p<sub>3/2</sub> is also characteristic. The first observed BEs separation is 14.35 eV which is comparable to V<sup>4+</sup> in VO<sub>2</sub> (13.7 - 14.5 eV). The second observed BEs separation is 12.84 eV which is comparable to V<sup>5+</sup> in V<sub>2</sub>O<sub>5</sub> (12.6 - 12.8 eV) [186]. The observed BE of W4f<sub>7/2</sub> level is 36.39 eV (Figure 6.15) which is very close to that of W<sup>6+</sup> in WO<sub>3</sub> (35.4 - 36.6 eV) or in Al<sub>2</sub>(WO<sub>4</sub>)<sub>3</sub> (35.8 - 36.7 eV) [118]. Therefore, the XPS measurements confirm the presence of mixed valence states of vanadium(IV and V) and the single valence state of tungsten(VI).

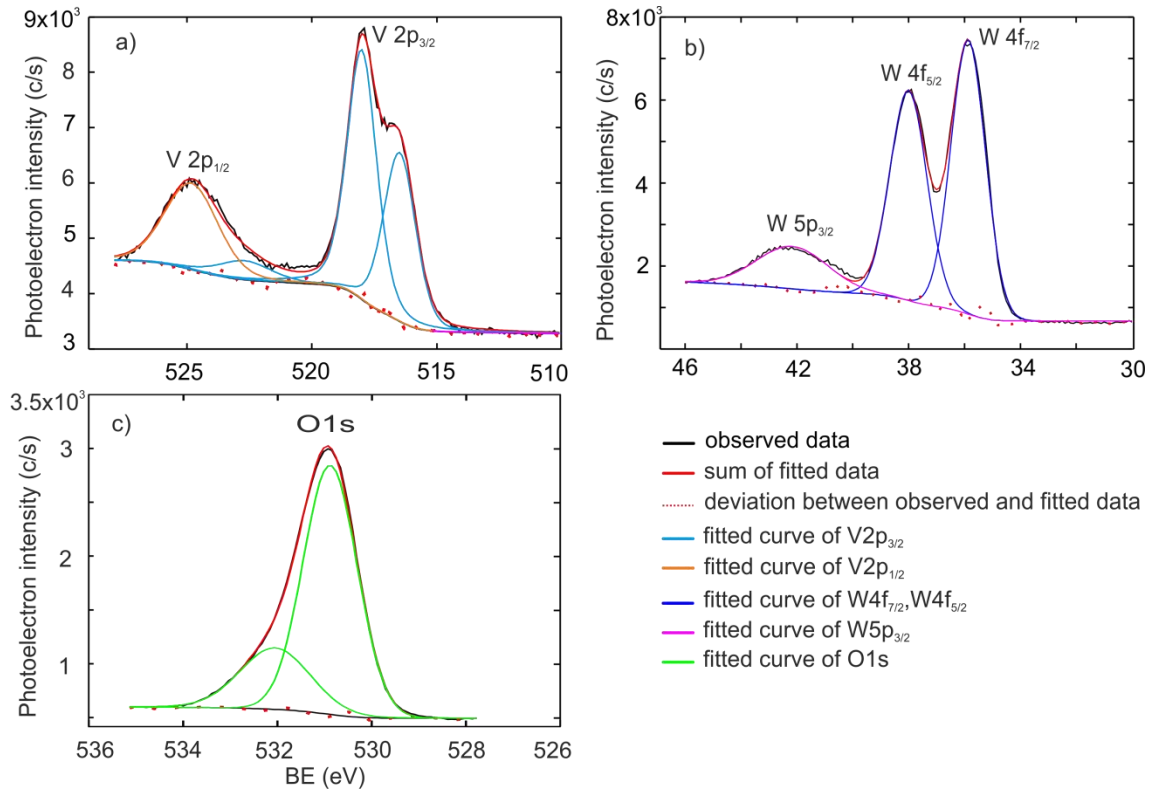


Figure 6.15 XPS spectra of  $\alpha_{II}-(V^{IV}_{0.2}V^V_{0.6}W^{VI}_{0.2})OPO_4$  with fitted curves for V2p (a), W4f (b), and O1s (c).

### 6.5.3 UV/Vis/NIR spectroscopy

Powders and single-crystals (Figure 6.7a) of stoichiometric  $\beta$ -V<sup>V</sup>OPO<sub>4</sub> exhibit a bright yellow (lemon) color due to a strong absorption at  $\tilde{\nu} = 24500 \text{ cm}^{-1}$  with a shoulder at  $26700 \text{ cm}^{-1}$  (Figure 6.16). Another strong absorption band is observed at  $\tilde{\nu} = 33800 \text{ cm}^{-1}$  with a shoulder at  $\tilde{\nu} \approx 38000 \text{ cm}^{-1}$ . In agreement with DFT calculations on the electronic structure of  $\beta$ -VOPO<sub>4</sub> [187] we assign these bands to transitions from the valence band (mainly s- and p-orbitals of oxygen atoms O1, O2, and O3) to the lowest states of the conduction band, which in a simplified picture correspond to the empty *d*-orbitals of V<sup>5+</sup>. The occurrence of several ligand-metal charge-transfer transitions LMCT(O<sup>2-</sup> → V<sup>5+</sup>) is the consequence of a strong ligand-field splitting of the vanadium 3*d*-orbitals {  $E(d_{xy}) \ll E(d_{x^2-y^2}) \ll E(d_{z^2})$  }.

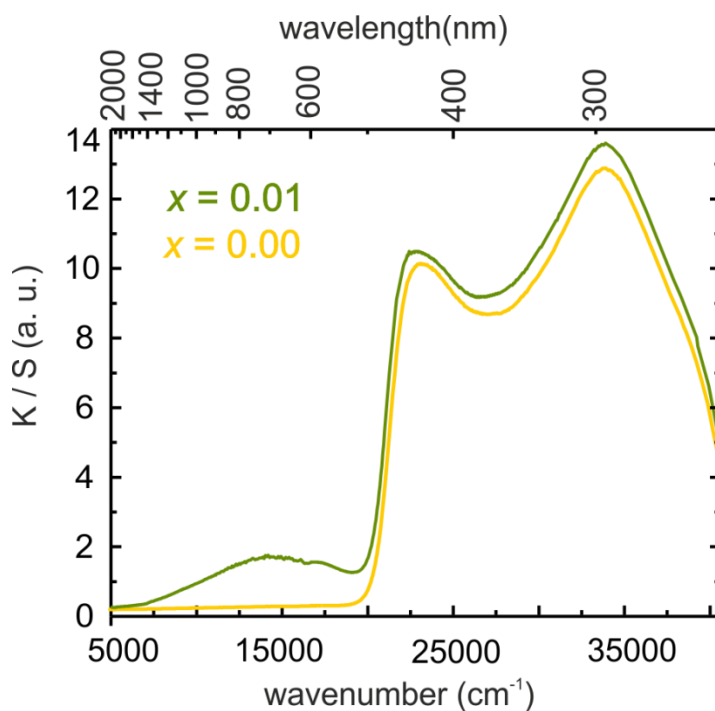


Figure 6.16 UV/Vis/NIR powder reflectance spectra of  $(V_{1-x}W_x)OPO_4$  ( $\beta$ -VOPO<sub>4</sub> structure type) with  $x = 0.00$  (stoichiometric bright yellow) and  $x = 0.01$  (olive).

Though the description of the electronic structure of  $\beta$ -VOPO<sub>4</sub> in [187] considered by and large is correct, here it is emphasized that the experimentally observed transition energies are about 8000 to 10000  $\text{cm}^{-1}$  higher than the calculated ones, reported in [187]. On the other hand, one may take the ligand field transitions for the  $[(V^{IV}=O)O_5]$  chromophore, which is geometrically quite similar to the  $[(V^V=O)O_5]$  group in the vanadyl(V) phosphates, for an estimate of the expected  $d$ -orbital splitting. Electronic transitions for the aquo-complex  $[(V^{IV}=O)(H_2O)_5]^{2+}$  [188, 189] and the chromophore  $[(V^{IV}=O)O_5]$  in  $Ag_6(V^{IV}O)_2(P_2O_7)(PO_4)_2$  [190] (in parentheses) are reported to occur at  $\tilde{\nu} \approx 13000$  (9500)  $\text{cm}^{-1}$  for the transitions  $d_{xy} \rightarrow d_{xy-yz}$  and  $\tilde{\nu} \approx 16000$  (14800)  $\text{cm}^{-1}$  for  $d_{xy} \rightarrow d_{x^2-y^2}$ . These energies agree remarkably well with the energy differences between the first, second and third LMCT( $O^{2-} \rightarrow V^{5+}$ ) at 24500  $\text{cm}^{-1}$ , 33800  $\text{cm}^{-1}$ , and 38000  $\text{cm}^{-1}$  in the vanadyl(V) phosphates.

Crystals of  $(V_{0.99}W_{0.01})OPO_4$  ( $\beta$ -VOPO<sub>4</sub> structure type) are dark green (see Figure 6.7b). Its powder reflectance spectrum (see Figure 6.16) shows a broad band around 14300  $\text{cm}^{-1}$  with weak shoulders at 10500 and 17300  $\text{cm}^{-1}$  in contrast to pure  $\beta$ -VOPO<sub>4</sub>. These transitions are assigned to inter-valence charge-transfer transitions IVCT( $V^{4+} \rightarrow V^{5+}$ ). Two further strong absorption bands are observed at  $\tilde{\nu} = 22800$  (shoulder at 24300)  $\text{cm}^{-1}$

and  $\tilde{\nu} = 33800$  (shoulder at  $38000$ )  $\text{cm}^{-1}$ . The former two are shifted by about  $2000 \text{ cm}^{-1}$  to lower energy with respect to  $\beta\text{-VOPO}_4$ , while the latter appear at the same energies.

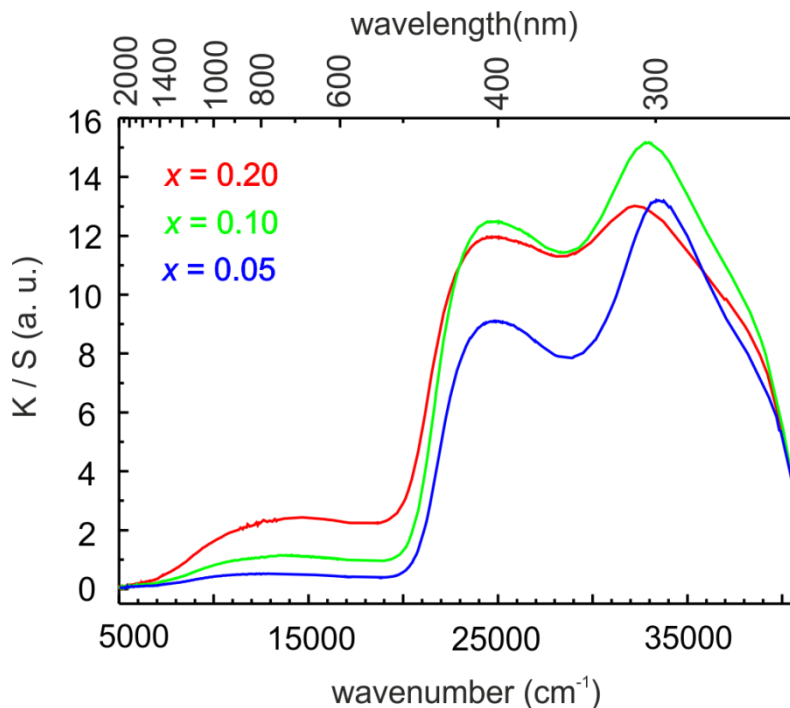


Figure 6.17 UV/Vis/NIR powder reflectance spectra of  $(V_{1-x}W_x)OPO_4$  ( $\alpha_{II}\text{-VOPO}_4$  structure type) with  $x = 0.05, 0.10,$  and  $0.20$ .

Powders of phosphates  $(V_{1-x}W_x)OPO_4$  with higher tungsten content ( $\alpha_{II}\text{-VOPO}_4$  structure type;  $x = 0.05, 0.10,$  and  $0.20$ ) show olive to dark greenish color. Despite their structural difference  $V_{0.99}W_{0.01}OPO_4$  and the solid solution  $V_{1-x}W_xOPO_4$  ( $x = 0.05, 0.10,$  and  $0.20$ ) exhibit very similar electronic absorption spectra (see Figure 6.17) with a broad band due to IVCT ( $V^{4+} \rightarrow V^{5+}$ ) at  $\tilde{\nu} = 14000 \text{ cm}^{-1}$ , broad bands due to LMCT( $O^{2-} \rightarrow V^{5+}$ ) at  $\tilde{\nu} = 25200 \text{ cm}^{-1}$  and at  $32500$  to  $33800 \text{ cm}^{-1}$  with a shoulder at  $\tilde{\nu} \approx 38000 \text{ cm}^{-1}$ . For increasing tungsten content ( $x = 0.10, 0.20$ ) the intensity of the IVCT at  $\tilde{\nu} = 14000 \text{ cm}^{-1}$  increases.

Mildly reducing conditions or too high temperatures during synthesis cause the formation of slightly oxygen deficient  $\beta\text{-VO}_{1-\delta}PO_4$  which shows an olive color for powder samples. Single crystals of this slightly under-stoichiometric material are dichroic (yellow/green) due to the additional electronic transition at  $\tilde{\nu} = 15700 \text{ cm}^{-1}$  (see Figure 6.18). Due to the strong orientation dependence of this excitation parallel to the crystallographic  $a$ -axis of the  $\beta\text{-VOPO}_4$  structure, which corresponds to the direction of the  $\dots\text{O}=\text{V}-\text{O}=\text{V}-\text{O}=\text{V}-\dots$  chains this transition is assigned to the IVCT( $V^{4+} \rightarrow V^{5+}$ ). The amount of

$V^{4+}$  in nonstoichiometric  $\beta\text{-VO}_{1-\delta}\text{PO}_4$  is even less than 1%. Thus, it is too low to allow  $d-d$  transitions of reasonable intensity. Furthermore, the orientation dependence of this electronic transition cannot be explained by  $d-d$  transitions on  $V^{4+}$ , but agrees well with the one expected for the electric dipole allowed IVCT( $V^{4+} \rightarrow V^{5+}$ ).

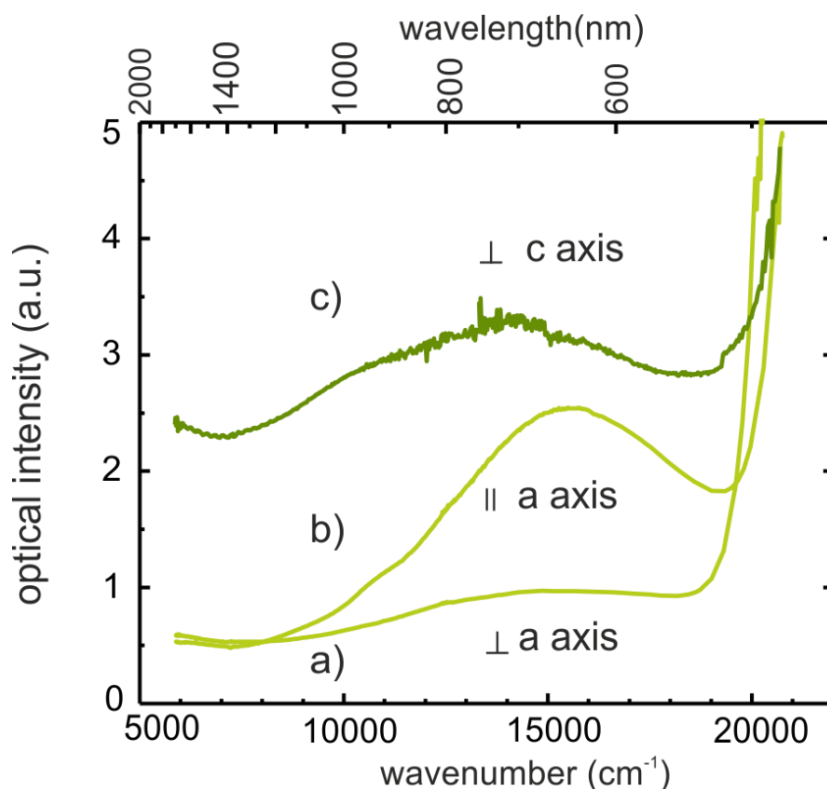


Figure 6.18 Polarized single crystal UV/Vis/NIR absorption spectra of slightly oxygen-deficient  $\beta\text{-VO}_{1-\delta}\text{PO}_4$  (a, b) and  $\alpha_{II}\text{-(V}_{0.90}\text{W}_{0.10})\text{OPO}_4$  (c). Due to very thin plate like crystals, measurements of the spectra with light polarized along the  $c$ -axis of  $\alpha_{II}\text{-(V}_{0.90}\text{W}_{0.10})\text{OPO}_4$  was not possible.

#### 6.5.4 Magnetic behavior of $\alpha_{II}\text{-(V}_{1-x}\text{W}_x)\text{OPO}_4$

The temperature dependence of the reciprocal molar magnetic susceptibility  $\chi_m^{-1}$  of  $(V_{0.90}W_{0.10})\text{OPO}_4$  (powder) and  $(V_{0.74}W_{0.26})\text{OPO}_4$  (crushed single crystals) was measured using a vibrating sample magnetometer (VSM) as a function of temperature ( $2 \leq T \leq 300$  K; Figure 6.19). A diamagnetic correction was applied to the observed weight data according to the method of atom and group increments [129].



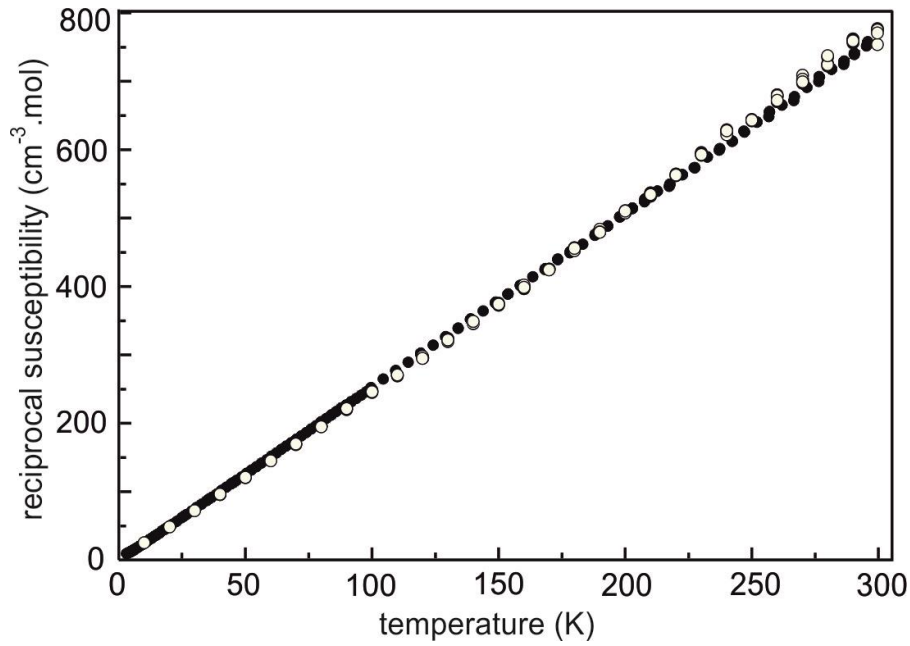


Figure 6.19 Reciprocal molar susceptibility  $\chi_{\text{mol}}^{-1}$  vs. temperature of  $(V^{IV}_{0.10}V^V_{0.80}W^{VI}_{0.10})OPO_4$  (open circles,  $\mu_{\text{exp}} = 1.74 \mu_B / V^{4+}$ ) and  $(V^{IV}_{0.26}V^V_{0.48}W^{VI}_{0.26})OPO_4$  (black circles,  $\mu_{\text{exp}} = 1.62 \mu_B / V^{4+}$ ).

Over the whole temperature range Curie behavior [130] with constant magnetic moments  $\mu_{\text{exp}} = 1.74 \mu_B / V^{4+}$  and  $1.62 \mu_B / V^{4+}$ , respectively is observed. These moments are close to the spin-only value of  $1.73 \mu_B$  for one unpaired electron. Apparently, the orbital contribution to the magnetic moment is almost completely extinguished due to the low symmetry ligand field around the  $V^{4+}$  ions. The slightly smaller  $\mu_{\text{exp}}$  for  $(V^{IV}_{0.26}V^V_{0.48}W^{VI}_{0.26})OPO_4$  might point to a small uncertainty in its chemical composition ( $x = 0.24$  instead of  $0.26$ ) which was taken from the structure refinement (Table 6.4).

### 6.5.5 Electronic conductivity of $\alpha_{II}-(V_{0.74}W_{0.26})OPO_4$

The electrical resistance of selected crushed crystal of  $(V^{IV}_{0.26}V^V_{0.48}W^{VI}_{0.26})OPO_4$  was measured by a Keithley 2400 sourcemeter over the temperature range 309 to 390K with 80C535 microcontroller and PT 100 temperature sensor. The sample (diameter  $d = 2$  mm, length  $l = 0.54$  mm) was placed inside a silica tube and two ends of the sample were contacted by gold (disc) electrodes. The gold electrodes were made by electroplating of nickel electrodes. The current was measured by applying an electrical potential difference of 0.3 Volt which was controlled by the Keithley 2400 source meter.

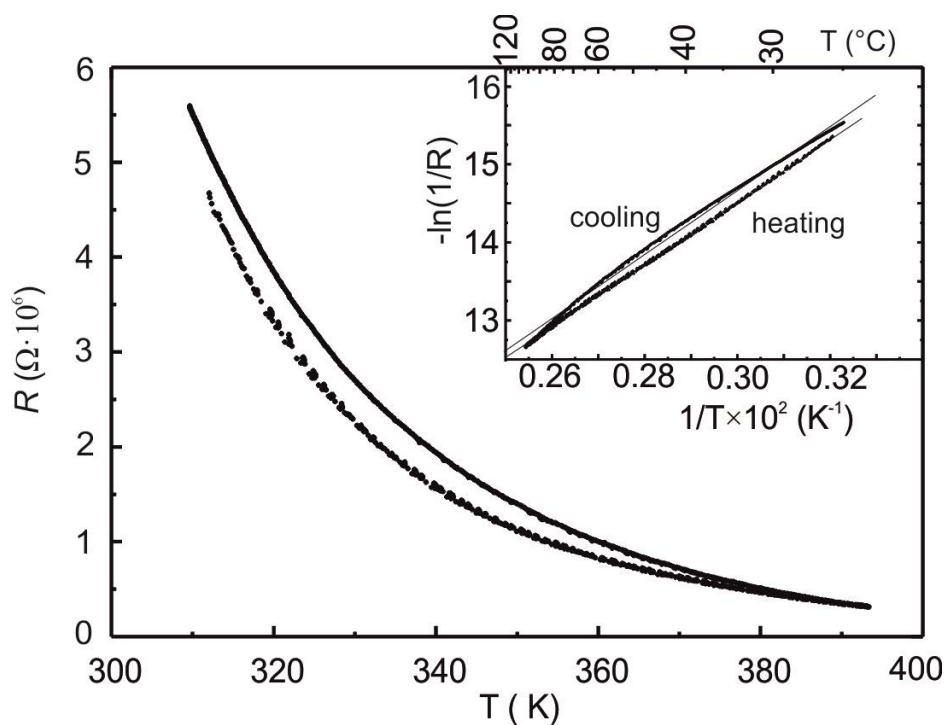


Figure 6.20 Temperature dependent resistance of  $\alpha_{II}-(V^{IV}_{0.26}V^V_{0.48}W^{VI}_{0.26})OPO_4$  (crushed crystals obtained from CVT).

Figure 6.20 shows the typical semiconducting behavior of  $(V^{IV}_{0.26}V^V_{0.48}W^{VI}_{0.26})OPO_4$ . The band gap was estimated to  $E_g = 0.7$  eV from the Arrhenius plot  $\ln(1/R)$  vs.  $(1/T)$  (Figure 6.20 inset). This value is in good agreement with the optical band gap observed for phosphates  $(V_{1-x}W_x)OPO_4$  (Figure 6.19). Thus, a hopping mechanism according to a *Robin and Day* Class II mixed-valent compound [191] appears to be a reasonable assumption. In this context it is worth mentioning that semiconducting behavior has been reported many years ago for pure as well as for tungsten-doped V-P-O glasses [192, 193]. Only recently it was shown by contactless *in-situ* conductivity measurements, that selective oxidation catalyst behavior of vanadyl pyrophosphate catalysts is related to *p*-type semiconducting behavior [194].

The linear *I-V* curves (current-voltage) of  $(V^{IV}_{0.26}V^V_{0.48}W^{VI}_{0.26})OPO_4$  (Figure 6.21) obtained at different temperature (300-353 K) indicate the homogenous semiconducting behavior of the material which follow the ohmic law.

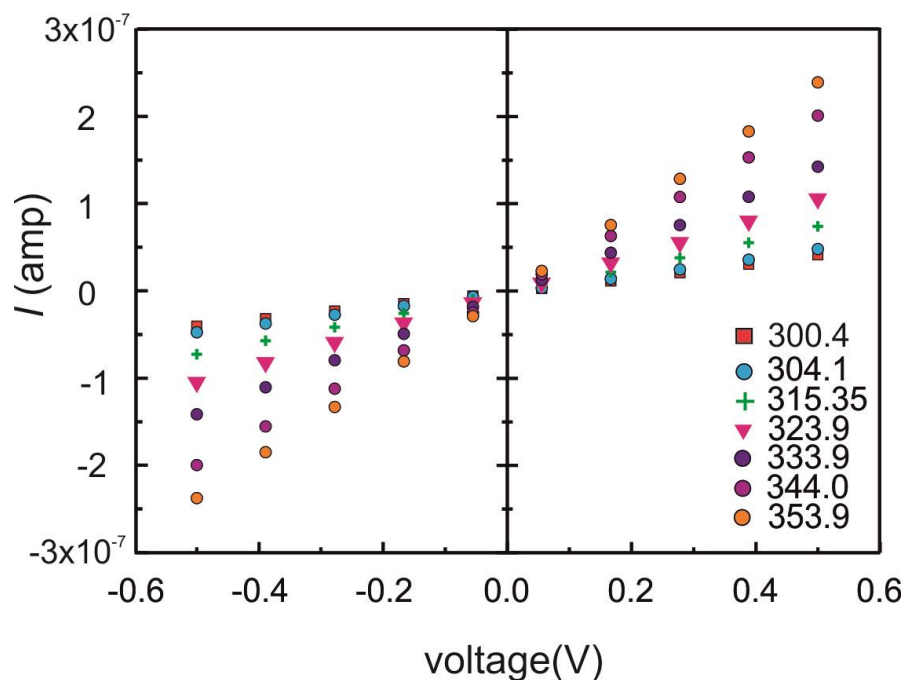


Figure 6.21 The  $I$ - $V$  relationship of  $(V^{IV}_{0.26}V^V_{0.48}W^{VI}_{0.26})OPO_4$  ( $\alpha_{II}$ -VOPO<sub>4</sub> type).

### 6.5.6 <sup>31</sup>P-MAS-NMR spectra of $\alpha_{II}$ -(V<sub>1-x</sub>W<sub>x</sub>)OPO<sub>4</sub>

<sup>31</sup>P-MAS-NMR spectra of paramagnetic  $\alpha_{II}$ -V<sup>V</sup>OPO<sub>4</sub> type solid solution  $(V^{IV}_xV^V_{1-2x}W^{VI}_x)OPO_4$ , ( $0.04 \leq x \leq 0.26$ ) also confirm formation of single phase materials. For  $\alpha_{II}$ -VOPO<sub>4</sub> the single isotropic <sup>31</sup>P-MAS-NMR chemical shift is reported at  $\delta_{iso} = -20.5$  ppm [195] which comply with the crystal structure containing only one independent phosphorus site at Wyckoff position of  $2b$ . The <sup>31</sup>P-MAS-NMR measurements of weakly paramagnetic solid solution  $(V^{IV}_xV^V_{1-2x}W^{VI}_x)OPO_4$  ( $\alpha_{II}$ - type) with  $x = 0.05$  and  $0.20$  also showed single resonance line at  $\delta_{iso} = -19.0$  and  $-17.6$  ppm, respectively (see Table 6.6 and Figure 6.22). The downfield shift of the resonance lines with increasing tungsten concentration is attributed to inductive effect. The broadening of the resonance line with increasing paramagnetic species (see Table 6.6) is the consequences of coupling between the <sup>31</sup>P nuclei and the  $3d^1$  electron of vanadium(IV) ions and anisotropic magnetic susceptibility [196].

Table 6.6 Summary of isotropic chemical shifts  $\delta_{iso}$  in <sup>31</sup>P-MAS-NMR spectra of members of the solid solution  $(V_{1-x}W_x)OPO_4$ ;  $0 \leq x \leq 0.20$ .

phosphate	$\delta_{iso}$ (ppm)	FWHM (Hz)	reference
$\alpha_{II}$ -V <sup>V</sup> OPO <sub>4</sub>	-20.5	--	[195]
$\alpha_{II}$ -(V <sup>IV</sup> <sub>0.05</sub> V <sup>V</sup> <sub>0.90</sub> W <sup>VI</sup> <sub>0.05</sub> )OPO <sub>4</sub>	-19.0	810	[this thesis]
$\alpha_{II}$ -(V <sup>IV</sup> <sub>0.20</sub> V <sup>V</sup> <sub>0.60</sub> W <sup>VI</sup> <sub>0.20</sub> )OPO <sub>4</sub>	-17.6	1360	[this thesis]

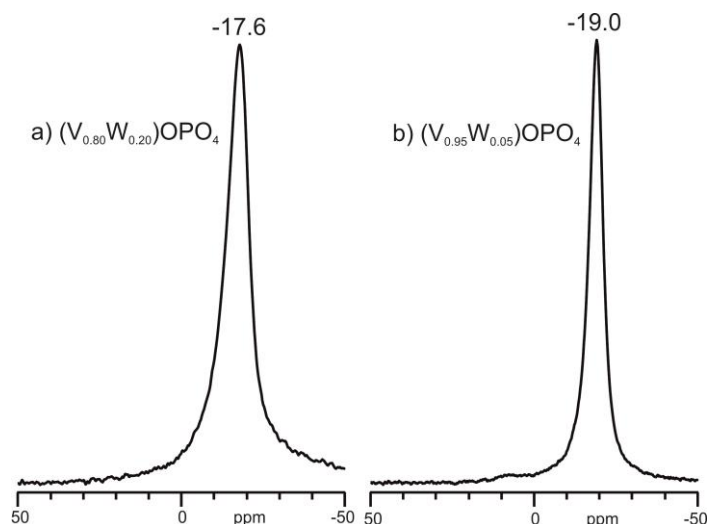


Figure 6.22 Room temperature  $^{31}\text{P}$ -MAS-NMR spectra of  $(V_{1-x}W_x)OPO_4$ ;  $x = 0.20$  (a) and  $x = 0.05$  (b) (both  $\alpha_{\text{II}}$ - $VOPO_4$  structure type) measured at spin rates 15 KHz.

### 6.6 The solid solution $(V_{1-x}W_x)OPO_4$ ( $WOPO_4$ type) at high tungsten concentration ( $0.67 \leq x \leq 1$ )

Substitution of pentavalent tungsten in  $W^{\text{V}}OPO_4$  (upper phase boundary) by two-thirds of hexavalent tungsten and one-third of trivalent vanadium allows the formation of lower phase boundary composition  $(V^{\text{III}}_{0.33}W^{\text{VI}}_{0.67})OPO_4$  ( $W^{\text{V}}OPO_4$  type). This substitution actually mimics the overall metal oxidation state of +5. The redox stability of  $V^{3+}$  towards  $W^{5+}$  and/or  $W^{6+}$  in the solid solution  $(V_{1-x}W_x)OPO_4$  in the range  $0.67 \leq x \leq 1.0$  can be formulated as  $(V^{\text{III}}_{1-x}W^{\text{V}}_{3x-2}W^{\text{VI}}_{2(1-x)})OPO_4$  which is in agreement with the oxygen co-existence pressures of their corresponding oxides (see Figure 6.1b) [136].

In this subchapter, synthesis of the solid solution  $(V_{1-x}W_x)OPO_4$ ;  $0.67 \leq x \leq 1.0$ , ( $WOPO_4$  type) at high tungsten concentration of the quasi-binary section  $VOPO_4 - WOPO_4$  by different synthetic routes and their characterization by Guinier photographs is described.

**Vapour phase moderated solid state synthesis.** Microcrystalline powders of solid solution  $(V_{1-x}W_x)OPO_4$ ;  $0.67 < x < 1.0$  ( $WOPO_4$  type) was prepared from mixtures of  $\beta$ - $VOPO_4$  and  $WOPO_4$  according to (eq. 6.1) in sealed silica ampoules by vapor phase moderated solid state reaction at  $800^\circ\text{C}$  using chlorine as mineralizer (Figure 6.23 and Table 6.2). The procedure for this synthesis technique is already described in section 6.3. Aiming at the synthesis of the LPB composition by vapor phase moderated solid state synthesis at  $800^\circ\text{C}$  leads to formation of  $V^{\text{III}}(W^{\text{VI}}O_2)(P_2O_7)(PO_4)$  [197] (Table 6.2) which is the thermodynamically stable phase for the composition  $(V^{\text{III}}_{0.33}W^{\text{VI}}_{0.67})OPO_4$  (see Chapter 8).

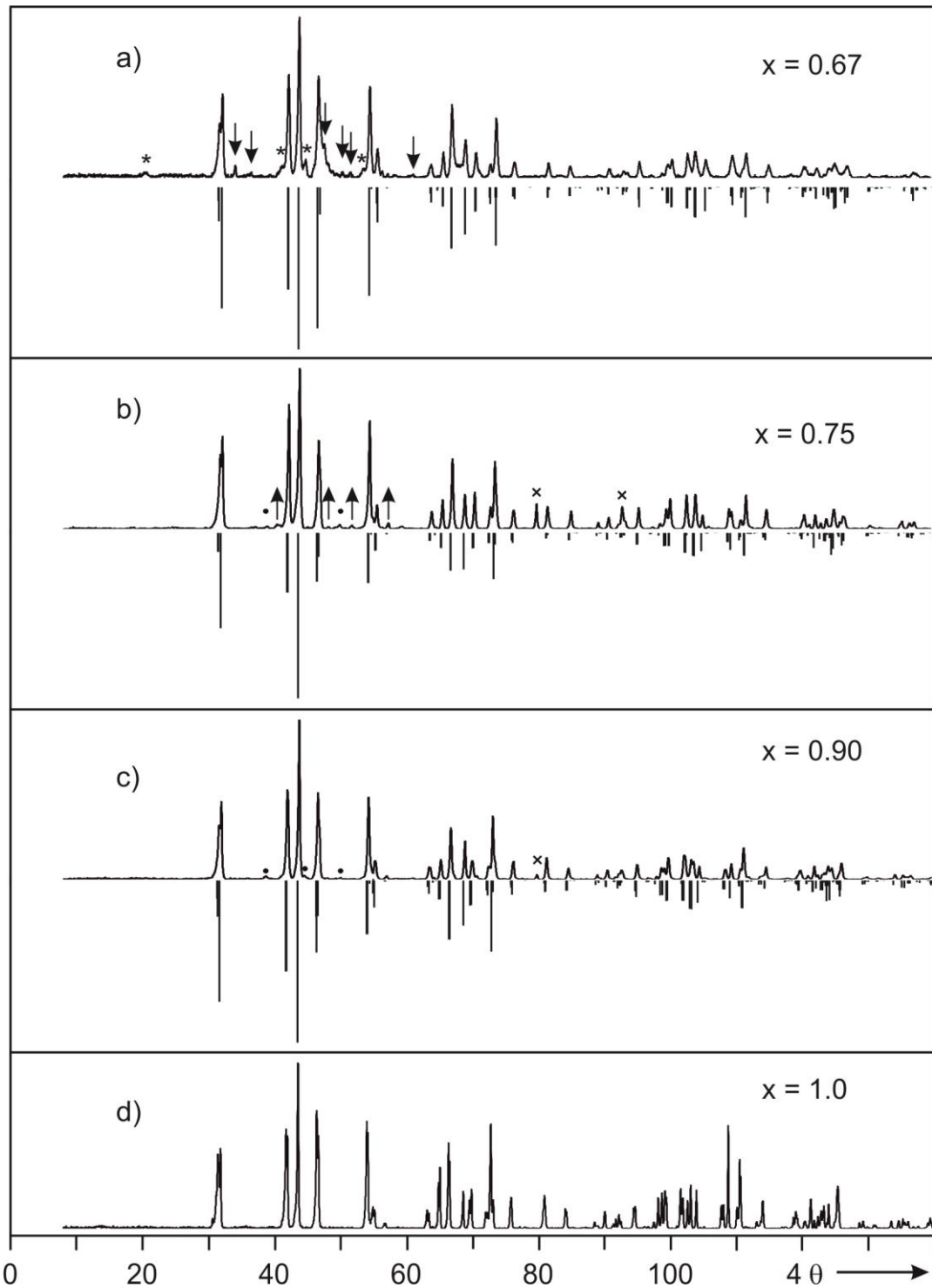


Figure 6.23 Guinier-photographs of members of the solid solution  $(V_{1-x}W_x)OPO_4$ ; (WOPO<sub>4</sub> type) with  $x = 0.67$  (a), 0.75 (b), 0.90 (c), and 1.0 (d) compared to the simulations based on the single-crystal data of WOPO<sub>4</sub> [this thesis]. Asterisks, down arrows, black dots, cross, and up arrows indicate P<sub>4</sub>W<sub>8</sub>O<sub>32</sub> [95], V(WO<sub>2</sub>)<sub>2</sub>(P<sub>2</sub>O<sub>7</sub>)(PO<sub>4</sub>) [this thesis], WP<sub>2</sub>O<sub>7</sub> [94], Pt and unknown phase, respectively. The samples were obtained via SCS followed by heating in argon atmosphere (a), by vapor phase moderated solid state reactions (b) and (c), and by CVT (d).

**Solution combustion synthesis** (followed by heating in argon flow,  $p(O_2) \approx 20$  ppm). The LPB member  $(V^{III}_{0.33}W^{VI}_{0.67})OPO_4$  ( $WOPO_4$  structure type) of the solid solution is synthesized via SCS followed by heating the combustion product in an argon flow,  $p(O_2) \approx 20$  ppm (see Table 6.3). The procedure of SCS is described in section 6.3. The low oxygen pressure is required to set the appropriate oxidation state of  $V^{3+}$  and  $W^{5+/6+}$ .

Experiments aiming at the synthesis of  $(V^{III}_{0.333}W^{VI}_{0.667})OPO_4$  ( $W^VOPO_4$  structure type) via SCS followed by heating (800 °C) in air lead to oxidation of the material. XRPD of the obtained grey powders show the pattern of  $m-W^{VI}_2O_3(PO_4)_2$  [78, 79, this thesis]) with a small hump which might be amorphous vanadium phosphate. On further heating the sample melted. The solidified melt showed weak reflections of  $m-W^{VI}_2O_3(PO_4)_2$ .

**Three step synthesis** (SCS, reduction by moist  $H_2$  flow, and sealed tube reaction at elevated temperature). One of the members of  $W^VOPO_4$  type solid solution  $(V_{0.2}W_{0.8})OPO_4$  which was obtained by *vapor phase moderated solid state reaction* as mentioned before was also synthesized by a three step procedure (see Figure 6.24 and Table 6.3).

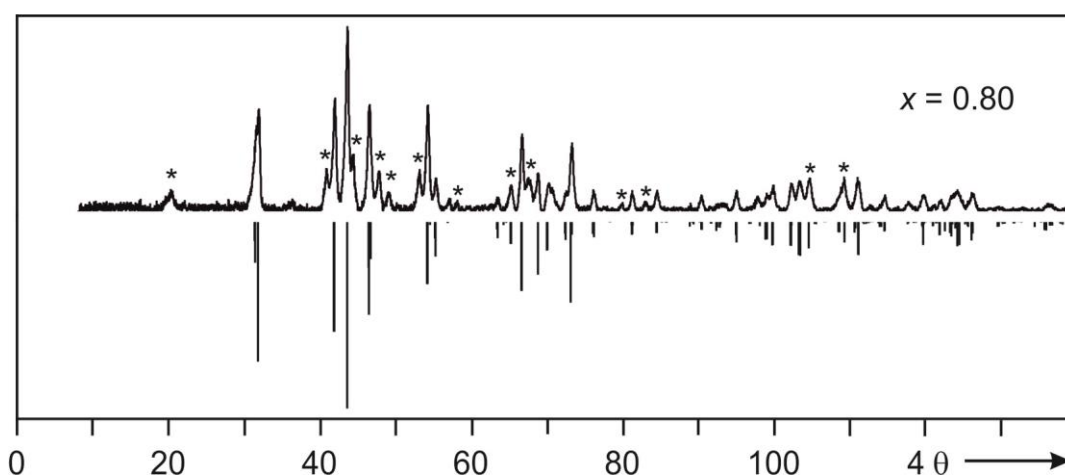


Figure 6.24 Guinier photograph of  $(V_{0.20}W_{0.80})OPO_4$  (member of  $WOPO_4$  type solid solution) obtained by a three step procedure (a), compared to simulation (b) based on the single-crystal data of  $WOPO_4$  [this thesis], mixed occupancy of the W sites by V and W, asterisks indicate a small impurity of  $(WO_3)_8(PO_2)_4$  [95].

Immediately after ignition at 450 °C followed by heating at this temperature the XRPD shows the formation of a phase with structure related *cub*- $WO_3$  [252] (details are discussed in Chapter 9). Subsequent heating of the intermediate at 550 °C for one day, 600 °C for another day, 700 °C for five days and 750 °C for two days in air led to

formation grey powders of  $m-W_2O_3(PO_4)_2$  [78]. Reduction of the combustion product, however, by moist hydrogen at 550 °C for two days changed its color from grey to violet-blue without significant change of its XRPD. The violet-blue color already indicates the partial reduction of  $W^{6+} \rightarrow W^{5+}$  and  $V^{5+} \rightarrow V^{3+}$ . Heating of the partially reduced violet-blue powders at 800 °C in sealed silica tubes ( $l \approx 11$  cm and  $d \approx 1.5$  cm) for seven days led to the formation of the solid solution  $((V_{1-x}W_x)OPO_4; x = 0.80; W^V OPO_4$  structure type) with a small impurity of  $(WO_3)_8(PO_2)_4$  [95]. Nevertheless, the reduction temperature (550 °C) is not high enough for equilibrating the formation of the solid solution. Therefore, heating at relatively high temperature, 800 °C, in sealed tubes for seven days of the partially reduced blue products obtained at low temperature (550 °C) is required for the formation of the solid solution.

The formation of partially reduced states, W(V) and V(III) in the solid solution is evidenced by two separate reduction experiments with  $m-W^{VI}_2O_3(PO_4)_2$  and  $\beta-V^V OPO_4$  by moist hydrogen. Reduction of the former compound at 550° C leads only to a color change from white-grey to deep blue, without changing the crystal structure. The color change indicates partial reduction of W(VI) to W(V) (see Figure 14.2c). The deep blue color of substoichiometric  $WO_{2.96}$  is also accounted for the partially reduction of stoichiometric  $WO_3$  [198]. Subsequent heating of the partially reduced  $W^{VI}_2O_3(PO_4)_2$  at relatively high temperature, 800 °C, in sealed silica tube led to the formation of a two phase mixture. One is partially reduced phase,  $(P_2O_4)_4(W^{VI}O_3)_4(W^V O_3)_8$  [98] and the other is the fully oxidized phase  $m-W^{VI}_2O_3(PO_4)_2$  (Figure 14.3) at the ratio of (wt) 10 % and 90 %, respectively. This weight ratio allows an estimate for the initial amount of  $W^{5+}$  in the violet-blue “ $W^{VI}_2O_3(PO_4)_2$ ”. The estimated degree of reduction is about 4%. The possibility of thermal reduction of  $m-W_2O_3(PO_4)_2$  is excluded since it is stable up to 1000 °C for several days in air. Reduction of  $\beta-V OPO_4$  by moist hydrogen followed by heating in evacuated sealed tube at 700 °C for one day lead to the formation of single phase  $V^{III}PO_4$  [83] as shown in Section 11.2 (and also see Figure 14.4). Therefore, these two separate reduction reactions followed by heating in sealed ampoules at higher temperature suggest that the treatment of the reaction intermediate of the aiming solid solution by moist  $H_2$  at 550 °C allows the reduction of V(V) to V(III) and partial reduction of W(VI) to W(V). Further reduction by moist hydrogen of  $m-W^{VI}_2O_3(PO_4)_2$  and  $\beta-V^V OPO_4$  at 700 and 900° C, respectively leads to formation of WP [105] (Figure 14.2d) and  $\beta-V_2OPO_4$  [148] (Figure 14.4d), accordingly.

The solid solution  $(V^{III}_{1-x}W^V_{3x-2}W^{VI}_{2(1-x)})OPO_4$ ;  $0.67 \leq x \leq 1.0$  with  $WOPO_4$  structure type is obtained by substitution of pentavalent tungsten (62 pm) by trivalent vanadium (64 pm) and hexavalent tungsten (60 pm). The substitution leads to shrinking of average ionic radii of the metal ions which follow Vegard's rule as shown in Figure 6.25. (see Table 14.6). Assigning of the Guinier photographs of the members of solid solutions ( $WOPO_4$  structure type) are provided in Table 14.20 to Table 14.23.

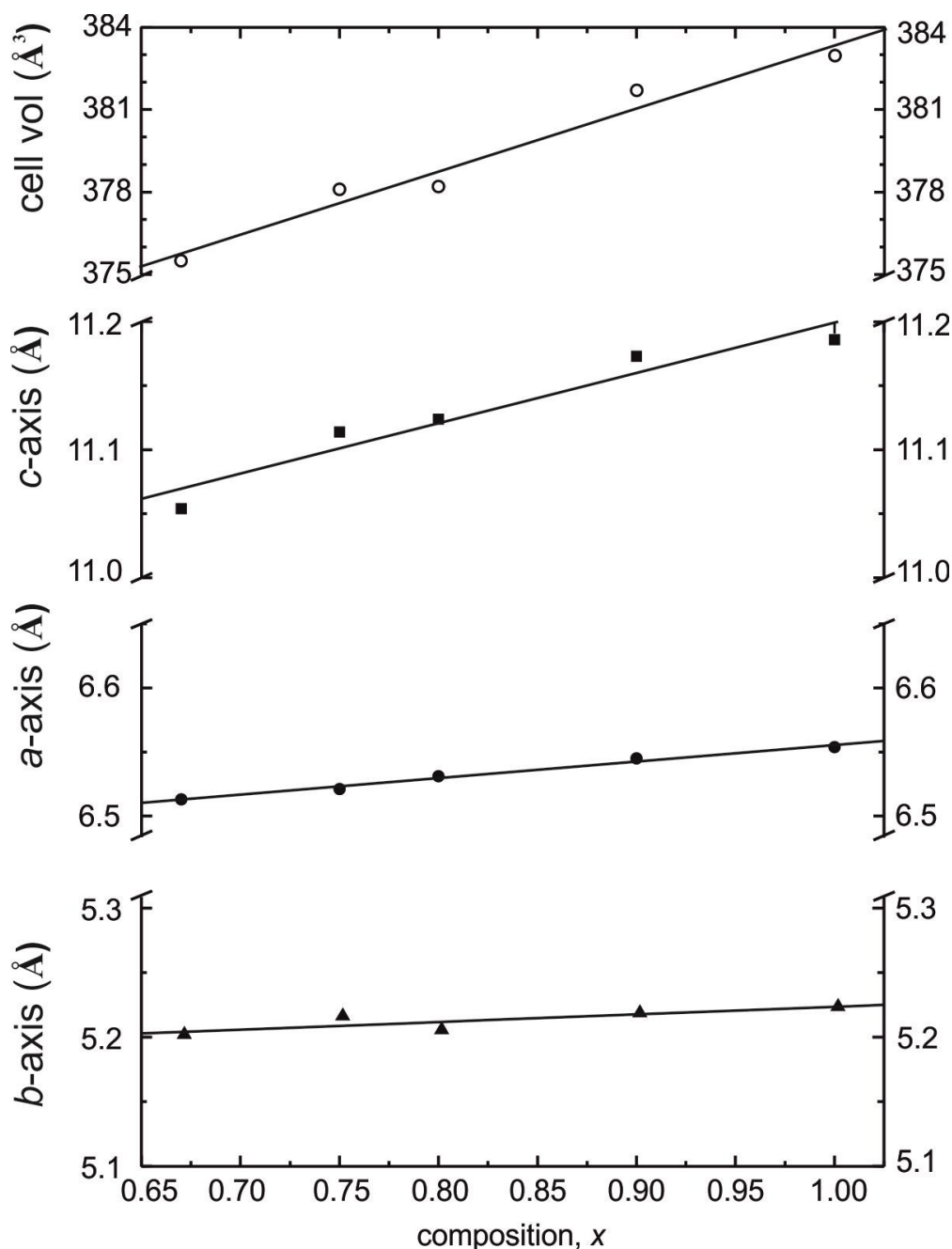


Figure 6.25 Variation of lattice parameters of members of  $WOPO_4$  structure type solid solution  $(V^{III}_{1-x}W^V_{3x-2}W^{VI}_{2(1-x)})OPO_4$  with  $0.67 \leq x \leq 1.0$ .



## 6.7 Conclusion

Reactions between  $V^V OPO_4$  and  $W^V OPO_4$  aiming at  $(V_{1-x}W_x)OPO_4$  lead to solid solutions  $(V^{IV}_x V^V_{1-2x} W^{VI}_x)OPO_4$ ;  $\beta$ - $VOPO_4$  structure type for  $0.0 \leq x \leq 0.01$  and  $\alpha_{II}$ - $VOPO_4$  structure type for  $0.04 \leq x \leq 0.26$  and  $WOPO_4$  structure type  $(V^{III}_{1-x} W^{V}_{3x-2} W^{VI}_{2(1-x)})OPO_4$  for  $0.67 \leq x \leq 1.0$ . These isomorphous substitutions in  $V^V OPO_4$  structure type suggest a quite unexpected crystal chemical similarity of  $V^{5+}$  to  $V^{4+}/W^{6+}$  combinations whereas in the solid solution ( $0.67 \leq x \leq 1.0$ ) with  $W^V OPO_4$  structure type the observed chemical similarity is  $W^{5+}$  to  $V^{3+}/W^{6+}$ . Assumptions in earlier publications [161] on a stabilization of the  $\alpha_{II}$ - $VOPO_4$  structure type with respect to the  $\beta$ - form by incorporation of larger cations are confirmed by these results.

As the metal-oxygen distances show, substitution of vanadium by tungsten in the  $\alpha_{II}$ - $VOPO_4$  structure type will modify the inter-layer interactions and, correspondingly, the Lewis acid-base and intercalation behavior of  $\alpha_{II}$ - $VOPO_4$ . The given charge distribution complies with the results of EPR, XPS, and magnetic measurements. One of the most notable properties of the solid solutions  $(V^{IV}_x V^V_{1-2x} W^{VI}_x)OPO_4$  ( $0.01 \leq x \leq 0.26$ ) is setting of the mean oxidation states of vanadium from 4.65 to 4.99 which is one of the criteria to be a good catalyst material for butane based MA production [22]. In contrast to pure, stoichiometric  $VOPO_4$  the solid solutions show a strong IVCT( $V^{4+} \rightarrow V^{5+}$ ) transition centered around  $13500 \text{ cm}^{-1}$ , which, together with a LMCT( $O^{2-} \rightarrow V^{5+}$ ) at about  $25000 \text{ cm}^{-1}$ , explains their olive to dark-green color. According to these properties the solid solutions have to be regarded as class II mixed-valent compounds within the classification scheme of *Robin and Day*. Accordingly, semiconducting behavior with rather low band gap is observed. All these properties suggest that phosphates  $(V_{1-x}W_x)OPO_4$  ( $0.04 \leq x \leq 0.26$ ) should show catalytic activity and selectivity in the oxidation of *n*-butane to MA. This expectation was eventually confirmed (see Chapter 12).

## 7 Solid solutions $(V_{1-x}Mo_x)OPO_4$

### 7.1 Introduction

The unexpected formation of various solid solutions  $(V_{1-x}W_x)OPO_4$  raised the question about the redox and structural chemistry in the quasi-binary system  $MoOPO_4$ - $VOPO_4$ . The isotopic crystal structures among the several polymorphs of  $MoOPO_4$  and  $VOPO_4$  (e.g.  $\beta_I$ - $MoOPO_4$  [88] and  $\beta$ - $VOPO_4$  [161];  $\beta$ - $MoOPO_4$  [202] and  $\varepsilon$ - $VOPO_4$  [164];  $\alpha$ - $MoOPO_4$  [203] and  $\alpha_{II}$ - $VOPO_4$  [160]) as well as the diagonal relationship V/Mo suggested mutual solubility. Differences in the redox behavior of  $Mo^{5+}$  and  $W^{5+}$  (see Figure 7.1b) made these investigations even more interesting with respect to possible new catalyst materials for selective oxidation of short-chain hydrocarbons.

In this chapter, the solid solution formation between  $V^V OPO_4$  and  $Mo^V OPO_4$  is investigated. For characterization XRPD, EPR spectra, UV/Vis/NIR spectra,  $^{31}P$ -MAS-NMR spectra, magnetic behaviour and electronic conductivity have been measured.

### 7.2 Equilibrium phases in systems $MoO_x/VO_y/PO_{2.5}$

$$(2.0 \leq x \leq 3.0; 1.5 \leq y \leq 2.5)$$

The quaternary system Mo/V/P/O can be represented by a Gibbs phase tetrahedron as shown in Figure 7.1a where the quasi-ternary section  $MoO_3/VO_{2.5}/PO_{2.5}$  is the fully oxidized plane (the oxygen co-existence pressures for the binary systems are shown in Figure 7.1b, [136]).

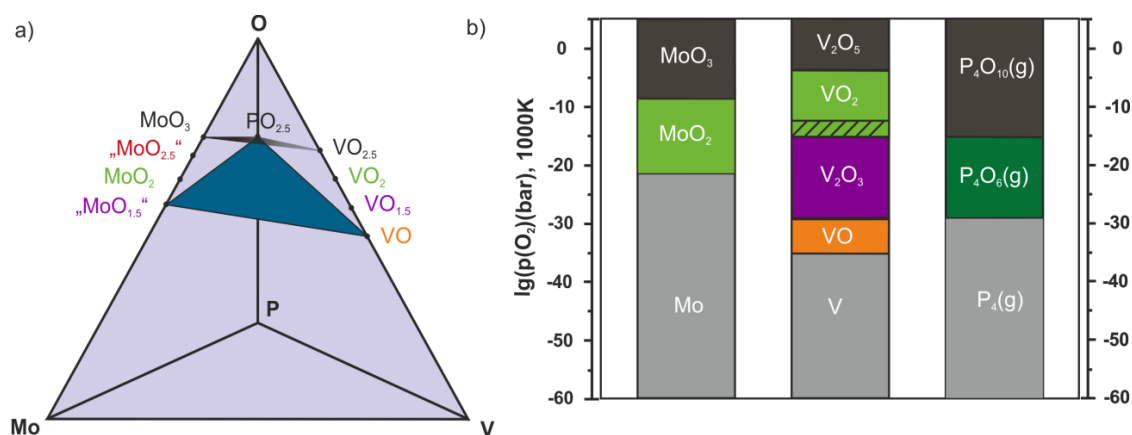


Figure 7.1 The quaternary system Mo/V/P/O with quasi-ternary oxide systems (a) and the oxygen co-existence pressure diagram of Mo, V, and P oxides (b) [136].

The other quasi-ternary section “ $MoO_{1.5}$ ”/ $VO/PO_{2.5}$  is the lowest oxidized plane, which is still containing phosphates  $\beta$ - $V_2OPO_4$  [148] and  $Mo(PO_3)_3$  [199] as equilibrium phases. These two planes and all other possible quasi ternary sections between these two planes are represented as phase triangle by the projection at the intersection of the phase tetrahedron as shown in Figure 7.2.

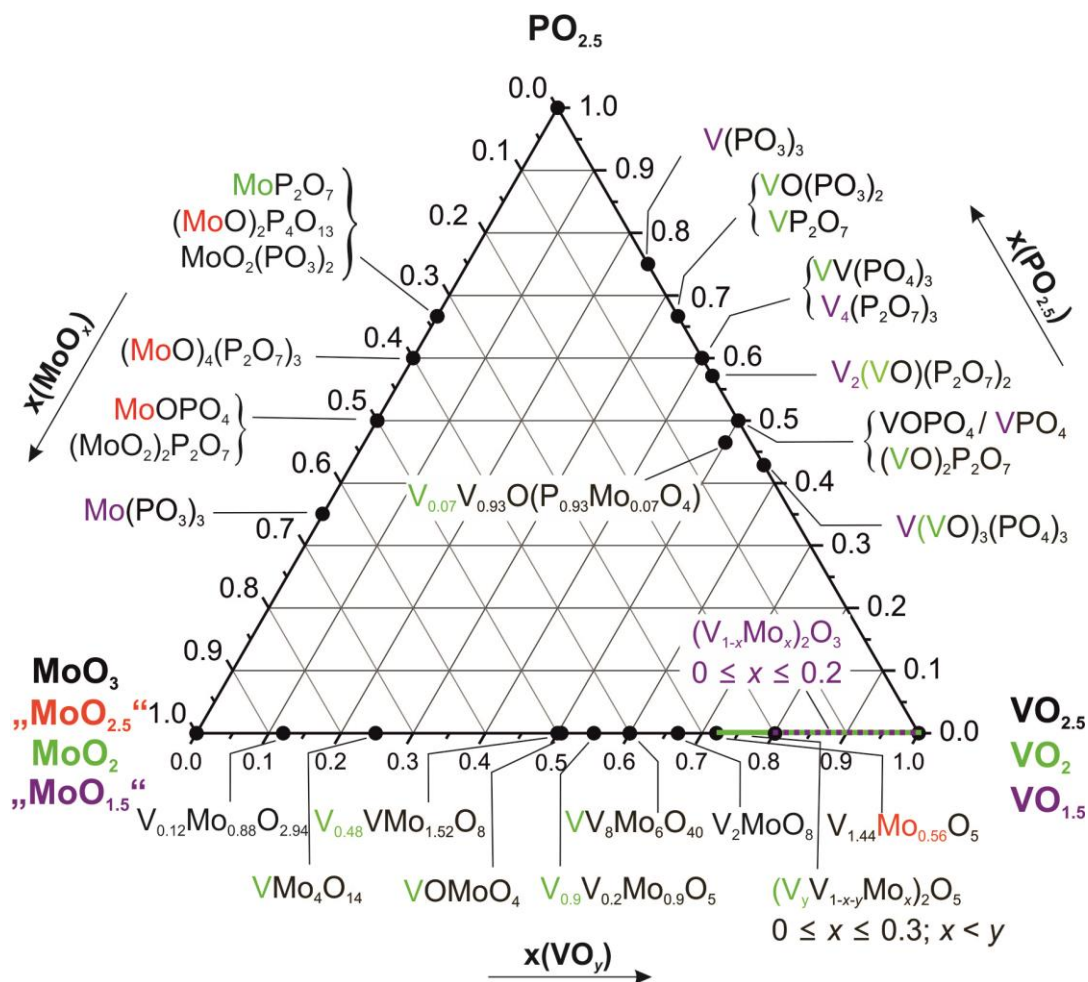


Figure 7.2 Visualization of compounds in systems  $MoO_x/VO_y/PO_{2.5}$ , ( $2.0 \leq x \leq 3.0$ ;  $1.5 \leq y \leq 2.5$ ), the reduced phases with Mo(V), M(IV) and M(III); (M: Mo, V) are indicated by red, green and violet color, respectively.

The quaternary system Mo/V/P/O is also part of the present investigation. The redox properties of the quasi-binary oxide systems,  $MoO_x-VO_y$ ,  $VO_y-PO_{2.5}$ ,  $PO_{2.5}-MoO_x$  ( $2.0 \leq x \leq 3.0$ ;  $1.5 \leq y \leq 2.5$ ) will be helpful to explore the quaternary system. Therefore compounds known in these quasi-binary oxides are shown in Figure 7.2 and given in Table 7.1. In the quaternary system Mo/V/P/O only one compound  $(V^{IV}O)_{0.07}(V^{VO})_{0.93}(P^{VO}O_4)_{0.93}(M^{VI}O_4)_{0.07}$  [138] is known in literature which is located on the quasi-binary line between  $V^{VO}OP^{VO}O_4$  and  $V^{IV}OMo^{VI}O_4$  (see Figure 7.2).

Table 7.1 Crystallographic information on molybdenum phosphates MoO<sub>x</sub>-PO<sub>2.5</sub> and molybdenum vanadium oxides MoO<sub>x</sub>-VO<sub>y</sub> (2.0 ≤ x ≤ 3.0; 1.5 ≤ y ≤ 2.5), a summary on vanadium phosphates was given in Table 6.1, S.G.: space group, Z: formula units per unit cell.

Phase	S.G., Z	Unit cell parameters (Å, °)	Ref.
Mo(PO <sub>3</sub> ) <sub>3</sub>	<i>Ia</i> , 12	10.819(1), 19.515(3), 9.609(1), 97.74(1)	[199]
MoOP <sub>2</sub> O <sub>7</sub>	<i>Pbcm</i> , 2	7.683(5), 7.436(5), 4.889(3)	[200]
α-(MoO) <sub>2</sub> P <sub>2</sub> O <sub>7</sub>	<i>P2/c</i> , 16	17.8161(1), 10.3675(5), 17.8089(1), 90.2009(2)	[80, 88]
γ-(MoO) <sub>2</sub> P <sub>2</sub> O <sub>7</sub>	<i>Pnma</i> , 4	12.58(1), 6.338(5), 10.38(1)	[80, 201]
δ-(MoO) <sub>2</sub> P <sub>2</sub> O <sub>7</sub>	<i>C222</i> <sub>1</sub> , 2	16.221(1), 3.8936(3), 6.2772(4)	[202]
α-MoOPO <sub>4</sub>	<i>P4/n</i> , 2	6.1768(3), 4.2932(3)	[203]
β-MoOPO <sub>4</sub>	<i>Cc</i> , 4	7.4043(3), 7.2128(3), 7.2876(3), 118.346(2)	[202]
β <sub>1</sub> -MoOPO <sub>4</sub>	<i>Pnma</i> , 2	7.704(2), 6.301(2), 7.080(2)	[88]
(MoO) <sub>4</sub> (P <sub>2</sub> O <sub>7</sub> ) <sub>3</sub>	<i>P2</i> <sub>1</sub> <i>2</i> <sub>1</sub> <i>2</i> <sub>1</sub> , 36	23.514(1), 23.514(1), 31.912(5)	[204, 88]
MoO <sub>2</sub> (PO <sub>3</sub> ) <sub>2</sub>	<i>Pbcm</i> , 2	7.683(5), 7.426(5), 4.889(3)	[200]
(MoO) <sub>2</sub> P <sub>4</sub> O <sub>13</sub>	<i>P2</i> <sub>1</sub> <i>/c</i> , 2	8.3068(8), 6.5262(6), 10.718(1), 106.705(8)	[205]
(MoO) <sub>2</sub> P <sub>4</sub> O <sub>13</sub>	<i>Pn</i> , 42	24.133(2), 19.579(1), 25.109(2), 99.962(3)	[206]
MoP <sub>2</sub> O <sub>7</sub>	<i>Pa</i> $\bar{3}$ , 4	7.944(1)	[207]
V <sup>V</sup> <sub>0.12</sub> Mo <sup>VI</sup> <sub>0.88</sub> O <sub>2.94</sub>	<i>P6</i> <sub>3</sub> , 6	10.593(1), 3.6944(4)	[208]
(V <sub>0.07</sub> Mo <sub>0.93</sub> ) <sub>5</sub> O <sub>14</sub>	<i>tetragonal</i>	22.83900, 3.99000	[209]
V <sup>IV</sup> <sub>0.48</sub> V <sup>V</sup> Mo <sup>VI</sup> <sub>1.52</sub> O <sub>8</sub>	<i>P2</i> <sub>1</sub> <i>/a</i> , 4	19.433(2), 7.2646(6), 4.1198(4), 90.65	[210]
V <sup>IV</sup> OMo <sup>VI</sup> O <sub>4</sub>	<i>P4/n</i> , 2	6.6078(2), 4.2646(3)	[211]
V <sup>IV</sup> <sub>0.9</sub> V <sup>V</sup> <sub>0.2</sub> Mo <sup>VI</sup> <sub>0.9</sub> O <sub>5</sub>	<i>C2/m</i> , 2	12.1230(3), 3.7168(1), 4.0336(1), 90.625	[212]
V <sup>IV</sup> V <sup>V</sup> <sub>8</sub> Mo <sup>VI</sup> <sub>6</sub> O <sub>40</sub>	<i>C2</i> , 1	19.365(3), 3.626(1), 4.124(1), 90.61	[213]
V <sup>V</sup> <sub>2</sub> Mo <sup>VI</sup> O <sub>8</sub>	<i>C2</i> , 2	19.398(9), 3.629(1), 4.117(1), 90.34	[214]
V <sup>V</sup> <sub>2</sub> Mo <sup>VI</sup> O <sub>8</sub> (Ht)	<i>Cmm2</i> , 2	19.4, 3.62, 4.13	[215]
V <sup>V</sup> <sub>1.44</sub> Mo <sup>V</sup> <sub>0.56</sub> O <sub>5</sub>	<i>C2</i> , 2	11.809(2), 3.652(1), 4.174(1), 90.56	[216]
(V <sup>IV</sup> <sub>y</sub> V <sup>V</sup> <sub>1-x-y</sub> Mo <sup>VI</sup> <sub>x</sub> ) <sub>2</sub> O <sub>5</sub>	<i>Pmnm</i> , 2	11.563(2), 3.5765(7), 4.333(1)	[217,
(0 ≤ x ≤ 3.0; x < y)		for x = 0.10	218]
(V <sup>III</sup> <sub>1-x</sub> Mo <sup>III</sup> <sub>x</sub> ) <sub>2</sub> O <sub>3</sub>	<i>R</i> $\bar{3}$ c, 6	4.9290(2), 4.9290(2), 14.1888(5)	[219]
(0 ≤ x ≤ 0.2)		for x = 0.10	

### 7.3 Synthesis and crystallization

Single-phase powders of solid solutions (V<sub>1-x</sub>Mo<sub>x</sub>)OPO<sub>4</sub> with two different structure types (0 ≤ x ≤ 0.30, thermodynamically stable β-VOPO<sub>4</sub> structure type [161]; 0 ≤ x ≤ 0.20, thermodynamically metastable γ-VOPO<sub>4</sub> structure type [162]) have been synthesized (see Figure 7.3 and Figure 7.4) via *solution combustion synthesis* followed by heating of the combustion products in air at higher temperature (see Table 7.2).

In SCS the precursor materials (NH<sub>4</sub>)<sub>6</sub>Mo<sub>7</sub>O<sub>24</sub>·4H<sub>2</sub>O, NH<sub>4</sub>VO<sub>3</sub>, and (NH<sub>4</sub>)<sub>2</sub>HPO<sub>4</sub> were used as source of MoO<sub>3</sub>, V<sub>2</sub>O<sub>5</sub>, and P<sub>4</sub>O<sub>10</sub>, respectively. Glycine (CH<sub>2</sub>NH<sub>2</sub>COOH) is used as fuel/chelator due to satisfactory performances for the synthesis of the solid solution (V<sub>1-x</sub>W<sub>x</sub>)OPO<sub>4</sub> (0 ≤ x ≤ 0.26). Moreover, glycine is also used for Cr<sub>2</sub>O<sub>3</sub> and related oxides of the elements of group VIB [44]. Nitric acid was used as oxidizer. The precursor materials with appropriate molar ratios (see Table 7.2) were dissolved in a minimum amount of water together with HNO<sub>3</sub> (oxidizer). The fuel is added to the clear solution with continuous stirring. The ratio of  $n(\text{metal}):n(\text{glycine}):n(\text{HNO}_3) = 1:1.5:8$  was kept. Eventually, the solution was dried to a gel on a hot plate at  $\vartheta \approx 100$  °C. The dry mass was ignited in a preheated (400 °C) muffle furnace and subsequently heated there for ten minutes. After that the reaction intermediate was allowed to cool slowly to room temperature.

Typically, after combustion all reaction mixtures go through various thermodynamically metastable polymorphs ( $\alpha_{\text{I}}$ -VOPO<sub>4</sub> [159],  $\alpha_{\text{II}}$ -VOPO<sub>4</sub> [160],  $\gamma$ -VOPO<sub>4</sub> [162],  $\varepsilon$ -VOPO<sub>4</sub> [164],  $\omega$ -VOPO<sub>4</sub> type [165, 166]) upon annealing at relatively low temperature (see Table 7.2). Eventually, the  $\gamma$ -VOPO<sub>4</sub> structure type solid solution (V<sub>1-x</sub>Mo<sub>x</sub>)OPO<sub>4</sub> (x = 0.02, 0.10, and 0.20) was obtained reproducibly as a single phase material (see Figure 7.4). Although this metastable  $\gamma$ -VOPO<sub>4</sub> polymorph was also observed with higher molybdenum content composition (up to x = 0.40), it was not single phase. It is worth to be noted that the  $\gamma$ -VOPO<sub>4</sub> type polymorph was not observed during the formation of tungsten substituted VOPO<sub>4</sub>. Metastable polymorphs of  $\omega$ - and  $\gamma$ -VOPO<sub>4</sub> structure type convert into phases with VOPO<sub>4</sub>·2H<sub>2</sub>O [173] structure type after keeping on lab bench (see Figure 7.5 and Figure 7.6, respectively).

Subsequent heating of these reaction intermediates in air with quenching and grinding in intermediate steps leads to the formation of powders of the thermodynamically stable solid solution (V<sub>1-x</sub>Mo<sub>x</sub>)OPO<sub>4</sub> (0 ≤ x ≤ 0.3) with  $\beta$ -VOPO<sub>4</sub> structure type (Figure 7.3). The reaction intermediates and the final thermodynamically stable products are monitored by XRPD (see Table 7.2).

Table 7.2 Experiments aiming at the synthesis of solid solutions (V<sub>1-x</sub>Mo<sub>x</sub>)OPO<sub>4</sub> (0 ≤ x ≤ 1.0) via SCS followed by heating in air, heating protocol  $\vartheta$  (°C) and  $t$  (h).

$x$	Starting Materials	Amount (mg)	$\vartheta$ (°C)	$t$ (h)	Reaction Products (according to IP Guinier photograph)
0.0	NH <sub>4</sub> VO <sub>3</sub>	1169.92	500	0.1	$\alpha_1$ -VOPO <sub>4</sub> , VOPO <sub>4</sub> ·2H <sub>2</sub> O <sup>a)</sup>
	(NH <sub>4</sub> ) <sub>2</sub> HPO <sub>4</sub>	1320.85	600	24	$\alpha_1$ -VOPO <sub>4</sub> , VOPO <sub>4</sub> ·2H <sub>2</sub> O <sup>a)</sup>
	(NH <sub>4</sub> ) <sub>6</sub> Mo <sub>7</sub> O <sub>24</sub> ·4H <sub>2</sub> O	---	725	72	$\beta$ -VOPO <sub>4</sub>
0.005	NH <sub>4</sub> VO <sub>3</sub>	3259.12	400	0.1	$\alpha_1$ -(V <sub>0.995</sub> Mo <sub>0.005</sub> )OPO <sub>4</sub>
	(NH <sub>4</sub> ) <sub>2</sub> HPO <sub>4</sub>	3698.08	500	24	$\alpha_1$ -(V <sub>0.995</sub> Mo <sub>0.005</sub> )OPO <sub>4</sub> , (V <sub>0.995</sub> Mo <sub>0.005</sub> )OPO <sub>4</sub> ·2H <sub>2</sub> O <sup>a)</sup>
	(NH <sub>4</sub> ) <sub>6</sub> Mo <sub>7</sub> O <sub>24</sub> ·4H <sub>2</sub> O	24.80	600	24	$\alpha_1$ -(V <sub>0.995</sub> Mo <sub>0.005</sub> )OPO <sub>4</sub> , (V <sub>0.995</sub> Mo <sub>0.005</sub> )OPO <sub>4</sub> ·2H <sub>2</sub> O <sup>a)</sup>
			600	120	$\alpha_1$ + $\gamma$ -(V <sub>0.995</sub> Mo <sub>0.005</sub> )OPO <sub>4</sub> , (V <sub>0.995</sub> Mo <sub>0.005</sub> )OPO <sub>4</sub> ·2H <sub>2</sub> O <sup>a)</sup>
			700	48	$\beta$ -(V <sub>0.995</sub> Mo <sub>0.005</sub> )OPO <sub>4</sub>
0.01	NH <sub>4</sub> VO <sub>3</sub>	3242.68	400	0.1	$\alpha_1$ -(V <sub>0.99</sub> Mo <sub>0.01</sub> )OPO <sub>4</sub> , (V <sub>0.99</sub> Mo <sub>0.01</sub> )OPO <sub>4</sub> ·2H <sub>2</sub> O <sup>a)</sup>
	(NH <sub>4</sub> ) <sub>2</sub> HPO <sub>4</sub>	3698.00	500	24	$\alpha_1$ -(V <sub>0.99</sub> Mo <sub>0.01</sub> )OPO <sub>4</sub> , (V <sub>0.99</sub> Mo <sub>0.01</sub> )OPO <sub>4</sub> ·2H <sub>2</sub> O <sup>a)</sup>
	(NH <sub>4</sub> ) <sub>6</sub> Mo <sub>7</sub> O <sub>24</sub> ·4H <sub>2</sub> O	49.54	600	24	$\alpha_1$ -(V <sub>0.99</sub> Mo <sub>0.01</sub> )OPO <sub>4</sub> , (V <sub>0.99</sub> Mo <sub>0.01</sub> )OPO <sub>4</sub> ·2H <sub>2</sub> O <sup>a)</sup>
			700	48	$\beta$ -(V <sub>0.99</sub> Mo <sub>0.01</sub> )OPO <sub>4</sub>
0.02	NH <sub>4</sub> VO <sub>3</sub>	1146.45	400	0.1	amorphous
	(NH <sub>4</sub> ) <sub>2</sub> HPO <sub>4</sub>	1320.56	500	24	$\delta$ -(V <sub>0.98</sub> Mo <sub>0.02</sub> )OPO <sub>4</sub>
	(NH <sub>4</sub> ) <sub>6</sub> Mo <sub>7</sub> O <sub>24</sub> ·4H <sub>2</sub> O	35.33	600	24	$\gamma$ -(V <sub>0.98</sub> Mo <sub>0.02</sub> )OPO <sub>4</sub>
			650	144	$\beta$ -(V <sub>0.98</sub> Mo <sub>0.02</sub> )OPO <sub>4</sub>
0.05	NH <sub>4</sub> VO <sub>3</sub>	4445.27	400	0.1	amorphous
	(NH <sub>4</sub> ) <sub>2</sub> HPO <sub>4</sub>	5282.90	500	24	$\varepsilon$ -(V <sub>0.95</sub> Mo <sub>0.05</sub> )OPO <sub>4</sub> , (V <sub>0.95</sub> Mo <sub>0.05</sub> )OPO <sub>4</sub> ·2H <sub>2</sub> O <sup>a)</sup>
	(NH <sub>4</sub> ) <sub>6</sub> Mo <sub>7</sub> O <sub>24</sub> ·4H <sub>2</sub> O	353.30	650	168	$\beta$ -(V <sub>0.95</sub> Mo <sub>0.05</sub> )OPO <sub>4</sub>
0.07	NH <sub>4</sub> VO <sub>3</sub>	2175.88	400	0.1	amorphous
	(NH <sub>4</sub> ) <sub>2</sub> HPO <sub>4</sub>	2641.82	600	24	$\gamma$ -(V <sub>0.93</sub> Mo <sub>0.07</sub> )OPO <sub>4</sub> , (V <sub>0.93</sub> Mo <sub>0.07</sub> )OPO <sub>4</sub> ·2H <sub>2</sub> O <sup>a)</sup>
	(NH <sub>4</sub> ) <sub>6</sub> Mo <sub>7</sub> O <sub>24</sub> ·4H <sub>2</sub> O	247.30	650	300	$\beta$ -(V <sub>0.93</sub> Mo <sub>0.07</sub> )OPO <sub>4</sub>
0.08	NH <sub>4</sub> VO <sub>3</sub>	2152.42	400	0.1	amorphous
	(NH <sub>4</sub> ) <sub>2</sub> HPO <sub>4</sub>	2641.62	600	24	$\gamma$ -(V <sub>0.92</sub> Mo <sub>0.08</sub> )OPO <sub>4</sub> , (V <sub>0.92</sub> Mo <sub>0.08</sub> )OPO <sub>4</sub> ·2H <sub>2</sub> O <sup>a)</sup>
	(NH <sub>4</sub> ) <sub>6</sub> Mo <sub>7</sub> O <sub>24</sub> ·4H <sub>2</sub> O	282.53	650	300	$\beta$ -(V <sub>0.92</sub> Mo <sub>0.08</sub> )OPO <sub>4</sub>
0.10	NH <sub>4</sub> VO <sub>3</sub>	1473.95	400	0.1	amorphous
	(NH <sub>4</sub> ) <sub>2</sub> HPO <sub>4</sub>	1848.78	500	24	$\gamma$ -(V <sub>0.90</sub> Mo <sub>0.10</sub> )OPO <sub>4</sub>
	(NH <sub>4</sub> ) <sub>6</sub> Mo <sub>7</sub> O <sub>24</sub> ·4H <sub>2</sub> O	247.27	600	48	$\gamma$ -(V <sub>0.90</sub> Mo <sub>0.10</sub> )OPO <sub>4</sub>
			650	300	$\beta$ -(V <sub>0.90</sub> Mo <sub>0.10</sub> )OPO <sub>4</sub>
0.20	NH <sub>4</sub> VO <sub>3</sub>	2620.38	400	0.1	amorphous
	(NH <sub>4</sub> ) <sub>2</sub> HPO <sub>4</sub>	3697.75	500	24	$\omega$ -(V <sub>0.80</sub> Mo <sub>0.20</sub> )OPO <sub>4</sub> <sup>b)</sup>
	(NH <sub>4</sub> ) <sub>6</sub> Mo <sub>7</sub> O <sub>24</sub> ·4H <sub>2</sub> O	988.80	550	24	$\gamma$ -(V <sub>0.80</sub> Mo <sub>0.20</sub> )OPO <sub>4</sub>
	O		600	24	$\varepsilon$ -(V <sub>0.80</sub> Mo <sub>0.20</sub> )OPO <sub>4</sub>
			650	144	$\beta$ -(V <sub>0.80</sub> Mo <sub>0.20</sub> )OPO <sub>4</sub>
0.25	NH <sub>4</sub> VO <sub>3</sub>	1228.38	400	0.1	amorphous
	(NH <sub>4</sub> ) <sub>2</sub> HPO <sub>4</sub>	1849.09	500	24	$\alpha_{II}$ -, $\varepsilon$ -(V <sub>0.75</sub> Mo <sub>0.25</sub> )OPO <sub>4</sub>
	(NH <sub>4</sub> ) <sub>6</sub> Mo <sub>7</sub> O <sub>24</sub> ·4H <sub>2</sub> O	617.93	600	96	$\alpha_{II}$ -, $\varepsilon$ -, $\gamma$ -(V <sub>0.75</sub> Mo <sub>0.25</sub> )OPO <sub>4</sub>
			600	500	$\beta$ -(V <sub>0.75</sub> Mo <sub>0.25</sub> )OPO <sub>4</sub>
			650	24	$\beta$ -(V <sub>1-x</sub> Mo <sub>x</sub> )OPO <sub>4</sub> <sup>d)</sup>
0.30	NH <sub>4</sub> VO <sub>3</sub>	343.95	400	0.1	amorphous
	(NH <sub>4</sub> ) <sub>2</sub> HPO <sub>4</sub>	554.62	500	24	$\alpha_{II}$ -, $\omega$ -(V <sub>0.70</sub> Mo <sub>0.30</sub> )OPO <sub>4</sub> <sup>b)</sup>
	(NH <sub>4</sub> ) <sub>6</sub> Mo <sub>7</sub> O <sub>24</sub> ·4H <sub>2</sub> O	222.55	600	96	$\alpha_{II}$ -, $\gamma$ -, $\beta$ -(V <sub>0.70</sub> Mo <sub>0.30</sub> )OPO <sub>4</sub>
			600	500	$\beta$ -(V <sub>0.70</sub> Mo <sub>0.30</sub> )OPO <sub>4</sub>
			650	96	$\beta$ -(V <sub>1-x</sub> Mo <sub>x</sub> )OPO <sub>4</sub> <sup>d)</sup>
0.35	NH <sub>4</sub> VO <sub>3</sub>	760.34	400	0.1	amorphous
	(NH <sub>4</sub> ) <sub>2</sub> HPO <sub>4</sub>	1320.76	500	24	$\omega$ -(V <sub>0.65</sub> Mo <sub>0.35</sub> )OPO <sub>4</sub> <sup>b)</sup>
	(NH <sub>4</sub> ) <sub>6</sub> Mo <sub>7</sub> O <sub>24</sub> ·4H <sub>2</sub> O	617.93	600	24	$\gamma$ - + $\varepsilon$ -(V <sub>1-x</sub> Mo <sub>x</sub> )OPO <sub>4</sub>
			600	200	$\gamma$ - + $\beta$ -(V <sub>1-x</sub> Mo <sub>x</sub> )OPO <sub>4</sub>
			650	96	$\beta$ -(V <sub>0.70</sub> Mo <sub>0.30</sub> )OPO <sub>4</sub> <sup>d)</sup>

0.40	NH <sub>4</sub> VO <sub>3</sub>	491.33	400	0.1	amorphous
	(NH <sub>4</sub> ) <sub>2</sub> HPO <sub>4</sub>	924.63	500	24	$\omega$ - <sup>b)</sup> + $\gamma$ -(V <sub>1-x</sub> Mo <sub>x</sub> )OPO <sub>4</sub>
	(NH <sub>4</sub> ) <sub>6</sub> Mo <sub>7</sub> O <sub>24</sub> ·4H <sub>2</sub> O	494.35	600	96	$\gamma$ - + $\varepsilon$ -(V <sub>1-x</sub> Mo <sub>x</sub> )OPO <sub>4</sub>
			650	96	$\beta$ -(V <sub>1-x</sub> Mo <sub>x</sub> )OPO <sub>4</sub> <sup>d)</sup>
0.67	NH <sub>4</sub> VO <sub>3</sub>	360.38	400	0.1	Keggin <sup>c)</sup>
	(NH <sub>4</sub> ) <sub>2</sub> HPO <sub>4</sub>	1232.80	400	12	amorphous
	(NH <sub>4</sub> ) <sub>6</sub> Mo <sub>7</sub> O <sub>24</sub> ·4H <sub>2</sub> O	1104.70	500	24	amorphous <sup>d)</sup>
0.75	NH <sub>4</sub> VO <sub>3</sub>	273.03	400	0.1	Keggin <sup>c)</sup>
	(NH <sub>4</sub> ) <sub>2</sub> HPO <sub>4</sub>	1232.85	400	12	amorphous
	(NH <sub>4</sub> ) <sub>6</sub> Mo <sub>7</sub> O <sub>24</sub> ·4H <sub>2</sub> O	1235.85	475	144	amorphous
			500	24	amorphous <sup>d)</sup>
0.85	NH <sub>4</sub> VO <sub>3</sub>	245.70	400	0.1	Keggin <sup>c)</sup>
	(NH <sub>4</sub> ) <sub>2</sub> HPO <sub>4</sub>	1849.23	400	24	amorphous
	(NH <sub>4</sub> ) <sub>6</sub> Mo <sub>7</sub> O <sub>24</sub> ·4H <sub>2</sub> O	2101.07	450	96	amorphous
	O		475	168	amorphous <sup>d)</sup>
0.90	NH <sub>4</sub> VO <sub>3</sub>	163.83	400	0.1	Keggin <sup>c)</sup>
	(NH <sub>4</sub> ) <sub>2</sub> HPO <sub>4</sub>	1849.90	400	24	amorphous
	(NH <sub>4</sub> ) <sub>6</sub> Mo <sub>7</sub> O <sub>24</sub> ·4H <sub>2</sub> O	2224.70	450	96	amorphous
			475	168	amorphous <sup>d)</sup>
0.95	NH <sub>4</sub> VO <sub>3</sub>	54.60	400	0.1	Keggin <sup>c)</sup>
	(NH <sub>4</sub> ) <sub>2</sub> HPO <sub>4</sub>	1233.0	400	96	MoO <sub>3</sub>
	(NH <sub>4</sub> ) <sub>6</sub> Mo <sub>7</sub> O <sub>24</sub> ·4H <sub>2</sub> O	1565.40	475	144	$\alpha$ -(MoO <sub>2</sub> ) <sub>2</sub> P <sub>2</sub> O <sub>7</sub>
1.0	(NH <sub>4</sub> ) <sub>2</sub> HPO <sub>4</sub>	1843.40	400	0.1	amorphous
	(NH <sub>4</sub> ) <sub>6</sub> Mo <sub>7</sub> O <sub>24</sub> ·4H <sub>2</sub> O	2465.50	500	24	amorphous
			600	24	$\alpha$ -(MoO <sub>2</sub> ) <sub>2</sub> P <sub>2</sub> O <sub>7</sub>

<sup>a)</sup> hydration of  $\alpha_1$ - and/or  $\gamma$ -VOPO<sub>4</sub> type, <sup>b)</sup> high temperature polymorph [166], <sup>c)</sup> (NH<sub>4</sub>)<sub>3</sub>[PW<sub>12</sub>O<sub>40</sub>]·xH<sub>2</sub>O [171] type,

<sup>d)</sup> solidified melt.

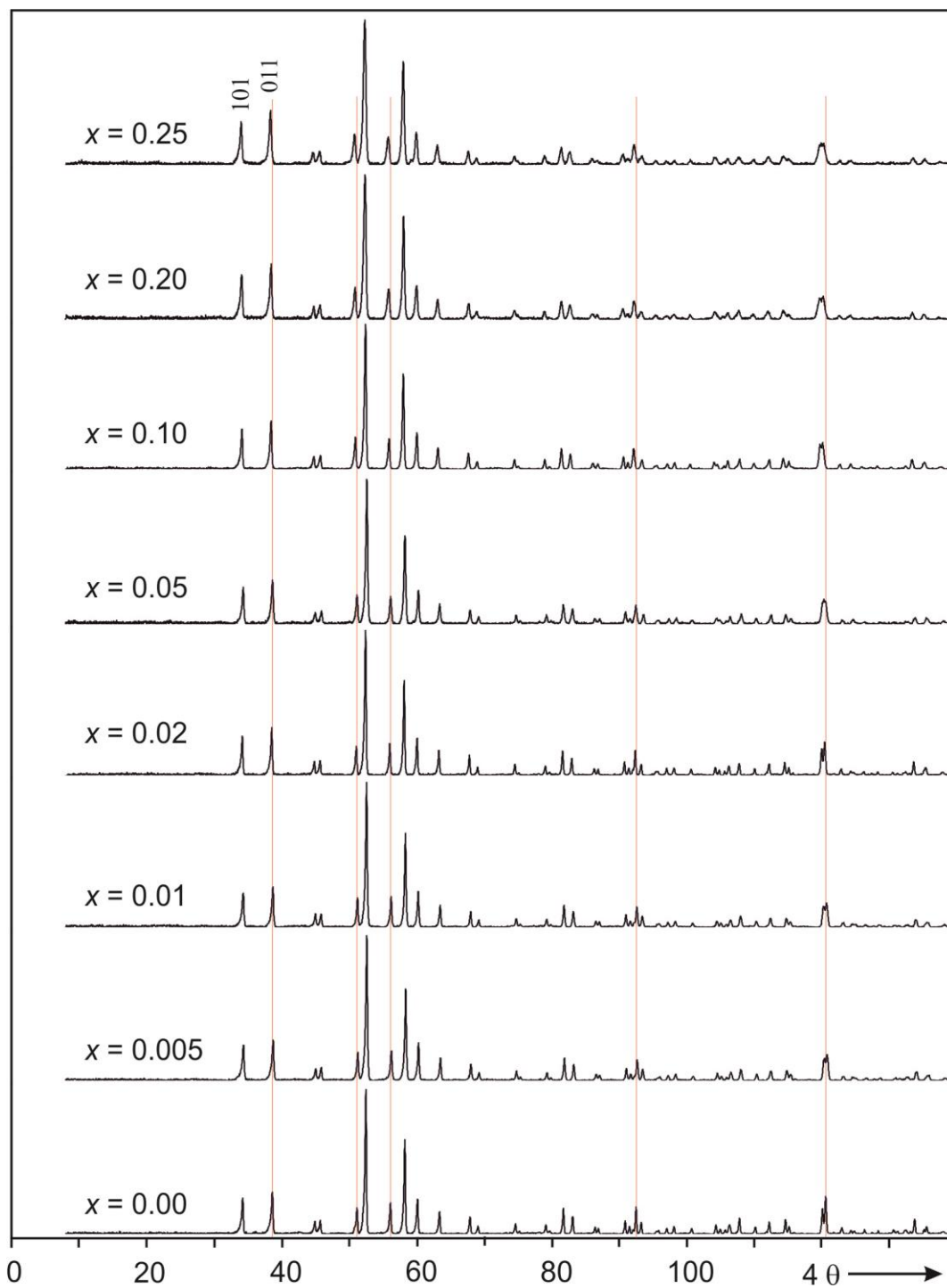


Figure 7.3 Comparison of Guinier photographs of members of the solid solution  $(V_{1-x}Mo_x)OPO_4$ ;  $0.0 \leq x \leq 0.30$  ( $\beta$ - $VOPO_4$  structure type [161]) obtained via SCS followed by heating in air ( $\vartheta = 725^\circ\text{C}$  for  $x = 0.0$ , decreasing to  $\vartheta = 600^\circ\text{C}$  for  $x = 0.30$ ).



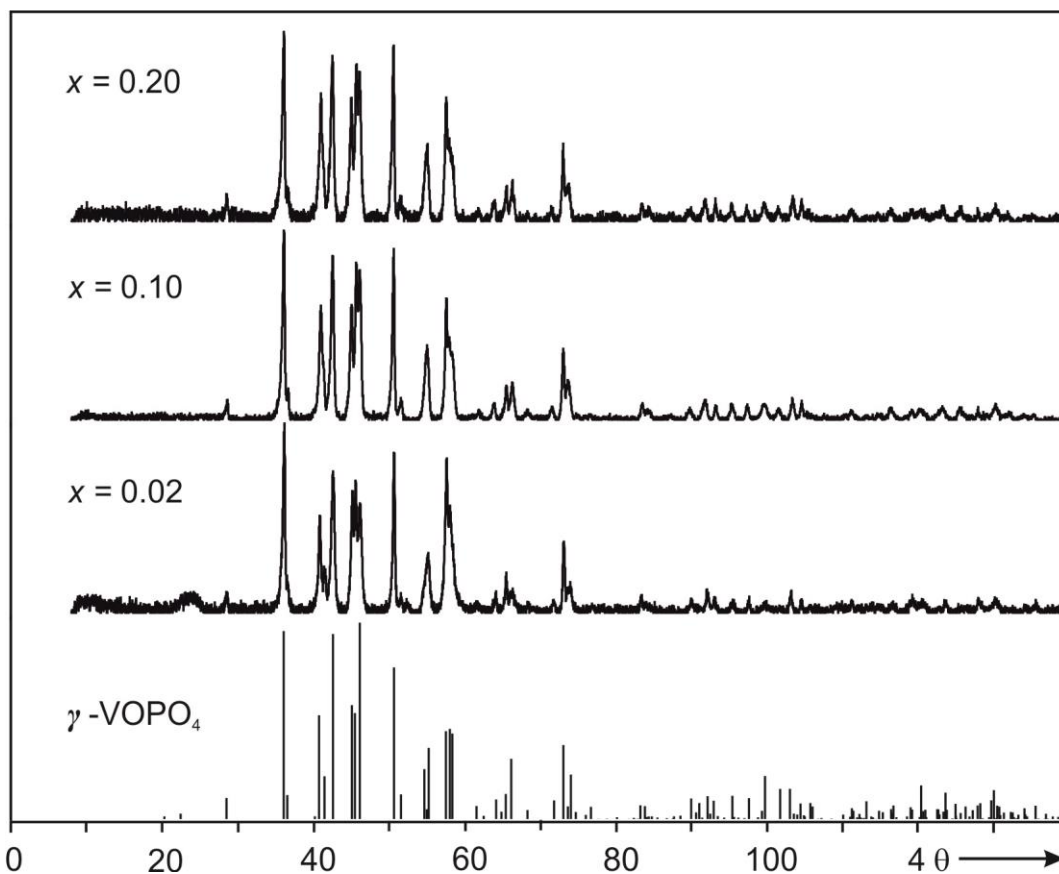


Figure 7.4 Comparison of Guinier photographs of members of the metastable solid solution  $(V_{1-x}Mo_x)OPO_4$ ;  $0.0 \leq x \leq 0.20$  ( $\gamma$ - $VOPO_4$  structure type) with the simulation based on data of  $\gamma$ - $VOPO_4$  [162]).

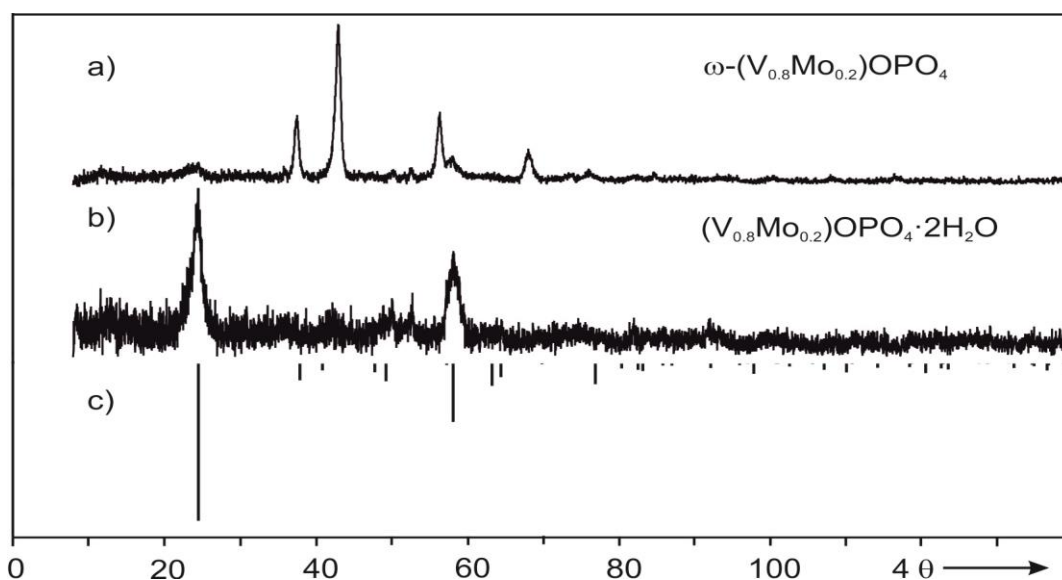


Figure 7.5 Conversion of the member of solid solution  $(V_{0.8}Mo_{0.2})OPO_4$  ( $\omega$ - $VOPO_4$  (ht) type [166]) (a), into  $(V_{0.8}Mo_{0.2})OPO_4 \cdot 2H_2O$  (b) by absorbing  $H_2O$  from lab. atmosphere, and a simulated XRPD pattern of  $(V_{0.8}Mo_{0.2})OPO_4 \cdot 2H_2O$  (c), structure model  $VOPO_4 \cdot 2H_2O$  [173] with adjusted lattice parameters,  $a = 6.131 \text{ \AA}$  and  $c = 7.216 \text{ \AA}$ .

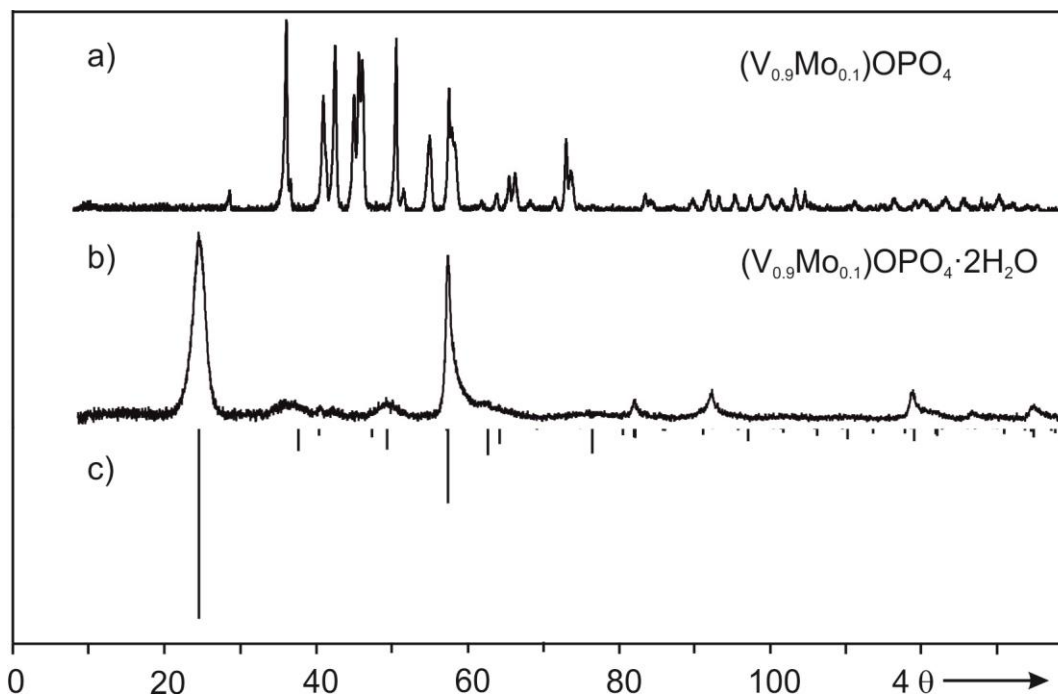


Figure 7.6 Conversion of the member of solid solution  $(V_{0.9}Mo_{0.1})OPO_4$  ( $\gamma$ - $VOPO_4$  type [162]) (a), into  $(V_{0.9}Mo_{0.1})OPO_4 \cdot 2H_2O$  (b) by absorbing  $H_2O$  from lab. atmosphere, and a simulated XRPD pattern of  $(V_{0.9}Mo_{0.1})OPO_4 \cdot 2H_2O$  (c) (structure model  $VOPO_4 \cdot 2H_2O$  [173]), with adjusted lattice parameters,  $a = 6.201$  and  $c = 7.189 \text{ \AA}$ .

Experiments aiming at further extension of the solubility of  $MoOPO_4$  in  $VOPO_4$  according to  $(V_{1-x}Mo_x)OPO_4$  ( $0.35 \leq x \leq 0.40$ ) via SCS followed by heating in air at  $600 \text{ }^\circ\text{C}$  led to the formation of a mixture of phases with  $\gamma$ -,  $\epsilon$ -, and  $\beta$ - $VOPO_4$  structure type (see Table 7.2). Further heating (at  $650 \text{ }^\circ\text{C}$ ) led to melting of the samples. The solidified melt showed weak reflections of a  $\beta$ - $VOPO_4$  type solid solution according to XRPD together with a broad hump (see Figure 7.7) which indicates the presence of amorphous materials. The silica ampoule was attacked by the melt and the EDX measurement confirmed the presence of small amounts of Si in the molten sample.

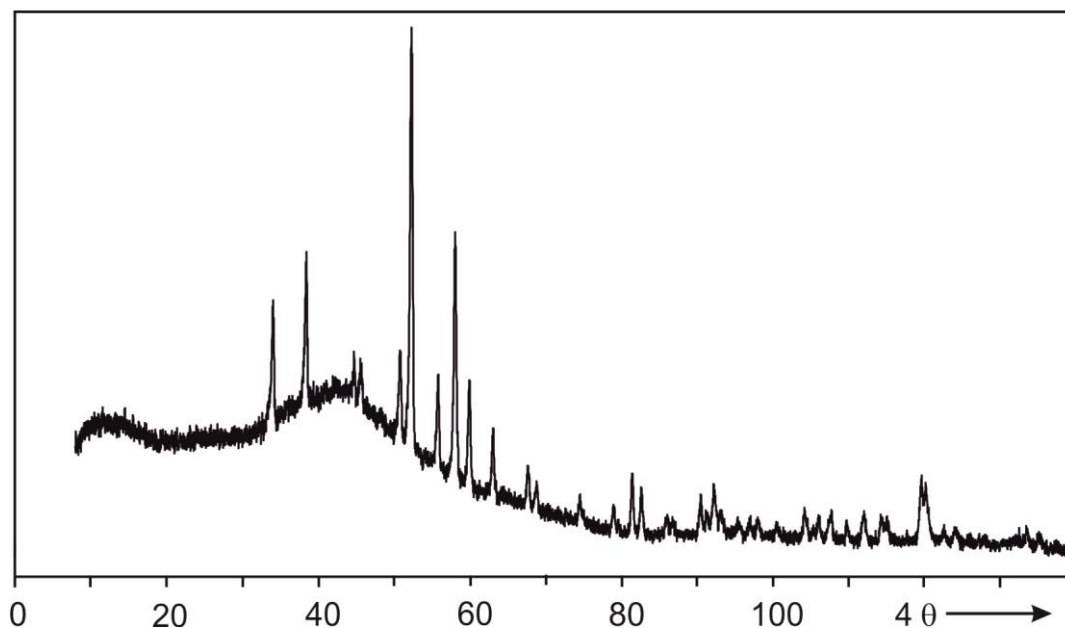


Figure 7.7 Guinier photograph of the solidified melt of “ $(V_{0.60}Mo_{0.40})OPO_4$ ” showing rather bad signal to noise ratio and a hump around  $40 \approx 42^\circ$  indicating the presence of amorphous material.

At  $x > 0.4$  the synthetic procedure (Table 7.2) led to melting of the batches. The quenched melts were amorphous according to XRPD. Only at the highest molybdenum concentration crystalline  $\alpha$ - $(MoO_2)_2P_2O_7$  [80, 88] was observed. From XRPD (Figure 14.5) and  $^{31}P$ -MAS-NMR no hints on incorporation of  $VOPO_4$  into  $(MoO_2)_2P_2O_7$ , e.g. as  $(MoO_2)_{2-x}(VO)_{2x}(P_2O_7)_{1-2x}(PO_4)_{2x}$  were obtained.

**Crystallization.** Single crystals of  $(V_{0.90}Mo_{0.10})OPO_4$  ( $\beta$ - $VOPO_4$  structure type, molybdenum content according to structure refinement and EDX analysis) were obtained from a melt of composition  $(V_{0.80}Mo_{0.20})OPO_4$  by slow cooling. The olive green powder sample obtained via SCS followed by heating in air was transferred into silica ampoule ( $l = 9$  cm,  $d = 1.5$  cm) and then evacuated and sealed. The ampoule was heated at  $730^\circ C$  (ramp  $50^\circ h^{-1}$ ) to melt the sample. The melt was kept at this temperature for five hours then cooled to  $650^\circ C$  at the rate of  $1^\circ h^{-1}$ . Afterwards the furnace was switched off and allowed to cool to RT.

#### 7.4 X-ray single crystal structure refinement of $\beta$ - $(V_{0.90}Mo_{0.10})OPO_4$

An olive green single crystal of  $(V_{0.90}Mo_{0.10})OPO_4$  ( $\beta$ - $VOPO_4$  structure type) was selected carefully under a polarizing microscope and glued on a thin vitreous silica fiber. Diffraction data was collected on a  $\kappa$ -CCD diffractometer (Enraf-Nonius Inc.) controlled by

the HKL2000 software [177] using graphite-monochromated Mo-K $\alpha$  ( $\lambda = 0.71073$  Å) radiation at ambient temperature. Crystal system and lattice type were determined from simulated precession photographs. For the crystal structure refinement the starting parameters were taken from  $\beta$ -VOPO<sub>4</sub> [161]. Full-matrix least-squares refinement was carried out using SHELX-97 [123] in the WinGX [124] framework. The best result of the refinement was obtained by setting the mixed occupancy vanadium/molybdenum to 1:0.1 which is obtained from single crystals EDX analyses. No hints were found for the presence of a superstructure due to vanadium/molybdenum ordering. Details regarding single crystal data collection and structure refinement of (V<sub>0.90</sub>Mo<sub>0.10</sub>)OPO<sub>4</sub> are summarized in Table 7.3.

Table 7.3 Summary of crystallographic data and information on x-ray single-crystal structure refinement of  $\beta$ -(V<sub>0.90</sub>Mo<sub>0.10</sub>)OPO<sub>4</sub>.

	<b>V<sub>0.90</sub>Mo<sub>0.10</sub>PO<sub>5</sub></b>
Structural formula	$\beta$ -(V <sub>0.90</sub> Mo <sub>0.10</sub> )OPO <sub>4</sub>
Formula weight	166.41
Crystal system	orthorhombic
Space group	<i>Pnma</i>
<i>T</i> (K)	293(2)
$\lambda$ (Å)	0.71073
<i>a</i> (Å)	7.7720(5)
<i>b</i> (Å)	6.1532(4)
<i>c</i> (Å)	6.9900(3)
<i>V</i> (Å <sup>3</sup> )	334.28(3)
<i>Z</i>	4
<i>D</i> <sub>calc</sub> (g·cm <sup>-3</sup> )	3.307
$\mu$ (mm <sup>-1</sup> )	3.41
Crystal dimensions (mm <sup>3</sup> )	0.07×0.01×0.01
Crystal color	olive green
<i>F</i> (0 0 0)	320
Measured refls.	4833
Independent refls.	778
Absorption correction	analytical
No. of parameters	42
Theta range (°)	3.9 - 34.9
Index ranges	$-12 \leq h \leq 12$ ; $-9 \leq 0 \leq 7$ ; $-6 \leq l \leq 11$
<i>GOOF</i>	1.06
<i>R</i> <sub>int</sub>	0.089
<i>R</i> ( <i>F</i> )/ <i>wR</i> ( <i>F</i> <sup>2</sup> ) <sup>b)</sup> [ <i>I</i> > 2 $\sigma$ ( <i>I</i> ) <sup>a)</sup>	0.046, 0.102
<i>R</i> ( <i>F</i> )/ <i>wR</i> ( <i>F</i> <sup>2</sup> ) <sup>b)</sup> (all data) <sup>a)</sup>	0.089, 0.115
<i>A</i> , <i>B</i> <sup>b)</sup>	0.054, 0

<sup>a)</sup>  $R_1 = \sum ||F_o| - |F_c|| / \sum |F_o|$ ,  $F^2 > 2\sigma(F^2)$ .  $w = 1/[\sigma^2(F_o^2) + (A \cdot P)^2 + B \cdot P]$ ,  $P = (F_o^2 + 2F_c^2)/3$ .

Comparison of the observed powder diffraction pattern of  $(V_{0.90}Mo_{0.10})OPO_4$  to the simulation based on the data from the single crystal structure refinement is shown in Figure 7.8. The final atomic coordinates and anisotropic displacement parameters, and selected inter-atomic distances are provided in Table 14.25, Table 14.26, and Table 14.27, respectively.

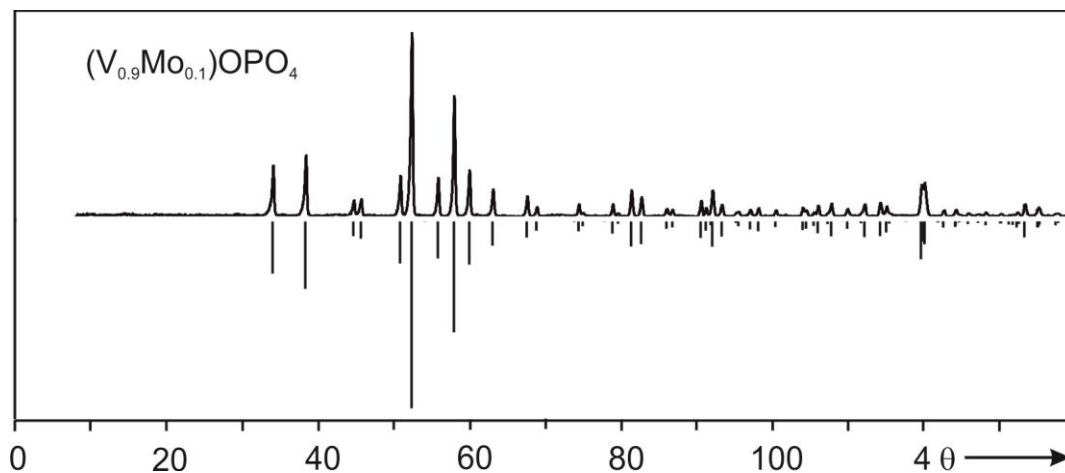


Figure 7.8 Guinier-photograph  $(V_{0.9}Mo_{0.1})OPO_4$  ( $\beta$ - $VOPO_4$  structure type) compared to the simulation based on the data from the single crystal structure refinement [this thesis] with mixed V/Mo occupancy on metal site.

## 7.5 Results and discussion

The solid solutions  $(V_{1-x}Mo_x)OPO_4$ ;  $\beta$ - $VOPO_4$  type ( $0.0 \leq x \leq 0.30$ ) and  $\gamma$ - $VOPO_4$  type, ( $0.0 \leq x \leq 0.20$ ) are obtained with high reproducibility via SCS followed by heating the combustion product in air. The former one is thermodynamically stable and the latter one is thermodynamically metastable. To prevent the highly hygroscopic  $(V_{1-x}Mo_x)OPO_4$  ( $\gamma$ - $VOPO_4$  structure type) from being hydrated, rapid cooling to room temperature and storage avoiding moisture is required. The maximum temperature required to obtain the thermodynamically stable phase depends on the concentration of molybdenum. With increasing concentration the required temperature decreases. The lower phase boundary  $(V_{1-x}Mo_x)OPO_4$  ( $x = 0$ ) was obtained at 725 °C, the upper phase boundary ( $x = 0.30$ ) was obtained at 600 °C. At higher temperatures the powders of the corresponding composition started to melt.

Careful inspection of the XRPD patterns of members of the  $\beta$ - $VOPO_4$  type solid solution showed that the intensity of the (011) reflection increases with the Mo concentration (Figure 7.3). The XRPD of the two members at  $x = 0.30$  and 0.20 of the

solid solution  $(V_{1-x}Mo_x)OPO_4$  are compared with simulations using adjusted lattice parameters (see Figure 7.9).

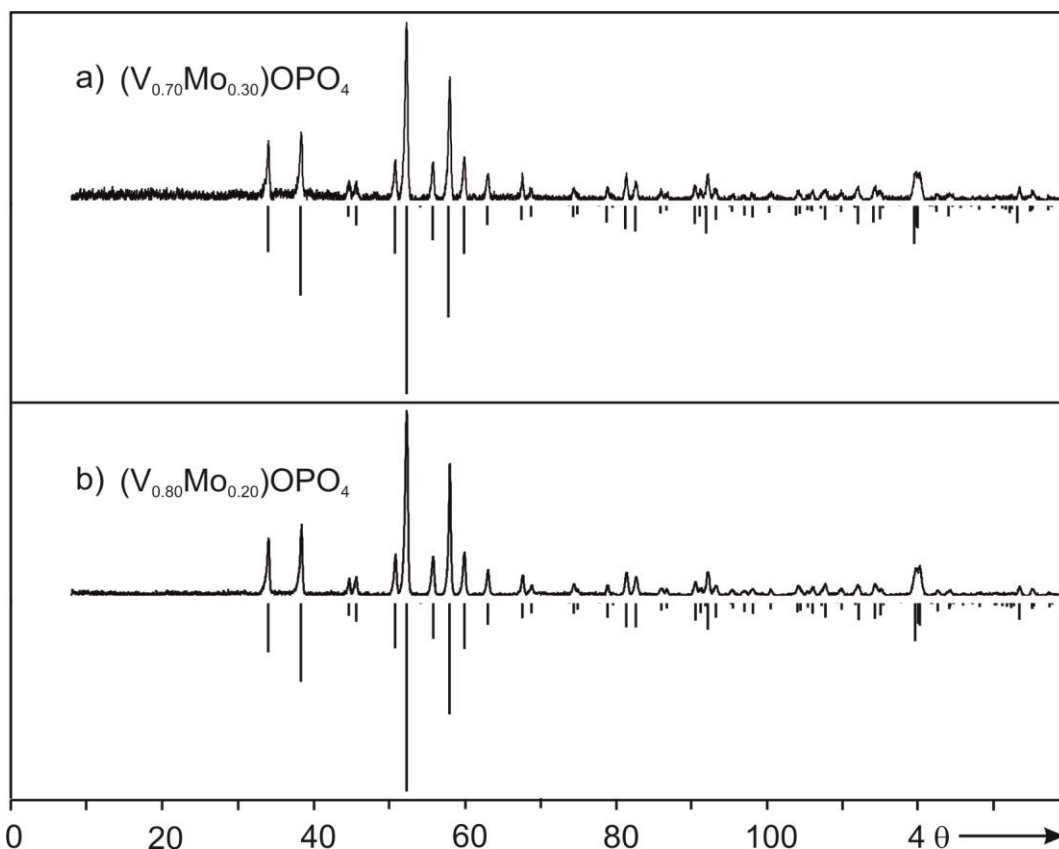


Figure 7.9 Guinier-photographs of two members of the solid solution  $(V_{1-x}Mo_x)OPO_4$  ( $\beta$ -VOPO<sub>4</sub> structure type) at  $x = 0.30$  (a) and  $x = 0.20$  (b), compared to simulations based on the single crystal structure refinement of  $(V_{0.90}Mo_{0.10})OPO_4$  [this thesis,  $\beta$ -type] with adjusted lattice parameters.

The crystal structure of  $\beta$ -VOPO<sub>4</sub> is 3D network of VO<sub>6</sub> octahedra and PO<sub>4</sub> tetrahedra (see Figure 6.11) whereas  $\alpha_{II}$ -VOPO<sub>4</sub> shows a layer type structure (see Figure 6.10). The pattern of changes in unit cell parameters of molybdenum substituted VOPO<sub>4</sub> ( $\beta$ -VOPO<sub>4</sub> structure type) is comparable to tungsten substituted VOPO<sub>4</sub> ( $\alpha_{II}$ -type) as shown in Figure 7.10 (see also Table 14.24). This can be attributed to similar distances in the MO<sub>6</sub> octahedra. Therefore the oxidation states in  $(V_{1-x}Mo_x)OPO_4$  ( $0 \leq x \leq 0.30$ ,  $\beta$ -VOPO<sub>4</sub> type) are expected to be  $(V^{IV}_x V^V_{1-2x} Mo^{VI}_x)OPO_4$  which is similar to  $(V^{IV}_x V^V_{1-2x} W^{VI}_x)OPO_4$  ( $0.0 \leq x \leq 0.26$ ,  $\alpha_{II}$ -VOPO<sub>4</sub> type). Crystal chemical similarity of V<sup>5+</sup> with V<sup>4+</sup>/Mo<sup>6+</sup> combination is already reported in mixed oxides,  $V^{IV}_{0.48}V^V Mo^{VI}_{1.52}O_8$  [210] and  $V^{IV}_{0.9}V^V_{0.2}Mo^{VI}_{0.9}O_5$  [212]. Heterovalent substitution of pentavalent vanadium (54 pm) in VOPO<sub>4</sub> by combination of hexavalent molybdenum (59 pm) and tetravalent vanadium (58 pm) leads to an increase of the  $b$ - and  $c$ - axes as a consequence of increasing the

distances  $d(V-O_{eq})$ . However, the  $a$ -axis, along the chain of short long short distances  $d(O_{ax}=V-O_{ax})$  is decreased. Comparing the isotypic pair of pure phases, the short-long-short distances in  $\beta$ -VOPO<sub>4</sub> [161] {4.155(1) Å} is larger than that of  $\beta$ -MoOPO<sub>4</sub> [88] {4.06(5) Å} as shown in Figure 7.11. Therefore, in Mo substituted  $\beta$ -VOPO<sub>4</sub> type solid solution the shrinkage of the distance along the chain is quite as expected. Fully assigned Guinier photographs of the members of the solid solution  $(V_{1-x}Mo_x)OPO_4$ ;  $0.0 \leq x \leq 0.30$  ( $\beta$ -VOPO<sub>4</sub> structure type) are provided in Table 14.28 to Table 14.33.

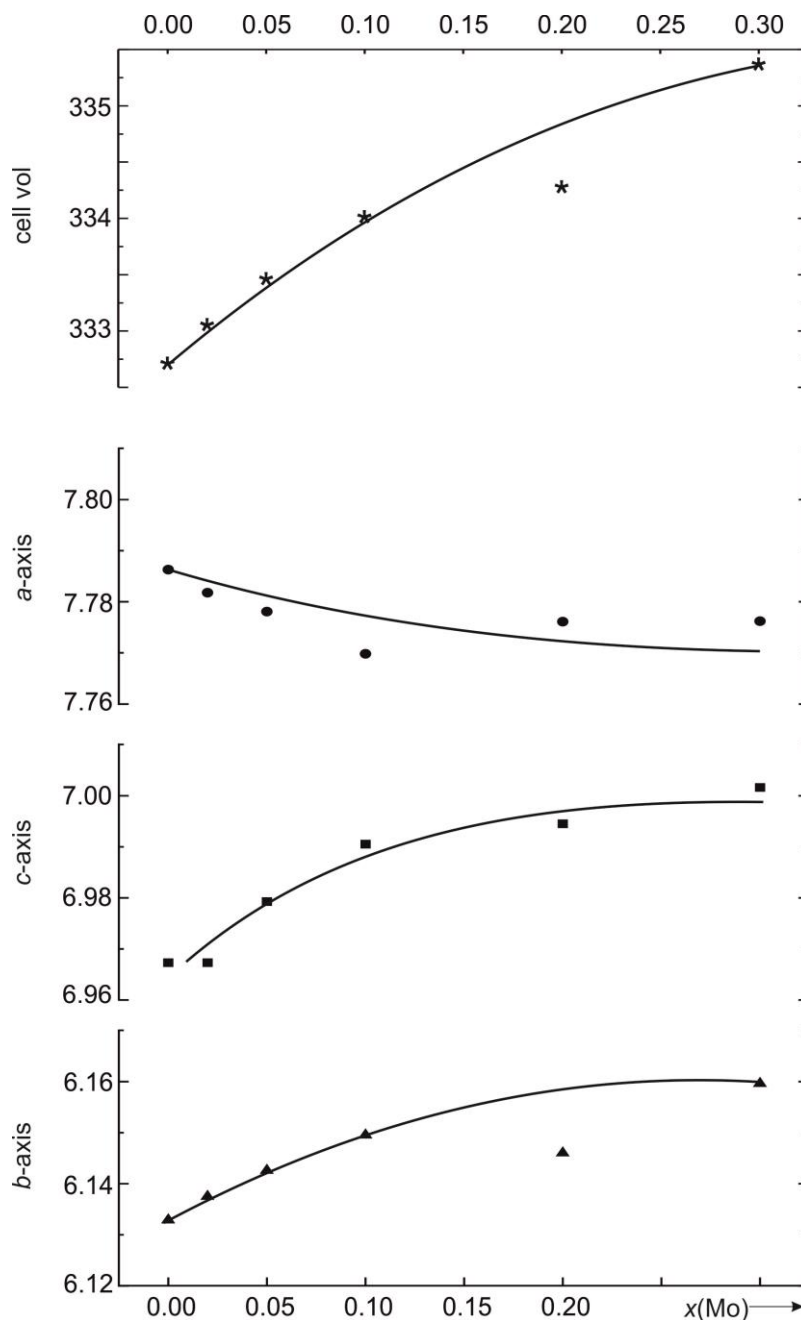


Figure 7.10 Variation of lattice parameters and cell volume ( $\text{\AA}^3$ ) of members of the solid solution  $(V_{1-x}Mo_x)OPO_4$ ;  $0.0 \leq x \leq 0.30$  ( $\beta$ -VOPO<sub>4</sub> structure type).

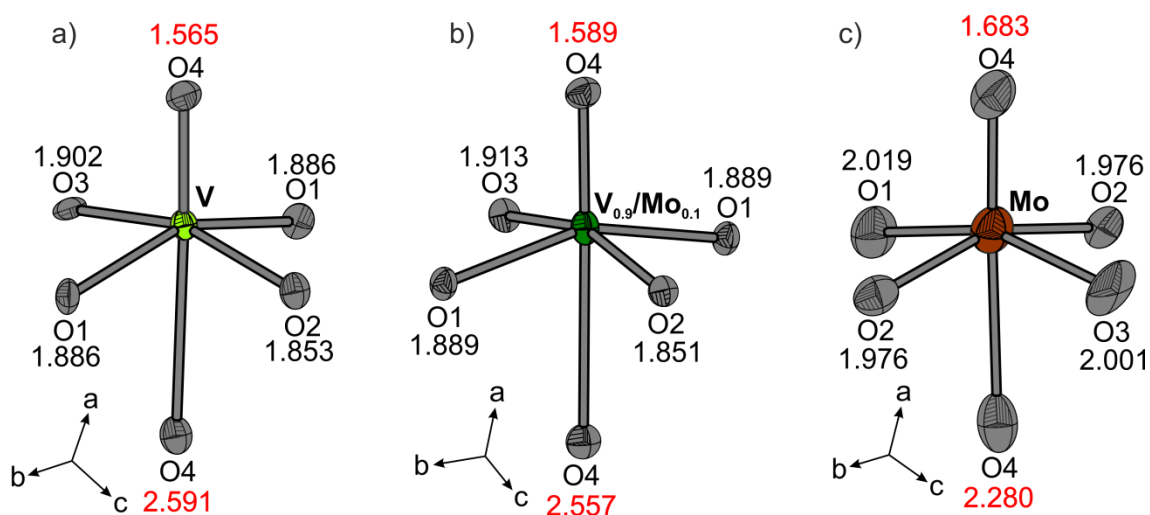


Figure 7.11 Comparison of the co-ordination polyhedra  $[MO_6]$  in  $\beta$ -VOPO<sub>4</sub> [161] (a),  $(V_{0.90}Mo_{0.10})OPO_4$  [this thesis] (b), and  $\beta$ -MoOPO<sub>4</sub> (c) [88]. ORTEP style graphics (ellipsoids are at 50% probability level, software: DIAMOND [128]).

The crystal structure of  $\gamma$ -VOPO<sub>4</sub> (thermodynamically metastable) is presented in Figure 7.12 [162]. It consists of chains of VO<sub>6</sub> octahedra, VO<sub>5</sub> square pyramids, and PO<sub>4</sub> tetrahedra.

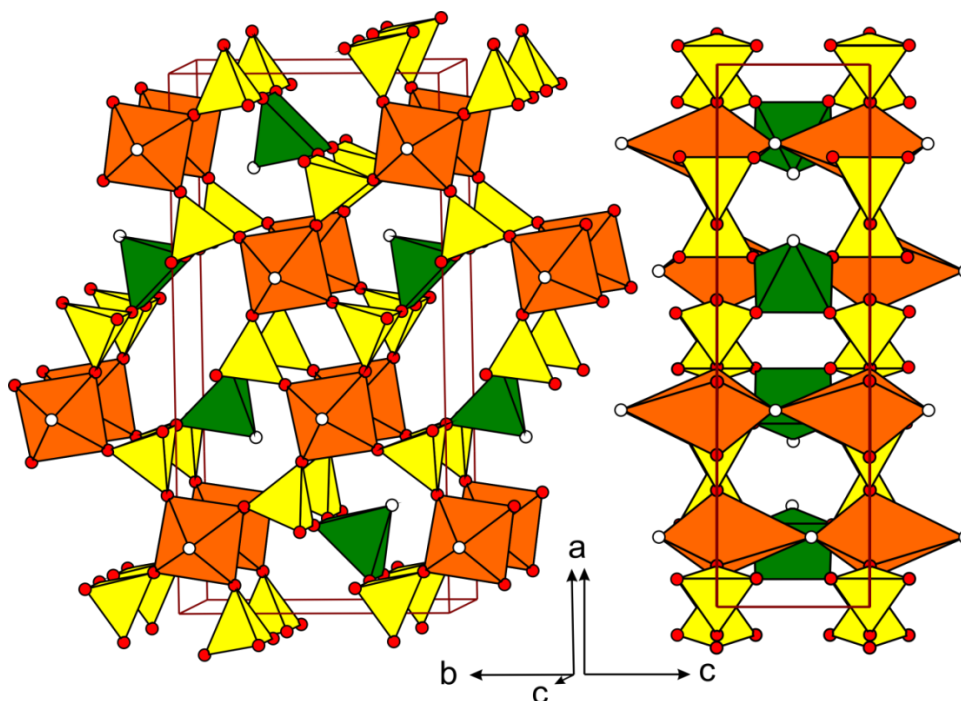


Figure 7.12 Crystal structure of  $\gamma$ -VOPO<sub>4</sub> [162].  $[VO_6]$  octahedra: orange,  $[VO_5]$  square pyramids: green,  $[PO_4]$  tetrahedra: yellow, open circles represent oxygen atoms of vanadyl(V) groups  $(V=O)^{3+}$ .



The calculated XRPD patterns of the solid solution  $(V_{1-x}Mo_x)OPO_4$  ( $\gamma$ -type) revealed that molybdenum ions substitute only for vanadium in octahedral coordination (Figure 7.13). The charge distribution of both  $\beta$ - and  $\gamma$ -type solid solution is assumed to be  $(V_x^{IV}V_{1-2x}^V Mo_x^{VI})OPO_4$ . Experimental evidence is provided and discussed in section 7.6.

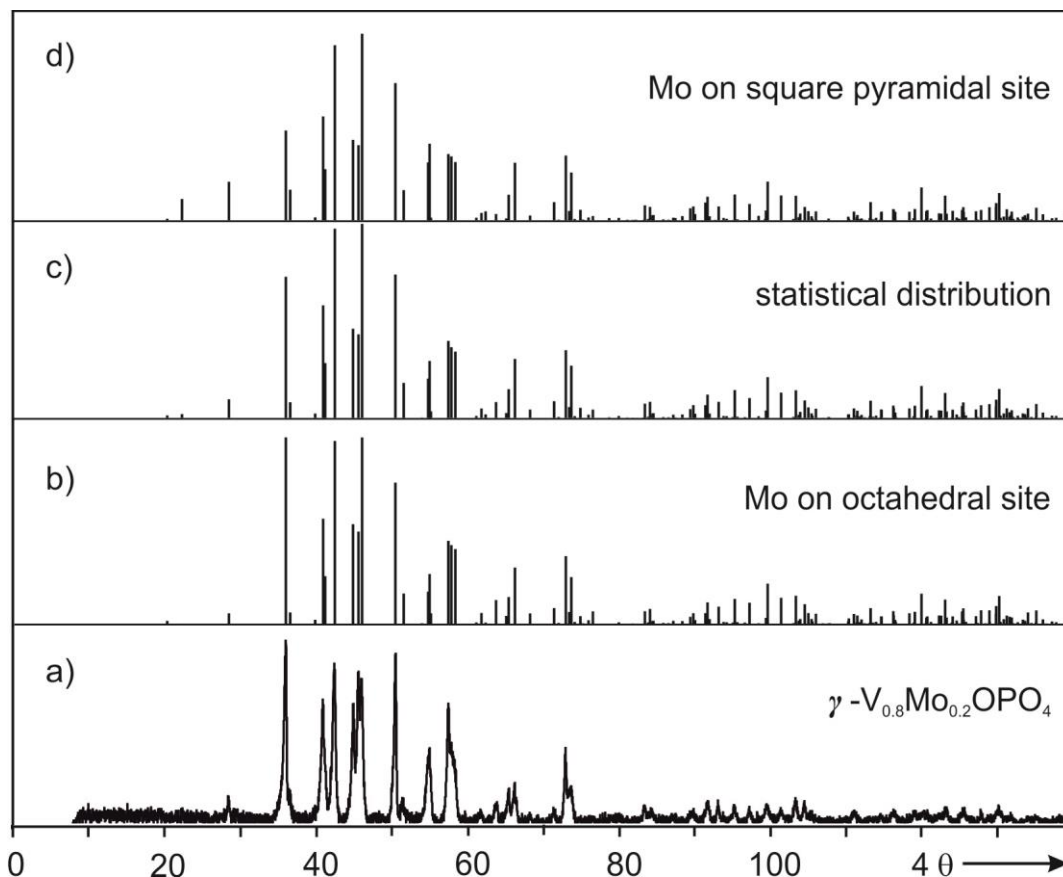


Figure 7.13 Guinier photograph of  $(V_{0.8}Mo_{0.2})OPO_4$ ,  $\gamma$ -VOPO<sub>4</sub> structure type (a) obtained by SCS compared to simulated patterns based on the structure model of  $\gamma$ -VOPO<sub>4</sub> [162] with different metal distributions. Mo in octahedral metal site (b) which shows best fit with the experimental XRPD, in contrast to Mo in statistical distribution of metal sites (c) and in square pyramidal metal site (d).

The heterovalent substitution of pentavalent vanadium ions (54 pm) in  $\gamma$ -VOPO<sub>4</sub> by combination of hexavalent molybdenum (59 pm) and tetravalent vanadium (58 pm) leads to an increase of the  $b$ -axis as a consequence of increasing the distances  $d(V-O_{eq})$  as shown in Table 7.4. Assignment of the Guinier photographs of the members of solid solutions  $(V_{1-x}Mo_x)OPO_4$ ;  $0.0 \leq x \leq 0.20$  ( $\gamma$ -VOPO<sub>4</sub> structure type) is provided in Table 14.34 and Table 14.35.

Table 7.4 Lattice parameters of members of the solid solution (V<sub>1-x</sub>Mo<sub>x</sub>)OPO<sub>4</sub>; 0.0 ≤ x ≤ 0.20 ( $\gamma$ -VOPO<sub>4</sub> structure type [162], space group: *Pbam*).

Composition, <i>x</i>	<i>a</i> (Å)	<i>b</i> (Å)	<i>c</i> (Å)	<i>V</i> (Å <sup>3</sup> )
0.0 <sup>a)</sup>	17.3970(23)	8.8199(2)	4.9079(1)	753.07
0.10	17.327(2)	8.875(2)	4.918(1)	756.3(2)
0.20	17.318(4)	8.880(3)	4.915(1)	755.9(3)

7) from reference [162]

It is worth to mention that an experiment aiming at co-substitution molybdenum and tungsten according to (Mo<sub>x</sub>W<sub>x</sub>V<sub>1-2x</sub>)OPO<sub>4</sub> (*x* = 0.10) via SCS (combustion at 400 °C) followed by heating in air at 700 °C led to a two phase mixture, one with  $\alpha_{II}$ - and the other with  $\beta$ -VOPO<sub>4</sub> structure type. This result is not totally unexpected. Since incorporation of Mo (0 ≤ *x* ≤ 0.30) and W (0.04 ≤ *x* ≤ 0.26) individually in VOPO<sub>4</sub> as (M<sub>x</sub>V<sub>1-x</sub>)OPO<sub>4</sub> (*M*: Mo or W) leads to  $\beta$ - and  $\alpha_{II}$ -VOPO<sub>4</sub> structure type solid solutions, respectively.

## 7.6 Charge distribution in (V<sub>1-x</sub>Mo<sub>x</sub>)OPO<sub>4</sub>

EPR spectroscopic studies of  $\beta$ - and  $\gamma$ -(V<sub>1-x</sub>Mo<sub>x</sub>)OPO<sub>4</sub> were performed in the research group of Prof. Schiemann, Univ. Bonn. Evidence for the presence of paramagnetic V<sup>4+</sup> ions in the solid solutions (V<sub>1-x</sub>Mo<sub>x</sub>)OPO<sub>4</sub> ( $\beta$ -VOPO<sub>4</sub> structure type) has been obtained from EPR measurements of powder samples. Since V<sup>5+</sup> and Mo<sup>6+</sup> are EPR silent, all obtained spectra are attributed to V<sup>4+</sup> ions. For the magnetically dilute solid solutions (V<sup>IV</sup><sub>x</sub>V<sup>V</sup><sub>1-2x</sub>Mo<sup>VI</sup><sub>x</sub>)OPO<sub>4</sub> with *x* = 0.005, 0.01 and 0.02 (all  $\beta$ -VOPO<sub>4</sub> structure type) the EPR spectra are very similar showing a resonance which is typical for tetragonally distorted octahedral coordination of a vanadyl(IV) cation (see Figure 7.14). The hyperfine coupling with the <sup>51</sup>V nucleus is nicely resolved. For *x* = 0.30 the spectrum appears to be distinctly different, which can be attributed to the high concentration of paramagnetic V<sup>4+</sup> ions and their interactions. The EPR spectra of Mo doped  $\beta$ -VOPO<sub>4</sub> structure type solid solutions show a pattern similar to one observed for W doped  $\beta$ -VOPO<sub>4</sub> [197, this thesis, see Figure 7.15]. Therefore, *g* and *A* tensors for Mo-doped phases are also expected to have axial symmetry (see section 6.5.1).

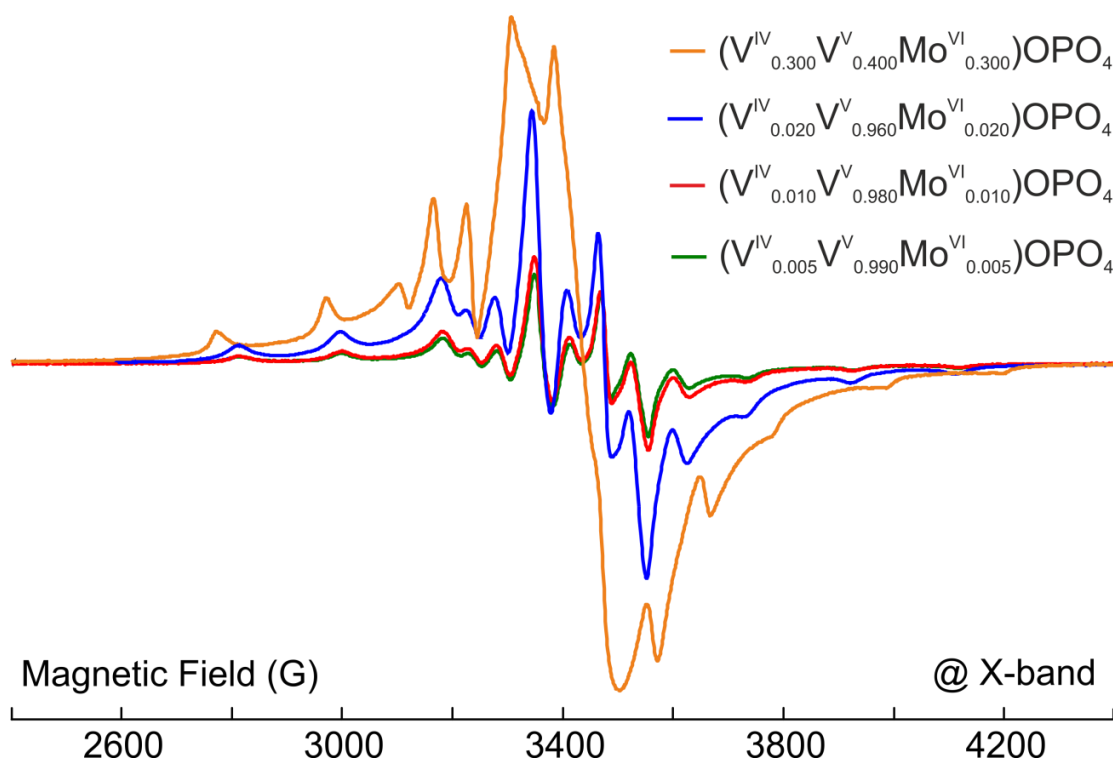


Figure 7.14 Continuous wave X-band powder EPR spectra of  $(V^{IV}_x V^V_{1-2x} Mo^{VI}_x)OPO_4$ ;  $x = 0.005, 0.01, 0.02$  and  $0.30$  (all  $\beta$ -VOPO<sub>4</sub> structure type [161]) measured at RT.

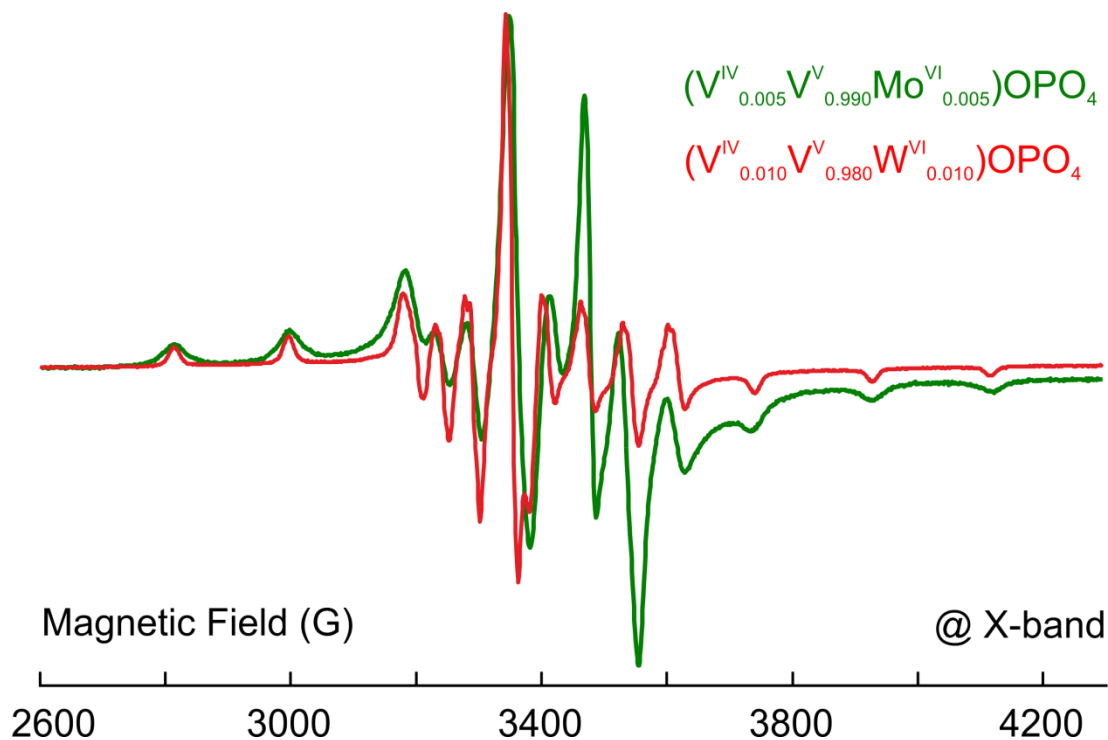


Figure 7.15 Comparison of X-band powder CW-EPR spectra (measured at RT) of  $(V^{IV}_{0.005} V^V_{0.990} Mo^{VI}_{0.005})OPO_4$  (green) and  $(V^{IV}_{0.010} V^V_{0.980} W^{VI}_{0.010})OPO_4$  (red, both are  $\beta$ -VOPO<sub>4</sub> structure type).

The EPR spectra of Mo substituted  $\gamma$ -VOPO<sub>4</sub> also showed an axial  $g$ -tensor with hyperfine coupling which is typical for  $V^{4+}$  ions ( $^{51}V$ ) (see Figure 7.16). To determine the tensors, better resolved spectra from additional measurements at higher frequencies than X-band are necessary.

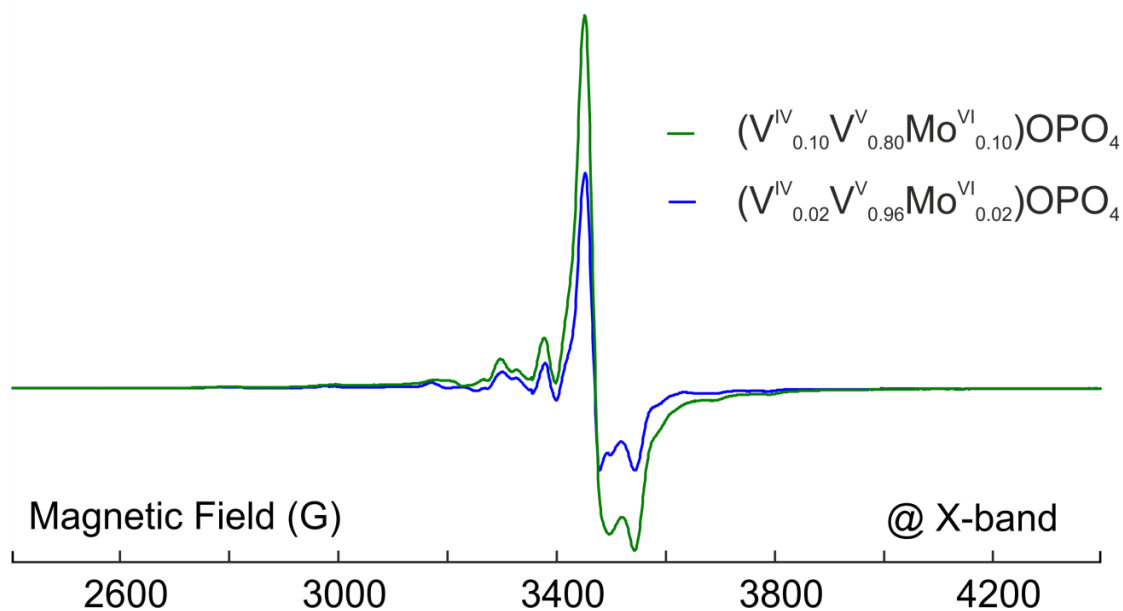


Figure 7.16 Continuous wave (CW) X-band powder EPR spectra (measured at RT) of  $(V^{IV}_x V^V_{1-2x} Mo^{VI}_x)OPO_4$ ;  $x = 0.02$  and  $0.10$  ( $\gamma$ -VOPO<sub>4</sub> structure type).

The observed powder reflectance spectra of the solid solution  $(V_{1-x}Mo_x)OPO_4$  ( $\beta$ -VOPO<sub>4</sub> structure type [161]) shown in Figure 7.17 are quite similar to those obtained for the solid solution  $(V_{1-x}W_x)OPO_4$  ( $\alpha_{II}$ -VOPO<sub>4</sub> structure type [160]). The intensity of the absorption bands increases with the Mo concentration. The color of the solid solution  $(V_{1-x}Mo_x)OPO_4$  ( $0 \leq x \leq 0.30$ ;  $\beta$ -VOPO<sub>4</sub> structure type) changes from bright yellow (for  $x = 0.0$ ) to deep olive green (for  $x = 0.3$ ) with increasing Mo concentration as shown in Figure 7.18. The color change can be attributed to heterovalent substitution of  $V^{5+}$  by combination of  $Mo^{6+}$  and  $V^{4+}$ . The assignment of the absorption bands follows the one given for  $(V_{1-x}W_x)OPO_4$  (see Figure 6.17). In spite of the structural difference solid solutions  $(V_{1-x}Mo_x)OPO_4$  with  $\gamma$ - and  $\beta$ -VOPO<sub>4</sub> structure type exhibit similar powder reflectance spectra (see Figure 7.17 and Figure 7.19).

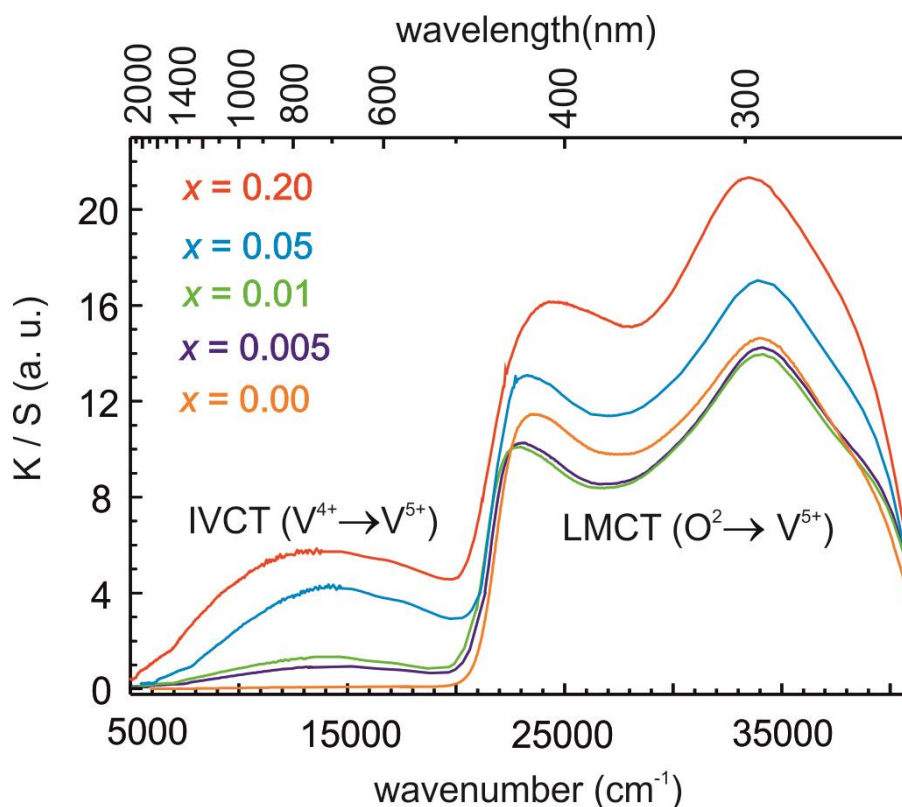


Figure 7.17 UV/Vis/NIR powder reflectance spectra of  $(V_{1-x}Mo_x)OPO_4$ ;  $x = 0.00, 0.005, 0.01, 0.05, \text{ and } 0.20$  ( $\beta$ -VOPO<sub>4</sub> structure type).

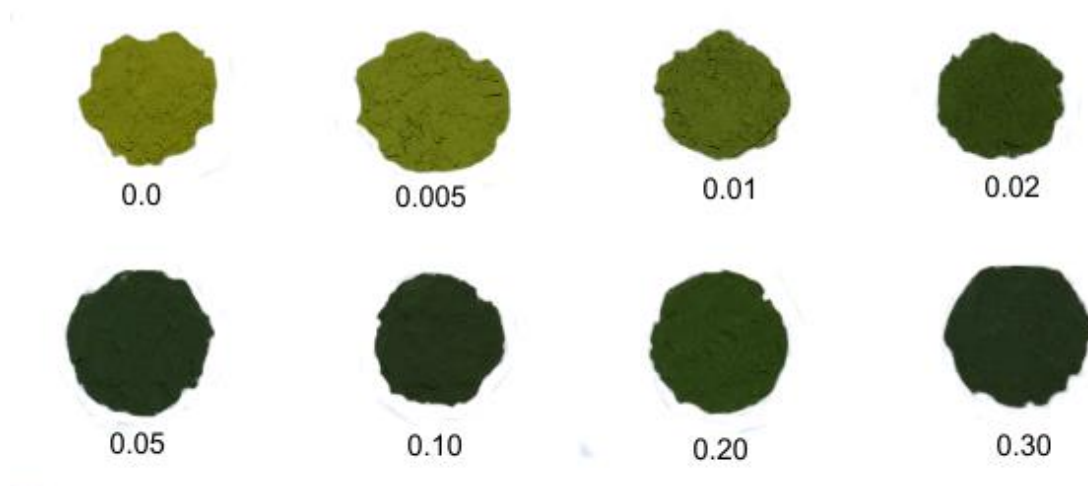


Figure 7.18 Photographs of microcrystalline powders of members of the solid solution  $(V_{1-x}Mo_x)OPO_4$ ;  $0 \leq x \leq 0.30$  ( $\beta$ -VOPO<sub>4</sub> type [161]) obtained via SCS followed by heating in air.

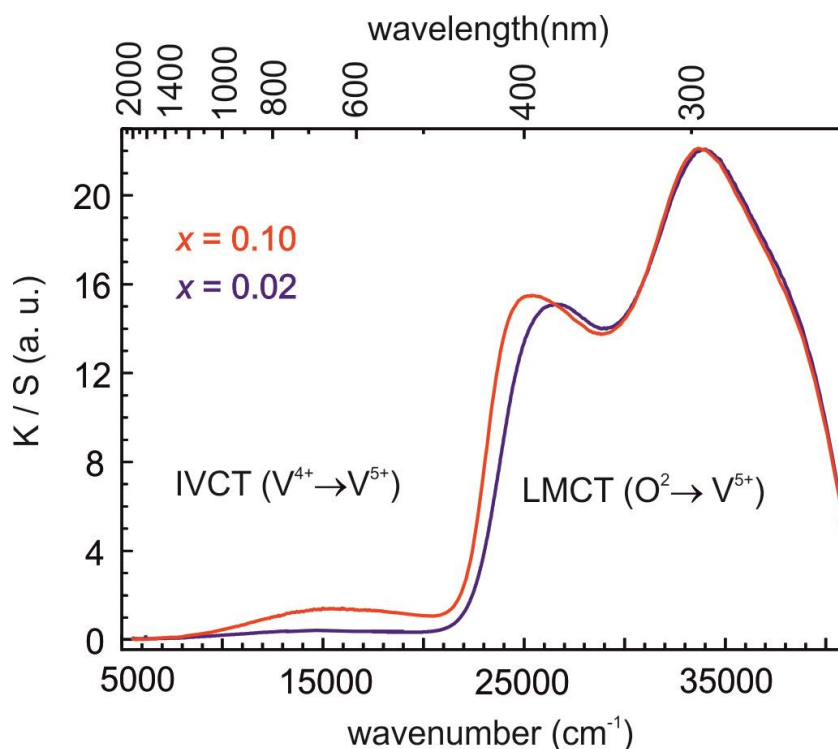


Figure 7.19 UV/Vis/NIR powder reflectance spectra of  $(V_{1-x}Mo_x)OPO_4$ ;  $x = 0.02$ , and  $0.10$  ( $\gamma$ - $VOPO_4$  structure type).

**Molar magnetic susceptibility**  $\chi_m^{-1}$  of  $(V_{0.80}Mo_{0.20})OPO_4$  powder ( $\beta$ - $VOPO_4$  structure type) was measured using a VSM as a function of temperature ( $2 \leq T \leq 300$  K, Figure 7.20). According to the method of atom and group increments [129] a diamagnetic correction was applied to the observed susceptibility.  $(V^{IV}_{0.20}V^{V}_{0.60}Mo^{VI}_{0.20})OPO_4$  exhibits paramagnetic behavior (Figure 7.20). An effective magnetic moment,  $\mu_{eff} = 1.14\mu_B/V^{4+}$  ion is calculated (eq. 3.34). The moment is markedly lower than the spin-only value of  $1.73\mu_B$  for one unpaired electron. The observed reduced magnetic moment is not obvious till now.

**The electrical resistance** of a pellet  $(V^{IV}_{0.20}V^{V}_{0.60}Mo^{VI}_{0.20})OPO_4$  ( $d = 2$  mm,  $l = 0.54$  mm) was measured in the temperature range 311 to 470 K (for details see section 6.5.5). Typical semiconducting behavior was observed (Figure 7.21). From the Arrhenius plot  $\ln(1/R)$  vs.  $(1/T)$  the calculated band gap is  $E_g = 0.84$  eV (Figure 7.21, inset). This value is in good agreement with the optical band gap observed for phosphates  $(V_{1-x}Mo_x)OPO_4$  from the onset of the IVCT Figure 7.17. Semiconducting behavior has already been reported for pure V-P-O glasses, molybdenum doped V-P-O glasses [220] as well as for tungsten doped V-P-O glasses [192, 193]. Thus, according to *Robin and Day*, the solid

solutions can be assumed as Class II mixed-valent compound. For conductivity in such cases a hopping mechanism appears to be reasonable.

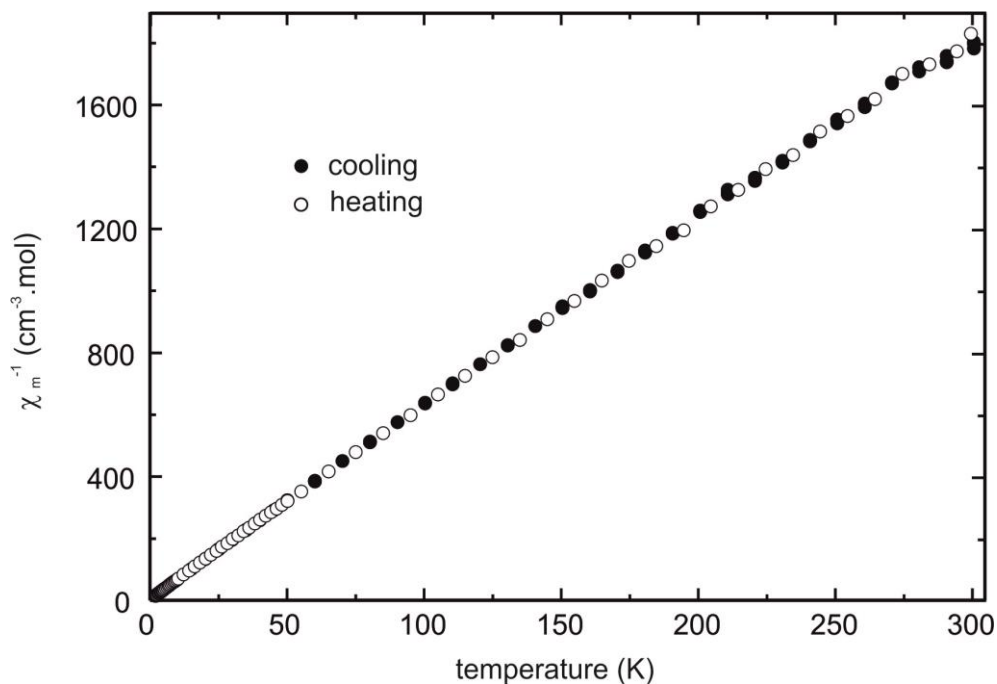


Figure 7.20 ( $V_{0.20}^{IV}V_{0.60}^V\text{Mo}_{0.20}^{VI}$ )OPO<sub>4</sub>. Reciprocal molar susceptibility vs. temperature.

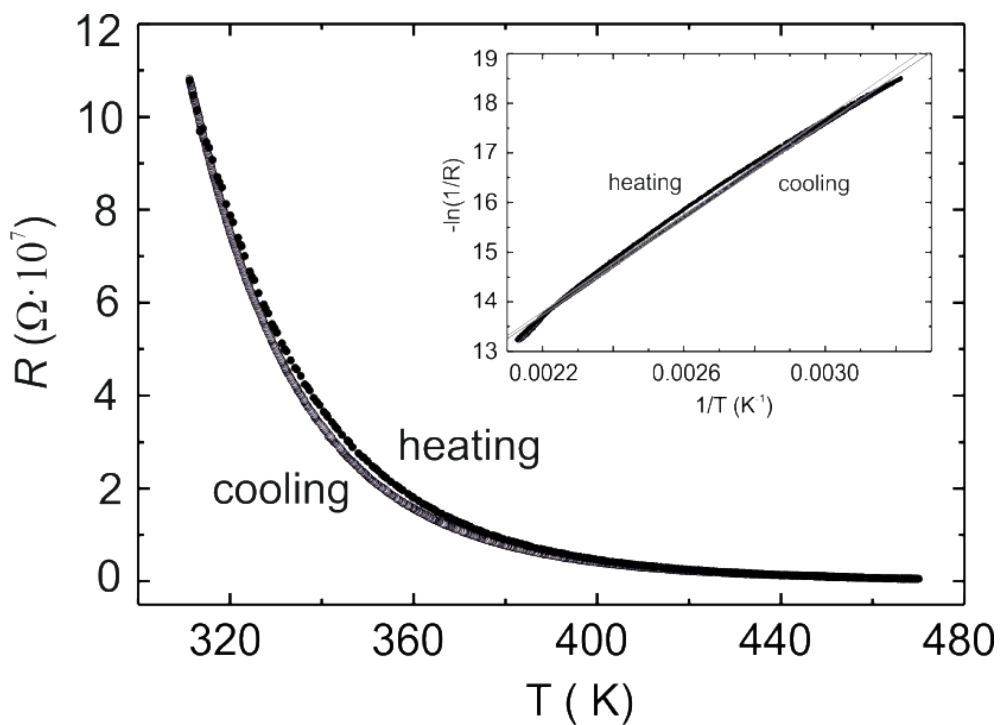


Figure 7.21 Temperature dependent resistance of ( $V_{0.20}^{IV}V_{0.60}^V\text{Mo}_{0.20}^{VI}$ )OPO<sub>4</sub> powder ( $\beta$ -VOPO<sub>4</sub> structure type [161]).

**<sup>31</sup>P-MAS-NMR spectra.** The formation of solid solutions (V<sub>1-x</sub>Mo<sub>x</sub>)OPO<sub>4</sub> ( $\beta$ - and  $\gamma$ -VOPO<sub>4</sub> structure type) as pure phase is also revealed by <sup>31</sup>P-MAS-NMR spectra. For  $\beta$ -VOPO<sub>4</sub> a single isotropic resonance is reported at  $\delta_{\text{iso}} = -10.9$  ppm [221] which complies with the crystal structure containing only one independent phosphorus at Wyckoff position 4c. The <sup>31</sup>P-MAS-NMR measurements of the weakly paramagnetic solid solution (V<sub>1-x</sub>Mo<sub>x</sub>)OPO<sub>4</sub> ( $\beta$ -VOPO<sub>4</sub> structure type) with  $x = 0.05$  and  $0.20$  also showed just a single resonance at  $\delta_{\text{iso}} = -10.5$  and  $-10.0$  ppm, respectively (see Figure 7.22a and Table 7.5). The broadening of the resonance peak with increasing amount of paramagnetic species (see also Table 7.5) is the consequence of coupling between the <sup>31</sup>P nuclei and the 3d<sup>1</sup> electron of vanadium(IV) and its anisotropic magnetic susceptibility [196]. The downfield shift of the resonance lines with increasing molybdenum concentration is attributed to an inductive effect. This effect is also observed for the  $\gamma$ -type solid solution (Figure 7.22b) as well as for the dihydrate (V<sub>1-x</sub>Mo<sub>x</sub>)OPO<sub>4</sub>·2H<sub>2</sub>O (Figure 7.22c).

Table 7.5 Summary of isotropic chemical shifts  $\delta_{\text{iso}}$  in <sup>31</sup>P-MAS-NMR spectra of members of the solid solutions (V<sub>1-x</sub>Mo<sub>x</sub>)OPO<sub>4</sub>;  $0.02 \leq x \leq 0.20$  and reference compounds.

orthophosphate ( $Q^\circ$ )	Wyckoff position of P	$\delta_{\text{iso}}$ (ppm)	FWHM (Hz)	reference
$\beta$ -V <sup>V</sup> OPO <sub>4</sub>	4c	-11.5		[195]
$\beta$ -V <sup>V</sup> OPO <sub>4</sub>	4c	-10.9		[221]
$\beta$ -(V <sup>IV</sup> <sub>0.05</sub> V <sup>V</sup> <sub>0.90</sub> Mo <sup>VI</sup> <sub>0.05</sub> )OPO <sub>4</sub>	4c	-10.5	610	[this thesis]
$\beta$ -(V <sup>IV</sup> <sub>0.20</sub> V <sup>V</sup> <sub>0.60</sub> Mo <sup>VI</sup> <sub>0.20</sub> )OPO <sub>4</sub>	4c	-10.0	705	[this thesis]
$\gamma$ -V <sup>V</sup> OPO <sub>4</sub>	4g, 4g	(-21.2, -17.3) <sup>b)</sup> , (1:1) <sup>a)</sup>		[195]
$\gamma$ -(V <sup>IV</sup> <sub>0.10</sub> V <sup>V</sup> <sub>0.80</sub> Mo <sup>VI</sup> <sub>0.10</sub> )OPO <sub>4</sub>	4g, 4g	-18.4, 6.8 <sup>c)</sup>	1340	[this thesis]
$\gamma$ -(V <sup>IV</sup> <sub>0.20</sub> V <sup>V</sup> <sub>0.60</sub> Mo <sup>VI</sup> <sub>0.20</sub> )OPO <sub>4</sub>	4g, 4g	-17.7	1500	[this thesis]
V <sup>V</sup> OPO <sub>4</sub> ·2H <sub>2</sub> O	2b	3.9		[222]
(V <sup>IV</sup> <sub>0.02</sub> V <sup>V</sup> <sub>0.96</sub> Mo <sup>VI</sup> <sub>0.02</sub> )OPO <sub>4</sub> ·2H <sub>2</sub> O	2b	6.2	400	[this thesis]

<sup>a)</sup> intensity ratio of the resonance, <sup>b)</sup> shoulder at -14.3 ppm, <sup>c)</sup> due to partially hydration of the parent  $\gamma$ -phase

Two resonances are reported for  $\gamma$ -VOPO<sub>4</sub> (two Wyckoff positions of P atom 4g, 4g) at -21.2 and -17.3 ppm with a shoulder at -14.3 ppm. The <sup>31</sup>P-MAS-NMR measurements of the weakly paramagnetic solid solution (V<sub>1-x</sub>Mo<sub>x</sub>)OPO<sub>4</sub> ( $\gamma$ -VOPO<sub>4</sub> type) with  $x = 0.10$  and  $0.20$  show broad resonances at  $\delta_{\text{iso}} = -17.7$  and  $-18.4$  ppm, respectively. The impurity signal at  $\delta_{\text{iso}} = 6.8$  ppm in Figure 7.22b is due to partial conversion of (V<sub>0.90</sub>Mo<sub>0.10</sub>)OPO<sub>4</sub> ( $\gamma$ -VOPO<sub>4</sub> type) into (V<sub>0.90</sub>Mo<sub>0.10</sub>)OPO<sub>4</sub>·2H<sub>2</sub>O (VOPO<sub>4</sub>·2H<sub>2</sub>O type [173]). This is revealed



by comparing resonance signal observed at  $\delta_{iso} = 6.2$  ppm of  $(V_{0.98}Mo_{0.02})OPO_4 \cdot 2H_2O$  (see Figure 7.22c). The di-hydrated phases are formed from their parent phases  $\gamma-(V_{1-x}Mo_x)OPO_4$  due to absorbing water from laboratory atmosphere. This is confirmed by taking XRPD after  $^{31}P$ -MAS-NMR measurement.

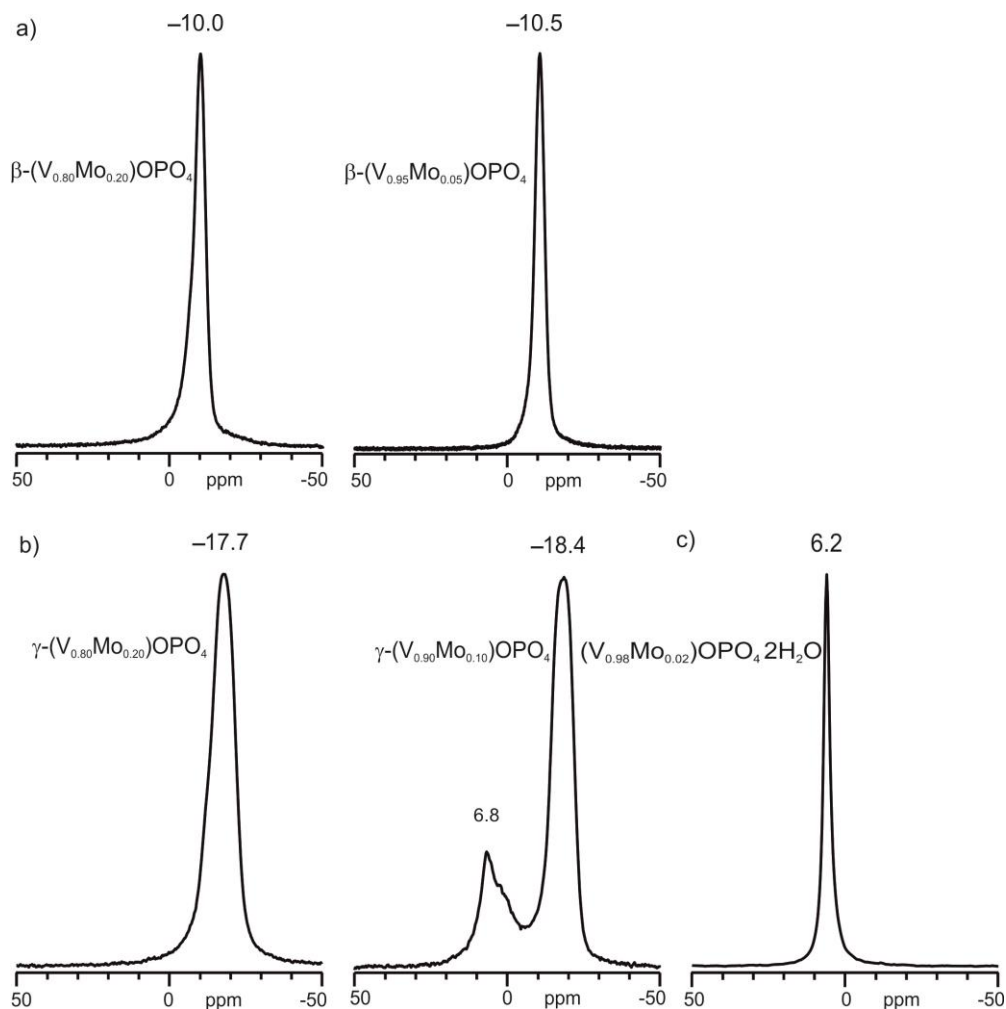


Figure 7.22 Room temperature  $^{31}P$ -MAS-NMR spectra of paramagnetic solid solution  $(V_{1-x}Mo_x)OPO_4$ ;  $x = 0.05, 0.20$ ,  $\beta$ - $VOPO_4$  structure type (a),  $x = 0.10, 0.20$ ,  $\gamma$ - $VOPO_4$  structure type (b),  $x = 0.02$ ,  $VOPO_4 \cdot 2H_2O$  structure type (c). In fig (b) the impurity signal at 6.8 ppm is due to partial conversion into  $VOPO_4 \cdot 2H_2O$  type [173] phase. All spectra were measured at rotation frequency of 15 KHz.

## 7.7 Conclusion

Thermodynamically stable single phase solid solution  $(V^{IV}_xV^{V}_{1-2x}Mo^{VI}_x)OPO_4$ ;  $\beta$ - $VOPO_4$  structure type [161] for  $0.0 \leq x \leq 0.30$  is obtained by SCS followed by heating the combustion products in air. The temperature required to obtain the thermodynamically stable phase decreased with increasing Mo concentration. The lower phase boundary

compound  $(V_{1-x}Mo_x)OPO_4$  ( $x = 0$ ) was obtained at 725 °C and the upper phase boundary compound ( $x = 0.30$ ) was obtained at 600 °C in air. A thermodynamically metastable  $\gamma$ -VOPO<sub>4</sub> structure type solid solution is obtained for  $0.0 \leq x \leq 0.20$  at lower temperature then  $\beta$ -type solid solution (Figure 7.23).

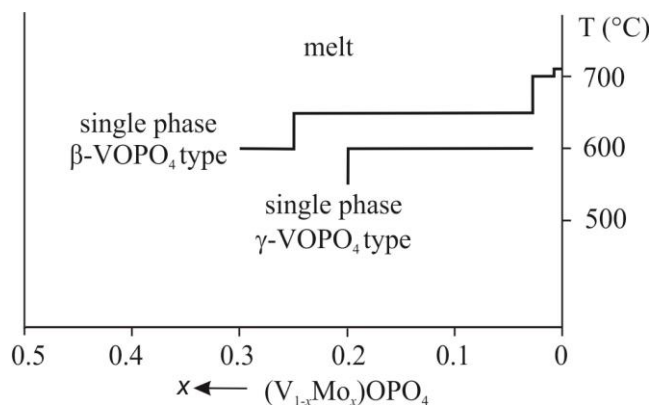


Figure 7.23 Structure types, their homogeneity ranges, and formation temperatures in the quasi-binary system MoOPO<sub>4</sub>-VOPO<sub>4</sub>.

The color of the members of the Mo substituted  $\beta$ -VOPO<sub>4</sub> type solid solution revealed the existence of  $V^{4+}$  within the structure which is identified by the weak and broad IVCT ( $V^{4+} \rightarrow V^{5+}$ ) electronic transition observed around at  $\tilde{\nu} = 14300 \text{ cm}^{-1}$  and broad LMCT [ $O^{2-}(s,p) \rightarrow V^{5+}(d)$ ] absorption band observed at  $\tilde{\nu} = 23500$  (shoulder at 25500)  $\text{cm}^{-1}$ . The variation of lattice parameters is also noticed which is similar to tungsten substituted  $\alpha_{II}$ -VOPO<sub>4</sub> structure type solid solution. Furthermore, the unexpected crystal chemical combination of  $V^{5+}$  to  $V^{4+}/Mo^{6+}$  is also supported by EPR, and the conductivity measurement. <sup>31</sup>P-MAS-NMR spectra of  $\beta$ -type solid solution showed single isotropic resonance which corroborate the crystal structure. For Mo substituted  $\gamma$ -VOPO<sub>4</sub> structure type solid solution the single isotropic resonance is observed instead of two which might be attributed to single metal site occupancy by Mo (only octahedra) out of two metal sites. The resonance signals are shifted to the up field with increasing Mo concentration due to inductive effect. Several further metastable polymorphs ( $\alpha_I$ -,  $\alpha_{II}$ -,  $\gamma$ -,  $\omega$ -,  $\omega$  (ht)-,  $\epsilon$ -VOPO<sub>4</sub> structure type) were also observed as intermediates steps during the heating procedure after SCS whereas only the  $\alpha_I$ -form was obtained during the synthesis of tungsten substituted VOPO<sub>4</sub>. The metastable polymorphs are sensitive to air. They absorb water at laboratory environment and transformed into the dihydrated phase reversibly.

## 8 Metal(III) tungstenyl(VI) ortho-pyrophosphates

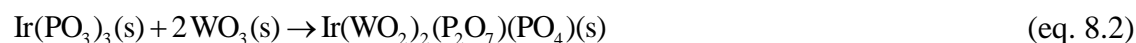
### 8.1 Introduction

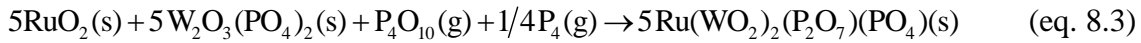
A plethora of anhydrous mixed transition metal phosphates are reported in literature [1, 2, 78]. The highest numbers of examples are known for mixed transition metals with combinations of oxidation states (II, II), (II, III), and (II, IV). Phosphates with cations in the oxidation states (I, II), (I, III), and (I, IV) are similarly well investigated. There are also some examples of anhydrous phosphates with cations in the oxidation states (I, V), (II, V), and (IV, V). According to literature the hexavalent transition metals, molybdenum or tungsten form mixed metal phosphates only with tetravalent zirconium [223, 224]. Phosphates with mixed transition metals containing hexavalent tungsten besides trivalent cation were hitherto completely unknown. First hints on vanadium(III) tungstenyl(VI) orthopyrophosphate  $V^{III}(W^{VI}O_2)_2(P_2O_7)(PO_4)$  were obtained during the studies on solid solution formation between  $V^VOPO_4$  and  $W^VOPO_4$  [197, this thesis]. On the other hand, only very few anhydrous transition metal phosphates show the presence of both ortho- and pyrophosphate units within their structures. One example is provided via partial substitution of molybdenum by tungsten in  $KMo^{IV}_2O(P_2O_7)(PO_4)$  [225].

In this chapter two different synthesis techniques, SCS and vapor phase moderated solid state reactions as well as single crystal structure analysis of some of the title compounds are reported. In addition, characterization of some members of this class of phosphates was carried out by electron diffraction, magnetic measurements, XPS, EPR,  $^{31}P$ -MAS-NMR and UV/Vis/NIR spectra.

### 8.2 Synthesis and crystallization

The new polynary phosphates  $M^{III}(W^{VI}O_2)_2(P_2O_7)(PO_4)$  ( $M$ : V, Cr, Mo, Ru, Rh, Ir) are thermodynamically stable solids which can be obtained from various starting materials by vapor phase moderated solid state reactions in sealed evacuated silica tubes ( $l = 11$  cm,  $d = 1.5$  cm) in the temperature range 800 to 950 °C (see Table 8.1 and Figure 8.3) according to (eq. 8.1) to (eq. 8.4). Small amounts of  $Cl_2$  are used as mineralizer.





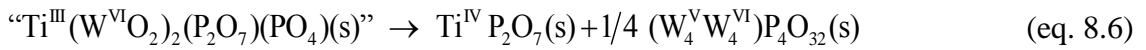
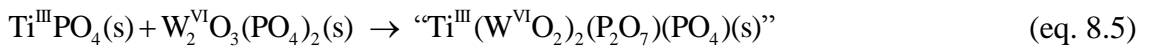
Appropriate amounts of the corresponding reactants (see Table 8.1) were finely ground in an agate mortar and transferred to the cleaned and dry silica tube (preheated at 800 °C for about five hours). The charged tubes were then evacuated and sealed under vacuum. Subsequently, the ampoules containing the reaction mixture were preheated at 550 °C for two days prior to the final equilibration temperature. An argon filled glove bag was used for manipulation of  $\text{P}_4\text{O}_{10}$  due to its hygroscopic nature.

Table 8.1 Experiments aiming at the synthesis of phosphates  $M^{\text{III}}(\text{W}^{\text{VI}}\text{O}_2)_2(\text{P}_2\text{O}_7)(\text{PO}_4)$  via vapor phase moderated solid state reactions in sealed ampoules using  $\text{Cl}_2$  (from  $\text{PtCl}_2$ ) as mineralizer, heating protocol  $\vartheta$  (°C) and  $t$  (d).

<i>M</i>	Starting Materials	Amount (mmol)	$\vartheta$ (°C); $t$ (d)	$\text{PtCl}_2$ (mg)	Reaction Products (according to IP-Guinier-photographs)
V <sup>a)</sup>	$\text{VPO}_4$ $\text{W}_2\text{O}_3(\text{PO}_4)_2$	(0.43) (0.43)	800; 8	6.0	$\text{V}^{\text{III}}(\text{W}^{\text{VI}}\text{O}_2)_2(\text{P}_2\text{O}_7)(\text{PO}_4)$
V <sup>a)</sup>	$\text{VOPO}_4$ $\text{WOPO}_4$	(0.40) (0.80)	800; 7	5.0	$\text{V}^{\text{III}}(\text{W}^{\text{VI}}\text{O}_2)_2(\text{P}_2\text{O}_7)(\text{PO}_4)$
V <sup>b)</sup>	$\text{VOPO}_4$ $\text{WOPO}_4$	(0.40) (0.60)	800; 8	20.5	$(\text{V}^{0.6\text{III}}\text{V}^{0.4\text{IV}})(\text{V}^{\text{IV}}\text{O}_2)_{0.2}(\text{W}^{\text{VI}}\text{O}_2)_{1.8}(\text{P}_2\text{O}_7)(\text{PO}_4)$
Cr <sup>a)</sup>	$\text{CrPO}_4$ $\text{W}_2\text{O}_3(\text{PO}_4)_2$	(0.50) (0.50)	950; 5	6.7	$\text{Cr}^{\text{III}}(\text{WO}_2)_2(\text{P}_2\text{O}_7)(\text{PO}_4)$
Cr <sup>b)</sup>	$\text{CrPO}_4$ $\text{W}_2\text{O}_3(\text{PO}_4)_2$	(0.67) (0.50)	950; 5	6.6	$\text{Cr}^{\text{III}}(\text{WO}_2)_2(\text{P}_2\text{O}_7)(\text{PO}_4)$ , $(\text{W}^{\text{VI}}_{0.87}\text{Cr}^{\text{III}}_{0.17}\text{O}_3)_8(\text{PO}_2)_4$ <sup>d)</sup>
Ru	$\text{RuO}_2$ $\text{W}_2\text{O}_3(\text{PO}_4)_2$ $\text{P}_4\text{O}_{10}$ $\text{P}_4$	(0.58) (0.58) (0.12) (0.03)	950; 13	6.7	$\text{Ru}^{\text{III}}(\text{WO}_2)_2(\text{P}_2\text{O}_7)(\text{PO}_4)$
Rh	$\text{RhPO}_4$ $\text{W}_2\text{O}_3(\text{PO}_4)_2$	(0.25) (0.25)	950; 6	5.5	$\text{Rh}^{\text{III}}(\text{WO}_2)_2(\text{P}_2\text{O}_7)(\text{PO}_4)$
Ir	$\text{Ir}(\text{PO}_3)_3$ $\text{WO}_3$	(0.25) (0.50)	875; 6	6.9	$\text{Ir}^{\text{III}}(\text{WO}_2)_2(\text{P}_2\text{O}_7)(\text{PO}_4)$
Mo	$\text{MoO}_2$ $\text{W}_2\text{O}_3(\text{PO}_4)_2$ $\text{P}_4\text{O}_{10}$ $\text{P}_4$	(0.60) (0.58) (0.12) (0.03)	900; 9	5.9	$\text{Mo}^{\text{III}}(\text{W}^{\text{VI}}\text{O}_2)_2(\text{P}_2\text{O}_7)(\text{PO}_4)$ , $\text{W}^{\text{V}}\text{OPO}_4$ , $\text{P}_4\text{W}^{\text{V,VI}}_8\text{O}_{32}$ <sup>c)</sup> , $\text{Mo}^{\text{IV}}\text{P}_2\text{O}_7$
Ti	$\text{TiPO}_4$ $\text{W}_2\text{O}_3(\text{PO}_4)_2$	(0.50) (0.50)	950; 7	160 (I <sub>2</sub> )	$\text{Ti}^{\text{IV}}\text{P}_2\text{O}_7$ , $\text{P}_8\text{W}^{\text{V,VI}}_{12}\text{O}_{52}$ <sup>e)</sup>
Sb <sup>e)</sup>	$\text{Sb}_2\text{O}_3$ $\text{W}_2\text{O}_3(\text{PO}_4)_2$ $(\text{NH}_4)_2\text{HPO}_4$	(0.50) (1.00) (1.01)	200; 0.2 400; 2 650; 2 750; 2 800; 5 900; 3		$o\text{-W}_2\text{O}_3(\text{PO}_4)_2$ , $\text{SbPO}_4$ $o\text{-W}_2\text{O}_3(\text{PO}_4)_2$ , phase X2 <sup>f)</sup> $o\text{-W}_2\text{O}_3(\text{PO}_4)_2$ , $m\text{-W}_2\text{O}_3(\text{PO}_4)_2$ , phase X2 <sup>f)</sup> $m\text{-W}_2\text{O}_3(\text{PO}_4)_2$ , $\text{SbOPO}_4$

<sup>a)</sup> upper phase boundary, <sup>b)</sup> lower phase boundary, <sup>c)</sup> MPTB with  $m = 4$  [95], <sup>d)</sup> chromium doped MPTB type with  $m = 4$  [see Chapter 10], <sup>e)</sup> solid state reaction in air, <sup>f)</sup> see figure Figure 14.6 (Appendix).

Experiments aiming at the synthesis of  $\text{Mo}^{\text{III}}(\text{W}^{\text{VI}}\text{O}_2)_2(\text{P}_2\text{O}_7)(\text{PO}_4)$  led to four phase mixtures of  $\text{Mo}^{\text{IV}}\text{P}_2\text{O}_7$  [207],  $\text{W}^{\text{V}}\text{OPO}_4$  [90, 91, this thesis], and  $(\text{W}^{\text{V},\text{VI}}\text{O}_3)_8(\text{PO}_2)_4$  [95] along with the target compound (see Figure 14.7). Experiments for the synthesis of the  $\text{Sb}^{3+}$  containing phosphate led to the formation of  $o\text{-W}_2\text{O}_3(\text{PO}_4)_2$ ,  $m\text{-W}_2\text{O}_3(\text{PO}_4)_2$ , and phase X2 (unknown phase, see Figure 14.6 and Table 8.1 ) at 750 °C. This unknown phase is stable up to 850 °C. Upon further heating the mixture leads to the fully oxidized products  $\text{SbOPO}_4$  [226] and  $m\text{-W}_2\text{O}_3(\text{PO}_4)_2$ . Instead of “ $\text{Ti}^{\text{III}}(\text{W}^{\text{VI}}\text{O}_2)_2(\text{P}_2\text{O}_7)(\text{PO}_4)$ ” the formation of  $\text{Ti}^{\text{IV}}\text{P}_2\text{O}_7$  [227] and  $(\text{W}^{\text{V},\text{VI}}\text{O}_3)_{12}(\text{P}_2\text{O}_4)_4$  [98] was observed, obviously due to the redox reaction (eq. 8.6).



The formation of the mixed ortho-pyrophosphate,  $\text{V}^{\text{III}}(\text{W}^{\text{VI}}\text{O}_2)_2(\text{P}_2\text{O}_7)(\text{PO}_4)$  from two orthophosphates,  $\text{V}^{\text{V}}\text{OPO}_4$  and  $\text{W}^{\text{V}}\text{OPO}_4$  can be described as a combined acid-base (Lux-Flood [228, 229]) and redox reaction as shown in (eq. 8.7) and (eq. 8.8).



Eventually, a small homogeneity range was observed for  $(\text{V}_{1-x}\text{W}_x)\text{OPO}_4$  in the range  $0.60 \leq x \leq 0.67$  where the upper phase boundary composition ( $\text{V}:\text{W} = 1:2$ ) is  $\text{V}(\text{WO}_2)(\text{P}_2\text{O}_7)(\text{PO}_4)$  according to (eq. 8.4) and the lower phase boundary composition ( $\text{V}:\text{W} = 2:3$ ) is  $\text{V}(\text{VO}_2)_{0.2}(\text{WO}_2)_{1.8}(\text{P}_2\text{O}_7)(\text{PO}_4)$  according to (eq. 8.9) (see Table 8.1).



Reference experiments with the ratio of chromium and tungsten, at 1:2 (UPB) and 2:3 (LPB) led to the formation of single phase  $\text{Cr}(\text{WO}_2)_2(\text{P}_2\text{O}_7)(\text{PO}_4)$  and two phase mixtures ( $\text{Cr}(\text{WO}_2)_2(\text{P}_2\text{O}_7)(\text{PO}_4)$  and  $(\text{Cr}_{1/6}\text{W}_{5/6}\text{O}_3)_8(\text{PO}_2)_4$  [MPTB type with  $m = 4$ , see Chapter 10]), respectively (see Table 8.1 and Figure 8.1).

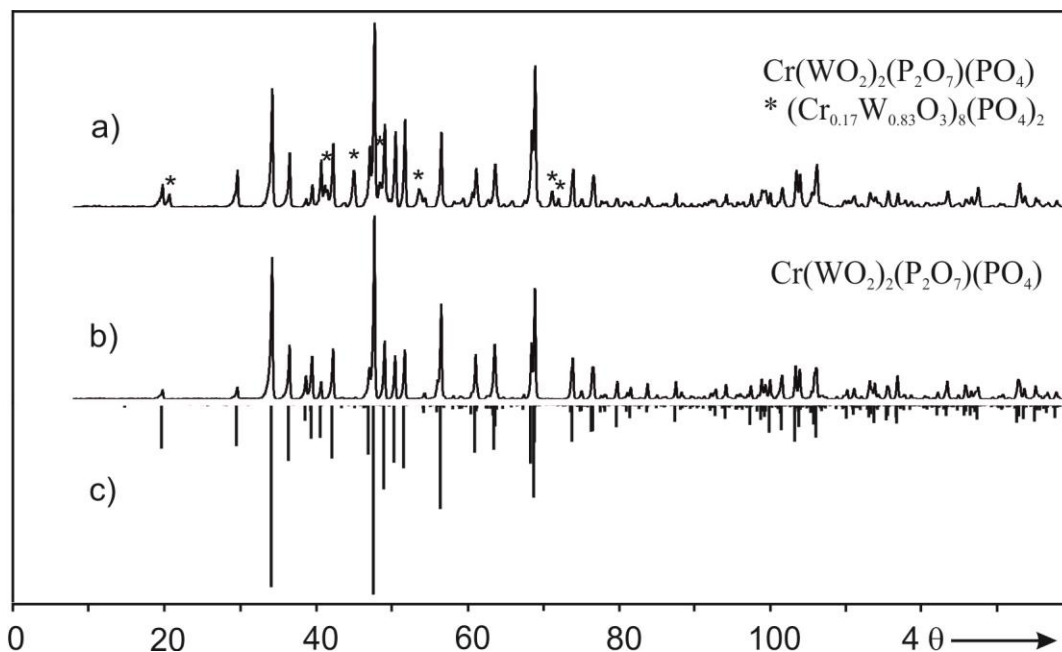


Figure 8.1 Comparison of Guinier photographs of products from experiments aiming at the synthesis of  $\text{Cr}^{\text{III}}(\text{W}^{\text{VI}}\text{O}_2)_{1.8}(\text{Cr}^{\text{III}}\text{O}_2)_{0.2}(\text{P}_2\text{O}_7)(\text{PO}_4)$  (a) and  $\text{Cr}(\text{WO}_2)_2(\text{P}_2\text{O}_7)(\text{PO}_4)$  (b) to simulated XRPD based on structure data of  $\text{Rh}(\text{WO}_2)_2(\text{P}_2\text{O}_7)(\text{PO}_4)$  [this thesis] with adjusted lattice parameters (c). Asterisks indicate mixed-metal MPTB phase ( $m = 4$ )  $(\text{Cr}_{0.17}\text{W}_{0.83}\text{O}_3)_8(\text{PO}_2)_4$  [see Chapter 10].

The existence of a narrow homogeneity range for vanadium tungstenyl(VI) orthophosphate-pyrophosphate is also observed in SCS experiments followed by subsequent annealing at various oxygen partial pressures. Heating the reaction intermediate after combustion at two different oxygen partial pressures,  $p(\text{O}_2) = 1000 \text{ ppm O}_2$  and  $p(\text{O}_2) \approx 20 \text{ ppm}$  (4N argon flow), leads to different reaction products, depending on the molar ratio of  $n(\text{V}) : n(\text{W})$  in the starting materials. The oxygen pressure was controlled via potentiometric measurement (SGM5EL  $\text{ZrO}_2$  electrolysis cell and SGM7 oxygen analyzer; ZIROX<sup>®</sup> company, Greifswald, Germany, [230, 231]). At the reduced oxygen pressure, at molar ratio  $n(\text{V}):n(\text{W}) = 1:2$  the upper phase boundary, ( $x = 0.67$ ) leads to formation of the single-phase product,  $\text{V}^{\text{III}}(\text{W}^{\text{VI}}\text{O}_2)_2(\text{P}_2\text{O}_7)(\text{PO}_4)$ . Whereas for the molar ratio  $n(\text{V}):n(\text{W}) = 2:3$  (lower phase boundary,  $x = 0.60$ ) a mixture of  $\text{V}^{\text{III}}(\text{W}^{\text{VI}}\text{O}_2)_2(\text{P}_2\text{O}_7)(\text{PO}_4)$  and  $(\text{V}_{0.17}\text{W}_{0.83}\text{O}_3)_8(\text{PO}_2)_4$  [197, Chapter 10] was observed. However, at higher the oxygen pressure ( $p(\text{O}_2) = 1000 \text{ ppm}$ ) the lower phase boundary composition leads to formation of  $(\text{V}^{\text{III}}_{0.6}\text{V}^{\text{IV}}_{0.4})(\text{V}^{\text{IV}}\text{O}_2)_{0.2}(\text{W}^{\text{VI}}\text{O}_2)_{1.8}(\text{P}_2\text{O}_7)(\text{PO}_4)$  (Figure 8.2 and Table 8.2) as single phase product. Here the higher oxygen partial pressure ( $p(\text{O}_2) = 1000 \text{ ppm}$ ) partially oxidizes  $\text{V}^{3+}$  to  $\text{V}^{4+}$ .

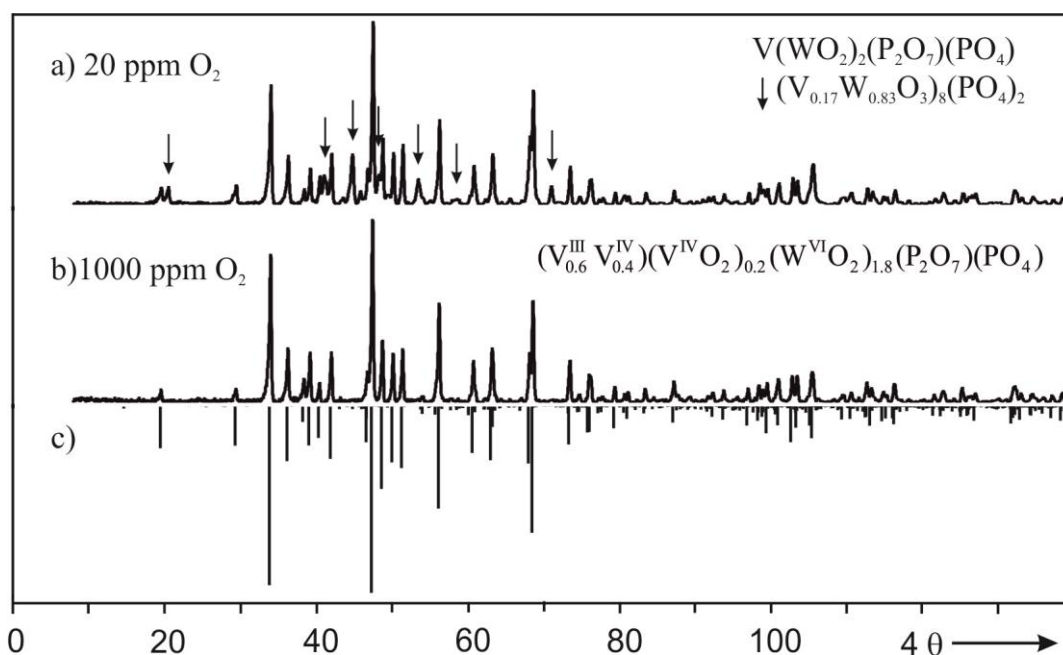


Figure 8.2 Comparison of Guinier photographs of products from experiments aiming at the synthesis of the lpb composition  $(V_{0.6}^{III}V_{0.4}^{IV})(W^{VI}O_2)_{1.8}(V^{III}O_2)_{0.2}(P_2O_7)(PO_4)$  with  $x = 0.60$  at ca. 20 ppm  $O_2$  (a) and at 1000 ppm  $O_2$  (b), and simulated XRPD pattern of  $V(WO_2)_2(P_2O_7)(PO_4)$  (c), down arrows in (a) indicate mixed-metal MPTB  $(V_{0.17}W_{0.83}O_3)_8(PO_2)_4$  [197, Chapter 10].

SCS followed by subsequent heating of the reaction intermediate after combustion was applied to synthesis of phosphates  $M^{III}(W^{VI}O_2)_2(P_2O_7)(PO_4)$  with  $M$ :  $Sc^{3+}$ ,  $V^{3+}$ ,  $Cr^{3+}$ ,  $Fe^{3+}$ , and  $In^{3+}$  (see Table 8.2). The  $V^{3+}$  containing compound was synthesized by subsequent heating under reduced oxygen pressure ( $p(O_2) \approx 20$  ppm i.e. 4N argon flow, see Table 8.2). Heating at higher oxygen pressure would oxidize  $V^{3+}$ . The mixed ortho-pyrophosphates  $M^{III}(W^{VI}O_2)_2(P_2O_7)(PO_4)$  do not form with  $M = RE^{3+}$  (La, Nd, Sm, Gd, Yb, see Table 8.2).  $RE^{3+}$  are just too big to fit into the octahedral voids. After prolonged heating at temperatures up to 1000 °C solidified melts were obtained. Their XRPD pattern showed the reflections of  $REPO_4$ ,  $m-W_2O_3(PO_4)_2$  and weak reflections of  $WO_3$  which is one of the thermal decomposition products of  $m-W_2O_3(PO_4)_2$ . For SCS the precursor materials  $NH_4VO_3$ ,  $(NH_4)_6W_{12}O_{39} \cdot 4.8H_2O$ ,  $Cr(NO_3)_3 \cdot 9H_2O$ , and  $(NH_4)_2HPO_4$  were used as source of  $V_2O_5$ ,  $WO_3$ ,  $Cr_2O_3$  and  $P_4O_{10}$ , respectively (see Table 8.2). Glycine and nitric acid were used as fuel and oxidizer, accordingly. The ratio of  $n(\text{metal}):n(\text{glycine}):n(\text{HNO}_3) = 1:3:8$  was used. The procedure for SCS was similar to the descriptions in sections 2.7 and 6.3.

Table 8.2 Experiments aiming at the synthesis of phosphates  $M^{\text{III}}(\text{W}^{\text{VI}}\text{O}_2)_2(\text{P}_2\text{O}_7)(\text{PO}_4)$  via SCS followed by heating in air. For the vanadium phosphate various  $p(\text{O}_2)$  were used, heating protocol  $\vartheta$  ( $^{\circ}\text{C}$ ) and  $t$  (d).

<i>M</i>	Starting Materials (mmol)	$\vartheta$ ( $^{\circ}\text{C}$ ); <i>t</i> (d)	Reaction Products (according to IP-Guinier photographs)
Al	$\text{Al}(\text{NO}_3)_3 \cdot 9\text{H}_2\text{O}$	(3.0) 400; 0.07	Keggin <sup>h</sup>
	$(\text{NH}_4)_6\text{W}_{12}\text{O}_{39} \cdot 4.8\text{H}_2\text{O}$	(0.50) 550; 1	“ <i>t</i> - $\text{WO}_3$ ” <sup>f</sup>
	$(\text{NH}_4)_2\text{HPO}_4$	(9.0) 650; 1	“ <i>t</i> - $\text{WO}_3$ ” <sup>f</sup>
		700; 2	“ <i>t</i> - $\text{WO}_3$ ” <sup>f</sup>
		850; 1	<i>m</i> - $\text{W}_2\text{P}_2\text{O}_{11}$ , <i>o</i> - $\text{W}_2\text{P}_2\text{O}_{11}$
	950; 6	<i>m</i> - $\text{W}_2\text{P}_2\text{O}_{11}$	
Sc	$\text{Sc}_2\text{O}_3$	(0.66) 500; 0.07	amorphous
	$(\text{NH}_4)_6\text{W}_{12}\text{O}_{39} \cdot 4.8\text{H}_2\text{O}$	(0.23) 600; 1	“ <i>t</i> - $\text{WO}_3$ ” <sup>f</sup>
	$(\text{NH}_4)_2\text{HPO}_4$	(4.00) 700; 5	“ <i>t</i> - $\text{WO}_3$ ” <sup>f</sup>
		850; 3	“ <i>t</i> - $\text{WO}_3$ ” <sup>f</sup> , <i>m</i> - $\text{W}_2\text{P}_2\text{O}_{11}$
	950; 4	$\text{Sc}^{\text{III}}(\text{W}^{\text{VI}}\text{O}_2)_2(\text{P}_2\text{O}_7)(\text{PO}_4)$ , <i>m</i> - $\text{W}_2\text{P}_2\text{O}_{11}$	
V <sup>a)</sup>	$\text{NH}_4\text{VO}_3$	(9.90) 400; 0.06	Keggin <sup>h</sup>
	$(\text{NH}_4)_6\text{W}_{12}\text{O}_{39} \cdot 4.8\text{H}_2\text{O}$	(1.68) 400; 0.3	Keggin <sup>h</sup> “ <i>c</i> - $\text{WO}_3$ ” <sup>g</sup>
	$(\text{NH}_4)_2\text{HPO}_4$	(30.0) 425; 1	“ <i>c</i> - $\text{WO}_3$ ” <sup>g</sup>
		600; 1	“ <i>c</i> - $\text{WO}_3$ ” <sup>g</sup>
		780; 2 <sup>c)</sup>	$(\text{V}_{0.33}\text{W}_{0.67})\text{OPO}_4$ <sup>i)</sup>
	900; 2 <sup>c)</sup>	$\text{V}^{\text{III}}(\text{W}^{\text{VI}}\text{O}_2)_2(\text{P}_2\text{O}_7)(\text{PO}_4)$	
V <sup>b)</sup>	$\text{NH}_4\text{VO}_3$	(0.80) 400; 0.06	Keggin <sup>h</sup>
	$(\text{NH}_4)_6\text{W}_{12}\text{O}_{39} \cdot 4.8\text{H}_2\text{O}$	(0.10) 400; 0.3	Keggin <sup>h</sup> , “ <i>c</i> - $\text{WO}_3$ ” <sup>g</sup>
	$(\text{NH}_4)_2\text{HPO}_4$	(2.00) 850; 9 <sup>c)</sup>	$\text{V}^{\text{III}}(\text{W}^{\text{VI}}\text{O}_2)_2(\text{P}_2\text{O}_7)(\text{PO}_4)$ , $(\text{W}_{0.83}\text{V}_{0.17}\text{O}_3)_8(\text{PO}_2)_4$
		950; 3 <sup>d)</sup>	$(\text{V}^{\text{III}}_{0.6}\text{V}^{\text{IV}}_{0.4})(\text{W}^{\text{VI}}\text{O}_2)_{1.8}(\text{V}^{\text{IV}}\text{O}_2)_{0.2}(\text{P}_2\text{O}_7)\text{PO}_4$
Cr	$\text{Cr}(\text{NO}_3)_3 \cdot 9\text{H}_2\text{O}$	(2.85) 400; 0.06	Keggin <sup>h</sup>
	$(\text{NH}_4)_6\text{W}_{12}\text{O}_{39} \cdot 4.8\text{H}_2\text{O}$	(0.47) 450; 1	amorphous
	$(\text{NH}_4)_2\text{HPO}_4$	(8.55) 650; 1	“ <i>c</i> - $\text{WO}_3$ ” <sup>g</sup>
		800; 2	“ <i>c</i> - $\text{WO}_3$ ” <sup>g</sup>
		850; 2	$(\text{Cr}_{0.33}\text{W}_{0.67})\text{OPO}_4$ <sup>i)</sup>
	950; 3	$\text{Cr}^{\text{III}}(\text{W}^{\text{VI}}\text{O}_2)_2(\text{P}_2\text{O}_7)(\text{PO}_4)$	
Fe	$\text{FePO}_4$	(6.60) 400; 0.06	Keggin <sup>h</sup>
	$(\text{NH}_4)_6\text{W}_{12}\text{O}_{39} \cdot 4.8\text{H}_2\text{O}$	(1.12) 450; 1	amorphous
	$(\text{NH}_4)_2\text{HPO}_4$	(13.4) 700; 2	“ <i>c</i> - $\text{WO}_3$ ” <sup>g</sup>
		800; 10	$(\text{Cr}_{0.33}\text{W}_{0.67})\text{OPO}_4$ <sup>i)</sup>
	900; 3	$\text{Fe}^{\text{III}}(\text{W}^{\text{VI}}\text{O}_2)_2(\text{P}_2\text{O}_7)(\text{PO}_4)$	
In	$\text{InCl}_3$	(2.37) 400; 0.06	Keggin <sup>h</sup>
	$(\text{NH}_4)_6\text{W}_{12}\text{O}_{39} \cdot 4.8\text{H}_2\text{O}$	(0.40) 500; 1	amorphous
	$(\text{NH}_4)_2\text{HPO}_4$	(7.11) 600; 1	“ <i>c</i> - $\text{WO}_3$ ” <sup>g</sup>
		700; 5	“ <i>c</i> - $\text{WO}_3$ ” <sup>g</sup>
		800; 6	“ <i>c</i> - $\text{WO}_3$ ” <sup>g</sup> , <i>m</i> - $\text{W}_2\text{P}_2\text{O}_{11}$
	900; 3	$\text{In}^{\text{III}}(\text{W}^{\text{VI}}\text{O}_2)_2(\text{P}_2\text{O}_7)(\text{PO}_4)$ , <i>m</i> - $\text{W}_2\text{P}_2\text{O}_{11}$	
Lu	$\text{LuCl}_3 \cdot 6\text{H}_2\text{O}$	(0.90) 500; 0.17	
	$(\text{NH}_4)_6\text{W}_{12}\text{O}_{39} \cdot 4.8\text{H}_2\text{O}$	(0.15) 600; 1	“ <i>c</i> - $\text{WO}_3$ ” <sup>g</sup>
	$(\text{NH}_4)_2\text{HPO}_4$	(2.73) 800; 4	$\text{LuPO}_4$ , <i>m</i> - $\text{W}_2\text{P}_2\text{O}_{11}$
		900; 168	$\text{LuPO}_4$ , <i>m</i> - $\text{W}_2\text{P}_2\text{O}_{11}$
	1000; 6 <sup>e)</sup>	$\text{LuPO}_4$ , <i>m</i> - $\text{W}_2\text{P}_2\text{O}_{11}$ , $\text{WO}_3$	
La	$\text{LaPO}_4$	(0.90) 500; 0.06	
	$(\text{NH}_4)_6\text{W}_{12}\text{O}_{39} \cdot 4.8\text{H}_2\text{O}$	(0.15) 600; 1	
	$(\text{NH}_4)_2\text{HPO}_4$	(1.82) 800; 2	
	950; 5 <sup>e)</sup>	$\text{LaPO}_4$ , $\text{W}_2\text{P}_2\text{O}_{11}$ , $\text{WO}_3$	



Nd	Nd(NO <sub>3</sub> ) <sub>3</sub> ·6H <sub>2</sub> O	(0.90)	500; 0.06	
	(NH <sub>4</sub> ) <sub>6</sub> W <sub>12</sub> O <sub>39</sub> ·4.8 H <sub>2</sub> O	(0.15)	600; 1	“c-WO <sub>3</sub> ” <sup>g)</sup>
	(NH <sub>4</sub> ) <sub>2</sub> HPO <sub>4</sub>	(2.73)	800; 4	NdPO <sub>4</sub> , <i>m</i> -W <sub>2</sub> O <sub>3</sub> (PO <sub>4</sub> ) <sub>2</sub>
			900; 7	NdPO <sub>4</sub> , <i>m</i> -W <sub>2</sub> O <sub>3</sub> (PO <sub>4</sub> ) <sub>2</sub>
			1000; 6 <sup>e)</sup>	NdPO <sub>4</sub> , <i>m</i> -W <sub>2</sub> O <sub>3</sub> (PO <sub>4</sub> ) <sub>2</sub> , WO <sub>3</sub>
Sm	SmPO <sub>4</sub>	(0.90)	500; 0.06	
	(NH <sub>4</sub> ) <sub>6</sub> W <sub>12</sub> O <sub>39</sub> ·4.8H <sub>2</sub> O	(0.15)	600; 0.2	
	(NH <sub>4</sub> ) <sub>2</sub> HPO <sub>4</sub>	(1.83)	700; 1	
			750; 2	
			900; 3	SmPO <sub>4</sub> , <i>m</i> -W <sub>2</sub> O <sub>3</sub> (PO <sub>4</sub> ) <sub>2</sub>
1000; 2 <sup>e)</sup>			SmPO <sub>4</sub> , <i>m</i> -W <sub>2</sub> P <sub>2</sub> O <sub>11</sub> , WO <sub>3</sub>	
Yb	YbPO <sub>4</sub>	(0.90)	500; 0.06	
	(NH <sub>4</sub> ) <sub>6</sub> W <sub>12</sub> O <sub>39</sub> ·4.8H <sub>2</sub> O	(0.15)	600; 0.2	
	(NH <sub>4</sub> ) <sub>2</sub> HPO <sub>4</sub>	(1.82)	700; 1	
			750; 2	YbPO <sub>4</sub> , <i>m</i> -W <sub>2</sub> O <sub>3</sub> (PO <sub>4</sub> ) <sub>2</sub>
			900; 3 <sup>e)</sup>	YbPO <sub>4</sub> , <i>m</i> -W <sub>2</sub> P <sub>2</sub> O <sub>11</sub> , WO <sub>3</sub>

a) upper phase boundary, b) lower phase boundary, c) under argon  $p(\text{O}_2) \approx 20$  ppm, d)  $p(\text{O}_2) = 1000$  ppm, e) about to melt, f) phosphates with structure type of tetragonal WO<sub>3</sub> [249] see Chapter 9, g) phosphates with structure type of cubic WO<sub>3</sub> [252, 253] see Chapter 9, h) (NH<sub>4</sub>)<sub>3</sub>[PW<sub>12</sub>O<sub>40</sub>]·*x*H<sub>2</sub>O [232] type, i) WOPO<sub>4</sub> structure type.

In the SCS process the reaction proceeds from the amorphous material through several intermediates to the final thermodynamically stable compound. A typical sequence of reaction intermediates shows with increasing temperature a Keggin type solid presumably (NH<sub>4</sub>)<sub>3</sub>[PW<sub>12</sub>O<sub>40</sub>]·*x*H<sub>2</sub>O → amorphous material → phosphate with ReO<sub>3</sub> related XRPD pattern [252, 253] ((*M*<sup>III</sup><sub>0.167</sub>W<sup>VI</sup><sub>0.333</sub>P<sup>V</sup><sub>0.50</sub>)O<sub>2.5</sub>□<sub>0.5</sub>; *M*: V, Cr, Fe, In) → phosphate with WOPO<sub>4</sub> structure type [90, this thesis] ((*M*<sup>III</sup><sub>0.333</sub>W<sup>VI</sup><sub>0.667</sub>)OPO<sub>4</sub>; *M*: V, Cr, Fe) → thermodynamically stable phase (*M*<sup>III</sup>(W<sup>VI</sup>O<sub>2</sub>)<sub>2</sub>(P<sub>2</sub>O<sub>7</sub>)(PO<sub>4</sub>); *M*: Sc, V, Cr, Fe, and In) as shown in Table 8.2. Formation of the solid reaction intermediates with cubic and tetragonal WO<sub>3</sub> structure type and WOPO<sub>4</sub> structure type will be discussed in Chapter 9. The XRPD patterns showing the sequential phase formation with temperature are shown in Figure 14.9 to Figure 14.11 (Appendix). The x-ray powder diffraction patterns and unit cell parameters of all the isotopic ortho-pyrophosphates are shown in Figure 8.3 and Table 8.3, respectively. Assigning of the Guinier photographs of the phosphates *M*(WO<sub>2</sub>)<sub>2</sub>(P<sub>2</sub>O<sub>7</sub>)(PO<sub>4</sub>) are provided in Table 14.38 to Table 14.47 (Appendix).

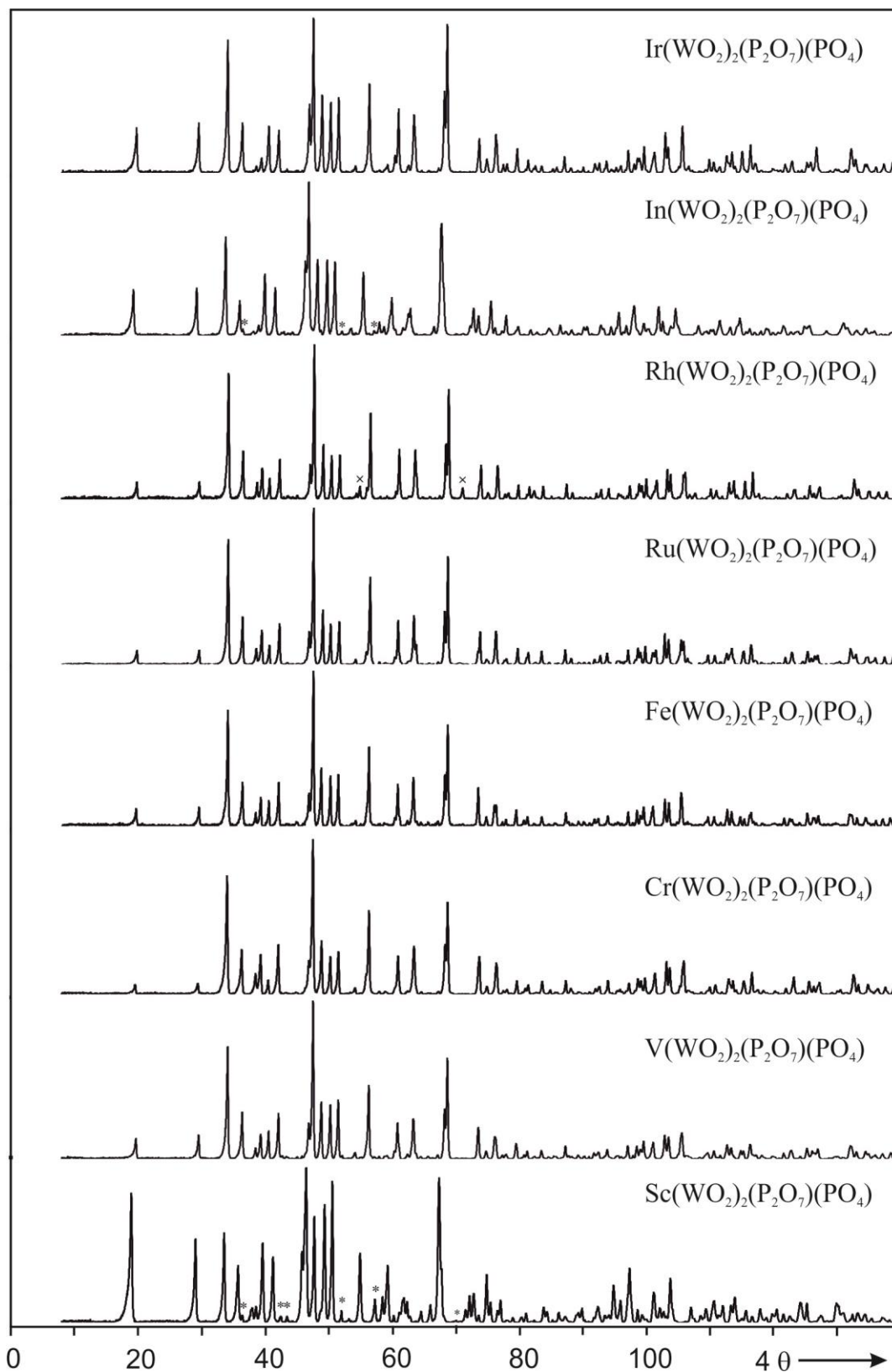


Figure 8.3 Comparison of the Guinier photographs of  $M^{\text{III}}(\text{W}^{\text{VI}}\text{O}_2)_2(\text{P}_2\text{O}_7)(\text{PO}_4)$  where  $M^{\text{III}}$ : Sc, V, Cr, Fe, Ru, Rh, In, and Ir. Small impurities of  $m\text{-W}_2\text{O}_3(\text{PO}_4)_2$  [76, 77, 78] and  $(\text{Rh}_{0.667}\text{W}_{0.333})\text{O}_2$  [233] are indicated by (\*) and ( $\times$ ), respectively.

Table 8.3 Lattice parameters and colors of anhydrous ortho-pyrophosphates  $M^{\text{III}}(\text{W}^{\text{VI}}\text{O}_2)_2(\text{P}_2\text{O}_7)(\text{PO}_4)$  ( $C2/c$ ,  $Z = 16$ , from IP-Guinier photographs,  $\text{Cu-K}\alpha_1$ ).

M	Color	$a$ (Å)	$b$ (Å)	$c$ (Å)	$\beta$ (°)
Sc	grey	38.210(7)	12.919(2)	9.608(2)	102.10(1)
V <sup>a)</sup>	brown	37.169(3)	12.7899(8)	9.476(1)	102.319(8)
V <sup>b)</sup>	brown	37.171(3)	12.788(1)	9.4852(8)	102.278(8)
Cr	green	37.016(3)	12.756(1)	9.428(1)	102.275(9)
Fe	blueish	37.187(4)	12.789(1)	9.484(1)	102.36(1)
Mo <sup>c)</sup>	bronze	37.355(7)	12.902(2)	9.550(2)	102.33(1)
Ru	bronze	37.054(4)	12.807(1)	9.454(1)	102.14(1)
Rh	olive green	37.043(3)	12.7786(9)	9.434(1)	102.245(2)
In	bluish	37.839(7)	12.930(3)	9.530(2)	102.15(2)
Ir	brown	37.113(2)	12.819(1)	9.4610(8)	102.314(6)

<sup>a)</sup> upper phase boundary  $\text{V}^{\text{III}}(\text{W}^{\text{VI}}\text{O}_2)_2(\text{P}_2\text{O}_7)(\text{PO}_4)$  <sup>b)</sup> lower phase boundary  $(\text{V}_{0.6}^{\text{III}}\text{V}_{0.4}^{\text{IV}})(\text{V}^{\text{IV}}\text{O}_2)_{0.2}(\text{W}^{\text{VI}}\text{O}_2)_{1.8}(\text{P}_2\text{O}_7)(\text{PO}_4)$

<sup>c)</sup> “ $\text{Mo}(\text{WO}_2)_2(\text{P}_2\text{O}_7)(\text{PO}_4)$ ” was formed besides several neighbouring phases ( $\text{WOPO}_4$ ,  $\text{MoP}_2\text{O}_7$ ,  $\text{W}_8\text{P}_4\text{O}_{32}$ , see Table 8.2). Therefore, its Mo/W ratio is not yet accurately established. The oxygen co-existence pressures of molybdenum and tungsten oxides [136] suggest  $\text{Mo}^{4+}$  besides  $\text{W}^{5+}$  and  $\text{W}^{6+}$ . Thus, a Mo/W ratio similar to the V/W ratio at the upper phase boundary seems reasonable.

Single crystals of  $M^{\text{III}}(\text{WO}_2)_2(\text{P}_2\text{O}_7)(\text{PO}_4)$ ;  $M^{\text{III}}$ : V, Ru, Rh (see Figure 8.4) were obtained during vapour phase moderated solid state reactions using  $\text{Cl}_2$  (from in situ decomposition of  $\text{PtCl}_2(\text{s}) \rightarrow \text{Pt}(\text{s}) + \text{Cl}_2(\text{g})$  at the synthesis temperature).

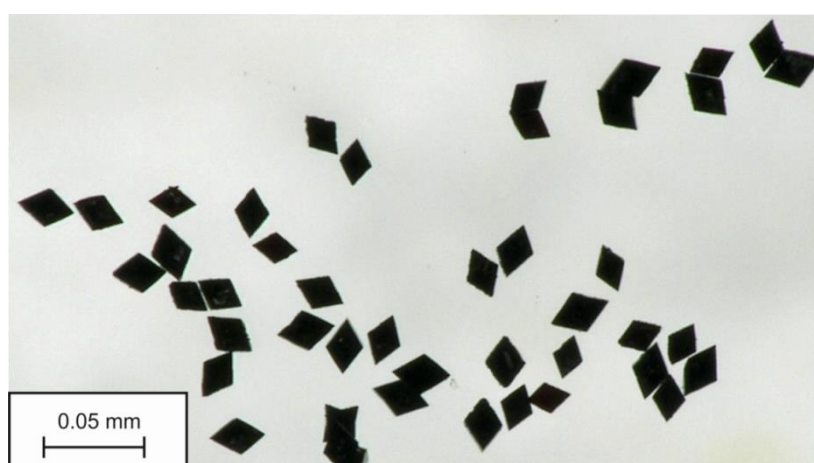


Figure 8.4 Microphotograph of brown crystals of  $\text{V}(\text{WO}_2)_2(\text{P}_2\text{O}_7)(\text{PO}_4)$  obtained by vapor phase moderated solid state reaction.

### 8.3 Single crystal structure analysis

Despite extended search all crystals under investigation turned out to be multiply intergrown. In case of  $V(WO_2)_2(P_2O_7)PO_4$  eventually a crystal showing only very small additional domains was found. Data were collected by a  $\kappa$ -CCD diffractometer (Enraf-Nonius Inc.) using the software HKL Denzo [177]. Data reduction and cell refinement were performed with the software HKL Scalepack [177]. Due to their weak intensity the additional domains were ignored during further data processing. An empirical (“multi-scan”) absorption correction was applied to the data set. The structure was solved in space group  $C2/c$  by Direct methods with SHELX-97 [123] which disclosed the metal and phosphorus sites as well as some oxygen atoms. After initial refinement cycles six and seven independent sites were localized for the metal and phosphorus atoms, respectively. The missing oxygen atoms were localized from subsequent  $\Delta$ -Fourier syntheses. Full-matrix least-squares refinement was carried out using SHELX-97 in the WinGX [124] framework. In the course of the refinement disorder V/W on metal sites  $M1$  to  $M6$  was introduced. In the refinement the overall ratio  $n(V):n(W)$  was constraint to the ideal chemical composition (SUMP in SHELX). It is quite remarkable, that the displacement ellipsoids for  $M5$  and  $M6$ , each site accommodating about 50% V and W, are about twice as large as the ellipsoids for  $M1$  to  $M4$  (about 75% W and 25% V). There is no hint on correlation of refinement parameters, e.g. s.o.f. and  $U_{ij}$  for sites  $M5$  and  $M6$ . Indeed vanadium and tungsten are occupying slightly different positions within the coordination polyhedra. Such an interpretation is in agreement with the tendency of  $W^{6+}$  to adopt off-center positions in octahedral environment, while coordination polyhedra around  $V^{3+}$  do generally not show such distortion. An refinement with split sites was unsuccessful.

X-ray diffraction data of  $Ru(WO_2)_2(P_2O_7)PO_4$  and  $Rh(WO_2)_2(P_2O_7)PO_4$  were collected on a Stoe IPDS diffractometer. Data collection and cell refinement were controlled by the software STOE X-AREA [234] and data reduction was performed using the software STOE X-RED [235]. The crystal structure analysis of  $Ru(WO_2)_2(P_2O_7)(PO_4)$  is obviously hampered by the low quality of diffraction data obtained from the highly intergrown crystals. Three domains with volumes of 88%, 10%, 2% were observed and accounted for in the refinement (TWIN with HKLF5 in SHELX).

The diffraction data was transformed (STOE X-RED) into a data file containing intensity data for all reflections of the three domains as HKLF5-1 format (SHELX). For the structure refinement coordinates of  $V(WO_2)_2(P_2O_7)PO_4$  were used as starting parameters. In contrast to the vanadium compound only small site disorder Ru/W was observed, with W preferring *M1* to *M4* and Ru sites *M5* and *M6*. Reasonable refinement of the Ru/W occupancy without high correlations between the overall scale factor, site occupation factors and displacement parameters was only possible after introducing the total number of ruthenium and tungsten atoms per unit cell as restraint (SUMP in SHELX-97). In the final stages of the refinement anisotropic displacement parameters were introduced for the metal and phosphorus sites. For oxygen atoms only isotropic displacement parameters were allowed, otherwise many of these atoms became “NPD”. It should be pointed out that without the high-angle reflections ( $2\theta_{\max} = 50^\circ$  instead of  $75^\circ$ ) no improvement in residual was observed and, even worse, most metal and phosphorus sites became “NPD”, too.

The single crystal data set for  $Rh(WO_2)_2(P_2O_7)(PO_4)$  is strongly affected by multiple intergrown domains. The structure refinement by using the HKLF5.1 file is not reasonable. Therefore, structure refinement was performed using the HKLF4 of only one domain data allowing only isotropic displacement parameters for the lighter atoms (P, O) and no mixed-occupancy of Rh/W.

The observed powder diffraction patterns of  $M(WO_2)_2(P_2O_7)(PO_4)$  with *M*: V, Ru, Rh are compared to the simulations which are based on the data from single crystal structure refinement in Figure 8.5. The powder patterns of phosphates  $M(WO_2)_2(P_2O_7)(PO_4)$  with *M*: Cr, Fe, Mo, In, Ir are nicely matched by simulations (see Appendix, Figure 14.12) based on mixed metal distribution of  $V(WO_2)_2(P_2O_7)(PO_4)$  structure model (see Table 8.5).

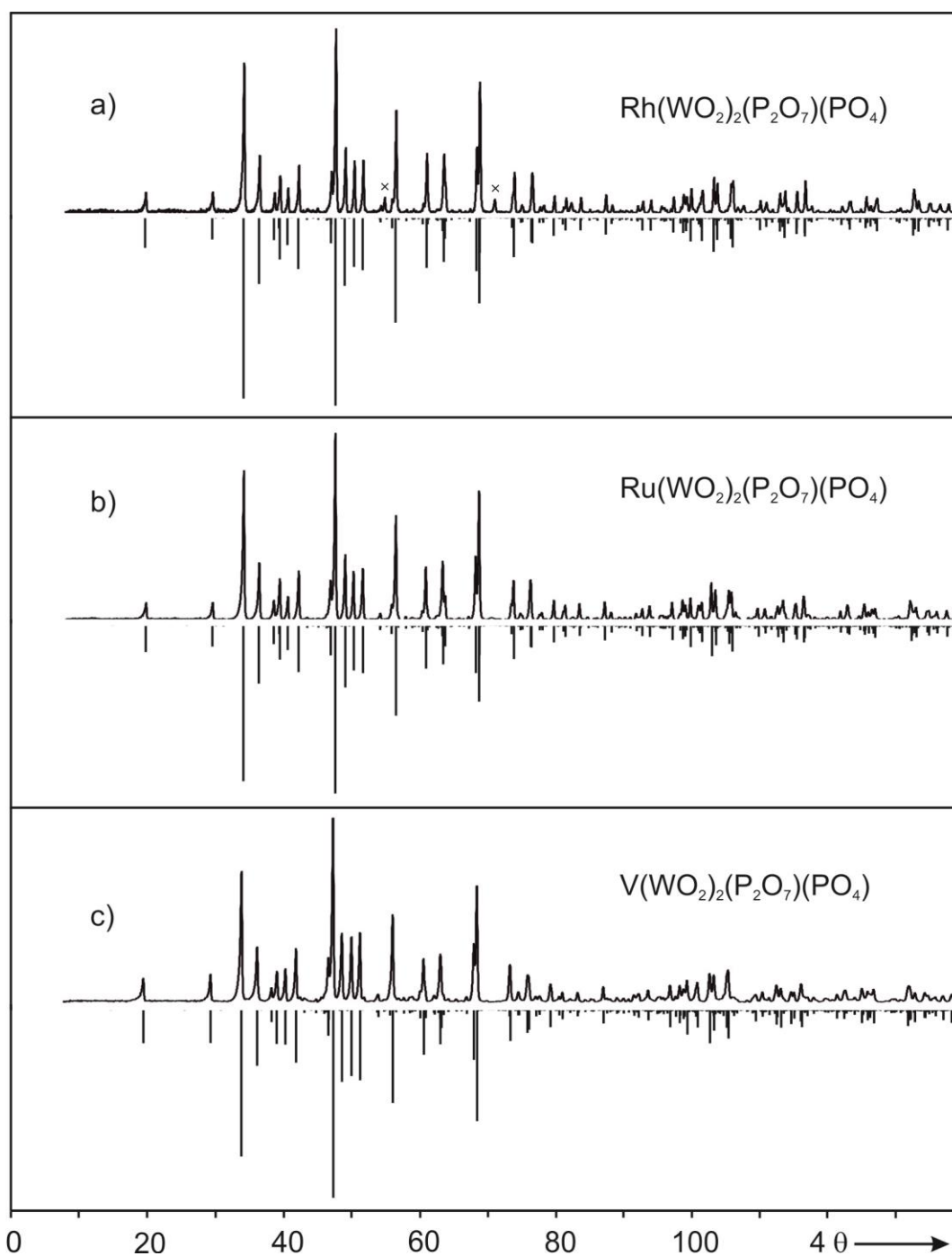


Figure 8.5 Guinier photographs of  $\text{Ru}(\text{WO}_2)_2(\text{P}_2\text{O}_7)(\text{PO}_4)$  (a),  $\text{Rh}(\text{WO}_2)_2(\text{P}_2\text{O}_7)(\text{PO}_4)$  (b), and  $\text{V}(\text{WO}_2)_2(\text{P}_2\text{O}_7)(\text{PO}_4)$  (c) obtained from vapor phase moderated solid state reactions (see Table 8.1), compared to the simulated diffraction pattern based on the models from the crystal structure refinements (Table 8.5 to Table 8.7). Crosses indicate small impurity of  $(\text{Rh}_{0.667}\text{W}_{0.333})\text{O}_2$  [233].

Details regarding single crystal data collection and structure refinements of  $V(WO_2)_2(P_2O_7)(PO_4)$ ,  $Ru(WO_2)_2(P_2O_7)(PO_4)$ , and  $Rh(WO_2)_2(P_2O_7)(PO_4)$  are summarized in Table 8.4. Atomic coordinates and selected inter-atomic distances are given in Table 8.5 to Table 8.8. Anisotropic displacement parameters for V and Ru compounds are provided in Table 14.36 and Table 14.37, respectively.

Table 8.4 Summary of crystallographic data and information on x-ray single crystal structure refinements of  $M(WO_2)_2(P_2O_7)(PO_4)$  with  $M$ : V, Ru, Rh.

Formula	$V(WO_2)_2(P_2O_7)(PO_4)$	$Ru(WO_2)_2(P_2O_7)(PO_4)$	$Rh(WO_2)_2(P_2O_7)(PO_4)$
$M_r$	751.53	801.66	803.50
Cryst. Size (mm <sup>3</sup> )	0.05 × 0.04 × 0.01	0.06 × 0.03 × 0.02	0.05 × 0.02 × 0.01
Crystal system	monoclinic	Monoclinic	monoclinic
Space group	$C2/c$ (15)	$C2/c$ (15)	$C2/c$ (15)
$a$ (Å) <sup>a)</sup>	37.169(3)	37.054(4)	37.043(3)
$b$ (Å) <sup>a)</sup>	12.7899(8)	12.807(1)	12.7768(9)
$c$ (Å) <sup>a)</sup>	9.476(1)	9.454(1)	9.434(1)
$\beta$ (°) <sup>a)</sup>	102.319(8)	102.139(12)	102.245(9)
$V$ (Å <sup>3</sup> ) <sup>a)</sup>	4401.5(7)	4386.44	4363.92(7)
$Z$	16	16	16
$D_{x\text{-ray}}$ (g cm <sup>-3</sup> )	4.56	4.84	4.90
$\mu(MoK\alpha)$ (cm <sup>-1</sup> )	22.34	22.73	23.08
$F(000)$	5376	5712	5728
$hkl$ range	$-59 \leq h \leq +59$ ; $-20 \leq k \leq +20$ ; $-15 \leq l \leq +15$	$-62 \leq h \leq +61$ ; $0 \leq k \leq +22$ ; $0 \leq l \leq +15$	$-58 \leq h \leq +58$ ; $-19 \leq k \leq +19$ ; $-13 \leq l \leq +14$
Theta ranges (°)	2.9 - 35.0	3.87 - 36.34	2.69 - 34.37
Absor. correction	multi-scan	numerical	numerical
Refl. measured	101357	10856	56097
Refl. unique	9610	10544	8919
$R_{int}$	0.082	-- <sup>b)</sup>	0.254
Param. refined	378	237	199
$R(F)/wR(F^2)$ <sup>c)</sup>	0.065 / 0.14	0.076 / 0.16	0.083 / 0.20
$[I > 2\sigma(I)]$			
$A, B$ <sup>c)</sup>	0.0, 590.88	0.0, 307.37	0.025, 0.0
GooF ( $F^2$ )	1.23	1.03	0.94
$\Delta\rho$ (max/min) (e Å <sup>-3</sup> )	4.37 / -3.54	4.03 / -5.46	5.90 / -3.90

<sup>a)</sup> lattice parameters from powder XRPD, <sup>b)</sup> for HKLF5-1 formate data file  $R_{int}$  is not generated, <sup>c)</sup>  $R_1 = \sum ||F_o| - |F_c|| / \sum |F_o|$ ,  $F^2 > 2\sigma(F^2)$ ;  $w = 1/[\sigma^2(F_o^2) + (A \cdot P)^2 + B \cdot P]$ ,  $P = (F_o^2 + 2F_c^2)/3$

Table 8.5 Atomic coordinates and isotropic displacement parameters ( $\text{\AA}^2$ ) with estimated standard deviations in parentheses of  $\text{V}(\text{WO}_2)_2(\text{P}_2\text{O}_7)(\text{PO}_4)$ .

Atom	x	y	z	<i>s.o.f</i>	$U_{\text{iso}}$ ( $\text{\AA}^2$ ) <sup>a)</sup>
W1	0.18983(1)	0.38971(7)	0.70035(5)	0.757(2)	0.0097(1)
V1				0.243(2)	
W2	0.43697(1)	0.62648(4)	0.71596(5)	0.761(3)	0.0106(2)
V2				0.239(3)	
W3	0.43736(2)	0.12477(4)	0.67821(6)	0.732(3)	0.0110(2)
V3				0.268(3)	
W4	0.31577(2)	0.63836(4)	0.31011(6)	0.733(3)	0.0111(2)
V4				0.267(3)	
W5	0.25650(3)	0.51498(7)	0.9975(1)	0.50(2)	0.0248(3)
V5				0.50(2)	
W6	0.50737(3)	0.75148(7)	0.0059(1)	0.514(4)	0.0276(3)
V6				0.486(4)	
P1	0.36797(7)	0.7899(2)	0.5881(3)	1	0.0074(4)
P2	0.36328(7)	0.2715(2)	0.5629(3)	1	0.0069(4)
P3	0.38429(7)	0.5243(2)	0.9484(3)	1	0.0065(4)
P4	0.24585(7)	0.1852(2)	0.7679(3)	1	0.0078(4)
P5	0.38538(7)	0.9655(2)	0.4092(3)	1	0.0074(4)
P6	1/2	0.4325(3)	3/4	1	0.0079(6)
P7	1/2	0.9354(3)	3/4	1	0.0077(6)
O1	0.2936(2)	0.5732(6)	0.1470(8)	1	0.014(1)
O2	0.4664(2)	0.0041(6)	0.7579(9)	1	0.013(1)
O3	0.4138(2)	0.5680(6)	0.8818(9)	1	0.013(1)
O4	0.3439(2)	0.7160(7)	0.4837(9)	1	0.017(2)
O5	0.4035(2)	0.2414(6)	0.6036(1)	1	0.014(2)
O6	0.3898(2)	0.8608(1)	0.499(1)	1	0.017(2)
O7	0.2147(2)	0.2611(6)	0.7820(9)	1	0.013(2)
O8	0.4112(2)	0.0445(7)	0.4993(1)	1	0.018(2)
O9	0.5112(2)	0.8683(7)	0.8854(9)	1	0.017(2)
O10	0.3984(3)	0.7323(1)	0.6934(8)	1	0.012(1)
O11	0.2163(3)	0.4666(6)	0.8407(8)	1	0.012(1)
O12	0.3602(2)	0.3842(6)	0.493(1)	1	0.019(2)
O13	0.1548(2)	0.5030(6)	0.6179(9)	1	0.012(1)
O14	0.3464(3)	0.7252(7)	0.1937(9)	1	0.017(2)
O15	0.4706(2)	0.1696(6)	0.5820(9)	1	0.013(1)
O16	0.4686(2)	0.6958(6)	0.8508(8)	1	0.012(1)
O17	0.2639(2)	0.6334(7)	0.8793(9)	1	0.016(2)
O18	0.2912(2)	0.5676(6)	0.4236(9)	1	0.013(1)
O19	0.4549(2)	0.1953(6)	0.8425(8)	1	0.013(1)
O20	0.4655(2)	0.5004(7)	0.7359(1)	1	0.020(2)
O21	0.3963(2)	0.0596(7)	0.7684(8)	1	0.015(1)
O22	0.2191(2)	0.4102(6)	0.5763(8)	1	0.011(1)
O23	0.3989(2)	0.5367(7)	0.5854(1)	1	0.018(2)
O24	0.2820(2)	0.7537(7)	0.281(1)	1	0.019(2)
O25	0.1573(3)	0.2980(7)	0.554(1)	1	0.020(2)
O26	0.1529(2)	0.3606(6)	0.8306(9)	1	0.016(2)
O27	0.4968(3)	0.3648(7)	0.6153(9)	1	0.021(2)
O28	0.3569(2)	0.4614(6)	0.8402(9)	1	0.014(1)
O29	0.2515(2)	0.1035(6)	0.8880(9)	1	0.017(2)
O30	0.4558(2)	0.6736(7)	0.5669(9)	1	0.016(2)

<sup>a)</sup>  $U_{\text{iso}} = (1/3) \sum_i \sum_j U_{ij} a_i \cdot a_j$



Table 8.6 Atomic coordinates and isotropic displacement parameters ( $\text{\AA}^2$ ) with estimated standard deviations in parentheses of  $\text{Ru}(\text{WO}_2)_2(\text{P}_2\text{O}_7)(\text{PO}_4)$ .

Atom	<i>x</i>	<i>y</i>	<i>z</i>	<i>s.o.f</i>	$U_{\text{iso}}$ ( $\text{\AA}^2$ ) <sup>a)</sup>
W1	0.19039(2)	0.38812(4)	0.70072(6)	0.981(3)	0.0047(1)
Ru1				0.019(3)	
W2	0.43787(2)	0.62614(4)	0.71482(6)	0.965(6)	0.0046(2)
Ru2				0.035(6)	
W3	0.43810(2)	0.12477(4)	0.68160(6)	0.972(6)	0.0048(2)
Ru3				0.028(6)	
W4	0.31486(2)	0.63659(4)	0.30749(6)	0.985(6)	0.0049(2)
Ru4				0.015(6)	
W5	0.2559(3)	0.51414(7)	0.9965(1)	0.046(6)	0.0047(3)
Ru5				0.954(2)	
W6	0.50571(3)	0.75096(8)	0.0032(1)	0.050(6)	0.0058(6)
Ru6				0.950(6)	
P1	0.3670(1)	0.7894(3)	0.5852(4)	1	0.0047(6)
P2	0.3628(1)	0.2716(3)	0.5626(4)	1	0.0047(6)
P3	0.3848(1)	0.5260(3)	0.9505(4)	1	0.0048(6)
P4	0.2457(1)	0.1839(3)	0.7646(4)	1	0.0066(6)
P5	0.3858(1)	0.9662(3)	0.4099(4)	1	0.0052(6)
P6	1/2	0.4305(4)	3/4	1	0.0055(9)
P7	1/2	0.9340(4)	3/4	1	0.0051(9)
O1	0.2953(3)	0.5688(8)	0.151(1)	1	0.014(2)
O2	0.4673(3)	0.0040(8)	0.765(1)	1	0.011(2)
O3	0.4133(3)	0.5728(7)	0.878(1)	1	0.009(2)
O4	0.3418(3)	0.7225(8)	0.4805(1)	1	0.014(2)
O5	0.4033(3)	0.2395(8)	0.603(1)	1	0.011(2)
O6	0.3891(3)	0.8604(8)	0.498(1)	1	0.014(2)
O7	0.2147(3)	0.2599(7)	0.786(1)	1	0.010(2)
O8	0.4114(3)	0.0421(8)	0.502(1)	1	0.011(2)
O9	0.5149(3)	0.8719(8)	0.886(1)	1	0.016(2)
O10	0.3976(3)	0.7283(8)	0.684(1)	1	0.012(1)
O11	0.2158(3)	0.4657(7)	0.839(1)	1	0.007(2)
O12	0.3605(3)	0.3852(8)	0.498(1)	1	0.012(2)
O13	0.1547(3)	0.5007(8)	0.617(1)	1	0.011(2)
O14	0.3467(3)	0.7231(8)	0.195(1)	1	0.012(2)
O15	0.4695(3)	0.1666(8)	0.578(1)	1	0.011(2)
O16	0.4669(3)	0.7013(7)	0.844(1)	1	0.010(2)
O17	0.2673(3)	0.6351(8)	0.884(1)	1	0.014(2)
O18	0.2911(3)	0.5713(8)	0.425(1)	1	0.011(2)
O19	0.4551(3)	0.1974(7)	0.838(1)	1	0.009(2)
O20	0.4669(3)	0.5026(8)	0.754(1)	1	0.014(2)
O21	0.3971(3)	0.0596(8)	0.769(1)	1	0.009(2)
O22	0.2187(3)	0.4082(7)	0.575(1)	1	0.008(2)
O23	0.4002(2)	0.5308(9)	0.588(1)	1	0.018(2)
O24	0.2808(3)	0.7521(8)	0.267(1)	1	0.014(2)
O25	0.1580(3)	0.2956(8)	0.557(1)	1	0.013(2)
O26	0.1526(3)	0.3586(8)	0.827(1)	1	0.012(2)
O27	0.4917(3)	0.3681(8)	0.613(1)	1	0.016(2)
O28	0.3579(3)	0.4576(8)	0.846(1)	1	0.013(2)
O29	0.2549(3)	0.1090(8)	0.888(1)	1	0.012(2)
O30	0.4569(3)	0.6667(7)	0.569(1)	1	0.009(2)

<sup>a)</sup>  $U_{\text{iso}} = (1/3) \sum_i \sum_j U_{ij} a_i \cdot a_j \cdot a_i \cdot a_j$

Table 8.7 Atomic coordinates and isotropic displacement parameters ( $\text{\AA}^2$ ) with estimated standard deviations in parentheses of  $\text{Rh}(\text{WO}_2)_2(\text{P}_2\text{O}_7)(\text{PO}_4)$ .

Atom	<i>x</i>	<i>y</i>	<i>z</i>	$U_{\text{iso}}$ ( $\text{\AA}^2$ ) <sup>a)</sup>
W1	0.19094(5)	0.3886(1)	0.6997(2)	0.0190(3)
W2	0.43829(4)	0.6253(1)	0.7153(2)	0.0148(3)
W3	0.43856(4)	0.1242(2)	0.6834(2)	0.0176(6)
W4	0.31463(4)	0.6362(1)	0.3083(2)	0.0262(8)
Rh5	0.25525(7)	0.5129(2)	0.9977(3)	0.020(1)
Rh6	0.50574(7)	0.7511(2)	0.0022(3)	0.019(1)
P1	0.3671(2)	0.7876(6)	0.5876(9)	0.012(2)
P2	0.3632(2)	0.2715(6)	0.5586(9)	0.011(2)
P3	0.3855(3)	0.5253(8)	0.957(1)	0.024(2)
P4	0.2451(3)	0.1800(8)	0.764(1)	0.024(2)
P5	0.3862(3)	0.9654(9)	0.414(1)	0.031(2)
P6	½	0.4308(9)	¾	0.014(2)
P7	½	0.9343(9)	¾	0.012(2)
O1	0.2947(6)	0.565(2)	0.150(3)	0.019(5)
O2	0.4668(6)	0.007(2)	0.764(2)	0.013(5)
O3	0.4119(6)	0.569(2)	0.875(3)	0.022(2)
O4	0.3419(7)	0.723(2)	0.481(3)	0.029(5)
O5	0.4028(6)	0.237(2)	0.604(3)	0.022(5)
O6	0.3897(7)	0.862(2)	0.498(3)	0.032(6)
O7	0.2155(7)	0.253(2)	0.786(3)	0.029(6)
O8	0.4107(6)	0.044(2)	0.502(3)	0.020(5)
O9	0.5180(6)	0.874(2)	0.890(3)	0.020(5)
O10	0.3971(5)	0.727(2)	0.678(2)	0.016(4)
O11	0.2157(6)	0.467(2)	0.843(3)	0.025(5)
O12	0.3605(6)	0.384(2)	0.494(3)	0.027(2)
O13	0.1557(6)	0.501(2)	0.618(2)	0.018(4)
O14	0.3462(6)	0.725(2)	0.194(3)	0.025(5)
O15	0.4711(7)	0.167(2)	0.574(3)	0.026(6)
O16	0.4672(6)	0.701(2)	0.840(3)	0.018(5)
O17	0.2657(8)	0.632(2)	0.878(3)	0.036(7)
O18	0.2903(5)	0.576(2)	0.424(2)	0.008(4)
O19	0.4550(7)	0.197(2)	0.835(3)	0.025(5)
O20	0.4659(7)	0.508(2)	0.754(3)	0.025(6)
O21	0.3968(6)	0.059(2)	0.771(2)	0.016(4)
O22	0.2177(6)	0.406(2)	0.576(3)	0.022(5)
O23	0.4018(6)	0.531(2)	0.589(3)	0.023(5)
O24	0.2804(6)	0.756(2)	0.260(2)	0.021(5)
O25	0.1573(6)	0.300(2)	0.556(3)	0.024(5)
O26	0.1534(6)	0.359(2)	0.831(2)	0.020(4)
O27	0.4885(8)	0.369(3)	0.614(3)	0.041(7)
O28	0.3582(8)	0.454(2)	0.847(3)	0.038(6)
O29	0.2564(6)	0.111(2)	0.889(2)	0.019(5)
O30	0.4566(9)	0.666(2)	0.570(3)	0.049(8)

<sup>a)</sup>  $U_{\text{iso}} = (1/3) \sum_i \sum_j U_{ij} a_i \cdot a_j \cdot a_i$

Table 8.8 Selected interatomic distances (Å) of phosphates  $M(\text{WO}_2)_2(\text{P}_2\text{O}_7)(\text{PO}_4)$ ;  $M$ : V, Ru, Rh with estimated standard deviations in parentheses.

	V	Ru	Rh		V	Ru	Rh
W1 – O22	1.781(7)	1.77(1)	1.70(2)	W2 – O16	1.774(7)	1.74(1)	1.71(2)
– O11	1.770(7)	1.76(1)	1.77(3)	– O30	1.806(8)	1.75(1)	1.73(3)
– O13	1.988(7)	2.01(1)	1.99(2)	– O20	1.914(8)	1.91(1)	1.80(3)
– O25	2.005(8)	2.01(1)	1.99(2)	– O10	1.913(8)	1.96(1)	1.98(2)
– O7	1.960(8)	1.96(2)	2.05(3)	– O23	1.947(8)	2.05(1)	2.00(2)
– O26	2.063(8)	2.06(1)	2.08(2)	– O3	2.082(8)	2.07(1)	2.08(2)
W3 – O19	1.793(7)	1.75(1)	1.71(3)	W4 – O18	1.795(7)	1.77(1)	1.73(2)
– O15	1.776(7)	1.76(1)	1.82(2)	– O1	1.792(8)	1.74(1)	1.77(2)
– O2	1.938(7)	1.96(1)	1.89(2)	– O28	1.961(8)	1.97(1)	1.95(3)
– O5	1.979(8)	1.99(1)	1.99(2)	– O24	1.914(8)	1.93(1)	1.98(2)
– O21	2.072(8)	2.06(1)	2.08(2)	– O4	2.008(8)	2.05(1)	2.05(3)
– O8	2.038(8)	2.07(1)	2.08(2)	– O14	2.065(8)	2.07(1)	2.09(2)
M5 – O11	1.964(7)	1.96(1)	1.93(3)	M6 – O15	1.954(7)	1.96(1)	1.89(2)
– O1	1.900(8)	1.97(1)	1.94(3)	– O16	1.956(7)	1.96(1)	1.97(2)
– O18	1.909(7)	1.94(1)	1.96(2)	– O19	1.902(8)	1.97(2)	1.99(3)
– O17	1.934(8)	1.98(1)	1.99(2)	– O9	1.901(8)	1.98(1)	2.00(2)
– O22	1.958(7)	1.96(1)	2.00(2)	– O30	1.932(8)	1.99(1)	2.00(3)
– O29	1.918(7)	2.01(1)	2.01(2)	– O27	1.898(8)	1.98(1)	2.03(3)
P1 – O10	1.526(8)	1.52(1)	1.47(2)	P2 – O14	1.504(9)	1.50(1)	1.45(2)
– O4	1.514(9)	1.49(1)	1.47(3)	– O5	1.509(8)	1.53(1)	1.50(2)
– O26	1.503(9)	1.50(1)	1.50(2)	– O25	1.496(9)	1.50(1)	1.55(3)
– O6	1.573(8)	1.57(1)	1.62(3)	– O12	1.576(8)	1.58(1)	1.59(3)
P3 – O23	1.508(8)	1.49(1)	1.46(3)	P4 – O17	1.515(8)	1.52(1)	1.45(3)
– O3	1.485(8)	1.50(1)	1.48(2)	– O29	1.523(8)	1.49(1)	1.46(2)
– O12	1.584(8)	1.58(1)	1.57(3)	– O7	1.536(8)	1.55(1)	1.48(3)
– O28	1.512(8)	1.53(1)	1.57(3)	– O24	1.535(8)	1.54(1)	1.54(2)
P5 – O8	1.521(8)	1.51(1)	1.48(3)	P6 – O27	1.523(8)	1.50(1)	1.49(3)
– O21	1.508(8)	1.52(1)	1.51(2)	– O27	1.523(8)	1.50(1)	1.49(3)
– O6	1.574(8)	1.59(1)	1.53(3)	– O20	1.528(8)	1.54(1)	1.61(3)
– O13	1.514(8)	1.53(1)	1.57(2)	– O20	1.528(8)	1.54(1)	1.61(3)
P7 – O9	1.524(8)	1.52(1)	1.55(2)				
– O9	1.524(8)	1.52(1)	1.55(2)				
– O2	1.540(8)	1.54(1)	1.57(2)				
– O2	1.540(8)	1.54(1)	1.57(2)				

**Description.** The crystal structure of the polynary phosphates  $M^{\text{III}}(\text{W}^{\text{VI}}\text{O}_2)_2(\text{P}_2\text{O}_7)(\text{PO}_4)$  is built from  $[\text{M}^{\text{III}}\text{O}_6]$ ,  $[(\text{W}^{\text{VI}}\text{O}_2)\text{O}_4]$ ,  $[\text{PO}_4]$ , and  $[\text{P}_2\text{O}_7]$  units (see Figure 8.7). The coordination polyhedra of those building units are shown in Figure 8.6. All oxygen atoms exhibit coordination number, c. n. ( $\text{O}^{2-}$ ) = 2, (M-O-P, M-O-W, W-O-P, and P-O-P).



The four equatorial oxygen atoms of the fairly regular octahedra  $[MO_6]$  are connected with crystallographically four different  $[WO_6]$  via  $M-O-W$  bridging oxygen. The remaining two axial oxygen atoms are connected with two different  $PO_4$  tetrahedra. Crystallographically two independent  $[MO_6]$  octahedra are bridged by two opposite oxygen atoms of  $PO_4$  groups. The remaining two oxygen atoms of  $PO_4$  connect two different  $WO_6$ . The two oxygen atoms with short  $d(W-O)$  of  $WO_6$  octahedra are sharing corners with two  $MO_6$ . Of the remaining four oxygen atoms three are connected with three different  $P_2O_7$  units and the fourth is connected to  $PO_4$ . The  $P_2O_7$  unit shares its six corners with six different octahedra  $[WO_6]$ .

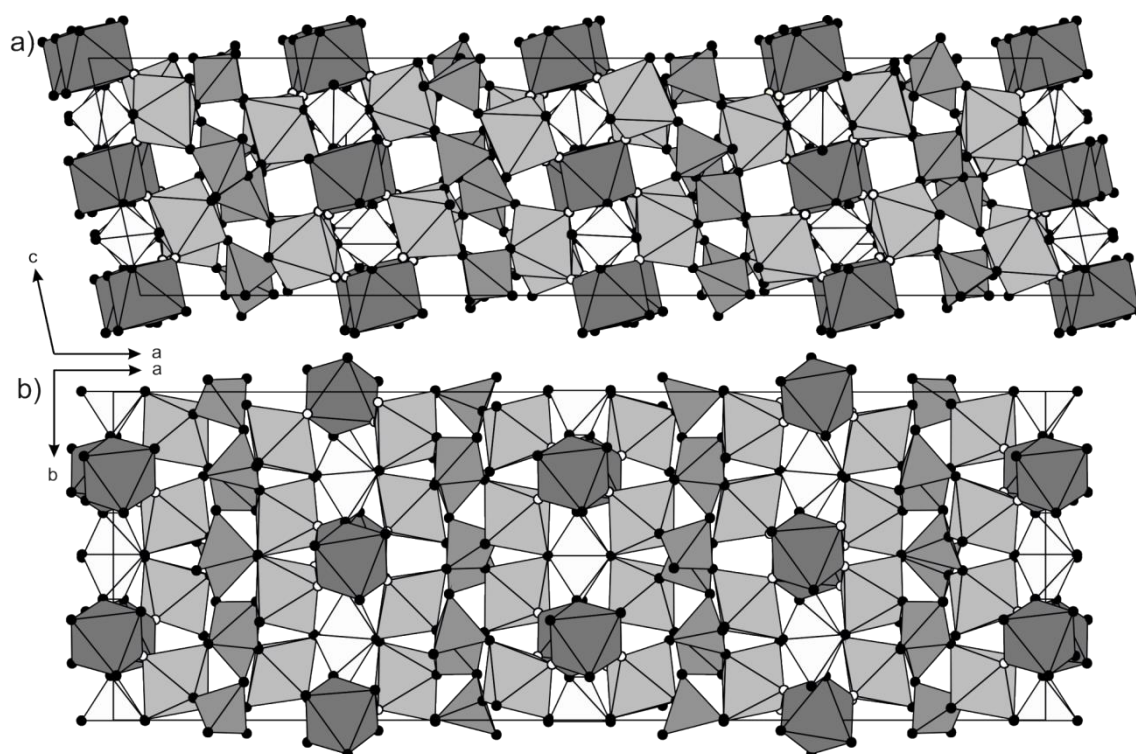


Figure 8.7 Crystal structure of polynary phosphate  $V^{III}(W^{VI}O_2)_2(P_2O_7)PO_4$  projected along the crystallographic  $b$ -axis (a); and  $c$ -axis (b). Dark grey fairly regular octahedra  $VO_6$  (2 sites) show an occupancy of about  $V_{0.5}W_{0.5}$ , light grey distorted octahedra  $WO_6$  (4 sites,  $WO_2^{2+}$  groups) show an occupancy of about  $V_{0.25}W_{0.75}$ , medium grey  $[P_2O_7]$  group and white  $[PO_4]$  tetrahedra, white circles represent oxygen atoms of tungstenyl(VI) groups  $(WO_2)^{2+}$ .

The XRPD pattern of  $Sc(WO_2)_2(P_2O_7)(PO_4)$  shows a remarkably different intensity distribution compared to all other isotopic compounds. This observation is best matched by a simulated diffraction pattern based on fully statistical occupancy by Sc and W of the sites  $M1$  to  $M4$  and exclusive occupancy by W of the two sites  $M5$  and  $M6$  shown in

Figure 8.8a and b. Figure 8.8c shows simulated diffraction patterns of  $\text{ScW}_2\text{P}_3\text{O}_{15}$  based on the ordered structure like  $\text{Rh}(\text{WO}_2)_2(\text{P}_2\text{O}_7)(\text{PO}_4)$  where the intensity distribution is not comparable with the Guinier photograph (see Figure 8.8a).

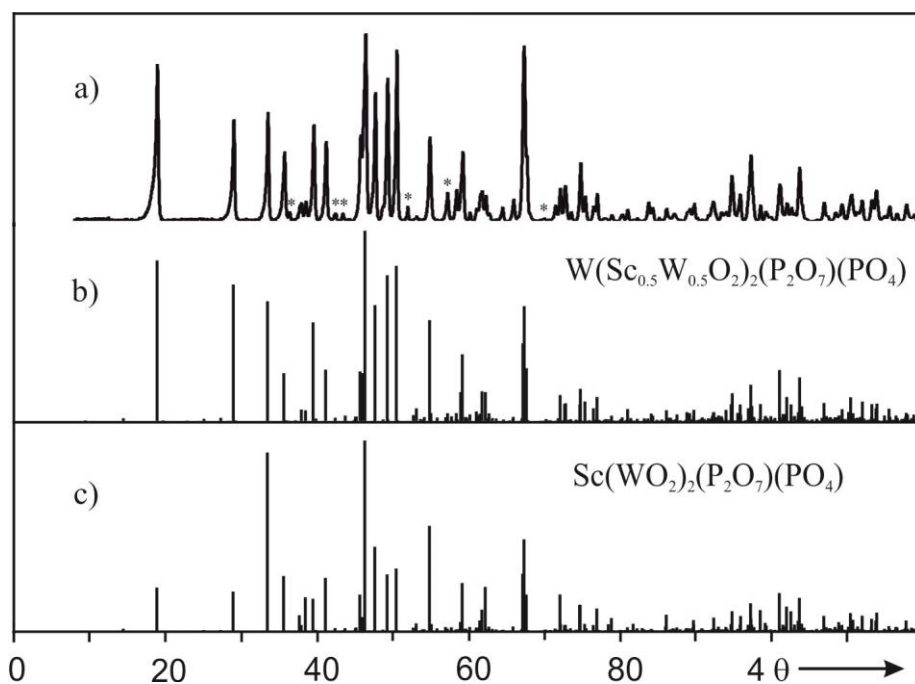


Figure 8.8 Scandium(III) tungstenyl(VI) ortho-pyrophosphate. Comparison of the observed XRPD pattern (a) to simulations based on the structure of  $\text{Rh}^{\text{III}}(\text{W}^{\text{VI}}\text{O}_2)_2(\text{P}_2\text{O}_7)(\text{PO}_4)$  (Sc substituting Ru on sites  $M5$  and  $M6$ , no Sc/W disorder) (c) and full inversion of the occupancy of the sites  $M5$  and  $M6$  according to  $\text{W}(\text{Sc}_{1/2}\text{W}_{1/2}\text{O}_2)_2(\text{P}_2\text{O}_7)(\text{PO}_4)$  (b). A small impurity of  $m\text{-W}_2\text{O}_3(\text{PO}_4)_2$  is indicated by (\*).

**Electron diffraction and HRTEM.** All the Electron diffraction and HRTEM studies were performed in the research group of Prof. Dr. Werner Mader, University of Bonn, Germany. TEM studies were conducted on transmission electron microscopes (i) FEI-Philips CM300 UT/FEG operated at 300 kV and (ii) FEI-Philips CM30 T/LaB<sub>6</sub>, operated at 300 kV, both equipped with a Gatan CCD for image recording and with a Thermo NSS system for EDX analysis using HPG<sub>e</sub> and Si(Li) Nanotracer detectors, respectively. The powder samples were prepared both dispersed in *cyclo*-hexane by ultrasonication and without dispersion in a solvent on holey carbon films supported on a copper grid. Electron diffraction pattern and HRTEM image simulation were carried out using the JEMS software package [236]

TEM investigations on  $V(WO_2)_2(P_2O_7)(PO_4)$  confirmed the lattice parameters found by the Guinier XRD measurements and are corroborating the structure model. The crystals were found mainly in a  $\langle 0\ 1\ 2 \rangle$  orientation on the TEM grids and due to the limitation in tilting angle main zone axis orientations were not adjustable. Figure 8.9 shows a typical bright field (BF) TEM image of a crushed  $V(WO_2)_2(P_2O_7)(PO_4)$  sample with crystals of different sizes and an electron diffraction (ED) pattern in the predominant  $[012]$  orientation. The  $d$ -values of the marked reflections were determined as \*:  $18.3\ \text{\AA}\ d_{(\bar{2}00)}$  and \*\*:  $5.3\ \text{\AA}\ d_{(0\ 2\ 1)}$  and are in agreement with the values from XRD. The composition of the crystals measured by EDX was found to match the ratio of V:W:P = 1:2:3 as given by the chemical formula  $V(WO_2)_2(P_2O_7)(PO_4)$  (c.f. Figure 14.13). In Figure 14.14 and Figure 14.15 the ED patterns of different zone axis of  $V(WO_2)_2(P_2O_7)(PO_4)$  and  $Cr(WO_2)_2(P_2O_7)(PO_4)$  are shown to be consistent with simulated ED patterns using the crystallographic data from single crystal investigation (Table 8.4).

HRTEM investigations on  $V(WO_2)_2(P_2O_7)(PO_4)$  were unfortunately complicated by beam damage processes [237] that caused an amorphization of the crystals starting from the thin areas and propagating inwards even when low electron doses were applied. Thus, neither informative HRTEM studies on thin crystal edges nor focus series techniques were possible. Figure 8.10 shows a HRTEM image along  $[0\ 1\ 2]$  of a  $V(WO_2)_2(P_2O_7)(PO_4)$  crystal with an amorphous region in left part of the picture. The dominant lattice fringes found in the HRTEM image have spacings of  $d_{\{2\ 0\ 0\}} = 9.1\ \text{\AA}$ . An enlargement of the boxed area is shown in Figure 8.10 b and c with a HRTEM simulation as overlay. The simulation succeeded convincingly with a sample thickness  $d = 43\ \text{nm}$  and a defocus  $\Delta f = -7.5\ \text{nm}$  using crystal data of the structure model for  $V(WO_2)_2(P_2O_7)(PO_4)$  Table 8.4.

Due to the sample thickness and to the superimposed position of atoms in the  $[0\ 1\ 2]$  orientation no further improvement of the structure model can be gained by HRTEM as to be seen by the overlay of the structure model in polyhedra presentation. The prominent bright contrasts on the  $\{2\ 0\ 0\}$  lattice planes correspond to the layers consisting of  $(W,V)O_6$  octahedra and  $PO_4$  tetrahedra, whereas the layers of  $P_2O_7$  units appear as faint contrasts in between. No extended defects like stacking faults or twin domain boundaries were found in HRTEM images of  $V(WO_2)_2(P_2O_7)(PO_4)$ . Figure 8.10 shows a well ordered array of atoms with no hints on twinning or disorder. This observation is in contrast to multiple twinning found for  $V(WO_2)_2(P_2O_7)(PO_4)$  by x-ray diffraction studies.



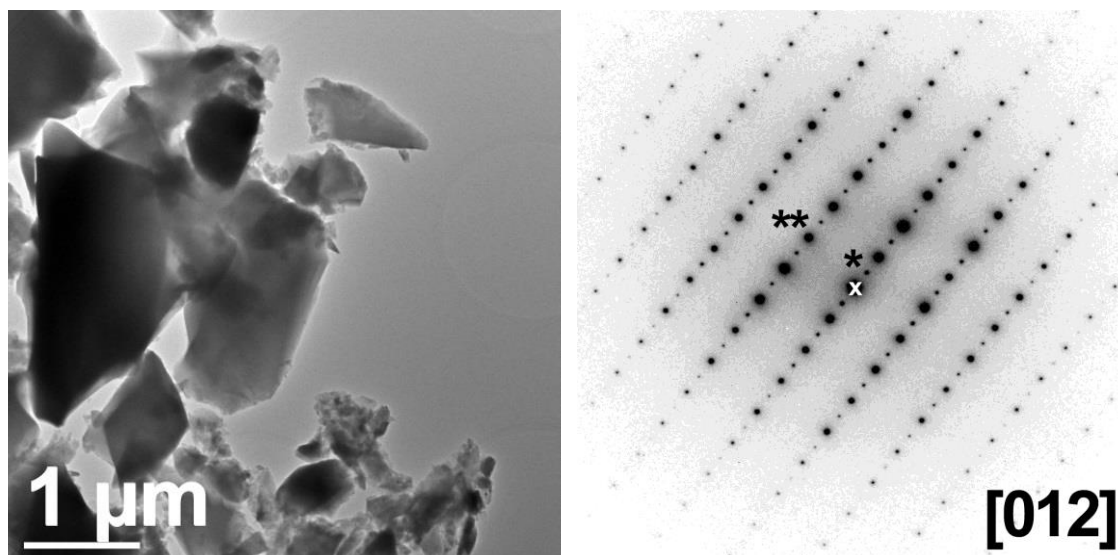


Figure 8.9 BF TEM image of crushed  $V(WO_2)_2(P_2O_7)(PO_4)$  crystals (left) and ED pattern along  $[012]$ ; \* :  $18.3 \text{ \AA } d(\bar{2}00)$ ; \*\* :  $5.3 \text{ \AA } d(021)$  (right).

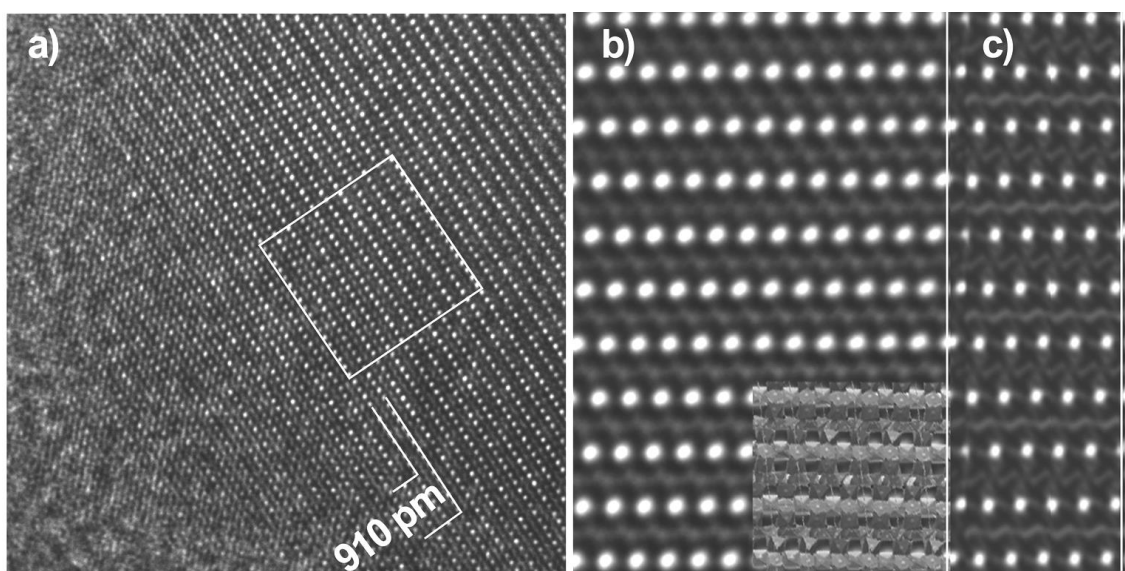


Figure 8.10 HRTEM image of  $V(WO_2)_2(P_2O_7)(PO_4)$  along  $[012]$  (a); enlargement of the boxed area with a polyhedra drawing of the structure model (b); HRTEM simulation:  $d = 43$ ;  $\Delta f = -7.5 \text{ nm}$  (c).

**$^{31}\text{P}$ -MAS-NMR spectra.** The x-ray single crystal, ED, as well as the HRTEM analysis showed the existence of two  $(P_2O_7)^{4-}$  and three  $(PO_4)^{3-}$  units within the structure of phosphates  $M^{\text{III}}(W^{\text{VI}}O_2)_2(P_2O_7)(PO_4)$ . Further evidence for the presence of  $(P_2O_7)^{4-}$  and  $(PO_4)^{3-}$  anions is revealed by  $^{31}\text{P}$ -MAS-NMR spectra of the diamagnetic phosphates  $M(WO_2)_2(P_2O_7)(PO_4)$  with  $M$ : Sc, In, Ir (see Figure 8.11). Although the mixed ortho-pyrophosphates are structurally closely related the solid state  $^{31}\text{P}$ -MAS-NMR spectra



are surprisingly different. For comparison  $^{31}\text{P}$ -MAS-NMR spectra of  $\text{InPO}_4$ ,  $\text{WOP}_2\text{O}_7$  and  $m\text{-W}_2\text{O}_3(\text{PO}_4)_2$  were also measured. These are shown in Figure 8.11. The isotropic chemical shift parameters obtained for ortho-pyrophosphates and the reference phosphates are summarized in Table 8.9. Chemical shifts are reported in parts per million (ppm) from an external standard of 85%  $\text{H}_3\text{PO}_4$ .

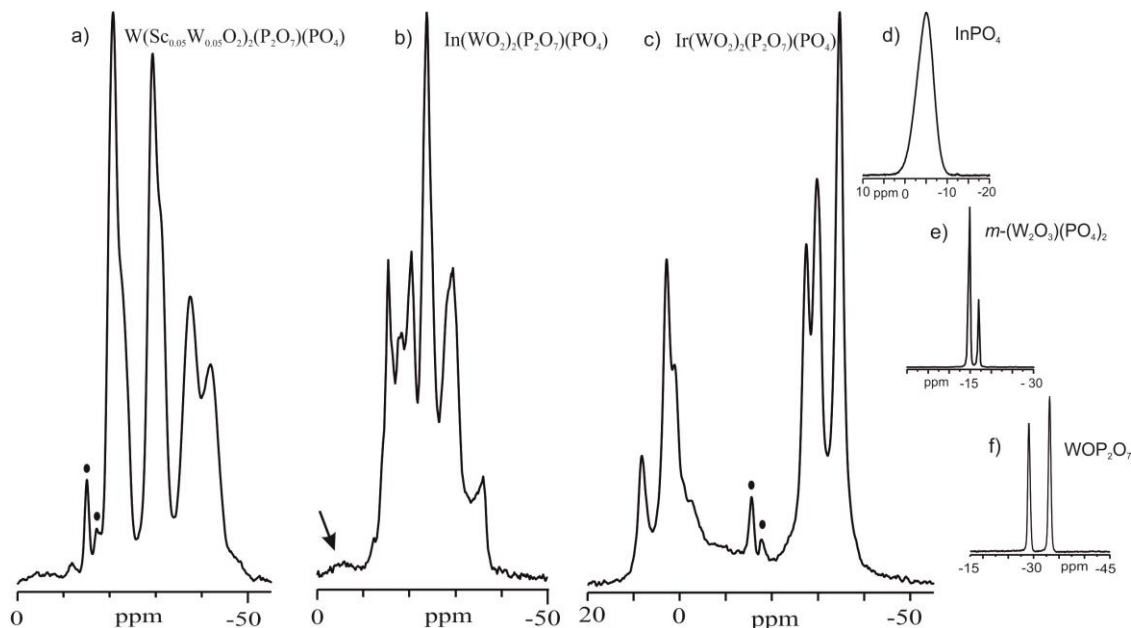


Figure 8.11 Room temperature  $^{31}\text{P}$ -MAS-NMR spectra of  $\text{W}(\text{Sc}_{0.5}\text{W}_{0.5}\text{O}_2)_2(\text{P}_2\text{O}_7)(\text{PO}_4)$  (a),  $\text{In}(\text{WO}_2)_2(\text{P}_2\text{O}_7)(\text{PO}_4)$  (b), and  $\text{Ir}(\text{WO}_2)_2(\text{P}_2\text{O}_7)(\text{PO}_4)$  (c),  $\text{InPO}_4$  [87, this thesis] (d),  $m\text{-W}_2\text{O}_3(\text{PO}_4)_2$  [this thesis] (e), and  $\text{WO}(\text{P}_2\text{O}_7)$  [this thesis] (f). Resonances from an impurity of  $m\text{-W}_2\text{O}_3(\text{PO}_4)_2$  are indicated by ( $\bullet$ ).

The structure models of the mixed ortho-pyrophosphates  $M(\text{WO}_2)_2(\text{P}_2\text{O}_7)(\text{PO}_4)$  with  $M$ : V, Ru, Rh (Table 8.5 to Table 8.7) consist of seven phosphorus sites,  $5 \times (8f)$  and  $2 \times (4e)$  in space group  $C2/c$  ( $1^{\text{st}}$  setting). Four of the  $(8f)$  sites correspond to phosphorus in pyrophosphate groups, one  $(8f)$  and the two  $(4e)$  sites are related to orthophosphate groups. Resonances related to orthophosphate are typically found at lower field than those of pyrophosphate groups [238]. Thus, the broad resonance at  $-20.7$  ppm (integral of resonance  $A_o = 3.93 \text{ cm}^2$ ) in the spectrum of  $\text{Sc}(\text{WO}_2)_2(\text{P}_2\text{O}_7)(\text{PO}_4)$  is assigned to the three orthophosphate groups, while the resonances at  $-29.3$ ,  $-37.4$ , and  $-41.8$  ppm are related to  $\text{Q}^1$  phosphate groups (pyrophosphate).

Table 8.9 Summary of  $^{31}\text{P}$ -MAS-NMR isotropic chemical shifts  $\delta_{\text{iso}}$  of phosphates  $M(\text{WO}_2)_2(\text{P}_2\text{O}_7)(\text{PO}_4)$  with  $M$ : Sc, In, Ir, and reference compounds. A: Integrated intensities of resonances.

phosphate	$\delta_{\text{iso}}$ (ppm); A (a. u.)	Ref.
$\text{InPO}_4$	-5.1; 1	this thesis
$m\text{-W}_2\text{O}_3(\text{PO}_4)_2$	-15.2, -17.4; 3:1 <sup>a)</sup>	this work
$\text{ReO}_2(\text{PO}_4)$	-6.8, -11.4, -13.8; 1:1:1 <sup>a)</sup>	[239]
$\text{WOP}_2\text{O}_7$	-29.0, -33.1; 1:1 <sup>a)</sup>	this thesis
$(\text{MoO}_2)_2\text{P}_2\text{O}_7$	-21.2, -23.9, -27.0, -28.8; 3:1:1:3 <sup>a)</sup>	[80]
$\text{W}(\text{Sc}_{0.5}\text{W}_{0.5}\text{O}_2)_2(\text{P}_2\text{O}_7)(\text{PO}_4)$	-15.0 <sup>b)</sup> , -17.9 <sup>b)</sup> , -20.7, (-29.3, -37.4, -41.8); 1:2 <sup>a, c)</sup>	this thesis
$\text{In}(\text{WO}_2)_2(\text{P}_2\text{O}_7)(\text{PO}_4)$	-15.2 <sup>b)</sup> , -17.6 <sup>b)</sup> , -18.2, -20.3, -23.6, -28.2, -29.3, -35.9	this thesis
$\text{Ir}(\text{WO}_2)_2(\text{P}_2\text{O}_7)(\text{PO}_4)$	(8.1, 2.7, 0.9), -15.7 <sup>b)</sup> , -17.9 <sup>b)</sup> , (-27.4; -29.7, -34.6); 1:2 <sup>a, c)</sup>	this thesis
$\text{Ir}(\text{PO}_3)_3$ (C-type)	-4.8, -7.2, -13.0, -17.3, -18.9, -27.3, -30.9; 1:1:1:3:1:1:1 <sup>a)</sup>	[240]

<sup>a)</sup> Intensity ratio of the observed resonances, <sup>b)</sup> Resonances observed in the spectra of the mixed ortho-pyrophosphates are related to an impurity of  $m\text{-W}_2\text{O}_3(\text{PO}_4)_2$  [76, 77, 78], <sup>c)</sup> Due to limited spectral resolution intensity ratios are given for groups of resonances in parentheses.

The integrals of these three resonances sum up to  $A_p = 7.85 \text{ cm}^2$ . The ratio orthophosphate /pyrophosphate  $A_o:A_p = 1:2$  corresponds nicely to the one expected from the structure model. Resonances at -15.2 and -17.6 ppm point to an impurity of  $m\text{-W}_2\text{O}_3(\text{PO}_4)_2$  which was also been identified from the XRPD pattern of the material. The  $^{31}\text{P}$ -MAS-NMR spectrum  $\text{In}(\text{WO}_2)_2(\text{P}_2\text{O}_7)(\text{PO}_4)$  shows badly resolved at least seven isotropic resonances with different width and relative intensities. The observed resonances are at  $\delta_{\text{iso}} = -15.2, -17.6, -18.2, -20.3, -23.6, -29.3, -35.9$  ppm. While the resonances at -15.2 and -17.6 ppm are again related to an impurity of  $m\text{-W}_2\text{O}_3(\text{PO}_4)_2$  [78] there is no immediate assignment of the main resonances to ortho- and pyrophosphate. The bad resolution can be attributed to dipolar coupling of  $^{31}\text{P}$  with the indium nuclei which results in peak broadening as also seen for pure  $\text{InPO}_4$  (see Figure 8.11d). In  $\text{Ir}(\text{WO}_2)_2(\text{P}_2\text{O}_7)(\text{PO}_4)$  the resonances in the  $^{31}\text{P}$ -MAS-NMR span over an unexpectedly wide range. The integrals  $A_o = 3.0 \text{ cm}^2$  (resonances in the range  $10 \geq \delta_{\text{iso}} \geq -2$  ppm) and  $A_p = 5.5 \text{ cm}^2$  (resonances in the range  $-20 \geq \delta_{\text{iso}} \geq -40$  ppm) show a ratio  $A_o:A_p = 1:1.8$  which is in agreement with the structure model.

**X-ray photoelectron spectroscopy.** The oxidation states of tungsten and vanadium in  $V(WO_2)_2(P_2O_7)PO_4$  (obtained from  $VOPO_4$  and  $WOPO_4$  in 1:2 molar ratio by vapor phase moderated solid state reaction) were identified by XPS measurements (see Table 8.10 and Figure 8.12). The instrumental parameters for the XPS measurement are similar to those as described in section 6.5.2. The binding energies (BEs) of tungsten were referenced to that of C1s level at 285.0 eV whereas for vanadium, the best energy reference is, O1s at 530.0 eV for  $V_2O_5$ .

Table 8.10 XPS results of  $V^{III}(W^{VI}O_2)_2(P_2O_7)(PO_4)$  and literature value.

component	BEs (eV)		$\Delta$ (eV)	Ref.
	Observed	Corrected		
O 1s	531.18	530.00		[this thesis, 186]
V 2p <sub>3/2</sub>	516.20	515.02	14.98	[this thesis]
		515.15	14.84	$V^{III}_2O_3$ [186]
		515.7	14.40	$V^{III}_2O_3$ [184]
		515.65	14.35	$V^{IV}O_2$ [186]
		516.20	13.70	$V^V_2O_5$ [184]
C 1s	284.47	285.00		
W 4f <sub>7/2</sub>	35.97	36.50	--	[this thesis]
		35.4 - 36.6	--	$W^{VI}O_3$ [118]
		35.8 - 36.7	--	$Al_2(W^{VI}O_4)_3$ [118]

$$\Delta = |O1s - V2p_{3/2}|$$

The XP spectra of V2p<sub>3/2</sub> and Wf<sub>7/2</sub> show that vanadium and tungsten both are present in a single valence state. The corrected binding energies (BE) for an electron in the vanadium 2p<sub>3/2</sub> state is 515.02 eV. (Figure 8.12a) which is very close to that of  $V_2O_3$  [184, 185]. The separation of BEs between O1s and V2p<sub>3/2</sub> is also representative. The observed BE separation is 14.98 eV which is comparable to  $V^{3+}$  in  $V_2O_3$  (14.4 - 14.84 eV). The observed BE of the W4f<sub>7/2</sub> level is 36.50 eV (Figure 8.12b) which is very close to that of  $W^{6+}$  in  $WO_3$  (35.4 - 36.6 eV) or in  $Al_2(WO_4)_3$  (35.8 - 36.7eV) [118]. Therefore, the XPS measurements confirm the exclusive valence states vanadium(III) and tungsten(VI).

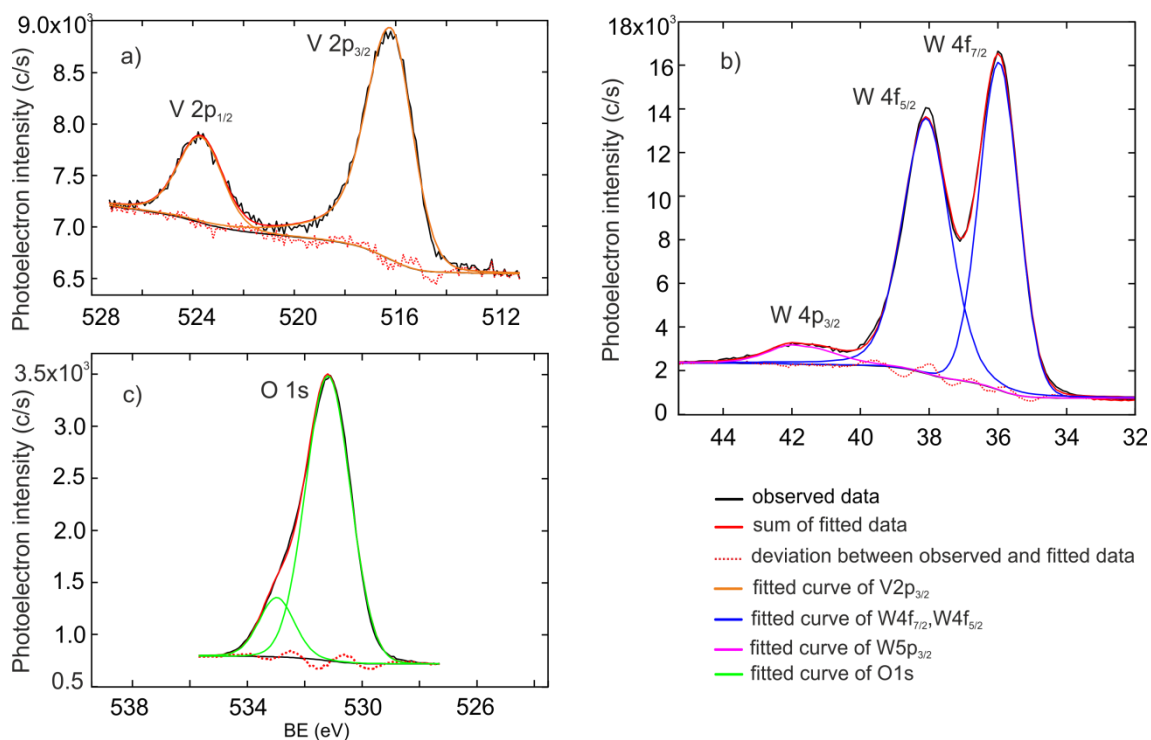


Figure 8.12 XPS spectra of  $V^{III}(W^{VI}O_2)_2(P_2O_7)PO_4$  with fitted curves for V2p (a), W4f (b), and O1s (c).

**UV/Vis/NIR spectroscopy.** The crystal structure of  $Cr(WO_2)_2(P_2O_7)PO_4$  consists of  $[Cr^{III}O_6]$  chromophores. These chromophores are fairly regular octahedra where the bond distances are  $1.90 \text{ \AA} \leq d(Cr-O) \leq 1.96 \text{ \AA}$ . The second-sphere ligands of the chromophore consist of four  $W^{6+}$  and two  $P^{5+}$ ,  $[(O_3P-O)_2-Cr-((O=W=O)O_4)_4]$ . Due to the presence of the strong  $\pi$ -acceptor  $W^{6+}(d^0)$  in the second-ligand sphere a larger ligand field splitting might have been expected, which is not corroborated by the powder reflectance spectrum of  $Cr(WO_2)_2(P_2O_7)PO_4$  (Figure 8.13).  $10 Dq$  for  $Cr(WO_2)_2(P_2O_7)PO_4$  corresponds to the mean energy (at  $\tilde{\nu} \approx 14000 \text{ cm}^{-1}$ ) of the split bands ( ${}^4B_{1g} \rightarrow {}^4E_g$  and  ${}^4B_{1g} \rightarrow {}^4B_{2g}$  at  $\tilde{\nu} \approx 11900$  and  $15500 \text{ cm}^{-1}$ , respectively). For the expected band at  $20000$  to  $28000 \text{ cm}^{-1}$  just the first split term ( ${}^4B_{1g} \rightarrow {}^4E_g$ ) is observed at  $\tilde{\nu} \approx 21000 \text{ cm}^{-1}$ . The second one ( ${}^4B_{1g} \rightarrow {}^4A_{2g}$ ) is obscured, as is the third absorption band, possibly at about  $30000$  to  $35000 \text{ cm}^{-1}$  which is in agreement with the result obtained for  $Cr^{III}_4(P_2O_7)_3$  [1]. Thus, determination of the Racah parameter  $B$  is rendered impossible. The strong absorption band at  $\tilde{\nu} \approx 27500 \text{ cm}^{-1}$  (with shoulder at  $38000 \text{ cm}^{-1}$ ) corresponds presumably to LMCT ( $O^{2-} \rightarrow W^{6+}$ ).

The powder reflectance spectrum of  $\text{Fe}(\text{WO}_2)_2(\text{P}_2\text{O}_7)\text{PO}_4$  (Figure 8.13) shows a LMCT at  $\tilde{\nu} \approx 29000 \text{ cm}^{-1}$  (with shoulder at  $38000 \text{ cm}^{-1}$ ). Two electronic transitions of  $\text{Fe}^{3+}$  are observed at  $\tilde{\nu} \approx 12500 \text{ cm}^{-1}$  and  $16000 \text{ cm}^{-1}$  which could be assigned to  ${}^6\text{A}_{1g} \rightarrow {}^4\text{T}_{1g}$  and  ${}^6\text{A}_{1g} \rightarrow {}^4\text{T}_{2g}$ , respectively [1]. On the other hand the bluish color of the iron compound suggest a small oxygen deficiency which leads to an IVCT ( $\text{Fe}^{2+} \rightarrow \text{Fe}^{3+}$ ).

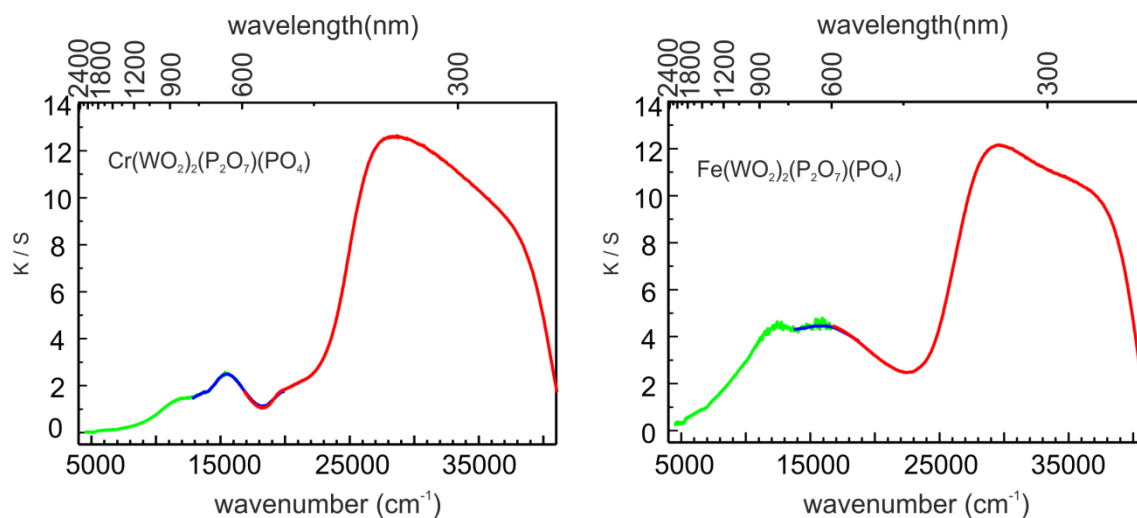


Figure 8.13 UV/Vis/NIR powder reflectance spectra of  $\text{Cr}^{\text{III}}(\text{W}^{\text{VI}}\text{O}_2)_2(\text{P}_2\text{O}_7)\text{PO}_4$  and  $\text{Fe}^{\text{III}}(\text{W}^{\text{VI}}\text{O}_2)_2(\text{P}_2\text{O}_7)\text{PO}_4$ .

**Magnetic behavior.** Molar susceptibility,  $\chi_{\text{mol}}$  and its reciprocal,  $\chi_{\text{mol}}^{-1}$  as a function of temperature ( $2 \leq T \leq 300 \text{ K}$ ) are shown in Figure 8.14 for  $\text{V}^{\text{III}}(\text{W}^{\text{VI}}\text{O}_2)_2(\text{P}_2\text{O}_7)\text{PO}_4$ ,  $\text{Cr}^{\text{III}}(\text{W}^{\text{VI}}\text{O}_2)_2(\text{P}_2\text{O}_7)\text{PO}_4$ , and  $\text{Fe}^{\text{III}}(\text{W}^{\text{VI}}\text{O}_2)_2(\text{P}_2\text{O}_7)\text{PO}_4$ . For the chromium and iron compound at higher temperature Curie-Weiss behavior [130] is observed with constant magnetic moments (calculated from 50 – 300 K) and negative paramagnetic Curie temperatures:  $\mu_{\text{exp}}/\mu_{\text{B}} = 3.90$  per  $\text{Cr}^{3+}$  and  $5.89$  per  $\text{Fe}^{3+}$ ;  $\theta_{\text{p}}(\text{Cr}) = -38.8 \text{ K}$  and  $\theta_{\text{p}}(\text{Fe}) = -23.9 \text{ K}$ . These moments are close to  $3.87\mu_{\text{B}}$  for  $d^3$  and  $5.92\mu_{\text{B}}$  for  $d^5$  (high spin) systems. At very low temperature the iron and chromium containing phosphates show weak antiferromagnetic coupling. For  $\text{V}^{\text{III}}(\text{W}^{\text{VI}}\text{O}_2)_2(\text{P}_2\text{O}_7)\text{PO}_4$  the graph of reciprocal susceptibility vs. temperature is slightly bent, thus indicating a temperature dependent magnetic moment ranging from  $2.7 \mu_{\text{B}}$  at 300 K down to  $1.2 \mu_{\text{B}}$  at 4 K. These values are typically observed for  $\text{V}^{3+}$  in distorted octahedra [241, 242, 243].

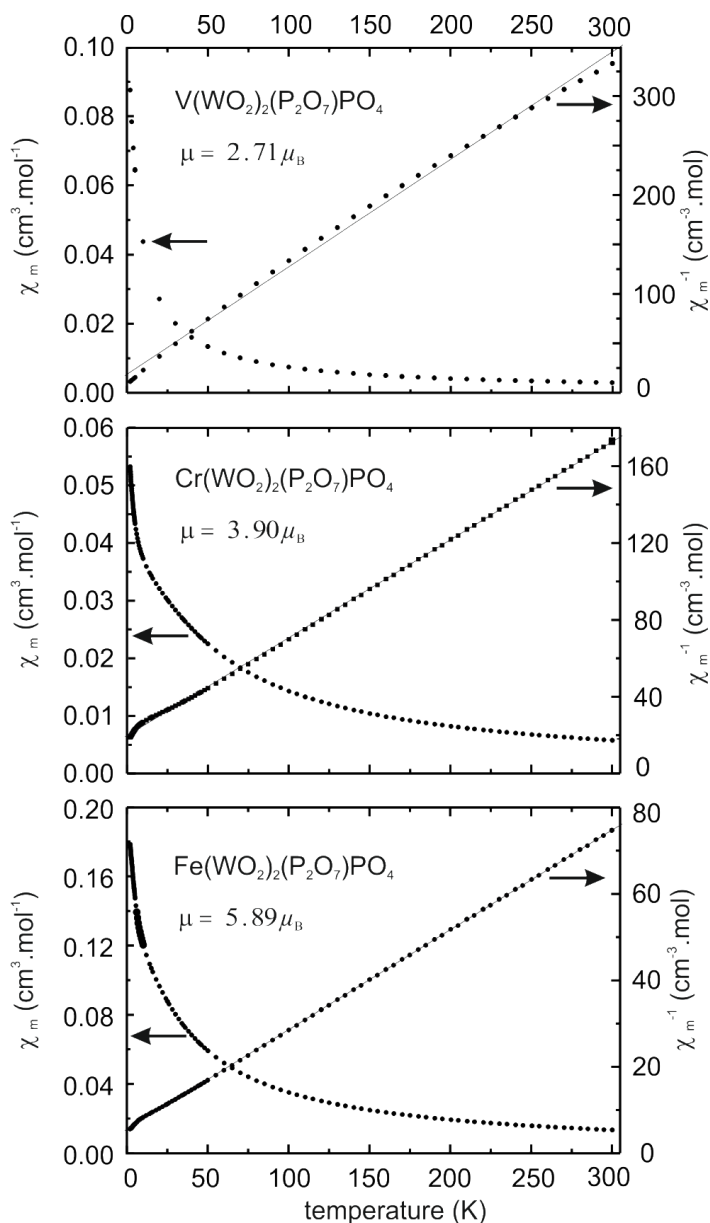


Figure 8.14 Temperature dependence molar susceptibility,  $\chi_{mol}$  and its reciprocal  $\chi_{mol}^{-1}$  of  $M^{III}(WO_2)_2(P_2O_7)PO_4$ ,  $M$ : V, Cr, Fe.

**EPR studies.** X-band EPR spectra of the Fe and Cr containing ortho-pyrophosphates are shown in Figure 8.15. The observed EPR spectrum of  $FeW_2P_3O_{15}$  shows an isotropic resonance with  $g = 2.00 \pm 0.01$  which is typical for  $Fe^{3+}$  ions in the sense that for high spin  $Fe^{3+}$  ( $d^5$ ) ion in ground state,  ${}^6A_1$  with  $S = 5/2$ ,  $L = 0$ , a single EPR line is expected at a  $g$ -value close to free electron value of  $g = 2.0023$  [244]. In addition, no hyperfine interaction in the EPR spectrum is observed due to its non-magnetic nucleus.

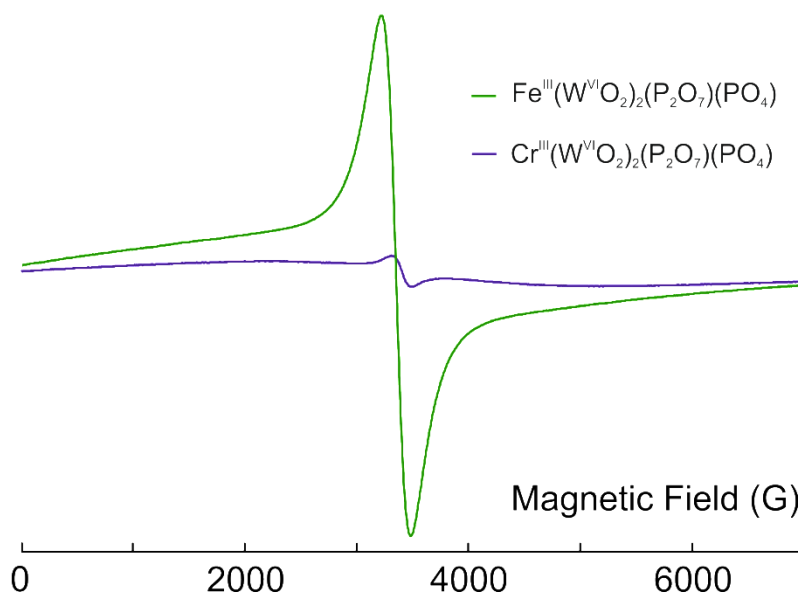


Figure 8.15 Room temperature continuous wave (CW) X-band powder EPR spectra of  $\text{Cr}^{\text{III}}(\text{W}^{\text{VI}}\text{O}_2)_2(\text{P}_2\text{O}_7)\text{PO}_4$  and  $\text{Fe}^{\text{III}}(\text{W}^{\text{VI}}\text{O}_2)_2(\text{P}_2\text{O}_7)\text{PO}_4$ .

Although for the  $\text{Cr}^{3+}$  ion ( $d^3$ ,  $S = 3/2$ ) three EPR resonance lines are expected, in the powder EPR pattern only the perpendicular component is visible. Moreover, the  $\text{Cr}^{3+}$  ion exhibits zero field splitting (zfs). Taking into consideration a high zfs a single resonance is predicted with  $g = 4.0$ , considering no zfs a single resonance line is anticipated with  $g \sim 1.98$ . Furthermore, the most abundant  $^{52}\text{Cr}$  nucleus ( $I = 0$ ) doesn't exhibit any hyperfine structure. The observed single resonance line with  $g = 1.97$  for  $\text{Cr}^{3+}$  is close to the expected value.

## 8.4 Conclusion

Reactions between  $\text{V}^{\text{V}}\text{OPO}_4$  and  $\text{W}^{\text{V}}\text{OPO}_4$  with 1:2 molar ratio in sealed silica tubes lead to the formation of the hitherto unknown  $\text{V}^{\text{III}}(\text{W}^{\text{VI}}\text{O}_2)_2(\text{P}_2\text{O}_7)(\text{PO}_4)$  with new crystal structure type. This formation can be interpreted as a combined acid-base and redox reaction. Single crystal (obtained via vapor phase moderated solid state reaction using chlorine as mineralizer) structure analysis revealed fairly regular  $\text{VO}_6$  octahedra and distorted  $\text{WO}_6$  octahedra with two short  $\text{W}=\text{O}$  distances as building units together with  $\text{P}_2\text{O}_7$  and  $\text{PO}_4$ . Eight isotopic compounds were synthesized with trivalent Sc, Cr, Fe, Mo, Ru, Rh, In, and Ir instead of  $\text{V}^{3+}$ . While in  $\text{VW}_2\text{P}_3\text{O}_{15}$  and  $\text{RuW}_2\text{P}_3\text{O}_{15}$  mixed metal occupancy are observed, the single crystal structure analysis of rhodium containing

phosphates showed ordered distribution where the tungsten exclusively occupies four out of the six metal sites and the remaining two are occupied by trivalent rhodium. In contrast, the scandium compound, probably due to the large ionic radius of  $\text{Sc}^{3+}$  showed inverted metal distribution where the metal sites M5 and M6 are exclusively occupied by tungsten and the sites W1 to W4 are statistically occupied by Sc/W. Such a disorder is proposed by the intensity distribution of the powder diffraction pattern. Although the x-ray single crystal structure model of  $\text{VW}_2\text{P}_3\text{O}_{15}$  is supported by the ED and HRTEM studies, no hints on twinning or disorder is observed by these techniques. The existence of ortho- and pyrophosphate units was confirmed by  $^{31}\text{P}$ -MAS-NMR studies. Magnetic measurements and EPR studies confirm the above mentioned charge distribution. A small homogeneity range  $0.60 \leq x \leq 0.67$  was observed for the vanadium compound. With respect to its formulation as the upper phase boundary composition (V:W = 1:2) is  $\text{V}^{\text{III}}(\text{W}^{\text{VI}}\text{O}_2)(\text{P}_2\text{O}_7)(\text{PO}_4)$  and the lower phase boundary composition (V:W = 2:3) is  $\text{V}^{\text{III}}_{0.6}\text{V}^{\text{IV}}_{0.4}(\text{V}^{\text{IV}}\text{O}_2)_{0.2}(\text{W}^{\text{VI}}\text{O}_2)_{1.8}(\text{P}_2\text{O}_7)(\text{PO}_4)$ .



## 9 Metastable tungsten phosphates with structures related to $\text{ReO}_3$ and $\text{WOPO}_4$

### 9.1 Introduction

Plenty of literature is available about different modifications and polymorphic forms of tungsten(VI) oxide. Some of the literature is even contradictory. Several polymorphs ( $\alpha$ -,  $\beta$ -,  $\gamma$ -,  $\delta$ -,  $\varepsilon$ -) of  $\text{W}^{\text{VI}}\text{O}_3$  [245, 246, 247, 248, 249] are reported which are stable in certain temperature ranges and should transform reversibly (see Figure 9.1).

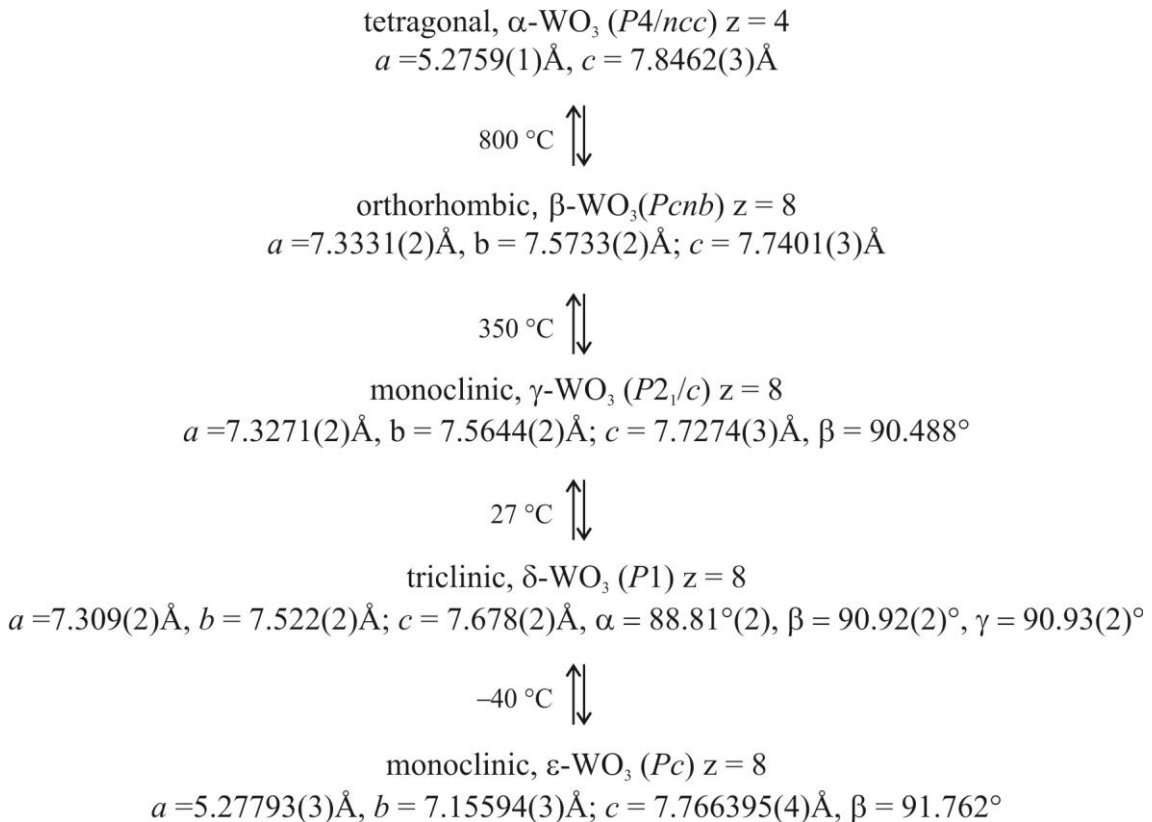


Figure 9.1 Summary on phase transitions and structural parameters of  $\text{WO}_3$  [245, 246, 247, 248, 249].

The existence of various modifications of  $\text{WO}_3$  can be related to a displacement of the tungsten atoms away from the center of its ideal octahedron. For  $\alpha$ - $\text{WO}_3$  the displacement of tungsten is toward a corner of the octahedron, in case of  $\beta$ -,  $\gamma$ -,  $\delta$ - toward an edge, and in  $\varepsilon$ - $\text{WO}_3$  toward a face of the octahedron [249]. In addition to the aforementioned thermodynamically stable phases the higher symmetric polymorphs (metastable phases) like hexagonal- $\text{WO}_3$  [250, 251] and cubic- $\text{WO}_3$  [252, 253] (Table 9.1) were obtained by dehydration of certain precursor compounds. These polymorphs cannot be obtained

reversibly from the other known polymorphs. *Cub*- $\text{WO}_3$  obtained by dehydration of precursors like  $\text{H}_2\text{WO}_4 \cdot \text{H}_2\text{O}$  [253] or  $\text{WO}_3 \cdot \text{H}_2\text{O}$  [254] was characterized by high temperature x-ray diffraction of a material. Though the cubic  $\text{WO}_3$  is documented [252], it is not well characterized due to difficulties in synthesis of chemically pure material.

Siedle et al. [255] claimed the formation of pure *cub*- $\text{WO}_3$  by pyrolysis of aluminum tungstophosphate  $[\text{Al}(\text{H}_2\text{O})_6]\text{PW}_{12}\text{O}_{40} \cdot 4\text{H}_2\text{O}$  at  $T > 500$  °C with the release of  $\text{P}_4\text{O}_{10}$ . They also reported the formation of pure orthorhombic  $\text{WO}_3$  [249] upon heating of  $(\text{NH}_4)_3\text{PW}_{12}\text{O}_{40} \cdot 13\text{H}_2\text{O}$  at 600 °C. In both cases the incorporation of foreign elements within the cubic structure was excluded by the authors. Soaking at high temperature  $\text{WO}_3$  generally transforms to its higher symmetric forms ( $\alpha$ - or  $\beta$ -[249]). *Cub*- $\text{WO}_3$  ( $\text{ReO}_3$  structure type) and high symmetric  $\text{WO}_3$  polymorphs are metastable. At room temperature the monoclinic ( $\gamma$ - $\text{WO}_3$ ) phase [264] is thermodynamically stable.

Formation of stoichiometric  $\text{WO}_3$  is very much temperature and  $p(\text{O}_2)$  dependent. Reduction of tungsten trioxide leading to  $\text{WO}_{3-x}$  is attributed to crystallographic shear planes (CS) and pentagonal column (PC) as shown in Figure 9.2a and b, respectively. The reduced homologous series are  $\text{W}_n\text{O}_{3n-1}$ ;  $25 \leq n \leq 50$  ( $\{102\}$  CS phases,  $\text{WO}_{2.96}$ ) [256], and  $\text{W}_n\text{O}_{3n-2}$ ;  $12 \leq n \leq 32$  (Magnéli phase or  $\{103\}$  CS phases,  $\text{WO}_{2.90}$  [257],  $\text{W}_{24}\text{O}_{70}$  [258]). The PC2 phases are  $\text{WO}_{2.83}$  ( $\text{W}_{24}\text{O}_{68}$ ) [259, 260], and  $\text{WO}_{2.72}$  ( $\text{W}_{18}\text{O}_{49}$ ) [261]. Another stoichiometric, reduced oxide is  $\text{W}^{\text{IV}}\text{O}_2$  [262].

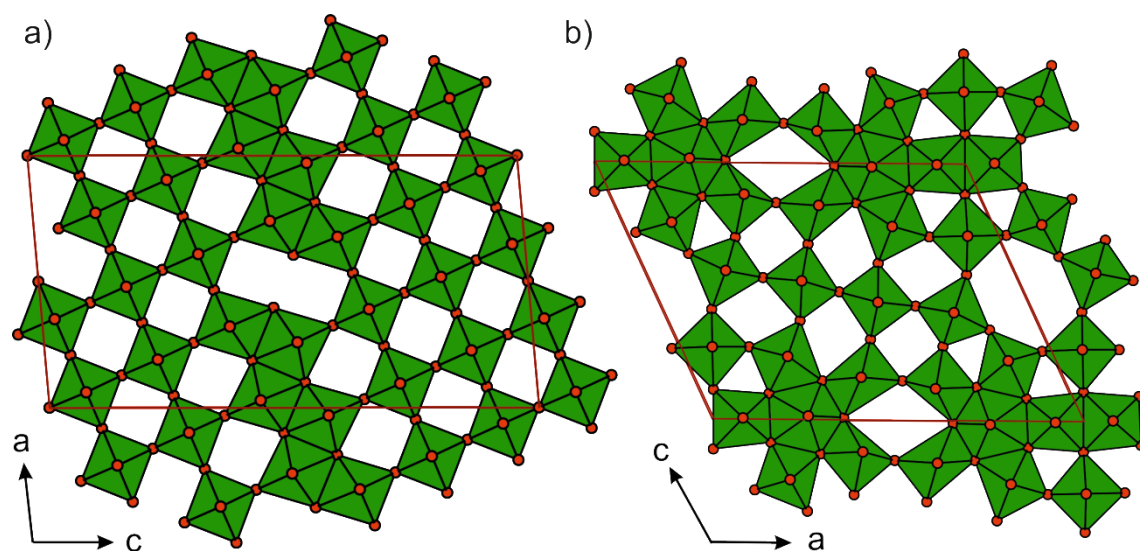


Figure 9.2 Crystal structures of  $\text{WO}_{2.90}$  ( $\text{W}_{20}\text{O}_{58}$ ) showing the CS $\{103\}$  plane [257] (a) and  $\text{WO}_{2.72}$  ( $\text{W}_{18}\text{O}_{49}$ ) showing the pentagonal columns of  $\text{WO}_7$  pentagonal bipyramids with edge sharing and hexagonal tunnels [261] (b).

Table 9.1 Summary of the crystallographic information on the existing compounds in system W-O, S.G.: space group, Z: formula units per unit cell.

Phases	S.G., Z	Unit cell parameters ( $\text{\AA}$ , $^\circ$ )	Lit.
$c\text{-WO}_3$	$Pm\bar{3}m$ , 1	3.838	[252]
$h\text{-WO}_3$	$P6/mmm$ , 3	7.298(2), 3.899(2)	[250]
$\alpha\text{-WO}_3$	$P4/nmm$ , 2	5.250(2), 3.915(2)	[245]
$\alpha\text{-WO}_3$	$P4/ncc$ , 4	5.2806(1), 7.8496(3)	[249]
$\alpha\text{-WO}_3$	$P4/ncc$ , 4	5.2759(1), 7.8462(3)	[249]
$\beta\text{-WO}_3$	$Pbcn$ , 8	7.3903(2), 7.5655(2), 7.7875(3)	[249]
$\beta\text{-WO}_3$	$Pbcn$ , 8	7.3612(2), 7.5739(2), 7.7620(3)	[249]
$\beta\text{-WO}_3$	$Pbcn$ , 8	7.3331(2), 7.5733(2), 7.7401(3)	[249]
$\beta\text{-WO}_3$	$Pnma$ , 8	7.570(4), 7.341(4), 7.754(4)	[263]
$\gamma\text{-WO}_3$	$P2_1/n$ , 8	7.3, 7.53, 7.68, 90.9	[264]
$\delta\text{-WO}_3$	$P\bar{1}$ , 8	7.309(2), 7.522(2), 7.678(2), 88.81(2), 90.92(2), 90.93(2)	[247]
$\varepsilon\text{-WO}_3$	$Pc$ , 4	5.27793(3), 5.15594(3), 7.66392(4), 91.762	[248]
$\text{WO}_{2.96}$	$P2/c$ , 50	11.9, 3.826, 59.64, 98.4	[256]
$\text{WO}_{2.9}$	$P2/m$ , 20	12.1, 3.78, 23.4, 90.95	[257]
$\text{WO}_{2.82}$	--	19.31, 3.781, 17.07, 104.4	[260]
$\text{WO}_{2.72}$	$P2/m$ , 18	18.32, 3.79, 14.04, 115.2	[261]
$\text{W}^{\text{IV}}\text{O}_2$	$P2_1/c$ , 4	5.5769(2), 4.8986(1), 5.6644(2), 120.678(1)	[262]

The structure families of MPTB or DPTB show how phosphate can be incorporated into the  $\text{WO}_3$  lattice. The members of MPTB are partially reduced phases and can be written as  $(\text{PO}_2)_4(\text{W}^{\text{V}}\text{O}_3)_4(\text{W}^{\text{VI}}\text{O}_3)_{2m}$  ( $0 \leq m \leq 12$ ). In contrast, the 2<sup>nd</sup> member,  $\text{WOPO}_4$  has neither tungsten 6+ nor  $\text{ReO}_3$  type slabs.  $\text{WOPO}_4$  contains tungsten in a single valence state (5+) and zig-zag chains of  $\text{WO}_6$  corner sharing octahedra separated by  $\text{PO}_4$  units. Phosphates with  $\text{WOPO}_4$  structure type containing hexavalent tungsten were hitherto unknown.

In this chapter, synthesis of thermodynamically metastable phosphates with structures related to those of  $\text{cub-WO}_3$ ,  $\text{tet-WO}_3$  or  $\text{WOPO}_4$  will be described. In addition to  $\text{WO}_3$  and  $\text{P}_2\text{O}_5$  these phosphates may contain further oxides of tri- and tetravalent metals. Their characterization by XRPD is presented. Furthermore, characterization of some of these phosphates was carried out by electron diffraction, magnetic measurements,  $^{31}\text{P}$ -MAS-NMR and UV/Vis/NIR spectroscopy.

## 9.2 Synthesis

In SCS experiments aiming at the synthesis of  $M^{\text{III}}(\text{W}^{\text{VI}}\text{O}_2)_2(\text{P}_2\text{O}_7)(\text{PO}_4)$  (see Chapter 8) thermodynamically metastable phosphates were observed as intermediates with XRPD pattern related to those of (1) *cub*- and *tet*-WO<sub>3</sub> type  $\{(M^{\text{III}}_{0.17}\text{W}^{\text{VI}}_{0.33}\text{P}_{0.50})\text{O}_{2.5}\square_{0.5}$ ;  $M$ : Sc, V, Cr, Fe, In} and, at increasing temperature, (2) to the WOPO<sub>4</sub> structure type  $\{(M^{\text{III}}_{0.333}\text{W}^{\text{VI}}_{0.667})\text{OPO}_4$ ;  $M$ : V, Cr, Fe}. The procedure for SCS was already described in section 8.2 (see also Table 9.2).

Table 9.2 Experiments aiming at the synthesis of phosphates  $M^{\text{III}}(\text{W}^{\text{VI}}\text{O}_2)_2(\text{P}_2\text{O}_7)(\text{PO}_4)$  by SCS followed by heating in air. For vanadium the use of various  $p(\text{O}_2)$  is given as footnotes, heating protocol  $\vartheta$  (°C) and  $t$  (d).

<i>M</i>	Starting Materials (mmol)	$\vartheta$ (°C); <i>t</i> (d)	Reaction Products (according to IP-Guinier photographs)	
Al	Al(NO <sub>3</sub> ) <sub>3</sub> ·9H <sub>2</sub> O	(3.0)	400; 0.07	Keggin <sup>h)</sup>
	(NH <sub>4</sub> ) <sub>6</sub> W <sub>12</sub> O <sub>39</sub> ·4.8H <sub>2</sub> O	(0.50)	550; 1	“ <i>t</i> -WO <sub>3</sub> ” <sup>f)</sup>
	(NH <sub>4</sub> ) <sub>2</sub> HPO <sub>4</sub>	(9.0)	650; 1	“ <i>t</i> -WO <sub>3</sub> ” <sup>f)</sup>
			700; 2	“ <i>t</i> -WO <sub>3</sub> ” <sup>f)</sup>
			850; 1	<i>m</i> -W <sub>2</sub> P <sub>2</sub> O <sub>11</sub> , <i>o</i> -W <sub>2</sub> P <sub>2</sub> O <sub>11</sub>
		950; 6	<i>m</i> -W <sub>2</sub> P <sub>2</sub> O <sub>11</sub>	
Sc	Sc <sub>2</sub> O <sub>3</sub>	(0.66)	500; 0.07	amorphous
	(NH <sub>4</sub> ) <sub>6</sub> W <sub>12</sub> O <sub>39</sub> ·4.8H <sub>2</sub> O	(0.23)	600; 1	“ <i>t</i> -WO <sub>3</sub> ” <sup>f)</sup>
	(NH <sub>4</sub> ) <sub>2</sub> HPO <sub>4</sub>	(4.00)	700; 5	“ <i>t</i> -WO <sub>3</sub> ” <sup>f)</sup>
			850; 3	“ <i>t</i> -WO <sub>3</sub> ” <sup>f)</sup> , <i>m</i> -W <sub>2</sub> P <sub>2</sub> O <sub>11</sub>
			950; 4	Sc <sup>III</sup> (W <sup>VI</sup> O <sub>2</sub> ) <sub>2</sub> (P <sub>2</sub> O <sub>7</sub> )(PO <sub>4</sub> ), <i>m</i> -W <sub>2</sub> P <sub>2</sub> O <sub>11</sub>
V <sup>a)</sup>	NH <sub>4</sub> VO <sub>3</sub>	(9.90)	400; 0.06	Keggin <sup>h)</sup>
	(NH <sub>4</sub> ) <sub>6</sub> W <sub>12</sub> O <sub>39</sub> ·4.8H <sub>2</sub> O	(1.68)	400; 0.3	Keggin <sup>h)</sup> “ <i>c</i> -WO <sub>3</sub> ” <sup>g)</sup>
	(NH <sub>4</sub> ) <sub>2</sub> HPO <sub>4</sub>	(30.0)	425; 1	“ <i>c</i> -WO <sub>3</sub> ” <sup>g)</sup>
			600; 1	“ <i>c</i> -WO <sub>3</sub> ” <sup>g)</sup>
			780; 2 <sup>c)</sup>	(V <sub>0.33</sub> W <sub>0.67</sub> )OPO <sub>4</sub> <sup>i)</sup>
		900; 2 <sup>c)</sup>	V <sup>III</sup> (W <sup>VI</sup> O <sub>2</sub> ) <sub>2</sub> (P <sub>2</sub> O <sub>7</sub> )(PO <sub>4</sub> )	
V <sup>b)</sup>	NH <sub>4</sub> VO <sub>3</sub>	(0.80)	400; 0.06	Keggin <sup>h)</sup>
	(NH <sub>4</sub> ) <sub>6</sub> W <sub>12</sub> O <sub>39</sub> ·4.8H <sub>2</sub> O	(0.10)	400; 0.3	Keggin <sup>h)</sup> , “ <i>c</i> -WO <sub>3</sub> ” <sup>g)</sup>
	(NH <sub>4</sub> ) <sub>2</sub> HPO <sub>4</sub>	(2.00)	850; 9 <sup>c)</sup>	V <sup>III</sup> (W <sup>VI</sup> O <sub>2</sub> ) <sub>2</sub> (P <sub>2</sub> O <sub>7</sub> )(PO <sub>4</sub> ), (W <sub>0.83</sub> V <sub>0.17</sub> O <sub>3</sub> ) <sub>8</sub> (PO <sub>2</sub> ) <sub>4</sub>
			950; 3 <sup>d)</sup>	(V <sup>III</sup> <sub>0.6</sub> V <sup>IV</sup> <sub>0.4</sub> )(W <sup>VI</sup> O <sub>2</sub> ) <sub>1.8</sub> (V <sup>IV</sup> O <sub>2</sub> ) <sub>0.2</sub> (P <sub>2</sub> O <sub>7</sub> )PO <sub>4</sub>
Cr	Cr(NO <sub>3</sub> ) <sub>3</sub> ·9H <sub>2</sub> O	(2.85)	400; 0.06	Keggin <sup>h)</sup>
	(NH <sub>4</sub> ) <sub>6</sub> W <sub>12</sub> O <sub>39</sub> ·4.8H <sub>2</sub> O	(0.47)	450; 1	amorphous
	(NH <sub>4</sub> ) <sub>2</sub> HPO <sub>4</sub>	(8.55)	650; 1	“ <i>c</i> -WO <sub>3</sub> ” <sup>g)</sup>
			800; 2	“ <i>c</i> -WO <sub>3</sub> ” <sup>g)</sup>
			850; 2	(Cr <sub>0.33</sub> W <sub>0.67</sub> )OPO <sub>4</sub> <sup>i)</sup>
		950; 3	Cr <sup>III</sup> (W <sup>VI</sup> O <sub>2</sub> ) <sub>2</sub> (P <sub>2</sub> O <sub>7</sub> )(PO <sub>4</sub> )	
Fe	FePO <sub>4</sub>	(6.60)	400; 0.06	Keggin <sup>h)</sup>
	(NH <sub>4</sub> ) <sub>6</sub> W <sub>12</sub> O <sub>39</sub> ·4.8H <sub>2</sub> O	(1.12)	450; 1	amorphous
	(NH <sub>4</sub> ) <sub>2</sub> HPO <sub>4</sub>	(13.4)	700; 2	“ <i>c</i> -WO <sub>3</sub> ” <sup>g)</sup>
			800; 10	(Cr <sub>0.33</sub> W <sub>0.67</sub> )OPO <sub>4</sub> <sup>i)</sup>
		900; 3	Fe <sup>III</sup> (W <sup>VI</sup> O <sub>2</sub> ) <sub>2</sub> (P <sub>2</sub> O <sub>7</sub> )(PO <sub>4</sub> )	

In	InCl <sub>3</sub>	(2.37)	400; 0.06	Keggin <sup>h)</sup>
	(NH <sub>4</sub> ) <sub>6</sub> W <sub>12</sub> O <sub>39</sub> ·4.8H <sub>2</sub> O	(0.40)	500; 1	amorphous
	(NH <sub>4</sub> ) <sub>2</sub> HPO <sub>4</sub>	(7.11)	600; 1	“c-WO <sub>3</sub> ” <sup>g)</sup>
			700; 5	“c-WO <sub>3</sub> ” <sup>g)</sup>
			800; 6	“c-WO <sub>3</sub> ” <sup>g)</sup> , <i>m</i> -W <sub>2</sub> P <sub>2</sub> O <sub>11</sub>
		900; 3	In <sup>III</sup> (W <sup>VI</sup> O <sub>2</sub> ) <sub>2</sub> (P <sub>2</sub> O <sub>7</sub> )(PO <sub>4</sub> ), <i>m</i> -W <sub>2</sub> P <sub>2</sub> O <sub>11</sub>	
Lu	LuCl <sub>3</sub> ·6H <sub>2</sub> O	(0.90)	500; 0.17	
	(NH <sub>4</sub> ) <sub>6</sub> W <sub>12</sub> O <sub>39</sub> ·4.8H <sub>2</sub> O	(0.15)	600; 1	“c-WO <sub>3</sub> ” <sup>g)</sup>
	(NH <sub>4</sub> ) <sub>2</sub> HPO <sub>4</sub>	(2.73)	800; 4	LuPO <sub>4</sub> , <i>m</i> -W <sub>2</sub> P <sub>2</sub> O <sub>11</sub>
			900; 168	LuPO <sub>4</sub> , <i>m</i> -W <sub>2</sub> P <sub>2</sub> O <sub>11</sub>
		1000; 6 <sup>e)</sup>	LuPO <sub>4</sub> , <i>m</i> -W <sub>2</sub> P <sub>2</sub> O <sub>11</sub> , WO <sub>3</sub>	
La	LaPO <sub>4</sub>	(0.90)	500; 0.06	
	(NH <sub>4</sub> ) <sub>6</sub> W <sub>12</sub> O <sub>39</sub> ·4.8H <sub>2</sub> O	(0.15)	600; 1	
	(NH <sub>4</sub> ) <sub>2</sub> HPO <sub>4</sub>	(1.82)	800; 2	
			950; 5 <sup>e)</sup>	LaPO <sub>4</sub> , W <sub>2</sub> P <sub>2</sub> O <sub>11</sub> , WO <sub>3</sub>
Nd	Nd(NO <sub>3</sub> ) <sub>3</sub> ·6H <sub>2</sub> O	(0.90)	500; 0.06	
	(NH <sub>4</sub> ) <sub>6</sub> W <sub>12</sub> O <sub>39</sub> ·4.8 H <sub>2</sub> O	(0.15)	600; 1	“c-WO <sub>3</sub> ” <sup>g)</sup>
	(NH <sub>4</sub> ) <sub>2</sub> HPO <sub>4</sub>	(2.73)	800; 4	NdPO <sub>4</sub> , <i>m</i> -W <sub>2</sub> O <sub>3</sub> (PO <sub>4</sub> ) <sub>2</sub>
			900; 7	NdPO <sub>4</sub> , <i>m</i> -W <sub>2</sub> O <sub>3</sub> (PO <sub>4</sub> ) <sub>2</sub>
1000; 6 <sup>e)</sup>			NdPO <sub>4</sub> , <i>m</i> -W <sub>2</sub> O <sub>3</sub> (PO <sub>4</sub> ) <sub>2</sub> , WO <sub>3</sub>	
Sm	SmPO <sub>4</sub>	(0.90)	500; 0.06	
	(NH <sub>4</sub> ) <sub>6</sub> W <sub>12</sub> O <sub>39</sub> ·4.8H <sub>2</sub> O	(0.15)	600; 0.2	
	(NH <sub>4</sub> ) <sub>2</sub> HPO <sub>4</sub>	(1.83)	700; 1	
			750; 2	
			900; 3	SmPO <sub>4</sub> , <i>m</i> -W <sub>2</sub> O <sub>3</sub> (PO <sub>4</sub> ) <sub>2</sub>
1000; 2 <sup>e)</sup>			SmPO <sub>4</sub> , <i>m</i> -W <sub>2</sub> P <sub>2</sub> O <sub>11</sub> , WO <sub>3</sub>	
Yb	YbPO <sub>4</sub>	(0.90)	500; 0.06	
	(NH <sub>4</sub> ) <sub>6</sub> W <sub>12</sub> O <sub>39</sub> ·4.8H <sub>2</sub> O	(0.15)	600; 0.2	
	(NH <sub>4</sub> ) <sub>2</sub> HPO <sub>4</sub>	(1.82)	700; 1	
			750; 2	YbPO <sub>4</sub> , <i>m</i> -W <sub>2</sub> O <sub>3</sub> (PO <sub>4</sub> ) <sub>2</sub>
900; 3 <sup>e)</sup>			YbPO <sub>4</sub> , <i>m</i> -W <sub>2</sub> P <sub>2</sub> O <sub>11</sub> , WO <sub>3</sub>	
V/Fe	NH <sub>4</sub> VO <sub>3</sub>	(6.0)	400; 0.06	“c-WO <sub>3</sub> ” <sup>g)</sup>
	FePO <sub>4</sub>	(6.0)	450; 1	“c-WO <sub>3</sub> ” <sup>g)</sup>
	(NH <sub>4</sub> ) <sub>6</sub> W <sub>12</sub> O <sub>39</sub> ·4.8H <sub>2</sub> O	(1.5)		
	(NH <sub>4</sub> ) <sub>2</sub> HPO <sub>4</sub>	(24.0)		

<sup>a)</sup> upper phase boundary, <sup>b)</sup> lower phase boundary, <sup>c)</sup> under argon  $p(\text{O}_2) \approx 20$  ppm, <sup>d)</sup>  $p(\text{O}_2) = 1000$  ppm, <sup>e)</sup> about to melt, <sup>f)</sup> phosphates with structure type of tetragonal WO<sub>3</sub> [249], <sup>g)</sup> phosphates with structure type of cubic WO<sub>3</sub> [252, 253] see, <sup>h)</sup> (NH<sub>4</sub>)<sub>3</sub>[PW<sub>12</sub>O<sub>40</sub>]·*x*H<sub>2</sub>O [232] type, <sup>i)</sup> WOPO<sub>4</sub> structure type.

In SCS process, the reaction proceeds from the amorphous combustion product through several reaction intermediates to the final thermodynamically stable compound. A typical sequence of reactions shows with increasing temperature a Keggin type solid presumably (NH<sub>4</sub>)<sub>3</sub>[PW<sub>12</sub>O<sub>40</sub>]·*x*H<sub>2</sub>O → amorphous material → ReO<sub>3</sub> related XRPD pattern [252, 253]  $\{(M^{\text{III}}_{0.167}W^{\text{VI}}_{0.333}P^{\text{V}}_{0.50})\text{O}_{2.5}\square_{0.5}\}$ ; *M*: V, Cr, Fe, In} → phosphate with WOPO<sub>4</sub> structure type [90, this thesis]  $\{(M^{\text{III}}_{0.333}W^{\text{VI}}_{0.667})\text{OPO}_4\}$ ; *M*: V, Cr, Fe} → thermodynamically stable phase  $\{M^{\text{III}}(\text{W}^{\text{VI}}\text{O}_2)_2(\text{P}_2\text{O}_7)(\text{PO}_4)\}$ ; *M*: Sc, V, Cr, Fe, In} as shown in Table 9.2. The XRPD patterns of the sequential changes with temperatures are shown in Figure 9.3 for *M*: Cr and in Figure 14.8 to Figure 14.11 (Appendix) for *M*: Sc, V, Fe, In.

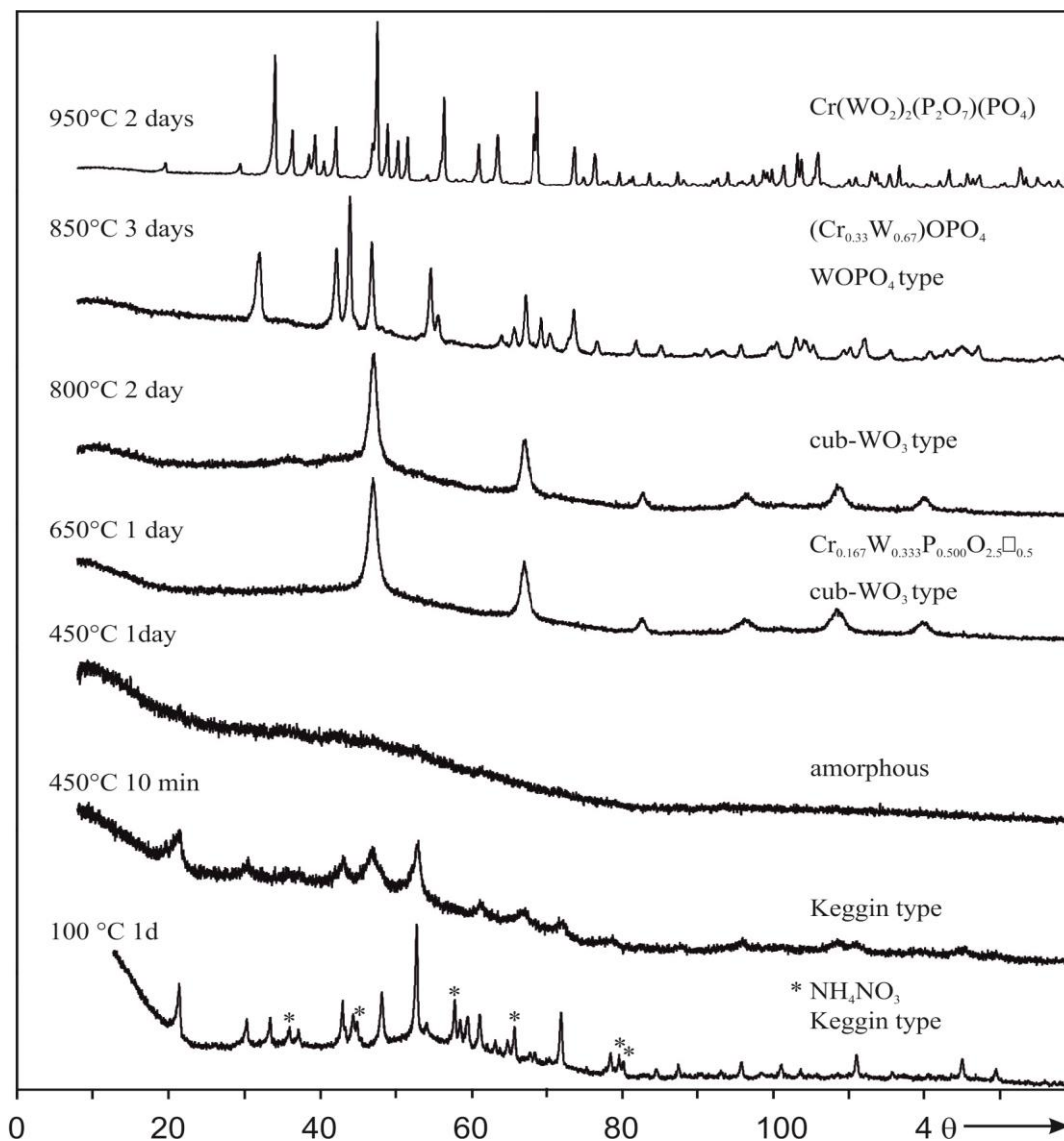


Figure 9.3 Powder diffraction patterns showing the progress of phase formation with temperature during SCS followed by heating in air. The formation of two metastable phases, *cub*- $\text{WO}_3$  and  $\text{WOPO}_4$  type prior to the occurrence of the thermodynamically stable phase  $\text{Cr}(\text{WO}_2)_2(\text{P}_2\text{O}_7)(\text{PO}_4)$  is obvious.

Immediately after combustion/ignition (400 °C) the XRPD pattern shows the weak reflections of Keggin type along with indication of amorphous solids (Figure 9.3). On subsequent heating the XRPD pattern of the reaction intermediate shows the formation of amorphous solid which is important for obtaining the desired phase, inasmuch as it approves the required homogeneous distribution of all the components. However, the formation of amorphous solids is not frequently detectable due to thermodynamic and kinetic effects. The thermodynamically metastable *cub*- $\text{WO}_3$  structure type phosphates were obtained at low temperature around 500 °C. These are stable up to 800 °C (see Table 9.2).  $\text{V}^{3+}$ ,  $\text{Cr}^{3+}$ ,  $\text{Fe}^{3+}$ ,  $\text{In}^{3+}$  form phosphate with *cub*- $\text{WO}_3$  structure type, however  $\text{Sc}^{3+}$  forms

*tet*- $\text{WO}_3$  structure type (Figure 9.7). Eventually for the vanadium containing compound a homogeneity range  $(\text{V}_{0.5-x}\text{W}_x\text{P}_{0.5})\text{O}_{2.5+\delta}$  ( $0.25 \leq x \leq 0.50$ ) with *cub*- $\text{WO}_3$  structure type was obtained (see Figure 9.4 and Table 6.3). Attempts for co-doping by Fe and V according to  $(\text{Fe}_{0.1}\text{V}_{0.1}\text{W}_{0.3}\text{P}_{0.5})\text{O}_{2.5+\delta}$  via SCS led also to the formation of a phase with *cub*- $\text{WO}_3$  structure type (Table 9.2 and Figure 9.5).

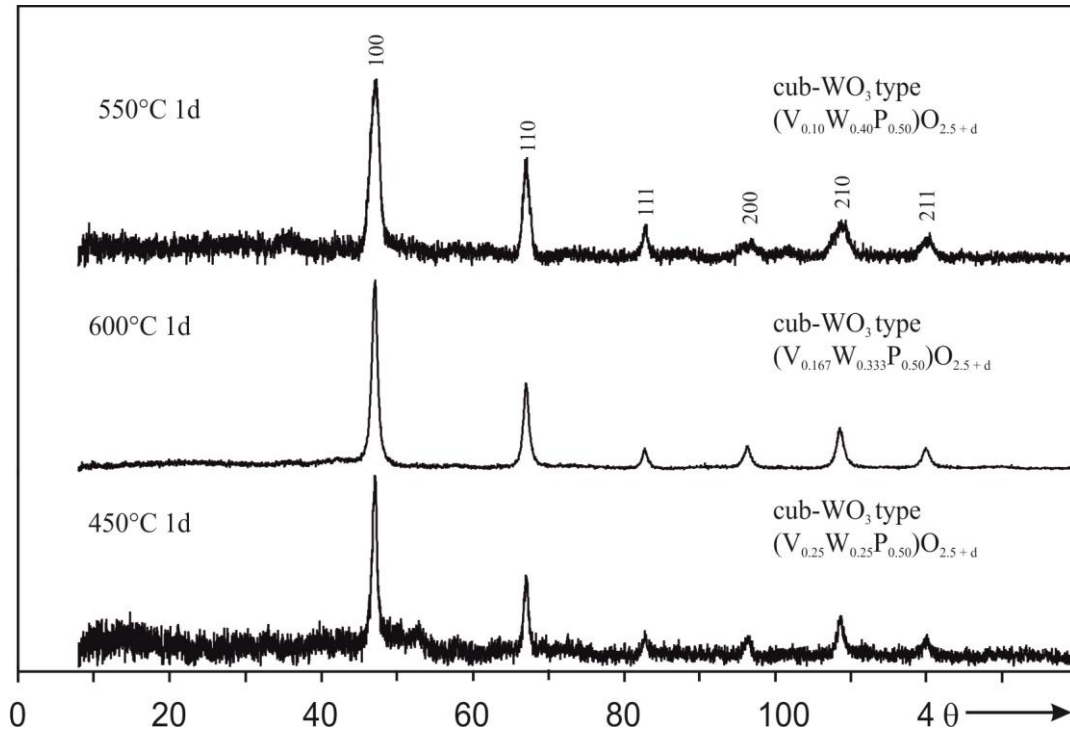


Figure 9.4 XRPD patterns of members of the solid solution  $(\text{V}_{1-x}\text{W}_x\text{P}_{0.5})\text{O}_{2.5+\delta}$  ( $0.25 \leq x \leq 0.50$ ) with *cub*- $\text{WO}_3$  structure type obtained via SCS followed by heating in air.

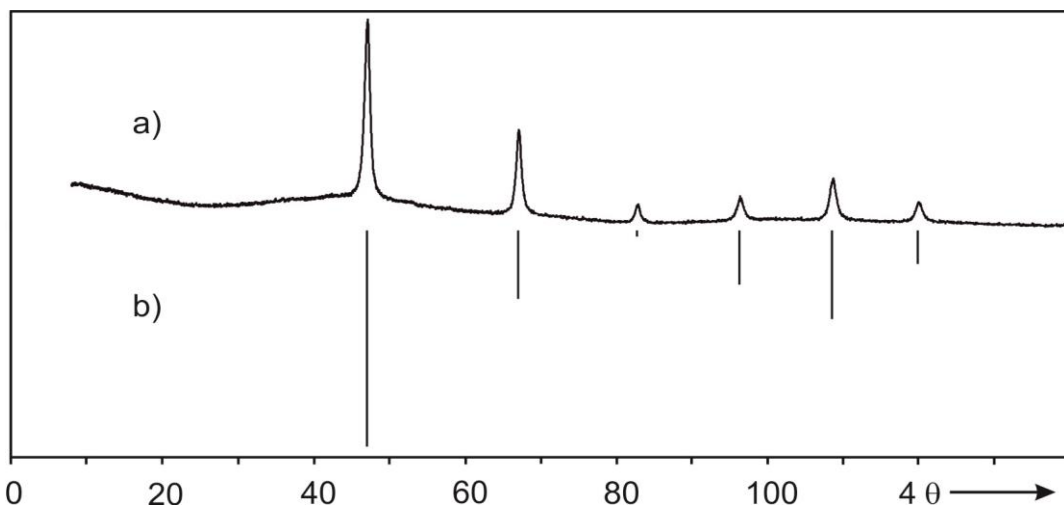


Figure 9.5 Guinier photograph of  $(\text{Fe}_{0.10}\text{V}_{0.10}\text{W}_{0.30}\text{P}_{0.5})\text{O}_{2.5+\delta}$  (*cub*- $\text{WO}_3$  structure type) (a) obtained by via SCS followed by heating in air at 450 °C for one day, compared with the simulated pattern (b) with adjusted lattice parameter (structure model *cub*- $\text{WO}_3$  [252]).

Phosphates related to *cub*- or *tet*-WO<sub>3</sub> structure were obtained even in the simple binary oxide system WO<sub>3</sub> – PO<sub>2.5</sub> via SCS followed by heating in air (see Table 9.3 and Figure 9.6). Some of the reported experiments (Table 9.3) were carried out by Markus Weber [265]. Details of the SCS were given in sections 2.7 and 8.2.

Table 9.3 Experiments aiming at the synthesis of (W<sub>1-x</sub>P<sub>x</sub>)O<sub>3-x/2</sub>□<sub>x/2</sub> (0 ≤ x ≤ 0.5) via SCS, molar ratio of metal:glycine:nitric acid is 1:3:6, heating protocol *g* (°C) and *t* (h).

<b>W:P (x)</b>	<b>Starting Solids</b>	<b>Amount (mmol)</b>	<b><i>g</i> (°C)</b>	<b><i>t</i> (h)</b>	<b>Reaction Products (according to IP Guinier photograph)</b>
12:0 (0.0)	(NH <sub>4</sub> ) <sub>6</sub> W <sub>12</sub> O <sub>39</sub> ·xH <sub>2</sub> O (NH <sub>4</sub> ) <sub>2</sub> HPO <sub>4</sub>	0.66 ----	400	0.1	<i>h</i> -WO <sub>3</sub> <sup>a)</sup>
			500	96	<i>m</i> -WO <sub>3</sub> <sup>b)</sup>
			650	48	<i>m</i> -WO <sub>3</sub> <sup>b)</sup>
12:1 (0.077)	(NH <sub>4</sub> ) <sub>6</sub> W <sub>12</sub> O <sub>39</sub> ·xH <sub>2</sub> O (NH <sub>4</sub> ) <sub>2</sub> HPO <sub>4</sub>	1.02 1.05	400	0.1	Keggin <sup>c)</sup> , “ <i>t</i> -WO <sub>3</sub> ” <sup>d)</sup>
			600	240	“ <i>t</i> -WO <sub>3</sub> ” <sup>d)</sup> , <i>m</i> -WO <sub>3</sub> <sup>b)</sup>
			900	48	<i>m</i> -WO <sub>3</sub> <sup>b)</sup> , <i>m</i> -(W <sub>2</sub> O <sub>3</sub> )(PO <sub>4</sub> ) <sub>2</sub>
12:2 (0.14)	(NH <sub>4</sub> ) <sub>6</sub> W <sub>12</sub> O <sub>39</sub> ·xH <sub>2</sub> O (NH <sub>4</sub> ) <sub>2</sub> HPO <sub>4</sub>	0.66 1.35	400	0.1	“ <i>t</i> -WO <sub>3</sub> ” <sup>d)</sup> , Keggin <sup>c)</sup>
			500	72	“ <i>t</i> -WO <sub>3</sub> ” <sup>d)</sup> , <i>m</i> -WO <sub>3</sub> <sup>b, f)</sup>
			650	72	“ <i>t</i> -WO <sub>3</sub> ” <sup>d)</sup> , <i>m</i> -WO <sub>3</sub> <sup>b, f)</sup>
12:4 (0.25)	(NH <sub>4</sub> ) <sub>6</sub> W <sub>12</sub> O <sub>39</sub> ·xH <sub>2</sub> O (NH <sub>4</sub> ) <sub>2</sub> HPO <sub>4</sub>	0.66 2.70	400	0.1	Keggin <sup>c)</sup>
			500	72	“ <i>t</i> -WO <sub>3</sub> ” <sup>d)</sup>
			500	144	“ <i>t</i> -WO <sub>3</sub> ” <sup>d)</sup>
12:6 (0.33)	(NH <sub>4</sub> ) <sub>6</sub> W <sub>12</sub> O <sub>39</sub> ·xH <sub>2</sub> O (NH <sub>4</sub> ) <sub>2</sub> HPO <sub>4</sub>	0.66 4.06	400	0.1	Keggin <sup>c)</sup>
			500	5	Keggin <sup>c)</sup>
			650	72	“ <i>t</i> -WO <sub>3</sub> ” <sup>d, f)</sup>
			800	72	<i>m</i> -WO <sub>3</sub> <sup>b)</sup> , <i>m</i> -(W <sub>2</sub> O <sub>3</sub> )(PO <sub>4</sub> ) <sub>2</sub>
12:9 (0.43)	(NH <sub>4</sub> ) <sub>6</sub> W <sub>12</sub> O <sub>39</sub> ·xH <sub>2</sub> O (NH <sub>4</sub> ) <sub>2</sub> HPO <sub>4</sub>	0.66 6.08	400	0.1	Keggin <sup>c)</sup>
			500	24	amorphous
			650	2	“ <i>t</i> -WO <sub>3</sub> ” <sup>d, f)</sup>
12:12 (0.5)	(NH <sub>4</sub> ) <sub>6</sub> W <sub>12</sub> O <sub>39</sub> ·xH <sub>2</sub> O (NH <sub>4</sub> ) <sub>2</sub> HPO <sub>4</sub>	1.00 12.0	400	0.1	Keggin <sup>c)</sup>
			500	24	amorphous
			600	24	“ <i>c</i> -WO <sub>3</sub> ” <sup>e)</sup>
			700	120	<i>o</i> -(W <sub>2</sub> O <sub>3</sub> )(PO <sub>4</sub> ) <sub>2</sub> , “ <i>t</i> -WO <sub>3</sub> ” <sup>d, f)</sup>
			900	144	<i>m</i> -(W <sub>2</sub> O <sub>3</sub> )(PO <sub>4</sub> ) <sub>2</sub> , <i>m</i> -WO <sub>3</sub> <sup>f)</sup>
12:24 (0.67)	(NH <sub>4</sub> ) <sub>6</sub> W <sub>12</sub> O <sub>39</sub> ·xH <sub>2</sub> O (NH <sub>4</sub> ) <sub>2</sub> HPO <sub>4</sub>	0.66 16.21	400	0.1	Keggin <sup>c)</sup>
			500	96	<i>o</i> -(W <sub>2</sub> O <sub>3</sub> )(PO <sub>4</sub> ) <sub>2</sub>
			650	72	<i>o</i> -(W <sub>2</sub> O <sub>3</sub> )(PO <sub>4</sub> ) <sub>2</sub>

<sup>a)</sup> hexagonal WO<sub>3</sub> [250], <sup>b)</sup> monoclinic WO<sub>3</sub> [264], <sup>c)</sup> (NH<sub>4</sub>)<sub>3</sub>[PW<sub>12</sub>O<sub>40</sub>]·xH<sub>2</sub>O [171], <sup>d)</sup> phosphates with structure type of tetragonal WO<sub>3</sub> [249], <sup>e)</sup> phosphates with structure type of cubic WO<sub>3</sub> [252], <sup>f)</sup> very small amount.

Increasing the amount of P<sub>2</sub>O<sub>5</sub> in WO<sub>3</sub> led to the formation of phosphates with structures related to higher symmetric WO<sub>3</sub>. According to Guinier photographs a single phase solid with the structure type of *cub*-WO<sub>3</sub> was obtained at *x* = 0.5. At 0.25 ≤ *x* < 0.50 phases with *tet*-WO<sub>3</sub> related structure [249] were formed (see Table 9.3 and Figure 9.6). At the ranges of 0.077 ≤ *x* < 0.25 the XRPD pattern revealed the formation of mostly *tet*-



$\text{WO}_3$  type phosphate along with one very weak additional reflection. This reflection might be attributed to  $m\text{-WO}_3$  [264]. Even with small amount of  $\text{P}_2\text{O}_5$  the formation of  $o\text{-W}_2\text{O}_3(\text{PO}_4)_2$  [75] or  $m\text{-W}_2\text{O}_3(\text{PO}_4)_2$  [76, 77, 78] was observed upon advanced heat treatment. At  $x < 0.08$  the metastable phase with hexagonal- $\text{WO}_3$  [250] was formed as intermediate. It is worth to be mentioned here that slow evaporating of same precursor material leads to the formation of *mono*- $\text{WO}_3$  instead of *hex*- $\text{WO}_3$ . For  $x > 0.5$  no formation of phases with structures related to  $\text{WO}_3$  was observed. Instead  $m\text{-W}_2\text{O}_3(\text{PO}_4)_2$  and/or  $\text{WOP}_2\text{O}_7$  did occur.

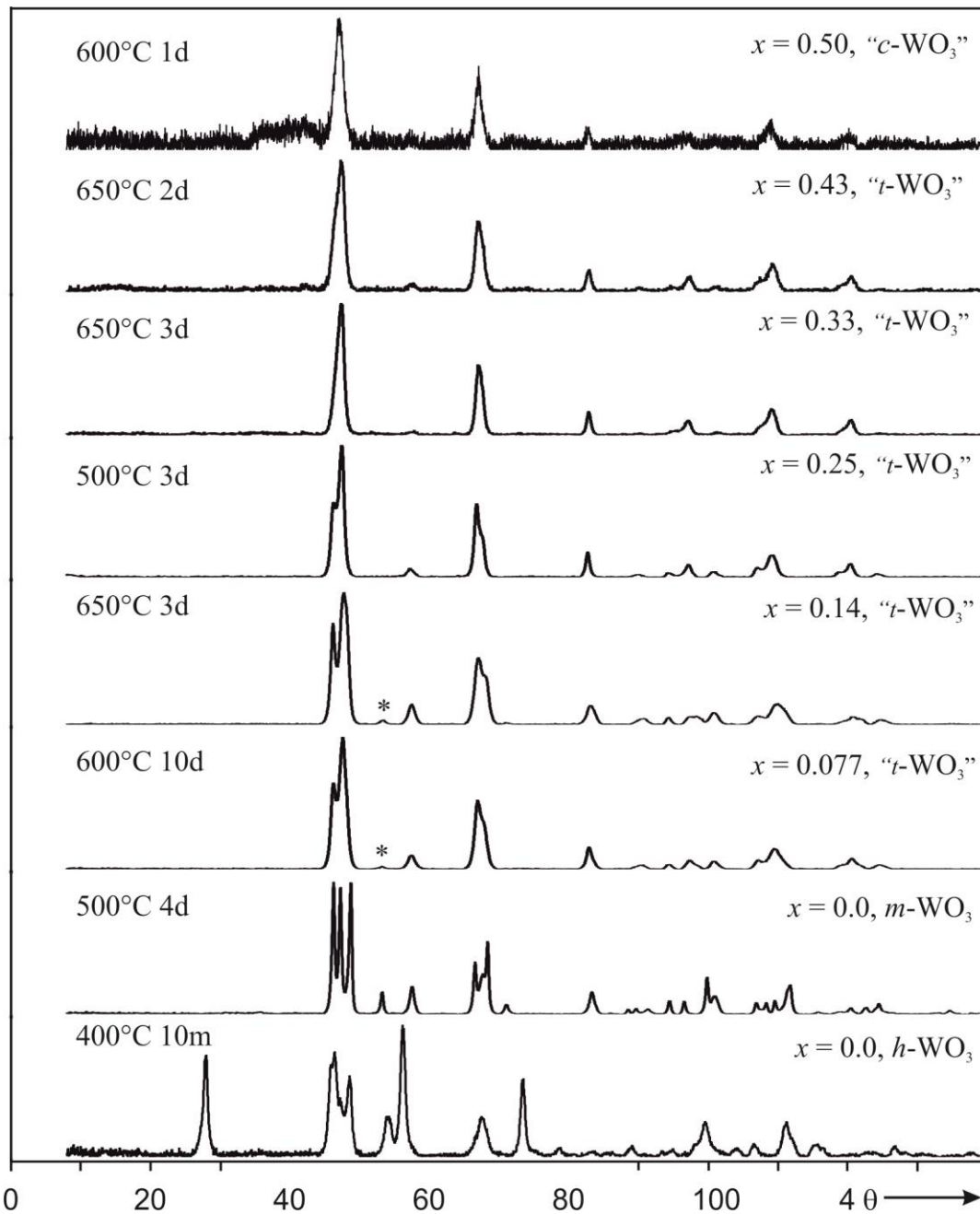


Figure 9.6 Comparison of Guinier photographs of  $(\text{W}_{1-x}\text{P}_x)\text{O}_{3-x/2}\square_{x/2}$ ;  $0 \leq x < 0.5$  obtained by SCS followed by heating in air. Asterisks indicate small impurities of  $m\text{-WO}_3$ .

### 9.3 X-ray powder pattern

The XRPD patterns of the reaction intermediates  $(M^{\text{III}}_{0.167}W^{\text{VI}}_{0.333}P_{0.50})O_{2.5}\square_{0.5}$  ( $M$ : Sc, V, Cr, Fe, In) with structures related to *cub*- and *tet*-WO<sub>3</sub> [252, 253, 249] are compared to simulated diffraction patterns with adjusted lattice parameters (see Figure 9.7). The simulated diffraction patterns based on mixed occupancy of all cations at the single metal site of *cub*-WO<sub>3</sub> and *tet*-WO<sub>3</sub> nicely match the observed Guinier photographs. The lattice parameters are distinctly different from those of pure *cub*-WO<sub>3</sub> (Table 9.4) which provides evidence for the incorporation of further cations into the structure. Assignment of the Guinier photographs of the phosphates with structures related to *cub*- and *tet*-WO<sub>3</sub>, are provided in Table 14.48 to Table 14.57. The XRPD pattern of  $(Fe_{0.1}V_{0.1}W_{0.3}P_{0.5})O_{2.5+\delta}$  (*cub*-WO<sub>3</sub> related structure) matches nicely to the simulated pattern (see Figure 9.5). The assignment of the XRPD pattern is provided in Table 14.56.

Table 9.4 Lattice parameters of the metastable phosphates with crystal structures related to *cub*-/*tet*-WO<sub>3</sub>.

Composition	Sym.	<i>a</i> (Å)	<i>c</i> (Å)	V(Å <sup>3</sup> )	Ref.
WO <sub>3</sub>	cub.	3.838(2)		56.53	[252]
$(V_{0.25}W^{\text{VI}}_{0.25}P^{\text{V}}_{0.50})O_{2.5+\delta}$	cub.	3.7732(9)		53.72(4)	this thesis
$(V_{0.167}W^{\text{VI}}_{0.333}P^{\text{V}}_{0.50})O_{2.5+\delta}$	cub.	3.7708(8)		53.62(3)	this thesis
$(V_{0.10}W^{\text{VI}}_{0.40}P^{\text{V}}_{0.50})O_{2.5+\delta}$	cub.	3.770(1)		53.60(4)	this thesis
$(Cr^{\text{III}}_{0.167}W^{\text{VI}}_{0.333}P^{\text{V}}_{0.50})O_{2.5}\square_{0.5}$	cub.	3.7712(9)		53.63(4)	this thesis
$(Fe^{\text{III}}_{0.167}W^{\text{VI}}_{0.333}P^{\text{V}}_{0.50})O_{2.5}\square_{0.5}$	cub.	3.766(2)		53.40(9)	this thesis
$(In^{\text{III}}_{0.167}W^{\text{VI}}_{0.333}P^{\text{V}}_{0.50})O_{2.5}\square_{0.5}$	cub.	3.761(5)		53.2(2)	this thesis
$(Fe^{\text{III}}_{0.1}V_{0.1}W^{\text{VI}}_{0.4}P^{\text{V}}_{0.50})O_{2.5+\delta}$	cub.	3.7732(8)		53.72(4)	this thesis
$(W^{\text{VI}}_{0.50}P^{\text{V}}_{0.50})O_{2.75}$	cub.	3.771(2)		52.62(8)	this thesis
WO <sub>3</sub> <sup>a)</sup>	tet.	5.2885(5)	7.8626(8)	219.9(1)	[249]
$(W^{\text{VI}}_{0.75}P^{\text{V}}_{0.25})O_{2.875}$	tet.	5.290(2)	7.698(3)	215.4(1)	this thesis
$(Sc^{\text{III}}_{0.167}W^{\text{VI}}_{0.333}P^{\text{V}}_{0.50})O_{2.5}\square_{0.5}$	tet.	5.2760(6)	7.717(2)	214.82(6)	this thesis

<sup>a)</sup> lattice parameters obtained at 800 °C

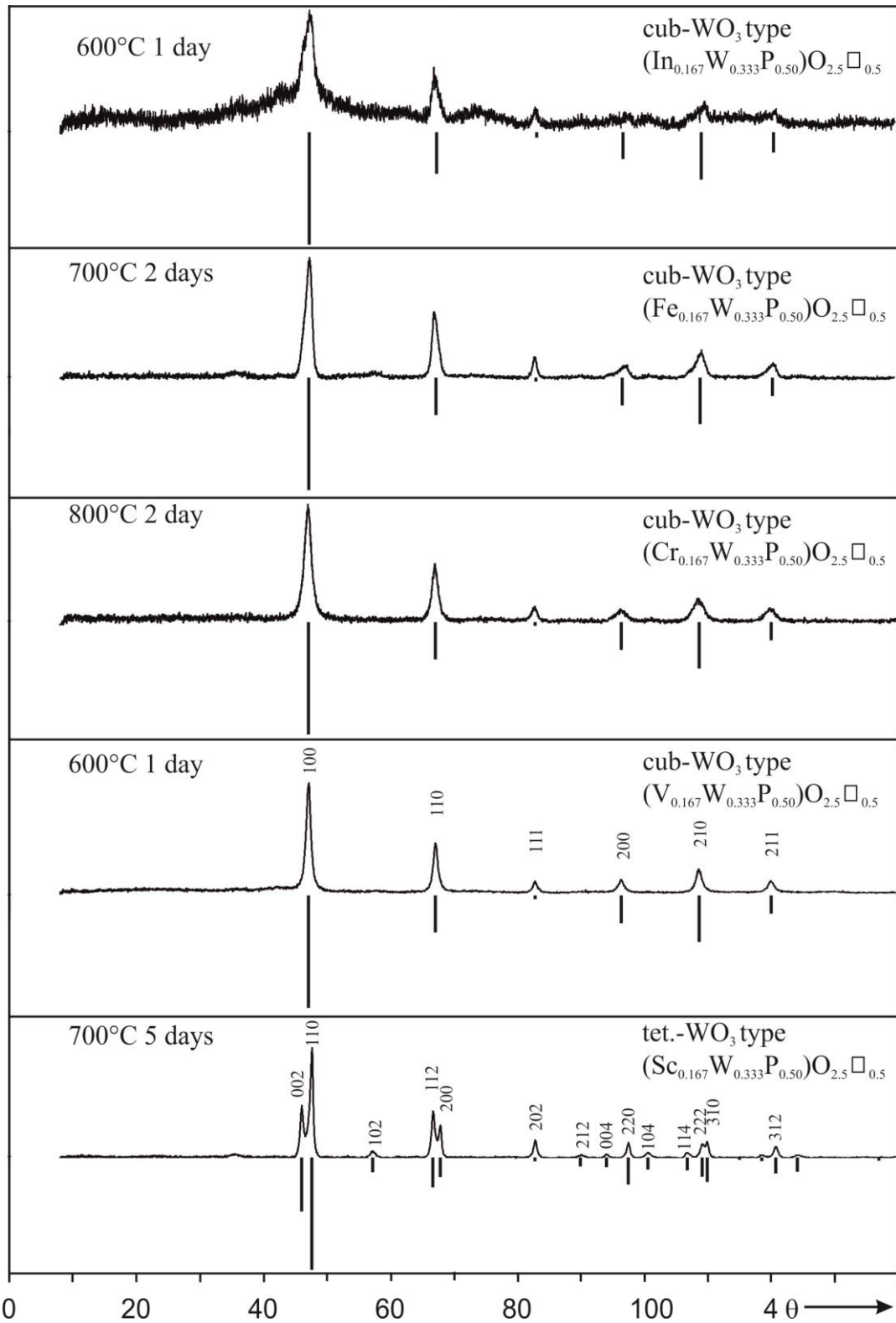


Figure 9.7 Guinier photographs of metastable phosphates  $(M^{\text{III}}_{0.167}W^{\text{VI}}_{0.333}P_{0.50})O_{2.5}\square_{0.5}$  and simulated patterns based on the structure model of *cub*- $\text{WO}_3$  [252], for  $M$ : V, Cr, Fe, In and *tet*- $\text{WO}_3$  [249] for  $M$ : Sc with adjusted lattice parameters.

## 9.4 Transmission Electron Microscopy (TEM)

All electron diffraction and HRTEM studies were performed in the research group of Prof. Dr. Werner Mader, University of Bonn, Germany. The TEM studies were conducted using a Philips CM30 @300 kV microscope with Si(Li) “Thermo nano trace” EDX detector. For HRTEM  $(\text{Cr}^{\text{III}}_{0.167}\text{W}^{\text{VI}}_{0.333}\text{P}^{\text{V}}_{0.50})\text{O}_{2.5}\square_{0.5}$  and  $(\text{W}^{\text{VI}}_{0.5}\text{P}^{\text{V}}_{0.5})\text{O}_{2.75}\square_{0.25}$  were selected because of their stability in air and well defined oxidation states.

For TEM studies the sample was prepared by two methods, a dry and a suspension method. In the first the probe was poured directly on a “quantifoil” carbon foil supported by copper mesh. In the later the probe was suspended in cyclohexane in ultrasonic bath and a droplet of the suspension was given on supported “quantifoil” carbon foil. The samples prepared in both ways showed more or less agglomerated “flakes” of the materials.

Unfortunately, none of the samples were stable under the electron beam. Amorphization of the sample was observed during electron beam irradiation. Neither Bragg peaks nor Scherrer rings were observed as shown in Figure 9.8. One of the important findings of the HRTEM technique is that the size of the flakes was in the nano range (ca. 10-20 nm). The broad FWHM of the reflection profiles in the Guinier photographs point also to nano-scale particles (see Figure 9.7). The EDX analysis of  $(\text{Cr}^{\text{III}}_{0.167}\text{W}^{\text{VI}}_{0.333}\text{P}^{\text{V}}_{0.50})\text{O}_{2.5}\square_{0.5}$  showed the homogeneous distribution of the elements (Table 9.5).

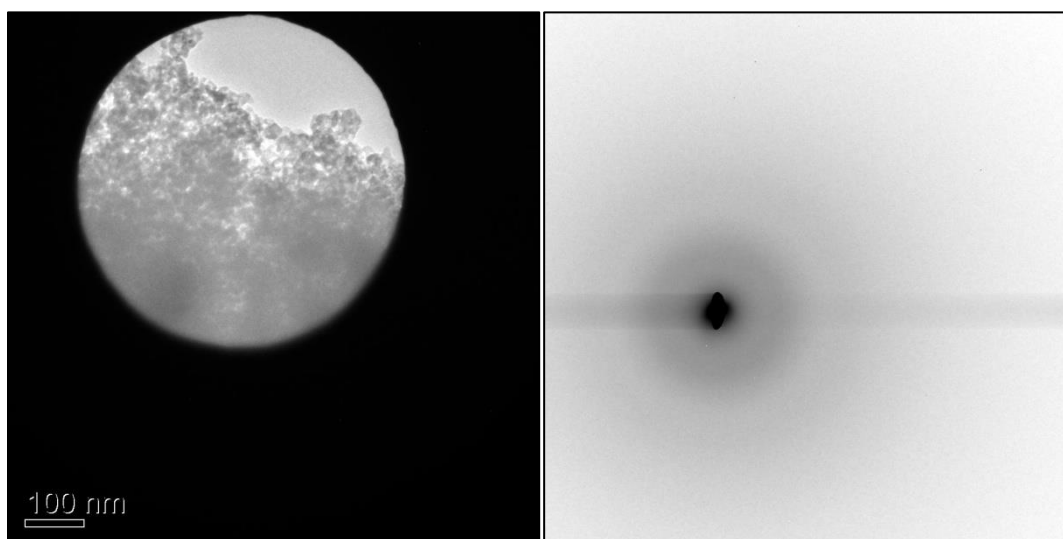


Figure 9.8 TEM image showing an volume of  $(\text{Cr}_{0.17}\text{W}_{0.33}\text{P}_{0.50})\text{O}_{2.5}\square_{0.5}$  selected by a “selected area aperture” for diffraction (left), inverted electron diffraction pattern (right).

Table 9.5 EDX analysis of powder sample of  $\text{cub}-(\text{Cr}_{0.17}\text{W}_{0.33}\text{P}_{0.50})\text{O}_{2.5}\square_{0.5}$ .

	Cr (%)	W (%)	P (%)
spot 1	16.30	31.18	52.47
spot 2	18.73	36.78	44.49
spot 3	15.93	31.67	52.40
spot 4	18.22	34.90	46.88
area	17.43	35.63	46.94
average	17.32	34.03	48.64
theory	16.7	33.3	50.0

## 9.5 $^{31}\text{P}$ -MAS-NMR spectroscopy

The  $^{31}\text{P}$ -MAS-NMR spectra of  $(\text{W}_{1-x}\text{P}_x)\text{O}_{3-x/2}\square_{x/2}$ ;  $x = 0.25, 0.33$  and  $0.50$  exhibit broad isotropic signals at  $-12.6, -12.2,$  and  $-16.4$  ppm (with sharp signal at  $-12.6$  ppm), respectively as shown at Figure 9.9. Due to broad isotropic signals it is not convenient to discuss about the assignment. Although at  $x = 0.25$  and  $0.33$  the reaction intermediate products are phosphate with  $t$ - $\text{WO}_3$  structure type and at  $x = 0.50$  it was  $c$ - $\text{WO}_3$  structure type (according to XRPD, Figure 9.6). The broad signals in  $^{31}\text{P}$ -MAS-NMR spectra of  $(\text{W}_{1-x}\text{P}_x)\text{O}_{3-x/2}\square_{x/2}$  can be attributed to disorder structure as well as presence of amorphous meta-phosphoric acid within the sample which is revealed by small hump at  $\sim 0$  ppm (indicated by down arrow in Figure 9.9). Therefore, the solid  $(\text{W}_{0.67}\text{P}_{0.33})\text{O}_{2.83}\square_{0.17}$  was heated with distilled water for five minutes to remove the amorphous meta-phosphoric acid. After heating with water the remaining solid was filtered, dried and checked again by  $^{31}\text{P}$ -MAS-NMR study, x-ray powder diffraction, and EDX analysis. The mixture of that solid with water was strong acidic in nature that might be due to hydrolysis of the solid amorphous meta-phosphate to ortho-phosphoric acid.

$^{31}\text{P}$ -MAS-NMR resonance of the washed sample at  $\sim 0.2$  ppm (Figure 9.9d) reveals presence of remaining meta-phosphoric acid. This might be due to shorter heating time with water lead to incomplete hydrolysis of meta-phosphoric acid. The expected and observed second highest intense signal at  $-12.2$  ppm was present before and after leaching which is related to  $t$ - $\text{WO}_3$  structure type phosphate. After leaching a new sharp and highest intense resonance at  $-15.5$  ppm might be due to  $c$ - $\text{WO}_3$  structure type. Before heating with water, the signal for cubic structure type was hidden under broad signal due to its less quantity.

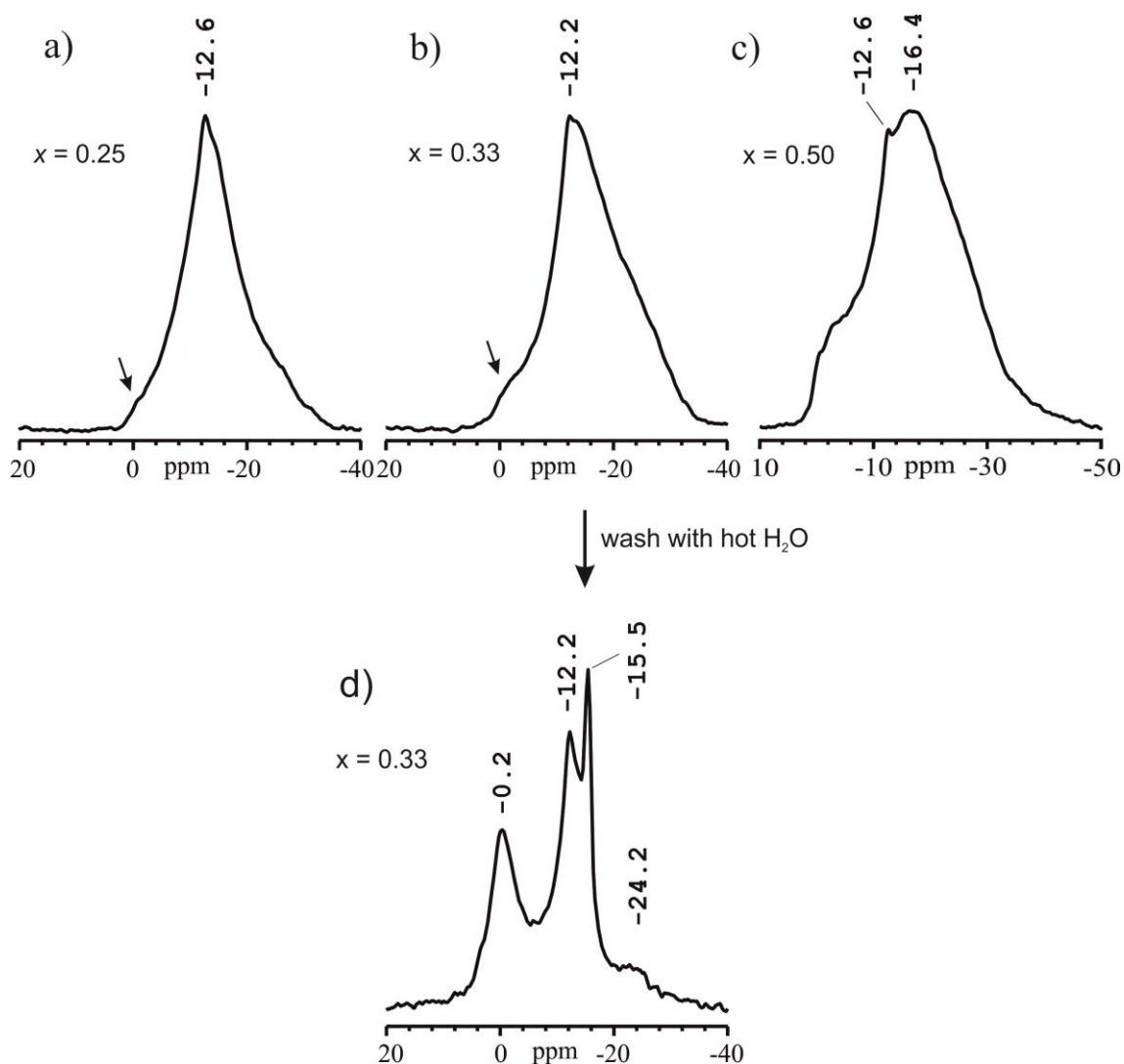


Figure 9.9  $^{31}\text{P}$ -MAS-NMR spectra of  $(\text{W}_{1-x}\text{P}_x)\text{O}_{3-x/2}\square_{x/2}$ ;  $x = 0.25$ , (a),  $x = 0.33$  (b),  $x = 0.50$  (c) obtained by SCS followed by heating in air at  $500^\circ\text{C}$ ,  $650^\circ\text{C}$  and  $500^\circ\text{C}$ , respectively and after leaching with hot water of sample *b* (d).

A broad hump in the XRPD pattern (no background correction) of  $(\text{W}_{0.67}\text{P}_{0.33})\text{O}_{2.83}\square_{0.17}$  indicates presence of amorphous materials (Figure 9.10a). After leaching with hot water the Guinier photograph shows no hints on amorphous material in that sample (Figure 9.10b). According to EDX analysis, after leaching with water the sample,  $(\text{W}_{0.67}\text{P}_{0.33})\text{O}_{2.83}\square_{0.17}$  contain ~61% less phosphorus than before (see Table 9.6) as a consequence of removal of amorphous meta-phosphoric acid during treatment with water.

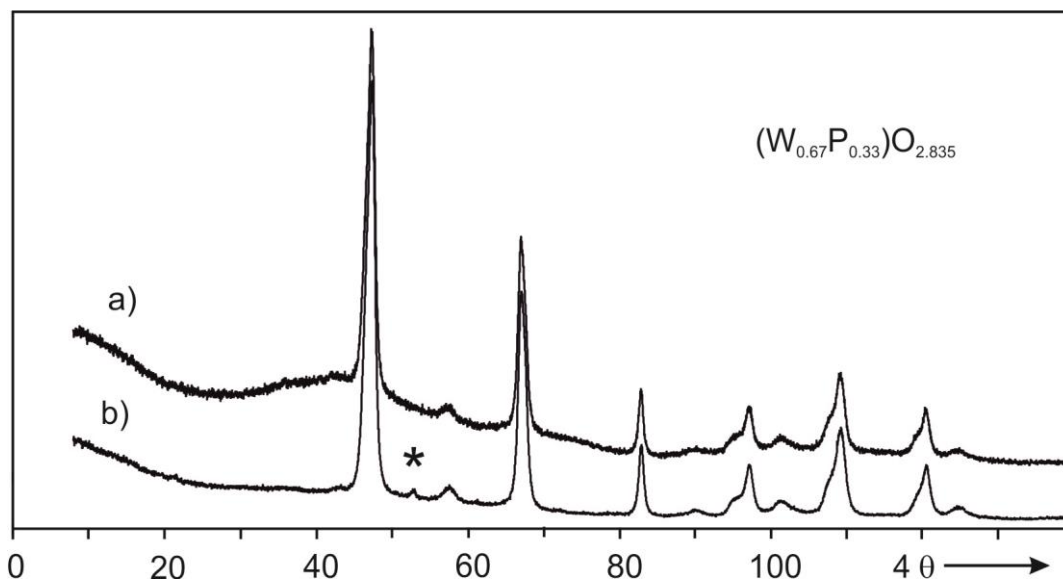


Figure 9.10 Comparison of Guinier photographs (no background correction) of  $(\text{W}_{0.67}\text{P}_{0.33})\text{O}_{2.835}$  (phosphate with *tet*-  $\text{WO}_3$  related, P:W = 6:12) obtained via SCS followed by heating at 650 °C (a) then leaching with hot water (b). Asterisk (\*) indicate might be the appearance of monoclinic  $\text{WO}_3$  phase.

Table 9.6 EDX analysis of powder samples of  $(\text{W}_{0.67}\text{P}_{0.33})\text{O}_{2.83}\square_{0.17}$  before and after leaching with hot water.

Nominal $x$	Before washing			After washing		
	P (%)	W (%)	P : W	P (%)	W (%)	P : W
<b>0.33</b>						
spot 1	33.67	66.33		17.08	82.92	
spot 2	30.81	69.19		15.76	84.24	
spot 3	30.25	69.75		11.28	88.72	
spot 4	32.00	68.00		16.64	83.36	
average	31.68	68.32	<b>5.6 : 12</b>	15.19	84.81	<b>2.2 : 12</b>
theory	33.3	66.7	<b>6 : 12</b>			

To correlate the reaction progress, one sample with particular composition  $(\text{W}_{0.923}\text{P}_{0.077})\text{O}_{2.962}\square_{0.038}$  was annealed at three different temperatures and characterized by XRPD and  $^{31}\text{P}$ -MAS-NMR spectra (see Figure 9.11).

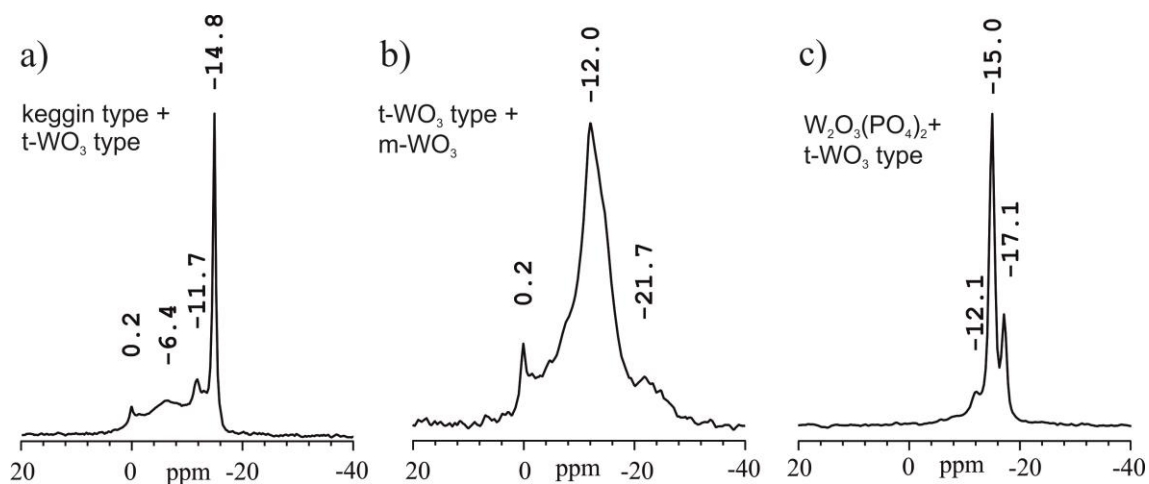


Figure 9.11 Development of  $^{31}\text{P}$ -MAS-NMR spectra  $(\text{W}_{0.923}\text{P}_{0.077})\text{O}_{2.962}$  obtained via SCS followed by heating at three different temperatures 400 °C (a), 600 °C (b), and 900 °C (c).

The  $^{31}\text{P}$ -MAS-NMR spectra of the solid  $(\text{W}_{0.923}\text{P}_{0.077})\text{O}_{2.962}\square_{0.038}$  obtained at 400 °C exhibit one most intense and sharp resonance at  $-14.8$  ppm, one weakest signal at  $-0.2$  and one weak signal at  $-11.7$  ppm. These resonances correspond to the Keggin ion  $(\text{PW}_{12}\text{O}_{40})^{3-}$  [232], orthophosphoric acid, and phosphate with  $t\text{-WO}_3$  structure type, accordingly which complies with the XRPD results.

The  $^{31}\text{P}$ -MAS-NMR spectrum of the annealed powder (600 °C) of this composition shows a broad, intense resonance at  $-12$  ppm with weak one at around  $0.2$  ppm. According to XRPD the composition is mainly  $t\text{-WO}_3$  structure type with very small impurities of  $m\text{-WO}_3$ .

The strongest resonance at  $-15.0$  and rather weak signal at  $-17.1$  ppm of this composition prepared at 900 °C corresponds to  $m\text{-W}_2\text{O}_3(\text{PO}_4)_2$  (see section 5.4). Although this phase is minor according to Guinier photograph, the other main phase is pure  $m\text{-WO}_3$  which is  $^{31}\text{P}$ -MAS-NMR inactive. The remaining very weak signal at  $-12.1$  ppm is due to  $tet\text{-WO}_3$  type phosphate. Interestingly, the  $tet\text{-WO}_3$  type phosphate was not possible to detect by Guinier photograph due to overlapping of its x-ray diffraction peaks with  $m\text{-WO}_3$ .

The ranges of  $^{31}\text{P}$ -MAS-NMR resonance signals for pyrophosphates like  $\text{WO}(\text{P}_2\text{O}_7)$  ( $\delta_{\text{iso}} = -29.0, -33.1$  ppm) [section 8.3] and  $\alpha\text{-(MoO}_2)_2(\text{P}_2\text{O}_7)$  ( $\delta_{\text{iso}} = -21.2, -23.9, -27.0, -28.8$  ppm) [80] suggested that the  $cub$  or  $tet\text{-WO}_3$  type phosphates belongs to only  $\text{PO}_4$  units rather than  $\text{P}_2\text{O}_7$ . The  $^{31}\text{P}$ -MAS-NMR signal for  $cub\text{-(In}^{\text{III}}_{0.17}\text{W}^{\text{VI}}_{0.33}\text{P}_{0.50})\text{O}_{2.5}\square_{0.5}$  at  $\delta_{\text{iso}} = -20.6$  ppm also indicate the presence of only  $\text{PO}_4$  unit (Figure 14.16).



## 9.6 Mixed metal phosphates with WOPO<sub>4</sub> structure type

Thermodynamically metastable phases ( $M^{\text{III}}_{0.333}W^{\text{VI}}_{0.667}$ )OPO<sub>4</sub> with  $M$ : V, Cr, and Fe (WOPO<sub>4</sub> structure type) are obtained by advanced heating (for V,  $p(\text{O}_2) \approx 20$  ppm and for Cr, Fe in air) of the first reaction intermediate ( $M^{\text{III}}_{0.17}W^{\text{VI}}_{0.33}P_{0.50}$ )O<sub>2.5</sub>□<sub>0.5</sub> (diffraction patterns related to *cub*-WO<sub>3</sub> structure). Like the trivalent rare earth cations scandium and indium do not lead to formation the second intermediate, the WOPO<sub>4</sub> related phase. This could be attributed to their larger ionic radii. Tungstenyl(V) phosphate W<sup>V</sup>OPO<sub>4</sub> is chemically modified by heterovalent substitution of pentavalent tungsten (62 pm, [266]) by of two-thirds hexavalent tungsten (60 pm, [266]) and one third of trivalent metal ions. Overall, substitution of W<sup>5+</sup> in WOPO<sub>4</sub> by  $M^{3+}/W^{6+}$  leads to a shrinking of all lattice parameters (see Table 9.7). Comparison of the Guinier photographs of metastable phases ( $M^{\text{III}}_{0.333}W^{\text{VI}}_{0.667}$ )OPO<sub>4</sub>;  $M$ : V, Cr, Fe with pure WOPO<sub>4</sub> are shown in Figure 9.12. Assigning of all the Guinier photographs of WOPO<sub>4</sub> structure type phases are provided in Table 14.23, Table 14.59, Table 14.60, and Table 14.61.

Table 9.7 Lattice parameters of phosphates ( $M^{\text{III}}_{0.333}W^{\text{VI}}_{0.667}$ )OPO<sub>4</sub>;  $M$ : V, Cr, Fe, Mo, S.G.  $P2_1/m$ , i.r. of W<sup>5+</sup> and W<sup>6+</sup> are 62 and 60 pm, respectively [266].

$M^{\text{III}}$	i.r. $M^{3+}$ (pm)	$a$ (Å)	$b$ (Å)	$c$ (Å)	$\beta$ (°)	Ref.
-	-	6.5538(4)	5.2237(8)	11.1866(8)	90.332(7)	[this thesis] <sup>a)</sup>
V	64.0	6.513(2)	5.202(1)	11.054(2)	90.12(1)	[this thesis]
Cr	61.5	6.474(1)	5.1569(4)	11.049(1)	90.11(1)	[this thesis]
Fe	64.5	6.516(1)	5.1771(6)	11.054(1)	90.20(1)	[this thesis]
Mo	69.0	6.5418(6)	5.2176(5)	11.1730(7)	90.307(6)	[this thesis]

<sup>a)</sup> lattice parameters of WOPO<sub>4</sub> [this thesis].

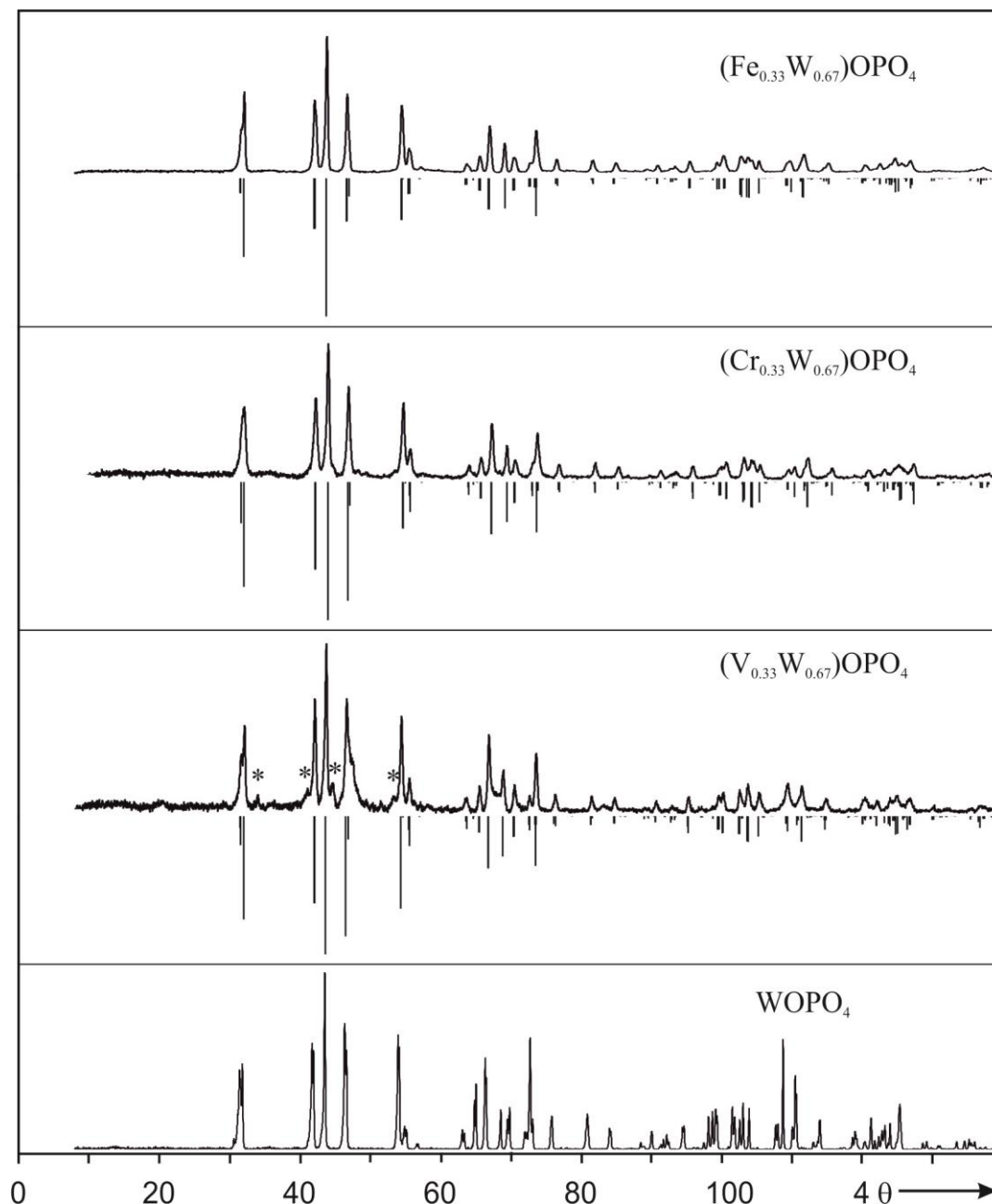
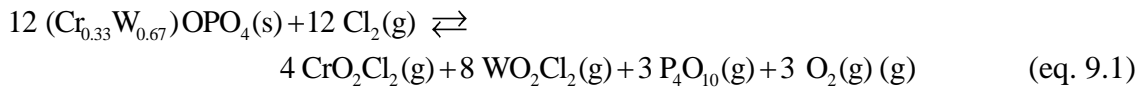


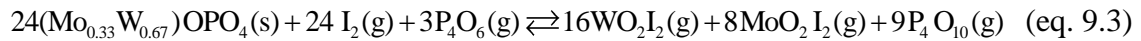
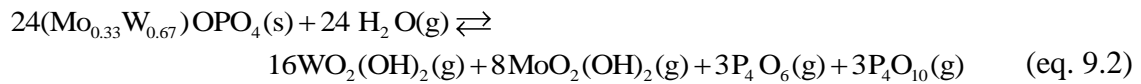
Figure 9.12 Comparison of the Guinier photographs of  $(M^{\text{III}}_{0.33}W^{\text{VI}}_{0.67})\text{OPO}_4$ ;  $M$ : V, Cr, Fe ( $\text{WOPO}_4$  structure type) with their simulated pattern based on the single crystal data of  $\text{WOPO}_4$  [this thesis] with adjusted lattice parameters, the W sites are statistically occupied by  $\text{Mo}_{0.33}\text{W}_{0.67}$ . \* indicate small impurities of  $(\text{W}_{0.83}\text{V}_{0.17}\text{O}_3)_8(\text{PO}_2)_4$  [197].

The metastable phosphate  $(\text{Cr}_{0.333}\text{W}_{0.667})\text{OPO}_4$  was crystallized by CVT in sealed silica tube via endothermic reaction using chlorine as transport agent in a temperature gradient  $1050 \rightarrow 900^\circ\text{C}$  for 30 days. Crystallization of metastable compounds via CVT is only seldomly observed and quite remarkable [43, 121]. The large temperature gradient ( $\Delta T = 150^\circ\text{C}$ ) allows the supersaturation of the gas phases which leads to the crystallisation of

the metastable phosphate. According to the literature, CVT of WO<sub>3</sub> [116, 121], Cr<sub>2</sub>O<sub>3</sub> [267] and anhydrous phosphates [43, 267] using chlorine as transport agent, the most effective gaseous transport species are expected to be CrO<sub>2</sub>Cl<sub>2</sub>, WO<sub>2</sub>Cl<sub>2</sub>, P<sub>4</sub>O<sub>10</sub> and O<sub>2</sub>. Therefore, CVT of (Cr<sub>0.333</sub>W<sub>0.667</sub>)OPO<sub>4</sub> is expected to proceed according to (eq. 9.1). The source material was Cr<sub>4</sub>[Si<sub>2</sub>O(PO<sub>4</sub>)<sub>6</sub>] [1]. The longer reaction period at high temperature and the transporting agent, Cl<sub>2</sub> are responsible for the incorporation of Si from the wall of silica ampoule. Incorporation of Si from the ampoule during CVT reaction using Cl<sub>2</sub> as TA is already reported [1].



Single crystals of (Mo<sup>III</sup><sub>0.333</sub>W<sup>VI</sup><sub>0.667</sub>)OPO<sub>4</sub> were obtained by CVT in sealed silica tube via endothermic reaction at temperature gradient 1000 → 900 °C for seven days using iodine as transport agent. According to the literature, CVT of anhydrous tungsten phosphate, WOPO<sub>4</sub> [this thesis], WP<sub>2</sub>O<sub>7</sub> [268], anhydrous molybdenum phosphate [88], and MoO<sub>2</sub> [269] using iodine as transport agent, the most effective gaseous transport species are expected to be MoO<sub>2</sub>I<sub>2</sub>, WO<sub>2</sub>I<sub>2</sub>, P<sub>4</sub>O<sub>10</sub> and P<sub>4</sub>O<sub>6</sub>. Therefore, CVT of (Mo<sub>0.333</sub>W<sub>0.667</sub>)OPO<sub>4</sub> is expected to proceed according to (eq. 9.2) and (eq. 9.3).



## 9.7 Single crystal structure refinements of (M<sup>III</sup><sub>0.333</sub>W<sup>VI</sup><sub>0.667</sub>)OPO<sub>4</sub> (M: Cr, Mo)

Single crystals of (Cr<sup>III</sup><sub>0.333</sub>W<sup>VI</sup><sub>0.667</sub>)OPO<sub>4</sub> and (Mo<sup>III</sup><sub>0.333</sub>W<sup>VI</sup><sub>0.667</sub>)OPO<sub>4</sub> with dimension of 0.06×0.06×0.06 and 0.2×0.1×0.08 mm<sup>3</sup>, respectively were carefully selected with visual judgment under a polarizing microscope, picked and glued on a thin vitreous silica glass fiber. Diffraction data were collected on a Bruker AXS BV and κ-CCD (Enraf-Nonius Inc.) diffractometer, respectively and controlled by HKL2000 software [177] using graphite monochromated Mo-Kα (λ = 0.71073 Å) radiation at ambient temperature. Crystal system and lattice type were determined from simulated precession photographs.

For the structure refinements coordinates of WOPO<sub>4</sub> [this thesis] were used as starting parameters with space group *P*2<sub>1</sub>/*m*. Full-matrix least-squares refinement was carried out by using SHELX-97 [123] in the WinGX [124] framework. After the initial

refinement cycles two independent sites for the metal and the phosphorus atoms were localized. However, the displacement parameters were unreasonable for these metal sites. This problem was solved by allowing for mixed occupancy of the metal sites by tungsten and chromium or molybdenum and the residuals dropped significantly. The free mixed occupancy Mo/W and anisotropic displacement parameters for all atoms were allowed to refine  $(\text{Mo}_{0.32}\text{W}_{0.68})\text{OPO}_4$ . The anisotropic displacement parameters for  $(\text{Mo}_{0.33}\text{W}_{0.67})\text{OPO}_4$  are given in appendix, Table 14.58. Whereas for  $(\text{Cr}_{0.33}\text{W}_{0.67})\text{OPO}_4$  the mixed occupancy Cr/W was set to 0.33/0.67 and anisotropic ADPs was allowed only for metal and phosphorus atoms. Otherwise, the refinement with free mixed occupancy Cr/W was exploded. Moreover, the anisotropic displacement parameters of two oxygen atoms, O6 and O7 (bridging oxygen of metal atoms, M2-O6-M2 and M1-O7-M1) was unreasonable. Eventually, the crystal of  $(\text{Cr}^{\text{III}}_{0.333}\text{W}^{\text{VI}}_{0.667})\text{OPO}_4$  turned out to be twinned with the twin components related by a twofold rotation parallel to (1 0 0). Taking the twinning into account the residuals reduced even further. No hints were found for the presence of a superstructure for Cr compound however threefold superstructure was observed for the Mo compound. Empirical absorption correction was done with multiscan [270] for both compounds. In Figure 9.13 the observed powder diffraction patterns of  $(\text{Cr}_{0.33}\text{W}_{0.67})\text{OPO}_4$  and  $(\text{Mo}_{0.33}\text{W}_{0.67})\text{OPO}_4$  are compared to simulations based on their single crystal structure refinements.

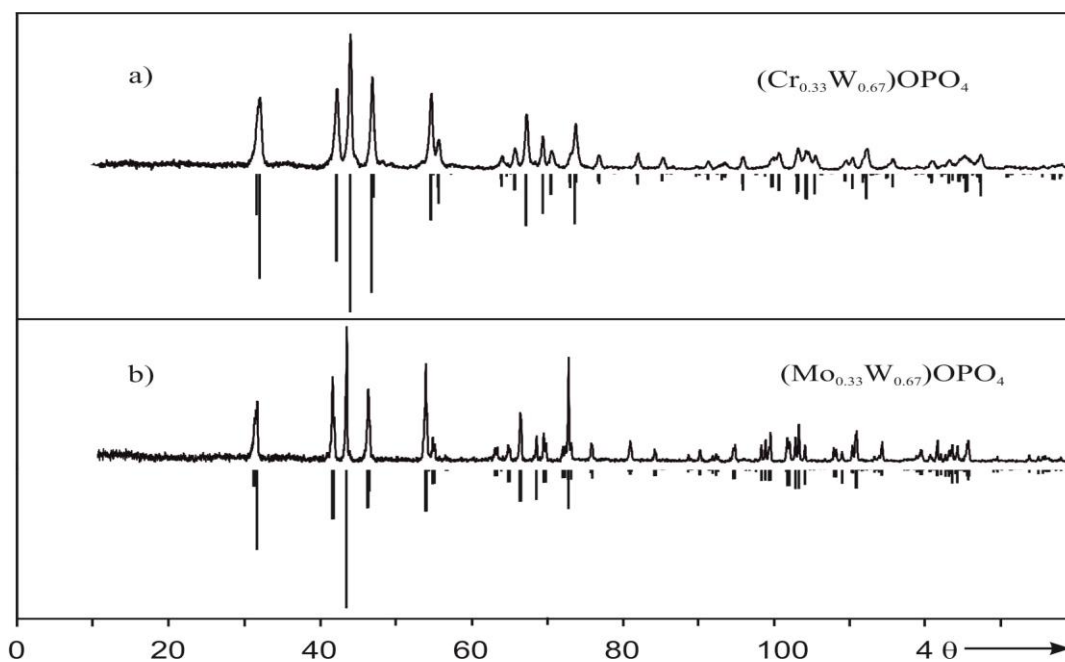


Figure 9.13 Guinier photographs of  $(\text{Cr}^{\text{III}}_{0.333}\text{W}^{\text{VI}}_{0.667})\text{OPO}_4$  (powder from SCS; a) and  $(\text{Mo}^{\text{III}}_{0.333}\text{W}^{\text{VI}}_{0.667})\text{OPO}_4$  (powder from selected crystals; b) are compared to the simulated diffraction patterns based on data sets from the crystal structure refinements [this thesis].

Details regarding data collection and structure refinements are summarized in Table 9.8. The final atomic coordinates and isotropic displacement parameters are listed in Table 9.9 and Table 9.10, respectively. Selected inter-atomic distances are reported in Table 9.11.

Table 9.8 Crystallographic data and information on x-ray single-crystal structure refinements of (Cr<sub>0.333</sub>W<sub>0.667</sub>)OPO<sub>4</sub> and (Mo<sub>0.333</sub>W<sub>0.667</sub>)OPO<sub>4</sub>.

Empirical formula	(Cr <sub>0.333</sub> W <sub>0.667</sub> )PO <sub>5</sub>	(Mo <sub>0.333</sub> W <sub>0.667</sub> )PO <sub>5</sub>
Structural formula	(W <sub>0.67</sub> Cr <sub>0.33</sub> O <sub>3</sub> ) <sub>4</sub> (PO <sub>2</sub> ) <sub>4</sub>	(W <sub>0.67</sub> Mo <sub>0.33</sub> O <sub>3</sub> ) <sub>4</sub> (PO <sub>2</sub> ) <sub>4</sub>
Formula weight	251.30	265.81
Crystal system	Monoclinic (11)	Monoclinic (11)
Space group	<i>P</i> 2 <sub>1</sub> / <i>m</i>	<i>P</i> 2 <sub>1</sub> / <i>m</i>
<i>T</i> (K)	293	293
$\lambda$ (Å)	0.71073	0.71073
<i>a</i> (Å) <sup>a)</sup>	6.474(1)	6.5417(6)
<i>b</i> (Å) <sup>a)</sup>	5.1569(4)	5.2176(5)
<i>c</i> (Å) <sup>a)</sup>	11.049(1)	11.1730(7)
$\beta$ <sup>a)</sup>	90.11(1)	90.307(6)
<i>V</i> <sup>a)</sup> (Å <sup>3</sup> )	368.87(9)	381.36(5)
<i>Z</i>	4	4
<i>D</i> <sub>calc</sub> (g·cm <sup>-3</sup> )	4.478	5.096
$\mu$ (mm <sup>-1</sup> )	24.37	25.27
Dimensions (mm <sup>3</sup> )	0.06×0.06×0.06	0.2×0.1×0.08
Color	green	dark brown
<i>F</i> (0 0 0)	449	513
Measured refls.	13046	16276
Independent refls.	1782	1832
Absorption corr.	multiscan	multiscan
No. of parameters	71	82
Theta range (°)	1.8 - 34.9	2.91 - 34.97
Index ranges	-10 ≤ <i>h</i> ≤ 10, -8 ≤ <i>k</i> ≤ 8, -17 ≤ <i>l</i> ≤ 17	-10 ≤ <i>h</i> ≤ 6, -8 ≤ <i>k</i> ≤ 8, -13 ≤ <i>l</i> ≤ 18
Twin	1 0 0 0 -1 0 0 0 -1	-
BASF	0.48	-
<i>GOOF</i>	1.10	1.31
<i>R</i> <sub>int</sub>	0.053	0.071
<i>R</i> indices	0.051, 0.123	0.035, 0.080
[ <i>I</i> > 2σ( <i>I</i> ): <i>R</i> <sub>1</sub> <sup>b)</sup> , w <i>R</i> <sub>2</sub> <sup>c)</sup>		
<i>R</i> indices	0.057, 0.127	0.037, 0.081
(all data): <i>R</i> <sub>1</sub> , w <i>R</i> <sub>2</sub>		

<sup>a)</sup> lattice parameters are from powder pattern, <sup>b)</sup>  $R_I = \frac{\|F_o\| - \|F_c\|}{\|F_o\|}$ ,  $F^2 > 2\sigma(F^2)$ , <sup>c)</sup>  $w = 1/[\sigma^2(F_o^2) + (AP)^2 + BP]$ ,  $P = (F_o^2 + 2F_c^2)/3$ .

Table 9.9 Atomic coordinates and isotropic displacement parameters ( $\text{\AA}^2$ ) for  $(\text{Cr}_{0.33}\text{W}_{0.67})\text{OPO}_4$  ( $\text{WOPO}_4$  structure type) with estimated standard deviations in parentheses.

Atom	<i>x</i>	<i>y</i>	<i>z</i>	<i>s.o.f</i>	$U_{\text{eq}}$ ( $\text{\AA}^2$ ) <sup>a)</sup>
W1/Cr1	0.6676(2)	¼	0.55794(8)	0.67/0.33	0.0212(2)
W2/Cr2	0.8312(2)	¼	0.06167(7)	0.67/0.33	0.0200(2)
P1	0.03330(9)	¼	0.3426(4)	1	0.0260(10)
P2	0.4704(7)	¼	-0.1542(5)	1	0.0253(10)
O1	0.692(4)	¼	-0.0874(15)	1	0.054(5)
O2	0.835(2)	¼	0.4167(13)	1	0.034(3)
O3	0.975(3)	¼	0.2109(10)	1	0.037(4)
O4	0.514(3)	¼	0.7103(13)	1	0.040(4)
O5	0.6243(15)	0.0281(19)	0.1310(10)	1	0.040(2)
O6	0	0	0	1	0.049(4)
O7	½	0	½	1	0.058(5)
O8	0.1895(17)	0.0727(19)	0.3796(12)	1	0.047(3)

$$^a) U_{\text{eq}} = (1/3) \sum_i \sum_j U_{ij} a_i \cdot a_j \cdot a_i \cdot a_j$$

Table 9.10 Atomic coordinates and isotropic displacement parameters ( $\text{\AA}^2$ ) for  $(\text{Mo}_{0.33}\text{W}_{0.67})\text{OPO}_4$  ( $\text{WOPO}_4$  structure type) with estimated standard deviations in parentheses.

Atom	<i>x</i>	<i>y</i>	<i>z</i>	<i>s.o.f</i>	$U_{\text{eq}}$ ( $\text{\AA}^2$ ) <sup>a)</sup>
W1/Mo1	0.66839(5)	¼	0.56121((3)	0.68/0.32	0.0103(1)
W2/Mo2	0.83170(5)	¼	0.06125(3)	0.68/0.32	0.0130(1)
P1	0.0288(3)	¼	0.3447(2)	1	0.0127(4)
P2	0.4708(3)	¼	-0.1556(2)	1	0.0124(4)
O1	-0.331(1)	¼	-0.0824(8)	1	0.037(2)
O2	0.829(1)	¼	0.4134(7)	1	0.033(2)
O3	0.978(1)	¼	0.2125(6)	1	0.029(2)
O4	0.522(2)	¼	0.71220(6)	1	0.027(2)
O5	0.646(2)	-0.0101(2)	0.1278(7)	1	0.078(4)
O6	0	0	0	1	0.041(3)
O7	½	0	½	1	0.045(3)
O8	0.147(2)	0.013(2)	0.3743(7)	1	0.080(4)

$$^a) U_{\text{eq}} = (1/3) \sum_i \sum_j U_{ij} a_i \cdot a_j \cdot a_i \cdot a_j$$

Table 9.11 Selected interatomic distances ( $\text{\AA}$ ) of  $(\text{Cr}_{0.33}\text{W}_{0.67})\text{OPO}_4$  and  $(\text{Mo}_{0.33}\text{W}_{0.67})\text{OPO}_4$  with estimated standard deviations in parentheses.

$(\text{Cr}_{0.33}\text{W}_{0.67})\text{OPO}_4$		$(\text{Mo}_{0.33}\text{W}_{0.67})\text{OPO}_4$	
type	distances	type	distances
W1/Cr1 – O7	1.8065(8)	W1/Mo1 – O7	1.8400(2)
– O7	1.8065(8)	– O7	1.8400(2)
– O4	1.98(2)	– O4	1.941(7)
– O2	1.87(1)	– O2	1.960(8)
– O8	2.01(1)	– O8	1.965(7)
– O8	2.01(1)	– O8	1.965(7)
W2/Cr2 – O6	1.834(1)	W2/Mo2 – O6	1.8402(2)
– O6	1.834(1)	– O6	1.8402(2)
– O3	1.86(2)	– O3	1.943(7)
– O1	1.92(2)	– O1	1.953(8)
– O5	1.93(1)	– O5	1.973(7)
– O5	1.93(1)	– O5	1.973(7)
P1 – O8	1.45(1)	P1 – O8	1.497(8)
– O8	1.45(1)	– O8	1.497(8)
– O3	1.54(2)	– O3	1.515(8)
– O2	1.52(2)	– O2	1.516(8)
P2 – O5	1.61(1)	P2 – O5	1.495(8)
– O5	1.61(1)	– O5	1.495(8)
– O1	1.59(2)	– O1	1.518(8)
– O4	1.48(2)	– O4	1.516(7)

Both octahedra  $[\text{M1O}_6]$  and  $[\text{M2O}_6]$  in  $(\text{Mo}^{\text{III}}_{0.333}\text{W}^{\text{VI}}_{0.667})\text{OPO}_4$  are equally distorted with two short distances ( $d(\text{M1-O7}) = 1.8400(2) \text{ \AA}$  and  $d(\text{M2-O6}) = 1.8402(2) \text{ \AA}$ ) and four long distances ( $1.941(7) \leq d(\text{M1-O}) \leq 1.965(7) \text{ \AA}$  and  $1.943(7) \leq d(\text{M2-O}) \leq 1.973(7) \text{ \AA}$ ). This phenomenon is also observed in pure  $\text{WOPO}_4$  [this thesis]. However, in  $(\text{Cr}^{\text{III}}_{0.333}\text{W}^{\text{VI}}_{0.667})\text{OPO}_4$  ( $\text{WOPO}_4$  structure type) the octahedra  $[\text{M2O}_6]$  are less distorted compared to  $[\text{M1O}_6]$  with two short distances ( $d(\text{M1-O7}) = 1.8065(8) \text{ \AA}$  and  $d(\text{M2-O6}) = 1.835(1) \text{ \AA}$ ) and four long distances ( $1.98(2) \leq d(\text{M1-O}) \leq 2.027(9) \text{ \AA}$  and  $1.86(1) \leq d(\text{M2-O}) \leq 1.915(8) \text{ \AA}$ ) as shown in Table 9.9 and Figure 9.14. The short distances along the bridging oxygen of two octahedra  $[\text{MO}_6]$  can be defined by Pauling second rule. Crystallographically two independent  $[\text{PO}_4]$  units are distorted ( $1.44(1) \leq d(\text{P1-O}) \leq 1.55(2) \text{ \AA}$ ) and ( $1.50(2) \leq d(\text{P2-O}) \leq 1.607(8) \text{ \AA}$ ) whereas in pure  $\text{WOPO}_4$  structure it is fairly regular.

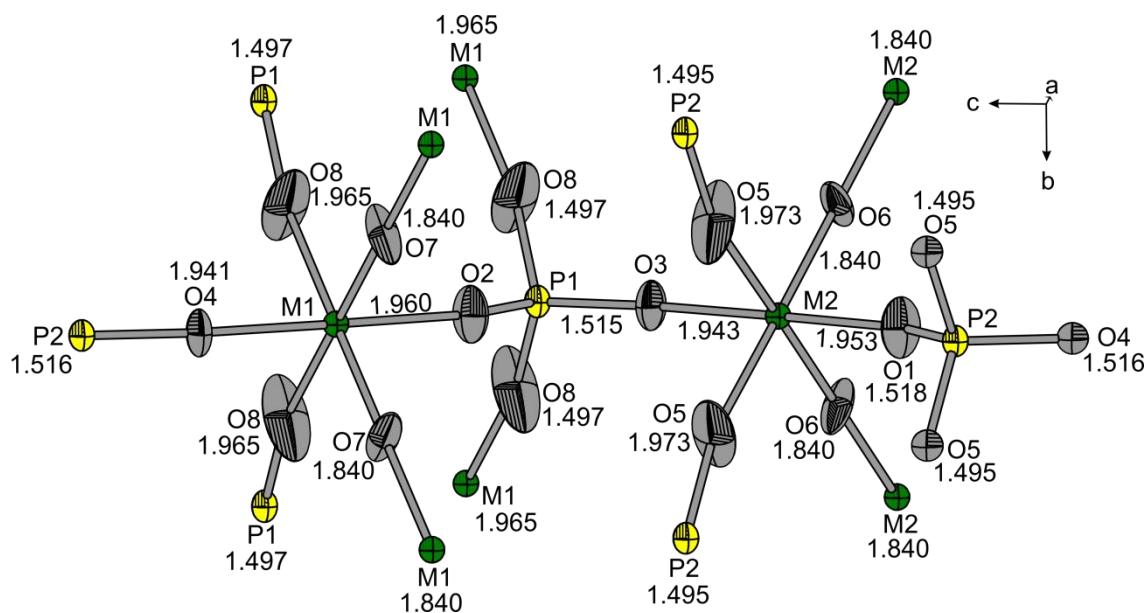


Figure 9.14 ORTEP representation (Ellipsoids are at 50% probability level, software DIAMOND [128]) of  $[(\text{Mo}/\text{W})\text{O}_6]$ , and  $[\text{PO}_4]$  groups in  $(\text{Mo}_{0.33}\text{W}_{0.67})\text{OPO}_4$ .

### 9.8 Magnetic behavior of $(\text{M}_{0.333}\text{W}_{0.667})\text{OPO}_4$ ; $M$ : Cr, Fe

Magnetic molar susceptibility,  $\chi_{\text{mol}}$  and its reciprocal,  $\chi_{\text{mol}}^{-1}$  as a function of temperature ( $2 \leq T \leq 300$  K) of powder samples of  $(\text{M}^{\text{III}}_{0.333}\text{W}^{\text{VI}}_{0.667}\text{O})\text{PO}_4$  ( $M$ : Cr and Fe) are shown in Figure 9.15. Over the whole temperature range Curie-Weiss behavior [130] with constant magnetic moment,  $\mu_{\text{exp}} = 3.85 \mu_{\text{B}}/\text{Cr}^{3+}$  and  $5.85 \mu_{\text{B}}/\text{Fe}^{3+}$  respectively, are observed where  $\theta_{\text{P}} = -6.3\text{K}$  and  $-14.8$  K, accordingly. These moments are close to the spin-only value of  $3.87\mu_{\text{B}}$  ( $d^3$ ) and  $5.92\mu_{\text{B}}$  ( $d^5$ , high spin) corresponding to  $\text{Cr}^{3+}$  and  $\text{Fe}^{3+}$ , respectively.

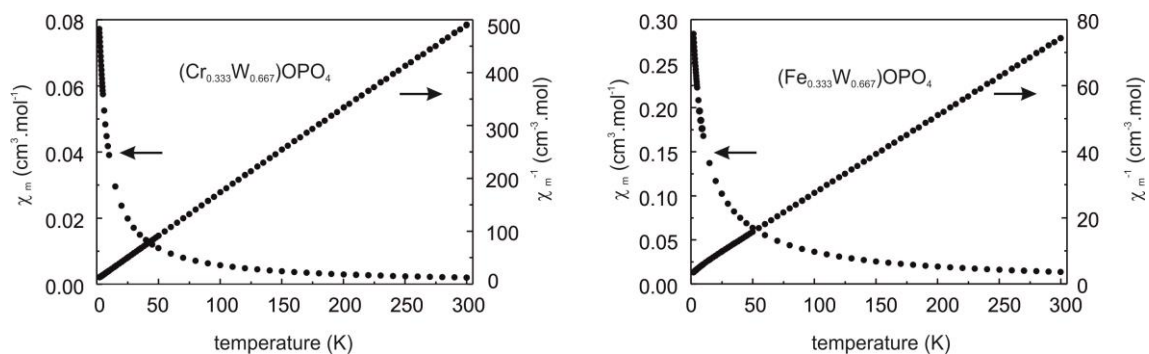


Figure 9.15 Temperature dependence of molar susceptibility,  $\chi_{\text{mol}}$  and its reciprocal  $\chi_{\text{mol}}^{-1}$  of  $(\text{Cr}^{\text{III}}_{0.333}\text{W}^{\text{VI}}_{0.667})\text{OPO}_4$  and  $(\text{Fe}^{\text{III}}_{0.333}\text{W}^{\text{VI}}_{0.667})\text{OPO}_4$ .



## 9.9 Discussion

SCS followed by heating in air at relatively low temperature lead to the formation of *cub*- $\text{WO}_3$  structure type phosphates,  $(M^{\text{III}}_{0.167}W^{\text{VI}}_{0.333}P^{\text{V}}_{0.50})\text{O}_{2.5}\square_{0.5}$  ( $M$ : V, Cr, Fe, In) whereas with scandium the *tet*- $\text{WO}_3$  structure type is adopted. All these phases are thermodynamically metastable, upon further heat treatment they are transformed via another metastable phase  $(M^{\text{III}}_{0.333}W^{\text{VI}}_{0.667})\text{OPO}_4$  ( $\text{WOPO}_4$  structure type) to the thermodynamically most stable phase,  $M(\text{WO}_2)_2(\text{P}_2\text{O}_7)\text{PO}_4$ .

The chemical composition of the thermodynamically metastable *cub*- and/or *tet*- $\text{WO}_3$  type phases  $(M^{\text{III}}_{0.167}W^{\text{VI}}_{0.333}P_{0.500})\text{O}_{2.5}\square_{0.5}$  were derived from its successor  $M^{\text{III}}W^{\text{VI}}_2P^{\text{V}}_3\text{O}_{15}$ . The molar ratio of the cations to oxygen in synthesized *cub*-/*tet*- $\text{WO}_3$  type phosphates is 1:2.5 which is remarkably less than in  $\text{WO}_3$  (1:3). A lot of structural variability or flexibility is expected in *cub*-/*tet*- $\text{WO}_3$  type phosphates as a consequence of oxygen vacancy. That means it can possibly accommodate tetravalent or even pentavalent cations instead of trivalent ions due to its oxygen vacancy. Since the metastable compounds with Sc, Cr, Fe, In are synthesized in air, the oxidation states of these metals and tungsten are set. For vanadium it could be +4 and/or +5. Whatever the oxidation states of vanadium(IV and/or V) due to the structural flexibility it could adopt any one or the mixed valence states. Therefore, due to the redox stability of vanadium with tungsten the solid solution  $(\text{V}_{0.5-x}\text{W}_x\text{P}_{0.5})\text{O}_{2.5+\delta}$  with  $0.25 \leq x \leq 0.5$  (*cub*- $\text{WO}_3$  structure type; [252]) is observed.

Without a further metal in the quasi-binary system  $\text{WO}_3$ - $\text{PO}_{2.5}$  the *cub*- $\text{WO}_3$  structure type phosphate was formed only at the composition  $(W^{\text{VI}}_{0.5}P^{\text{V}}_{0.50})\text{O}_{2.75}\square_{0.25}$ . The XRPD pattern as well as the  $^{31}\text{P}$ -MAS-NMR spectrum of the sample showed however the presence of some amorphous metaphosphoric acid. Under electron beam both the samples  $(W^{\text{VI}}_{0.5}P^{\text{V}}_{0.50})\text{O}_{2.75}\square_{0.25}$  and  $(\text{Cr}^{\text{III}}_{0.167}W^{\text{VI}}_{0.333}P^{\text{V}}_{0.50})\text{O}_{2.5}\square_{0.5}$  turned into amorphous material.

The most important quarry is how the tetrahedral  $\text{PO}_4$  groups fit into the *cub*- $\text{WO}_3$  structure where all the polyhedra are ideal octahedra. Trivalent 3d transition metals (V, Cr, Fe) fit easily into the *cub*- $\text{WO}_3$  structure. Tungstenyl bonds ( $\text{W}=\text{O}$ ) are generated upon incorporation of  $\text{P}_2\text{O}_5$  in the  $\text{WO}_3$  lattice e.g. *m*-/*o*- $\text{W}_2\text{O}_3(\text{PO}_4)_2$  [76, 77, 78]. The polyhedral connectivity in *cub*- or *tet*-  $\text{WO}_3$  structure type phosphate is most likely to be as in  $\text{W}_2\text{O}_3(\text{PO}_4)_2$ . Moreover, in  $(\text{V}_{1-x}\text{W}_x\text{P}_{0.50})\text{O}_{2.5+\delta}\square_{0.5-\delta}$ ;  $0.25 \leq x \leq 0.50$  (*cub*- or *tet*- $\text{WO}_3$  structure type) the vanadium could also lead to  $(\text{V}=\text{O})^{3+}$  or  $(\text{V}=\text{O})^{2+}$  groups. The

$^{31}\text{P}$ -MAS-NMR studies reveal the existence of  $\text{PO}_4$  instead of  $\text{P}_2\text{O}_7$  units. Since all kinds of terminal group ( $\text{E}=\text{O}$ ) are able to activate the C-H bond [271] and adaptation as mixed valence states of vanadium(IV, V) in presence of tungsten as a consequence of structural flexibility the *cub*- or *tet*-  $\text{WO}_3$  structure type phosphate might be a good candidate as catalyst material for the partial oxidation of *n*-butane to MA. One of the other potential applications of those materials would be as electrolyte in solid oxide fuel cell (SOFC).

The reduced phase  $\text{W}^{\text{V}}\text{OPO}_4$  (2<sup>nd</sup> member of MPTB series) is chemically modified by solution combustion synthesis followed by heating in air into oxidized phase,  $(\text{M}^{\text{III}}_{0.33}\text{W}^{\text{VI}}_{0.67}\text{O})\text{PO}_4$ . Substitution of W(V) by the combination of tungsten(VI) and metal(III) in 2/3 and 1/3 atomic ratio, respectively ( $\text{M}^{3+}$ : V, Cr, Fe). Heating the reaction intermediate of vanadium was carried out in low oxygen pressure ( $p(\text{O}_2) \approx 20$  ppm) to allow the lower oxidation state of vanadium ( $\text{V}^{3+}$ ). All these synthesised compounds are thermodynamically metastable as the consequence of transformation into another new structure type phase,  $\text{M}^{\text{III}}(\text{W}^{\text{VI}}\text{O}_2)_2(\text{P}_2\text{O}_7)(\text{PO}_4)$  upon heating at higher temperature. It was also reported the formation of perovskite structure type bronzes  $\text{M}_x\text{WO}_3$  with *M*: Co, Ni [272], Eu [273], Fe [274] however with very low limiting value of *M* cations. This heterovalent substitution maintained the charge to mass balance. Although the crystallization of the metastable phases by CVT is rather unusual, the crystallization  $(\text{Cr}^{\text{III}}_{0.33}\text{W}^{\text{VI}}_{0.67}\text{O})\text{PO}_4$  by CVT technique with larger temperature gradient ( $\Delta T = 150^\circ\text{C}$ ) and longer reaction time permit supersaturation which is favourable for the crystallization of metastable phase. The EDX analyses as well as single crystal structure refinements of  $(\text{Cr}^{\text{III}}_{0.33}\text{W}^{\text{VI}}_{0.67}\text{O})\text{PO}_4$  and  $(\text{Mo}^{\text{III}}_{0.33}\text{W}^{\text{VI}}_{0.67}\text{O})\text{PO}_4$  confirm the mixed occupancy of metal with statistical distribution. Furthermore the magnetic measurement of powder samples of  $(\text{M}^{\text{III}}_{0.33}\text{W}^{\text{VI}}_{0.67}\text{O})\text{PO}_4$  (*M*: Cr, Fe) comply the existence of only trivalent metal center together with hexavalent tungsten.

## 10 Mixed metal monophosphate tungsten bronzes $(W_{1-x}M_x)_8(PO_2)_4$ ( $M$ : Cr, V)

### 10.1 Introduction

It was shown for the monophosphate tungsten bronze  $W^V OPO_4$ , which is  $(WO_3)_{2m}(PO_2)_4$  with  $m = 2$  [90, 91, this thesis]) that co-substitution of pentavalent tungsten by hexavalent tungsten and trivalent cations is possible (e.g.  $Cr^{III}_{1/3}W^{VI}_{2/3}OPO_4$ , section 9.2). In further experiments the possibility to modify  $(W^V O_3)_4(W^{VI} O_3)_4(PO_2)_4$  (MPTB with  $m = 4$ ) via substituting  $W^{5+}$  by  $W^{6+}$  and another transition metal of appropriate oxidation state is explored. The substituted phases with  $m = 4$  “ $(M^{III}_{1/6}W^{VI}_{5/6}O_3)_8(PO_2)_4$ ” ( $M$ : V and Cr) were chosen as target compounds. The crystal structure of  $(WO_3)_8(PO_2)_4$  [95] was refined in space group  $P2_12_12_1$  with anisotropic displacement parameters only for tungsten. Moreover, according to the authors [95], introduction of an absorption correction led to physically meaningless displacement parameters. The crystal structure of  $(WO_3)_{2m}(PO_2)_4$ ;  $m = 4$  [95] can be described as corner sharing  $WO_6$  octahedra forming  $ReO_3$  type slabs, which are separated by  $PO_4$  tetrahedra as visualized in Figure 10.1. The integer  $m$  defining the MPTB phase can be interpreted as the width of the  $ReO_3$  related slabs ( $m = 4$ , four octahedra wide).

Here the syntheses of these mixed-metal MPTBs by three different techniques, classical solid state reaction, vapour phase moderated solid state reaction, and SCS together with their characterization by XRPD are reported.

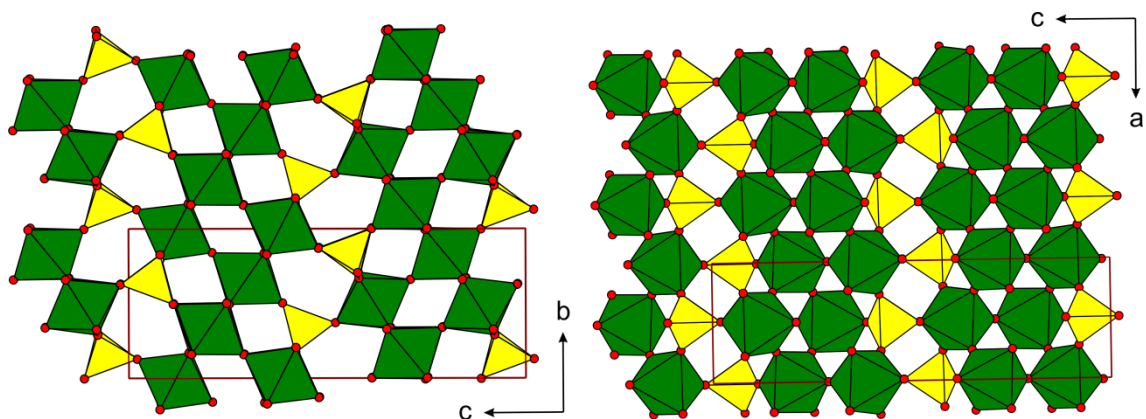


Figure 10.1 Crystal structure of  $(W^{V,VI}O_3)_8(PO_2)_4$  [95], green and yellow represent  $[WO_6]$  and  $[PO_4]$  polyhedra, respectively.

## 10.2 Synthesis

Synthesis aiming at the chromium tungsten bronze  $(Cr^{III}_{1/6}W^{VI}_{5/6}O_3)_8(PO_2)_4$  were carried out by vapour phase moderated solid state reaction and via SCS followed by heating in air.

In vapour phase moderated solid state reaction  $m$ - $W_2O_3(PO_4)_2$  (0.4 mmol; 242.22 mg),  $WO_3$  (1.2 mmol; 278.30 mg), and  $CrPO_4$  (0.4 mmol; 58.84 mg) were ground in an agate mortar to an intimate mixture. The mixture was transferred into a cleaned, preheated silica tube and the tube was sealed under vacuum with addition of a small amount of  $Cl_2$  (in situ decomposition from  $PtCl_2$ ) as mineralizer. The sealed tube was preheated at 800 °C for two days before setting the final temperature to 1000 °C for three weeks. According to XRPD (see Figure 10.2) the reaction product is containing the target compound  $(Cr^{III}_{1/6}W^{VI}_{5/6}O_3)_8(PO_2)_4$  besides a very small impurity of monoclinic  $WO_3$  [264].

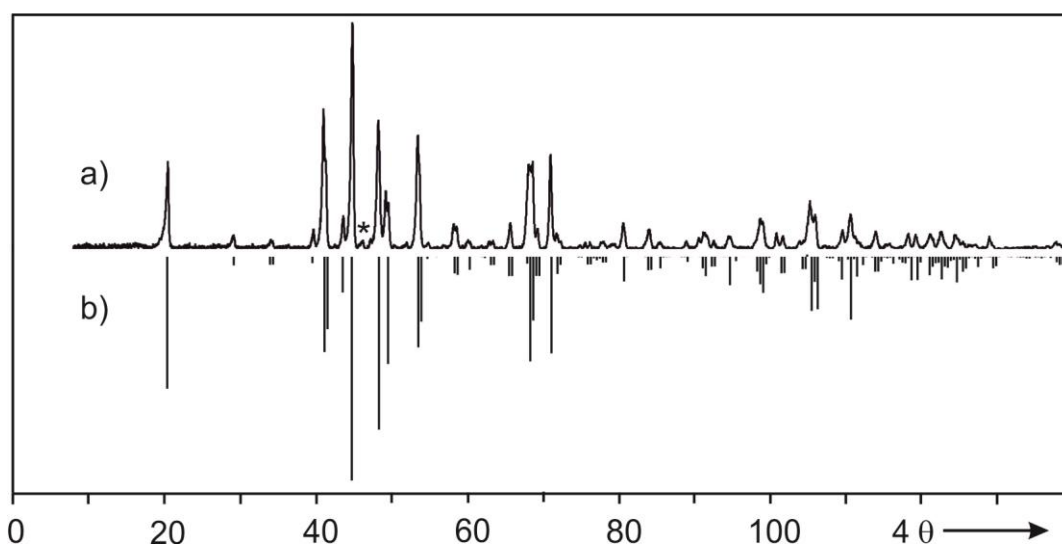


Figure 10.2 Synthesis of  $(Cr^{III}_{1/6}W^{VI}_{5/6}O_3)_8(PO_2)_4$ . Guinier photograph of the product obtained by vapour phase moderated solid state reaction (a), simulation based on the data of  $(W^{V,VI}O_3)_8(PO_2)_4$  [95] however transformed into monoclinic symmetry ( $P2_1$ ) with statistical Cr/W distribution of metal sites and adjusted lattice parameters (see section 10.3). Asterisks indicate a very small impurity of  $m$ - $WO_3$  [264].

In SCS the precursor materials  $(NH_4)_6W_{12}O_{39} \cdot 4.8H_2O$ ,  $Cr(NO_3)_3 \cdot 9H_2O$  and  $(NH_4)_2HPO_4$  were taken as source of  $WO_3$ ,  $Cr_2O_3$  and  $P_4O_{10}$ . Glycine was taken as chelator/fuel and  $HNO_3$  as oxidizer. The ratio of  $n(\text{metal}):n(\text{glycine}):n(HNO_3) = 1:3:8$  was used. The details

of SCS are described in section 2.7. Immediately after combustion the XRPD (Figure 10.3) of the solid intermediate shows weak reflections of a Keggin type phase, presumably  $(NH_4)_3[PW_{12}O_{40}] \cdot xH_2O$  [171]. Heat treatment at 650 °C for one day leads to the formation of a metastable phosphate  $(Cr^{III}_{0.11}W^{VI}_{0.56}P_{0.33})O_{2.67}\square_{0.33}$  related to the *cub*- $WO_3$  structure. Details regarding phases related to *cub*- $WO_3$  were discussed in Chapter 9. Further heating at 1000 °C for ten days forms chromium tungsten bronze,  $(Cr^{III}_{1/6}W^{VI}_{5/6}O_3)_8(PO_2)_4$  with a very small amount of *m*- $WO_3$  [264] as impurity. The phase formation on heating is shown by a series of XRPDs in Figure 10.3.

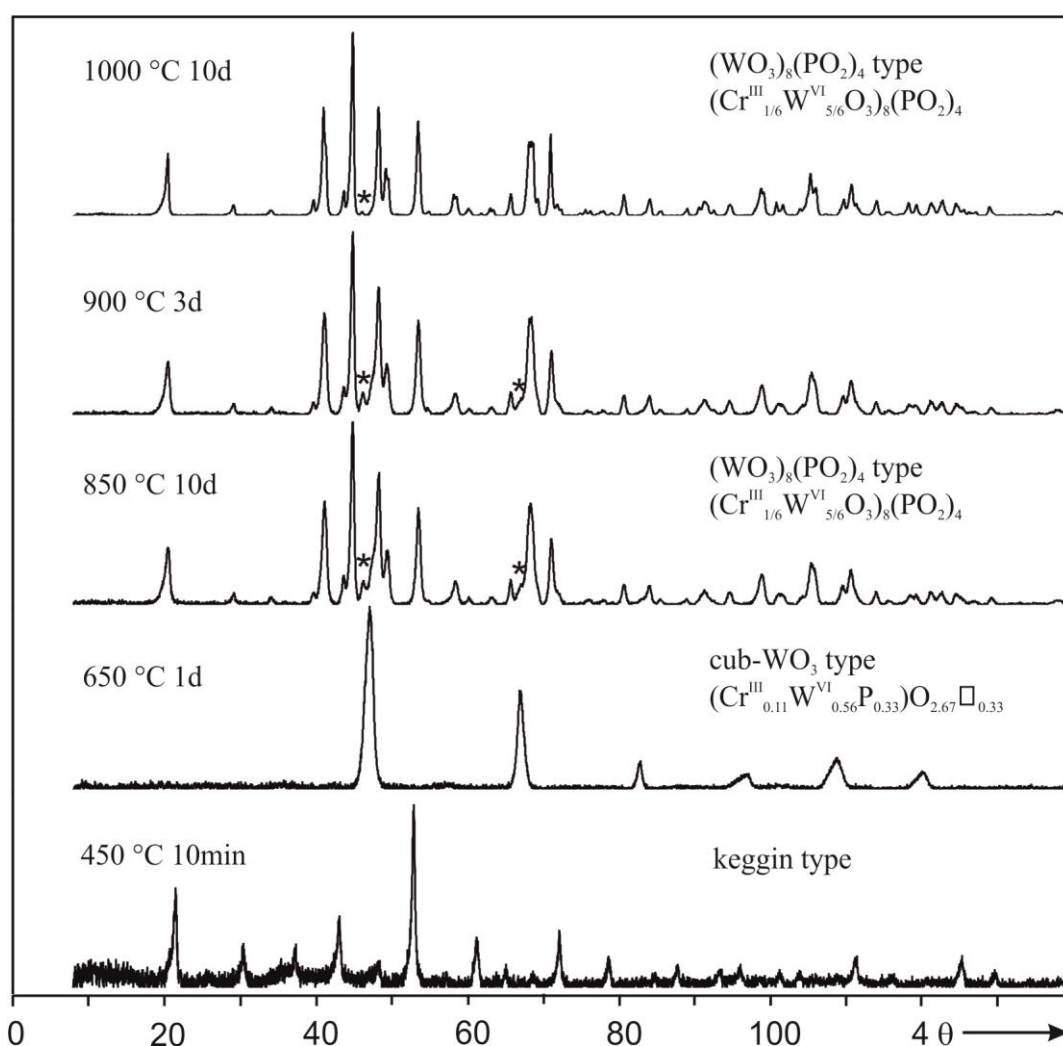


Figure 10.3 Phases obtained during annealing in air after ignition in SCS aiming at  $(Cr^{III}_{1/6}W^{VI}_{5/6}O_3)_8(PO_2)_4$ . Asterisks indicate small impurity of *m*- $WO_3$  [264].

Syntheses aiming at the MPTB with  $m = 4$  containing vanadium were performed by three different techniques, classical solid state reaction, vapour phase moderated solid state reaction, and via SCS followed by annealing. Due to the different possible oxidation states of vanadium several compositions may be envisaged: “ $(V^{III}_{1/6}W^{VI}_{5/6}O_3)_8(PO_2)_4$ ”, “ $(V^{IV}_{1/4}W^{VI}_{3/4}O_3)_8(PO_2)_4$ ”, and “ $(V^V_{1/2}W^{VI}_{1/2}O_3)_8(PO_2)_4$ ”. Even a homogeneity range, as indicated in Figure 10.4 could be possible.

Experiments aiming at the synthesis of  $(V^{III}_{1/6}W^{VI}_{5/6}O_3)_8(PO_2)_4$  (point A in Figure 10.4 and Table 10.1) were performed by vapour phase moderated solid state reaction. The sealed tube containing the reaction mixture was preheated at 550 °C for one day before heating at the final equilibration temperature 800 °C for seven days. According to the Guinier photograph a three phase mixture of  $(V^{III}_{1/6}W^{VI}_{5/6}O_3)_8(PO_2)_4$ ,  $V(WO_2)_2(P_2O_7)(PO_4)$  [this thesis Chapter 8], and  $WO_3$  [264] was obtained. Several further attempts aiming at synthesis of the target compound  $(V^{III}_{1/6}W^{VI}_{5/6}O_3)_8(PO_2)_4$  with slightly different composition (Figure 10.4 and Table 10.1) by classical solid state reactions lead to mixtures of phases (Figure 10.5).

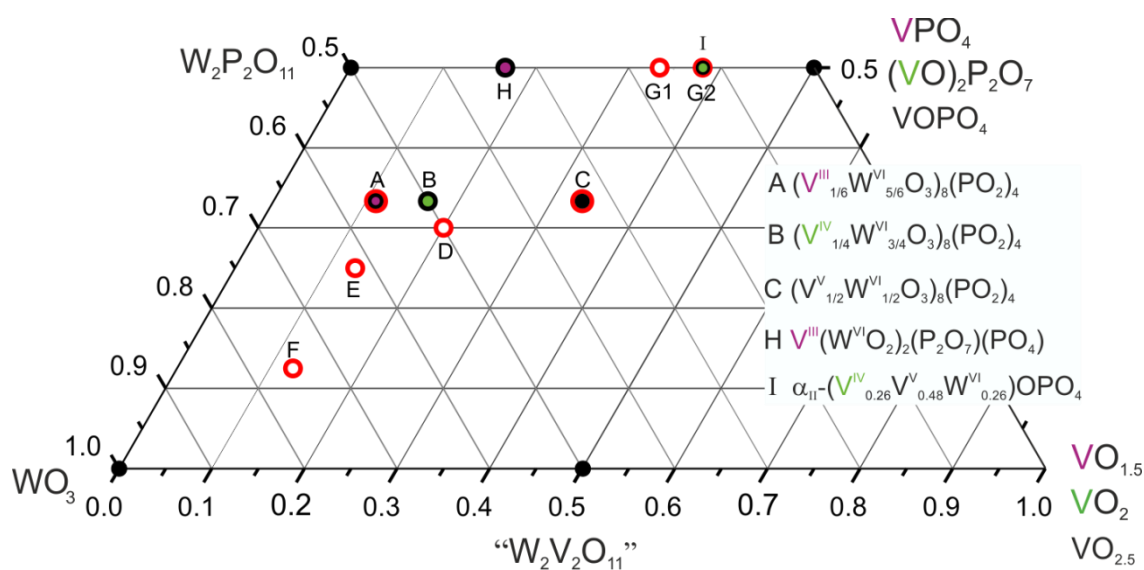


Figure 10.4 Visualization of the three calculated stoichiometric compositions (A, B, C) of vanadium-tungsten mixed transition metal MPTBs. Experiments are indicated by red circles.

Table 10.1 Experiments aiming at the synthesis of vanadium containing MPTB  $(V_xW_{1-x}O_3)_8(PO_2)_4$ , heating protocol  $\vartheta$  ( $^{\circ}C$ ) and  $t$  (d).

Exp.	Starting Materials	Amount (mg)	Exp. Condition	$\vartheta$ ( $^{\circ}C$ ), $t$ (d)	Reaction Products (according to IP Guinier photographs)
A	$W_2P_2O_{11}$ $WO_3$ $VPO_4$	242.40 278.27 58.37	$PtCl_2$ 7.5 mg <sup>a)</sup>	550, 1 850, 7	$(W_{1-x}V_xO_3)_8(PO_4)_2$ , $WO_3$ , $V(WO_2)_2(P_2O_7)(PO_4)$
C	$VOPO_4$ $WO_3$	647.64 927.35	powder	650, 3 <sup>b)</sup> 750, 10 <sup>b)</sup>	$(W_{1-x}V_xO_3)_8(PO_4)_2$ , $WO_3$
D	$VOPO_4$ $W_2P_2O_{11}$ $WO_3$	809.6 757.5 2318.3	powder	800, 17 <sup>b)</sup>	$(W_{1-x}V_xO_3)_8(PO_4)_2$ , $WO_3$
E	$NH_4VO_3$ $(NH_4)_2HPO_4$ $WO_3$	1738.8 396.2 175.5	pellet	400, 0.2 <sup>b)</sup> 600, 1 <sup>a)</sup>	$(W_{1-x}V_xO_3)_8(PO_4)_2$ , $WO_3$
F	$VOPO_4$ AMTH <sup>c)</sup>	838.05 600.0	pellet	500, 1 <sup>b)</sup> 800, 6 <sup>a)</sup>	$(W_{1-x}V_xO_3)_8(PO_4)_2$ , $WO_3$
G1	$(VO)_2P_2O_7$ $W_2P_2O_{11}$	102.6 100.9	$PtCl_2$ 53 mg <sup>a)</sup>	700, 2 800, 7	$(W_{1-x}V_xO_3)_8(PO_4)_2$ , $\alpha$ - $(VO)(PO_3)_2$ , $\alpha_{II}$ - $(V_{0.74}W_{0.26})OPO_4$ , $V(WO_2)_2(P_2O_7)(PO_4)$
G2	$(VO)_2P_2O_7$ $W_2P_2O_{11}$	369.4 242.3	$PtCl_2$ 50 mg <sup>a)</sup>	500, 7 800, 7	$(W_{1-x}V_xO_3)_8(PO_4)_2$ , $\alpha$ - $(VO)(PO_3)_2$ , $(VO)_2(P_2O_7)$ , $\alpha_{II}$ - $(V_{0.74}W_{0.26})OPO_4$

<sup>a)</sup> Sealed tube experiment, <sup>b)</sup> in air, <sup>c)</sup>  $(NH_4)_6W_{12}O_{39} \cdot 4.8H_2O$

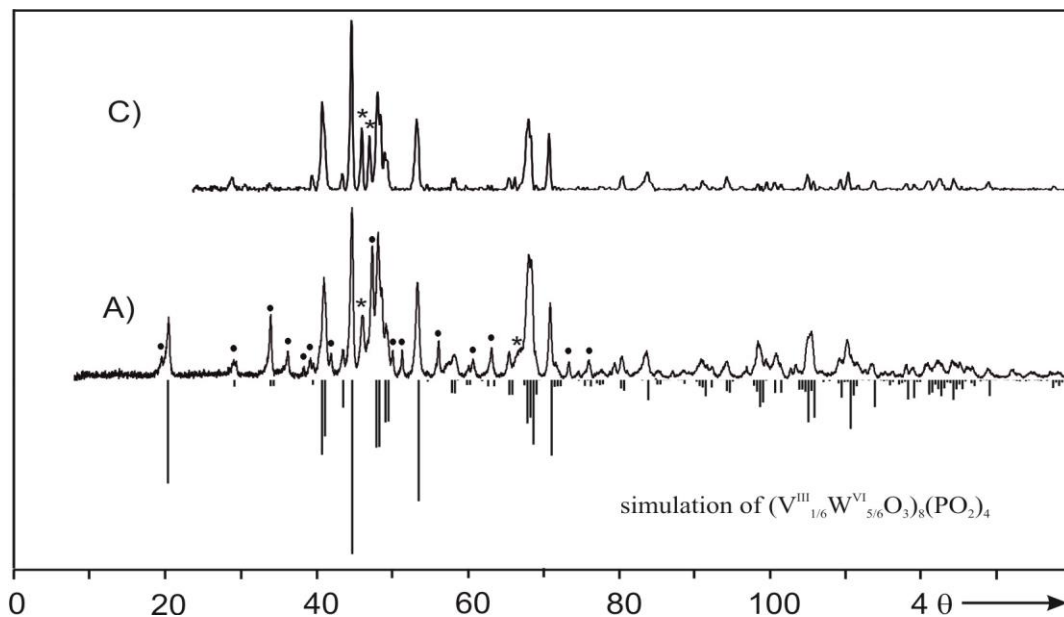


Figure 10.5 Reaction products in experiments aiming at the synthesis of  $(V^{III}_{1/6}W^{VI}_{5/6}O_3)_8(PO_2)_4$  (A, middle) and  $(V^{V}_{3/6}W^{VI}_{3/6}O_3)_8(PO_2)_4$  (C, top). Simulation based on data of  $(WO_3)_8(PO_2)_4$  [95] (bottom) however through transforming the cell from  $P2_12_12_1$  to  $P2_1$  with statistical distribution of V/W in metal sites and adjusted lattice parameters. Asterisks and black dots indicate  $m$ - $WO_3$  [264] and  $V(WO_2)_2(P_2O_7)(PO_4)$  [this thesis], respectively.

For SCS the starting materials  $(NH_4)_6W_{12}O_{39} \cdot 4.8H_2O$ ,  $NH_4VO_3$  and  $(NH_4)_2HPO_4$  were used. Glycine was taken as chelator/fuel and  $HNO_3$  as oxidizer. The ratio of  $n(\text{metal}):n(\text{glycine}):n(HNO_3) = 1:3:8$  was used. The details of SCS are described in section 2.7. The final annealing was performed at reduced oxygen pressure ( $p(O_2) \approx 20$  ppm) in order to set the oxidation state of vanadium to 3+. Immediately after ignition at 550 °C the intermediate solid was a phase with *tet*- $WO_3$  structure type with composition  $(V_{0.11}W^{VI}_{0.56}P_{0.33})O_{2.67+\delta}$  (see Figure 10.6).

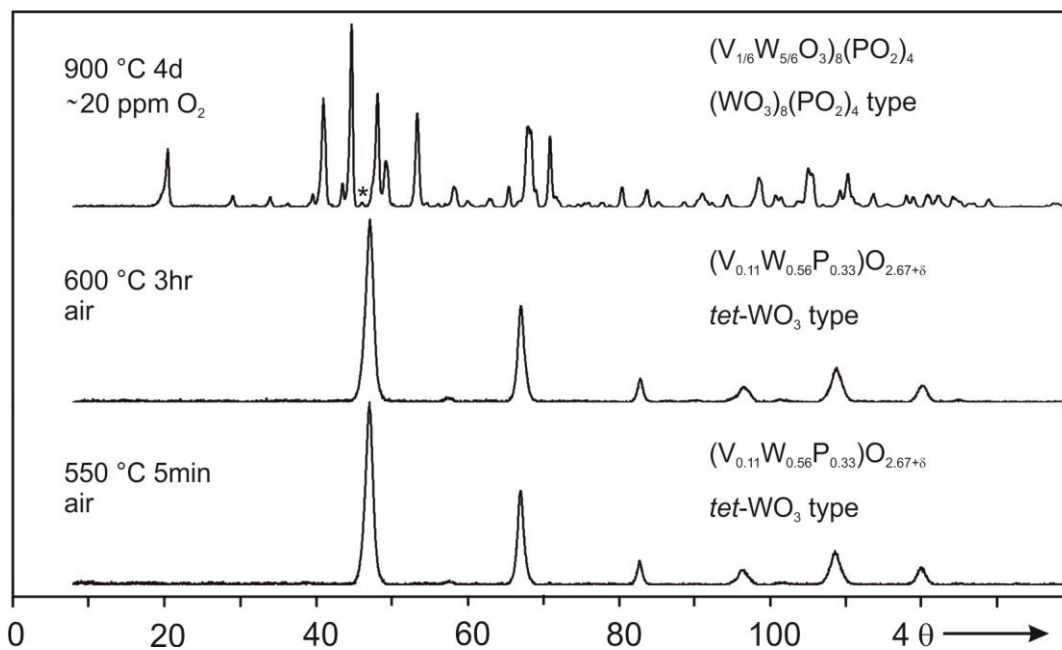


Figure 10.6 Phases obtained during SCS aiming at  $(V^{III}_{1/6}W^{VI}_{5/6}O_3)_8(PO_2)_4$ . Asterisks indicate a very small impurity of *m*- $WO_3$  [264].

### 10.3 Results and discussion

It is possible to substitute  $W^{5+}$  in  $(W^{V,VI}O_3)_8(PO_2)_4$  by appropriate amounts of  $Cr^{3+}$  and  $W^{6+}$ . The lattice parameters for  $(Cr^{III}_{1/6}W^{VI}_{5/6}O_3)_8(PO_2)_4$  are  $a = 6.483(2)$  Å,  $b = 5.215(1)$  Å,  $c = 17.221(1)$  Å,  $\beta = 90.32(3)^\circ$  (Table 10.2) determined from the XRPD pattern of selected crystals obtained from vapor phase moderated solid state reaction with space group  $P2_1$  which is transformed from  $P2_12_12_1$  of  $(W^{V,VI}O_3)_8(PO_2)_4$ . In contrast to the structure model of the pure MPTB reported in literature [95] ( $P2_12_12_1$   $a = 6.569(1)$  Å,  $b = 5.285(2)$  Å,  $c = 17.351(3)$  Å) the mixed-metal MPTB shows a monoclinic unit cell. Thermal decomposition of  $(Cr^{III}_{1/6}W^{VI}_{5/6}O_3)_8(PO_2)_4$  is observed at above 1000 °C. According to XRPD pattern the decomposition products are *m*- $W_2O_3(PO_4)_2$  [76, 78],  $WO_3$  [264], and  $\alpha$ - $CrPO_4$  [275].



Orientating experiments indicate that the formation of a MPTB phase with  $m = 4$  containing vanadium is also possible. The experiments do yet not allow determination of its accurate composition nor of a homogeneity range. The vanadium containing phase  $(V_xW^{VI}_{1-x}O_3)_8(PO_2)_4$  is observed over a wide compositional range as equilibrium phase in the Gibbs phase tetrahedron V/W/P/O. Crystals from experiment G2 were selected for a powder diffraction pattern (Figure 10.7) to determine the lattice parameters.

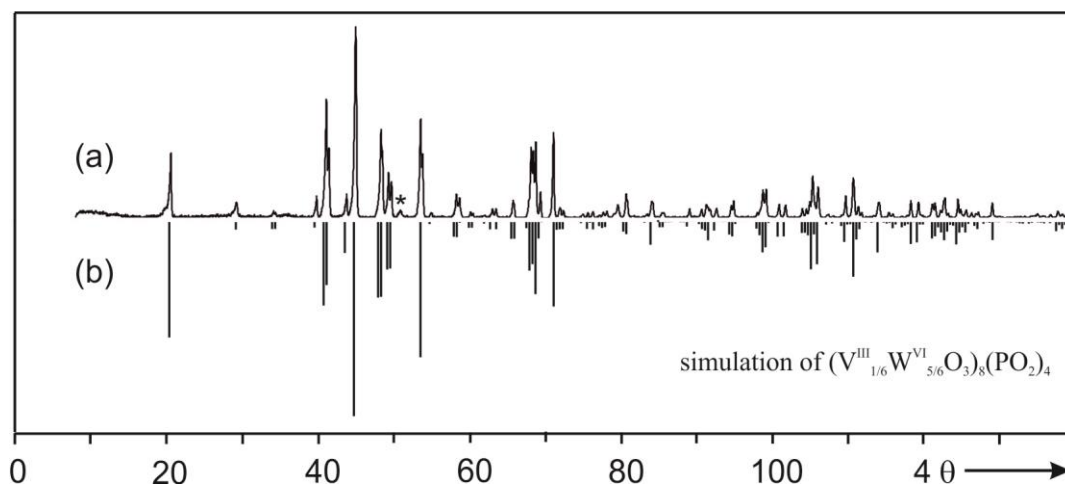


Figure 10.7 Guinier photograph of  $(V^{III}_{1/6}W^{VI}_{5/6}O_3)_8(PO_2)_4$ , obtained from crystals of experiment G2 (Table 10.1), showing the splitting of some of reflections (a) which is explained by the simulation based on data of  $(WO_3)_8(PO_2)_4$ , S. G.  $P2_12_12_1$  [95] however with transforming into lower symmetry ( $P2_1$ ) and statistical distribution of V and W in metal sites and adjusted lattice parameters. Asterisks indicate little impurity.

The lattice parameters obtained from G2 are given in Table 10.2. Overall, substitution of  $W^{5+}$  in  $(WO_3)_8(PO_2)_4$  by  $M^{3+}/W^{6+}$  leads to a shrinking of all lattice parameters. Assignments of all the Guinier photographs of  $(WO_3)_8(PO_2)_4$  structure type phases are provided in Table 14.62 and Table 14.63. The split reflections in XRPD as observed in Figure 10.7 indicate lower symmetry of the vanadium containing MPTB in contrast to that of the pure MPTB phase.

Table 10.2 Lattice parameters of  $(M^{III}_{1/6}W^{VI}_{5/6}O_3)_8(PO_2)_4$ ; ( $M$ : V, Cr) space group  $P2_1$ ; ionic radii (i.r.) of  $W^{5+}$  and  $W^{6+}$  are 62 and 60 pm, respectively [266].

$M^{III}$	i.r. of $M^{III}$ (pm)	$a$ (Å)	$b$ (Å)	$c$ (Å)	$\beta$ (°)	Ref.
–	–	6.569(1)	5.285(2)	17.351(3)	90.0	[95] <sup>1)</sup>
V	64.0	6.4929(8)	5.2217(5)	17.322(3)	90.486(7)	this thesis
Cr	61.5	6.483(2)	5.215(1)	17.22(1)	90.32(3)	this thesis

<sup>1)</sup> lattice parameters of  $(WO_3)_8(PO_2)_4$ ;  $a' = b$ ;  $b' = a$ ;  $c' = c$

Single crystals of “ $(V^{III}_{1/6}W^{VI}_{5/6}O_3)_8(PO_2)_4$ ” and  $(Cr^{III}_{1/6}W^{VI}_{5/6}O_3)_8(PO_2)_4$  were obtained by vapor phase moderated solid state reactions. The single crystal structure refinements of both showed unreasonable anisotropic displacement parameters for some oxygen atoms, unrealistic occupancy parameters at the metal sites, and high residuals,  $R_1 > 7\%$ . The monoclinic distortion of the unit cell was however confirmed by the measurements. It is worth to mention that the EDX analysis of the selected crystals comply with the target composition. It is emphasized that during SCS of  $(M^{III}_{1/6}W^{VI}_{5/6}O_3)_8(PO_2)_4$  ( $M$ : V, Cr) solid reaction intermediate were observed with diffraction pattern similar to that of  $ReO_3$  though different lattice parameters as given in Table 10.3.

Table 10.3 Lattice parameters of metastable phosphates with structure related to *cub-tet*- $WO_3$  type obtained via SCS followed by heating in air.

Composition	Symmetry	$a$ (Å)	$c$ (Å)	$V$ (Å <sup>3</sup> )	Ref.
$WO_3$	cubic	3.838(2)		56.53	[252]
$(Cr^{III}_{0.11}W^{VI}_{0.56}P^V_{0.33})O_{2.67+\delta}$	cubic	3.773(1)		53.72(5)	this thesis
$WO_3$	tetragonal	5.2885(5)	7.8626(8)	219.9(1)	[249] <sup>1)</sup>
$(V_{0.11}W^{VI}_{0.56}P^V_{0.33})O_{2.67+\delta}$	tetragonal	5.325(2)	7.57(1)	214.6(3)	this thesis

<sup>1)</sup> lattice parameters obtained at 800 °C

# 11 Access to thermodynamically metastable oxo-compounds via reduction by moist hydrogen

## 11.1 Introduction

VPO<sub>4</sub> can be synthesized reducing  $\beta$ -VOPO<sub>4</sub> by VP in sealed ampoules [83]. However these experiments are not suitable for upscaling. In the first part of this chapter, results of experiments on the reduction of  $\beta$ -VOPO<sub>4</sub> by moist hydrogen at various temperatures are reported.

Among the several polymorphs of vanadium(IV) oxide, semiconducting *mon*-VO<sub>2</sub>(M) [276] has attracted a lot of interest due to its unique reversible phase transition close to room temperature (340 K) to the metallic phase VO<sub>2</sub>(R) with tetragonal rutile type structure. Two other well characterized polymorphs of VO<sub>2</sub> are V<sup>IV</sup>O<sub>2</sub>(A) [277] and V<sup>IV</sup>O<sub>2</sub>(B) [278] which are thermodynamically metastable with low and high temperature modifications (LTP and HTP) each. Other reported polymorphs of vanadium(IV) oxide are VO<sub>2</sub>(BCC) [279], VO<sub>2</sub>(C) [280], VO<sub>2</sub>(D) [281], VO<sub>2</sub>(N) [280]. These are not well characterized. Recently, the layered structure of VO<sub>2</sub>(B) has drawn the attention of scientist due to its potential application as a cathode material in Li-ion batteries [282, 283, 284]. The preparation of VO<sub>2</sub>(B) was reported in literature by hydrothermal synthesis [278, 285, 286] or stepwise reduction of a vanadium oxide precursor under different reaction atmosphere [287]. Another metastable oxide of vanadium is V<sub>4</sub>O<sub>9</sub> structurally represented as (V<sup>IV</sup>O)<sub>2</sub>V<sup>V</sup><sub>2</sub>O<sub>7</sub>, which was first reported in 1970 [288]. It contains mixed-valent of vanadium(IV, V) and is isotypic to (VO)<sub>2</sub>P<sub>2</sub>O<sub>7</sub> [10]. Due to structural similarity V<sub>4</sub>O<sub>9</sub> is of interest for catalytic testing. However, preparation of V<sub>4</sub>O<sub>9</sub> by classical solid state reaction from an appropriate mixture of V<sub>2</sub>O<sub>5</sub> and V<sub>2</sub>O<sub>3</sub> or VO<sub>2</sub> is impossible. Recently, it was shown that V<sub>4</sub>O<sub>9</sub> can be obtained as part of a two phase mixture from V<sub>2</sub>O<sub>5</sub> reducing by sulfur vapor at 400 °C [289].

In the second part of this chapter an improved synthesis for V<sub>4</sub>O<sub>9</sub> is reported. Preparation of the metastable VO<sub>2</sub>(B) from V<sub>2</sub>O<sub>5</sub> is also reported.

The term “moist hydrogen” means hydrogen saturated with H<sub>2</sub>O(g) at 293 K. The saturation pressure of water at 293 K is given as  $p_{\text{sat}}(\text{H}_2\text{O}) = 0.023$  bar [290]. For H<sub>2</sub>/H<sub>2</sub>O gas mixture the equilibrium pressure  $p(\text{O}_2)$  can be calculated from (eq. 11.1) and (eq. 11.2).



$$K_p = \frac{p^2(\text{H}_2\text{O})}{p^2(\text{H}_2) \cdot p(\text{O}_2)} \quad (\text{eq. 11.2})$$

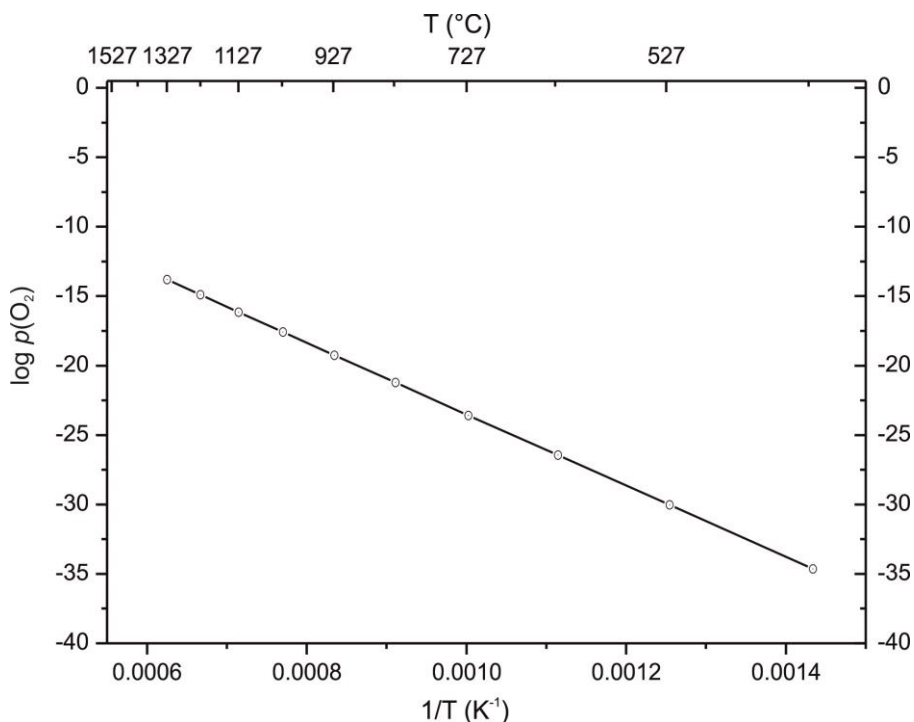
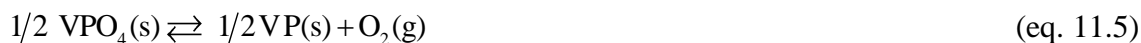


Figure 11.1 Diagram of  $\log p(\text{O}_2)$  vs.  $1/T$  for a gas mixture  $\text{H}_2/\text{H}_2\text{O}$   $\{p(\text{total}) = 1 \text{ bar}, p(\text{H}_2\text{O}) = 0.023 \text{ bar}\}$ .

## 11.2 Reduction of $\beta\text{-VOPO}_4$

In the system V/P/O several compounds are known at a ratio metal:phosphorus = 1,  $\text{V}^{\text{V}}\text{OPO}_4$  [161],  $(\text{V}^{\text{IV}}\text{O})_2\text{P}_2\text{O}_7$  [10],  $\text{V}^{\text{III}}\text{PO}_4$  [83], VP [84]. The formation of any one of the above mentioned phosphates depends on the oxygen partial pressure and temperature. This is expressed by the decomposition reactions (eq. 11.3) to (eq. 11.5).



Using (eq. 11.6) and the thermodynamic data listed in Table 11.1 allows calculation of the barogram for the coexisting phases  $\text{VOPO}_4 \rightarrow (\text{VO})_2\text{P}_2\text{O}_7 \rightarrow \text{VPO}_4 \rightarrow \text{VP}$  (see Figure 11.2).

$$\log p(\text{O}_2) = \log K_p = -\frac{\Delta_R H}{4.567T} + \frac{\Delta_R S}{4.567} \quad (\text{eq. 11.6})$$

$$K_p = \frac{a^2\{(\text{VO})_2(\text{P}_2\text{O}_7)\} \cdot a(\text{O}_2)}{a^4(\text{VOPO}_4)} = a(\text{O}_2) \quad (\text{eq. 11.7})$$

Table 11.1 Thermodynamic data of the coexisting phases in  $\text{VPO}_n$  ( $n = 5, 4.5, 4, 0$ ) [291].

Phase	$\Delta_R H_{298}$ (kcal·mol <sup>-1</sup> )	$S_{298}$ (cal·mol <sup>-1</sup> ·K <sup>-1</sup> )	A <sup>a)</sup>	B <sup>a)</sup>	C <sup>a)</sup>
VOPO <sub>4</sub>	-412.5	29.32	32.2	17.5	-8.5
(VO) <sub>2</sub> P <sub>2</sub> O <sub>7</sub>	-792.2	54.1	53.6	42.2	-11.62
VPO <sub>4</sub>	-365.8	28.6	23.625	21.78	-4.575
VP	-61	12	10.75	2.5	-

<sup>a)</sup> coefficients for calculating the specific heat,  $C_{p,T} = a + b \cdot T + c \cdot T^{-2} + d \cdot T^2$  [291].

Figure 11.2, the plot of  $\log p(\text{O}_2)$  vs. inverse temperature shows the coexistence ranges of the respective phases. The barogram shows that in an atmosphere of commercial argon ( $p(\text{O}_2) \approx 20$  ppm)  $\text{V}^{\text{V}}\text{OPO}_4$  decomposes to  $(\text{V}^{\text{IV}}\text{O})_2\text{P}_2\text{O}_7$  at  $780 \leq T \leq 1150$  °C. In other words,  $(\text{V}^{\text{IV}}\text{O})_2\text{P}_2\text{O}_7$  can be synthesised from  $\text{V}^{\text{V}}\text{OPO}_4$  at  $p(\text{O}_2) \approx 20$  ppm in the temperature range 780 to 1150 °C. Above the latter temperature  $(\text{V}^{\text{IV}}\text{O})_2\text{P}_2\text{O}_7$  decomposes to  $\text{V}^{\text{III}}\text{PO}_4$ . It can be seen from the barogram that  $\text{VPO}_4$  will already form at lower temperatures if  $p(\text{O}_2)$  in the gas flow is lowered. At  $p(\text{O}_2) \approx 10^{-16}$  bar temperatures below 600 °C are sufficient to reduce  $(\text{VO})_2\text{P}_2\text{O}_7$  to  $\text{VPO}_4$  while at  $p(\text{O}_2) \approx 10^{-30}$  bar and  $T > 600$  °C reduction to VP should occur. The reduction of  $\beta\text{-V}^{\text{V}}\text{OPO}_4$  to  $(\text{V}^{\text{IV}}\text{O})_2\text{P}_2\text{O}_7$  according to the barogram has been confirmed several times [133]. Therefore, the upscaled synthesis of  $\text{VPO}_4$  via reduction of  $\beta\text{-VOPO}_4$  by moist hydrogen was tested.

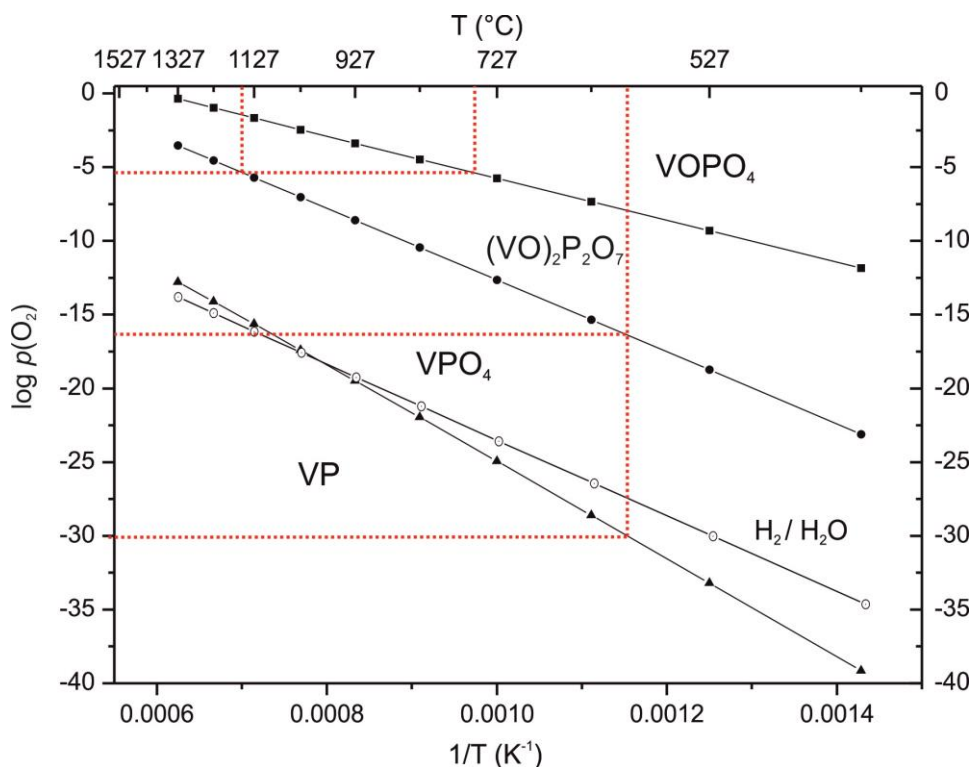


Figure 11.2 Barogram of the coexisting phases  $VPO_n$  ( $n = 5, 4.5, 4, 0$ ) [this thesis, for thermodynamic data see Table 11.1].

### 11.2.1 Experimental

A silica boat charged with  $\beta$ - $V^V OPO_4$  [161] ( $m \sim 700$  mg) was placed in a horizontal tubular furnace which was equipped with silica tube and controlled by Ni/Ni-Cr thermocouple. Commercial  $H_2$  was passed through a  $H_2O$  bubbler where the  $H_2$  is saturated with  $H_2O$ . Argon was passed for 30 minutes through the reaction tube before  $H_2$  gas to remove air inside the tube. The flow of  $H_2$  gas was controlled by a valve. Furnace temperature was raised by  $50^\circ h^{-1}$ .

### 11.2.2 Results and discussion

Reduction of  $\beta$ - $VOPO_4$  by moist hydrogen leads to different products depending on temperature (see Figure 11.3). At  $T \leq 350$  °C no reaction was observed apart from a color change (bright yellow  $\rightarrow$  olive green) pointing to very small oxygen deficiency. At 450 °C formation of  $(VO)_2P_2O_7$  was detected. The mechanistic transformation of  $\beta$ - $VOPO_4$  to  $(VO)_2P_2O_7$  due to reduction, as a consequence of ordered crystallographic shear planes was already explained in [292]. From 450 to 700 °C  $VPO_{4-m1}$ , a new polymorph of  $VPO_4$  was obtained. Reduction at  $600 \leq T \leq 800$  °C led to the formation of  $VPO_{4-m2}$  (isotypic to  $Fe(VO)_2(P_2O_7)(PO_4)$  [133]), a further, hitherto unknown

polymorph of  $\text{VPO}_4$ . At  $T \geq 900$  °C decomposition of  $\beta\text{-VOPO}_4$  led to formation of mostly  $\beta\text{-V}_2\text{OPO}_4$  [148] and  $\text{PO}_x(\text{g})$ . The thermodynamically stable  $\text{VPO}_4$  polymorph (space group  $Cmcm$  [83]) was never observed as single phase product in these experiments. Either  $\beta\text{-V}_2\text{OPO}_4$  or  $\text{VPO}_4\text{-m2}$  were present as impurity phase.

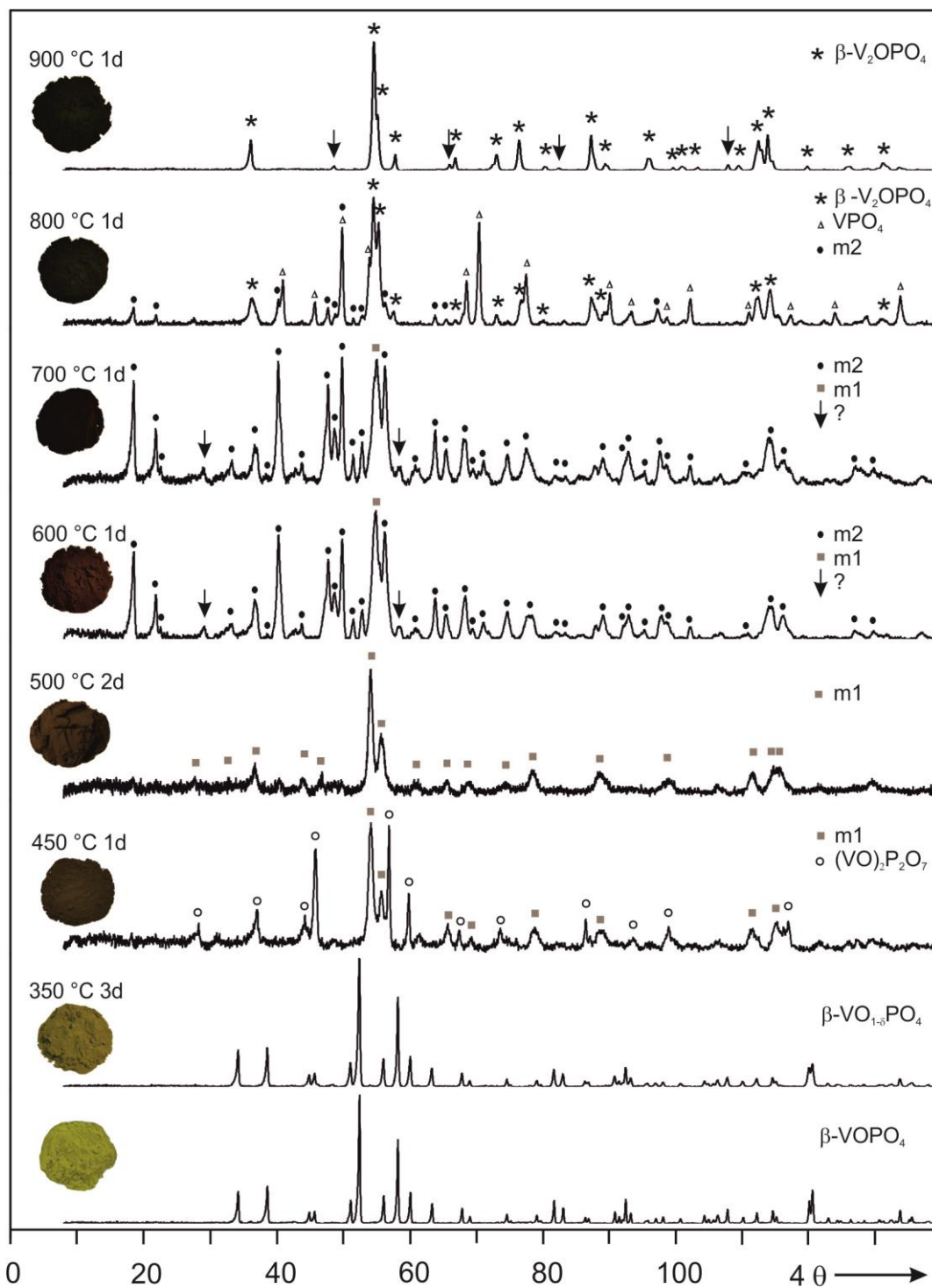


Figure 11.3 Reduction of  $\beta\text{-VOPO}_4$  by moist hydrogen at different temperatures. (○)  $(\text{VO})_2\text{P}_2\text{O}_7$  [10], (■)  $\text{VPO}_4\text{-m1}$  [this thesis], (●)  $\text{VPO}_4\text{-m2}$  phase [this thesis], (Δ)  $\text{VPO}_4$  [83], and (\*) indicate  $\beta\text{-V}_2\text{OPO}_4$  [148]. The down arrow indicates unassigned reflections.

Heat treatment of  $VPO_4$ -m1 in evacuated sealed tube ( $l \approx 9$  cm,  $d \approx 1.5$  cm,  $V \approx 16$  cm<sup>3</sup>) at 550 °C with small amounts of iodine as mineralizer led to transformation to single phase  $V^{III}PO_4$  in its thermodynamically stable form [83]. This confirms the metastability of  $VPO_4$ -m1 as well as the oxidation state +3 of vanadium. Keeping the metastable phases several weeks at laboratory atmosphere both polymorphs are stable according to Guinier photographs.

For further confirmation of the oxidation state of vanadium, stepwise oxidation of  $VPO_4$ -m1 was performed in sealed silica tubes ( $l \approx 9$  cm,  $d \approx 1.5$  cm,  $V \approx 16$  cm<sup>3</sup>) with  $O_2$  (in situ decomposition of  $Ag_2O$ ) at 450 °C for two days. Stepwise oxidation of  $VPO_4$ -m1 leads to  $(V^{IV}O)_2P_2O_7$  [10] and  $V^VOPO_4$  according to (eq. 11.8) and (eq. 11.9), respectively. For the oxidation reaction the ampoule was designed as shown in Figure 11.4.

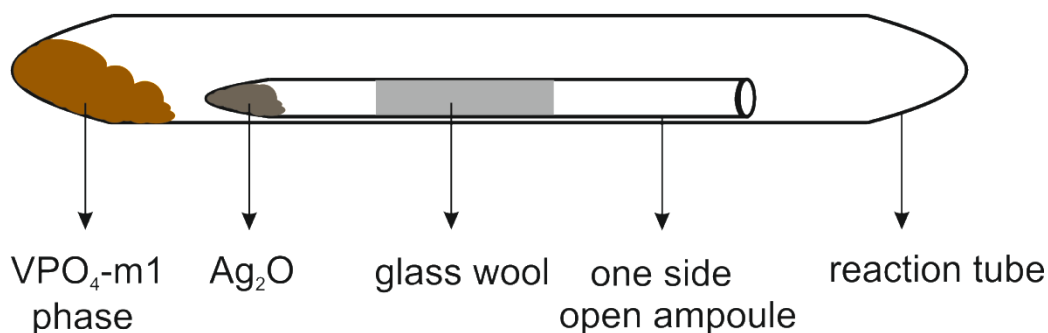
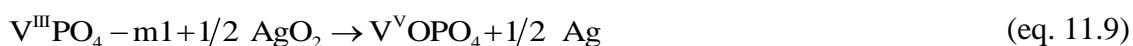
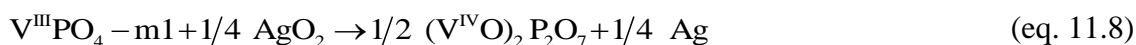


Figure 11.4 Sketch of the reaction tube designed for stepwise oxidation of  $VPO_4$ -m1 to  $(V^{IV}O)_2P_2O_7$  and  $\beta$ - $V^VOPO_4$ .

These two oxidation experiments confirm the oxidation state +3 of vanadium in  $VPO_4$ -m1. To check for the existence of any other polymorph, metastable  $VPO_4$ -m1 was heated in a sealed tube in a small temperature interval without allowing equilibration to the thermo-dynamically stable  $VPO_4$  phase. For that purpose all the reactions were performed in the same furnace at the same position to rule out any type of temperature error. All these experiments show that  $VPO_4$ -m1 directly converts to the stable polymorph (see Figure 14.17).



### 11.2.3 Characterization of $V^{III}PO_4$ -m1

Since the low temperature phase m1 is thermodynamically metastable, it is difficult to grow single crystals. However, two slightly different structure models could be derived from its XRPD pattern.

**First structure model for  $VPO_4$ -m1 based on  $\beta$ - $VOPO_4$ .** The first structure model of  $VPO_4$ -m1, shown in Figure 11.5b, is derived from  $\beta$ - $V^V OPO_4$  (space group  $Pnma$ ;  $a = 7.7863(5) \text{ \AA}$ ,  $b = 6.1329(3) \text{ \AA}$ , and  $c = 6.9673(5) \text{ \AA}$  [161]. Assignment of the reflections leads to  $a = 7.341 \text{ \AA}$ ,  $b = 6.389 \text{ \AA}$ ,  $c = 7.329 \text{ \AA}$  (Table 11.2). For  $VPO_4$ -m1 the shrinkage of the  $a$ -axis is attributed to removal of vanadyl oxygen from the chain of corner sharing  $VO_6$  octahedra along the crystallographic  $a$ -axis. Its worth to note that the square planar coordination polyhedra  $VO_4$  was not reported earlier. The simulation of the XRPD pattern derived from  $\beta$ - $VOPO_4$  structure nicely matches with the experimental Guinier photograph except for one diffraction peak indicated by arrow in Figure 11.6c. Moreover, there are several weaker reflections which are not explained by this structural model.

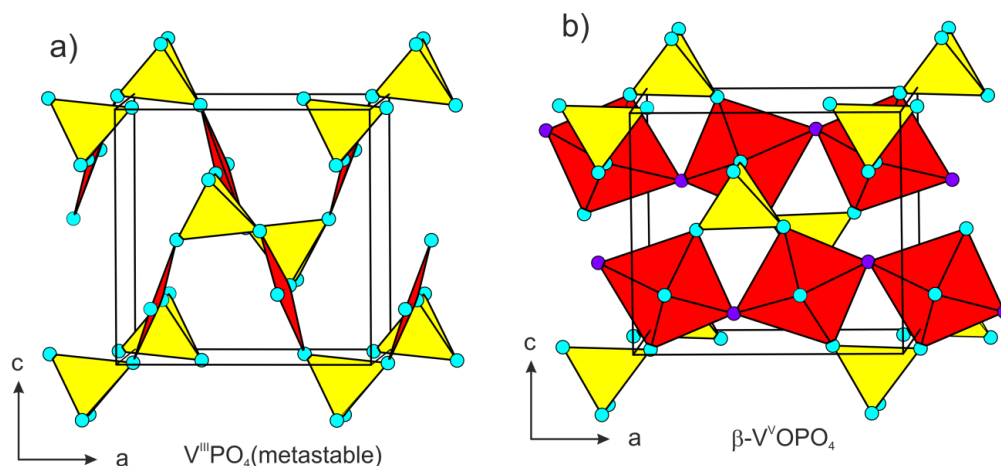


Figure 11.5 First structure model of metastable  $V^{III}PO_4$ -m1 (a) with square planar  $[VO_4]$  derived by removing the vanadyl oxygen from  $\beta$ - $V^V OPO_4$  (b) [161].

Table 11.2 Atomic coordinates for the first structure model of metastable  $VPO_4$ -m1, S.G.  $Pnma$ ;  $a = 7.341 \text{ \AA}$ ,  $b = 6.389 \text{ \AA}$ ,  $c = 7.329 \text{ \AA}$  based on  $\beta$ - $VOPO_4$ .

Atom	$x$	$y$	$z$
V1	0.1383	1/4	0.7622
P1	0.3756	1/4	0.3778
O1	0.2208	1/4	0.5272
O2	0.3608	0.0590	0.2785
O3	0.0465	1/4	0.0080

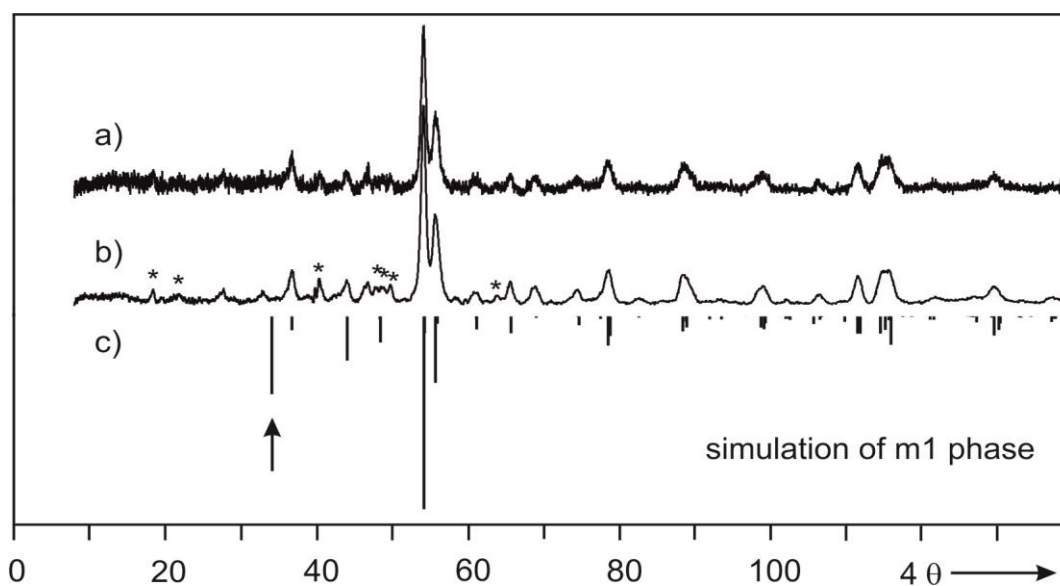
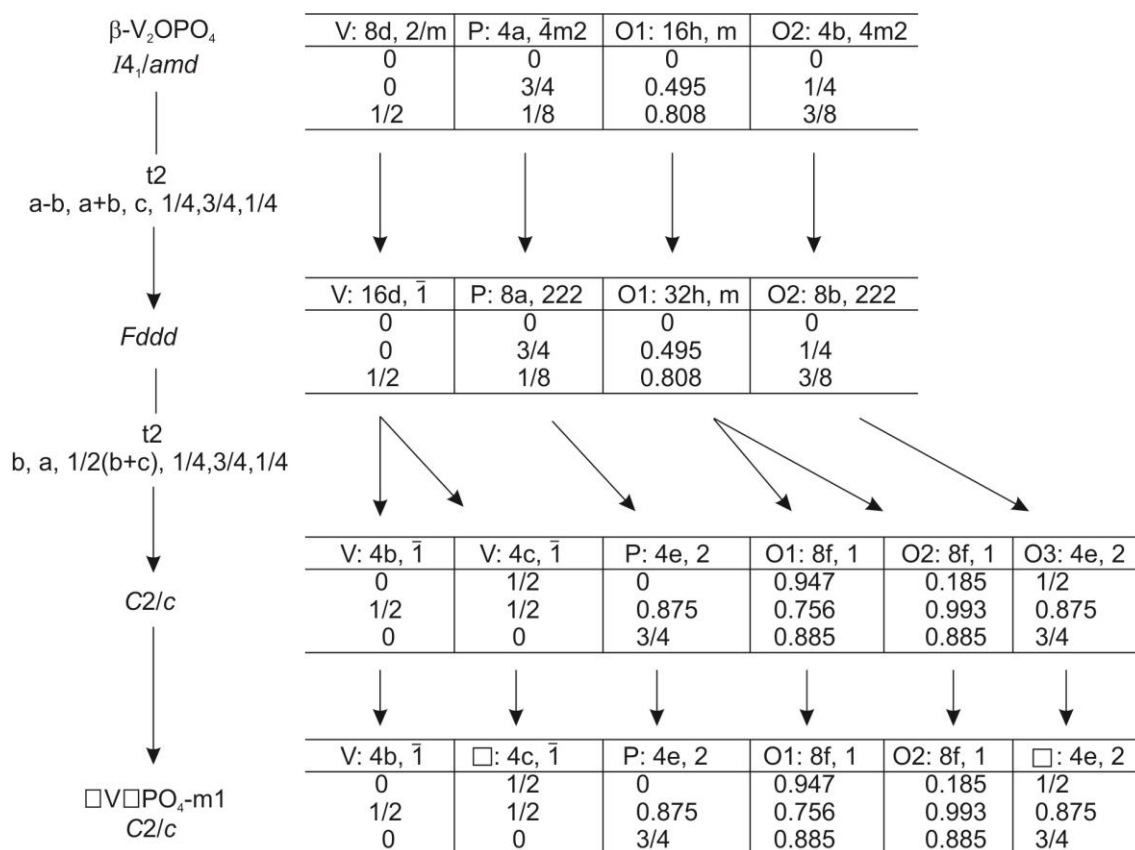
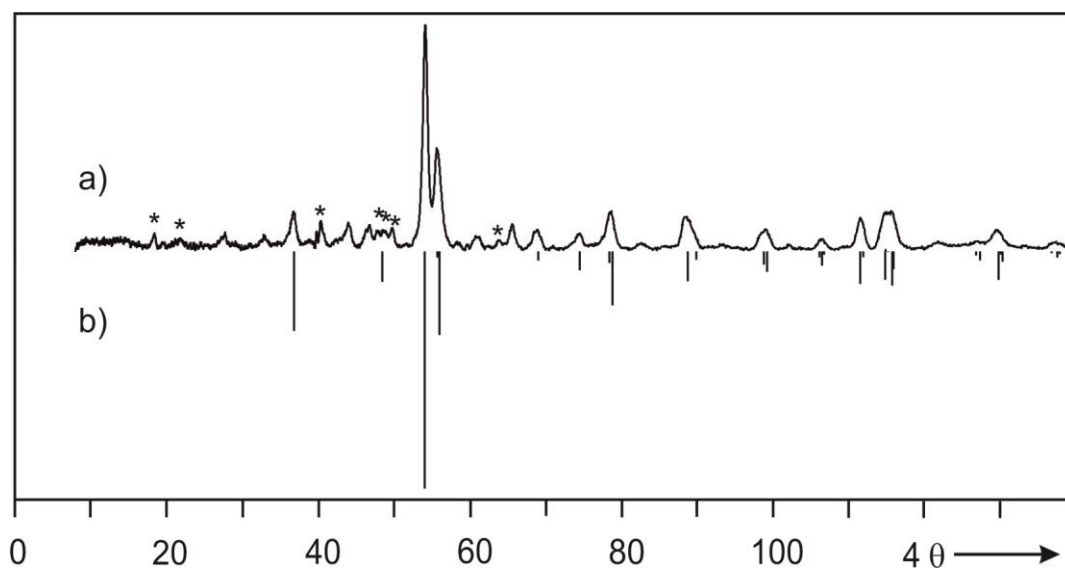


Figure 11.6 Guinier photographs of  $VPO_4$ -m1 with x-ray exposure time 15 min (a) and 5 hours (b), simulation based on the structure model related to  $\beta$ - $VOPO_4$  without vanadyl-oxygen atoms (square-planar  $VO_4$  groups) (c). Reflections marked by asterisks might originate from  $VPO_4$ -m2.

**Second structure model for  $VPO_4$ -m1 based on  $\beta$ - $V_2OPO_4$  and  $V_4O_3(PO_4)_3$ .** A second structure model for metastable  $VPO_4$ -m1 was derived from the Lipscombite structure type [293, 133] since the XRPD resembles those of  $\beta$ - $V_2OPO_4$  [148] and  $V_4O_3(PO_4)_3$  [31] both belonging to the Lipscombite/Lazulite structure family. The derivation of  $VPO_4$ -m1 (space group  $C2/c$ ;  $a = 7.73411 \text{ \AA}$ ,  $b = 7.33411 \text{ \AA}$ ,  $c = 7.36658 \text{ \AA}$ ,  $\beta = 119.854^\circ$ ) from  $\beta$ - $V_2OPO_4$  made use of group sub-group relations (see Table 11.3 and Figure 11.7). The simulated XRPD pattern derived from the  $\beta$ - $V_2OPO_4$  structure matches nicely with the experimental (see Figure 11.8). However, there are some reflections (indicated by asterisks in Figure 11.8) which are not explained by this structural model. Nevertheless many of unindexed reflections can be assigned by the current structure model through lowering the symmetry with threefold increase of  $c$ -axis. On the other hand, they are also overlap with the  $VPO_4$ -m2 phase. Therefore, assignment of these reflections is not unequivocal.

Table 11.3 Atomic coordinates for the second structure model of metastable  $VPO_4$ -m1 S.G.  $C2/c$ ;  $a = 7.73411 \text{ \AA}$ ,  $b = 7.33411 \text{ \AA}$ ,  $c = 7.36658 \text{ \AA}$ ,  $\beta = 119.854^\circ$  based on  $\beta$ - $V_2OPO_4$ .

Atom	$x$	$y$	$z$
V1	0	1/2	0
P1	0	0.875	$\frac{3}{4}$
O1	0.947	0.756	0.885
O2	0.185	0.993	0.885


 Figure 11.7 Second structure model of metastable  $\text{VPO}_4\text{-m1}$  derived from  $\beta\text{-V}_2\text{OPO}_4$ .

 Figure 11.8 Guinier photograph of  $\text{VPO}_4\text{-m1}$  (a) compared to the simulation based on the second structure model derived from  $\beta\text{-V}_2\text{OPO}_4$  (b), reflections marked by asterisks see text.

The second structure model for  $VPO_4$ -m1 derived from  $\beta$ - $V_2OPO_4$  [148] is shown in Figure 11.9. The strings of octahedra  $[VO_6]$  sharing faces along both  $a$ - and  $b$ -axis in  $\beta$ - $V_2OPO_4$  (see Figure 11.9a) is alternatively occupied by square planar  $[VO_4]$  and  $[\square O_4]$  with sharing corners in  $VPO_4$ -m1 (see Figure 11.9 b and c).

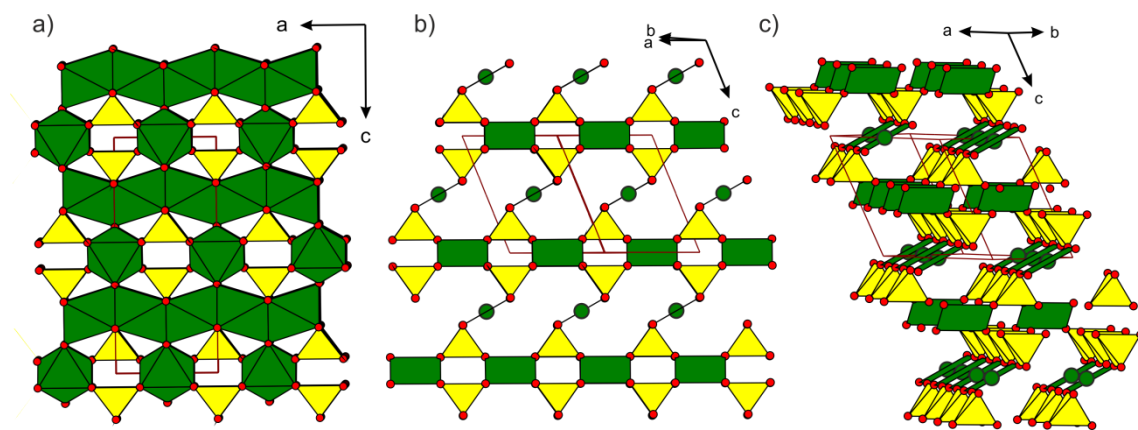


Figure 11.9 Second structure model of  $VPO_4$ -m1 with square planar  $[VO_4]$  (b) and (c) obtained from  $\beta$ - $V_2OPO_4$  (a).

Despite very long DFT calculations (PBE functional [294] and Pob.-T2VP basis set [295]) all attempts to relax the crystal structure of  $VPO_4$ -m1 failed. All the DFT calculation were performed in the research group of Prof. Thomas Bredow, Bonn University, Germany. Nevertheless these calculation predict a further polymorph for  $VPO_4$  with two slightly different unit cells. One adopts space group  $Pnma$  ( $a = 8.4891$  Å,  $b = 5.6533$  Å,  $c = 9.0598$  Å) and the other  $P2_1/m$  ( $a = 5.5289$  Å,  $b = 9.1850$  Å,  $c = 8.8903$  Å,  $\beta = 95.6362^\circ$ ). The orthorhombic structure can be described as corner sharing  $VO_4$  tetrahedra with four different  $PO_4$  units, thus forming a 3D structure with eight and four membered channels along the  $b$ -axis (Figure 11.10). The monoclinic structure model with  $P2_1/m$  is basically identical to the orthorhombic one. It is worth to be mentioned that they are, according to the DFT calculations, about  $39 \text{ kJmol}^{-1}$  more favorable than the thermodynamically stable phase of  $VPO_4$  ( $Cmcm$ ). These two predicted structure models have to be regarded as further polymorph expressing local minima in the energy hyper-surface of  $VPO_4$ . The simulated XRPD patterns of these two structures are shown in Figure 11.11. Atomic coordinates of the two structure models are given in Table 14.64.

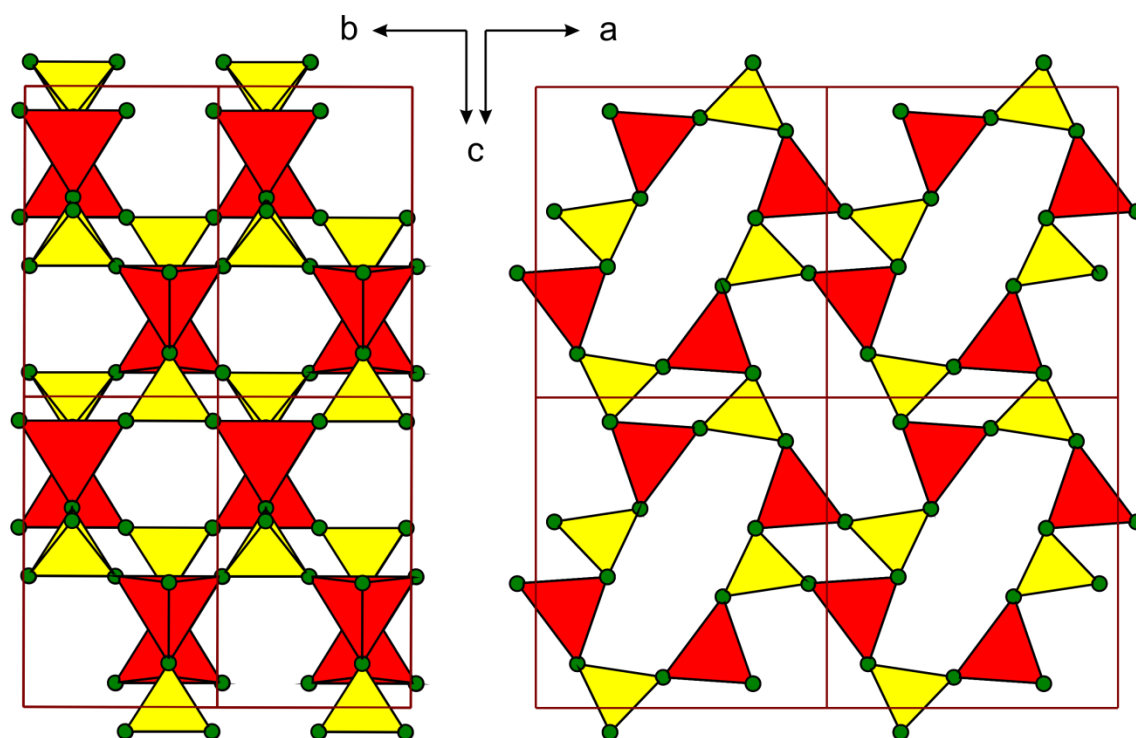


Figure 11.10 Predicted structure for new metastable  $VPO_4$  ( $Pnma$ ) polymorph with  $[VO_4]$  tetrahedra in red and  $PO_4$  in yellow obtained from DFT calculation.

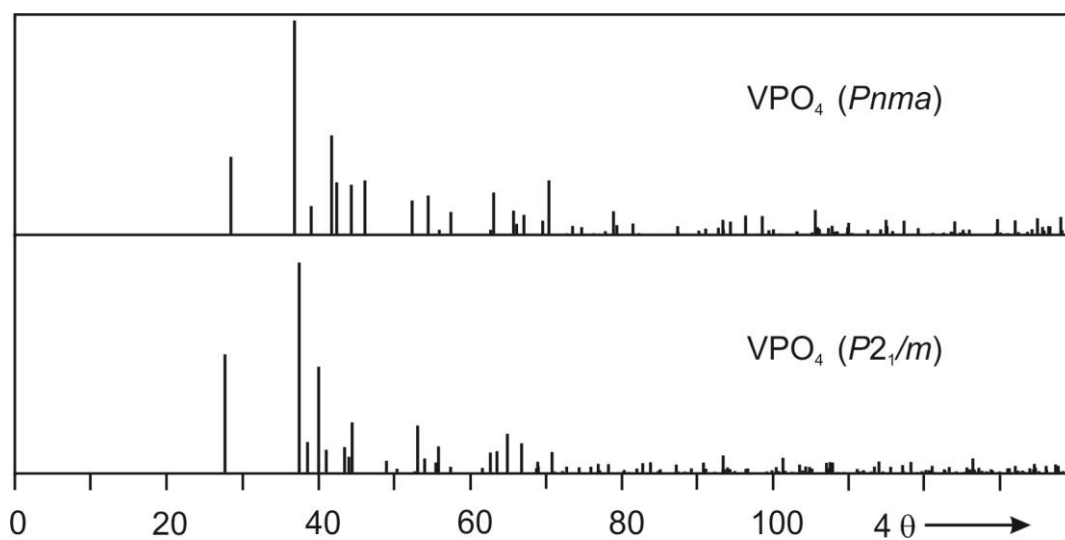


Figure 11.11 Simulated XRPD patterns of new metastable  $VPO_4$  polymorphs predicted by DFT calculation with  $Pnma$  (top) and  $P2_1/m$  (bottom). Both structure model consist of  $VO_4$  tetrahedra.

**Magnetic behavior of VPO<sub>4</sub>-m1.** The temperature dependent effective magnetic moment  $\mu_{\text{eff}}$  of V<sup>III</sup>PO<sub>4</sub>-m1 powder is shown in Figure 11.12. It was measured using a vibrating sample magnetometer (VSM) in the temperature range 2 to 300 K. The magnetic data was collected with field cooling at a magnetic flux density up to 10 kOe. A diamagnetic correction was applied to the observed data according to the method of atom and group increments [129]. The curve shows no hints on magnetic ordering.

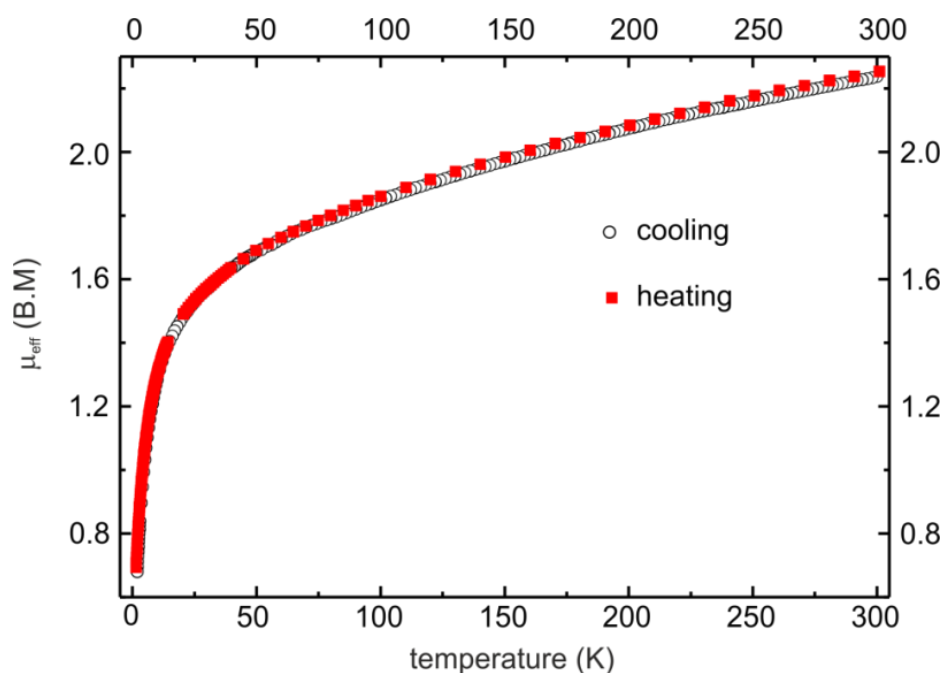


Figure 11.12 Temperature dependent effective magnetic moment of V<sup>III</sup>PO<sub>4</sub>-m1.

#### 11.2.4 Characterization of V<sup>III</sup>PO<sub>4</sub>-m2, V<sub>2</sub>(VO)(P<sub>2</sub>O<sub>7</sub>)(PO<sub>4</sub>)

The metastable phase VPO<sub>4</sub>-m2 is isotypic to “Fe<sup>II</sup>Fe<sup>III</sup>(V<sup>IV</sup>O)(P<sub>2</sub>O<sub>7</sub>)(PO<sub>4</sub>)” [133]. In a sealed tube in presence of mineralizer (I<sub>2</sub>) at 700 °C VPO<sub>4</sub>-m2 converts into thermodynamically stable VPO<sub>4</sub>. In VPO<sub>4</sub>-m2 the oxidation state of vanadium might be purely trivalent. The Guinier photograph of VPO<sub>4</sub>-m2 is compared with the simulation based on the relaxed crystal structure with adjusted lattice parameters [S.G.: *P2<sub>1</sub>/m*, *Z* = 2, *a* = 8.792(4) Å, *b* = 5.269(2) Å, *c* = 10.398(6) Å, *β* = 112.60(4)] determined from the experimental XRPD as shown in Figure 11.13. Assignment of the XRPD pattern is provided in Table 14.65.

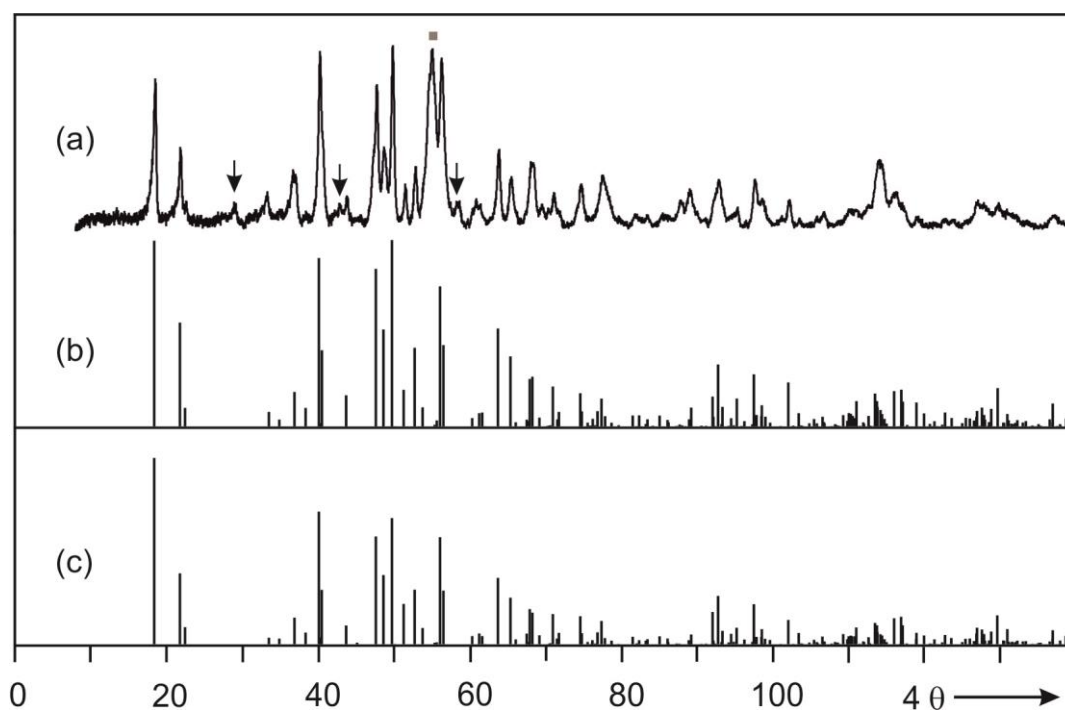


Figure 11.13 Guinier photograph of  $\text{VPO}_4\text{-m2}$ ,  $\text{V}_2(\text{VO})(\text{P}_2\text{O}_7)(\text{PO}_4)$  (a). Simulation based on single crystal data of  $\text{Fe}_2(\text{VO})(\text{P}_2\text{O}_7)(\text{PO}_4)$  [133] (b) via substituting the iron sites by vanadium, and simulation based on relaxed crystal structure (c). Adjusted lattice parameters from the experimental XRPD pattern are used for both cases. (■) and down arrows indicate reflections of  $\text{VPO}_4\text{-m1}$  and an unknown phase, respectively.

The crystal structure optimization for  $\text{VPO}_4\text{-m2}$  by DFT was successful (S.G.:  $P2_1/m$ ,  $Z = 2$ ,  $a = 8.80155 \text{ \AA}$ ,  $b = 5.34928 \text{ \AA}$ ,  $c = 10.4090 \text{ \AA}$ ,  $\beta = 112.0847^\circ$ ). The structure of  $\text{VPO}_4\text{-m2}$  consists of  $[\text{VO}_6]$  octahedra with orthophosphate and pyrophosphate anions forming a 3D network as shown in Figure 11.14. The structural derivation of  $\text{Fe}^{\text{II}}\text{Fe}^{\text{III}}(\text{V}^{\text{IV}}\text{O})(\text{P}_2\text{O}_7)(\text{PO}_4)$  from  $\beta\text{-V}_2\text{OPO}_4$  [148] (one member of the Lazulite family) was explained in details in ref [133]. The final atomic coordinates and selected interatomic distances of  $\text{VPO}_4\text{-m2}$  obtained by DFT calculation are provided in Table 11.4 and Table 14.66, respectively.

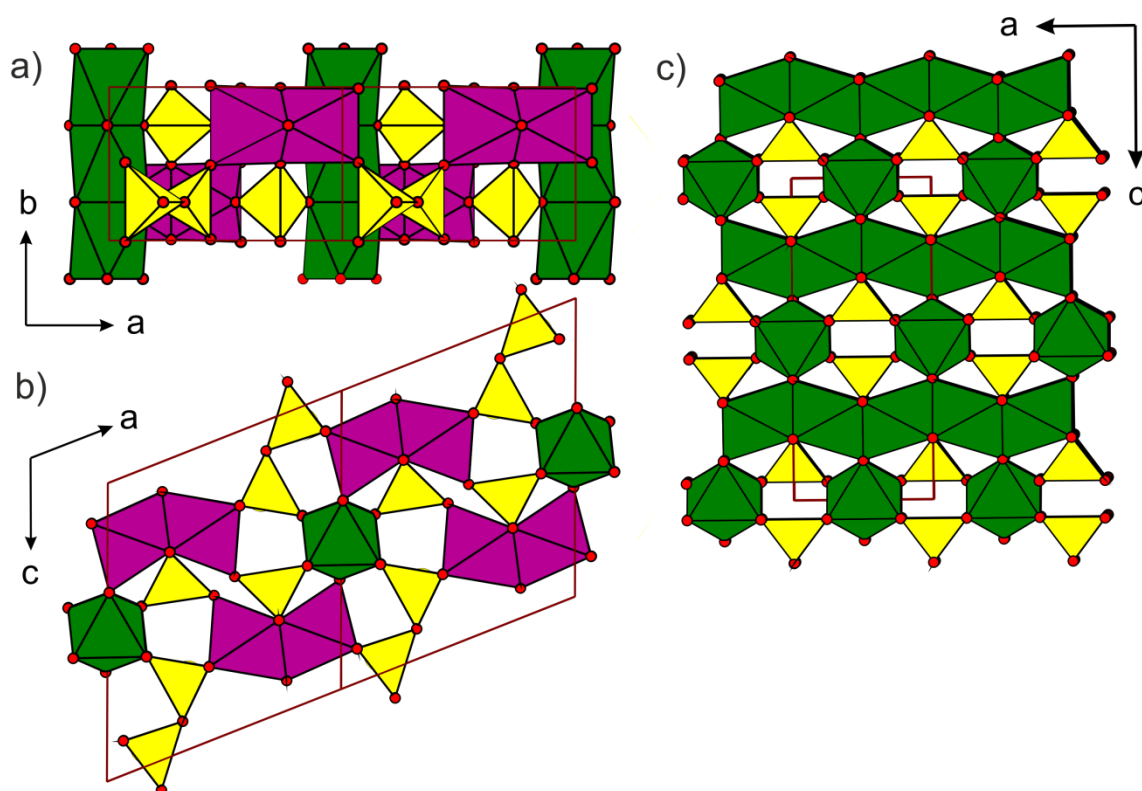


Figure 11.14 Polyhedral representation of the crystal structure of metastable  $VPO_4\text{-m}2$ ,  $V_2(\text{VO})(\text{P}_2\text{O}_7)(\text{PO}_4)$  (a) and (b), and  $\beta\text{-V}_2\text{OPO}_4$  [148] (c). Green strings of phase sharing  $\text{VO}_6$  octahedra, purple dimer of phase sharing  $\text{VO}_6$  octahedra, and yellow  $\text{PO}_4$  tetrahedra.

Table 11.4 Atomic coordinates of  $VPO_4\text{-m}2$ ,  $V_2(\text{VO})(\text{P}_2\text{O}_7)(\text{PO}_4)$  obtained by DFT calculation.

Atom	Wyck.Position	x	y	z
V1	2c	0	0	-1/2
V2	2e	-0.43175	-1/4	-0.28593
V3	2e	-0.077770	-1/4	-0.21903
P1	2e	0.28972	-1/4	0.40214
P2	2e	-0.16366	-1/4	0.06179
P3	2e	-0.34396	-1/4	0.24852
O1	2e	-0.16481	-1/4	0.36244
O2	2e	-0.32705	-1/4	0.09869
O3	2e	0.15341	-1/4	0.464812
O4	2e	0.46079	-1/4	-0.48470
O5	2e	-0.00615	-1/4	-0.37140
O6	4f	0.26534	-0.0055	0.31285
O7	2e	-0.23155	-1/4	-0.09940
O8	4f	-0.43341	-0.0092	0.25329
O9	4f	-0.06987	-0.0103	0.11884



### 11.3 Synthesis of the metastable vanadium oxides

#### $V^{IV}O_2(B)$ and $(V^{IV}O)_2V^V_2O_7$

##### 11.3.1 Experimental

The experimental set up for the synthesis of metastable  $VO_2(B)$  [278] and  $V_4O_9$  [288] (isotypic to  $(VO)_2P_2O_7$ ) from commercial  $V_2O_5$  via reduction by moist hydrogen flow ( $\approx 50$  bubbles  $\text{min}^{-1}$ ) was the same as described in section 11.2.1.

##### 11.3.2 Results and discussion

Reduction of  $V_2O_5$  by moist hydrogen leads to different products depending on temperatures as shown in Figure 11.15. At  $T < 300$  °C no reaction occurred. At 305 °C the reduction of  $V_2O_5$  started and after five days a mixture of  $VO_2(B)$  [278] and  $(VO)_2V_2O_7$  (“ $V_4O_9$ ”) [288] was obtained. Raising the temperature to  $T = 315$  °C formation of single phase metastable  $VO_2(B)$  [278] is accomplished. At 450 °C single phase  $V_2O_3$  [296] is obtained.

Attempts to get single phase  $(V^{IV}O)_2V^V_2O_7$  by reducing the reaction time were unsuccessful (Figure 14.18). Heating metastable  $V^{IV}O_2(B)$  in an evacuated sealed tube ( $l \approx 9$  cm,  $d \approx 1.5$  cm,  $V \approx 16$   $\text{cm}^3$ ) at 400 °C for one day transforms it into thermodynamically stable  $V^{IV}O_2(M)$  [276]. By electron microscopic and DSC studies the two steps transformation of  $VO_2(B) \rightarrow VO_2(A) \rightarrow VO_2(R)$  were already explained [297]. According to another literature [298] the intermediate polymorph  $VO_2(A)$  was not observed in this transformation. This complies to the observations reported here.

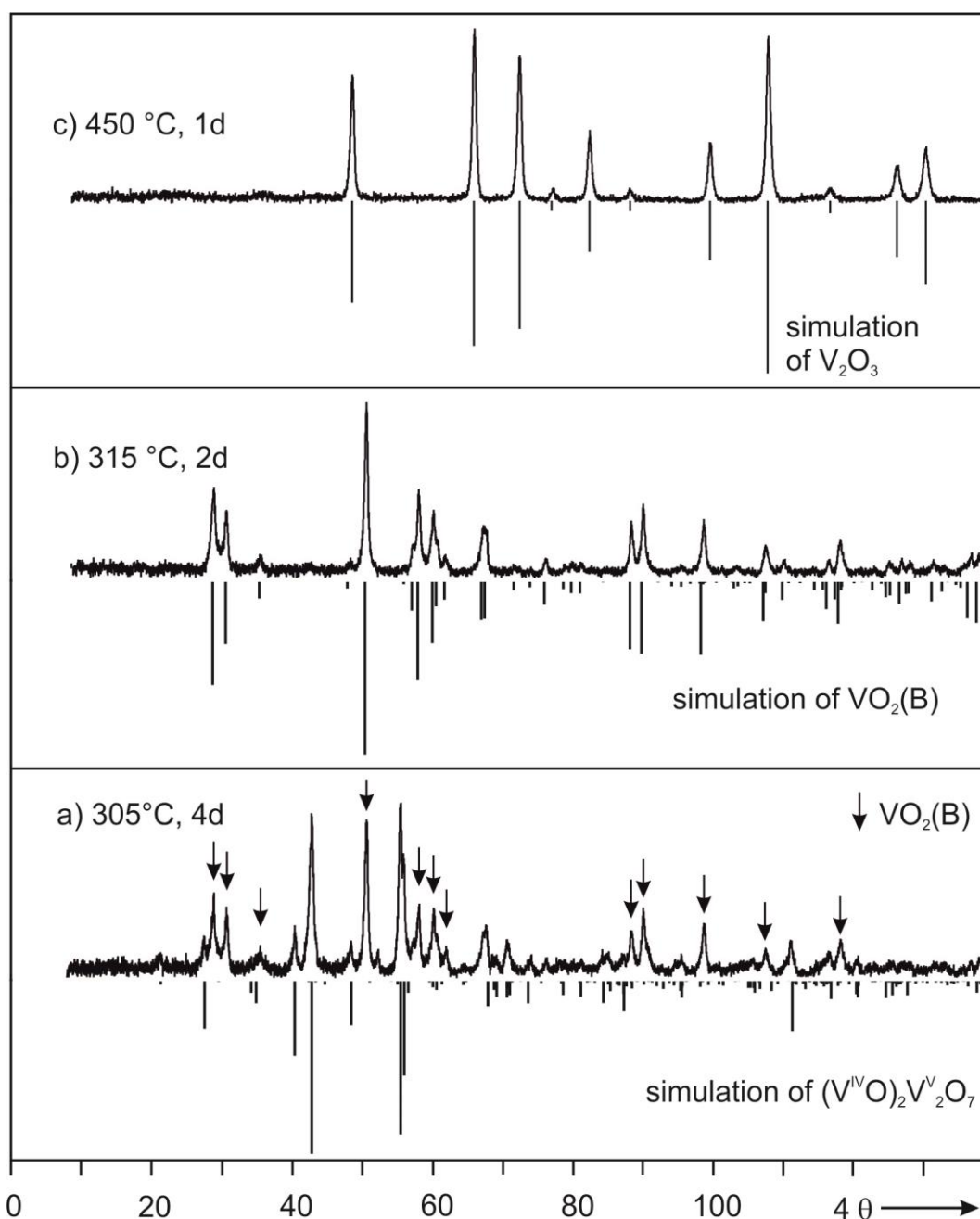


Figure 11.15 Reduction of  $V_2O_5$  by moist hydrogen at different temperatures.

The crystal structures of the vanadium oxides,  $V_2O_5$ ,  $V_4O_9$ ,  $VO_2(B)$  and  $VO_2(M)$  are shown in Figure 11.16.  $V_2O_5$  is made up of layers of  $VO_6$  octahedra sharing edges and corners along  $ab$ -plane which are interconnected by corner-sharing giving 3D structure. Mixed valence(IV,V) metastable  $V_4O_9$  adopts the  $(VO)_2P_2O_7$  structure type [10]. Metastable  $VO_2(B)$  is related to the  $V_2O_5$  structure. The difference is that each octahedra in  $V_2O_5$  is sharing 2 edges and 5 corners whereas in  $VO_2(B)$  sharing 4 edges and 4 corners with next neighbouring octahedra. The structure of  $VO_2(B)$  is also very close to the structure of  $V_6O_{13}$  [299].  $VO_2(M)$  is distorted rutile structure with chains of edge-

sharing octahedra along crystallographic  $a$ -axis. The distortion is due to pairing  $V^{4+}$ - $V^{4+}$  thus forming alternating short-long-short distances.

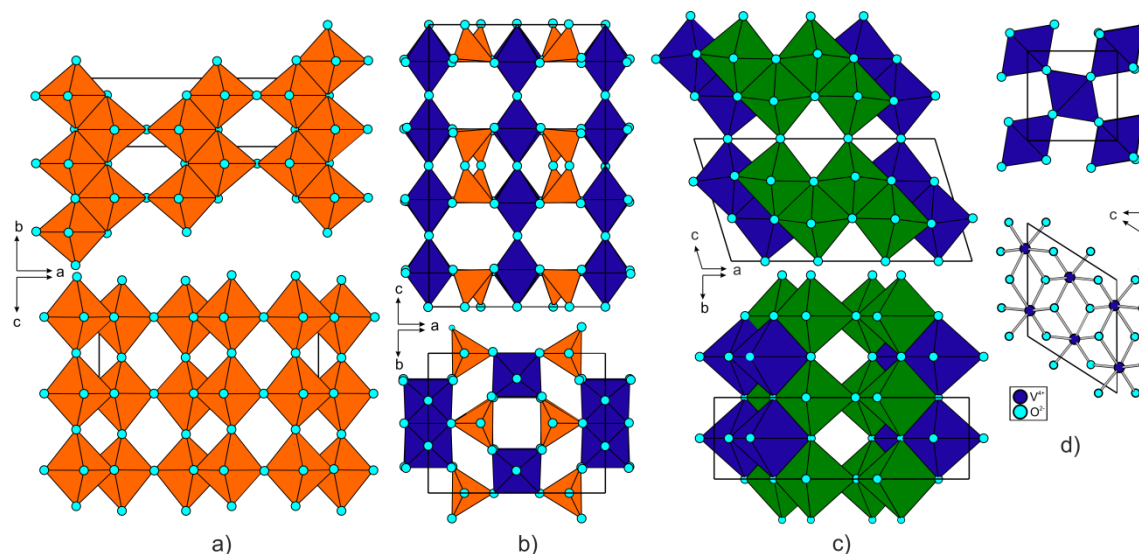


Figure 11.16 Crystal structures of  $V_2O_5$  (a), metastable  $(VO)_2V_2O_7$  (b), metastable  $VO_2(B)$  (c) related to  $V_2O_5$  structure, and  $VO_2(M)$  (d) distorted rutile structure type.

## 11.4 Conclusion

Moist hydrogen reduction of  $\beta$ - $VOPO_4$  [161] leads to two new metastable polymorphs of  $VPO_4$  (“m1” and “m2”). Two structure models for  $VPO_4$ -m1 are proposed. First one is based on the crystal structure of  $\beta$ - $VOPO_4$ . Second one is related to the crystal structures of the Lipscombite/Lazulite structure family, namely  $\beta$ - $V_2OPO_4$  [148] and  $V_4O_3(PO_4)_3$  [31]. Both structure models consist of square planar  $VO_4$  sharing corners with  $PO_4$  tetrahedra. It is worth to be mentioned that the existence of  $VO_4$  as a square planar polyhedra is the first example. Attempts to relax the structure of  $VPO_4$ -m1 led to another new metastable polymorph of  $VPO_4$ . The predicted structure consists of  $VO_4$  tetrahedra corner sharing with  $PO_4$  tetrahedra forming 3D network.

The second metastable phase  $VPO_4$ -m2 is isotypic to  $Fe^{II}Fe^{III}(V^{IV}O)(P_2O_7)(PO_4)$  [133]. DFT calculation allowed relaxation of the structure of  $VPO_4$ -m2. The oxidation state of vanadium in  $VPO_4$ -m2 is  $V^{3+}$  suggested by the sealed tube experiments. Considering the interatomic distances obtained from DFT calculation the oxidation states are  $V^{3+}/V^{3+}/V^{3+}$  instead of  $V^{2+}/V^{3+}/V^{4+}$ . The moist hydrogen reduction of  $V_2O_5$  leads to the formation of metastable  $V_4O_9$ , isotypic to  $(VO)_2P_2O_7$ . This technique also lead to the formation of single phase  $VO_2(B)$  and  $V_2O_3$ . This synthesis technique could also be used to selective reduction of metallyl bonds from oxides and oxy-phosphates.

## 12 Catalytic testing

### 12.1 Introduction

Several compounds described in this thesis for the first time have been tested for their use as catalyst material for selective oxidation of *n*-butane to MA (Table 12.1). The testing was done with batch sizes of 5-10 g. Their synthesis and characterizations are described in the respective chapters. The performance of a catalyst material mainly depends on three properties: activity, stability and selectivity.

**Conversion ( $X_A$ )** is expressed as the ratio of the converted amount of reactant *A* to the amount that has introduced into the reactor (eq. 12.1). In this regard the amount of desired product is not taken into account; it includes all types of reaction products.

$$X_A = \frac{n_{A,0} - n_A}{n_{A,0}} \quad (\text{eq. 12.1})$$

$n_{A,0}$  and  $n_A$  is the amount of reactant before and after reaction, respectively.

**Stability** of the catalyst material (thermal, mechanical, chemical) has an aspect on the total life time of a catalyst, which is crucial for an economic purpose.

**Selectivity ( $S_A$ )** is the fraction of the starting material *A* converted into desired reaction product only (eq. 12.2) and the maximum value of  $S_A$  could be 100%.

$$S_A = \frac{n_p |v_A|}{(n_{A,0} - n_A) v_p} \quad (\text{eq. 12.2})$$

$v_A$  and  $v_p$  are the stoichiometric coefficient of reactant and product and  $n_p$  is the amount of desired product.

The catalytic investigations of those phases were performed in the research laboratory of BasCat (UniCat BASF Joint Lab) TU Berlin. This is one of the project partners in **HT4CAT** (**H**igh **T**hroughput **C**omputing for Prediction and Modelling of new Lead Structures for Selective Oxidation **C**atalysts) funded by BASF SE.

## 12.2 Construction and operation of multi-tube fixed bed reactor

The substances were tested in 48-fold test reactor tubes with 1ml volume of test catalyst materials at average particle sizes between 500 to 1000 microns. To prevent hot spot formation and to avoid a temperature gradient in the reactor tubes the sample materials were diluted by placing alumina before and after it. First the samples were passed a various conditioning sequence, in which the temperature and the amount of feed gas mixture were slowly adjusted to the desired values.

The standard test procedure comprised a variation of the temperature from 380 to 450 °C and a feed gas supply of 2% *n*-butane: water in air at 2000 GHSV (Gaseous Hour Space Velocity). Meanwhile, the test parameters were adjusted repeatedly to track performance changes by changing test conditions. Reaction feed was controlled by a mass flow controller and the water was fed by mini pump. The analysis of the products was carried out "online" by using a gas chromatograph connected via heated lines to the reactor tubes. The data collection and monitoring of the reaction performance was accomplished automatically using the commercially available software "myhte" [300]. At every batch of catalytic test measurement 3 to 5 reactor tubes with commercially available VPP catalysts were distributed randomly and measured under the same conditions as internal standards.

## 12.3 Results and discussion

The results of the catalytic tests are summarized in Table 12.1. For the evaluation, the temperature is indicated where the highest conversion of *n*-butane was observed. To determine the selectivity a closed gaseous space was assumed and the measured MA, CO<sub>2</sub> and CO was extrapolated to 100%. Besides these three main products during the catalytic tests, the formation of acrolein, acetic acid, and acrylic acid as by-products was also monitored.

Table 12.1 Tested materials, results of catalytic testing and characterization of the catalyst materials after testing,  $S_{MA} = \{n(\text{MA}_{\text{product}})/n(\text{n-butane}_{\text{feed}})\} * 100$ ,  $X_{\text{n-butane}} = \{n(\text{All}_{\text{product}})/n(\text{n-butane}_{\text{feed}})\}$ .

substances	$\vartheta$ (°C)	$X_{\text{n-butane}}$ (%)	$S_{MA}$ (%)	after catalytic test (IP Guinier photograph)
$\text{V}^{\text{IV}}\text{O}_2(\text{M})$	450	12	-	$\text{VO}_2(\text{M}) + \text{V}_2\text{O}_3 + \text{V}_2\text{O}_5$
$\text{V}^{\text{IV}}\text{O}_2(\text{B})$ (metastable)	425	81	-	$\text{V}_2\text{O}_5$ <sup>a)</sup>
$\text{V}_2\text{O}_5$ (Merck)	450	38	-	$\text{V}_2\text{O}_5$
$\text{V}^{\text{III}}\text{PO}_4\text{-m1}$ (metastable)	450	50	57	$\text{V}^{\text{III}}\text{PO}_4\text{-m1}, (\text{V}^{\text{IV}}\text{O})_2\text{P}_2\text{O}_7, \beta\text{-V}^{\text{V}}\text{OPO}_4$
$(\text{V}^{\text{IV}}\text{O})_2\text{P}_2\text{O}_7$	450	17	77	$(\text{V}^{\text{IV}}\text{O})_2\text{P}_2\text{O}_7$ <sup>a)</sup>
$\beta\text{-V}^{\text{V}}\text{OPO}_4$	450	38	51	$\beta\text{-V}^{\text{V}}\text{OPO}_4$
$\beta\text{-}(\text{V}^{\text{IV}}_{0.01}\text{V}^{\text{V}}_{0.98}\text{W}^{\text{VI}}_{0.01})\text{OPO}_4$ <sup>b)</sup>	450	16	52	$\beta\text{-}(\text{V}^{\text{IV}}_{0.01}\text{V}^{\text{V}}_{0.98}\text{W}^{\text{VI}}_{0.01})\text{OPO}_4$ <sup>b)</sup>
$\alpha_{\text{II}}\text{-}(\text{V}^{\text{IV}}_{0.06}\text{V}^{\text{V}}_{0.88}\text{W}^{\text{VI}}_{0.06})\text{OPO}_4$ <sup>c)</sup>	450	20	63	$\alpha_{\text{II}}\text{-}(\text{V}^{\text{IV}}_{0.06}\text{V}^{\text{V}}_{0.88}\text{W}^{\text{VI}}_{0.06})\text{OPO}_4$ <sup>c)</sup>
$\alpha_{\text{II}}\text{-}(\text{V}^{\text{IV}}_{0.10}\text{V}^{\text{V}}_{0.80}\text{W}^{\text{VI}}_{0.10})\text{OPO}_4$ <sup>c)</sup>	450	28	51	$\alpha_{\text{II}}\text{-}(\text{V}^{\text{IV}}_{0.10}\text{V}^{\text{V}}_{0.80}\text{W}^{\text{VI}}_{0.10})\text{OPO}_4$ <sup>c)</sup>
$\alpha_{\text{II}}\text{-}(\text{V}^{\text{IV}}_{0.20}\text{V}^{\text{V}}_{0.60}\text{W}^{\text{VI}}_{0.20})\text{OPO}_4$ <sup>c)</sup>	450	32	45	$\alpha_{\text{II}}\text{-}(\text{V}^{\text{IV}}_{0.20}\text{V}^{\text{V}}_{0.60}\text{W}^{\text{VI}}_{0.20})\text{OPO}_4$ <sup>c)</sup>
$\beta\text{-}(\text{V}^{\text{IV}}_{0.20}\text{V}^{\text{V}}_{0.60}\text{Mo}^{\text{VI}}_{0.20})\text{OPO}_4$ <sup>b)</sup>	450	4	5	$\beta\text{-}(\text{V}^{\text{IV}}_{0.20}\text{V}^{\text{V}}_{0.60}\text{Mo}^{\text{VI}}_{0.20})\text{OPO}_4$ <sup>b)</sup>
$\gamma\text{-}(\text{V}^{\text{IV}}_{0.20}\text{V}^{\text{V}}_{0.60}\text{Mo}^{\text{VI}}_{0.20})\text{OPO}_4$ <sup>d)</sup>	450	4	5	$\gamma\text{-}(\text{V}^{\text{IV}}_{0.20}\text{V}^{\text{V}}_{0.60}\text{Mo}^{\text{VI}}_{0.20})\text{OPO}_4$ <sup>d)</sup>
$\text{cub}\text{-}(\text{V}_{0.10}\text{W}_{0.4}\text{P}_{0.50})\text{O}_{2.5+\delta}$ <sup>e)</sup>	450	8	26	$\text{cub}\text{-}(\text{V}_{0.10}\text{W}_{0.4}\text{P}_{0.50})\text{O}_{2.5+\delta}$ <sup>e)</sup>
$\text{cub}\text{-}(\text{V}_{0.167}\text{W}_{0.333}\text{P}_{0.50})\text{O}_{2.5+\delta}$ <sup>e)</sup>	450	20	26	$\text{cub}\text{-}(\text{V}_{0.167}\text{W}_{0.333}\text{P}_{0.50})\text{O}_{2.5+\delta}$ <sup>e)</sup>
$\text{cub}\text{-}(\text{V}_{0.25}\text{W}_{0.25}\text{P}_{0.50})\text{O}_{2.5+\delta}$ <sup>e)</sup>	450	37	32	$\text{cub}\text{-}(\text{V}_{0.25}\text{W}_{0.25}\text{P}_{0.50})\text{O}_{2.5+\delta}$ <sup>e)</sup>
$\text{cub}\text{-}(\text{Fe}_{0.60}\text{V}_{0.6}\text{W}_{1.8}\text{P}_3)\text{O}_{15}$ <sup>e)</sup>	450	28	67	$\text{cub}\text{-}(\text{Fe}_{0.60}\text{V}_{0.6}\text{W}_{1.8}\text{P}_3)\text{O}_{15}$ <sup>e)</sup>
$(\text{Fe}^{\text{III}}_{0.33}\text{W}^{\text{VI}}_{0.67})\text{OPO}_4$ <sup>f)</sup>	450	2	-	$(\text{Fe}^{\text{III}}_{0.33}\text{W}^{\text{VI}}_{0.67})\text{OPO}_4$ <sup>a, f)</sup>
$\text{Fe}^{\text{III}}(\text{W}^{\text{VI}}\text{O}_2)_2(\text{P}_2\text{O}_7)\text{PO}_4$	450	4	-	$\text{Fe}^{\text{III}}(\text{W}^{\text{VI}}\text{O}_2)_2(\text{P}_2\text{O}_7)\text{PO}_4$
$\text{W}^{\text{V}}\text{OPO}_4$	450	4	25	$\text{W}^{\text{V}}\text{OPO}_4$ + unknown phase

<sup>a)</sup> traces of impurity, <sup>b)</sup>  $\beta\text{-VOPO}_4$  type, <sup>c)</sup>  $\alpha_{\text{II}}\text{-VOPO}_4$  type, <sup>d)</sup> metastable and  $\gamma\text{-VOPO}_4$  type, <sup>e)</sup>  $\text{ReO}_3$  type (metastable), <sup>f)</sup>  $\text{WOPO}_4$  type (metastable).

The majority of the samples tested for selective oxidation of *n*-butane to MA showed both activity and selectivity. Among them the reference  $(\text{V}^{\text{IV}}\text{O})_2\text{P}_2\text{O}_7$  prepared in this study was most selective with  $S_{MA} = 77\%$ , which is close to the value of the industrially used catalyst material. The next compound which showed high selectivity and a moderate activity was a new phase,  $(\text{Fe}_{0.1}\text{V}_{0.1}\text{W}_{0.3}\text{P}_{1.5})\text{O}_{2.5+\delta}$  (*cub*- $\text{WO}_3$  structure type [252]) which is thermodynamically metastable.  $\text{Fe}(\text{WO}_2)_2(\text{P}_2\text{O}_7)\text{PO}_4$  and  $(\text{Fe}_{0.33}\text{W}_{0.67})\text{OPO}_4$  prepared in this thesis for the first time showed almost no activity. This seems to indicate that vanadium is an essential component of catalyst materials. Oxides of vanadium at different oxidation states also showed high activity, especially the metastable  $\text{VO}_2(\text{B})$ . The oxides, however didn't show any selectivity. As a result, not only vanadium but also phosphorus seems essential for a good catalyst material. Tungsten substituted  $\alpha_{\text{II}}\text{-VOPO}_4$  also

showed both selectivity and activity. The activity increases with increasing the dopant concentration, in other words the activity depends on the concentration of tetravalent vanadium. However the selectivity decreases with increasing the concentration of  $V^{4+}$  ions. Among the members of the solid solution  $(V_{1-x}W_x)OPO_4$  the composition with  $x = 20$  showed moderate activity and selectivity. On the other hand surprisingly, molybdenum doped  $VOPO_4$  structure with  $\gamma$ - and  $\beta$ -type were quite inactive. All of the materials that showed catalytic activity and selectivity are thermally stable within the range of the catalytic tests and, most importantly, they are also chemically stable (except metastable  $VPO_{4-m1}$ ). The stability was checked by XRPD after the catalytic test.

It can be concluded that the ratio of  $V^{4+}/V^{5+}$  and the presence of P have a strong influence on both activity and selectivity for the catalytic reaction of *n*-butane based MA production. The most potential candidates which can replace the industrial VPP catalyst material are  $(Fe^{III}_{0.1}V^{IV}_{0.05}V^V_{0.05}W^{VI}_{0.3}P_{0.5})O_{2.5+\delta}$  and  $(V^{IV}_{0.2}V^V_{0.6}W^{VI}_{0.2})OPO_4$  (*cub*- $WO_3$  and  $\alpha_{II}$ - $VOPO_4$  structure type, respectively). The striking feature of the former phase is its enormous structural flexibility and the second phase has enormous active sites due to layered type surface planes in comparison to  $(V^{IV}_{0.2}V^V_{0.6}Mo^{VI}_{0.2})OPO_4$  ( $\beta$ - $VOPO_4$  structure type) which has 3D network structure.

## 13 Summary

This thesis reports on syntheses, crystallization, phase relations and redox phenomena in the quasi-ternary oxide systems  $\text{WO}_{2.5}/\text{VO}_{2.5}/\text{PO}_{2.5}$  and  $\text{MoO}_{2.5}/\text{VO}_{2.5}/\text{PO}_{2.5}$ . This work focused on finding new catalyst lead structures for the gas-phase oxidation of *n*-butane to maleic anhydride. Synthesis of the new anhydrous phosphates was performed in three different techniques, namely solution combustion synthesis, classical solid state reaction and vapor phase moderated solid state reaction. Crystallization was achieved mainly by CVT and vapor phase moderated solid state reaction. Characterization of the newly obtained phases was accomplished by x-ray single crystal analysis, electron diffraction analysis, HRTEM analysis, magnetic and conductivity measurement and several spectroscopic techniques (XPS, EPR, UV/Vis/NIR,  $^{31}\text{P}$ -MAS-NMR).

$\text{W}^{\text{V}}\text{OPO}_4$  (Chapter 5) belongs to the series of monophosphate tungsten bronzes  $(\text{WO}_3)_{2m}(\text{PO}_2)_4$  ( $m = 2$ , [90, 91]). The single crystal structure refinement of  $\text{WOPO}_4$   $\{P2_1/m, Z = 4, a = 6.5538(4) \text{ \AA}, b = 5.2237(8) \text{ \AA}, c = 11.1866(8) \text{ \AA}, \beta = 90.332(7)^\circ\}$  as well as the XRPD pattern shows monoclinic instead of the reported orthorhombic symmetry [90]. A significant improved structure model is provided.

**Phosphates**  $(M^{\text{III}}_{0.333}W^{\text{VI}}_{0.667})\text{OPO}_4$  ( $M$ : V, Cr, Fe, Mo;  $\text{W}^{\text{V}}\text{OPO}_4$  structure type, Chapter 9) have been synthesized by various methods (SCS, CVT, vapor phase moderated solid state reactions) and characterized. These are the first hetero-metallic examples of phases with MPTB structure type.  $\text{W}^{5+}$  is substituted by  $M^{3+}_{1/3}W^{6+}_{2/3}$ . Similar substitution was also observed for  $(\text{W}^{\text{V,VI}}\text{O}_3)_8(\text{PO}_2)_4$  (MBTB with  $m = 4$ ) leading to  $(M^{\text{III}}_{1/6}W^{\text{VI}}_{5/6}\text{O}_3)_8(\text{PO}_2)_4$  ( $M$ : V, Cr, Chapter 10).

**In the system W/V/P/O** along the quasi binary line  $\text{WOPO}_4$ - $\text{VOPO}_4$  solid solutions  $(\text{V}_{1-x}\text{W}_x)\text{OPO}_4$  with four different structure types have been identified (see Figure 13.1):  $0 \leq x \leq 0.01$ ,  $\beta$ - $\text{VOPO}_4$  structure type [161];  $0.04 \leq x \leq 0.26$ ,  $\alpha_{\text{II}}$ - $\text{VOPO}_4$  structure type [160] (Chapter 6);  $0.60 \leq x \leq 0.67$ ,  $\text{V}(\text{WO}_2)_2(\text{P}_2\text{O}_7)(\text{PO}_4)$  structure type (Chapter 8); and  $0.67 \leq x \leq 1$   $\text{WOPO}_4$  structure type [90, 91] (Chapter 6). The latter is probably thermodynamically metastable.



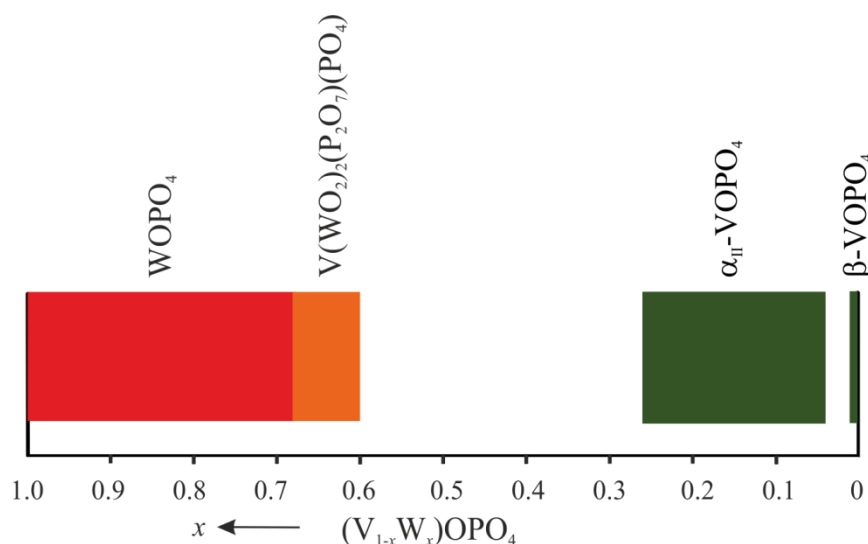
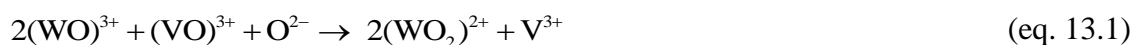


Figure 13.1 Solid solutions  $(V_{1-x}W_x)OPO_4$ . Structure types and compositional ranges.

For  $x = 0.50$  the formation of a four-phase equilibrium mixture of  $\alpha_{II}-(V_{0.74}W_{0.26})OPO_4$ ,  $m-(V^{IV}O)(PO_3)_2$  [167], a vanadium-doped mono-phosphate tungsten bronze of approximate composition  $(W_{5/6}V_{1/6}O_3)_8(PO_2)_4$  (Chapter 10) ( $(WO_3)_8(PO_2)_4$  structure type [95]) and a lower phase boundary composition  $V(W_{0.9}V_{0.1}O_2)_2(P_2O_7)PO_4$  which is extended up to  $x = 0.67$ ,  $V(WO_2)_2(P_2O_7)PO_4$  was observed. The oxidation states in the solid solutions  $(V_{1-x}W_x)OPO_4$  with  $\alpha_{II}$ - and  $\beta$ -VOPO<sub>4</sub> structure type have been established by various physical measurements (EPR, XPS, UV/Vis/NIR spectroscopy and magnetic measurements). Accordingly, the formulation  $(V^{IV}_xV^{V}_{1-2x}W^{VI}_x)OPO_4$  is appropriate. The solid solutions are Class II semiconductors ( $E_g \approx 0.7$  eV). In catalytic testing for *n*-butane oxidation to MA,  $(V_{0.8}W_{0.20})OPO_4$  ( $\alpha_{II}$ -VOPO<sub>4</sub> structure type) showed promising behavior (Activity  $X_{n\text{-butane}} = 32\%$ , Selectivity  $S_{MA} = 45\%$ , Chapter 12).

**The new polynary phosphate  $V^{III}(W^{VI}O_2)_2(P_2O_7)PO_4$  was synthesized and characterized.** Its composition corresponds to  $(V_{1-x}W_x)OPO_4$  with  $x = 0.67$ .  $V^{III}(W^{VI}O_2)_2(P_2O_7)PO_4$  is the first mixed transition metal phosphate combining oxidation states III+ and VI+. These are in agreement with the results of XPS, magnetic measurements and UV/Vis/NIR spectroscopy. Formation of new phase from VOPO<sub>4</sub> and WOPO<sub>4</sub> can be interpreted as a combined redox (eq. 13.1) and Lux-Flood acid-base reaction.(eq. 13.2).



A homogeneity range according to  $(V_{1-x}W_x)OPO_4$  with  $0.60 \leq x \leq 0.67$  ( $V(WO_2)_2(P_2O_7)PO_4$  structure type) was detected. Crystallization was obtained during vapour phase moderated solid state reactions using  $Cl_2$  as mineralizer. Its crystal structure is visualized in Figure 13.2.

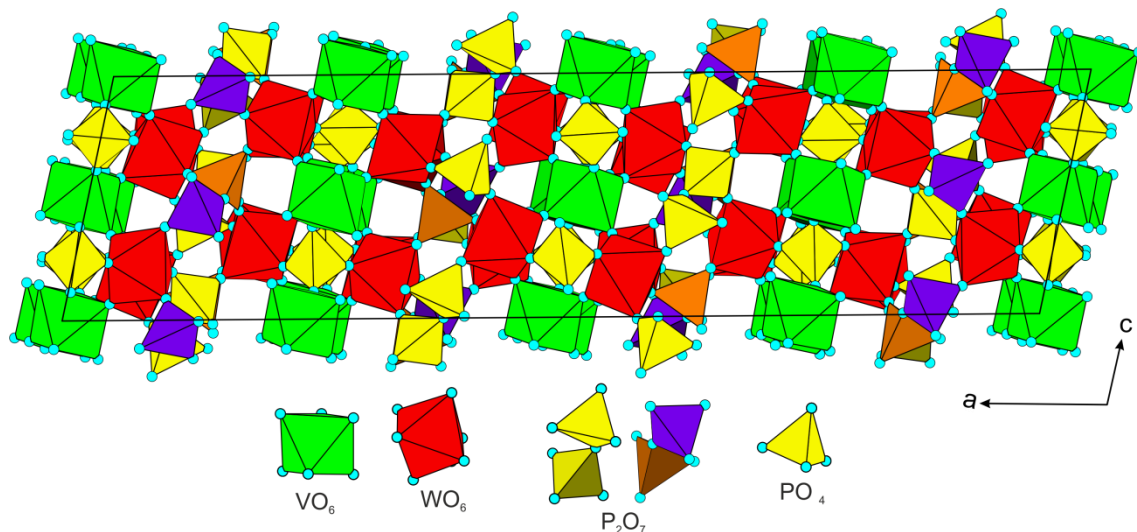
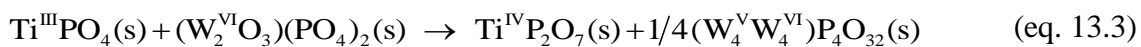


Figure 13.2 Crystal structure of new polynary phosphate  $V^{III}(W^{VI}O_2)_2(P_2O_7)PO_4$ . Fairly regular octahedra  $VO_6$  (2 sites) show an occupancy of about  $V_{0.5}W_{0.5}$ . Distorted octahedra  $WO_6$  (4 sites,  $WO_2^{2+}$  groups) show an occupancy of about  $V_{0.25}W_{0.75}$ .

The  $V^{III}(W^{VI}O_2)_2(P_2O_7)PO_4$  structure type shows a wide crystal chemical stability range allowing substitution of  $V^{3+}$  by several other trivalent ions ( $M^{3+}$ : Sc, Cr, Fe, Mo, Ru, Rh, Ir, In). However the strong reductant  $Ti^{3+}$  yielded different redox product as shown in (eq. 13.3).  $^{31}P$ -MAS-NMR studies of Sc, In, and Ir compound shows the presence of  $P_2O_7$  and  $PO_4$  units.



Monitoring the phase formation during the synthesis of  $M^{III}(W^{VI}O_2)_2(P_2O_7)PO_4$  via SCS and subsequent heating revealed the presence of various metastable reaction intermediates with structures related to the  $ReO_3$  and  $WOPO_4$  types. During annealing of the intermediate combustion products the following sequence of phases was typically observed (see Figure 13.3).

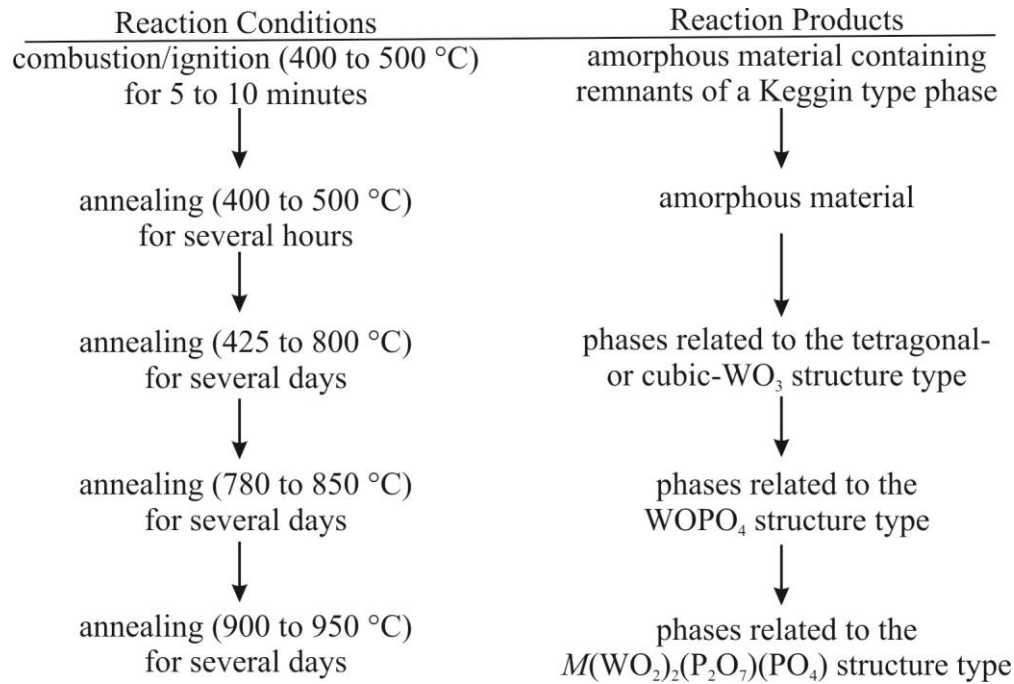


Figure 13.3 Schematic diagram of annealing condition and typically observed phases of post-SCS process ( $M$ : Sc, V, Cr, Fe, In).

In further experiments it was shown that solution combustion synthesis is a versatile method for obtaining various mixed metal phosphates with WO<sub>3</sub>-related structures. Thus the solid solution  $(\text{V}_x\text{W}_{0.5-x}\text{P}_{0.5})\text{O}_{2.5+\delta}$  ( $0.0 \leq x \leq 0.25$ ) as well as multi-metal phosphate  $(\text{Fe}_{0.1}\text{V}_{0.1}\text{W}_{0.3}\text{P}_{0.5})\text{O}_{2.5+\delta}$  were obtained as single phase material. It was shown that depending on  $p(\text{O}_2)$  during the post-combustion annealing, the oxidation states of vanadium in the solid solution can be set. Most remarkably,  $(\text{V}_{0.25}\text{W}_{0.25}\text{P}_{0.5})\text{O}_{2.5+\delta}$  as well as  $(\text{Fe}_{0.1}\text{V}_{0.1}\text{W}_{0.3}\text{P}_{0.5})\text{O}_{2.5+\delta}$  show very promising catalytic behavior in selective oxidation of  $n$ -butane to MA ( $(\text{V}_{0.25}\text{W}_{0.25}\text{P}_{0.5})\text{O}_{2.5+\delta}$ : Activity  $X_{n\text{-butane}} = 37\%$ , Selectivity  $S_{\text{MA}} = 32\%$  and  $(\text{Fe}_{0.1}\text{V}_{0.1}\text{W}_{0.3}\text{P}_{0.5})\text{O}_{2.5+\delta}$ : Activity  $X_{n\text{-butane}} = 28\%$ , Selectivity  $S_{\text{MA}} = 67\%$ ).

**In the system Mo/V/P/O** (Chapter 7) along the quasi-binary line of MoOPO<sub>4</sub>-VOPO<sub>4</sub> solid solutions  $(\text{V}_{1-x}\text{Mo}_x)\text{OPO}_4$  with two different structure types have been obtained by SCS followed by heating in air:  $0.0 \leq x \leq 0.30$  thermodynamically stable  $\beta$ -VOPO<sub>4</sub> [161] structure type;  $0.0 \leq x \leq 0.20$  thermodynamically metastable  $\gamma$ -VOPO<sub>4</sub> [162] structure type (Figure 13.4). With increasing Mo concentration the temperature required to obtain the thermodynamically stable phase decreased (725 °C for  $x = 0.0$  and 600 °C for  $x = 0.30$ ) and the color of the material changes from bright yellow to olive green. The EPR, <sup>31</sup>P-MAS-NMR, UV/Vis/NIR spectra as well as the magnetic and conducting

behavior of these solid solutions are quite similar to the tungsten substituted solid solutions. Therefore the oxidation states according to  $(V^{IV}_x V^{V}_{1-2x} Mo^{VI}_x)OPO_4$  are suggested.

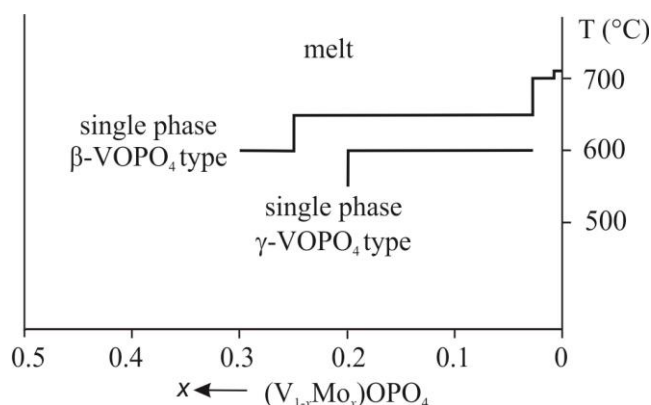


Figure 13.4 Structure types, their homogeneity ranges, and formation temperatures in the quasi-binary system  $MoOPO_4$ - $VOPO_4$ .

**Reduction of  $\beta$ - $VOPO_4$**  (Chapter 11) by moist hydrogen led to the two new metastable phases  $VPO_4$ -m1 (at 500 °C) and  $VPO_4$ -m2 (at 700 °C). For  $VPO_4$ -m1 two structure models are proposed. One is derived from  $\beta$ - $VOPO_4$  [161] and the other from  $\beta$ - $V_2OPO_4$  [148] (Figure 13.5 a and b). Both structure models lead to square-planar  $VO_4$  units which are sharing corners with  $PO_4$  tetrahedra.

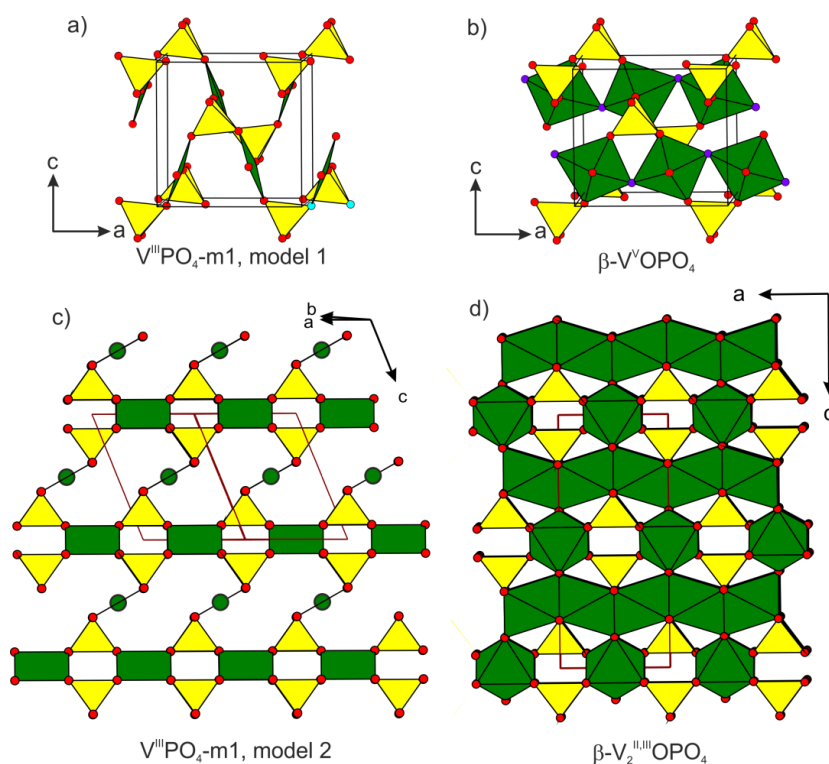


Figure 13.5 Structural derivation of  $V^{III}PO_4$ -m1, model 1 (a) and  $V^{III}PO_4$ -m1, model 2 (c) derived from  $\beta$ - $VOPO_4$  (b) and  $\beta$ - $V_2OPO_4$  (d), respectively.

For none of the two structure models of  $VPO_4$ -m1 via DFT calculation was successful. These calculations suggested a completely different structure built from  $VO_4$  tetrahedra and  $PO_4$  tetrahedra.

For the second metastable polymorph  $VPO_4$ -m2 relaxation of the structure model via DFT confirmed its relationship to  $Fe^{II}Fe^{III}(V^{IV}O)(P_2O_7)(PO_4)$  [133] (Figure 13.6). The DFT results suggest, however, vanadium adopts just the oxidation state III+.

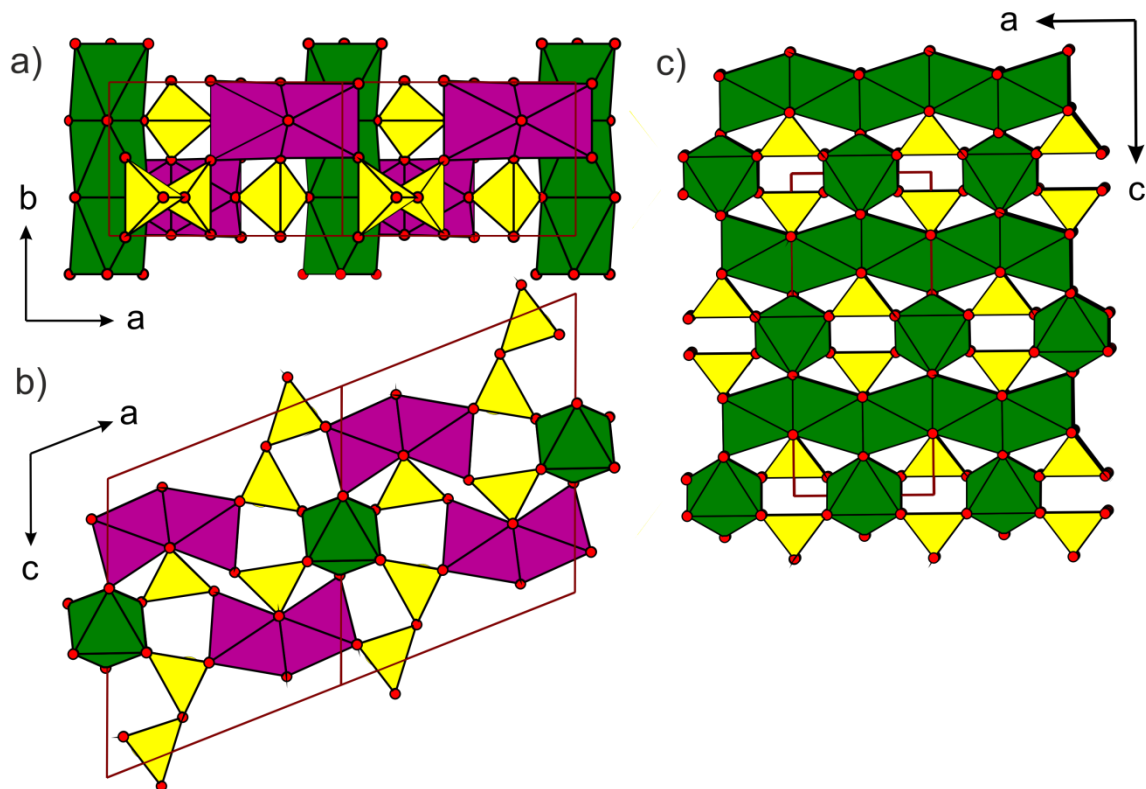


Figure 13.6 Polyhedral representation of the structures of metastable  $VPO_4$ -m2,  $V_2(VO)(P_2O_7)(PO_4)$  (a) and (b), and  $\beta$ - $V_2OPO_4$  [148] (c). Green: string of phase sharing  $VO_6$  octahedra, purple: dimer of phase sharing  $VO_6$  octahedra, and yellow:  $PO_4$  tetrahedra.

**Reduction of  $V_2O_5$  by moist  $H_2$**  led to the formation of two metastable phases  $V^{IV,V}O_9$  [288] (isotypic to  $(VO)_2P_2O_7$  [10]) and  $V^{IV}O_2(B)$  [278] and the thermodynamically stable phase  $V_2O_3$  [296] at 305, 315, and 450 °C, respectively.

## 14 Appendix

### 14.1 The crystal structures of $m$ -W<sub>2</sub>O<sub>3</sub>(PO<sub>4</sub>)<sub>2</sub> and WOPO<sub>4</sub> revisited

Table 14.1 Atomic coordinates and isotropic displacement parameters ( $\text{\AA}^2$ ) for WOPO<sub>4</sub> with estimated standard deviations in parentheses.

Atom	<i>x</i>	<i>y</i>	<i>z</i>	$U_{\text{eq}}$ ( $\text{\AA}^2$ ) <sup>a)</sup>
W1	0.66892(4)	¼	0.56096(2)	0.00566(9)
W2	0.83175(4)	¼	0.06151(2)	0.00573(9)
P1	0.0278(3)	¼	0.34510(16)	0.0075(3)
P2	0.4709(3)	¼	-0.15525(17)	0.0073(3)
O1	-0.3334(10)	¼	-0.050(7)	0.0294(18)
O2	0.8286(10)	¼	0.4128(6)	0.0231(15)
O3	0.9823(10)	¼	0.2130(5)	0.0202(14)
O4	0.5229(10)	¼	0.7124(5)	0.0150(12)
O5	0.6463(12)	0.0056(16)	0.1274(5)	0.0538(23)
O6	0	0	0	0.0252(16)
O7	½	0	½	0.0304(19)
O8	0.1478(11)	0.0171(16)	0.3755(6)	0.0550(23)

<sup>a)</sup>  $U_{\text{eq}} = (1/3) \sum_i \sum_j U_{ij} a_i \cdot a_j \cdot a_i$

Table 14.2 Anisotropic displacement parameters ( $\text{\AA}^2$ ) for WOPO<sub>4</sub> with estimated standard deviations in parentheses.

Atom	$U_{11}$	$U_{22}$	$U_{33}$	$U_{23}$	$U_{13}$	$U_{12}$
W1	0.0074(2)	0.0045(2)	0.0048(2)	0	-0.0008(2)	0
W2	0.0070(2)	0.0049(2)	0.0055(2)	0	-0.0001(2)	0
P1	0.006(1)	0.014(2)	0.003(2)	0	-0.003(1)	0
P2	0.009(2)	0.006(2)	0.007(2)	0	-0.001(1)	0
O1	0.012(5)	0.067(10)	0.008(4)	0	-0.006(4)	0
O2	0.016(5)	0.030(6)	0.019(5)	0	0.005(4)	0
O3	0.017(5)	0.039(8)	0.011(5)	0	-0.006(4)	0
O4	0.019(5)	0.014(5)	0.004(4)	0	0.000(3)	0
O5	0.091(9)	0.060(7)	0.012(4)	-0.005(4)	0.015(5)	-0.063(7)
O6	0.062(7)	0.061(8)	0.040(6)	0.029(5)	0.026(5)	0.061(6)
O7	0.039(8)	0.024(7)	0.013(6)	0.005(5)	-0.004(5)	0.018(6)
O8	0.052(9)	0.029(8)	0.017(5)	-0.021(5)	0.016(6)	-0.028(7)

Table 14.3 Selected interatomic distances (Å) of WOPO<sub>4</sub> with estimated standard deviations in parentheses.

type	distances	type	distances	type	distances	type	distances
W1 – O7	1.8448(2)	W2 – O6	1.8474(2)	P1 – O8	1.491(3)	P2 – O5	1.506(6)
– O7	1.8448(2)	– O6	1.8474(2)	– O8	1.491(3)	– O5	1.506(6)
– O4	1.947(6)	– O3	1.962(6)	– O3	1.507(7)	– O1	1.507(7)
– O2	1.965(7)	– O1	1.962(7)	– O2	1.517(7)	– O4	1.526(6)
– O8	1.976(5)	– O5	1.971(6)				
– O8	1.976(5)	– O5	1.971(6)				

Table 14.4 Assignment of the Guinier photograph of WOPO<sub>4</sub>, S. G.  $P2_1/m$ ;  $a = 6.5541(4)$  Å,  $b = 5.2234(7)$  Å,  $c = 11.1862(8)$  Å,  $\beta = 90.331(6)^\circ$ .

$h$	$k$	$l$	$4\theta_{\text{calc}}$	$4\theta_{\text{obs}}$	$\Delta$	$I_{\text{calc}}$	$I_{\text{obs}}$
1	0	-1	31.235			136	
1	0	1	31.394	31.298	0.11	138	337
0	0	2	31.663	31.718	0.07	598	339
1	0	-2	41.603	41.678	0.12	348	576
1	0	2	41.843	41.849	0.01	345	550
1	1	0	43.476	43.540	0.10	1000	1000
1	1	1	46.376	46.395	0.04	236	510
0	1	2	46.562	46.593	0.05	192	325
1	1	-2	53.919	53.968	0.10	305	560
1	1	2	54.108	54.078	0.06	304	200
1	0	-3	54.857	54.938	0.16	89	157
1	0	3	55.135	55.118	0.03	87	102
2	0	-1	56.620	56.669	0.10	10	24
2	0	1	56.800	56.819	0.04	12	17
2	0	-2	63.071	63.112	0.10	47	108
2	0	2	63.397	63.413	0.04	46	86
0	0	4	63.952	64.003	0.12	10	12
1	1	-3	64.849	64.893	0.10	92	150
1	1	3	65.088	65.103	0.04	94	119
0	2	0	68.612	68.614	0.01	220	165
1	0	-4	69.551	69.594	0.11	104	123
1	0	4	69.851	69.885	0.08	102	93
2	1	-2	72.037	72.085	0.12	61	139
2	1	2	72.327	72.345	0.05	60	143
0	1	4	72.822	72.805	0.04	296	323
2	0	3	73.158	73.185	0.07	77	129
0	2	2	75.982	75.935	0.12	75	185
3	0	-1	84.117	84.105	0.04	53	101
3	0	1	84.309	84.315	0.02	53	109
2	2	-2	94.569	94.603	0.11	64	158

2	2	2	94.802	94.813	0.03	62	152
2	2	-3	101.705	101.669	0.12	117	201
2	2	3	102.036	102.049	0.04	118	180
3	1	-3	102.749	102.769	0.07	139	189
3	1	3	103.241	103.239	0.01	141	217
0	1	6	104.079	104.078	0.00	107	126
1	3	0	108.963	108.945	0.06	103	119
4	0	-2	117.124	117.108	0.06	7	7
4	0	2	117.525	117.488	0.14	7	8
1	0	-7	118.804	118.806	0.01	18	17
4	1	-1	119.233	119.226	0.03	44	95
4	1	1	119.431	119.446	0.06	44	75
0	2	6	122.021	122.013	0.03	41	50
2	2	-5	122.586	122.613	0.10	53	55
2	2	5	123.073	123.082	0.03	54	66
3	1	-5	123.462	123.452	0.04	101	90
4	0	3	123.876	123.881	0.02	32	47
3	1	5	124.189	124.211	0.08	96	96
4	1	-3	128.885	128.865	0.08	20	25
4	1	3	129.454	129.455	0.00	18	32
0	0	8	133.707	133.689	0.07	24	24
2	1	-7	134.842	134.828	0.06	31	42
2	1	7	135.490	135.467	0.10	33	48

$\Delta = |\sin^2\theta_{\text{cat}} - \sin^2\theta_{\text{obs}}| \cdot 1000$ ; intensity normalized on 1000 for the strongest reflection



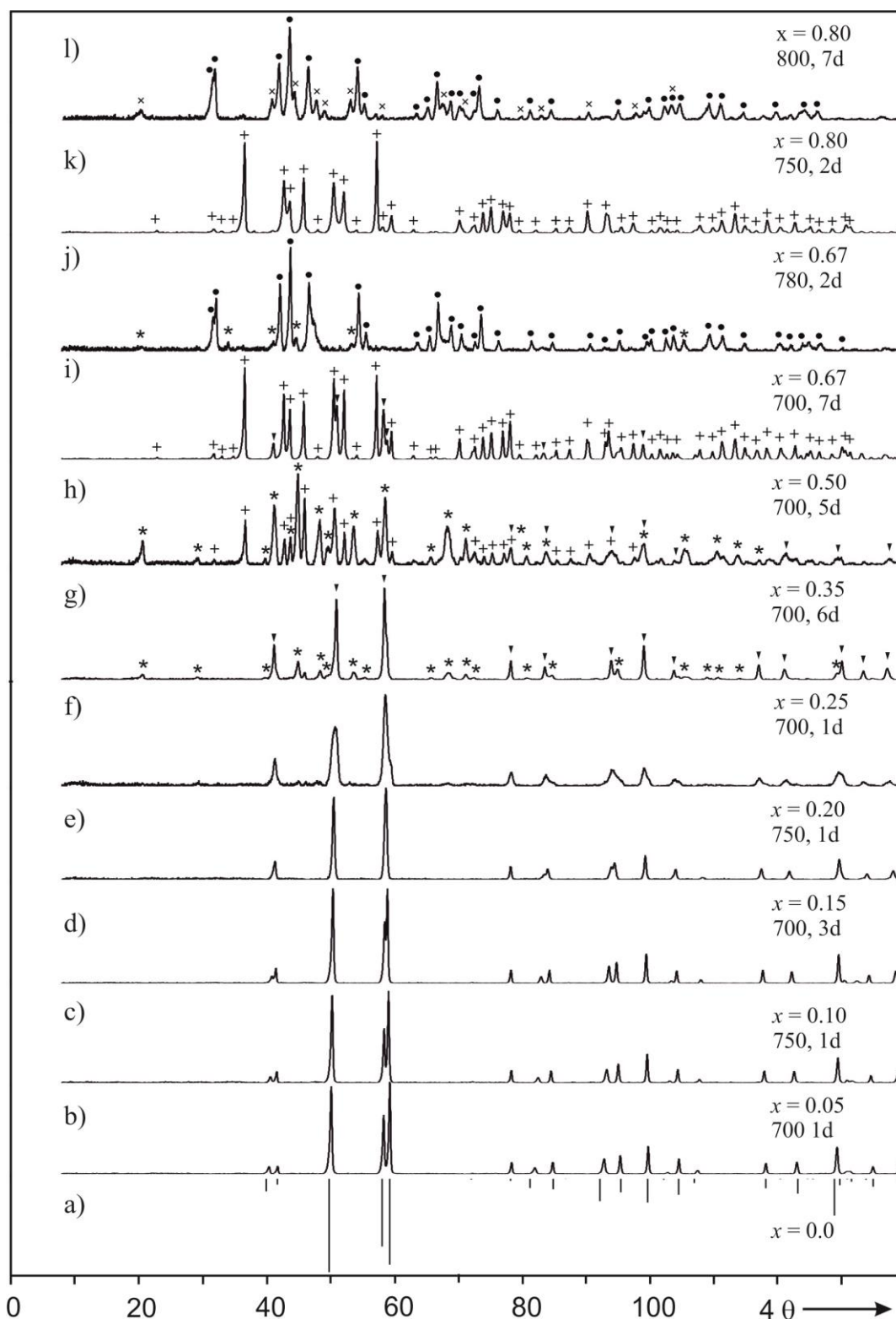
14.2 Solid solutions  $(V_{1-x}W_x)OPO_4$  ( $0 < x < 1.0$ )

Figure 14.1 Comparison of Guinier photographs of solid solutions  $(V_{1-x}W_x)OPO_4$ ;  $0 \leq x \leq 1.0$  obtained by SCS followed by heating in air with exceptions, where heating is done at argon (j), and at  $H_2$  flow followed by sealed tube experiment at  $800^\circ C$  (l), simulation of  $\alpha_{II}\text{-VOPO}_4$  [160] (a), the symbols (\*) represent  $(W_{0.83}V_{0.17}O_3)_8(PO_2)_4$  [this thesis], (†)  $\alpha_{II}\text{-(V}_{1-x}\text{W}_x)\text{OPO}_4$ , (×)  $(WO_3)_8(PO_2)_4$  [95], (+)  $m\text{-(W}_2\text{O}_3)(PO_4)_2$  [78].

Table 14.5 Lattice parameters of members of the solid solution  $(V_{1-x}W_x)OPO_4$ ;  $0.0 \leq x \leq 0.26$ . ( $\alpha_{II}$ -VOPO<sub>4</sub> structure type, S.G.  $P4/n$ ,  $Z = 4$ ).

composition, $x$	$a$ (Å)	$c$ (Å)	$V$ (Å <sup>3</sup> )
0.0 <sup>a)</sup>	6.014(7)	4.434(2)	160.37
0.05	6.0298(2)	4.3960(3)	159.83(1)
0.10 <sup>b)</sup>	6.0452(2)	4.3746(1)	159.67(1)
0.10	6.0505(2)	4.3621(6)	159.69(2)
0.125	6.0599(5)	4.3456(8)	159.57(3)
0.166	6.0729(3)	4.3295(6)	159.67(2)
0.20	6.0875(6)	4.3141(13)	159.87(5)
0.25	6.0892(4)	4.3116(9)	159.87(4)
0.26 <sup>b)</sup>	6.0978(2)	4.2994(1)	159.87(4)

<sup>a)</sup> lattice parameters according to reference [160], <sup>b)</sup> lattice parameters from single crystal [this thesis]

Table 14.6 Lattice parameters of members of WOPO<sub>4</sub> structure type solid solution  $(V^{III}_{1-x}W^{V}_{3x-2}W^{VI}_{2(1-x)})OPO_4$  ( $0.67 \leq x \leq 1.0$ ) S.G.  $P2_1/m$ ,  $Z = 4$ ). i.r. of  $W^{6+}$ ,  $W^{5+}$ , and  $V^{3+}$  are 60, 62, 64 pm, respectively [266].

composition, $x$	Average i.r. of metal ions, (pm)	$a$ (Å)	$b$ (Å)	$c$ (Å)	$\beta$ (°)	$V$ (Å <sup>3</sup> )
1.0	62.0	6.5538(4)	5.2237(8)	11.1866(8)	90.332(7)	382.97(7)
0.90	61.80	6.5450(11)	5.2189(9)	11.1739(14)	90.21(1)	381.7(1)
0.80 <sup>a)</sup>	61.60	6.531(1)	5.2056(7)	11.124(2)	90.12(1)	378.2(1)
0.75	61.50	6.521(1)	5.2164(7)	11.1143(8)	90.13(1)	378.1(1)
0.67 <sup>b)</sup>	61.32	6.513(2)	5.202(1)	11.054(2)	90.12(1)	374.5(2)

<sup>a)</sup> from three steps reactions, <sup>b)</sup> SCS followed by heating in argon atmosphere  $p(O_2) \approx 20$ ppm, others from vapor phase moderated solid state reactions

Table 14.7 Atomic coordinates and isotropic displacement parameters (Å<sup>2</sup>) for  $(V_{0.90}W_{0.10})OPO_4$  ( $\alpha_{II}$ -VOPO<sub>4</sub> structure type).

Atom	$x$	$y$	$z$	s. o. f.	$U_{eq}$ (Å <sup>2</sup> ) <sup>a)</sup>
V	1/4	1/4	0.2196(1)	0.897(2)	0.0098(1)
W	1/4	1/4	0.2196(1)	0.103(2)	0.0098(1)
P	1/4	-1/4	1/2	1	0.0086(2)
O1	0.3011(2)	-0.0506(2)	0.2960(3)	1	0.0111(3)
O2	1/4	1/4	-0.1497(6)	1	0.0153(4)

<sup>a)</sup>  $U_{eq} = (1/3) \sum_i \sum_j U_{ij} a_i \cdot a_j \cdot a_i \cdot a_j$

Table 14.8 Atomic coordinates and isotropic displacement parameters ( $\text{\AA}^2$ ) for  $(V_{0.74}W_{0.26})OPO_4$  ( $\alpha_{II}$ -VOPO<sub>4</sub> structure type).

Atom	x	y	z	s. o. f.	$U_{eq}$ ( $\text{\AA}^2$ ) <sup>a)</sup>
V	1/4	1/4	0.2232(1)	0.737(6)	0.0123(2)
W	1/4	1/4	0.2232(1)	0.263(6)	0.0123(2)
P	1/4	-1/4	1/2	1	0.0105(4)
O1	0.2979(4)	-0.0508(4)	0.2931(7)	1	0.0119(6)
O2	1/4	1/4	-0.1658(14)	1	0.0168(9)

$$^a) U_{eq} = (1/3) \sum_i \sum_j U_{ij} a_i \cdot a_j \cdot a_i \cdot a_j$$

Table 14.9 Anisotropic displacement parameters ( $\text{\AA}^2$ ) for  $(V_{0.90}W_{0.10})OPO_4$  ( $\alpha_{II}$ -VOPO<sub>4</sub> structure type).

Atom	U11	U22	U33	U23	U13	U12
V	0.0064(2)	0.0064(2)	0.0171(2)	0	0	0
W	0.0064(2)	0.0064(2)	0.0171(2)	0	0	0
P	0.0057(3)	0.0057(3)	0.0147(4)	0	0	0
O1	0.0101(6)	0.0063(5)	0.0170(6)	0.0022(4)	0.0011(4)	0.0006(4)
O2	0.0132(6)	0.0132(6)	0.0201(11)	0	0	0

Table 14.10 Anisotropic displacement parameters ( $\text{\AA}^2$ ) for  $(V_{0.74}W_{0.26})OPO_4$  ( $\alpha_{II}$ -VOPO<sub>4</sub> structure type).

Atom	U11	U22	U33	U23	U13	U12
V	0.0075(2)	0.0075(2)	0.0222(4)	0	0	0
W	0.0075(2)	0.0075(2)	0.0222(4)	0	0	0
P	0.0077(5)	0.0077(5)	0.0171(8)	0	0	0
O1	0.0114(14)	0.0071(11)	0.0176(12)	0.0023(9)	0.0007(8)	0.0006(8)
O2	0.0132(13)	0.0132(13)	0.0271(27)	0	0	0

Table 14.11 Interatomic distances ( $\text{\AA}$ ) for  $(V_{0.90}W_{0.10})OPO_4$  and  $(V_{0.74}W_{0.26})OPO_4$  ( $\alpha_{II}$ -VOPO<sub>4</sub> structure type).

	V(W)–O2	V(W)–O1 (4x)	V(W)–O2'	P–O1 (4x)
$(V_{0.90}W_{0.10})OPO_4$	1.615(3)	1.873(1)	2.762(1)	1.530(1)
$(V_{0.74}W_{0.26})OPO_4$	1.673(6)	1.882(3)	2.626(6)	1.533(3)

Table 14.12 Assignment of the Guinier photograph of  $\beta$ -VOPO<sub>4</sub>, S.G. *Pnma*;  $a = 7.7863(5)$  Å,  $b = 6.1329(4)$  Å,  $c = 6.9674(5)$  Å).

<i>h</i>	<i>k</i>	<i>l</i>	$4\theta_{\text{calc}}$	$4\theta_{\text{obs}}$	$\Delta$	$I_{\text{calc}}$	$I_{\text{obs}}$
1	0	1	34.125	34.105	0.03	312	250
0	1	1	38.528	38.471	0.08	302	292
1	1	1	44.833	44.788	0.07	83	90
2	0	0	45.644	45.629	0.03	90	98
0	0	2	51.095	51.095	0.00	201	184
2	0	1	52.397	52.416	0.04	1000	1000
1	0	2	56.072	56.019	0.11	211	218
0	2	0	58.191	58.170	0.04	590	655
2	1	1	60.070	60.042	0.06	237	243
1	1	2	63.335	63.344	0.02	142	156
1	2	1	67.845	67.836	0.02	97	120
2	0	2	69.038	69.056	0.05	45	57
2	2	0	74.591	74.588	0.01	53	74
1	2	2	81.693	81.718	0.07	144	180
0	1	3	83.085	83.078	0.02	107	122
1	1	3	86.413	86.388	0.07	41	49
3	0	2	86.882	86.888	0.02	34	41
2	0	3	90.869	90.857	0.04	84	93
2	2	2	91.507	91.537	0.10	46	55
3	1	2	92.020	92.007	0.04	24	32
0	3	1	92.481	92.487	0.02	127	190
4	0	0	93.237	93.236	0.00	79	83
4	0	1	97.033	97.035	0.01	35	40
4	1	0	98.115	98.114	0.00	47	52
2	3	1	104.337	104.321	0.06	46	65
0	0	4	104.979	105.000	0.07	35	35
3	0	3	105.706	105.710	0.01	23	30
3	2	2	106.276	106.289	0.05	40	46
1	3	2	106.442	106.429	0.05	30	42
4	0	2	107.817	107.788	0.10	80	111
3	1	3	110.176	110.196	0.07	47	50
4	1	2	112.230	112.224	0.02	81	85
4	2	1	115.147	115.151	0.02	51	55
2	1	4	120.123	120.096	0.10	197	177
0	4	0	120.628	120.646	0.06	123	262
3	2	3	122.933	122.963	0.11	32	45
2	4	1	133.778	133.758	0.08	81	104
4	3	1	135.521	135.515	0.02	14	34
4	2	3	140.165	140.167	0.01	49	53
4	3	2	144.465	144.479	0.06	41	45

$\Delta = |\sin^2\theta_{\text{calc}} - \sin^2\theta_{\text{obs}}| \cdot 1000$ ; intensity normalized at 1000 for the strongest reflection

Table 14.13 Assignment of the Guinier photograph of  $(V_{0.99}W_{0.01})OPO_4$  ( $\beta$ -VOPO<sub>4</sub> structure type, S.G. *Pnma*;  $a = 7.7794(5)$  Å,  $b = 6.1360(3)$ ,  $c = 6.9733(4)$  Å).

<i>h</i>	<i>k</i>	<i>l</i>	$4\theta_{\text{calc}}$	$4\theta_{\text{obs}}$	$\Delta$	$I_{\text{calc}}$	$I_{\text{obs}}$
1	0	1	34.122	34.059	0.08	307	291
0	1	1	38.502	38.471	0.05	317	355
1	1	1	44.821	44.823	0.00	80	102
2	0	0	45.685	45.663	0.04	92	105
0	0	2	51.051	51.046	0.01	205	183
2	0	1	52.422	52.406	0.03	1000	1000
1	0	2	56.039	55.998	0.08	209	229
0	2	0	58.160	58.159	0.00	591	635
2	1	1	60.084	60.069	0.03	240	261
1	1	2	63.299	63.281	0.04	138	161
1	2	1	67.816	67.793	0.06	96	162
2	0	2	69.032	69.004	0.07	47	55
2	2	0	74.592	74.596	0.01	54	84
2	1	2	75.169	75.147	0.06	21	24
2	2	1	79.092	79.129	0.10	55	75
1	2	2	81.647	81.630	0.05	143	199
0	1	3	83.015	83.021	0.02	109	133
1	1	3	86.351	86.362	0.03	42	58
3	0	2	86.906	86.923	0.05	33	38
2	0	3	90.831	90.855	0.07	85	111
2	2	2	91.481	91.495	0.04	48	58
0	3	1	92.428	92.425	0.01	129	246
4	0	0	93.324	93.316	0.03	78	78
4	0	1	97.111	97.088	0.07	36	43
4	1	0	98.194	98.189	0.02	48	56
2	3	0	100.723	100.730	0.02	25	47
2	3	1	104.308	104.322	0.05	47	70
0	0	4	104.883	104.872	0.04	36	32
3	0	3	105.697	105.703	0.02	23	30
3	2	2	106.278	106.303	0.09	39	77
4	0	2	107.872	107.844	0.10	79	94
3	1	3	110.163	110.166	0.01	47	52
4	1	2	112.278	112.287	0.03	83	84
2	3	2	114.587	114.578	0.03	75	121
2	1	4	120.049	120.042	0.03	198	194
0	4	0	120.560	120.552	0.03	123	248
1	4	1	126.288	126.266	0.09	15	31
4	1	3	128.408	128.427	0.07	18	34
2	4	1	133.726	133.740	0.06	83	121
4	3	1	135.548	135.552	0.02	14	70

$\Delta = |\sin^2\theta_{\text{calc}} - \sin^2\theta_{\text{obs}}| \cdot 1000$ ; intensity normalized at 1000 for the strongest reflection

Table 14.14 Assignment of the Guinier photograph of  $(V_{0.95}W_{0.05})OPO_4$  ( $\alpha_{II}$ -VOPO<sub>4</sub> structure type, S.G.  $P4/n$ ;  $a = 6.0297(2)$  Å,  $c = 4.3960(3)$  Å).

$h$	$k$	$l$	$4\theta_{\text{calc}}$	$4\theta_{\text{obs}}$	$\Delta$	$I_{\text{calc}}$	$I_{\text{obs}}$
0	0	1	40.366	40.328	0.06	122	65
1	1	0	41.631	41.639	0.01	75	91
1	0	1	50.094	50.105	0.02	1000	969
1	1	1	58.305	58.279	0.06	526	674
2	0	0	59.209	59.190	0.04	987	1000
2	1	1	78.314	78.316	0.00	31	160
0	0	2	82.056	82.046	0.03	120	62
2	2	0	84.722	84.706	0.05	91	160
1	1	2	92.880	92.876	0.01	263	139
3	1	0	95.302	95.286	0.05	116	282
3	0	1	99.687	99.665	0.07	323	414
3	1	1	104.497	104.474	0.08	53	204
2	1	2	107.514	107.523	0.03	9	35
3	2	1	118.094	118.099	0.02	44	162
4	0	0	122.913	122.927	0.05	189	181
3	1	2	129.315	129.313	0.01	260	294
4	1	1	134.863	134.859	0.02	53	124
4	2	0	139.357	139.375	0.07	45	122

$\Delta = |\sin^2\theta_{\text{cal}} - \sin^2\theta_{\text{obs}}| \cdot 1000$ ; intensity normalized at 1000 for the strongest reflection

Table 14.15 Assignment of the Guinier photograph of  $(V_{0.90}W_{0.10})OPO_4$  ( $\alpha_{II}$ -VOPO<sub>4</sub> structure type, S.G.  $P4/n$ ;  $a = 6.0503(3)$  Å,  $c = 4.3618(4)$  Å).

$h$	$k$	$l$	$4\theta_{\text{calc}}$	$4\theta_{\text{obs}}$	$\Delta$	$I_{\text{calc}}$	$I_{\text{obs}}$
0	0	1	40.682	40.636	0.07	90	64
1	1	0	41.487	41.478	0.01	120	135
1	0	1	50.292	50.252	0.07	1000	1000
1	1	1	58.425	58.434	0.02	520	632
2	0	0	59.002	58.964	0.08	870	951
2	1	1	78.286	78.311	0.07	10	156
2	2	0	84.418	84.414	0.01	120	142
1	1	2	93.413	93.425	0.04	240	142
3	1	0	94.956	94.945	0.04	200	222
3	0	1	99.53	99.525	0.02	260	367
3	1	1	104.312	104.303	0.03	90	161
3	2	1	117.835	117.845	0.04	70	147
4	0	0	122.447	122.451	0.02	150	142
3	1	2	129.518	129.513	0.02	120	284
4	1	1	134.511	134.506	0.02	20	92
4	2	0	138.812	138.82	0.03	140	154

$\Delta = |\sin^2\theta_{\text{cal}} - \sin^2\theta_{\text{obs}}| \cdot 1000$ ; intensity normalized at 1000 for the strongest reflection

Table 14.16 Assignment of the Guinier photograph of  $(V_{0.875}W_{0.125})OPO_4$  ( $\alpha_{II}$ -VOPO<sub>4</sub> structure type, S.G.  $P4/n$ ;  $a = 6.0599(5)$  Å,  $c = 4.3456(8)$  Å).

$h$	$k$	$l$	$4\theta_{\text{calc}}$	$4\theta_{\text{obs}}$	$\Delta$	$I_{\text{calc}}$	$I_{\text{obs}}$
0	0	1	40.839	40.740	0.15	87	70
1	1	0	41.422	41.391	0.05	122	158
1	0	1	50.393	50.303	0.17	1000	1000
1	1	1	58.490	58.472	0.04	435	703
2	0	0	58.908	58.893	0.03	922	912
2	1	1	78.281	78.296	0.04	50	175
0	0	2	83.052	83.037	0.04	111	42
2	2	0	84.282	84.348	0.19	99	114
3	1	0	94.800	94.848	0.15	119	194
3	0	1	99.466	99.467	0.00	312	367
3	1	1	104.236	104.206	0.10	46	141
3	2	1	117.724	117.748	0.09	52	140
4	0	0	122.237	122.224	0.05	176	100
3	1	2	129.632	129.626	0.02	239	294
3	3	0	130.536	130.525	0.04	56	25
4	1	1	134.359	134.401	0.17	59	77
4	2	0	138.567	138.545	0.09	46	116

$\Delta = |\sin^2\theta_{\text{calc}} - \sin^2\theta_{\text{obs}}| \cdot 1000$ ; intensity normalized at 1000 for the strongest reflection

Table 14.17 Assignment of the Guinier photograph of  $(V_{0.834}W_{0.166})OPO_4$  ( $\alpha_{II}$ -VOPO<sub>4</sub> structure type, S.G.  $P4/n$ ;  $a = 6.0729(3)$  Å,  $c = 4.3295(6)$  Å).

$h$	$k$	$l$	$4\theta_{\text{calc}}$	$4\theta_{\text{obs}}$	$\Delta$	$I_{\text{calc}}$	$I_{\text{obs}}$
0	0	1	40.992	40.958	0.05	72	77
1	1	0	41.333	41.338	0.01	147	170
1	0	1	50.482	50.495	0.02	1000	1000
1	1	1	58.535	58.579	0.10	397	735
2	0	0	58.779	58.750	0.06	890	897
2	1	1	78.240	78.273	0.09	60	151
0	0	2	83.374	83.353	0.06	107	55
2	2	0	84.093	84.113	0.06	103	139
1	1	2	93.931	93.930	0.00	250	145
3	1	0	94.585	94.570	0.05	119	208
3	0	1	99.349	99.347	0.01	307	329
3	1	1	104.103	104.124	0.07	43	133
3	2	1	117.546	117.543	0.01	56	140
4	0	0	121.948	121.979	0.12	169	120
3	1	2	129.693	129.710	0.06	230	280
3	3	0	130.222	130.219	0.01	57	41
4	1	1	134.125	134.114	0.04	61	92
4	2	0	138.228	138.208	0.08	47	137

$\Delta = |\sin^2\theta_{\text{calc}} - \sin^2\theta_{\text{obs}}| \cdot 1000$ ; intensity normalized at 1000 for the strongest reflection

Table 14.18 Assignment of the Guinier photograph of  $(V_{0.80}W_{0.20})OPO_4$  ( $\alpha_{II}$ -VOPO<sub>4</sub> structure type, S.G.  $P4/n$ ;  $a = 6.0875(6)$  Å,  $c = 4.3141(13)$  Å).

$h$	$k$	$l$	$4\theta_{\text{calc}}$	$4\theta_{\text{obs}}$	$\Delta$	$I_{\text{calc}}$	$I_{\text{obs}}$
0	0	1	41.140	41.082	0.09	63	41
1	1	0	41.232	41.212	0.03	168	192
1	0	1	50.562	50.537	0.05	1000	793
2	0	0	58.635	58.596	0.08	869	1000
2	1	1	78.182	78.209	0.08	68	124
2	2	0	83.881	83.880	0.00	106	128
3	1	0	94.344	94.299	0.14	120	226
3	0	1	99.208	99.197	0.04	303	198
3	1	1	103.944	103.933	0.04	40	92
3	2	1	117.338	117.300	0.14	59	96
3	1	2	129.727	129.731	0.02	223	206
4	0	0	137.849	137.885	0.15	164	80

$\Delta = |\sin^2\theta_{\text{calc}} - \sin^2\theta_{\text{obs}}| \cdot 1000$ ; intensity normalized at 1000 for the strongest reflection

Table 14.19 Assignment of the Guinier photograph of  $(V_{0.75}W_{0.25})OPO_4$  ( $\alpha_{II}$ -VOPO<sub>4</sub> structure type, S.G.  $P4/n$ ;  $a = 6.0928(8)$  Å,  $c = 4.3055(6)$  Å).

$h$	$k$	$l$	$4\theta_{\text{calc}}$	$4\theta_{\text{obs}}$	$\Delta$	$I_{\text{calc}}$	$I_{\text{obs}}$
0	0	1	41.164	41.129	0.05	50	180
1	0	1	50.577	50.575	0.0	1000	900
2	0	0	58.618	58.579	0.08	830	1000
2	1	1	78.179	78.186	0.02	80	172
2	2	0	83.856	83.816	0.12	110	103
3	1	0	94.316	94.316	0.0	120	221
3	0	1	99.195	99.185	0.03	290	438
3	1	1	103.929	103.924	0.02	40	119
2	1	2	108.441	108.413	0.1	10	70
3	2	1	117.316	117.299	0.06	60	180
4	0	0	121.586	121.617	0.12	160	112
3	1	2	129.742	129.772	0.12	210	195
4	1	1	133.825	133.799	0.1	70	108
4	2	0	137.804	137.816	0.05	50	138

$\Delta = |\sin^2\theta_{\text{calc}} - \sin^2\theta_{\text{obs}}| \cdot 1000$ ; intensity normalized at 1000 for the strongest reflection



Table 14.20 Assignment of the Guinier photograph of  $(V_{0.10}W_{0.90})OPO_4$  (WOPO<sub>4</sub> structure type, S.G.  $P2_1/m$ ;  $a = 6.5450(11)$  Å,  $b = 5.2189(9)$  Å,  $c = 11.1739(14)$  Å,  $\beta = 90.21(1)^\circ$ ).

$h$	$k$	$l$	$4\theta_{\text{calc}}$	$4\theta_{\text{obs}}$	$\Delta$	$I_{\text{calc}}$	$I_{\text{obs}}$
1	0	-1	31.306			112	
1	0	1	31.406	31.338	0.08	223	339
0	0	2	31.698	31.718	0.02	748	490
1	0	2	41.850	41.775	0.12	560	564
1	1	0	43.523	43.536	0.02	1000	1000
1	1	1	46.407	46.378	0.05	444	537
1	1	2	54.132	54.061	0.14	332	512
1	0	-3	54.973	54.931	0.08	80	119
1	0	3	55.149	55.101	0.10	166	112
2	0	-1	56.732	56.672	0.13	6	20
2	0	1	56.846	56.802	0.09	8	20
2	0	-2	63.216	63.233	0.04	40	76
2	0	2	63.422	63.383	0.09	82	72
0	0	4	64.024	64.113	0.21	14	12
1	1	-3	64.965	64.933	0.08	117	115
1	1	3	65.116	65.133	0.04	116	120
2	1	1	66.582	66.533	0.12	364	324
0	2	0	68.673	68.693	0.05	278	235
1	0	-4	69.688	69.713	0.06	155	106
1	0	4	69.877	69.883	0.01	152	114
1	2	1	75.925	75.932	0.02	44	110
3	0	-1	84.274	84.230	0.13	63	50
3	0	1	84.395	84.420	0.07	63	65
2	0	-5	98.497	98.483	0.05	92	68
2	0	5	98.853	98.912	0.20	91	70
1	2	-4	99.451	99.492	0.13	127	133
2	2	-3	101.884	101.920	0.12	125	150
2	2	3	102.092	102.080	0.04	126	140
3	1	-3	102.979	103.009	0.10	175	116
3	1	3	103.290	103.309	0.07	178	104
0	1	6	104.198	104.198	0.00	138	79
1	3	0	109.069	109.054	0.05	110	98
0	2	6	122.158	122.170	0.04	50	26

$\Delta = |\sin^2\theta_{\text{calc}} - \sin^2\theta_{\text{obs}}| \cdot 1000$ ; intensity normalized at 1000 for the strongest reflection

Table 14.21 Assignment of the Guinier photograph of  $(V_{0.20}W_{0.80})OPO_4$  (WOPO<sub>4</sub> structure type, S.G.  $P2_1/m$ ;  $a = 6.531(1)$  Å,  $b = 5.206(7)$  Å,  $c = 11.124(2)$  Å,  $\beta = 90.12(2)^\circ$ ).

<i>h</i>	<i>k</i>	<i>l</i>	$4\theta_{\text{calc}}$	$4\theta_{\text{obs}}$	$\Delta$	$I_{\text{calc}}$	$I_{\text{obs}}$
1	0	-1	31.413			101	
1	0	1	31.471	31.462	0.01	218	438
0	0	2	31.842	31.833	0.01	749	552
1	0	2	41.966	41.902	0.10	559	646
1	1	0	43.629	43.596	0.05	1000	1000
1	1	1	46.517	46.483	0.06	498	558
1	1	2	54.280	54.250	0.06	333	528
1	0	3	55.332	55.302	0.06	185	184
2	0	-2	63.437	63.406	0.07	40	64
2	0	2	63.557	63.536	0.05	87	84
1	1	3	65.322	65.308	0.03	118	141
2	1	1	66.725	66.710	0.03	370	384
0	2	0	68.855	68.873	0.04	283	202
1	0	4	70.136	70.145	0.02	151	150
2	0	3	73.356	73.278	0.20	69	342
0	2	2	76.284	76.251	0.09	82	93
1	2	2	81.331	81.335	0.01	66	90
2	2	-1	90.484	90.438	0.14	43	75
2	2	2	95.102	95.048	0.17	110	98
3	1	-3	103.345	103.346	0.01	178	153
3	1	3	103.526	103.556	0.10	182	151
0	1	6	104.678	104.695	0.06	142	150
1	3	0	109.370	109.352	0.06	110	148
3	2	1	111.240	111.301	0.22	177	147
1	3	-2	114.653	114.637	0.06	51	72
1	3	2	114.690	114.737	0.17	48	72
1	2	-6	126.229	126.342	0.03	61	90

$\Delta = |\sin^2\theta_{\text{cal}} - \sin^2\theta_{\text{obs}}| \cdot 1000$ ; intensity normalized at 1000 for the strongest reflection

Table 14.22 Assignment of the Guinier photograph of  $(V_{0.25}W_{0.75})OPO_4$  (WOPO<sub>4</sub> structure type, S G.  $P2_1/m$ ;  $a = 6.521(1)$  Å,  $b = 5.2164(7)$  Å,  $c = 11.1143(8)$  Å,  $\beta = 90.13(1)^\circ$ )

$h$	$k$	$l$	$4\theta_{\text{calc}}$	$4\theta_{\text{obs}}$	$\Delta$	$I_{\text{calc}}$	$I_{\text{obs}}$
1	0	-1	31.454			113	
1	0	1	31.517	31.519	0.00	115	454
0	0	2	31.869	31.820	0.06	576	558
1	0	2	42.018	41.997	0.03	361	776
1	1	0	43.599	43.609	0.02	1000	1000
1	1	1	46.495	46.493	0.00	295	544
1	1	2	54.275	54.243	0.06	304	673
1	0	3	55.394	55.354	0.08	106	144
2	0	-1	56.975	56.916	0.12	7	25
2	0	1	57.046	57.036	0.02	9	34
2	0	2	63.651	63.652	0.00	48	109
1	1	3	65.336	65.304	0.08	92	180
2	1	1	66.765	66.795	0.07	229	435
0	2	0	68.707	68.697	0.03	220	209
1	0	4	70.209	70.178	0.08	92	216
1	2	1	76.004	76.041	0.10	22	104
0	2	2	76.160	76.151	0.02	60	115
2	2	2	95.056	95.076	0.07	70	130
0	0	6	98.284	98.256	0.09	17	33
0	1	6	104.737	104.735	0.01	111	81
2	1	-5	105.489	105.495	0.02	4	10
2	1	5	105.703	105.705	0.01	5	15
1	1	-6	108.659	108.714	0.19	55	124
1	3	0	109.150	109.134	0.06	56	105
0	0	8	134.684	134.684	0.00	20	30
1	2	-7	141.766	141.736	0.12	28	22
1	2	7	141.892	141.916	0.10	31	28

$\Delta = |\sin^2\theta_{\text{calc}} - \sin^2\theta_{\text{obs}}| \cdot 1000$ ; intensity normalized at 1000 for the strongest reflection

Table 14.23 Assignment of the Guinier photograph of  $(V_{0.33}W_{0.67})OPO_4$  (WOPO<sub>4</sub> structure type, S.G.  $P2_1/m$ ;  $a = 6.513(2)$  Å,  $b = 5.202(1)$  Å,  $c = 11.056(2)$  Å,  $\beta = 90.12(2)^\circ$ )

<i>h</i>	<i>k</i>	<i>l</i>	$4\theta_{\text{calc}}$	$4\theta_{\text{obs}}$	$\Delta$	$I_{\text{calc}}$	$I_{\text{obs}}$
1	0	-1	31.531			85	
1	0	1	31.588	31.495	0.11	210	360
0	0	2	32.045	31.996	0.06	747	547
1	0	2	42.171	42.095	0.12	630	672
1	1	0	43.694	43.707	0.02	1000	1000
1	1	1	46.613	46.632	0.03	587	651
1	1	-2	54.386	54.382	0.01	334	562
1	0	3	55.640	55.574	0.13	216	179
2	0	-2	63.680	63.582	0.22	40	91
2	0	2	63.798	63.752	0.10	94	93
1	1	-3	65.512	65.574	0.15	120	170
2	1	-1	66.835	66.885	0.12	377	447
0	2	0	68.899	68.876	0.06	291	258
1	0	-4	70.446	70.527	0.20	151	150
1	0	4	70.554	70.627	0.19	149	164
2	0	3	73.684	73.669	0.04	63	372
0	2	2	76.414	76.330	0.23	73	96
1	2	-2	81.434	81.412	0.06	65	93
2	2	2	95.308	95.302	0.02	123	104
0	1	6	105.320	105.328	0.03	148	185
3	2	-1	111.426	111.423	0.01	182	148
3	2	1	111.482	111.543	0.22	186	149
2	0	-6	114.728	114.740	0.04	30	80
2	0	6	114.949	114.930	0.07	30	81
2	3	1	122.151	122.162	0.04	72	76
3	1	-5	124.889	124.858	0.12	134	96

$\Delta = |\sin^2\theta_{\text{calc}} - \sin^2\theta_{\text{obs}}| \cdot 1000$ ; intensity normalized at 1000 for the strongest reflection

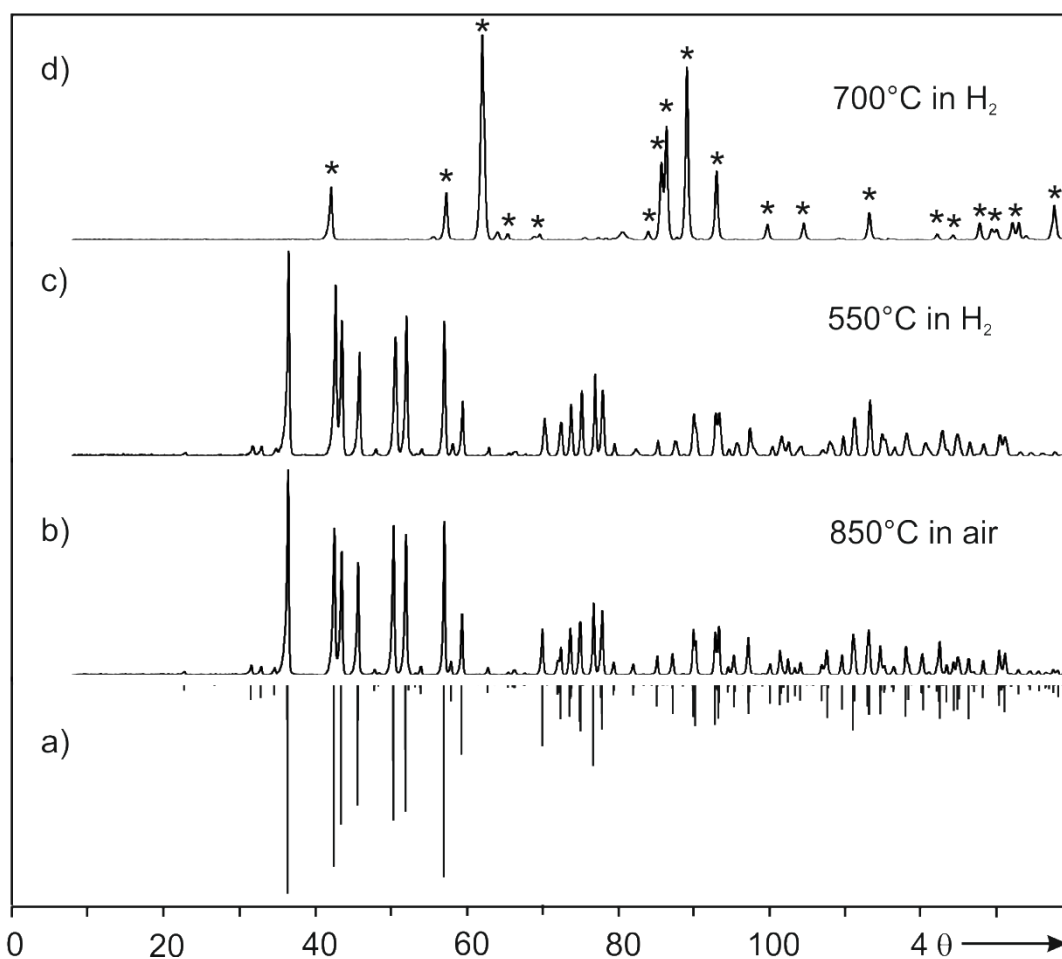


Figure 14.2 Reduction of  $m\text{-(W}_2\text{O}_3\text{)(PO}_4\text{)}_2$  (b) by moist  $\text{H}_2$  at different temperatures. At 550°C partially reduced violet  $m\text{-(W}_2\text{O}_{3-\delta}\text{)(PO}_4\text{)}_2$  (c), at 700°C black powder of WP [105] (d), and simulated pattern of  $m\text{-(W}_2\text{O}_3\text{)(PO}_4\text{)}_2$  (a) based on single crystal structure data [78].

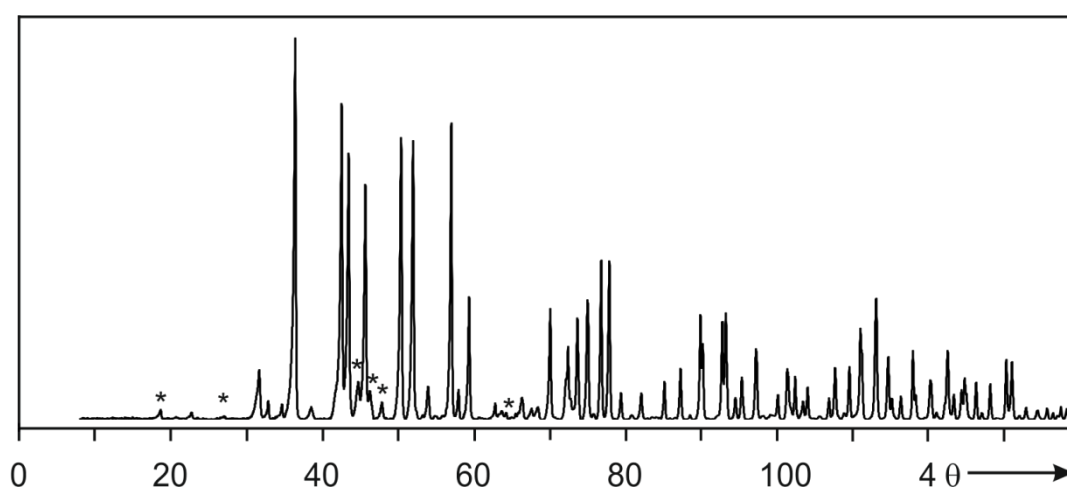


Figure 14.3 Guinier photograph of two phase mixture  $m\text{-(W}_2\text{O}_3\text{)(PO}_4\text{)}_2$  and  $\text{P}_8\text{W}^{\text{V,VI}}\text{O}_{52}$  (indicated by \*), obtained after partial reduction of  $m\text{-(W}_2\text{O}_3\text{)(PO}_4\text{)}_2$  [78] by moist  $\text{H}_2$  at 550 °C followed by heating in sealed silica ampoule at 800 °C.

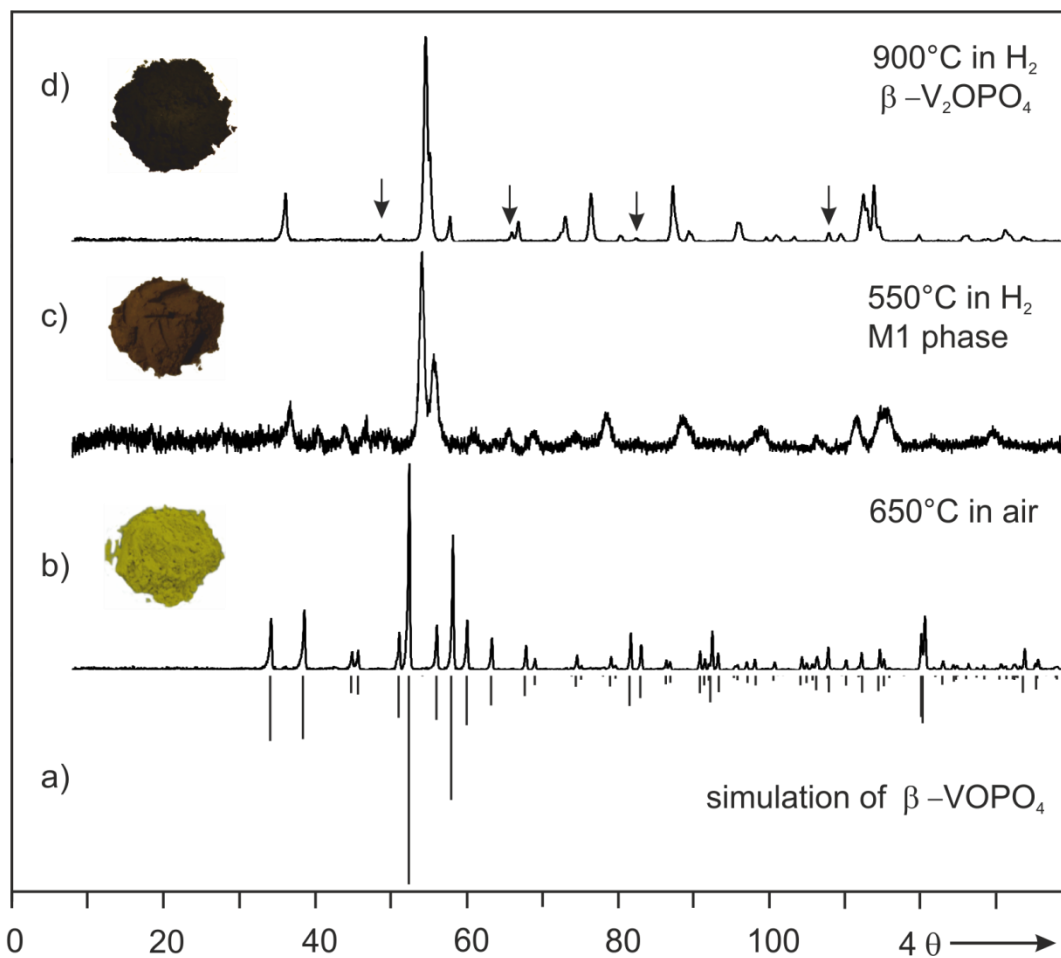


Figure 14.4 Reduction of  $\beta\text{-VOPO}_4$  (b) by moist  $\text{H}_2$  at different temperatures. At 550 and  $900^\circ\text{C}$  lead to metastable  $\text{VPO}_4\text{-m1}$  (c), and  $\beta\text{-V}_2\text{OPO}_4$  (d) [148], respectively. Simulation of  $\beta\text{-VOPO}_4$  (a) based on single crystal structure data [161]. Down arrows indicate small amount of unknown impurities.

### 14.3 Solid solutions ( $V_{1-x}Mo_x$ )OPO<sub>4</sub> ( $0 \leq x \leq 1.0$ )

Table 14.24 Lattice parameters of members of the solid solution ( $V_{1-x}Mo_x$ )OPO<sub>4</sub>;  $0.0 \leq x \leq 0.30$  ( $\beta$ -VOPO<sub>4</sub> structure type [161], space group: *Pnma*).

composition, <i>x</i>	<i>a</i> (Å)	<i>b</i> (Å)	<i>c</i> (Å)	Vol. (Å <sup>3</sup> )
0.0	7.7863(4)	6.1329(3)	6.9673(5)	332.71(3)
0.02	7.7818(7)	6.1375(4)	6.9673(7)	333.05(5)
0.05	7.7781(4)	6.1426(2)	6.9793(4)	333.46(3)
0.10	7.7698(6)	6.1495(6)	6.9905(5)	334.01(3)
0.20	7.7761(7)	6.1460(5)	6.9945(8)	334.28(65)
0.30	7.7762(7)	6.1596(7)	7.0016(8)	335.37(6)

Table 14.25 Atomic coordinates and isotropic displacement parameters (Å<sup>2</sup>) for ( $V_{0.90}Mo_{0.10}$ )OPO<sub>4</sub> ( $\beta$ -VOPO<sub>4</sub> structure type).

Atom	<i>x</i>	<i>y</i>	<i>z</i>	s. o. f.	$U_{eq}$ (Å <sup>2</sup> ) <sup>a)</sup>
V/Mo	0.1723(1)	1/4	0.2317(1)	0.45/0.05	0.0126(2)
P	0.8818(2)	1/4	0.8781(2)	1	0.0089(3)
O1	0.8765(3)	0.0499(4)	0.7494(3)	1	0.0130(5)
O2	0.7198(4)	1/4	0.0089(5)	1	0.0121(7)
O3	0.0466(4)	1/4	-0.0037(5)	1	0.0125(7)
O4	0.3620(5)	1/4	0.14697	1	0.0157(8)

<sup>a)</sup>  $U_{eq} = (1/3) \sum_i \sum_j U_{ij} a_i \cdot a_j \cdot a_i \cdot a_j$

Table 14.26 Anisotropic displacement parameters (Å<sup>2</sup>) for ( $V_{0.90}Mo_{0.10}$ )OPO<sub>4</sub> ( $\beta$ -VOPO<sub>4</sub> structure type).

Atom	$U_{11}$	$U_{22}$	$U_{33}$	$U_{23}$	$U_{13}$	$U_{12}$
V	0.0153(4)	0.0103(4)	0.0123(4)	0	-0.0025(3)	0
P	0.0114(6)	0.0078(6)	0.0076(5)	0	-0.0003(4)	0
O1	0.012(2)	0.013(2)	0.012(2)	0	0.001(1)	0
O2	0.011(2)	0.016(2)	0.011(2)	0	-0.006(1)	0
O3	0.016(1)	0.018(1)	0.013(3)	0	0.002(1)	0
O4	0.018(1)	0.009(1)	0.012(1)	0.0002(9)	0.0006(9)	-0.0003(9)

Table 14.27 Interatomic distances (Å) for ( $V_{0.90}Mo_{0.10}$ )OPO<sub>4</sub> ( $\beta$ -VOPO<sub>4</sub> structure type).

type	distance	type	distance
V(Mo) – O4	1.589(4)	P – O3	1.525(3)
– O2	1.851(4)	– O1	1.525(3)
– O1	1.889(3)	– O1	1.525(3)
– O1	1.889(3)	– O2	1.556(4)
– O3	1.913(3)		
– O4'	2.556(1)		

Table 14.28 Assignment of the Guinier photograph of  $(V_{0.99}Mo_{0.01})OPO_4$  ( $\beta$ -VOPO<sub>4</sub> structure type, S. G. *Pnma*;  $a = 7.7822(5)$  Å,  $b = 6.1352(7)$  Å,  $c = 6.9610(4)$  Å).

<i>h</i>	<i>k</i>	<i>l</i>	$4\theta_{\text{calc}}$	$4\theta_{\text{obs}}$	$\Delta$	$I_{\text{calc}}$	$I_{\text{obs}}$
1	0	1	34.123	34.160	0.05	310	237
0	1	1	38.511	38.559	0.07	308	280
2	0	0	45.669	45.653	0.03	91	95
0	0	2	51.069	51.101	0.06	203	92
2	0	1	52.412	52.418	0.01	1000	1000
1	0	2	56.052	56.041	0.02	210	215
0	2	0	58.169	58.157	0.03	591	650
2	1	1	60.077	60.053	0.05	238	248
1	1	2	63.313	63.307	0.01	140	154
1	2	1	67.824	67.830	0.01	97	110
2	0	2	69.034	69.018	0.04	46	53
2	2	0	74.589	74.599	0.03	53	60
2	1	2	75.173	75.188	0.04	20	24
1	2	2	81.662	81.660	0.01	144	153
0	1	3	83.042	83.048	0.02	108	111
1	1	3	86.375	86.394	0.06	42	42
3	0	2	86.897	86.903	0.02	34	40
2	0	3	90.846	90.829	0.05	84	88
3	1	2	92.030	92.018	0.04	23	44
0	3	1	92.444	92.438	0.02	127	143
4	0	0	93.290	93.287	0.01	79	79
4	0	1	97.080	97.094	0.05	25	35
4	1	0	98.162	98.143	0.06	47	42
2	3	1	104.315	104.298	0.06	46	43
0	0	4	104.921	104.918	0.01	35	32
3	2	2	106.275	106.317	0.15	39	50
4	0	2	107.850	107.836	0.05	79	79
3	1	3	110.168	110.155	0.04	47	42
4	1	2	112.259	112.284	0.09	82	63
2	3	2	114.600	114.603	0.01	74	63
4	2	1	115.176	115.203	0.10	51	39
0	1	5	138.043	138.063	0.08	19	22
4	2	3	140.166	140.134	0.13	49	30
1	1	5	140.438	140.424	0.06	20	32

$\Delta = |\sin^2\theta_{\text{cal}} - \sin^2\theta_{\text{obs}}| \cdot 1000$ ; intensity normalized at 1000 for the strongest reflectio



Table 14.29 Assignment of the Guinier photograph of  $(V_{0.98}Mo_{0.02})OPO_4$  ( $\beta$ -VOPO<sub>4</sub> structure type, *S. G. Pnma*;  $a = 7.7818(7)$  Å,  $b = 6.1375(4)$  Å,  $c = 6.9732(7)$  Å).

<i>h</i>	<i>k</i>	<i>l</i>	$4\theta_{\text{calc}}$	$4\theta_{\text{obs}}$	$\Delta$	$I_{\text{calc}}$	$I_{\text{obs}}$
1	0	1	34.118	34.075	0.06	308	272
0	1	1	38.497	38.444	0.08	314	330
1	1	1	44.813	44.756	0.09	81	98
2	0	0	45.672	45.648	0.04	92	102
0	0	2	51.052	50.997	0.10	205	201
2	0	1	52.410	52.389	0.04	1000	1000
1	0	2	56.037	55.994	0.09	210	220
0	2	0	58.146	58.157	0.02	592	656
2	1	1	60.070	60.070	0.00	240	257
1	1	2	63.294	63.284	0.02	139	174
1	2	1	67.802	67.788	0.03	96	140
2	0	2	69.023	69.019	0.01	46	57
2	2	0	74.572	74.594	0.06	54	78
2	1	2	75.158	75.194	0.10	21	19
3	1	1	79.696	79.727	0.08	14	23
1	2	2	81.635	81.677	0.12	143	169
0	1	3	83.013	83.028	0.04	109	118
1	1	3	86.347	86.369	0.07	41	46
3	0	2	86.889	86.919	0.09	34	45
2	0	3	90.824	90.819	0.02	85	95
0	3	1	92.407	92.429	0.07	128	173
4	0	1	97.082	97.079	0.01	36	51
4	1	0	98.163	98.139	0.08	48	51
2	3	0	100.696	100.718	0.07	26	44
2	3	1	104.282	104.276	0.02	47	55
0	0	4	104.884	104.866	0.06	35	37
3	0	3	105.682	105.676	0.02	23	31
4	0	2	107.846	107.835	0.04	80	83
2	3	2	114.563	114.560	0.01	75	91
0	4	0	120.529	120.524	0.02	123	202
2	4	1	133.690	133.666	0.10	82	95
4	2	3	140.141	140.155	0.06	50	45

$$\Delta = |\sin^2\theta_{\text{calc}} - \sin^2\theta_{\text{obs}}| \cdot 1000; \text{ intensity normalized at 1000 for the strongest reflection}$$

Table 14.30 Assignment of the Guinier photograph of  $(V_{0.95}Mo_{0.05})OPO_4$  ( $\beta$ -VOPO<sub>4</sub> structure type, S.G. *Pnma*;  $a = 7.7781(4)$  Å,  $b = 6.1426(2)$  Å,  $c = 6.9793(4)$  Å).

<i>h</i>	<i>k</i>	<i>l</i>	$4\theta_{\text{calc}}$	$4\theta_{\text{obs}}$	$\Delta$	$I_{\text{calc}}$	$I_{\text{obs}}$
1	0	1	34.109	34.115	0.01	302	270
0	1	1	38.464	38.479	0.02	333	310
1	1	1	44.790	44.784	0.01	77	88
2	0	0	45.693	45.675	0.03	94	93
0	0	2	51.006	50.968	0.07	210	198
2	0	1	52.418	52.409	0.02	1000	1000
1	0	2	56.000	55.971	0.06	208	212
0	2	0	58.097	58.122	0.05	593	648
2	1	1	60.065	60.073	0.02	245	233
1	1	2	63.249	63.255	0.01	134	153
1	2	1	67.754	67.786	0.08	94	111
2	0	2	69.003	69.007	0.01	48	57
2	2	0	74.547	74.558	0.03	55	68
2	1	2	75.130	75.148	0.05	24	25
3	1	1	79.709	79.689	0.06	14	19
1	2	2	81.571	81.589	0.05	142	141
0	1	3	82.937	82.939	0.00	112	110
1	1	3	86.277	86.289	0.04	42	48
3	0	2	86.889	86.879	0.03	33	36
2	0	3	90.774	90.778	0.01	87	89
0	3	1	92.326	92.338	0.04	131	139
4	0	0	93.342	93.358	0.05	78	71
4	0	1	97.121	97.117	0.01	38	37
4	1	0	98.200	98.217	0.06	49	41
2	3	0	100.637	100.636	0.00	27	32
2	3	1	104.218	104.225	0.02	48	51
0	0	4	104.785	104.785	0.00	37	34
4	0	2	107.863	107.843	0.07	79	74
3	1	3	110.109	110.112	0.01	46	43
2	3	2	114.486	114.470	0.06	77	72
0	4	0	120.418	120.396	0.08	123	180
2	4	1	133.590	133.595	0.02	84	68

$\Delta = |\sin^2\theta_{\text{calc}} - \sin^2\theta_{\text{obs}}| \cdot 1000$ ; intensity normalized at 1000 for the strongest reflection

Table 14.31 Assignment of the Guinier photograph of  $(V_{0.90}Mo_{0.10})OPO_4$  ( $\beta$ -VOPO<sub>4</sub> structure type, S.G. *Pnma*;  $a = 7.7698(6)$  Å,  $b = 6.1495(6)$  Å,  $c = 6.9905(5)$  Å).

<i>h</i>	<i>k</i>	<i>l</i>	$4\theta_{\text{calc}}$	$4\theta_{\text{obs}}$	$\Delta$	$I_{\text{calc}}$	$I_{\text{obs}}$
1	0	1	34.095	34.103	0.01	293	278
0	1	1	38.413	38.387	0.04	364	335
1	1	1	44.758	44.784	0.04	72	90
2	0	0	45.743	45.714	0.05	98	95
0	0	2	50.924	50.929	0.01	220	223
2	0	1	52.442	52.410	0.06	1000	1000
1	0	2	55.934	55.922	0.03	209	212
0	2	0	58.031	58.043	0.03	599	657
2	1	1	60.070	60.055	0.03	251	253
1	1	2	63.176	63.176	0.00	127	150
1	2	1	67.689	67.678	0.03	92	112
2	0	2	68.975	68.969	0.02	51	52
2	2	0	74.525	74.520	0.01	58	68
2	1	2	75.090	75.071	0.05	25	23
1	2	2	81.475	81.462	0.04	140	143
0	1	3	82.805	82.822	0.05	117	106
2	0	3	90.689	90.692	0.01	89	87
0	3	1	92.213	92.211	0.01	135	142
4	0	0	93.448	93.441	0.02	75	65
4	1	0	98.291	98.270	0.07	52	47
2	3	1	104.140	104.148	0.03	50	50
0	0	4	104.606	104.578	0.10	38	34
3	0	3	105.605	105.628	0.08	23	24
4	0	2	107.915	107.917	0.01	77	71
3	1	3	110.055	110.076	0.08	44	44
4	1	2	112.301	112.314	0.05	89	67

$\Delta = |\sin^2\theta_{\text{calc}} - \sin^2\theta_{\text{obs}}| \cdot 1000$ ; intensity normalized at 1000 for the strongest reflection

Table 14.32 Assignment of the Guinier photograph of  $(V_{0.80}Mo_{0.20})OPO_4$  ( $\beta$ -VOPO<sub>4</sub> structure type, S.G. *Pnma*;  $a = 7.7761(7)$  Å,  $b = 6.1460(5)$  Å,  $c = 6.9945(8)$  Å).

<i>h</i>	<i>k</i>	<i>l</i>	$4\theta_{\text{calc}}$	$4\theta_{\text{obs}}$	$\Delta$	$I_{\text{calc}}$	$I_{\text{obs}}$
1	0	1	34.071	34.042	0.04	275	311
0	1	1	38.415	38.369	0.07	422	374
1	1	1	44.751	44.728	0.04	61	92
2	0	0	45.705	45.659	0.08	104	98
0	0	2	50.894	50.915	0.04	235	216
2	0	1	52.402	52.397	0.01	1000	1000
1	0	2	55.899	55.871	0.06	197	203
0	2	0	58.064	58.083	0.04	593	658
2	1	1	60.043	60.024	0.04	365	232
1	1	2	63.152	63.167	0.03	112	154
1	2	1	67.706	67.699	0.02	86	111
2	0	2	68.926	68.920	0.02	55	64
2	2	0	74.528	74.512	0.04	62	68
2	1	2	75.052	75.022	0.08	38	35
1	2	2	81.475	81.493	0.05	135	134
0	1	3	82.768	82.773	0.02	125	100
1	1	3	86.114	86.113	0.00	45	45
2	0	3	90.628	90.642	0.04	93	78
0	3	1	92.260	92.252	0.02	141	141
4	0	1	97.130	97.160	0.10	46	38
4	0	2	107.826	107.823	0.01	74	65
4	1	2	112.221	112.218	0.01	97	59
2	4	1	133.513	133.518	0.02	90	59
4	2	3	139.992	139.986	0.02	58	49

$\Delta = |\sin^2\theta_{\text{calc}} - \sin^2\theta_{\text{obs}}| \cdot 1000$ ; intensity normalized at 1000 for the strongest reflection

Table 14.33 Assignment of the Guinier photograph of  $(V_{0.70}Mo_{0.30})OPO_4$  ( $\beta$ -VOPO<sub>4</sub> structure type, S.G. *Pnma*;  $a = 7.7762(7)$  Å,  $b = 6.1596(7)$  Å,  $c = 7.0016(8)$  Å).

<i>h</i>	<i>k</i>	<i>l</i>	$4\theta_{\text{calc}}$	$4\theta_{\text{obs}}$	$\Delta$	$I_{\text{calc}}$	$I_{\text{obs}}$
1	0	1	34.052	34.055	0.00	259	291
0	1	1	38.350	38.375	0.04	481	302
1	1	1	44.694	44.676	0.03	53	96
2	0	0	45.705	45.696	0.02	111	100
0	0	2	50.841	50.816	0.05	250	219
2	0	1	52.388	52.386	0.00	1000	1000
1	0	2	55.851	55.816	0.07	191	196
0	2	0	57.933	57.936	0.01	596	648
2	1	1	59.999	60.006	0.01	278	213
1	1	2	63.078	63.095	0.04	100	129
1	2	1	67.581	67.585	0.01	81	90
2	2	0	74.423	74.444	0.06	66	62
2	1	2	74.988	74.944	0.12	49	42
1	2	2	81.343	81.343	0.00	131	109
0	1	3	82.666	82.693	0.08	134	98
2	0	3	90.556	90.562	0.02	97	90
2	2	2	91.212	91.241	0.09	61	56
0	3	1	92.053	92.051	0.01	149	133
4	0	0	93.366	93.361	0.02	70	62
4	1	0	98.197	98.180	0.06	63	36
4	1	2	112.173	112.196	0.08	104	60
2	3	2	114.194	114.185	0.03	91	68

$\Delta = |\sin^2\theta_{\text{calc}} - \sin^2\theta_{\text{obs}}| \cdot 1000$ ; intensity normalized at 1000 for the strongest reflection

Table 14.34 Assignment of the Guinier photograph of  $(V_{0.90}Mo_{0.10})OPO_4$  ( $\gamma$ -VOPO<sub>4</sub> structure type, S.G. *Pbam*;  $a = 17.327(2)$  Å,  $b = 8.875(2)$  Å,  $c = 4.918(1)$  Å).

<i>h</i>	<i>k</i>	<i>l</i>	$4\theta_{\text{calc}}$	$4\theta_{\text{obs}}$	$\Delta$	$I_{\text{calc}}$	$I_{\text{obs}}$
2	1	0	28.549	28.491	0.06	57	113
0	0	1	36.040	36.029	0.02	1000	1000
3	1	0	36.622	36.620	0.00	61	173
4	0	0	40.970	40.944	0.04	564	607
1	1	1	42.525	42.516	0.01	980	867
2	2	0	44.985	45.018	0.06	533	611
4	1	0	45.649	45.648	0.00	494	832
2	1	1	46.127	46.119	0.01	999	793
3	2	0	50.577	50.563	0.03	756	904
3	1	1	51.602	51.583	0.04	163	124
1	2	1	55.069	55.056	0.03	267	400
4	2	0	57.553	57.558	0.01	444	643
2	2	1	57.939	57.898	0.09	421	442
4	1	1	58.465	58.398	0.14	401	364
6	0	0	61.878	61.921	0.10	59	62
2	3	0	63.880	63.872	0.02	128	96
5	2	0	65.523	65.523	0.00	144	188
5	1	1	66.335	66.284	0.12	302	205
0	0	2	73.013	73.067	0.14	363	381
7	2	0	83.497	83.491	0.02	68	97
7	1	1	84.158	84.152	0.02	81	66
0	4	1	89.546	89.533	0.04	38	72
4	4	0	91.831	91.854	0.07	115	115
6	3	1	95.390	95.374	0.05	134	94
8	3	0	104.609	104.635	0.09	79	109

$\Delta = |\sin^2\theta_{\text{cal}} - \sin^2\theta_{\text{obs}}| \cdot 1000$ ; intensity normalized at 1000 for the strongest reflection

Table 14.35 Assignment of the Guinier photograph of  $(V_{0.80}Mo_{0.20})OPO_4$  ( $\gamma$ -VOPO<sub>4</sub> structure type, S.G. *Pbam*;  $a = 17.318(4)$  Å,  $b = 8.880(3)$  Å,  $c = 4.915(11)$  Å).

<i>h</i>	<i>k</i>	<i>l</i>	$4\theta_{\text{calc}}$	$4\theta_{\text{obs}}$	$\Delta$	$I_{\text{calc}}$	$I_{\text{obs}}$
2	1	0	28.549	28.527	0.02	24	153
0	0	1	36.062	36.133	0.10	1000	1000
3	1	0	36.630	36.643	0.02	24	188
4	0	0	40.992	40.961	0.05	582	679
1	1	1	42.538	42.570	0.05	975	875
2	2	0	44.969	45.018	0.08	472	656
4	1	0	45.664	45.698	0.06	443	831
2	1	1	46.143	46.168	0.04	961	792
3	2	0	50.568	50.606	0.07	714	928
3	1	1	51.622	51.665	0.08	193	143
1	2	1	55.066	55.094	0.05	185	413
4	2	0	57.553	57.592	0.08	426	656
2	2	1	57.940	57.932	0.02	373	395
4	1	1	58.490	58.402	0.19	360	349
2	3	0	63.849	63.810	0.09	149	120
5	2	0	65.530	65.549	0.04	154	193
5	1	1	66.365	66.349	0.04	289	224
0	0	2	73.057	73.116	0.15	337	416
2	3	1	73.809	73.795	0.04	272	205
7	2	0	83.520	83.532	0.03	65	107
4	0	2	84.493	84.461	0.09	19	88
8	2	0	93.278	93.258	0.06	89	130
3	3	2	101.527	101.506	0.07	122	88
8	3	0	104.625	104.645	0.07	76	125

$\Delta = |\sin^2\theta_{\text{calc}} - \sin^2\theta_{\text{obs}}| \cdot 1000$ ; intensity normalized at 1000 for the strongest reflection

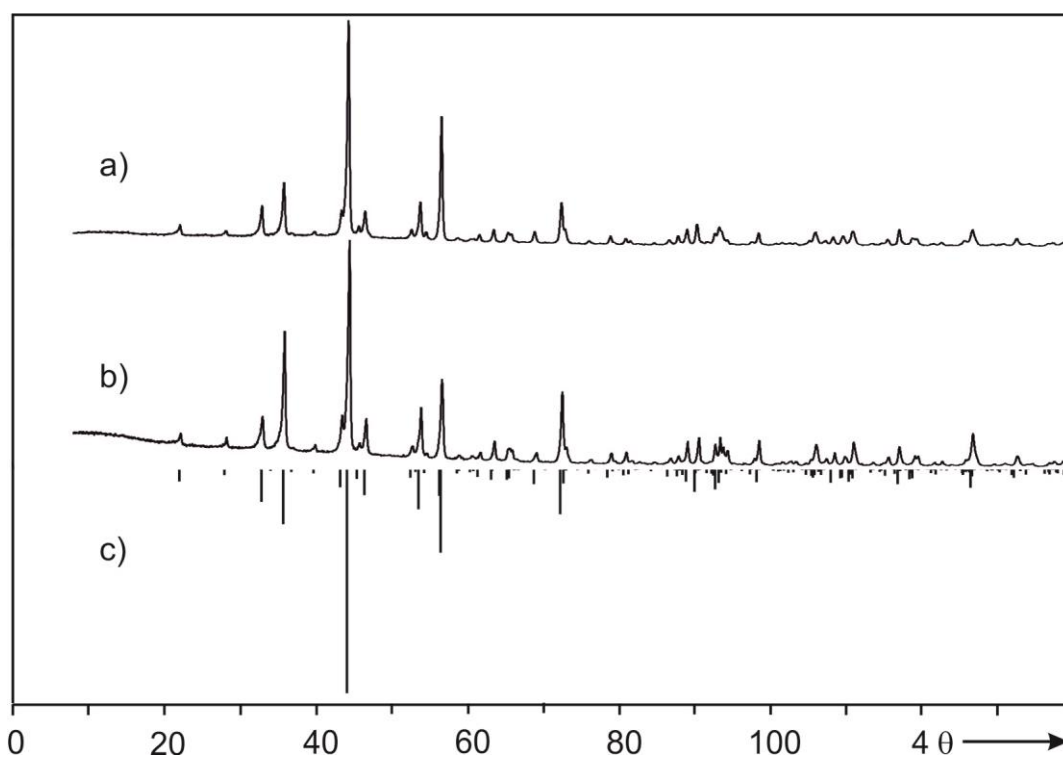


Figure 14.5 Comparison of the Guinier photographs aiming at the synthesis of “ $(V_{1-x}Mo_x)OPO_4$ ” at  $x = 0.95$  (a) and  $1.0$  (b) via SCS followed by heating in air with the simulation of  $\alpha-(MoO_2)_2P_2O_7$  [88] (c).



### 14.4 Metal(III) tungstenyl(VI) ortho-pyrophosphates

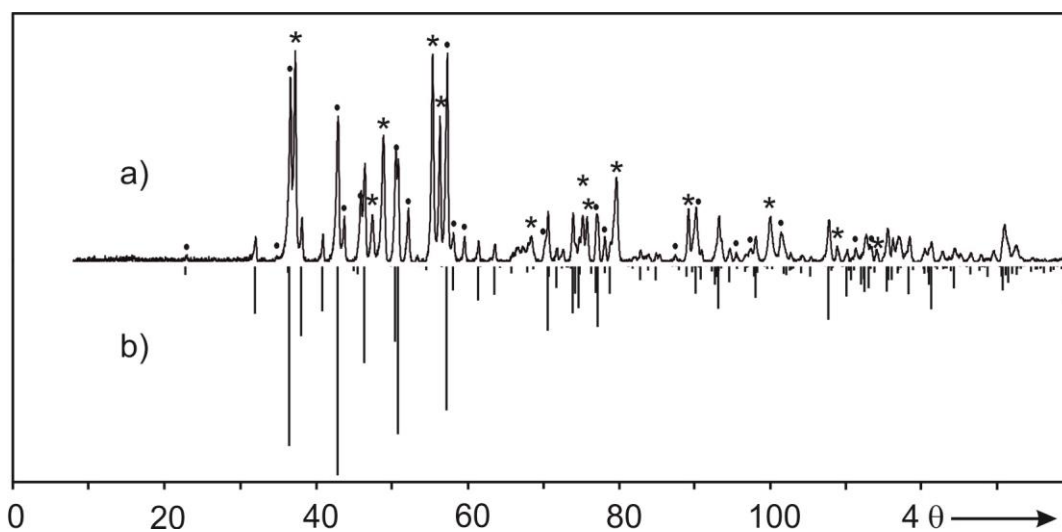


Figure 14.6 Aiming to the synthesis of “Sb(WO<sub>2</sub>)<sub>2</sub>(P<sub>2</sub>O<sub>7</sub>)(PO<sub>4</sub>)” (a) in air leads to multiphase mixture of *m*-W<sub>2</sub>O<sub>3</sub>(PO<sub>4</sub>)<sub>2</sub> (indicated by dots), a unknown phase X2 (indicated by \*) and *o*-W<sub>2</sub>O<sub>3</sub>(PO<sub>4</sub>)<sub>2</sub> shown as simulation of *o*-W<sub>2</sub>O<sub>3</sub>(PO<sub>4</sub>)<sub>2</sub> [75] (b).

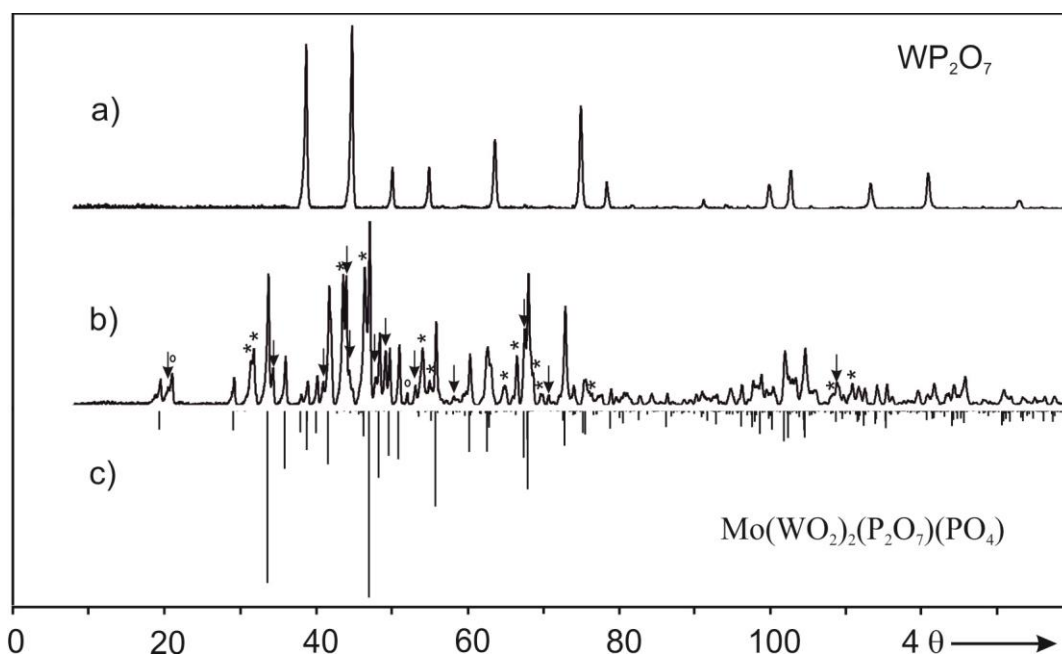


Figure 14.7 Synthesis of Mo(WO<sub>2</sub>)<sub>2</sub>(P<sub>2</sub>O<sub>7</sub>)(PO<sub>4</sub>) in sealed silica tube leads to the formation of multiphase mixtures: XRPD of mechanically separated black powders of MoP<sub>2</sub>O<sub>7</sub> [207] (a), bronze powders (b) comprising WOPO<sub>4</sub> [this thesis, 90, 91], (WO<sub>3</sub>)<sub>8</sub>(PO<sub>2</sub>)<sub>4</sub> [95] indicated by \* and down arrows, respectively. Simulation of Mo(WO<sub>2</sub>)<sub>2</sub>(P<sub>2</sub>O<sub>7</sub>)(PO<sub>4</sub>) (c) based on data of Ru(WO<sub>2</sub>)<sub>2</sub>(P<sub>2</sub>O<sub>7</sub>)(PO<sub>4</sub>) with adjusted lattice parameters, open circle indicate small impurity.

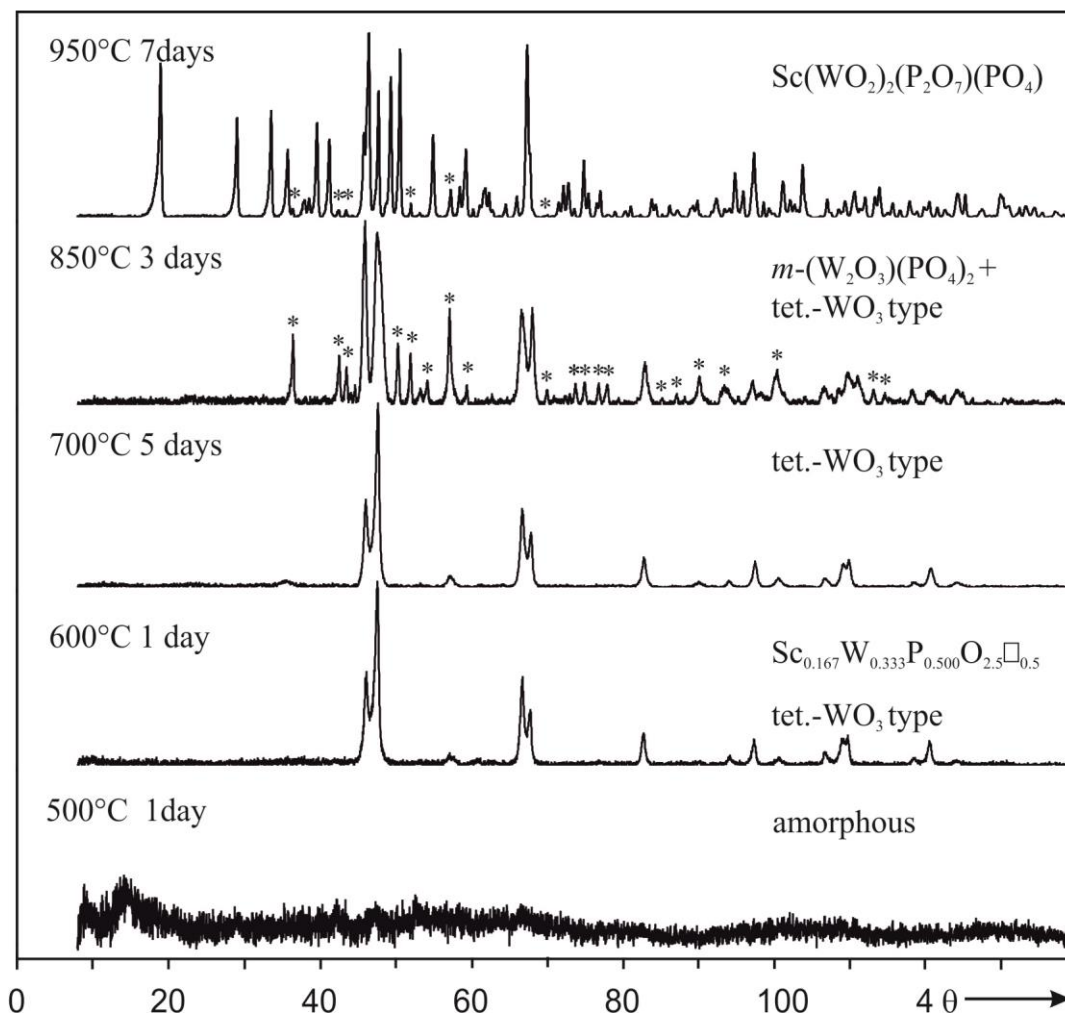


Figure 14.8 Sequential changes in powder diffraction patterns with temperatures during SCS followed by heating in air. The formation of two metastable phases, *tet*-WO<sub>3</sub> and WOPO<sub>4</sub> type prior to the occurrence of the thermodynamically stable phase Sc(WO<sub>2</sub>)<sub>2</sub>(P<sub>2</sub>O<sub>7</sub>)(PO<sub>4</sub>) is obvious. \* indicate *m*-(W<sub>2</sub>O<sub>3</sub>)(PO<sub>4</sub>)<sub>2</sub> [76, 77, 78].

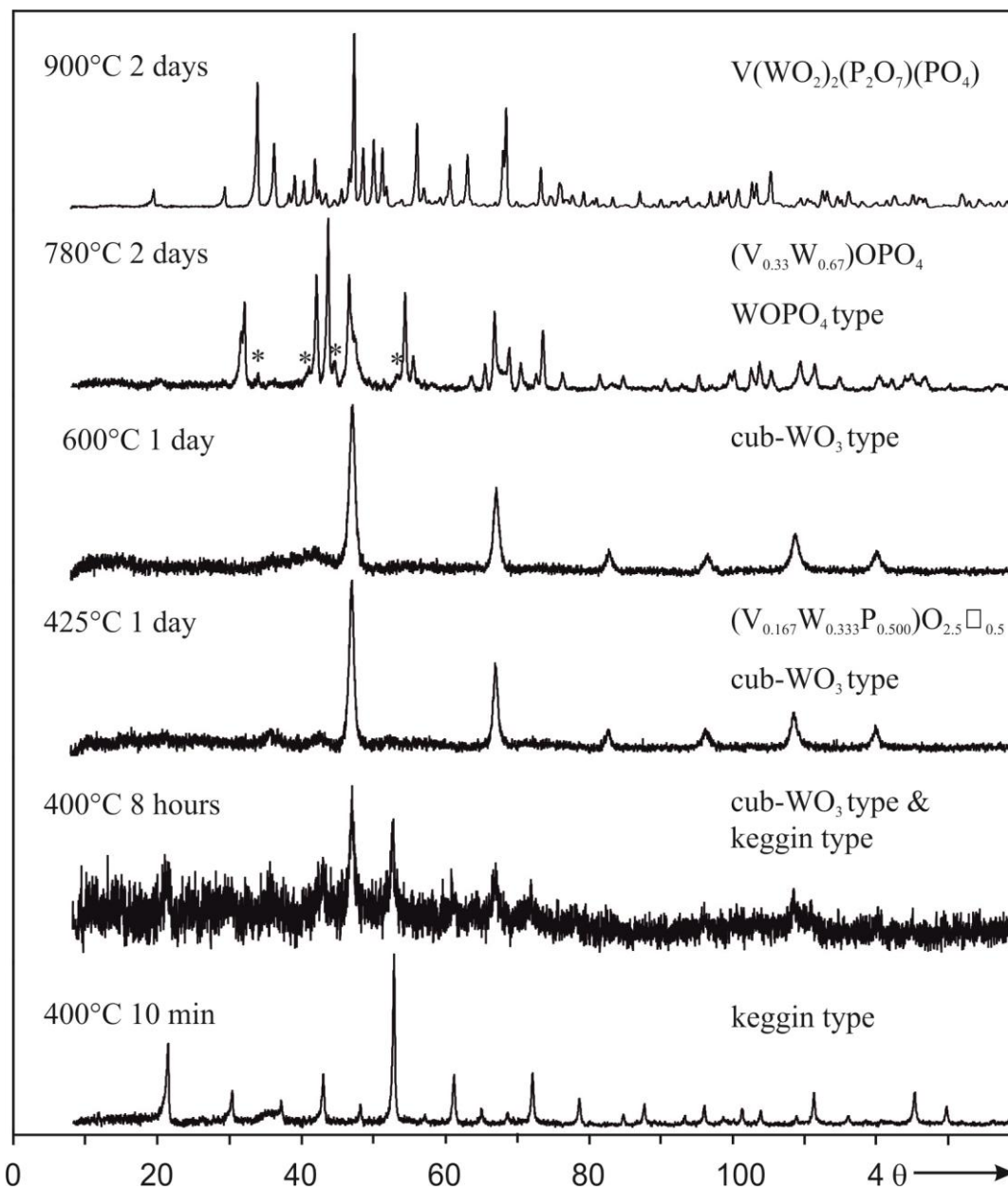


Figure 14.9 Sequential changes in powder diffraction patterns with temperatures during SCS followed by heating in air. The formation of two metastable phases, *cub*-WO<sub>3</sub> and WOPO<sub>4</sub> structure type prior to the occurrence of the thermodynamically stable phase V(WO<sub>2</sub>)<sub>2</sub>(P<sub>2</sub>O<sub>7</sub>)(PO<sub>4</sub>) is obvious.\* indicated (W<sub>0.83</sub>V<sub>0.17</sub>O<sub>3</sub>)<sub>8</sub>(PO<sub>2</sub>)<sub>4</sub>.

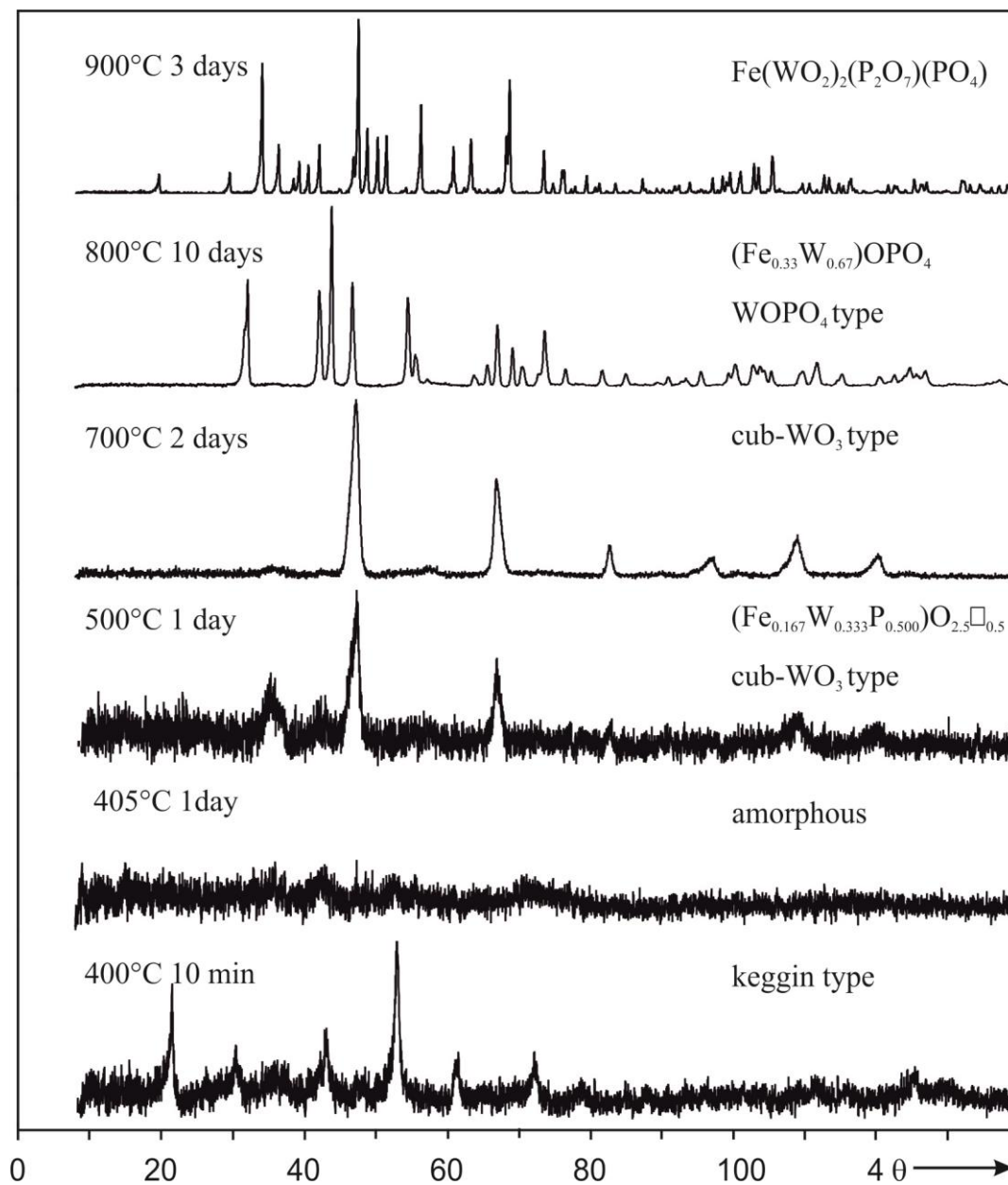


Figure 14.10 Sequential changes in powder diffraction patterns with temperatures during SCS followed by heating in air. The formation of two metastable phases, *cub-WO<sub>3</sub>* and *WOPO<sub>4</sub>* structure type prior to the occurrence of the thermodynamically stable phase  $\text{Fe}(\text{WO}_2)_2(\text{P}_2\text{O}_7)(\text{PO}_4)$  is obvious.

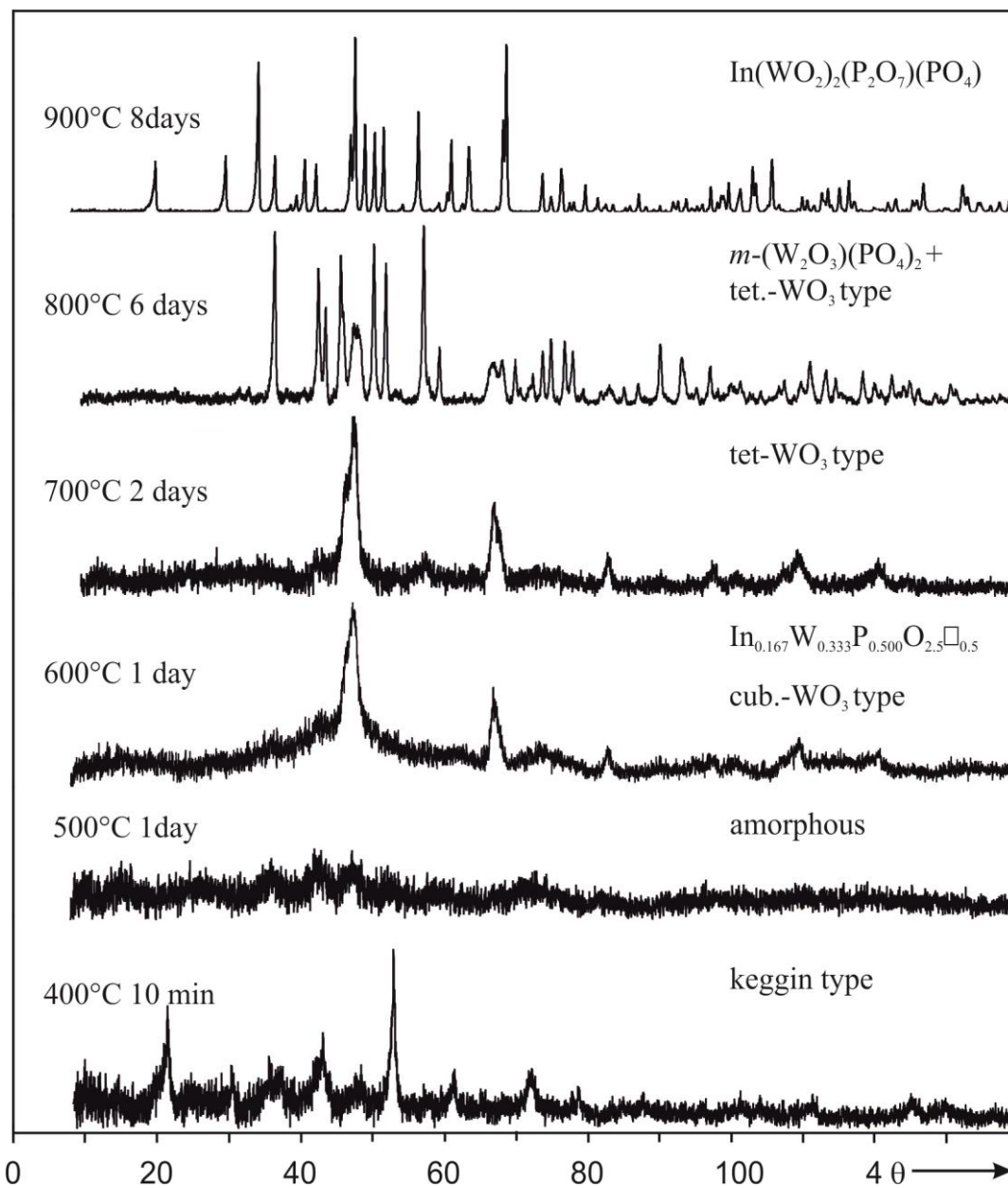


Figure 14.11 Sequential changes in powder diffraction patterns with temperatures during SCS followed by heating in air. The formation of two metastable phases, *cub*- $\text{WO}_3$  and  $\text{WOPO}_4$  structure type prior to the occurrence of the thermodynamically stable phase  $\text{In}(\text{WO}_2)_2(\text{P}_2\text{O}_7)(\text{PO}_4)$  is obvious.

Table 14.36  $V(\text{WO}_2)_2(\text{P}_2\text{O}_7)(\text{PO}_4)$ . Anisotropic displacement parameters ( $\text{\AA}^2$ ) with estimated standard deviations in parentheses.

Atom	$U_{11}$	$U_{22}$	$U_{33}$	$U_{23}$	$U_{13}$	$U_{12}$
W1	0.0095(2)	0.0089(2)	0.0105(2)	-0.0005(2)	0.0015(2)	0.0005(2)
V1						
W2	0.0104(2)	0.0103(2)	0.0105(2)	-0.0008(2)	0.0007(2)	0.0013(2)
V2						
W3	0.0112(2)	0.0110(2)	0.0113(2)	0.0011(2)	0.00341(16)	0.0020(2)
V3						
W4	0.0118(2)	0.0106(2)	0.0108(2)	0.0003(2)	0.0022(2)	0.0024(2)
V4						
W5	0.0313(5)	0.0196(4)	0.0232(4)	0.0100(3)	0.0053(3)	-0.0057(3)
V5						
W6	0.0376(6)	0.0207(4)	0.0251(5)	0.0110(3)	0.0080(4)	-0.0070(3)
V6						
P1	0.008(1)	0.0073(9)	0.007(1)	0.0007(8)	0.0014(8)	0.0010(8)
P2	0.007(1)	0.0063(9)	0.008(1)	0.0002(7)	0.0019(8)	0.0011(7)
P3	0.0060(9)	0.0061(9)	0.008(1)	-0.0016(7)	0.0023(8)	-0.0014(7)
P4	0.008(1)	0.0064(9)	0.009(1)	0.0000(8)	0.0019(8)	0.0001(8)
P5	0.007(1)	0.0063(9)	0.008(1)	0.0018(8)	-0.0004(8)	0.0007(7)
P6	0.007(1)	0.008(1)	0.009(1)	0	0.002(1)	0
P7	0.0065(1)	0.008(1)	0.008(1)	0	0.009(1)	0
O1	0.017(4)	0.014(3)	0.009(3)	-0.001(3)	0.000(3)	-0.002(3)
O2	0.012(3)	0.012(3)	0.015(3)	0.002(3)	0.003(3)	0.006(3)
O3	0.011(3)	0.017(3)	0.013(3)	0.002(3)	0.005(3)	-0.004(3)
O4	0.014(4)	0.019(4)	0.016(4)	0.006(3)	-0.000(3)	-0.002(3)
O5	0.012(3)	0.010(3)	0.017(4)	0.004(3)	0.000(3)	0.002(2)
O6	0.016(4)	0.012(3)	0.024(4)	0.011(3)	0.010(3)	0.003(3)
O7	0.014(3)	0.013(3)	0.013(3)	-0.001(3)	0.002(3)	0.006(3)
O8	0.016(4)	0.019(4)	0.016(4)	-0.005(3)	-0.003(3)	-0.008(3)
O9	0.017(4)	0.015(3)	0.017(4)	0.010(3)	0.001(3)	0.003(3)
O10	0.013(3)	0.012(3)	0.011(3)	0.002(2)	0.002(3)	0.003(3)
O11	0.012(3)	0.014(3)	0.008(3)	-0.003(3)	-0.002(2)	-0.002(3)
O12	0.017(4)	0.009(3)	0.034(5)	0.009(3)	0.011(3)	0.000(3)
O13	0.013(3)	0.007(3)	0.017(3)	0.002(3)	0.006(3)	0.002(2)
O14	0.026(4)	0.015(3)	0.013(3)	0.001(3)	0.013(3)	-0.003(3)
O15	0.010(3)	0.014(3)	0.017(3)	0.005(3)	0.007(3)	-0.003(3)
O16	0.008(3)	0.017(3)	0.009(3)	-0.001(3)	-0.001(2)	-0.003(3)
O17	0.019(4)	0.016(3)	0.011(3)	0.008(3)	-0.001(3)	-0.004(3)
O18	0.016(4)	0.012(3)	0.014(3)	0.004(3)	0.008(3)	-0.005(3)
O19	0.014(3)	0.014(3)	0.009(3)	-0.004(3)	-0.001(3)	0.001(3)
O20	0.015(4)	0.019(4)	0.026(4)	0.002(3)	0.002(3)	0.009(3)
O21	0.015(4)	0.021(4)	0.009(3)	0.001(3)	0.004(3)	-0.003(3)
O22	0.011(3)	0.012(3)	0.011(3)	0.001(3)	0.008(3)	0.000(2)
O23	0.017(4)	0.021(4)	0.012(3)	-0.005(3)	-0.004(3)	-0.001(3)
O24	0.015(4)	0.016(4)	0.025(4)	0.005(3)	0.002(3)	0.007(3)
O25	0.021(4)	0.021(4)	0.017(4)	-0.010(3)	0.003(3)	-0.005(3)
O26	0.017(4)	0.013(3)	0.018(4)	-0.002(3)	0.007(3)	-0.003(3)
O27	0.027(5)	0.022(4)	0.015(4)	-0.012(3)	0.006(3)	0.001(3)
O28	0.015(3)	0.016(3)	0.013(3)	-0.002(3)	0.006(3)	-0.006(3)
O29	0.022(4)	0.013(3)	0.015(4)	0.006(3)	0.005(3)	0.002(3)
O30	0.018(4)	0.017(4)	0.014(3)	0.005(3)	0.007(3)	-0.003(3)

Table 14.37 Ru(WO<sub>2</sub>)<sub>2</sub>(P<sub>2</sub>O<sub>7</sub>)(PO<sub>4</sub>). Anisotropic displacement parameters (Å<sup>2</sup>) with estimated standard deviations in parentheses.

<b>Atom</b>	$U_{11}$	$U_{22}$	$U_{33}$	$U_{23}$	$U_{13}$	$U_{12}$
W1 Ru1	0.0042(3)	0.0054(2)	0.0044(2)	-0.00008(18)	0.00075(18)	-0.0004(2)
W2 Ru2	0.0047(3)	0.0048(2)	0.0042(2)	-0.00002(19)	0.00039(18)	-0.0004(2)
W3 Ru3	0.0044(3)	0.0053(2)	0.0045(2)	-0.0005(2)	0.0009(2)	-0.0005(2)
W4 Ru4	0.0043(3)	0.0058(2)	0.0043(2)	0.00001(18)	0.00042(18)	-0.0007(2)
W5 Ru5	0.0046(5)	0.0052(4)	0.0044(5)	0.0003(3)	0.0010(3)	0
W6 Ru6	0.0054(5)	0.0066(5)	0.0054(5)	0.0012(4)	0.0007(3)	-0.0004(4)
P1	0.008(2)	0.005(1)	0.002(1)	0.002(1)	0.0012(12)	0.0004(12)
P2	0.005(2)	0.007(1)	0.0017(13)	0	-0.0007(12)	0.0013(12)
P3	0.003(2)	0.005(1)	0.006(2)	0.0001(12)	-0.0003(12)	-0.0013(12)
P4	0.007(2)	0.004(1)	0.010(2)	0.0003(12)	0.004(1)	-0.0009(12)
P5	0.003(2)	0.006(1)	0.006(2)	-0.0016(12)	0.0003(12)	-0.0005(12)
P6	0.007(2)	0.007(2)	0.002(2)	0	-0.0006(17)	0
P7	0.004(2)	0.009(2)	0.002(2)	0	-0.0012(17)	0

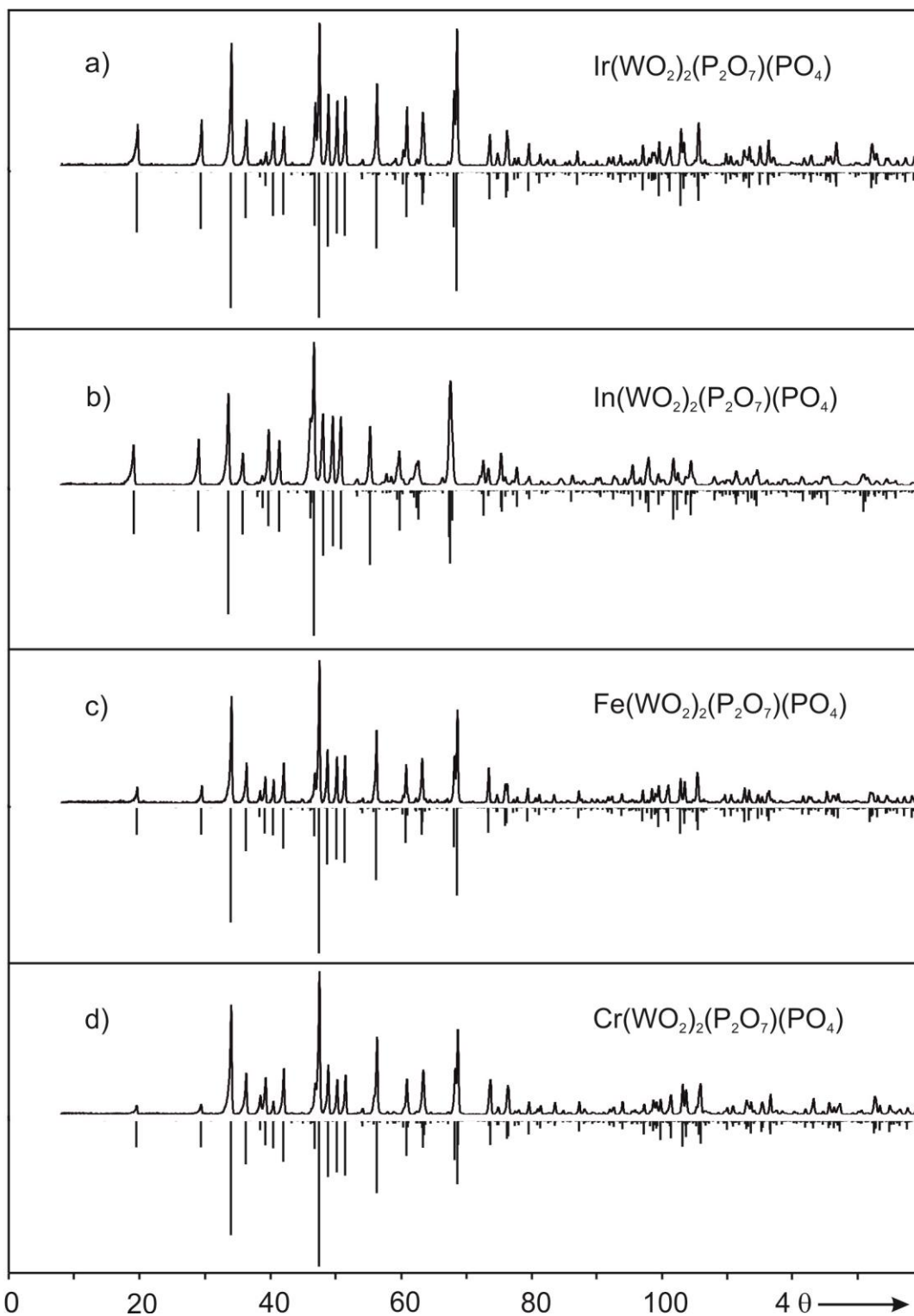


Figure 14.12 Guinier photographs of  $\text{Ir}(\text{WO}_2)_2(\text{P}_2\text{O}_7)(\text{PO}_4)$  (a),  $\text{In}(\text{WO}_2)_2(\text{P}_2\text{O}_7)(\text{PO}_4)$  (b),  $\text{Fe}(\text{WO}_2)_2(\text{P}_2\text{O}_7)(\text{PO}_4)$  (c), and  $\text{Cr}(\text{WO}_2)_2(\text{P}_2\text{O}_7)(\text{PO}_4)$  (d) obtained via SCS followed by heating in air except (a) which is obtained from vapor phase moderated solid state reactions (see Table 8.1 and Table 8.2), compared to the simulated diffraction patterns based on the model from the single crystal structure refinements (Table 8.5).



Table 14.38 Assignment of the Guinier photograph of  $W^{VI}(Sc^{III}_{0.5}W^{VI}_{0.5}O_2)_2(P_2O_7)(PO_4)$ , S.G.  $C2/c$ ;  $a = 38.201(7)$  Å,  $b = 12.919(8)$  Å,  $c = 9.608(2)$  Å,  $\beta = 102.10(1)^\circ$ .

<i>h</i>	<i>k</i>	<i>l</i>	$4\theta_{\text{calc}}$	$4\theta_{\text{obs}}$	$\Delta$	$I_{\text{calc}}$	$I_{\text{obs}}$
4	0	0	18.926	18.753	0.12	844	836
2	2	0	28.994	28.908	0.09	717	540
2	2	-1	33.508	33.452	0.07	629	580
2	2	1	35.693	35.668	0.03	251	369
8	0	0	37.983	37.955	0.04	60	96
4	0	-2	38.546	38.466	0.12	56	106
6	2	0	39.578	39.529	0.07	519	516
6	2	-1	41.217	41.183	0.05	269	424
4	0	2	45.775	45.764	0.02	260	460
6	2	1	46.442	46.396	0.08	1000	1000
8	0	-2	47.738	47.719	0.03	609	687
2	2	2	49.345	49.322	0.04	766	762
6	2	-2	50.574	50.554	0.04	816	914
10	2	-1	54.942	54.923	0.04	530	450
8	0	2	59.291	59.290	0.00	350	370
12	0	-2	61.864	61.834	0.07	156	161
2	2	-3	62.334	62.345	0.02	152	136
8	4	0	67.428	67.391	0.09	604	936
4	4	-2	67.760	67.771	0.03	276	350
10	2	-3	72.189	72.176	0.04	136	173
14	2	0	72.806	72.856	0.13	89	189
4	0	-4	74.886	74.888	0.01	169	311
14	2	-2	75.482	75.478	0.01	102	134
0	0	4	76.581	76.619	0.10	66	79
16	0	0	77.062	77.089	0.07	126	146
2	6	-1	86.218	86.243	0.07	57	67
18	2	-1	89.843	89.803	0.12	27	94
6	6	1	92.503	92.502	0.00	47	104
12	4	2	94.941	94.922	0.06	146	243
14	2	-4	95.998	95.971	0.09	87	144
16	4	-2	97.383	97.411	0.09	190	352
18	2	-3	98.681	98.720	0.13	84	85

$\Delta = |\sin^2\theta_{\text{cal}} - \sin^2\theta_{\text{obs}}| \cdot 1000$ ; intensity normalized at 1000 for the strongest reflection

Table 14.39 Assignment of the Guinier photograph of  $V^{III}(W^{VI}O_2)_2(P_2O_7)(PO_4)$ , S.G.  $C2/c$ ;  $a = 37.1696(31)$  Å,  $b = 12.7899(8)$  Å,  $c = 9.4769(13)$  Å,  $\beta = 102.319(8)^\circ$ .

<i>h</i>	<i>k</i>	<i>l</i>	$4\theta_{\text{calc}}$	$4\theta_{\text{obs}}$	$\Delta$	$I_{\text{calc}}$	$I_{\text{obs}}$
4	0	0	19.46	19.39	0.05	224	132
2	2	0	29.34	29.28	0.06	210	150
2	2	-1	33.90	33.85	0.06	959	707
2	2	1	36.19	36.19	0.00	293	296
0	0	2	38.31	38.27	0.05	83	68
4	0	-2	39.12	39.07	0.07	178	158
6	2	0	40.36	40.34	0.03	169	170
6	2	-1	41.93	41.92	0.02	281	273
4	0	2	46.67	46.70	0.06	191	227
6	2	1	47.38	47.38	0.01	1000	980
8	0	-2	48.67	48.66	0.02	442	360
2	2	2	50.08	50.10	0.03	299	336
6	2	-2	51.34	51.32	0.03	330	366
5	3	1	54.04	53.99	0.08	39	40
10	2	-1	56.17	56.16	0.03	548	460
6	2	2	60.20	60.18	0.03	46	51
8	0	2	60.70	60.69	0.01	248	229
2	2	-3	63.17	63.19	0.05	234	250
0	4	2	68.09	68.11	0.04	305	306
8	4	0	68.54	68.53	0.04	484	634
10	2	-3	73.43	73.44	0.04	192	198
8	4	-2	74.67	74.65	0.04	13	45
14	2	0	74.76	74.77	0.04	28	43
16	0	0	79.35	79.38	0.07	114	87
14	2	1	81.12	81.11	0.04	66	48
2	6	-1	87.15	87.14	0.03	86	82
18	2	-1	92.31	92.33	0.08	55	40
6	6	1	93.75	93.73	0.04	70	56
12	4	2	96.96	96.97	0.04	102	80
16	4	0	98.37	98.37	0.00	76	78
10	6	-1	98.90	98.89	0.02	55	63
16	4	-2	99.45	99.44	0.04	143	113
18	2	-3	100.98	100.97	0.02	101	97
4	4	4	102.78	102.79	0.03	191	150
2	6	-3	103.40	103.40	0.01	113	135
10	6	-3	110.57	110.57	0.01	46	49
16	4	2	113.26	113.24	0.07	92	69
0	8	0	115.20	115.23	0.09	54	52

$\Delta = |\sin^2\theta_{\text{calc}} - \sin^2\theta_{\text{obs}}| \cdot 1000$ ; intensity normalized at 1000 for the strongest reflection

Table 14.40 Assignment of the XRPD of  $(V_{0.6}^{III}V_{0.4}^{IV})(V_{0.1}^{IV}W_{0.9}^{VI}O_2)_2(P_2O_7)(PO_4)$ , S.G.  $C2/c$ ;  $a = 37.1714(31)$  Å,  $b = 12.7884(12)$  Å,  $c = 9.4852(8)$  Å,  $\beta = 102.278(8)^\circ$ .

$h$	$k$	$l$	$4\theta_{\text{calc}}$	$4\theta_{\text{obs}}$	$\Delta$	$I_{\text{calc}}$	$I_{\text{obs}}$
4	0	0	19.464	19.448	0.01	224	75
2	2	0	29.348	29.374	0.03	210	84
2	2	-1	33.897	33.938	0.05	959	749
2	2	1	36.180	36.225	0.06	292	275
0	0	2	38.271	38.343	0.10	83	105
4	0	-2	39.100	39.142	0.06	178	227
6	2	0	40.365	40.410	0.07	168	123
4	0	2	46.625	46.674	0.08	191	179
6	2	1	47.364	47.393	0.05	1000	980
8	0	-2	48.665	48.702	0.07	442	326
2	2	2	50.048	50.051	0.01	300	256
6	2	-2	51.331	51.360	0.05	330	302
5	3	1	54.025	53.987	0.07	39	35
10	2	-1	56.179	56.186	0.01	547	501
8	0	2	60.646	60.632	0.03	249	218
2	2	-3	63.128	63.131	0.01	234	289
0	4	2	68.076	68.108	0.08	305	284
8	4	0	68.548	68.537	0.03	484	566
10	2	-3	73.416	73.405	0.03	192	215
8	4	-2	74.673	74.674	0.00	13	42
16	0	0	79.339	79.353	0.04	114	106
14	2	1	81.092	81.112	0.06	66	55
8	4	2	83.318	83.352	0.10	36	60
2	6	-1	87.161	87.161	0.00	86	81
18	2	-1	92.307	92.320	0.04	55	53
6	6	1	93.744	93.720	0.08	70	70
12	4	2	96.917	96.900	0.06	102	72
16	4	0	98.364	98.340	0.08	76	89
10	6	-1	98.909	98.930	0.07	55	67
16	4	-2	99.461	99.480	0.06	143	96
18	2	-3	100.983	100.960	0.08	101	102
4	4	4	102.706	102.721	0.05	191	146
2	6	-3	103.383	103.371	0.04	114	143
2	2	5	105.247	105.231	0.05	46	132
12	4	-4	105.492	105.491	0.00	164	143
10	6	-3	110.565	110.572	0.03	46	51
16	4	2	113.207	113.193	0.05	92	72

$\Delta = |\sin^2\theta_{\text{calc}} - \sin^2\theta_{\text{obs}}| \cdot 1000$ ; intensity normalized at 1000 for the strongest reflection

Table 14.41 Assignment of the Guinier photograph of  $\text{Cr}^{\text{III}}(\text{W}^{\text{VI}}\text{O}_2)_2(\text{P}_2\text{O}_7)(\text{PO}_4)$ , S.G.  $C2/c$ ;  $a = 37.016(3) \text{ \AA}$ ,  $b = 12.756(1) \text{ \AA}$ ,  $c = 9.428(1) \text{ \AA}$ ,  $\beta = 102.275(9)^\circ$ .

<i>h</i>	<i>k</i>	<i>l</i>	$4\theta_{\text{calc}}$	$4\theta_{\text{obs}}$	$\Delta$	$I_{\text{calc}}$	$I_{\text{obs}}$
4	0	0	19.546	19.475	0.05	228	50
2	2	0	29.427	29.404	0.03	215	69
2	2	-1	34.019	33.982	0.05	961	820
2	2	1	36.317	36.316	0.00	293	285
0	0	2	38.503	38.479	0.03	81	124
4	0	-2	39.328	39.280	0.07	176	234
6	2	0	40.502	40.472	0.05	171	101
6	2	-1	42.093	42.074	0.03	280	269
4	0	2	46.886	46.871	0.03	192	175
6	2	1	47.554	47.552	0.00	1000	1000
2	2	2	50.291	50.266	0.05	301	251
6	2	-2	51.569	51.567	0.00	332	271
5	3	1	54.215	54.201	0.03	40	33
10	2	-1	56.401	56.363	0.08	548	548
6	2	2	60.441	60.448	0.02	47	39
8	0	2	60.959	60.938	0.05	250	247
2	2	-3	63.473	63.481	0.02	234	298
0	4	2	68.330	68.305	0.06	308	308
8	4	0	68.763	68.735	0.07	487	587
10	2	-3	73.788	73.779	0.02	192	221
14	2	0	75.053	75.020	0.09	29	44
16	0	0	79.683	79.663	0.06	115	170
14	2	1	81.442	81.444	0.00	66	59
2	6	-1	87.405	87.417	0.03	86	96
18	2	-1	92.700	92.709	0.03	55	55
6	6	1	94.031	94.019	0.04	71	79
12	4	2	97.327	97.330	0.01	103	69
16	4	0	98.742	98.760	0.06	76	110
10	6	-1	99.221	99.230	0.03	55	80
16	4	-2	99.865	99.900	0.12	144	103
18	2	-3	101.467	101.470	0.01	101	128
4	4	4	103.232	103.250	0.06	191	181
2	6	-3	103.783	103.800	0.06	114	163
10	6	-3	110.997	110.970	0.10	46	57
16	4	2	113.706	113.709	0.01	93	93

$\Delta = |\sin^2\theta_{\text{calc}} - \sin^2\theta_{\text{obs}}| \cdot 1000$ ; intensity normalized at 1000 for the strongest reflection

Table 14.42 Assignment of the Guinier photograph of  $\text{Fe}^{\text{III}}(\text{W}^{\text{VI}}\text{O}_2)_2(\text{P}_2\text{O}_7)(\text{PO}_4)$ , S.G.  $C2/c$ ;  $a = 37.187(4) \text{ \AA}$ ,  $b = 12.789(1) \text{ \AA}$ ,  $c = 9.484(1) \text{ \AA}$ ,  $\beta = 102.36(1)^\circ$ .

$h$	$k$	$l$	$4\theta_{\text{calc}}$	$4\theta_{\text{obs}}$	$\Delta$	$I_{\text{calc}}$	$I_{\text{obs}}$
4	0	0	19.463	19.424	0.03	232	116
2	2	0	29.347	29.337	0.01	217	125
2	2	-1	33.892	33.882	0.01	960	750
2	2	1	36.192	36.164	0.04	293	284
0	0	2	38.288	38.287	0.00	80	81
4	0	-2	39.086	39.047	0.06	176	187
6	2	0	40.362	40.319	0.06	173	152
6	2	-1	41.915	41.890	0.04	281	281
4	0	2	46.664	46.675	0.02	194	203
6	2	1	47.384	47.355	0.05	1000	1000
8	0	-2	48.626	48.627	0.00	448	368
2	2	2	50.073	50.068	0.01	304	326
6	2	-2	51.307	51.289	0.03	335	326
5	3	1	54.040	54.001	0.08	40	38
10	2	-1	56.150	56.123	0.06	549	515
6	2	2	60.194	60.186	0.02	48	58
8	0	2	60.695	60.656	0.09	251	266
2	2	-3	63.137	63.158	0.05	235	315
0	4	2	68.084	68.071	0.03	309	324
8	4	0	68.544	68.531	0.03	488	653
10	2	-3	73.370	73.363	0.02	192	235
16	0	0	79.331	79.336	0.01	115	138
8	4	2	83.354	83.357	0.01	35	57
2	6	-1	87.156	87.169	0.04	12	75
18	2	-1	92.268	92.250	0.06	55	41
6	6	1	93.752	93.730	0.07	71	62
12	4	2	96.961	96.991	0.10	103	89
16	4	0	98.356	98.371	0.05	76	101
10	6	-1	98.888	98.901	0.04	55	70
16	4	-2	99.407	99.421	0.05	144	122
4	4	4	102.759	102.751	0.03	192	160

$\Delta = |\sin^2\theta_{\text{calc}} - \sin^2\theta_{\text{obs}}| \cdot 1000$ ; intensity normalized at 1000 for the strongest reflection

Table 14.43 Assignment of the Guinier photograph of  $\text{Mo}^{\text{III}}(\text{W}^{\text{VI}}\text{O}_2)_2(\text{P}_2\text{O}_7)(\text{PO}_4)$ , S.G.  $C2/c$   $a = 37.355(7) \text{ \AA}$ ,  $b = 12.902(2) \text{ \AA}$ ,  $c = 9.550(2) \text{ \AA}$ ,  $\beta = 102.33(1)^\circ$ .

<i>h</i>	<i>k</i>	<i>l</i>	$4\theta_{\text{calc}}$	$4\theta_{\text{obs}}$	$\Delta$	$I_{\text{calc}}$	$I_{\text{obs}}$
4	0	0	19.372	19.288	0.06	120	135
2	2	0	29.102	29.074	0.03	120	146
2	2	-1	33.62	33.571	0.06	850	715
2	2	1	35.903	35.864	0.05	300	268
0	0	2	38.016	37.977	0.06	90	60
4	0	-2	38.835	38.828	0.01	200	131
6	2	0	40.093	40.069	0.04	140	160
4	0	2	46.347	46.327	0.04	130	
6	2	1	47.059	46.987	0.12	1000	982
8	0	-2	48.361	48.369	0.01	360	374
2	2	2	49.69	49.67	0.04	280	286
6	2	-2	50.958	50.951	0.01	300	326
10	2	-1	55.831	55.816	0.03	500	448
8	0	2	60.315	60.27	0.1	220	272
2	2	-3	62.664	62.642	0.05	200	309
0	4	2	67.509	67.495	0.04	250	417
8	4	0	68.022	68.025	0.01	410	713
10	2	-3	72.906	72.898	0.02	170	521
4	0	-4	75.358	75.389	0.08	110	130
6	2	3	75.638	75.609	0.08	110	138
16	0	0	78.947	78.95	0.01	90	85
2	6	-1	86.367	86.382	0.05	80	64
12	4	2	96.263	96.263	0.0	80	108
4	4	4	101.931	101.942	0.04	160	285
14	2	3	104.576	104.602	0.09	100	310

$\Delta = |\sin^2\theta_{\text{cal}} - \sin^2\theta_{\text{obs}}| \cdot 1000$ ; intensity normalized at 1000 for the strongest reflection

Table 14.44 Assignment of the Guinier photograph of  $\text{Ru}^{\text{III}}(\text{W}^{\text{VI}}\text{O}_2)_2(\text{P}_2\text{O}_7)(\text{PO}_4)$ , S.G.  $C2/c$   $a = 37.054(4) \text{ \AA}$ ,  $b = 12.807(1) \text{ \AA}$ ,  $c = 9.454(1) \text{ \AA}$ ,  $\beta = 102.139(12)^\circ$ .

$h$	$k$	$l$	$4\theta_{\text{calc}}$	$4\theta_{\text{obs}}$	$\Delta$	$I_{\text{calc}}$	$I_{\text{obs}}$
4	0	0	19.516	19.466	0.04	187	102
2	2	0	29.319	29.300	0.02	184	105
2	2	-1	33.908	33.930	0.03	921	818
2	2	1	36.177	36.220	0.06	311	314
0	0	2	38.376	38.388	0.02	80	107
8	0	0	39.175	39.201	0.04	33	203
6	2	0	40.394	40.435	0.06	174	125
6	2	-1	42.004	42.041	0.06	288	288
4	0	2	46.714	46.714	0.00	171	210
6	2	1	47.395	47.396	0.00	1000	1000
8	0	-2	48.872	48.860	0.02	407	341
2	2	2	50.103	50.112	0.02	300	263
6	2	-2	51.462	51.505	0.08	316	389
5	3	1	54.015	54.010	0.01	37	40
10	2	-1	56.314	56.344	0.06	514	578
6	2	2	60.219	60.198	0.04	44	55
8	0	2	60.752	60.749	0.01	205	281
2	2	-3	63.274	63.231	0.10	218	291
12	0	-2	63.574	63.591	0.04	106	132
0	4	2	68.069	68.082	0.03	291	312
4	4	-2	68.588	68.612	0.06	184	640
10	2	-3	73.671	73.670	0.00	184	144
4	0	-4	76.159	76.177	0.05	135	221
16	0	0	79.557	79.583	0.07	107	98
14	2	1	81.233	81.260	0.08	68	70
8	4	2	83.341	83.347	0.02	38	76
2	6	-1	87.054	87.068	0.04	87	93
12	0	-4	88.037	88.036	0.00	22	45
18	2	-1	92.575	92.573	0.01	52	76
6	6	1	93.656	93.650	0.02	67	76
12	4	2	96.985	96.958	0.09	97	82
16	4	0	98.497	98.492	0.02	76	93
16	4	-2	99.681	99.648	0.11	136	115

$\Delta = |\sin^2\theta_{\text{cal}} - \sin^2\theta_{\text{obs}}| \cdot 1000$ ; intensity normalized at 1000 for the strongest reflection

Table 14.45 Assignment of the Guinier photograph of  $\text{Rh}^{\text{III}}(\text{W}^{\text{VI}}\text{O}_2)_2(\text{P}_2\text{O}_7)(\text{PO}_4)$ , S.G.  $C2/c$ ;  $a = 37.043(3) \text{ \AA}$ ,  $b = 12.7768(9) \text{ \AA}$ ,  $c = 9.434(1) \text{ \AA}$ ,  $\beta = 102.245(9)^\circ$ .

<i>h</i>	<i>k</i>	<i>l</i>	$4\theta_{\text{calc}}$	$4\theta_{\text{obs}}$	$\Delta$	$I_{\text{calc}}$	$I_{\text{obs}}$
4	0	0	19.529	19.472	0.04	316	110
2	2	0	29.384	29.394	0.01	292	116
2	2	-1	33.978	33.969	0.01	961	791
2	2	1	36.268	36.301	0.04	294	310
0	0	2	38.472	38.463	0.01	60	97
4	0	-2	39.306	39.303	0.00	145	197
6	2	0	40.454	40.494	0.06	217	125
6	2	-1	42.051	42.056	0.01	282	253
4	0	2	46.839	46.849	0.02	221	227
6	2	1	47.497	47.479	0.03	1000	1000
8	0	-2	48.893	48.920	0.05	482	329
2	2	2	50.235	50.231	0.01	348	272
6	2	-2	51.527	51.552	0.05	379	285
5	3	1	54.141	54.133	0.02	44	38
10	2	-1	56.352	56.334	0.04	551	530
6	2	2	60.371	60.355	0.03	62	54
8	0	2	60.895	60.905	0.02	272	320
2	2	-3	63.417	63.446	0.07	234	303
10	4	2	68.239	68.236	0.01	339	352
8	4	0	68.670	68.666	0.01	525	673
10	2	-3	73.740	73.736	0.01	191	209
8	4	-2	74.869	74.846	0.06	8	46
6	2	3	76.454	76.446	0.02	136	220
14	2	1	81.356	81.355	0.00	67	80
8	4	2	83.545	83.554	0.03	29	79
2	6	-1	87.268	87.273	0.01	87	99
18	2	-1	92.622	92.610	0.04	55	64
6	6	1	93.886	93.879	0.02	71	69
12	4	2	97.203	97.207	0.01	112	86
16	4	0	98.629	98.646	0.05	69	100
10	6	-1	99.082	99.085	0.01	55	91
4	4	4	103.110	103.102	0.03	205	176

$\Delta = |\sin^2\theta_{\text{calc}} - \sin^2\theta_{\text{obs}}| \cdot 1000$ ; intensity normalized at 1000 for the strongest reflection



Table 14.46 Assignment of the Guinier photograph of  $\text{Ir}^{\text{III}}(\text{W}^{\text{VI}}\text{O}_2)_2(\text{P}_2\text{O}_7)(\text{PO}_4)$ , S.G.  $C2/c$ ;  $a = 37.113(2)$  Å,  $b = 12.819(1)$  Å,  $c = 9.4610(8)$  Å,  $\beta = 102.314(6)^\circ$ .

$h$	$k$	$l$	$4\theta_{\text{calc}}$	$4\theta_{\text{obs}}$	$\Delta$	$I_{\text{calc}}$	$I_{\text{obs}}$
4	0	0	19.497	19.474	0.02	436	286
2	2	0	29.291	29.267	0.03	407	295
2	2	-1	33.868	33.882	0.02	926	825
2	2	1	36.169	36.174	0.01	315	315
6	2	0	40.355	40.368	0.02	314	292
6	2	-1	41.929	41.939	0.01	295	263
4	0	2	46.750	46.763	0.02	250	446
6	2	1	47.395	47.403	0.01	1000	1000
8	0	-2	48.754	48.794	0.07	519	495
2	2	2	50.106	50.115	0.02	437	450
6	2	-2	51.368	51.385	0.03	451	475
5	3	1	53.998	54.007	0.02	48	46
10	2	-1	56.211	56.248	0.08	526	544
6	2	2	60.245	60.279	0.07	87	107
8	0	2	60.797	60.779	0.04	314	416
2	2	-3	63.233	63.240	0.02	221	368
0	4	2	68.024	68.040	0.04	382	496
8	4	0	68.475	68.490	0.04	577	960
10	2	2	74.668	74.680	0.03	50	82
14	2	0	74.835	74.840	0.01	48	52
4	0	-4	76.092	76.080	0.03	174	235
6	2	3	76.289	76.280	0.03	128	162
14	2	-2	77.303	77.300	0.01	55	55
0	0	4	77.882	77.890	0.02	43	59
2	6	-1	86.965	86.957	0.03	88	93
18	2	-1	92.422	92.404	0.06	51	60
6	6	1	93.588	93.583	0.02	70	70
12	4	2	96.985	96.970	0.05	126	140
14	2	-4	97.919	97.940	0.07	47	54
16	4	0	98.398	98.409	0.04	57	95
10	6	-1	98.762	98.789	0.09	54	86
16	4	-2	99.488	99.468	0.06	168	170
18	2	-3	101.121	101.117	0.01	104	125
4	4	4	102.832	102.826	0.02	223	251
2	6	-3	103.292	103.275	0.06	113	168
12	4	-4	105.572	105.563	0.03	193	297
16	4	2	113.327	113.334	0.03	109	129

$\Delta = |\sin^2\theta_{\text{calc}} - \sin^2\theta_{\text{obs}}| \cdot 1000$ ; intensity normalized at 1000 for the strongest reflection

Table 14.47 Assignment of the Guinier photograph of  $\text{In}^{\text{III}}(\text{W}^{\text{VI}}\text{O}_2)_2(\text{P}_2\text{O}_7)(\text{PO}_4)$ , S.G.  $C2/c$   $a = 37.839(7) \text{ \AA}$ ,  $b = 12.930(3) \text{ \AA}$ ,  $c = 9.530(2) \text{ \AA}$ ,  $\beta = 102.15(2)^\circ$ .

$h$	$k$	$l$	$4\theta_{\text{calc}}$	$4\theta_{\text{obs}}$	$\Delta$	$I_{\text{calc}}$	$I_{\text{obs}}$
4	0	0	19.111	19.050	0.04	336	270
2	2	0	29.002	29.065	0.07	304	314
2	2	-1	33.578	33.591	0.02	948	610
2	2	1	35.807	35.804	0.00	291	212
6	2	0	39.764	39.779	0.02	226	394
6	2	-1	41.406	41.401	0.01	281	300
4	0	2	46.191	46.226	0.06	225	432
6	2	1	46.721	46.696	0.04	1000	1000
8	0	-2	48.147	48.128	0.03	488	482
2	2	2	49.630	49.659	0.05	354	502
6	2	-2	50.858	50.841	0.03	385	465
10	2	-1	55.318	55.295	0.05	554	401
8	0	2	59.861	59.829	0.07	277	232
2	2	-3	62.740	62.751	0.02	231	177
8	4	0	67.607	67.625	0.04	531	707
10	2	-3	72.708	72.708	0.00	189	162
16	0	0	77.842	77.871	0.08	127	125
14	2	1	79.707	79.692	0.04	67	60

$\Delta = |\sin^2\theta_{\text{calc}} - \sin^2\theta_{\text{obs}}| \cdot 1000$ ; intensity normalized at 1000 for the strongest reflection

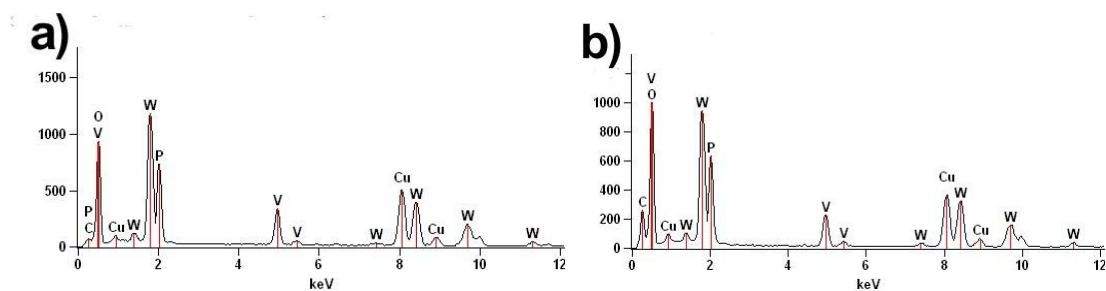


Figure 14.13 TEM EDX spectra of  $\text{V}(\text{WO}_2)_2(\text{P}_2\text{O}_7)(\text{PO}_4)$ ; V-K : W-L : P-K = 16.2(5) : 31.7(9) : 52.2(9) (a) and 16.8(7) : 29(1) : 53(2) (b) atom%. Cu and C from TEM grid.

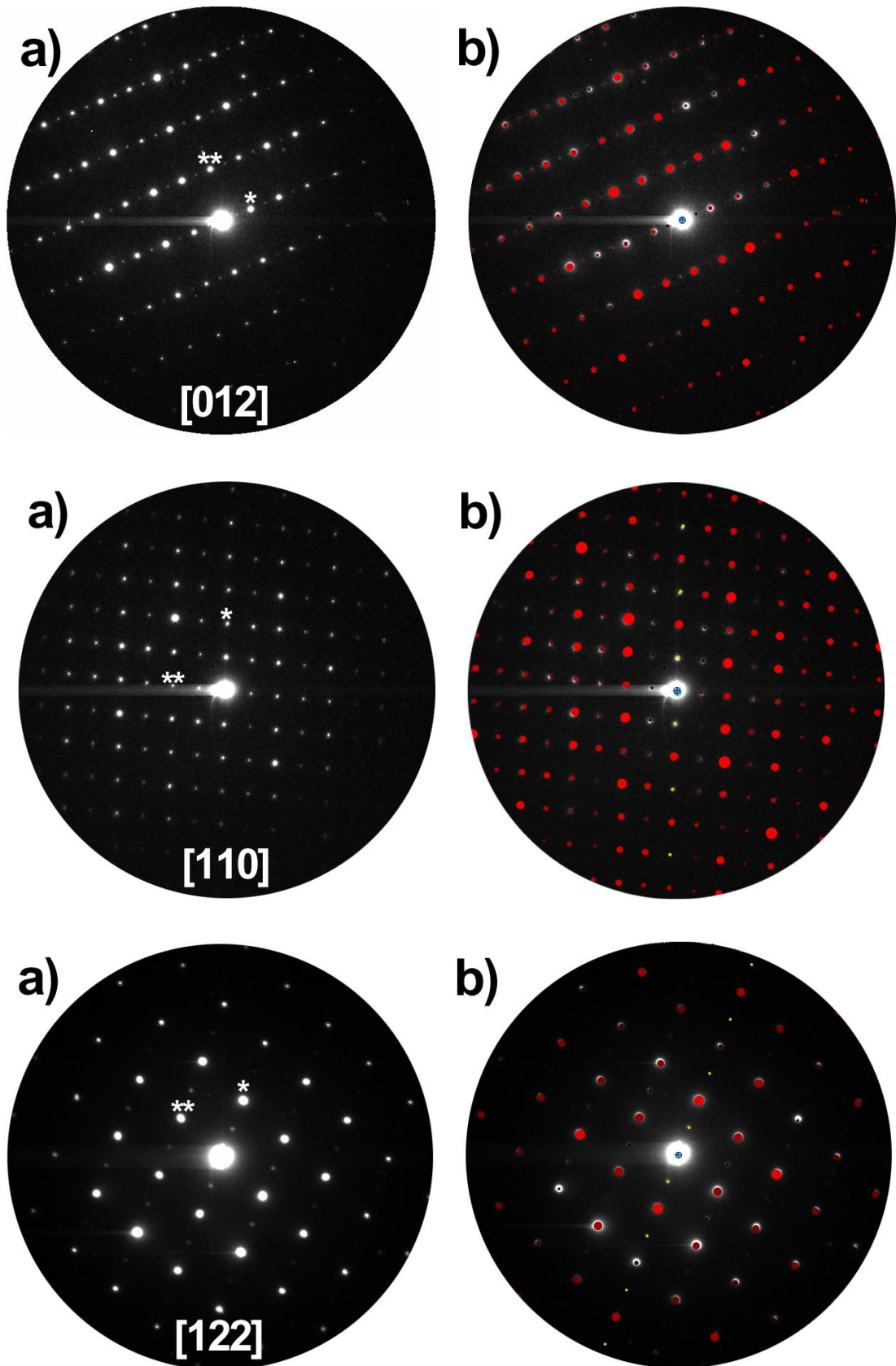


Figure 14.14 ED pattern (a) and ED simulation (b) based on the structure model of  $V(WO_2)_2(P_2O_7)(PO_4)$  (Table 8.5); Top:  $[012]$ : \* :  $(40\bar{2})$ ; \*\* :  $(\bar{2}21)$ ; Middle:  $[110]$ : \* :  $(00\bar{2})$ ; \*\* :  $(\bar{2}20)$ ; Bottom:  $[122]$ : \* :  $(40\bar{2})$  and \*\* :  $(\bar{2}21)$ .

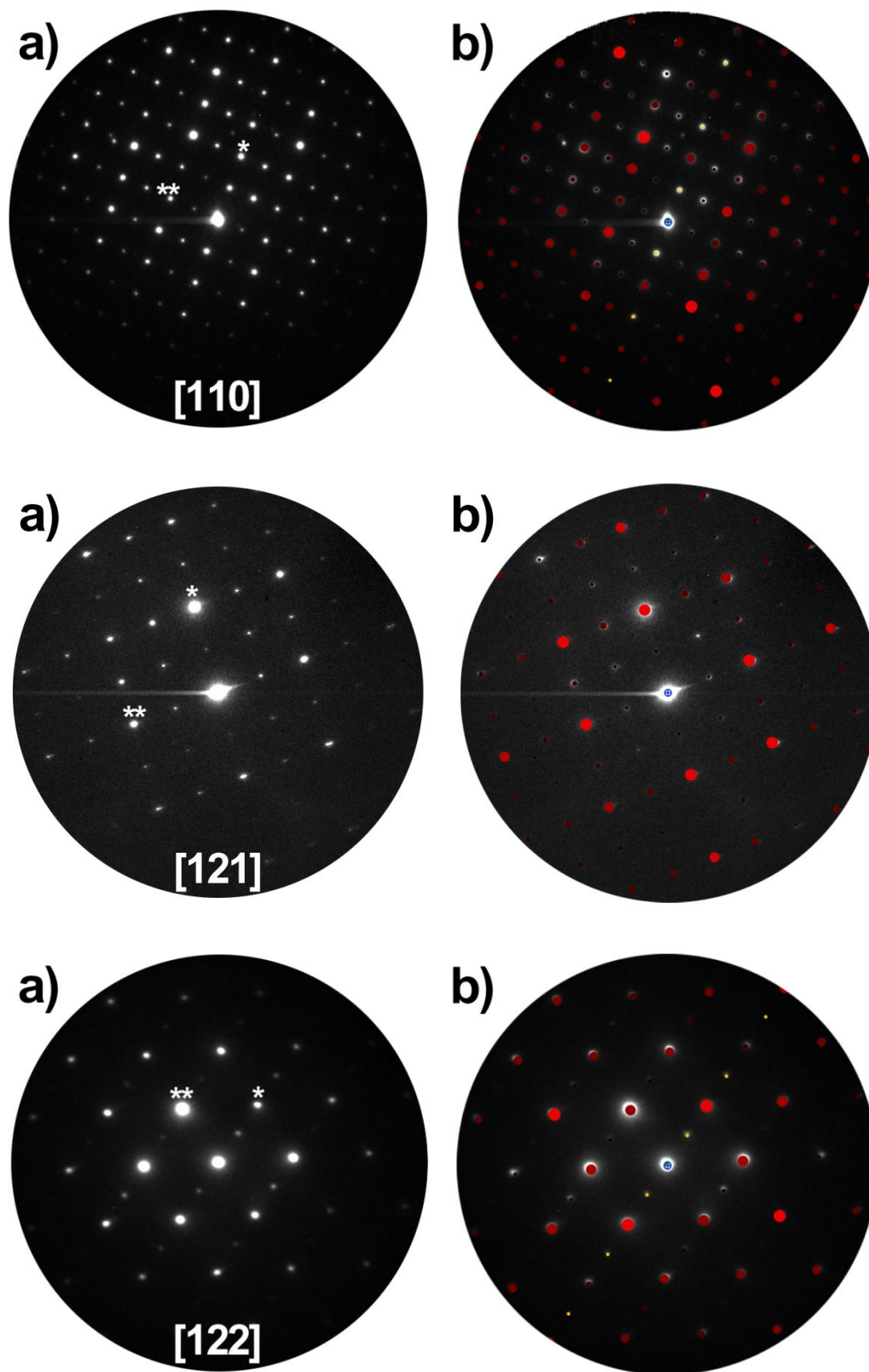


Figure 14.15 ED pattern (a) and ED simulation (b) based on the structure model of  $\text{Cr}(\text{WO}_2)_2(\text{P}_2\text{O}_7)(\text{PO}_4)$  (model from Table 8.5 with adjusted lattice parameters from powder XRPD); Top: [110]: \* :  $(00\bar{2})$ ; \*\* :  $(\bar{2}20)$ ; Middle: [121]: \* :  $(\bar{2}2\bar{2})$ ; \*\* :  $(\bar{2}21)$ ; Bottom: [122].

## 14.5 Metastable tungsten phosphates with structures related to $\text{ReO}_3$ and $\text{WOPO}_4$

Table 14.48 Assignment of the Guinier photograph of  $\text{cub}-(\text{V}_{0.25}\text{W}_{0.25}\text{P}_{0.50})\text{O}_{2.5+\delta}$ , S.G.  $Pm\bar{3}m$ ;  $a = 3.7732(9)$  Å.

$h$	$k$	$l$	$4\theta_{\text{calc}}$	$4\theta_{\text{obs}}$	$\Delta$	$I_{\text{calc}}$	$I_{\text{obs}}$
1	0	0	47.116	47.014	0.18	1000	1000
1	1	0	67.120	67.035	0.20	289	501
1	1	1	82.826	82.745	0.23	20	149
2	0	0	96.387	96.413	0.09	257	147
2	1	0	108.638	108.602	0.13	403	242
2	1	1	120.010	120.079	0.26	142	134

$\Delta = |\sin^2\theta_{\text{calc}} - \sin^2\theta_{\text{obs}}| \cdot 1000$ ; intensity normalized at 1000 for the strongest reflection

Table 14.49 Assignment of the Guinier photograph of  $\text{cub}-(\text{V}_{0.167}\text{W}_{0.333}\text{P}_{0.50})\text{O}_{2.5+\delta}$ , S.G.  $Pm\bar{3}m$ ;  $a = 3.7708(9)$  Å.

$h$	$k$	$l$	$4\theta_{\text{calc}}$	$4\theta_{\text{obs}}$	$\Delta$	$I_{\text{calc}}$	$I_{\text{obs}}$
1	0	0	47.147	47.013	0.23	1000	1000
1	1	0	67.164	67.145	0.05	330	499
1	1	1	82.881	82.812	0.20	33	139
2	0	0	96.453	96.522	0.22	248	125
2	1	0	108.714	108.715	0.01	414	226
2	1	1	120.095	120.094	0.00	162	126

$\Delta = |\sin^2\theta_{\text{calc}} - \sin^2\theta_{\text{obs}}| \cdot 1000$ ; intensity normalized at 1000 for the strongest reflection

Table 14.50 Assignment of the Guinier photograph of  $\text{cub}-(\text{V}_{0.10}\text{W}_{0.40}\text{P}_{0.50})\text{O}_{2.5+\delta}$ , S.G.  $Pm\bar{3}m$ ;  $a = 3.770(1)$  Å.

$h$	$k$	$l$	$4\theta_{\text{calc}}$	$4\theta_{\text{obs}}$	$\Delta$	$I_{\text{calc}}$	$I_{\text{obs}}$
1	0	0	47.151	47.094	0.10	1000	1000
1	1	0	67.170	67.035	0.33	359	576
1	1	1	82.889	82.775	0.33	44	202
2	0	0	96.462	96.493	0.10	242	123
2	1	0	108.724	108.731	0.03	421	191
2	1	1	120.107	120.159	0.20	176	145

$\Delta = |\sin^2\theta_{\text{calc}} - \sin^2\theta_{\text{obs}}| \cdot 1000$ ; intensity normalized at 1000 for the strongest reflection

Table 14.51 Assignment of the Guinier photograph of  $cub-(Cr_{0.167}W_{0.333}P_{0.50})O_{2.5}\square_{0.5}$ , S.G.  $Pm\bar{3}m$ ;  $a = 3.7712(9)$  Å.

$h$	$k$	$l$	$4\theta_{\text{calc}}$	$4\theta_{\text{obs}}$	$\Delta$	$I_{\text{calc}}$	$I_{\text{obs}}$
1	0	0	47.142	47.071	0.12	1000	1000
1	1	0	67.157	67.043	0.28	332	492
1	1	1	82.872	82.842	0.09	34	187
2	0	0	96.442	96.508	0.22	247	124
2	1	0	108.701	108.736	0.12	413	220
2	1	1	120.081	120.057	0.09	162	116

$\Delta = |\sin^2\theta_{\text{calc}} - \sin^2\theta_{\text{obs}}| \cdot 1000$ ; intensity normalized at 1000 for the strongest reflection

Table 14.52 Assignment of the Guinier photograph of  $cub-(Fe_{0.167}W_{0.333}P_{0.50})O_{2.5}\square_{0.5}$ , S.G.  $Pm\bar{3}m$ ;  $a = 3.766(2)$  Å.

$h$	$k$	$l$	$4\theta_{\text{calc}}$	$4\theta_{\text{obs}}$	$\Delta$	$I_{\text{calc}}$	$I_{\text{obs}}$
1	0	0	47.211	47.197	0.02	1000	1000
1	1	0	67.257	67.051	0.50	334	535
1	1	1	82.997	82.812	0.54	35	183
2	1	0	108.871	109.001	0.46	415	220
2	1	1	120.272	120.285	0.05	164	123

$\Delta = |\sin^2\theta_{\text{calc}} - \sin^2\theta_{\text{obs}}| \cdot 1000$ ; intensity normalized at 1000 for the strongest reflection

Table 14.53 Assignment of the Guinier photograph of  $cub-(In_{0.167}W_{0.333}P_{0.50})O_{2.5+\delta}$ , S.G.  $Pm\bar{3}m$ ;  $a = 3.761(5)$  Å.

$h$	$k$	$l$	$4\theta_{\text{calc}}$	$4\theta_{\text{obs}}$	$\Delta$	$I_{\text{calc}}$	$I_{\text{obs}}$
1	0	0	47.271	47.223	0.08	1000	1000
1	1	0	67.343	66.965	0.91	370	613
1	1	1	83.106	82.812	0.85	49	206
2	1	1	120.438	120.634	0.74	181	158

$\Delta = |\sin^2\theta_{\text{calc}} - \sin^2\theta_{\text{obs}}| \cdot 1000$ ; intensity normalized at 1000 for the strongest reflection

Table 14.54 Assignment of the Guinier photograph of  $cub-(W_{0.50}P_{0.50})O_{2.75}\square_{0.25}$ , S.G.  $Pm\bar{3}m$ ;  $a = 3.771(2)$  Å.

$h$	$k$	$l$	$4\theta_{\text{calc}}$	$4\theta_{\text{obs}}$	$\Delta$	$I_{\text{calc}}$	$I_{\text{obs}}$
1	0	0	47.145	46.974	0.30	1000	1000
1	1	0	67.161	67.000	0.39	398	572
1	1	1	82.877	82.736	0.41	61	234
2	0	0	96.448	96.360	0.28	236	173
2	1	0	108.708	108.835	0.45	431	217
2	1	1	120.088	120.139	0.19	196	163

$\Delta = |\sin^2\theta_{\text{calc}} - \sin^2\theta_{\text{obs}}| \cdot 1000$ ; intensity normalized at 1000 for the strongest reflection

Table 14.55 Assignment of the Guinier photograph of *tet*-(W<sub>0.75</sub>P<sub>0.25</sub>)O<sub>2.5+0.375</sub>, S.G. *P4/ncc*; *a* = 5.290(2) Å, *c* = 7.698(3) Å.

<i>h</i>	<i>k</i>	<i>l</i>	<b>4θ<sub>calc</sub></b>	<b>4θ<sub>obs</sub></b>	Δ	<b>I<sub>calc</sub></b>	<b>I<sub>obs</sub></b>
0	0	2	46.178	46.202	0.04	460	568
1	1	0	47.53	47.393	0.24	1000	1000
1	0	2	57.315	57.258	0.12	160	66
1	1	2	66.747	66.751	0.01	410	560
2	0	0	67.717	67.542	0.43	250	338
2	0	2	82.765	82.715	0.15	120	192
2	1	2	89.869	89.905	0.11	100	23
0	0	4	94.377	94.305	0.23	70	32
2	2	0	97.274	97.184	0.29	210	100
1	0	4	100.834	100.694	0.47	130	41
1	1	4	107.004	107.092	0.31	120	76
2	2	2	108.997	109.042	0.16	190	170
3	1	2	120.538	120.467	0.27	200	105
2	2	4	140.195	140.176	0.08	90	30

Δ = |sin<sup>2</sup>θ<sub>calc</sub> - sin<sup>2</sup>θ<sub>obs</sub>| · 1000; intensity normalized at 1000 for the strongest reflection

Table 14.56 Assignment of the Guinier photograph of *cub*-(Fe<sub>0.1</sub>V<sub>0.1</sub>W<sub>0.3</sub>P<sub>0.50</sub>)O<sub>2.5+δ</sub>, S.G. *Pm*  $\bar{3}m$ ; *a* = 3.7732(8) Å.

<i>h</i>	<i>k</i>	<i>l</i>	<b>4θ<sub>calc</sub></b>	<b>4θ<sub>obs</sub></b>	Δ	<b>I<sub>calc</sub></b>	<b>I<sub>obs</sub></b>
1	0	0	47.12	47.15	0.05	1000	1000
1	1	0	67.12	67.09	0.08	317	450
1	1	1	82.83	82.81	0.06	29	104
2	0	0	96.39	96.47	0.25	251	143
2	1	0	108.64	108.68	0.15	410	222
2	1	1	120.01	119.95	0.25	155	147

Δ = |sin<sup>2</sup>θ<sub>calc</sub> - sin<sup>2</sup>θ<sub>obs</sub>| · 1000; intensity normalized at 1000 for the strongest reflection

Table 14.57 Assignment of the Guinier photograph of  $tet\text{-(Sc}_{0.167}\text{W}_{0.333}\text{P}_{0.50})\text{O}_{2.5}\square_{0.5}$ , S.G.  $P4/ncc$ ;  $a = 5.2760(6)$  Å,  $c = 7.717(2)$  Å.

$h$	$k$	$l$	$4\theta_{\text{calc}}$	$4\theta_{\text{obs}}$	$\Delta$	$I_{\text{calc}}$	$I_{\text{obs}}$
0	0	2	46.058	45.975	0.14	480	479
1	1	0	47.661	47.588	0.13	1000	1000
1	1	2	66.757	66.71	0.11	270	429
2	0	0	67.908	67.901	0.01	180	300
2	0	2	82.854	82.852	0.01	40	166
0	0	4	94.12	94.112	0.03	90	38
2	2	0	97.556	97.54	0.05	240	143
1	1	4	106.835	106.844	0.03	110	52
2	2	2	109.199	109.211	0.04	170	129
3	1	0	109.98	109.93	0.18	220	150
3	1	2	120.788	120.795	0.02	140	105
2	2	4	140.221	140.221	0.0	110	34
4	0	0	142.922	142.933	0.05	90	31

$\Delta = |\sin^2\theta_{\text{calc}} - \sin^2\theta_{\text{obs}}| \cdot 1000$ ; intensity normalized at 1000 for the strongest reflection

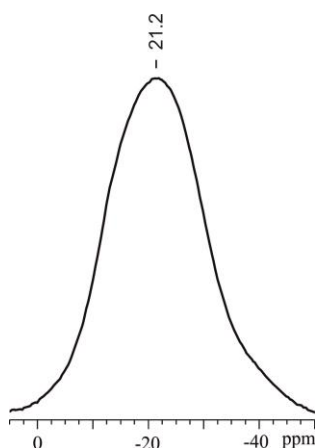


Figure 14.16  $^{31}\text{P}$ -MAS-NMR spectra of  $(\text{In}_{0.167}\text{W}_{0.333}\text{P}_{0.50})\text{O}_{2.5}\square_{0.5}$  ( $cub\text{-WO}_3$  type) obtained by SCS followed by heating in air at  $700$  °C. The broadness of the signal might be due to low crystallinity as well as coupling of In nuclei.



Table 14.58 Anisotropic displacement parameters ( $\text{\AA}^2$ ) for  $(\text{Mo}_{0.33}\text{W}_{0.67})\text{OPO}_4$  ( $\text{WOPO}_4$  structure type).

Atom	$U_{11}$	$U_{22}$	$U_{33}$	$U_{23}$	$U_{13}$	$U_{12}$
W1/Mo1	0.0085(2)	0.0117(2)	0.0108(2)	0	-0.0005(1)	0
W2/Mo2	0.0084(2)	0.0117(2)	0.0107(2)	0	-0.0006(1)	0
P1	0.0093(8)	0.0179(9)	0.0109(8)	0	-0.0008(6)	0
P2	0.0095(8)	0.0168(9)	0.0110(8)	0	-0.0005(6)	0
O1	0.018(3)	0.066(7)	0.025(4)	0	-0.008(3)	0
O2	0.019(3)	0.058(6)	0.023(3)	0	0.007(3)	0
O3	0.028(3)	0.044(5)	0.015(3)	0	-0.006(2)	0
O4	0.029(4)	0.040(5)	0.012(3)	0	0.006(2)	0
O5	0.104(7)	0.099(8)	0.032(4)	0.010(4)	-0.003(4)	-0.088(7)
O6	0.063(6)	0.044(5)	0.018(3)	-0.010(3)	-0.009(3)	0.040(5)
O7	0.058(6)	0.052(6)	0.024(4)	-0.017(4)	0.019(4)	-0.042(5)
O8	0.091(6)	0.109(9)	0.042(4)	0.030(5)	0.017(4)	0.085(7)

Table 14.59 Assignment of the XRPD of  $(\text{Fe}^{\text{III}}_{0.33}\text{W}^{\text{VI}}_{0.67})\text{OPO}_4$  ( $\text{W}^{\text{V}}\text{OPO}_4$  structure type) S.G.  $P2_1/m$ ;  $a = 6.5158(11)$   $\text{\AA}$ ,  $b = 5.1771(6)$   $\text{\AA}$ ,  $c = 11.0542(15)$   $\text{\AA}$ ,  $\beta = 90.20(1)^\circ$ .

$h$	$k$	$l$	$4\theta_{\text{calc}}$	$4\theta_{\text{obs}}$	$\Delta$	$I_{\text{calc}}$	$I_{\text{obs}}$
1	0	1	31.598	31.646	0.06	110	339
0	0	2	32.043	32.027	0.02	570	553
1	0	-2	42.044	42.087	0.07	368	540
1	1	0	43.817	43.780	0.06	1000	1000
1	1	1	46.743	46.705	0.07	311	567
1	1	-2	54.461	54.467	0.01	302	506
1	0	-3	55.495	55.528	0.07	115	162
2	0	1	57.134	57.130	0.01	8	20
2	0	-2	63.614	63.618	0.01	49	58
1	1	-3	65.564	65.610	0.11	90	120
1	1	3	65.713	65.710	0.01	91	119
2	1	1	66.979	67.001	0.05	226	335
0	1	4	73.671	73.706	0.09	275	313
1	2	1	76.532	76.568	0.10	21	60
2	1	3	81.803	81.790	0.04	13	70
2	2	-1	90.882	90.852	0.09	41	34
1	1	-5	93.434	93.432	0.01	13	25
2	2	-2	95.441	95.472	0.10	74	75
2	0	-5	99.427	99.441	0.05	82	67
2	2	-3	102.719	102.750	0.11	121	110
3	1	-3	103.682	103.680	0.01	139	100
0	1	6	105.377	105.369	0.03	112	74
3	2	1	111.707	111.715	0.03	138	122
2	3	-1	122.591	122.585	0.02	140	41
3	1	-5	124.815	124.783	0.13	102	70
0	3	4	127.000	126.980	0.08	97	63

$\Delta = |\sin^2\theta_{\text{calc}} - \sin^2\theta_{\text{obs}}| \cdot 1000$ ; intensity normalized on 1000 for the strongest reflection

Table 14.60 Assignment of the Guinier photograph of  $(\text{Cr}^{\text{III}}_{0.33}\text{W}^{\text{VI}}_{0.67})\text{OPO}_4$  ( $\text{W}^{\text{VOPO}_4}$  structure type, S.G.  $P2_1/m$ ;  $a = 6.4740(10)$  Å,  $b = 5.1569(4)$  Å,  $c = 11.0486(18)$  Å,  $\beta = 90.11(1)^\circ$ ).

$h$	$k$	$l$	$4\theta_{\text{calc}}$	$4\theta_{\text{obs}}$	$\Delta$	$I_{\text{calc}}$	$I_{\text{obs}}$
1	0	-1	31.679	31.661	0.02	87	154
1	0	1	31.731	31.832	0.12	212	391
0	0	2	32.060	31.962	0.12	759	510
1	0	2	42.286	42.190	0.15	634	596
1	1	0	44.035	44.014	0.03	1000	1000
1	1	1	46.935	46.901	0.06	580	659
1	1	-2	54.676	54.666	0.02	335	527
1	1	2	54.738	54.746	0.02	338	400
1	0	-3	55.646	55.597	0.10	100	193
1	0	3	55.738	55.768	0.06	217	178
2	0	1	57.456	57.460	0.01	4	27
2	0	-2	63.983	63.989	0.01	40	67
2	0	2	64.091		0	94	66
1	1	-3	65.768	65.751	0.04	120	117
1	1	3	65.847	65.852	0.01	120	136
2	1	-1	67.279	67.343	0.16	377	390
0	2	0	69.525	69.545	0.05	290	240
1	0	-4	70.546	70.516	0.07	153	108
1	0	4	70.645	70.646	0.00	151	120
0	1	4	73.768	73.778	0.03	365	335
0	2	2	76.994	76.960	0.09	74	106
1	2	-2	82.045	82.082	0.11	65	106
3	0	-1	85.272		0	54	62
3	0	1	85.336	85.382	0.14	55	84
2	2	-1	91.357	91.351	0.02	43	71
2	2	-2	95.921	95.959	0.12	75	103
1	2	-4	100.724	100.745	0.07	125	128
2	2	3	103.306	103.283	0.08	131	157
3	1	-3	104.291	104.252	0.13	182	127
3	1	3	104.453	104.421	0.11	188	135
0	1	6	105.478	105.510	0.11	149	106
1	3	0	110.484	110.464	0.07	110	89
3	2	1	112.328	112.331	0.01	184	174
1	3	2	115.840	115.835	0.02	47	74
2	3	-1	123.205	123.191	0.06	71	69
2	3	1	123.238	123.271	0.13	70	72
0	3	4	127.422	127.411	0.04	99	96

$\Delta = |\sin^2\theta_{\text{calc}} - \sin^2\theta_{\text{obs}}| \cdot 1000$ ; intensity normalized on 1000 for the strongest reflection

Table 14.61 Assignment of the Guinier photograph of  $(\text{Mo}^{\text{III}}_{0.33}\text{W}^{\text{VI}}_{0.67})\text{OPO}_4$  ( $\text{W}^{\text{V}}\text{OPO}_4$  structure type, S.G.  $P2_1/m$ ;  $a = 6.5418(6)$  Å,  $b = 5.2176(5)$  Å,  $c = 11.1730(7)$  Å,  $\beta = 90.307(6)^\circ$ ).

$h$	$k$	$l$	$4\theta_{\text{calc}}$	$4\theta_{\text{obs}}$	$\Delta$	$I_{\text{calc}}$	$I_{\text{obs}}$
1	0	1	31.442	31.339	0.12	120	381
0	0	2	31.701	31.679	0.03	580	488
1	0	-2	41.673	41.715	0.06	360	500
1	0	2	41.897	41.885	0.02	360	332
1	1	0	43.538	43.536	0.0	1000	1000
1	1	-1	46.336	46.378	0.07	280	537
1	1	-2	53.999	54.002	0.01	300	720
1	0	-3	54.942	54.932	0.02	100	190
1	0	3	55.201	55.232	0.06	100	140
2	0	-2	63.192	63.196	0.01	50	113
2	0	2	63.496	63.516	0.05	50	117
1	1	-3	64.943	64.927	0.04	90	135
1	1	3	65.166	65.147	0.04	90	106
2	1	-1	66.488	66.537	0.12	230	366
2	1	1	66.633	66.657	0.06	230	320
0	2	0	68.69	68.668	0.05	220	200
1	0	-4	69.654	69.629	0.06	90	217
1	0	4	69.933	69.929	0.01	90	145
2	1	-2	72.164	72.17	0.01	60	123
2	1	2	72.434	72.47	0.09	60	124
0	1	4	72.91	72.89	0.05	280	764
2	0	3	73.262	73.27	0.02	70	147
2	2	-2	94.716	94.697	0.06	70	108
2	2	2	94.933	94.957	0.08	70	136
2	2	-3	101.865	101.858	0.02	120	182
2	2	3	102.173	102.148	0.08	120	156
3	1	-3	102.947	102.958	0.04	140	188
3	1	3	103.405	103.378	0.09	140	265
0	1	6	104.21	104.228	0.06	110	133
1	3	0	109.1	109.089	0.04	100	85
2	3	1	121.719	121.73	0.04	50	163
0	2	6	122.177	122.18	0.01	40	68
2	2	-5	122.78	122.801	0.08	50	65
3	1	-5	123.693	123.701	0.03	100	135
3	1	5	124.371	124.381	0.04	100	130
4	1	3	129.683	129.661	0.09	20	50
0	0	8	133.885	133.881	0.02	20	57
2	1	-7	135.064	135.041	0.09	30	51
2	1	7	135.667	135.681	0.05	30	50

$$\Delta = |\sin^2\theta_{\text{calc}} - \sin^2\theta_{\text{obs}}| \cdot 1000; \text{ intensity normalized at 1000 for the strongest reflection}$$

## 14.6 Mixed metal monophosphate tungsten bronzes

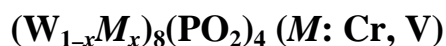


Table 14.62 Assignment of the Guinier photograph of  $(\text{Cr}^{\text{III}}_{1/6}\text{W}^{\text{VI}}_{5/6}\text{O}_3)_8(\text{PO}_2)_4$  {structure type  $(\text{WO}_3)_8(\text{PO}_2)_4$  [95]; S.G.  $P2_1$ ;  $a = 6.483(2) \text{ \AA}$ ,  $b = 5.216(1) \text{ \AA}$ ,  $c = 17.22(1) \text{ \AA}$ ,  $\beta = 90.32(3)^\circ$ }.

$h$	$k$	$l$	$4\theta_{\text{calc}}$	$4\theta_{\text{obs}}$	$\Delta$	$I_{\text{calc}}$	$I_{\text{obs}}$
0	0	2	20.533	20.596	0.05	590	316
1	0	1	29.228	29.277	0.05	39	93
0	1	2	39.773	39.808	0.05	29	126
0	0	4	41.234	41.208	0.04	426	635
1	0	3	41.419	41.478	0.09	325	385
1	1	0	43.704	43.788	0.14	160	193
1	1	1	44.956	45.028	0.12	1000	1000
1	1	-2	48.328	48.408	0.14	773	942
1	0	-4	49.484	49.447	0.07	480	290
1	0	4	49.745	49.717	0.05	0	218
1	1	-3	53.626	53.617	0.02	405	572
1	1	-4	60.33	60.386	0.12	59	58
2	1	1	65.885	65.895	0.02	87	150
2	1	-2	68.228	68.304	0.19	468	612
2	1	2	68.423	68.444	0.05	285	587
0	2	0	68.719	68.724	0.01	86	506
2	0	4	69.413	69.404	0.02	86	106
1	2	-3	80.786	80.751	0.1	111	156
2	2	0	89.107	89.128	0.06	24	72
2	2	-3	94.736	94.705	0.1	127	115
1	3	-1	109.759	109.767	0.03	103	145
3	2	-1	110.806	110.786	0.07	281	244
3	2	1	110.906	110.886	0.07	89	111

$\Delta = |\sin^2\theta_{\text{calc}} - \sin^2\theta_{\text{obs}}| \cdot 1000$ ; intensity normalized on 1000 for the strongest reflection

Table 14.63 Assignment of the Guinier photograph of  $(V^{III}_{1/6}W^{VI}_{5/6}O_3)_8(PO_2)_4$  {structure type  $(WO_3)_8(PO_2)_4$  [95], S.G.  $P2_1$ ;  $a = 6.4929(8) \text{ \AA}$ ,  $b = 5.2217(5) \text{ \AA}$ ,  $c = 17.322(3) \text{ \AA}$ ,  $\beta = 90.486(7)^\circ$ }.

$h$	$k$	$l$	$4\theta_{\text{calc}}$	$4\theta_{\text{obs}}$	$\Delta$	$I_{\text{calc}}$	$I_{\text{obs}}$
0	0	2	20.41	20.333	0.06	590	316
0	1	2	39.674	39.687	0.02	21	100
0	0	4	40.984	40.959	0.04	430	580
1	0	3	41.31	41.289	0.03	320	422
1	1	0	43.647	43.584	0.1	160	113
1	1	-1	44.797	44.776	0.04	1000	971
1	1	-2	48.19	48.211	0.04	390	475
1	1	2	48.39	48.341	0.09	388	420
1	0	-4	49.185	49.183	0.0	244	244
1	0	4	49.578	49.523	0.1	239	200
1	1	3	53.698	53.679	0.04	697	785
1	0	-5	58.176	58.205	0.06	75	114
1	0	5	58.597	58.595	0.0	78	100
2	0	-3	62.946	62.96	0.03	38	48
2	0	3	63.416	63.431	0.03	37	55
2	1	-1	65.658	65.623	0.08	86	90
2	1	-2	68.052	68.045	0.02	250	291
2	1	2	68.344	68.335	0.02	217	322
0	2	0	68.636	68.635	0.0	371	343
2	0	4	69.289	69.316	0.07	85	136
0	1	6	71.003	70.967	0.09	435	396
2	1	-3	71.931	71.948	0.04	40	50
2	1	3	72.35	72.328	0.06	37	40
2	2	-3	94.498	94.513	0.05	64	59
2	2	3	94.833	94.863	0.1	74	69
2	2	-4	98.693	98.702	0.03	156	141
2	2	4	99.125	99.122	0.01	130	127
2	0	-8	100.84	100.851	0.04	75	118
2	0	8	101.689	101.711	0.07	75	85
3	1	-5	105.26	105.259	0.0	244	241
3	1	5	106.032	106.018	0.05	218	196
1	3	-1	109.604	109.616	0.04	102	114
3	2	-1	110.615	110.625	0.04	281	212
1	3	2	111.334	111.315	0.07	90	54
3	1	-7	118.257	118.238	0.07	113	76

$\Delta = |\sin^2\theta_{\text{calc}} - \sin^2\theta_{\text{obs}}| \cdot 1000$ ; intensity normalized on 1000 for the strongest reflection

### 14.7 Access to thermodynamically metastable oxo-compounds via reduction by moist hydrogen

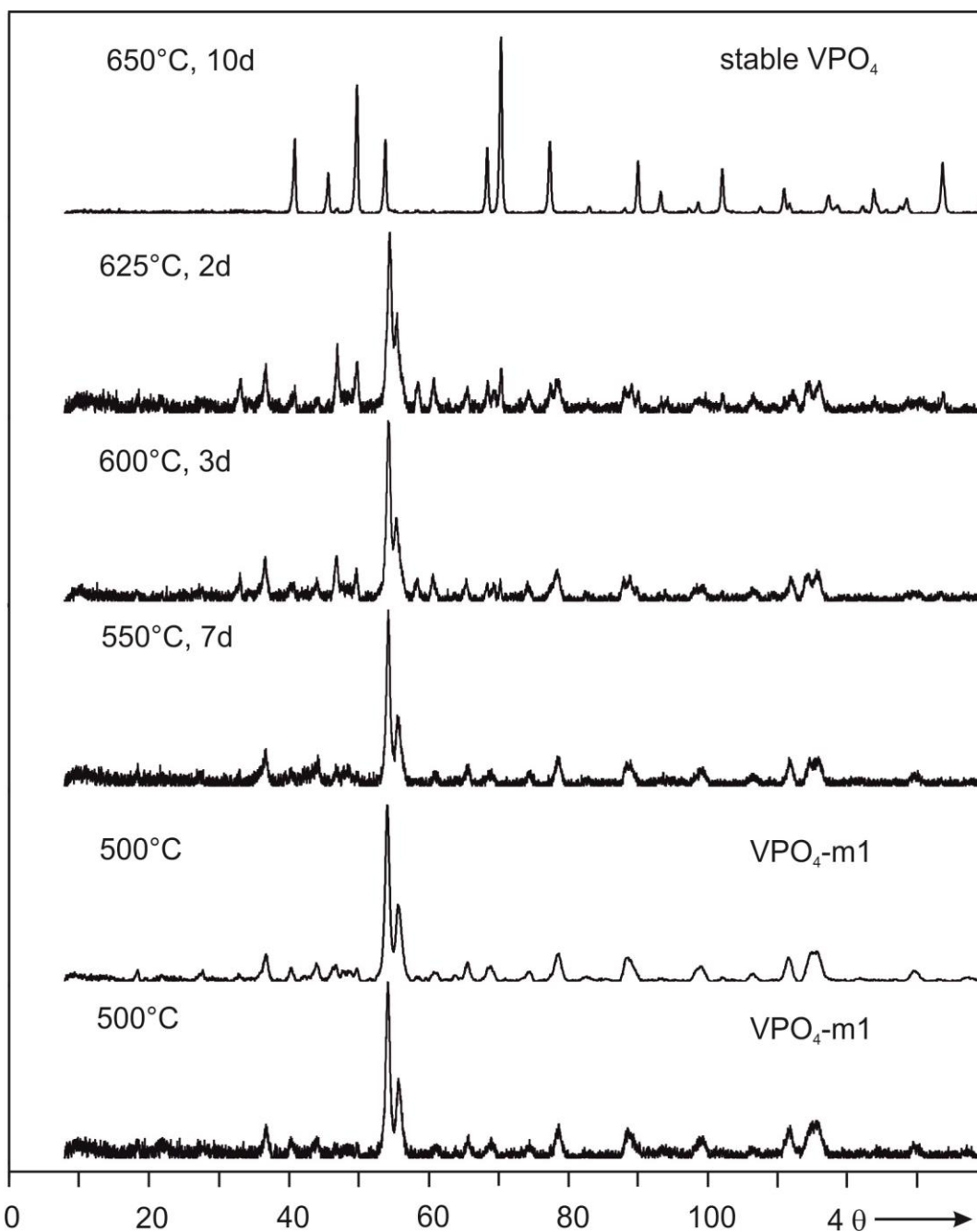


Figure 14.17 Monitoring the changes of metastable  $\text{VPO}_4\text{-m1}$  [this thesis] into thermodynamically stable  $\text{VPO}_4$  [83] phase from heating experiments in sealed silica ampoules by XRPD patterns. X-ray exposure time 15 min except 2<sup>nd</sup> pattern from bottom where the x-ray exposure time is 5 hours.

Table 14.64 Atomic coordinates of predicted new metastable polymorph of VPO<sub>4</sub> containing VO<sub>4</sub> and PO<sub>4</sub> tetrahedra obtained from DFT calculation, S.G. *Pnma*;  $a = 8.4891 \text{ \AA}$ ,  $b = 5.6533 \text{ \AA}$ ,  $c = 9.0598 \text{ \AA}$  (left) and S. G. *P2<sub>1</sub>/m*;  $a = 5.5289 \text{ \AA}$ ,  $b = 9.1850 \text{ \AA}$ ,  $c = 8.8903 \text{ \AA}$ ,  $\beta = 95.6362^\circ$  (right).

Atom	S. G. <i>Pnma</i>			S. G. <i>P2<sub>1</sub>/m</i>		
	<i>x</i>	<i>y</i>	<i>z</i>	<i>x</i>	<i>y</i>	<i>z</i>
V1	0.15257	1/4	0.34794	0.27636	0.35483	0.15180
P1	0.27626	1/4	0.02011	0.22521	0.03579	0.28650
O1	0.14251	1/4	0.14156	0.24850	0.15133	0.16218
O2	0.25450	0.02620	-0.07852	-0.02509	-0.04034	0.27383
O3	-0.06352	1/4	0.40083	0.41926	-0.41932	-0.23873
O4				0.25968	0.38605	-0.05882

Table 14.65 Assignment of the Guinier photograph of metastable VPO<sub>4</sub>-m2, V<sub>2</sub>(VO)(P<sub>2</sub>O<sub>7</sub>)(PO<sub>4</sub>) obtained by moist H<sub>2</sub> reduction of  $\beta$ -VOPO<sub>4</sub> at 700 °C for one day, S.G. *P2<sub>1</sub>/m*;  $a = 8.794(4) \text{ \AA}$ ,  $b = 5.269(2) \text{ \AA}$ ,  $c = 10.398(6) \text{ \AA}$ ,  $\beta = 112.60(4)^\circ$ .

<i>h</i>	<i>k</i>	<i>l</i>	$4\theta_{\text{calc}}$	$4\theta_{\text{obs}}$	$\Delta$	$I_{\text{calc}}$	$I_{\text{obs}}$
0	0	1	18.409	18.382	0.02	1000	808
1	0	0	21.782	21.734	0.04	560	418
1	0	-1	22.482	22.454	0.02	100	120
0	0	2	36.939	36.892	0.07	180	287
0	1	1	38.4	38.332	0.1	100	56
1	1	0	40.15	40.153	0.0	900	970
2	0	0	43.764	43.704	0.1	170	149
1	1	1	47.684	47.645	0.07	850	780
1	1	-2	48.672	48.625	0.08	520	421
1	0	2	49.792	49.766	0.05	1000	1000
3	0	-1	61.337	61.408	0.16	70	916
2	1	1	63.81	63.828	0.04	530	119
0	1	3	65.431	65.428	0.01	380	412
0	2	0	68.004	68.058	0.13	250	255
3	1	0	74.661	74.658	0.01	180	235
3	2	-1	92.875	92.856	0.06	330	225
3	1	2	95.337	95.315	0.07	150	256
2	0	4	102.151	102.173	0.07	230	152

$$\Delta = |\sin^2\theta_{\text{calc}} - \sin^2\theta_{\text{obs}}| \cdot 1000; \text{ intensity normalized at 1000 for the strongest reflection}$$

Table 14.66 Selected interatomic distances (Å) of  $VPO_4$ -m2,  $V_2(VO)(P_2O_7)(PO_4)$  obtained by DFT calculation with adjusted lattice parameters from the experimental XRPD pattern.

type	distances	type	distances	type	distances
V1 – O5	1.8925(7)	V2 – O4	1.9140(12)	V3 – O9	1.9002(7)
– O5	1.8925(7)	– O8	1.9223(5)	– O9	1.9002(7)
– O3	2.0167(6)	– O8	1.9223(5)	– O5	1.9162(10)
– O3	2.0167(6)	– O7	2.0582(13)	– O6	2.0612(8)
– O1	2.0707(8)	– O6	2.0847(6)	– O6	2.0612(8)
– O1	2.0707(8)	– O6	2.0847(6)	– O7	2.1611(9)
P1 – O4	1.5121(9)	P2 – O9	1.5003(5)	P3 – O8	1.5036(4)
– O3	1.5690(7)	– O9	1.5003(5)	– O8	1.5036(4)
– O6	1.5539(5)	– O7	1.5481(10)	– O1	1.5653(10)
– O6	1.5539(5)	– O2	1.6231(7)	– O2	1.6209(9)

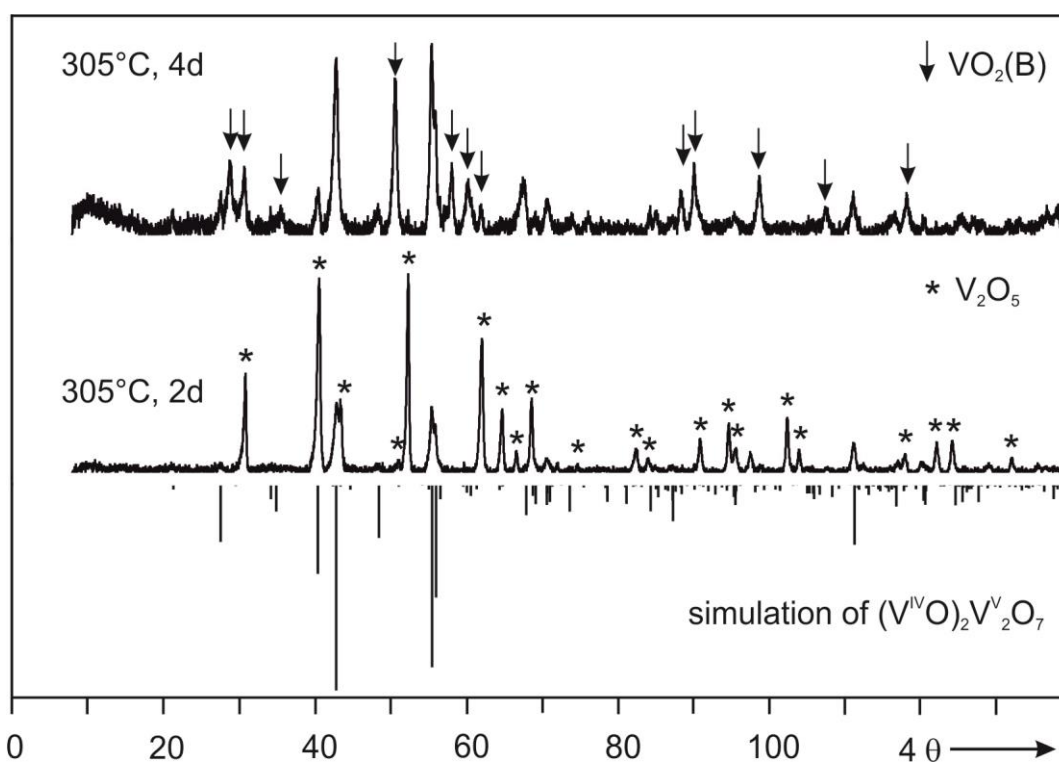


Figure 14.18 Monitoring the synthesis of  $V_4O_9$  by XRPD from the reduction process of  $V_2O_5$  with moist hydrogen.



## 15 References

- [1] R. Glaum, *Thesis of Habilitation (in german)*, University of Giessen, **1999**,  
URN: nbn:de:hebis:26-opus-1240.
- [2] G. Bergerhoff, R. Hundt, R. Sievers, I. D. Brown, *J. Chem. Inf. Comput. Sci.*  
**1983**, 23, 66; Inorganic Crystal Structure Database, (ICSD) FIZ/NIST, Germany  
/USA Vers. **2015**-1, FindIt Vers. 1.9.6.
- [3] Powder Diffraction File database (PDF-2), The International Center for  
Diffraction Data (ICDD) **2014**.
- [4] A. Durif, *Crystal Chemistry of Condensed Phosphates*, Plenum Press,  
New York, **1995**.
- [5] A. K. Padhi, K. S. N. Sawamy, J. B. Goodenough, *Electrochemical Soc. Meeting  
Abstracts* **1996**, 73.
- [6] Y. Si, H. R. Kunz, J. M. Fenton, *J. Electrochem. Soc.* **2004**, 151, 623.
- [7] P. M. Forster, J. Eckert, J.-S. Chang, S.-E. Park, G. Férey, A. K. Cheetham,  
*J. Am. Chem. Soc.* **2003**, 125, 1309.
- [8] L.-O. Hagman, P. Kierkegaard, *Acta. Chem. Scand.* **1968**, 22, 1822.
- [9] P. I. Tordjman, R. Masse, J. C. Guitel, *Z. Kristallogr.* **1974**, 139, 103.
- [10] Z. Hiroi, M. Azuma, Y. Fujishiro, T. Saito, M. Takano, F. Izumi, T. Kamiyama,  
T. Ikeda, *J. Solid State Chem.* **1999**, 146, 369.
- [11] E. Bordes, P. Courtine, *J. Catal.* **1979**, 57, 236.
- [12] R. Schlögl, *Modern Heterogenous Oxidation Catalysis* (Ed: N. Mizuno), Wiley  
VCH, Weinheim, **2009**.
- [13] P. K. Grasselli, *Top. Catal.* **1999**, 49, 141.
- [14] P. Mars, D. W. van Krevelen, *Chem. Eng. Sci. Suppl.* **1954**, 3, 3.
- [15] E. Heracleous, A. A. Lemonidou, *J. Cat.* **2006**, 237, 175.
- [16] T. K. Todorova, M. V. Gandglia-Pirovano, J. Sauer,  
*J. Phys. Chem. C* **2007**, 111, 5141.
- [17] R. I. Bergman, N. W. Frisch, *US Patent 3 293 268*, **1966**.
- [18] G. Centi, F. Trifiro, J. R. Ebner, V. M. Franchetti, *Chem. Rev.* **1988**, 88, 55.
- [19] J. W. Johnson, D. C. Johnston, A. J. Jacobson, J. F. Brody,  
*J. Am. Chem. Soc.* **1984**, 106, 8123.

- [20] M. E. Leonowicz, J. W. Brody, J. F. Brody, H. F. Shannon, J. M. Newsam, *J. Solid State Chem.* **1985**, *56*, 370.
- [21] N. Ballarini, F. Cavani, C. Cortelli, S. Ligi, F. Pierelli, F. Trifiro, C. Fumagalli, G. Mazzoni, T. Monti, *Top. Catal.* **2006**, *38*, 147.
- [22] V. A. Zazhigalov, A. I. Pyatnitskaya, I. V. Bacherikova, G. A. Komashko, G. Ladwig, V. M. Belousov, *React. Kinet. Catal. Lett.* **1983**, *23*, 119.
- [23] G. J. Hutchings, A. Desmartin-Chomel, R. Oller, J.-C. Volta, *Nature* **1994**, *368*, 41.
- [24] G. J. Hutchings, I. J. Ellison, M. T. Sananes, J.-C. Volta, *Catal. Lett.* **1996**, *38*, 231.
- [25] M. Conte, G. Budroni, J. K. Bartley, S. H. Taylor, A. F. Carley, A. Schmidt, D. M. Murphy, F. Girgsdies, T. Ressler, R. Schlögl, G. J. Hutchings, *Science* **2006**, *313*, 1270.
- [26] P. A. Agaskar, R. K. Grasselli, D. J. Buttrey, B. White, *Stud. Surf. Sci. Catal.* **1997**, *110*, 219.
- [27] M. E. Davis, C. J. Dillon, J. H. Holles, J. Labinger, *Angew. Chem. Int. Ed.* **2002**, *41*, 858.
- [28] V. V. Guliants, J. B. Benziger, S. Sundaresan, I. E. Wachs, A. M. Hirt, *Cat. Lett.* **1999**, *62*, 87.
- [29] A. A. Rownaghi, Y. H. T. Yap, F. Rezaei, *Cat. Lett.* **2009**, *130*, 504.
- [30] R. Glaum, E. Benser, H. Hibst, *Chem. Ing. Tech.* **2007**, *79*, 843.
- [31] E. Benser, R. Glaum, T. Dross, *Chem. Mater.* **2007**, *19*, 4341.
- [32] R. M. Contractor, H. E. Bergna, H. S. Horowitz, C. M. Blackstone, B. Malone, C. C. Torardi, B. Griffiths, U. Chowdry, A. W. Sleight, *Cat. Today* **1987**, *1*, 49.
- [33] P. K. Grasselli, *Top. Catal.* **2002**, *21*, 79.
- [34] J. L. Callahan, P. K. Grasselli, *AIChE J.* **1963**, *9*, 755.
- [35] F. Trifiro, R. K. Grasselli, *Top. Catal.* **2014**, *57*, 1188.
- [36] G. J. Hutchings, C. J. Kiely, M. T. S. Schulz, A. Burrows, J.-C. Volta, *Catal. Today* **1998**, *40*, 273.
- [37] B. K. Hodnett: *Heterogeneous Catalytic Oxidation*, John Wiley & Sons, Chichester, **2000**.
- [38] C. Schmitt, *Ph. D. Thesis*, University of Darmstadt, Germany **2009**.
- [39] G. Koyano, T. Okuhara, M. Misono, *J. Am. Chem. Soc.* **1998**, *120*, 767.
- [40] G. Schmidt, R. Grünh, *J. Cryst. Growth* **1982**, *57*, 585.
- [41] A. Schmidt, *Ph. D. Thesis*, University of Giessen, Germany **2002**.

- [42] H. Schäfer, *Chemische Transportreaktionen*, Verlag Chemie, Weinheim, **1962**.
- [43] M. Binnewies, R. Glaum, M. Schmidt, P. Schmidt, *Chemical Vapor Transport Reactions*, W. de Gruyter, Berlin/Boston, **2012**.
- [44] K. C. Patil, M. S. Hedge, T. Rattan, S. T. Aruna, *Chemistry of nanocrystalline oxide Materials*, World Scientific, Singapore, **2008**.
- [45] K. Deshpande, A. S. Mulasayan, A. Varma, *Chem. Mater.* **2004**, *24*, 4896.
- [46] I. Tanaka, M. Yao, M. Suzuki, K. Hikichi, T. Matsumoto, M. Kozasa, C. Katayama, *J. App. Crystallogr.* **1990**, *23*, 334.
- [47] H. Putz, K. Brandenburg, *Match! Phase Identification from powder diffraction*, ver. 1.11h, Crystal Impact, Bonn, Germany, <http://www.crystalimpact.com/match>.
- [48] Origin 6.1G, OriginLab Corporation, **1991-2000**.
- [49] K. Yvon, W. Jeitschko, E. Parthé, *J. Appl. Crystallogr.* **1977**, *10*, 73.
- [50] G. Meyer, J. Soose: "SOS-Programme zur Auswertung von Guinier-Aufnahmen", *Staatsexamensarbeit*, University of Giessen, **1980**.
- [51] P. E. Werner, L. Eriksson, M. Westdahl, *J. Appl. Cryst.* **1985**, *18*, 367.
- [52] A. Boultif, D. Louër, *J. Appl. Cryst.* **1991**, *24*, 987.
- [53] J. Visser, *J. Appl. Cryst.* **1966**, *2*, 89.
- [54] J. R. Carvajal, T. Roisnel: "FullProf98 and WinPLOTR: New Windows 95/NT Applications for Diffraction, Commission For Powder Diffraction", *IUCr., Newsletter N°20*, **1998**.
- [55] G. M. Sheldrick: *SHELXS-97: Program for crystal structure solution*, University of Göttingen, **1997**.
- [56] L. Palatinus, G. Chapuis, *J. Appl. Cryst.* **2007**, *40*, 786.
- [57] A. L. Patterson, *Phys. Rev.* **1934**, *46*, 372.
- [58] A. L. Patterson, *Z. Kristallogr.* **1935**, *A90*, 517.
- [59] J. Karle, H. Hauptmann, *Acta Crystallogr.* **1952**, *10*, 267.
- [60] H. Hauptmann, *Acta Crystallogr.* **1950**, *3*, 181.
- [61] G. Oszlanyi, A. Süto, *Acta Cryst.* **2004**, *A60*, 134.
- [62] L. Palatinus, *Acta Cryst.* **2004**, *A60*, 604.
- [63] J. Karle, H. Hauptmann, *Acta Crystallogr.* **1956**, *9*, 635.
- [64] W. Massa, *Crystal structure determination*, Springer-Verlag Berlin Heidelberg New York, **2004**.
- [65] P. Kubelka, F. Munk, *Z. Tech. Phys.* **1931**, *12*, 593.

- [66] E. Krausz, *Aust. J. Chem.* **1993**, *46*, 1041.
- [67] E. Krausz, *AOS news.* **1998**, *12*, 21.
- [68] S. Stoll, A. Schweiger, *J. Mag. Reson.* **2006**, *178*, 72.
- [69] M. Carlisle, J. Welch, D. Steele, M. Miller, *Spinsight Software*, Varian Associates Inc., U. S. A., **1998**.
- [70] [http://en.wikipedia.org/wiki/X-ray\\_photoelectron\\_spectroscopy](http://en.wikipedia.org/wiki/X-ray_photoelectron_spectroscopy), retrieve on July 2015.
- [71] MultiPak AES & XPS Data Reduction Software by ULVAC-PHI. Inc., Japan.
- [72] D. Newbury, *Advanced Scanning Electron Microscopy and X-ray Microanalysis*, Plenum Press, New York, **1987**.
- [73] Bedienungsanleitung, *PVSUPQ (EDAX-Analysensystem)*, Philips, Eindhoven, Netherland, **1986**.
- [74] H. G. von Schnering, J. Chang, K. Peters, E. M. Peters, F. R. Wagner, Y. Grin, G. Thiele, *Z. Anorg. Allg. Chem.* **2003**, *629*, 516.
- [75] M. Hanawa, H. Imoto, *J. Solid State Chem.* **1999**, *144*, 325.
- [76] P. Kierkegaard, *Acta Chem. Scand.* **1960**, *14*, 657.
- [77] P. Kierkegaard, S. Asbrink, *Acta Chem. Scand.* **1964**, *18*, 2329.
- [78] C. Litterscheid, *Ph. D. Thesis*, Bonn University, Germany **2009**, <http://hss.ulb.uni-bonn.de/2009/1928/1928.htm>.
- [79] P. Kierkegaard, *Acta Chem. Scand.* **1958**, *12*, 1715.
- [80] S. E. Lister, A. Soleilhavoup, R. L. Withers, P. Hodgkinson, J. S. O. Evans, *Inorg. Chem.* **2010**, *49*, 2290.
- [81] S. Geupel, K. Pilz, S. van Smaalen, F. Büllfeld, A. Prokofiev, W. Assmus, *Acta Cryst.* **2002**, *C58*, i9.
- [82] H.-J. Koo, M. Whangbo, P. D. VerNooy, C. C. Torardi, W. J. Marshall, *Inorg. Chem.* **2002**, *41*, 4664.
- [83] R. Glaum, R. Gruehn, *Z. Anorg. Allg. Chem.* **1992**, *198*, 41.
- [84] K. Selte, A. Kjekshus, A. F. Andresen, *Acta Chem. Scand.* **1972**, *26*, 4057.
- [85] M. Smirnov, N. Mazhenov, N. Aliouane, P. S. Gregoire, *J. Phys. Condes. Matt.* **2010**, *22*, 225403.
- [86] P. Royen, T. Korinth, *Z. Anorg. Allg. Chem.* **1957**, *291*, 227.
- [87] National Bureau of Standard, (U.S.), Circ. 539 8, 29, **1959**.

- [88] M. Saiful Islam, *Ph. D. Thesis*, Bonn University, Germany **2012**,  
<http://hss.ulb.uni-bonn.de/2012/2760/2760.htm>.
- [89] M. Westerland-Sundbäck, *Acta Chem. Scand.* **1971**, 25, 1429.
- [90] S.-L. Wang, C.-C. Wang, K.-H. Lii, *J. Solid State Chem.* **1989**, 82, 298.
- [91] N. Kinomura, M. Hirose, N. Kumada, F. Muto, *J. Solid State Chem.* **1988**, 77, 156.
- [92] H. Mathis, *Diploma Thesis*, University of Giessen, Germany **1990**.
- [93] A. Leclaire, J. Chardon, B. Raveau, *J. Solid State Chem.* **2000**, 155, 112.
- [94] V. V. Lisnyak, N. V. Stus, N. S. Slobodyanik, N. M. Belyavina, V. Ya. Maekiv,  
*J. Alloys Compd.* **2000**, 309, 83.
- [95] J. P. Giroult, M. Goreaud, Ph. Labbe, B. Raveau,  
*Acta Crystallogr.* **1981**, B37, 2139.
- [96] B. Domenges, M. Hervieu, B. Raveau, R. J. D. Tilley,  
*J. Solid State Chem.* **1984**, 54, 10.
- [97] P. Roussel, G. Mather, B. Domenges, D. Giroult, Ph. Labbe,  
*Acta Crystallogr.* **1998**, B54, 365.
- [98] B. Domenges, M. Goreaud, Ph. Labbe, B. Raveau,  
*Acta Crystallogr.* **1982**, B38, 1724.
- [99] J. P. Giroult, M. Goreaud, Ph. Labbe, B. Raveau,  
*J. Solid State Chem.* **1982**, 44, 407.
- [100] P. Roussel, O. Perez, Ph. Labbe, *Acta Crystallogr.* **2001**, B57, 603.
- [101] J. P. Giroult, M. Goreaud, Ph. Labbe, B. Raveau,  
*Acta Crystallogr.* **1980**, B36, 2570.
- [102] J. P. Giroult, M. Goreaud, Ph. Labbe, B. Raveau,  
*Acta Crystallogr.* **1991**, B37, 2139.
- [103] A. Magnéli, *Acta Chem. Scand.* **1948**, 2, 861.
- [104] L. Kihlberg, *Arkiv Kemi* **1963**, 21, 365.
- [105] R. Guerin, M. Sergent, J. Prigent, *Matt. Res. Bull.* **1975**, 10, 957.
- [106] R. Rühl, W. Jeitschko, *Monatshefte für Chemie* **1983**, 114, 817.
- [107] R. D. Blaugher, J. K. Hulm, P. N. Yocom,  
*J. Phys. Chem. Solids* **1965**, 26, 2037.
- [108] F. A. Cotton, G. Wilkinson, *Adv. Inorganic Chemistry*, New York, **1980**.
- [109] W. L. Hill, G. Faust, S. B. Hendricks, *J. Am. Chem. Soc.* **1943**, 65, 794.
- [110] J. R. van Wazer, *Phosphorus and its compounds*, Interscience, New York, **1988**.

- [111] B. D. Sharma, *Inorg. Chem.* **1987**, 26, 454.
- [112] M. Jansen, M. Möbs, *Inorg. Chem.* **1984**, 23, 4486.
- [113] M. Jansen, M. Voss, *Angew. Chem.* **1981**, 93, 120.
- [114] K. H. Jost, *Acta, Crystallogr.* **1966**, 21, 34.
- [115] K. H. Jost, *Acta, Crystallogr.* **1964**, 17, 1593.
- [116] G. Krabbes, U. Gerlach, E. Wolf, W. Reichelt, H. Oppermann, J. C. Launay, Proc 6th Symposium on *Material Science under Microgravity Conditions*, Bordeaux, **1986**.
- [117] D. Vogt, *Staatsexamensarbeit (in german)*, Bonn University, Germany **2006**.
- [118] W. Grünert, E. S. Shapiro, R. Feldhaus, K. Anders, G. V. Antoshin, Kh. M. Minachev, *J. Catal.* **1987**, 107, 522.
- [119] C. Sanchez, J. Livage, J. P. Launay, M. Fournier, Y. Jeannin, *J. Am. Chem. Soc.* **1982**, 104, 3194.
- [120] J. M. Fruchart, G. Herve, J. P. Launay, R. Massart, *J. Inorg. Nucl. Chem.* **1976**, 38, 127.
- [121] H. Schäfer, T. Grofe, M. Trenkel, *J. Solid State Chem.* **1973**, 8, 14.
- [122] Bruker **2007**, *Bruker APEX2 2009/2, Bruker SAINT 2009/2*, Bruker AXS Inc., Madison Wisconsin, USA.
- [123] G. M. Sheldrick, “*SHELX-97 (Includes SHELXS97, SHELXL97, CIFTAB) Programs for Crystal Structure Analysis (Release 97-2)*”, University of Göttingen, Germany **1998**.
- [124] L. J. Farrugia, *J. Appl. Cryst.* **1990**, 32, 837.
- [125] C. Schlenker, J. Dumas, M. Greenblatt, S. V. Smaalen, *Physics and chemistry of low-dimensional inorganic conductors, vol 354 of NATO A. S. I. Series B: Physics*, Plenum, NY, **1996**.
- [126] E. M. Levin, R. S. Roth, *J. Solid State Chem.* **1970**, 2, 250.
- [127] J. M. Longo, J. W. Pierce, J. A. Kafalas, *Mater. Res. Bull.* **1971**, 6, 1157.
- [128] H. Putz, K. Brandenburg, *Diamond-Crystal and molecular structure visualization, Crystal Impact*, Bonn, Germany, <http://www.crystalimpact.com/diamond>.
- [129] A. Weiss, H. Witte, *Magnetochemie*, Verlag Chemie, Weinheim, Germany, **1973**.
- [130] H. Lueken, *Magnetochemie*, Verlag Chemie, Weinheim, Germany, **1973**.
- [131] Z. S. Teweldemedhin, K. V. Ramanujachary, M. Greenblatt, *J. Solid State Chem.* **1991**, 95, 21.

- [132] T. Dross, *Ph. D. Thesis*, University of Giessen, Germany **2004**.
- [133] E. Benser, *Ph. D. Thesis*, Bonn University, Germany **2007**.
- [134] R. J. Cava, D. J. Kleinman, S. M. Zahurak, *Mat. Res. Bull.* **1983**, *18*, 869.
- [135] T. Ekström, R. J. D. Tilley, *J. Solid State Chem.* **1976**, *16*, 141.
- [136] P. Schmidt, *Habilitationsschrift*, TU Dresden,  
<http://nbn-resolving.de/urn:nbn:de:bsz:14-ds-1200397971615-40549>, **2007**.
- [137] C. Schmitt, L. Giebeler, R. Schierholz, S. Endres, C. Fasel, H. Vogel, H. Fuess, *Z. Phys. Chem.* **2007**, *221*, 1525.
- [138] A. Raminosona, E. Bordes, P. Courtine, *J. Solid State Chem.* **1987**, *68*, 1.
- [139] J. M. Longo, P. Kierkegaard, *Acta Chem. Scand.* **1966**, *20*, 72.
- [140] A. Leclaire, M. M. Borel, B. Raveau, *Z. Kristallogr.* **1997**, *212*, 837 .
- [141] A. Leclaire, H. Chahboun, D. Groult, B. Raveau, *Z. Kristallogr.* **1986**, *177*, 277 .
- [142] J. L. Hodeau, M. Gondrand, M. Labeau, J. C. Joubert, *Acta Crystallogr.* **1978**, *B34*, 3543.
- [143] S. Mondet, A. Rimsky, J. Borene, W. Freundlich, *Comptes Rendus Hebdomadaires des Seances de l'Academie des Sciences C, Sciences Chimiques* **1968**, *266*, 1145.
- [144] S. Mondet, *Comptes Rendus Hebdomadaires des Seances de l'Academie des Sciences C, Sciences Chimiques* **1968**, *267*, 1689.
- [145] M. Israelsson, L. Kihlberg, *Arkiv Kemi* **1969**, *30*, 129.
- [146] M. Israelsson, L. Kihlberg, *J. Solid State Chem.* **1970**, *1*, 469.
- [147] G. Heurung, R. Gruehn, *Z. Anorg. Allg. Chem.* **1984**, *513*, 175.
- [148] R. Glaum, R. Gruehn, *Z. Kristallogr.* **1989**, *186*, 91.
- [149] K. K. Palkina, S. I. Maksimova, N. T. Chibiskova, K. Schlesinger, G. Ladwig, *Z. Anorg. Allg. Chem.* **1985**, *529*, 89.
- [150] N. Middlemiss, F. C. Hawthorne, C. Calvo, *Canad. J. Chem.* **1977**, *55*, 1673.
- [151] S. A. Linde, Yu. E. Gorbunova, A. V. Lavrov, *Russian J. Inorg. Chem.* **1983**, *28*, 29.
- [152] J. W. Johnson, D. C. Johnston, H. E. King Jr., T. R. Halbert, J. F. Brody, D. P. Goshorn, *Inorg. Chem.* **1988**, *27*, 1646.
- [153] G. Rouse, C. Wurm, M. Morcrette, C. J. Rodriguez, J. Gaubicher, C. Masquelier, *Int. J. Inorg. Mater.* **2001**, *3*, 881.
- [154] Yu. E. Gorbunova, S. A. Linde, *Doklady Akademii Nauk SSSR* **1979**, *245*, 584.

- [155] P. T. Nguyen, R. D. Hoffman, A. W. Sleight, *Mater. Res. Bull.* **1995**, *30*, 1055.
- [156] S. N. Achary, S. J. Patwe, A. K. Tyagi, *J. Alloys Compd.* **2008**, *461*, 474.
- [157] V. V. Krasnikov, Z. A. Konstant, *Izvestiya Akademii Nauk SSSR, Neorganicheskie Materialy* **1979**, *15*, 2164.
- [158] S.-C. Yin, H. Grondey, P. Strobel, M. Anne, L. F. Nazar, *J. Am. Chem. Soc.* **2003**, *125*, 10402.
- [159] M. Tachez, F. R. Theobald, E. Bordes, *J. Solid State Chem.* **1981**, *40*, 280.
- [160] B. Jordan, C. Calvo, *Canad. J. Chem.* **1973**, *51*, 2621.
- [161] R. Gopal, C. Calvo, *J. Solid State Chem.* **1972**, *5*, 432.
- [162] R. L. Harlow, Z. G. Li, N. Herron, H. S. Horowitz, E. M. McCarron, J. W. Richardson. Jr., B. H. Toby *ICSD no. 415213*, **2005**.
- [163] F. Girgsdies, M. Schneider, A. Brueckner, T. Ressler, R. Schlögl, *Solid State Sci.* **2009**, *11*, 1258.
- [164] F. Girgsdies, W.-S. Dong, J. K. Bartley, F. J. Hutchings, R. Schlögl, T. Ressler, *Solid State Sci.* **2006**, *8*, 807.
- [165] P. Amoros, M. D. Marcos, M. Roca, J. Alamo, A. B.-Porter, D. B.-Porter, *J. Phys. Chem. Solids* **2001**, *62*, 1393.
- [166] H. Wibbeke, RWTH Aachen, Hüls AG, Marl, Germany, **1985**, ICSD entry: 370809.
- [167] E. V. Murashova, N. N. Chudinova, *Kristallografiya* **1994**, *39*, 145.
- [168] K. C. Patil, S. T. Aruna, S. Ekambaram, *Current Opinion Sol. St. Mat. Sci.* **1997**, *2*, 158.
- [169] J. J. Moore, H. J. Feng, *Prog. Mater. Sci.* **1995**, *39*, 243.
- [170] J. J. Moore, H. J. Feng, *Prog. Mater. Sci.* **1995**, *39*, 275.
- [171] V. Zubkov, Inst. of Solid State Chemistry, Ekaterinburg, Russia, ICDD Grant-in-Aid **1998**, Powder Diffraction File-2.
- [172] N. Middlemiss, C. Calvo, *Acta Crystallogr.* **1976**, *B32*, 2896.
- [173] H. R. Tietze, *Aus. J. Chem.* **1981**, *34*, 2035.
- [174] K. Meisel, *Z. Anorg. Allg. Chem.* **1932**, *207*, 121.
- [175] St. Fechter, S. Krüger, H. Oppermann, *Z. Anorg. Allg. Chem.* **1993**, *619*, 424.
- [176] W. Brückner, U. Gerlach, H. P. Brückner, W. Moldenhauer, H. Oppermann, *Phys. Status Solidi* **1977**, *42a*, 295.
- [177] Z. Otwinowski, W. Minor, *Methods in Enzymology A* **1997**, *276*, 307; C. W. Carter Jr., R. M. Sweet, Eds., p-307, Academic Press (New York).



- [178] L. Beneš, K. Melánová, J. Svoboda, V. Zima, *J. Incl. Phenom. Macrocycl. Chem.* **2012**, *73*, 33.
- [179] T. Lunkenbein, F. Girgsdies, A. Wernbacher, J. Noack, G. Auffermann, A. Yasuhara, A. K.-Hoffmann, W. Ueda, M. Eichelbaum, A. Trunschke, R. Schlögl, M. G. Willinger, *Angew. Chem. Int. Ed.* **2015**, *54*, 1.
- [180] V. Luca, D. J. MacLachlan, R. Bramley, *Phys. Chem. Chem. Phys.* **1999**, *1*, 2597.
- [181] G. Martini, M. F. Ottaviani, G. L. Seravalli, *J. Phys. Chem.* **1975**, *79*, 1716.
- [182] A. Bencini, D. Gatteschi, *EPR of Exchange Coupled Systems*, Springer, Berlin, **1990**.
- [183] T. Rojo, J. L. Mesa, M. I. Arriotua, J. M. Savariault, J. Galy, G. Villeneuve, D. Beltrán, *Inorg. Chem.* **1988**, *27*, 3904.
- [184] G. A. Sawatzky, D. Post, *Phys. Rev.* **1979**, *B20*, 1546.
- [185] E. Hryha, E. Rutqvist, L. Nyborg, *Surf. Interface Anal.* **2012**, *44*, 1022.
- [186] J. Mendialdua, R. Casanova, Y. Barbaux, *J. Electron Spectrosc. Relat. Phenom.* **1995**, *71*, 249.
- [187] M. G. Willinger, D. S. Su, R. Schlögl, *Phys. Rev.* **2005**, *B71*, 155118.
- [188] A. B. P. Lever, *Inorganic Electronic Spectroscopy*, Elsevier, Amsterdam, 2nd Ed. **1984**.
- [189] B. N. Figgis, M. A. Hitchman, *Ligand Field Theory and Its Applications*, Wiley-VCH, New York, **2000**.
- [190] R. Glaum, K. Wittich, D. Abdulin, O. Schiemann, A. Karpov, K. Dobner, F. Rosowski, *Z. Anorg. Allg. Chem.* **2015**, in preparation.
- [191] M. B. Robin, P. Day, *Adv. Inorg. Chem. Radiochem.* **1968**, *10*, 247.
- [192] F. R. Landsberger, P. J. Bray, *J. Chem. Phys.* **1970**, *53*, 2757.
- [193] R. H. Caley, M. Krishna Murthy, *J. Amer. Ceram. Soc.* **1970**, *53*, 254.
- [194] M. Eichelbaum, M. Hävecker, C. Heine, A. Karpov, C.-K. Dobner, F. Rosowski, A. Trunschke, R. Schlögl, *Angew. Chem.* **2012**, *124*, 6350.
- [195] F. B. Abdelouahab, R. Olier, N. Guilhaume, F. Lefebvre, J. C. Volta, *J. Cat.* **1992**, *134*, 151.
- [196] S. Ganapathy, R. G. Bryant, *J. Magn. Reson.* **1986**, *70*, 149.
- [197] S. C. Roy, R. Glaum, D. Abdullin, O. Schiemann, N. Q. Bac, K.-H. Lii, *Z. Anorg. Allg. Chem.* **2014**, *640*, 1876.
- [198] E. Gebert, R. J. Ackermann, *Inorg. Chem.* **1966**, *5*, 136.

- [199] I. M. Watson, M. M. Borel, J. Chardon, A. Leclaire, *J. Solid State Chem.* **1994**, *111*, 253.
- [200] P. Kierkegaard, *Arkiv Kemi* **1961**, *18*, 521.
- [201] P. Kierkegaard, *Arkiv Kemi* **1962**, *19*, 1.
- [202] S. E. Lister, V. J. Rixom, J. S. O. Evans, *Chem. Mater.* **2010**, *22*, 5279.
- [203] P. Kierkegaard, J. M. Longo, *Acta Chem. Scand.* **1970**, *24*, 427.
- [204] M. Lenz, *Ph. D. Thesis*, University of Giessen, Germany **1995**.
- [205] G. Costentin, A. Leclaire, M. M. Borel, A. Grandin, B. Raveau, *Z. Kristallogr.* **1992**, *201*, 53.
- [206] S. E. Lister, I. R. Evans, J. S. O. Evans, *Inorg. Chem.* **2009**, *48*, 9271.
- [207] A. Leclaire, M. M. Borel, A. Grandin, B. Raveau, *Eur. J. Solid State Inorg. Chem.* **1988**, *25*, 323.
- [208] Y.-T. Hu, P. K. Davis, *J. Solid State Chem.* **1993**, *105*, 489.
- [209] T. Ekström, R. J. D. Tilley, *J. Solid State Chem.* **1976**, *19*, 125.
- [210] J. Galy, F. Duc, G. Svensson, P. Baules, P. Rozier, P. Millet, *Solid State Sci.* **2005**, *7*, 726.
- [211] H. A. Eick, L. Kihlborg, *Acta Chimica Scand.* **1966**, *20*, 722.
- [212] F. Duc, S. Gonthier, M. Brunelli, J. C. Trombe, *J. Solid State Chem.* **2006**, *179*, 3591.
- [213] R. H. Jarman, P.G. Dickens, *Mat. Res. Bull.* **1982**, *17*, 325.
- [214] H. A. Eick, L. Kihlborg, *Acta Chem. Scand.* **1966**, *20*, 1658.
- [215] P. Pailleret, *Revue de Chimie Minerale* **1970**, *7*, 807.
- [216] L. Kihlborg, *Acta Chem. Scand.* **1967**, *21*, 2495.
- [217] F. Haaß, A. H. Adams, T. Buhrmester, G. Schimanke, M. Martin, H. Fuess, *Phys. Chem. Chem. Phys.* **2003**, *5*, 4317.
- [218] L. Kihlborg, P. Torbo, E. Östlund, G. Bloom, G. Hagen, *Acta Chem. Scand.* **1967**, *21*, 2495.
- [219] C. Tenailleau, E. Suard, J. Rodriguez-Carvajal, A. Gibaud, P. Lacorre, *J. Solid State Chem.* **2003**, *174*, 431.
- [220] A. Mansingh, A. Dhawan, M. Sayer, *J. Non-Cryst. Solids* **1979**, *33*, 351.
- [221] S. Titlbach, *Ph.D. thesis*, Bonn University, Germany, **2014**.  
<http://hss.ulb.uni-bonn.de/2014/3642/3642.htm>.

- [222] S. A. Ennaciri, C. R'kha, P. Bardoux, J. Livage, *Eur. J. Solid State Inorg. Chem.* **1993**, *30*, 227.
- [223] J. S. O. Evans, T. A. Mary, A. W. Sleight, *J. Solid State Chem.* **1995**, *120*, 101.
- [224] M. Cetinkol, A. P. Wilkinson, P. L. Lee, *J. Solid State Chem.* **2009**, *182*, 1304.
- [225] A. Benmoussa, A. Leclaire, A. Grandin, B. Raveau, *Acta. Cryst.* **1989**, *C45*, 1277.
- [226] Y. Piffard, S. Oyetola, A. Verbaere, M. Tournoux, *J. Solid State Chem.* **1986**, *63*, 81.
- [227] S. T. Norberg, G. Svensson, J. Albertsson, *Acta Cryst.* **2001**, *C57*, 225.
- [228] J. A. Duffy, *Geochimica Cosmochimica Acta* **1993**, *57*, 3961.
- [229] H. Flood, T. Förland, *Acta Chem. Scand.* **1947**, *1*, 592.
- [230] H. Peters, H.-H. Möbius, *Verfahren zur Gasanalyse bei erhöhten Temperaturen mit Hilfe galvanischer Festelektrolytelemente* (in german), patent no. DD 21673, **1958**.
- [231] M. Blum, K. Teske, R. Glaum, *Z. Anorg. Allg. Chem.* **2003**, *629*, 1709.
- [232] I. V. Kozhevnikov, A. Sinnema, R. J. J. Jansen, H. van Bekkum, *Cat. Lett.* **1994**, *27*, 187.
- [233] J. P. Badaud, J. Omaly, *Comptes Rendus Hebdomadaires des Seances de l'Academie des Sciences, Serie C, Sciences Chimiques* **1974**, *278*, 521.
- [234] Stoe & Cie (2002). *X-AREA*, Stoe-**2010**, Stoe & Cie GmbH, Darmstadt, Germany.
- [235] Stoe & Cie (2002). *X-RED*, Stoe-**2010**, Stoe & Cie GmbH, Darmstadt, Germany.
- [236] P. A. Stadelmann, *JEMS - EMS Java ver.* **2004**.
- [237] R. F. Egerton, P. Li, M. Malac, *Micron* **2004**, *35*, 399.
- [238] P. Hartmann, J. Vogel, B. Schnabel, *J. Magn. Res.* **1994**, *111*, 110.
- [239] M. S. Islam, R. Glaum, A. Pelka, J. Daniels, W. Hoffbauer, *Z. Anorg. Allg. Chem.* **2013**, *639*, 2463.
- [240] K. Panagiotidis, R. Glaum, W. Hoffbauer, J. Weber, J. Schmedt auf der Günne, *Z. Anorg. Allg. Chem.* **2008**, *634*, 2922.
- [241] B. N. Figgis, M. A. Hitchman, *Ligand field Theory and Its Applications*, Wiley-VCH, NY, **2000**.
- [242] B. N. Figgis, J. Lewis, F. Mabbs, *J. Chem. Soc.* **1960**, 2480.
- [243] A. K. Gregson, D. M. Doddrell, P. Healy, *Inorg. Chem.* **1978**, *17*, 1216.
- [244] R. Berger, J. Kliava, E. Yahiaoui, J. C. Bissey, P. K. Zinsou, P. Beziade, *J. Non-Cryst. Solids* **1995**, *180*, 151.

- [245] W. L. Khel, R. G. Hay, D. Wahl, *J. Appl. Phys.* **1952**, 23, 212.
- [246] E. Salje, K. Viswanathan, *Acta Crystallogr.* **1975**, A31, 356.
- [247] R. Diehl, G. Brandt, E. Salje, *Acta Crystallogr.* **1978**, B34, 1105.
- [248] P. M. Woodward, A. W. Sleight, T. Vogt, *J. Solid State Chem.* **1997**, 131, 9.
- [249] T. Vogt, P. M. Woodward, B. A. Hunter, *J. Solid State Chem.* **1999**, 144, 209.
- [250] B. Gerand, G. Nowogrocki, J. Guenot, M. Figlarz, *J. Solid State Chem.* **1979**, 29, 429.
- [251] B. Gerand, G. Nowogrocki, J. Guenot, M. Figlarz, *J. Solid State Chem.* **1981**, 38, 312.
- [252] L. S. Palatnik, O. A. Obol'yaninova, M. N. Naboka, N. T. Gladkikh, *Izvestiya Akademii Nauk SSSR*, **1973**, 9, 718.
- [253] C. Balázsi, M. F. Jahnke, I. Kostas, L. Petrás, J. Pfeifer, *Solid State Ionics* **2001**, 141, 411.
- [254] O. Yamaguchi, D. Tomihisa, H. Kawabata, K. Shimizu, *J. Am. Ceram. Soc.* **1987**, 70, C94.
- [255] A. R. Siedle, T. E. Wood, M. L. Brostrom, D. C. Koskenmaki, B. Montez, E. Oldfield, *J. Am. Chem. Soc.* **1989**, 111, 1665.
- [256] E. Gebart, R. J. Ackermann, *Inorg. Chem.* **1966**, 5, 136.
- [257] A. Magnéli, *Arkiv Kemi* **1949**, 1, 513.
- [258] M. Sundberg, *J. Solid State Chem.* **1980**, 35, 120.
- [259] R. Pickering, R. J. D. Tilley, *J. Solid State Chem.* **1976**, 16, 247.
- [260] J. Booth, T. Ekström, E. Iguchi, R. J. D. Tilley, *J. Solid State Chem.* **1982**, 41, 293.
- [261] A. Magnéli, *Arkiv Kemi* **1949**, 1, 223.
- [262] A. A. Bolzan, B. J. Kennedy, C. J. Howard, *Aust. J. Chem.* **1995**, 48, 1473.
- [263] E. Salje, *Acta Crystallogr.* **1977**, B33, 547.
- [264] S. Tanisaki, *J. Phys. Soc. Jpn.* **1960**, 15, 573.
- [265] M. Weber, *Beachlor Thesis*, Bonn University, **2014**.
- [266] A. Kelly, G. W. Groves, *Crystallography and Crystal defects*, Addison-Wesley, Reading, Mass. **1970**.
- [267] K. Nocker, R. Grünh, *Z. Anorg. Allg. Chem.* **1993**, 619, 1530.
- [268] H. Mathis, R. Glaum, R. Gruehn, *Acta Chem. Scand.* **1991**, 45, 781.
- [269] H. Schäfer, *J. Cryst. Growth* **1971**, 9, 17.
- [270] R. H. Blessing, *Acta Crystallogr.* **1995**, A51, 33.

- [271] N. Dietl, M. Schlangen, H. Schwarz, *Angew. Chem.* **2012**, *124*, 5638.
- [272] P. C. Pouchard, J. P. Chaminade, J. P. Doumerc, J. C. launay, P. Hagemuller, *Mat. Res. Bull.* **1972**, *7*, 223.
- [273] C. S. Dimbylow, I. J. McClolm, C. M. P. Barton, N. N. Greenwood, G. E. Turner, *J. Solid State Chem.* **1974**, *10*, 128.
- [274] I. J. McColm, C. M. P. Barton, N. N. Greenwood, R. J. D. Tilley, *J. Solid State Chem.* **1976**, *16*, 265.
- [275] R. Glaum, R. Gruehn, M. Möller, *Z. Anorg. Allg. Chem.* **1986**, *543*, 111.
- [276] J. M. Longo, P. Kierkegaard, *Acta Chem. Scand.* **1970**, *24*, 420.
- [277] Y. Oka, S. Sato, T. Yao, N. Yamamoto, Y. Ueda, A. Hayashi, *J. Solid State Chem.* **1998**, *141*, 594.
- [278] Y. Oka, S. Sato, T. Yao, N. Yamamoto, Y. Ueda, A. Hayashi, *J. Solid State Chem.* **1993**, *105*, 271.
- [279] Y. Wang, Z. Zang, Y. Zhu, Z. Li, R. Vijtai, L. Ci, M. P. Ajayan, *ACS Nano* **2008**, *2*, 1492.
- [280] Z. Gui, R. Fan, X. H. Chen, Y. C. Wu, *J. Solid State Chem.* **2001**, *157*, 250.
- [281] L. Liu, F. Cao, T. Yao, Y. Xu, M. Zhou, B. Qu, B. Pan, C. Wu, S. Wei, Y. Xie, *New J. Chem.* **2012**, *36*, 319.
- [282] W. Li, J. R. Dahn, D. S. Wainwright, *Science* **1994**, *264*, 1115.
- [283] C. Tsang, A. Manthiram, *J. Electrochem. Soc.* **1997**, *144*, 520.
- [284] Z. Gui, R. Fan, W. Q. Mo, X. H. Chen, L. Yang, S. Y. Zhang, S. Y. Hu, Z. Z. Wang, W. C. Fan, *Chem. Mater* **2002**, *14*, 5053.
- [285] K.-F. Zhang, S.-J. Bao, X. Liu, J. Shi, Z.-X. Su, H.-L. Li, *Mater. Res. Bull.* **2006**, *41*, 1985.
- [286] S. R. Popuri, M. Miclau, A. Artemenko, C. Labrugere, A. Villesuzanne, M. Pollet, *Inorg. Chem.* **2013**, *52*, 4780.
- [287] F. Theobald, R. Cabala, J. Bernard, *J. Solid State Chem.* **1976**, *17*, 431.
- [288] K.-A. Wilhelmi, K. Waltersson, *Acta Chem. Scand.* **1970**, *24*, 3409.
- [289] S. Yamazaki, Li Chang, K. Ohoyama, M. Nishi, M. Ichihara, H. Ueda, Y. Ueda, *J. Solid State Chem.* **2010**, *183*, 1496.
- [290] <http://infosee.ethz.ch/kilo/tabellen.html>.
- [291] I. Barin, O. Knacke, *Thermochemical Properties of Inorganic Substances*, Springer Verlag, Berlin, **1973**.

- [292] E. Bordes, *Catal. Today*, **1987**, *1*, 499.
- [293] M. Schöneborn, *Ph. D. Thesis*, Bonn University, Germany **2008**,  
<http://hss.ulb.uni-bonn.de/2008/1542/1542.htm>.
- [294] M. F. Peintinger, D. V. Oliveira, T. Bredow, *J. Compt. Chem.* **2013**, *34*, 451.
- [295] J. P. Perdew, K. Burke, M. Ernzerhof, *Phys. Rev. Lett.* **1997**, *78*, 1396.
- [296] M. G. Vincent, K. Yvon, J. Ashkenasi, *Acta. Crystallog.* **1980**, *A36*, 808.
- [297] Ch. Leroux, G. Nihoul, G. Van Tendeloo, *Phys. Rev.* **1998**, *B57*, 5111.
- [298] F. Theobald, *J. Less-Common Met.* **1977**, *53*, 55.
- [299] P. D. Dernier, *Mater. Res. Bull.* **1974**, *9*, 955.
- [300] M. Saupe, R. Födiche, A. Sundermann, S. A. Schunk, K. E. Finger,  
*QSAR Comb. Sci.* **2005**, *24*, 66.

The present research work has been carried out from June 2011 to July 2015 at the Institute of Inorganic Chemistry in Rheinischen Friedrich-Wilhelms-Universität Bonn under the supervision of Professor Dr. Robert Glaum.

It is my great pleasure to express my deepest gratitude and special appreciation to my Ph.D. supervisor **Professor Dr. Robert Glaum**. I am thankful to him for giving me the liberty to pursue the present research work. Without his motivation, genuine guidance, carefulness and continuous support it would not been possible to carry out this dissertation. I am very indebted to him for his scientific advices and insightful discussions. Professor Glaum is one of the perfectionist and smartest person I have ever met.

I am also thankful to the honorable members of my Ph.D. examination committee, Prof. Dr. Robert Glaum, Prof. Dr. Werner Mader, Prof. Dr. Thomas Bredow and Prof. Dr. Hartmut Schmieden.

I am grateful to Prof. Dr. Werner Mader and Dr. Wilfried Assenmacher for the electron diffraction and HRTEM measurements and interpretations.

It is my pleasure to thanks Prof. Thomas Bredow and his co-worker Daniel Vilela Olivera for the DFT calculation.

I express my gratitude to Prof. Dr. Olav Schiemann and his co-workers Dr. Yaser Nejaty Jahromy and Dinar Abdullin for EPR measurements and analyses.

I am thankful to Dr. Jörg Daniels, Dr. Gergor Schnakenburg and Charlotte Rödde for the x-ray single crystal data collections. My thanks also go to Volker Dittrich for the single crystal UV/Vis/NIR and powder reflectance measurements. A special thanks to Volker Bendisch for taking photographs of crystals. My thanks also go to Dr. Wilfried Hoffbauer and Branimir Raguž for the  $^{31}\text{P}$ -MAS-NMR, and Mr. Norbert Wagner for magnetic and electric conductivity measurements and Prof. Dr. Kwang-Hwa Lii and Nguyen Quang Bac, National Central University, Taiwan for XPS measurenents.

It is my great pleasure to be a part of this collaborative research project “HT4CAT” (**H**igh **T**hroughput **C**omputing for Prediction and Modelling of new Lead Structures for Selective Oxidation **C**atalysts) funded by BASF SE. I would like to extent my thanks to the project managers Dr. Cathrin Welker-Nieuwoudt (BASF. SE), Dr. Michael Göbel (BASF. SE), and Dr. Rute André (BASF. SE) as well as all the members Dr. Frank

Rosowski (BasCat), Dr. Raoul Naumann (BasCat), Prof. Dr. Geoffroy Hautier (UCL, Belgium), Dr. David Waroquiers (UCL, Belgium) Dr. Stephan Schenk (BASF, SE) of this project, not only for their scientific astute discussions but also for the pleasant project meetings.

I would like to take the opportunity to thank my M.Sc. supervisor Professor Dr. Altaf Hussain, Director of Centre for advanced research in sciences (CARS), University of Dhaka who inspired me in the field of Solid State Chemistry.

I also thank to my Bachelor students Markus Weber and Bryan Rosales for their involvement for some experiments during their stay in this laboratory.

It is my great pleasure to thank my former and current colleagues Dr. Muhammad Saiful Islam, Dr. Christian Litterscheid, Dr. Kosta Panagiotidis, Dr. Eva Hammer, Dr. Katharina Snyder, Dr. Sven Titlbach, Emma Mosymow, Rebecca Groher, Anna Bronova, Anke Schnabel, Halil Shaqiri, Knut Wittich, Jan-Peter Häbel, Thomas Linden, Andreas Schmitz, Sarah Kollek, Waldemar Grunwald, Dr. Frank Otto, Sylvia Lorraine Kunz, Lars Esser, Marie Stockhausen, Alex Karbstein, Nils Kannengiesser, Julius Schultz, and Prof. Dr. Aftab Ali Shaikh (University of Dhaka) for their cordial cooperation and to maintain a wonderful working atmosphere in this research group. I express my heartfelt thanks to all of my friends and well-wishers who inspired and helped me during this time.

I express my deepest and hearty thanks to my dearest parents, brothers, sisters and their families and relatives. Nothing would have been possible without their constant love, affection and support.



### Publications and Patent

1. "Synthesis and Crystal Structure of Metal(III) Tungsten(VI) Pyrophosphate Ortho-phosphates" Subrata Chandra Roy, Branimir Raguž, W. Assenmacher, Robert Glaum *Solid State Science*, **2015**, *49*, 18.
2. "Solid solution formation between vanadium(V) and tungsten(V) oxide phosphate" Subrata Chandra Roy, Robert Glaum, Dinar Abdullin, Olav Schiemann, Nguyen Quang Bac, Kwang-Hwa Lii, *Z. Anorg. Allg. Chem.* **2014**, *640*, 1876.
3. "Wolframphosphate der  $\text{ReO}_3$ -strukturfamilie", Cathrin Alexandra Welker-Nieuwoudt, Frank Rosowski, Michael Göbel, Robert Glaum, Subrata Chandra Roy, Geoffroy Hautier, David Waroquiers, Raoul Naumann D'Alnoncourt, Verena Stempel, , Stephanie Linke, Patentanmeldung durch BASF SE, July **2015** (0000078320EP01).
4. "Chemical modification of tungsten(V) oxide phosphates" Subrata Chandra Roy, Robert Glaum (in preparation).
5. "Synthesis and characterization of niobium-doped potassium tetragonal tungsten bronzes,  $\text{K}_x\text{Nb}_y\text{W}_{1-y}\text{O}_3$ " Tapas Debnath, Subrata Chandra Roy, Claus H. Rücher, Altaf Hussain, *J. Mater. Sci.* **2009**, *44*, 179.

### Presentation (oral)

1. Phase formation in quasi-binary system  $\text{W}^{\text{V}}\text{OPO}_4$ - $\text{V}^{\text{V}}\text{OPO}_4$  Subrata Chandra Roy, Robert Glaum, Bangladesh Crystallographic Association, 10 Jan. **2015**, Dhaka, Bangladesh.
2. Solid solution  $\text{W}^{\text{V}}\text{OPO}_4$ - $\text{V}^{\text{V}}\text{OPO}_4$ ? Subrata Chandra Roy, Institute of Inorganic Chemistry, Bonn University, Germany, 07 Nov. **2013**

### Presentation (poster)

1. "Solid solutions in quasi-binary system  $\text{V}^{\text{V}}\text{OPO}_4$ - $\text{Mo}^{\text{V}}\text{OPO}_4$ " Subrata Chandra Roy, Sarah Kollek, Robert Glaum, European Conference of Solid State Chemistry (ECSSC-XV), 23-26 August, **2015**, P197, Vienna, Austria.

2. “Syntheses, crystal structures and redox reactions in the quasi-binary system  $W^V OPO_4$ - $V^V OPO_4$ ” Subrata Chandra Roy, Robert Glaum, European Conference of Solid State Chemistry (ECSSC-XIV), 07-10 July, **2013**, P85, Bordeaux, France.
  
3. “Characterization of Niobium Substituted Potassium Tetragonal Tungsten Bronzes” Subrata Chandra Roy, Altaf Hussain, Asian Crystallographic Association of Japan/Crystallographic Society of Japan (AsCA/CrSJ’06), 20-23 Nov. **2006**, P224, Epochal Tsukuba, Japan.